NASA-CR-121234

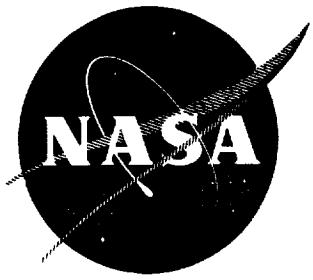

FINAL REPORT

INVESTIGATION OF GASEOUS PROPELLANT COMBUSTION AND ASSOCIATED INJECTOR/CHAMBER DESIGN GUIDELINES

by

D. F. Calhoon, J. I. Ito, and D. L. Kors

Aerojet Liquid Rocket Company
Sacramento, California 95813

prepared for

NATIONAL AERONAUTICS AND SPACE ADMINISTRATION

NASA Lewis Research Center
Contract NAS 3-14379
L. H. Gordon, Project Manager

1. Report No.	2. Government Accession No.	3. Recipient's Catalog No.
NASA CR-121234		

4. Title and Subtitle	5. Report Date
Investigation of Gaseous Propellant Combustion and Associated Injector/Chamber Design Guidelines	31 July 1973
	6. Performing Organization Code
7. Author(s)	8. Performing Organization Report No.
D. F. Calhoon, J. I. Ito and D. L. Kors	
	10. Work Unit No.
9. Performing Organization Name and Address	
Aerojet Liquid Rocket Company P. O. Box 13222 Sacramento, California 95813	11. Contract or Grant No. NAS 3-14379
	13. Type of Report and Period Covered
12. Sponsoring Agency Name and Address	Contractor Report
National Aeronautics and Space Administration Washington, D. C. 20546	14. Sponsoring Agency Code

15. Supplementary Notes

Project Manager, Larry H. Gordon
NASA Lewis Research Center, Cleveland, Ohio 44135

16. Abstract

Injector design criteria are provided for gaseous hydrogen-gaseous oxygen propellants. Design equations and procedures are presented which will allow an injector-chamber designer to a priori estimate the performance, compatibility & stability characteristics of prototype injectors. The data for these design criteria was obtained in a program which was structured to investigate the cold flow mixing characteristics of various element types and to determine how combustion influenced the mixing process. Experimental cold flow tests was conducted wherein the flow field downstream of prototype injection elements was sampled for mass and composition distributions. The effects of chamber length, element geometry, thrust per element, mixture ratio, impingement angle, and element spacing were evaluated for four element concepts and their derivatives. The data from this series of tests were reduced to a single valued mixing function that describes the mixing potential of the various elements. Limited sampling of a combustion flow field revealed that combustion effects impeded the mixing rate observed during cold flow tests. Single element hot-fire tests were conducted with four injector concepts. Performance, heat transfer and stability data were generated for various mixture ratios, propellant temperatures, chamber pressures, contraction ratios, and chamber lengths. A similar series of tests was conducted using full scale hardware. The test data was used to develop two design models; one analytical and the other empirical. Application of these models resulted in the design procedures described in the Handbook for Design of Gaseous Propellant Injectors, which is included as the last section of this report. This handbook includes techniques whereby the performance and chamber heat flux can be calculated directly, and the injector stability estimated in conjunction with existing models.

17. Key Words (Suggested by Author(s))	18. Distribution Statement
Injector Design; Combustion; Chamber Heat Flux; Turbulent Mixing Analysis; Gaseous Propellants; Stability	Unclassified - Unlimited

19. Security Classif. (of this report)	20. Security Classif. (of this page)	21. No. of Pages	22. Price*
Unclassified	Unclassified	302	

* For sale by the National Technical Information Service, Springfield, Virginia 22151

FOREWORD

This report was prepared for the NASA Lewis Research Center (LeRC) under Contract NAS 3-14379, by Aerojet Liquid Rocket Company (ALRC), Sacramento, California. The NASA Program Manager for this study was Mr. Larry H. Gordon. The study was performed during the period July 1971 to March 1973.

The ALRC Project Manager for this study was Mr. David L. Kors, Analytical Design Section, Design and Analysis Department. Mr. David F. Calhoon was principal investigator responsible for the daily program management. Mr. Jackson I. Ito was principal analyst and developed the analytical models that characterize the general combustion process.

In addition to the authors, many persons contributed significantly to this study effort, for which we are grateful. Mr. J. W. Salmon created and implemented the data management procedures used to handle the cold and hot flow data. Mr. D. M. Jassowski and his Aerophysics Laboratory personnel created and synthesized most of the equipment and procedures used to conduct the cold and hot flow testing. Mr. D. C. Rousar was responsible for all the single element and full scale heat transfer analysis. Mr. R. S. Gross and J. W. Holiday conducted the single element and full scale testing in the Physics Laboratory. Mr. J. L. Pieper was responsible for analyzing the performance of both the single element and full scale testing.

TABLE OF CONTENTS

		Page
I.	Summary	1
II.	Introduction	4
III.	Injector Design and Analysis	6
	A. Concept Screening	6
	B. Element Evaluation	9
	1. Shear Mixing Elements	9
	2. Momentum Mixing Elements	10
	C. Film vs Barrier Cooling Analysis	11
	D. Stability Considerations	12
	E. Element Selection	13
	F. Cold Flow Hardware Design	13
	1. Single Element Injector-Chamber	13
	2. Multiple Element Injector-Chamber	14
	3. Sampling Rake and Rake Assembly	14
IV.	Cold Flow Modeling	26
	A. Single Element Cold Flow	26
	B. Multiple Element Cold Flow	40
V.	Hot Flow Modeling	60
VI.	Single Element Injector Evaluation	64
	A. Test Articles	64
	B. Test Facility and Procedures	64
	C. Single Element Test Results	65
	1. Performance	65
	2. Heat Transfer	73
	3. Single Element Stability	77

TABLE OF CONTENTS (cont.)

		Page
VII.	Full Scale Injector Evaluation	94
	A. Description of Test Articles	94
	1. Injectors	94
	2. Chambers	97
	B. Test Facilities and Procedures	98
	C. Full Scale Test Results	98
	1. Performance	103
	2. Heat Transfer	111
	3. Stability	117
VIII.	Data Evaluation	141
	A. Introduction - Methods of Approach	141
	B. Discussion of Results - Empirical Approach	142
	1. Cold Flow Data and Correlations	142
	2. The Relationship Between Combustion Efficiency and E_m	148
	3. Discussion of Combustion Influences	149
	4. Empirical Heat Transfer Correlations	152
	5. Empirical Model ERE Prediction	153
	C. Discussion of Results - Analytical Approach	154
	1. Introduction	154
	2. Description of Generalized Analytical Model	156
	3. Analytical Data Correlation	161
	4. Generalized Chamber Wall Heat Flux Correlation	163
IX.	Conclusions	181

TABLE OF CONTENTS (cont.)

		Page
	APPENDICES	
Appendix A.	Analytical Mixing Model Description	182
Appendix B.	Cold Flow Test and Data Reduction Procedures	215
Appendix C.	Performance Evaluation Techniques	222
Appendix D.	Heat Transfer Evaluation Techniques	226
Appendix E.	Symbols and Abbreviations	229
Appendix F.	Distribution	234
References		244

LIST OF TABLES

Table		Page
I	Gas/Gas Injector Element Types and Derivatives	7
II	Element Concept Rating Chart	8
III	Single Element Cold Flow Test Summary	27
IV	Summary of Design and Operating Effects on Mixing Efficiency	36
V	Gas/Gas Multiple Element Cold Flow Data Summary	41
VI	Multiple Shear Co-Ax Element Cold Flow Summary Based on Recirculated Downstream Gases	43
VII	Single Element Hot Fire Test Series Performance Summary in English Units	66
VIII	Single Element Hot Fire Test Series Performance Summary in S.I. Units	68
IX	Stability Data for Single Element Injectors	70
X	Test Data for Deep Cup Premix, Triplet, -1 Zoned, and -2 Zoned Injectors	99
XI	Test Data for Deep Cup Premix, Triplet, -1 Zoned, and -2 Zoned Injectors	101
XII	Multi-Element Hot Fire Test Series Performance Summary in English Units	104
XIII	Multi-Element Hot Fire Test Series Performance Summary in S.I. Units	107
XIV	Injector Face Temperature	115
XV	Gas/Gas Injector Stability Data, Deep Cut Premix Injector and Triplet Injector	118
XVI	Comparison of Emperical Performance Prediction to Measured Data	155

LIST OF FIGURES

Figure		Page
1	Gaseous Injector Performance	16
2	Effect of Momentum Ratio on Premix Impinging Element Mixing Efficiency	17
3	Results of Barrier Cooling Analysis	18
4	Vacuum I_{sp} Loss for a Barrier Cooled Design	19
5	4,448 N (1000 lbf) Thrust H_2/O_2 Stability Map	20
6	Element Types Selected for Cold Flow Evaluation	21
7	Single Element Cold Flow Assembly	22
8	Single Element Cold Flow Designs	23
9	Multiple Element Cold Flow Assembly	24
10	Sampling Rake	25
11	Effect of Design Parameters on E_m	44
12	Coaxial Mixing Efficiency	45
13	The Effect of Thrust/Element on Mixing Efficiency of Shear Mixing Elements	46
14	The Effect of Oxidizer Swirl on Mixing Efficiency	47
15	Compatability Characteristics of Shear Mixing Elements	48
16	The Effect of Length on Mixing Efficiency for Premix Elements	49
17	The Parametric Influence of Various Design Variable on the Mixing Efficiency on Premix Triplet and Pentad Elements	50
18	Compatability Characteristics of Premix Elements	51
19	Doublet Element Mixing Efficiency	52
20	Compatability of a Like Doublet	53
21	Parallel Sheet Element Mixing Efficiency for Various Test Conditions	54
22	Compatability of Parallel Sheet Element	55
23	F-O-F Triplet Mixing Efficiencies as a Function of Test Conditions	56

LIST OF FIGURES (cont.)

Figure		Page
24	Triplet Element Compatability Characteristics	57
25	The Comparison of Multiple Element to Single Element Mixing Efficiency	58
26	The Comparison of Multiple Element to Single Element Mixing Efficiency	59
27	The Comparison of Hot and Cold Mixture Ratio Profiles for a Swirl Coaxial Element	62
28	Schematic of Swirl Element Combustion Process	63
29	Hot Fire Single Element Design Parameters	79
30	Single Element Thrust Chamber	80
31	Single Element Test Bay Schematic	81
32	Single Element Performance	82
33	Single Element Triplet Performance	83
34	Effect of Chamber Variables on Single Element Performance	84
35	The Effect of Tp and P_c on ERE	85
36	Single Element Heat Transfer Characteristics for Various Elements	86
37	Coaxial Element Heat Flux in Various Chambers	87
38	Swirl Coaxial Element (V_t/V_a = 0.5) Heat Transfer Characteristics	88
39	Swirl Coaxial Element (V_t/V_a = 1.0) Heat Transfer Characteristics	89
40	Premix Element Heat Transfer Characteristics in Various Chambers	90
41	Triplet Element Heat Transfer Characteristics	91
42	Triplet Axial and Circumferential Heat Flux Distribution for O/F = 4 and Chamber Pressure = 205 N/cm^2 (300 psia)	92
43	Low Frequency Stability Characteristics of Gaseous Injector Element	93
44	Deep Cup Premix Element Schematic	120

LIST OF FIGURES (cont.)

Figure		Page
45	Premix Injector	121
46	Triplet Injector	122
47	Zoned Injector	123
48	Barrier Injector Characteristics	124
49	Full Scale Chambers	125
50	Full Scale Test Hardware and Assembly	126
51	Effects of Mixture Ratio and Chamber Pressure on Full Scale Performance	127
52	Effect of Chamber Geometry on Full Scale Performance	128
53	The Effect of Mixing Parameter on Triplet Element Performance	129
54	Heat Flux for the Full Scale Injectors	130
55	Premix - Chamber Heat Flux Data (-1 Chamber)	131
56	Premix Chamber Heat Flux Using L = 7.6 cm (3.0-in.) Chambers	132
57	Premix Chamber Heat Flux for -1 + L* Chambers	133
58	Triplet Chamber Heat Flux in the CR 3.4, 7.6L Chamber	134
59	Triplet Chamber Heat Flux Using L = 7.6 cm (3.0-in.) Chamber	135
60	Triplet Chamber Heat Flux for -1 + L* Chamber	136
61	Zone -1 Triplet Chamber Heat Flux	137
62	Zone -2 Triplet Chamber Heat Flux	138
63	Throat Heat Transfer Characteristics	139
64	Test System Parameters Applicable to Stability Analysis	140
65	Coaxial and Increased Shear Coaxial Design Correlations	164
66	Swirler Design Correlations	165
67	Premix Elements Design Correlations	166
68	Triplet Element Design Correlations	167
69	Like Doublet Design Correlations	168
70	The Relationship Between $H_2/O_2, \eta_c$ and E_m	169

LIST OF FIGURES (cont.)

Figure		Page
71	Analytical Relationship Between Cold and Hot Fire Lengths	170
72	Relationship Between Chamber Length and Cold Flow Mixing Length	171
73	Chamber Heat Flux Characteristics of Gaseous Injector Elements	172
74	Predicted vs Measured Energy Release Efficiency	173
75	Generalized Mixing Correlation Chart	174
76	Combustion Influence Parameter vs Mixture Ratio GO_2/GH_2	175
77	Correlation of Analytical Model with Single Element Cold Flow Data - Coaxial and Triplet	176
78	Correlation of Analytical Model with Single Element Data - Swirl, Doublet and Premix	177
79	Correlation of Analytical Model with Single Element Combustion Data	178
80	Correlation Between Predicted and Measured Heat Flux	179
81	Correlation Between Predicted and Measured Heat Flux - Triplet	180
82	Schematic Velocity Decay Profile for Shear Mixing	208
83	The Effect of Boundary Layer Potential Flow Ratio upon the Dynamic Head Ratio	209
84	Local Dynamic Head Ratio for Fully Developed Boundary Layer Flow	210
85	Experimental Relationship Between Pressure Decay and Mass Diffusion	211
86	Dynamic Head Decay	212
87	Mole Fraction Decay	213
88	Analytical Correlation of Experimental Data	214
89	Cold Flow Facility	220
90	Data Acquisition - Reduction - Analysis System	221

I. SUMMARY

The broad objective of this program was to investigate injection, mixing and combustion processes using gaseous propellants over a range of operating conditions originally specified for the Space Shuttle Auxiliary Propulsion System. The end objective was to relate injector and chamber design parameters to combustion performance, chamber heat flux and combustion stability in the form of a step-by-step design handbook applicable to any selected operating condition or gaseous propellant combination.

The scope of the program was to include analysis, design, fabrication, and experimental tasks to develop the injector/chamber design criteria. The principal efforts in this program were to be devoted to evaluating various injector element configurations on the basis of single element cold flow and hot fire testing. Based on this evaluation and multiple element cold flow tests, full scale injectors were to be designed, fabricated and tested to verify the design criteria for high performance, low heat flux to the thrust chamber, and stability. The program was divided into five tasks: Task I - Injector Design Analysis, Task II - Cold Flow and Hot Flow Modeling, Task III - Single Element Hot Firing Evaluation, Task IV - Full Scale Injector Evaluation and Task V - Data Evaluation.

Task I was a concept screening and element evaluation effort which culminated in the selection of four element types for single element cold flow evaluation. The element concepts selected were: (1) the shear coaxial element, (2) the premix element, (3) the external impingement element and (4) elements for micro-orifice injectors. Each element concept included design geometry variations so that a total of 74 unique element designs were selected for detail design during this task. In addition, an analytical study was conducted to evaluate the effect on chamber heat flux and performance of a low mixture ratio barrier at the outer edge of the injector. The results of this analysis revealed that chamber heat flux could be lowered considerably by a low mixture ratio barrier, but that the performance penalty would be higher than if fuel film cooling were used to achieve the same chamber heat flux and wall temperature.

Task II was concerned with the fabrication, cold flow testing and analysis of both the single elements and multiple elements designed during Task I. The testing consisted of sampling the flow field in the chamber with a multi-element probe which was sequenced to measure both local total pressure (mass flux) and composition. From these measurements a mixing efficiency could be determined at any axial position in the chamber, and radial and circumferential gradients were evaluated to obtain chamber compatibility data. An evaluation of this data led to the following conclusions:

1. The shear coaxial element is a relatively low mixing rate concept but results in a fuel-rich composition at the outer wall.

2. Premix and external impingement elements are high mixing rate concepts. Nominal mixture ratio composition at the outer wall is characteristic of the premix concept, and the external impingement element when the optimum injection momentum ratio is selected.

3. Multi-element cold flow mixing efficiency was not noticeably different from comparable single element mixing efficiency.

In addition to the cold flow evaluations, limited combustion testing was conducted using the same measurement techniques. These experiments were conducted with the swirl coaxial element and conclusively demonstrated that combustion retards the mixing rate.

Task III involved design, fabrication and testing of single element thrusters to obtain combustion performance, chamber wall heat flux and stability data to compare with the cold flow data obtained during Task II. A total of 76 tests were conducted with 7 injector element designs which represented variations of the following element concepts: (1) premix, (2) triplet, (3) coaxial and (4) swirl coaxial. All of these injectors were evaluated with 3 different chamber geometries to permit evaluation of chamber length and contraction ratio changes. The results of this single element evaluation corresponded qualitatively with the Task II single element cold flow testing in both combustion performance (mixing efficiency) and chamber heat flux (composition at the wall). In addition low frequency instability was encountered under certain conditions on all element concepts except the premix.

Based on the results of Tasks I through III, 2 full scale injectors (premix and triplet) were designed during Task IV for maximum combustion performance and a third (triplet) injector was designed with a low mixture ratio (barrier cooled) outer row of elements to investigate chamber heat flux effects. The experimental data obtained during this task substantiated the design criteria developed during the earlier tasks: the injectors designed for high combustion performance achieved energy release efficiencies from 98.4 to 100% with a 7.6 (cm) 3.0 in. long chamber. The barrier cooled tests also substantiated the results of the Task I analysis, i.e., the performance penalty is excessive for the corresponding reduction in chamber wall heat flux. In addition, combustion was marginally stable during the premix tests and unstable at high frequencies during about 25% of the triplet tests.

The output of Task V, Data Evaluation, was two gaseous injector combustion models. The first model used the test data and correlated it directly with injector/chamber design parameters which are recognized from both theoretical and empirical standpoints as the controlling variables. This empirical model has the advantages of (1) inherently being the most accurate procedure for gaseous injectors which are to be designed within the operating envelopes and using the same propellants as this program, and (2) simplicity in the calculation procedure itself. However, it lacks generality since it

stressed utilization of the test data and did not concentrate on quantifying the mechanistic causal relationships of the mixing/combustion process itself. The second modeling approach had the objective of understanding the mixing/combustion process to the maximum extent possible, using both available theoretical knowledge and new techniques suggested and developed from close observation of the test data. It is somewhat more complex than the empirical model, but it has quantitatively characterized the mixing/combustion process for gaseous propellants so that it is general in nature and can handle all gaseous propellants and operating conditions. Both of these models have been summarized into step-by-step design procedures for gaseous injectors with the required information displayed in charts, graphs, and tables for clarity of presentation.

II. INTRODUCTION

In recent years, considerable effort has been devoted to increasing the level of knowledge concerning injection and combustion processes in rocket engines. The goal of these efforts has been to provide sufficient information for the reliable design of injectors having high performance, as well as being compatible with the chamber wall. Most of the work in this area has involved either liquid-liquid or gas-liquid propellant phases, with many different types of injector elements being characterized (e.g., like and unlike impinging doublet, triplet, pentad, and coaxial types). Characterization of these elements and complete injectors was accomplished by the use of cold flow tests with propellant simulant fluids to determine mass and mixture ratio distribution profiles. Determination of droplet size distribution was obtained by various experimental techniques. Using the experimental cold flow results, and correlating such results with hot firing tests, a comprehensive theoretical base has been obtained which permits the design of injectors having high performance as well as minimum interactions with the chamber wall.

The work described above has principally been associated with liquid-liquid propellant combinations. More recently, some attention has been directed to gas liquid combinations. However, to date no comprehensive effort has been directed toward developing similar technology which would permit the reliable design of gaseous propellant injectors. This program addresses that technology void.

The scope of this program encompassed the analytical screening and rating of a multitude of injector elements with the end objective being a comprehensive set of design criteria. These criteria should allow the future design of injectors for high performance, stable operation, and maximum compatibility with the thrust chamber, for any selected operating condition or gaseous propellant combination. The above was accomplished by single and multiple element cold flow tests to investigate the many variables which affect the mixing process. As part of this laboratory effort, sampling of a combustion gas flow field was accomplished to permit the effect of combustion on the mixing process to be explored. This was followed by single element hot fire testing to enable a correlation to be made with the previously obtained cold flow testing. The multiple element mixing process was then investigated on a hot fire basis. The last task was to correlate all the data generated on this and other programs using gaseous propellants and formulate a design approach for injectors and combustion chambers.

The significance of the work accomplished on this program can be divided into three primary areas. First is the comprehensive set of cold flow data which characterized the mixing process for 74 unique element designs over a range of operating conditions. Secondly, the influence of combustion on the mixing process has been determined for four different element types, using gaseous hydrogen, gaseous oxygen propellants. Thirdly, the first two items

have provided the experimental bases for the development of gaseous injector modeling procedures which can be used to determine optimum design parameters for most selected operating conditions and propellant combinations.

Documentation of the significant work is contained in the following sections of this report. In addition a supplemental Design Handbook is attached to the end of this report to specify the step-by-step calculations for the injector modeling procedures. This Design Handbook contains only the procedural steps with most of the required information displayed in charts, graphs, and tables for clarity of presentation. In addition, an example problem is included so that the reader can be assured that he is using the models correctly.

III. INJECTOR DESIGN AND ANALYSIS

The objective of this task was to evaluate and screen potential injection elements leading to the selection of four basic element concepts which have the potential for being high performing and, at the same time, meet other required injector design criteria for the Space Shuttle Attitude Control Propulsion System. The following sections discuss the results of this evaluation and selection process, as well as the cold flow hardware designed to incorporate the selected elements. Also as part of this task film vs barrier cooling studies were conducted and combustion stability characteristics were considered.

A. CONCEPT SCREENING

Potential injector design concepts for gaseous propellants evaluated in the screening process are shown in Table I. The left-hand column, labeled "Elements", catalogs basic element configurations. Design derivatives considered for each element are tabulated in the center column while the right hand column lists element geometry variations. The first two columns are starred (*) for those design concepts having test information available in the literature prior to the starting date of this contract. The applicable program has been keyed in the right-hand column. Examination of Table I reveals that there is at least some industry experience for seven of the twelve elements identified (column 1). The most in-depth experience appears to be with the shear elements.

The screening results are shown in Table II, where estimated ability to meet each of the defined evaluation criteria is designated by a number between 1 and 5 (1 is minimum ability and 5 is maximum ability). The elements are cataloged according to (1) external impingement, (2) premix, (3) shear, (4) micro-orifice and (5) reverse flow concepts. In a gross sense, this rating includes the orifice geometric derivatives listed in Table I for each design, since the particular orifice geometry which was estimated to be best for that element was used in determining the rating. For example, the F-O-F triplet has a non-circular jet (tri-slot) which was estimated to result in better compatibility, higher potential for decoupling the mixing/reaction processes, and a lower design/fabricability rating than a comparable circular-orifice triplet. In addition, the rating was based on equal thrust-per-element with the exception of the micro-orifice concept.

Using an equal weighting factor for each criteria, the evaluation results are summed in the right-hand column. Four element groupings resulted in at least one design derivative which was assessed a rating of 4. Based on this rating chart, the four element types and derivatives selected for further study were:

TABLE I

GAS/GAS INJECTOR ELEMENT TYPES AND DERIVATIVES

Elements	Basic Design Derivatives	Orifice Geometry Derivatives
I EXTERNAL IMPINGING		
* Doublets	* Like Doublets * Unlike Doublets	. Circular . Noncircular . Continuous Sheets (1) (2
* Triplets	* F-O-F O-F-O	. Circular (1) . Noncircular (6) . Continuous Sheets
Quadlets	O-F-O-F (Trans) O-O-F-F (CIS)	. Circular . Non circular
Pentads	F-F-O-F-F O-O-F-O-O	. Circular . Noncircular
II PREMIX		
* Triplets	* F-O-F O-F-O	. Circular . Noncircular (7)
Pentads	F-F-O-F-F O-O-F-O-O	. Circular . Noncircular
* Swirl	* O-Axial, F-Tang F-Axial, O-Tang	. Circular (8) . Noncircular
III SHEAR		
* Coaxial	* Fuel Annulus Oxidizer Annulus	. Circular (1),(6),(7),(11 . Noncircular . Swirler (6), (7) . Convolutions (9)
Showerhead	Both Propellants	. Circular ( ) . Noncircular
	One Propellant Plus Porous Face Plate	. Continuous Sheets ( )
IV MICRO-ORIFICE		
* Showerhead	* Both Propellants * Like Doublets Unlike Doublets	. Noncircular (3),(4),(5) . Noncircular (10)
Triplets	F-O-F O-F-O	

KEY:

* Elements and operation derivatives that have been tested with GH_2/GO_2
( ) Program definition for particular orifice geometry derivative

1. Contract NAS3-14347, "H-O Catalytic Ign. and Thruster Program" (TRW)
2. Contract NAS 3-14353, "High Pressure Reverse Flow APS Engine" (Bell)
3. Contract NAS8-21052, "Advanced Injector Concepts Investigation" (Aerojet)
4. Contract NAS 8-20672, "Stability Characterization of Advanced Inj." (Aerojet)
5. Aerojet IR&D Program
6. Contract NAS 3-14352, "Space Shuttle Auxiliary Propulsion System" (Rocketdyne)
7. Contract NAS 3-14354, "H-O APS Engines" (Aerojet)
8. Aerojet IR&D Program
9. Aerojet IR&D Program
10. Contract NAS 8-26188, "Space Shuttle Main Eng. Definition Study, Phase B (Aeroje
11. Contract NAS9-8285, "Apollo Optimized SPS Injector (OMS)" (Aerojet)

TABLE II

ELEMENT CONCEPT RATING CHART

	Performance		Compatibility			Insensitivity		
	Mixing Potential (High E_m)	Mixing/Reaction Decouple Potential	Inj Face	Chamber Wall	Stability Potential	to Engine Variables	Design and Fabricability	Weighted Average
EXTERNAL IMPINGEMENT								
Doublets								
Like	2	3	2	4	2	4	5	3
Unlike	4	2	2	3	3	2	5	3
Triplets								
F-O-F	5	3	3	4	4	3	4	(4)
O-F-O	5	3	2	2	4	3	4	3
Quadlets								
O-F-O-F	5	3	2	2	4	2	3	3
O-O-F-F	4	2	2	2	4	2	3	3
Pentads								
F-F-O-F-F	5	3	3	4	4	3	2	3
O-O-F-O-O	5	3	1	1	4	3	2	3
PREMIX								
Triplets	5	4	3	4	4	4	4	(4)
Pentads	4	4	3	4	4	4	3	4
Swirl	4	4	2	4	4	3	3	3
SHEAR ELEMENTS								
Coaxial	5	2	5	3	4	4	4	(4)
Showerhead	2	2	5	3	2	4	5	3
MICRO-ORIFICE								
Showerhead	5	3	5	5	2	4	2	4
Impinging Doublet	5	4	5	5	2	4	2	(4)
REVERSE FLOW	3	2	5	2	3	2	3	3

1. Shear Elements

   a. Coaxial

   b. Increased shear area coaxial

   c. Swirl coaxial

2. Premix Elements

   a. Triplet

   b. Pentad

3. External Impingement Elements

   a. Triplet (impingement angle $\pi/4$ rad (45°), $\pi/3$ rad (60°), and $\pi/2$ rad (90°))

4. Micro-Orifice Elements

   a. Parallel sheet

   b. Like Doublet

B. ELEMENT EVALUATION

1. Shear Mixing Elements

Shear mixing elements mix by turbulent diffusion through the shear mixing layer. In order to characterize this element analytically, the Aerojet Turbulent Mixing and Chemical Reactions Computer Program was used to parametrically investigate various coaxial element characteristics. This program models the interacting effects of mixing and reaction by solving the combined energy, streamwise momentum, and species equations using the Prandtl boundary layer approximation. A nominal (66.6 N) 15 lb_f thrust coaxial element was studied and the fuel annular area was varied from half that of the oxidizer area to twice the oxidizer area while mixture ratio was varied from one to sixteen.

The results of this study are shown in Figure 1a*, where the mixing efficiency E_m is plotted as a function of relative injection area and mixture ratio for a chamber length to element diameter ratio of 10. This analysis draws the conclusions that decreasing fuel annulus is in the direction of higher E_m. Experimental data pertinent to the coaxial element is shown in Figure 1b and 1c. The available gas-gas data for full scale coaxial elements is shown in Figure 1b while the results of an ALRC sponsored single element program are shown in Figure 1c. This data indicates that the following design parameters are important for shear mixing elements.

*For reader convenience, the figures appear at the end of each Roman Numeral section.

a. Relative area ratio

b. Relative velocity ratio

c. Absolute size

d. Shear area between the two propellants

e. Swirl

2. Momentum Mixing Elements

Since there is no available impinging mixing model which is computationally tractable, impinging elements must be evaluated empirically. Rupe and his coworkers at JPL as well as other investigators documented the results in the 1950's of an orderly investigation into the impingement mixing process for liquid propellants using inert propellant simulants (ref. 1, 2, 3, 4, and 5). By collecting immiscible fluids with a ganged probe, they were able to map mass and mixture ratio distributions for the common impinging elements (doublet, triplet, quadlet, and pentad) as a function of design and operating conditions. From his investigation, Rupe was able to correlate the maximum mixing potential for each of the elements using certain design variables. These correlations took the following form:

$$\left(\frac{\dot{w}_o}{\dot{w}_f}\right)^2 \cdot \frac{\rho_o}{\rho_f} \cdot \left(\frac{A_f}{A_o}\right)^a = K \qquad (1)$$

K and a are constants which must be determined empirically for each configuration. Rocketdyne used these correlations directly for gaseous propellants in Ref. 6 and concluded that the correlations were in fair agreement with the data. Aerojet's impinging premix (triplet) gas-gas cold flow data also was examined to determine applicability of the Rupe criterion. The results are shown on Figure 2 where it is apparent that the test data did correlate well with momentum ratio and geometry parameters.

Based on this work it was determined that the following physical and hydraulic parameters are important.

a. Relative stream momentum

b. Relative orifice size

c. Impingement angle

It was also inferred that the following parameters are likely to be important:

a. Physical size (thrust/element)

b. Spacing

c. Element orientation

C. BARRIER COOLING ANALYSIS

An evaluation of H_2 film cooling vs barrier cooling was conducted with the ground rule that the throat heat flux and wall temperature were to be maintained at 1960 watt/cm^2 (12 Btu/in.^{2}-sec) and 533°K (500°F) wall, respectively, based on chamber life considerations. This analysis was conducted using the mixing program developed in LeRC Contract NAS 3-14343, (Ref. 7). Performance was computed by a mass weighted average I_{sp} based on the barrier and free stream at their respective throat mixture ratios.

Barrier coolant characteristics were calculated using the Aerojet Barrier Film Cooling Program (BARFC). The BARFC Program is a film-cooling model, where mixing of the film coolant with the mainstream combustion products is calculated via an empirically adjusted entrainment model. BARFC is designed to calculate film temperature and mixture ratio profiles axially along the chamber contour. It considers the simultaneous effects of momentum, chemistry, and energy transport through the mixing layer. The profiles are coupled via empirically derived shape factors.

The Attitude Control Thruster hardware was modeled with the 19 cm (7.5-in.) long chamber composed of a cylindrical section and a 22° half-angle cone. Total weight flow was fixed at 1.55 kg/sec (3.45 lbm/sec) and an overall mixture ratio (O/F) of 4.0 was maintained. Barrier or film coolant was injected from the injector face.

Results are presented in Figure 3; no adjustment has been made other than use of the inferred entrainment factor multiplier. Wall temperature was taken to be 533°K (500°F) which is typical of throat values required to meet the originally specified cycle life (10^6 cycles). Heat fluxes of 1934 and 1960 watt/cm^2 (10 and 12 Btu/in.^{2}-sec), typical of those accompanying a 533°K (500°F) wall, were considered.

Figure 3a shows the heat flux at the throat vs the barrier flow/total flow (injection point) ratio for three barrier injection mixture ratios. For a constant heat flux (viz., wall temperature in a regeneratively cooled system), the barrier flow fraction must be increased as the mixture ratio increases to offset the higher combustion temperature. The heat transfer coefficient remains fairly constant over the range of mixture ratios and barrier temperatures predicted at the throat. Dashed lines on these figures represent extrapolations, necessitated because of convergence failure of the computer program.

Figure 3b is a cross plot of the preceding data and shows the injection barrier mixture ratio vs the barrier flow fraction for the two designated heat fluxes. The increased flow requirement with increasing mixture ratio is apparent.

Figure 3c is a plot of the barrier mixture ratio at the throat vs barrier flow fraction at the injection point, and it indicates that throat mixture ratio drops rapidly with increasing flow fraction. To achieve a given flux level, the barrier mixture ratio remains almost unchanged over a wide range of barrier flow fraction, reflecting the temperature sensitivity of flux since the heat transfer coefficient is approximately constant. The barrier flow fraction at the throat vs the injection barrier flow fraction is shown in Figure 3d for the three barrier injection mixture ratios. This figure also shows the two heat flux levels. Again, the dependence of heat flux on initial barrier mixture ratio is demonstrated.

Based on this analysis, the decrement in performance was computed using a mass weighted two stream tube model using the throat barrier mixture ratio and barrier percentage weight flow as defined on Figures 3c and 3d for a throat heat flux of 1960 watt/cm^2 (12 Btu/in.^{2}-sec). The core mixture ratio at the throat was then found by difference. The results of this performance analysis are shown on Figure 4. This analysis indicates that barrier cooling would penalize the engine system more than fuel film cooling [(Barrier O/F)$_{Inj}$ = 0] for the same chamber life requirements and that the performance penalty increases as (Barrier O/F)$_{Inj}$ is increased.

The effects of element characteristics was beyond the scope of this barrier cooling study, and therefore the results of this analysis did not influence directly the selection of element types for cold flow evaluation. However the analysis did provide a theoretical basis upon which to evaluate the full scale barrier cooled designs fabricated and tested in Task IV (See Section VII).

D. STABILITY CONSIDERATIONS

Stability characteristics of gas-gas systems are significantly different from liquid/liquid systems investigated to date. Recent experimental results at ALRC and work at Purdue University (Ref. 8) suggest that kinetics play the major roll in the stability of a gas-gas system rather than the generally accepted causal mechanisms for liquid injectors such as propellant mixing and vaporization. The influence of kinetics is based upon the observed sensitivity in the stability of a system to changes in mixture ratio. This effect is predicted with a model such as the Geode model (Ref. 8) which uses kinetics as the rate controlling process. The trends summarized in Figure 5 reflect a strong influence of mixture ratio and some effect of chamber pressure. Such trends in stability are apparent from the model of Reference 8 which gives the following expression for this energy release rate:

$$Q' = \bar{Q}\left[\frac{2\rho'}{\rho} + \frac{E}{R\bar{T}} + \frac{1}{2}\frac{T'}{\bar{T}}\right] \qquad (2)$$

where:

$(\bar{\ })$ = steady-state quantity

$(')$ = perturbation quantity

From this expression, it can be seen that, increasing temperature and pressure, and consequently, density, has a stabilizing effect. This would imply that, as the stoichiometric mixture is approached (which generally gives a near maximum steady-state temperature), the system becomes more stable. Such a trend is shown on Figure 5.

The significance of such a mechanism being the driver for unstable combustion is that the combustion process would not exhibit preferential frequency. This will make the use of conventional damping devices such as liners and baffles difficult because of their limited frequency range of effectiveness and could result in a major development hurdle for gas-gas systems. Also, with Kinetics playing such a key role in the stability area, it is difficult to select elements on the basis of stability characteristics. Therefore the primary criteria used for selecting the elements for cold flow evaluation were based primarily on the Concept Screening and Element Evaluation analyses discussed previously.

E. ELEMENT SELECTION

Based on the above analyses the element configurations listed in Figure 6 were synthesized and selected as the most promising concepts. The element geometry variations selected for cold flow evaluation are also included in Figure 6. These geometry variations were influenced by the full scale operating ranges specified for the Space Shuttle Attitude Control Thruster, which are tabulated below:

Thrust	1790 - 8900 N	(500-2000 lb)
Chamber Pressure	68 - 341 N/cm^2	(100-500 psia)
Mixture Ratio	3 - 5	
Propellant Inlet Temperature	167 - 333 °K	(300-600°R)
Propellants	O_2/H_2	

F. COLD FLOW HARDWARE DESIGN

1. Single Element Injector-Chamber

The single element hardware assembly is depicted in Figure 7, and the selected element designs are shown in Figure 8. Element configurations were changed by replacing the element plate and the oxidizer orifice plugs, Part Nos. 105 and 106, on Figure 7. The element plates shown in Figure 8 were removed and changed by unbolting the split ring (Part No. 103) and lifting out the remaining assembly, which then allowed access to the

element plate. The oxidizer plug access was through Part No. 101. The plug was removed and reinstalled by removing Part No. 101 from the assembly, extracting the tested plug, inserting a new seal, installing the new plug, and reassembling Part No. 101 to the test hardware. Hydrogen and nitrogen (the oxygen cold flow simulant) were introduced to the test article through Part Nos. 102 and 101, respectively.

A helium bleed circuit was incorporated into Part No. 104, which permitted helium to be injected axially through an annular Rigimesh plate that covered the injector face from the element to the chamber wall. This helium circuit was designed to suppress face recirculation using the criteria described in Reference 9. A recirculation parameter, C_T, is defined in Reference [9] which is a function of the source jet velocity, the field velocity, and the radius ratio of the jet to the chamber. A jet velocity of 91.5 m/sec (300 fps) a radius ratio of 0.17, and a field velocity of 7.61 m/sec (25 fps) suppressed face recirculation using the C_T criterion defined in Reference 9. The addition of a third fluid circuit does not compromise the resulting test data as the mass spectrometer used to probe the flow field has the capability of determining the mole fraction of any and all species.

2. Multiple Element Injector-Chamber

The design of this hardware was similar to that of the single element hardware, with the same consideration given to versatility of element configurations and test setup. The assembly of this hardware is shown in Figure 9 together with the elements and face geometry. The basic purpose of the multiple element test rig was to permit evaluation of inter element mixing effects. This was accomplished in two ways. (1) The radial spacing of the elements could be varied (three positions). The elements during testing were arranged in a square injection pattern as shown in Figure 9. During testing, the active elements were located in one of the three hole circles. The remaining holes were blocked with blank elements. (2) The elements were rotated with respect to each other such that the fuel-rich zones of one element were directed toward the oxidizer-rich zones of the adjacent element. Based on the single element cold flow work it was determined that the coaxial, swirl coaxial and premix triplet elements would be investigated. The 67N, (15 lb_f) elements are shown in detail in Figure 9. The helium face bleed shown in Figure 9 was not operational. It was eliminated because the test facility did not have the flow capacity to maintain the required He flow rate.

3. Sampling Rake and Rake Assembly

The sampling rake shown in Figure 10 was used to acquire mass and pressure data in the flow field downstream of the injector face. It was a multiple entry type probe with 20 active positions. Each entry port performed two functions: (1) it provided a local gas sample which was drawn from the flow field and routed to a mass spectrometer and (2) it served as a total pressure probe when the test apparatus was sequenced to the pressure scan mode.

The rake was located and held by the pintle assembly shown in Figure 7. The rake and instrumentation leads were routed through Part No. 406 and sealed against chamber pressure by a Swage-lock fitting. Provision was made to traverse the rake both axially and circumferentially. In operation, chamber pressure was set by the remotely controlled, belt driven pintle that enabled the throat area to be varied until the required pressure was obtained.

Figure 1a. Mixing Efficiency Predicted by Turbulent Mixing/Combustion Model (L/D = 10)

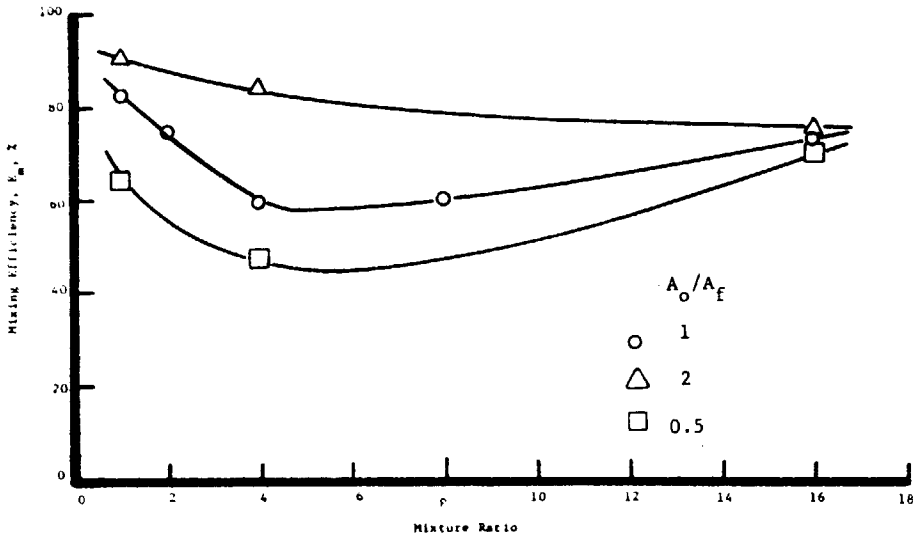

Figure 1b. Performance of Multi-Element Coaxial Injectors

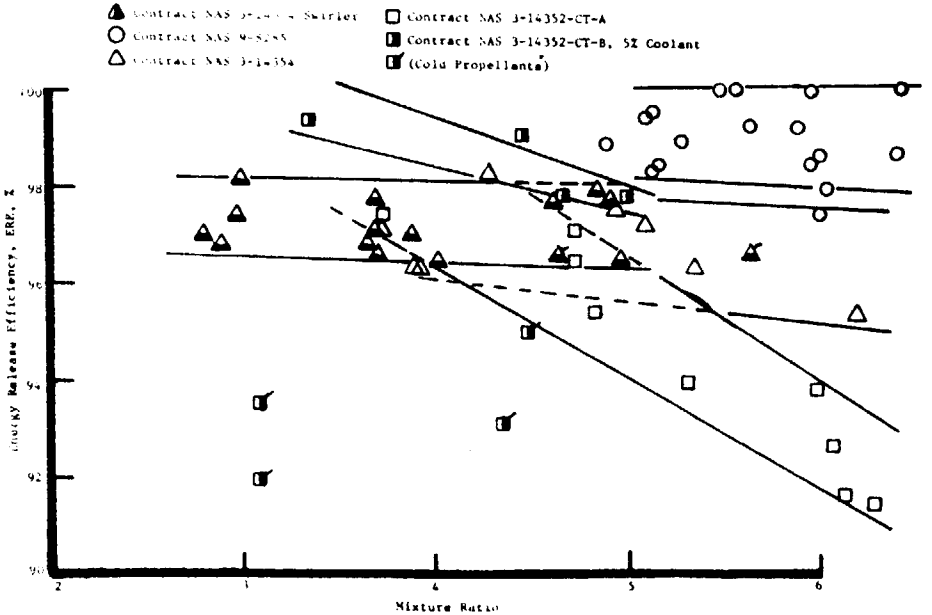

Figure 1c. Performance of Single Element Injectors

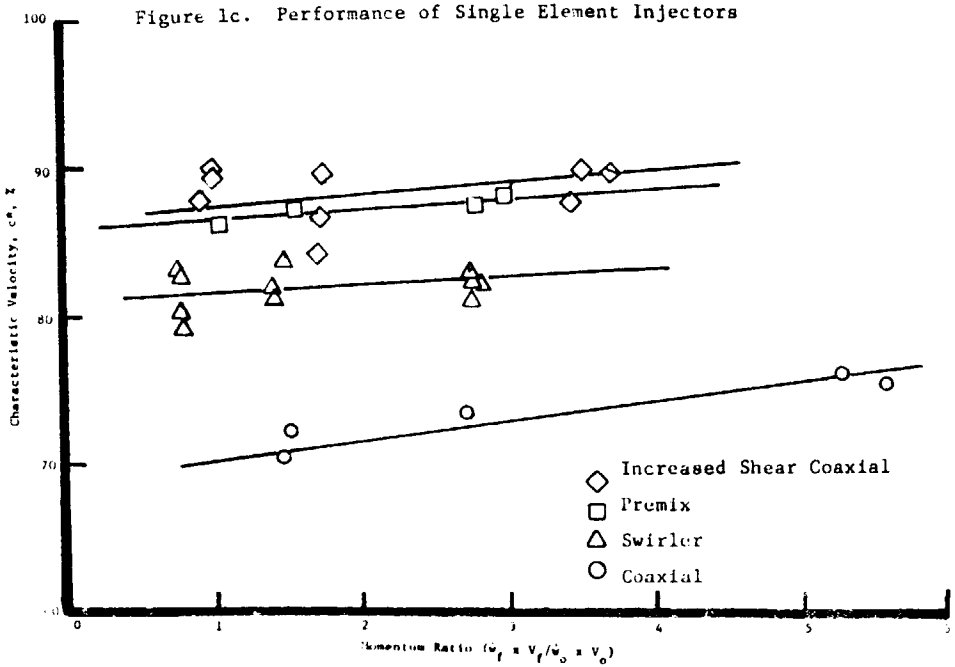

Figure 1. Gaseous Injector Performance

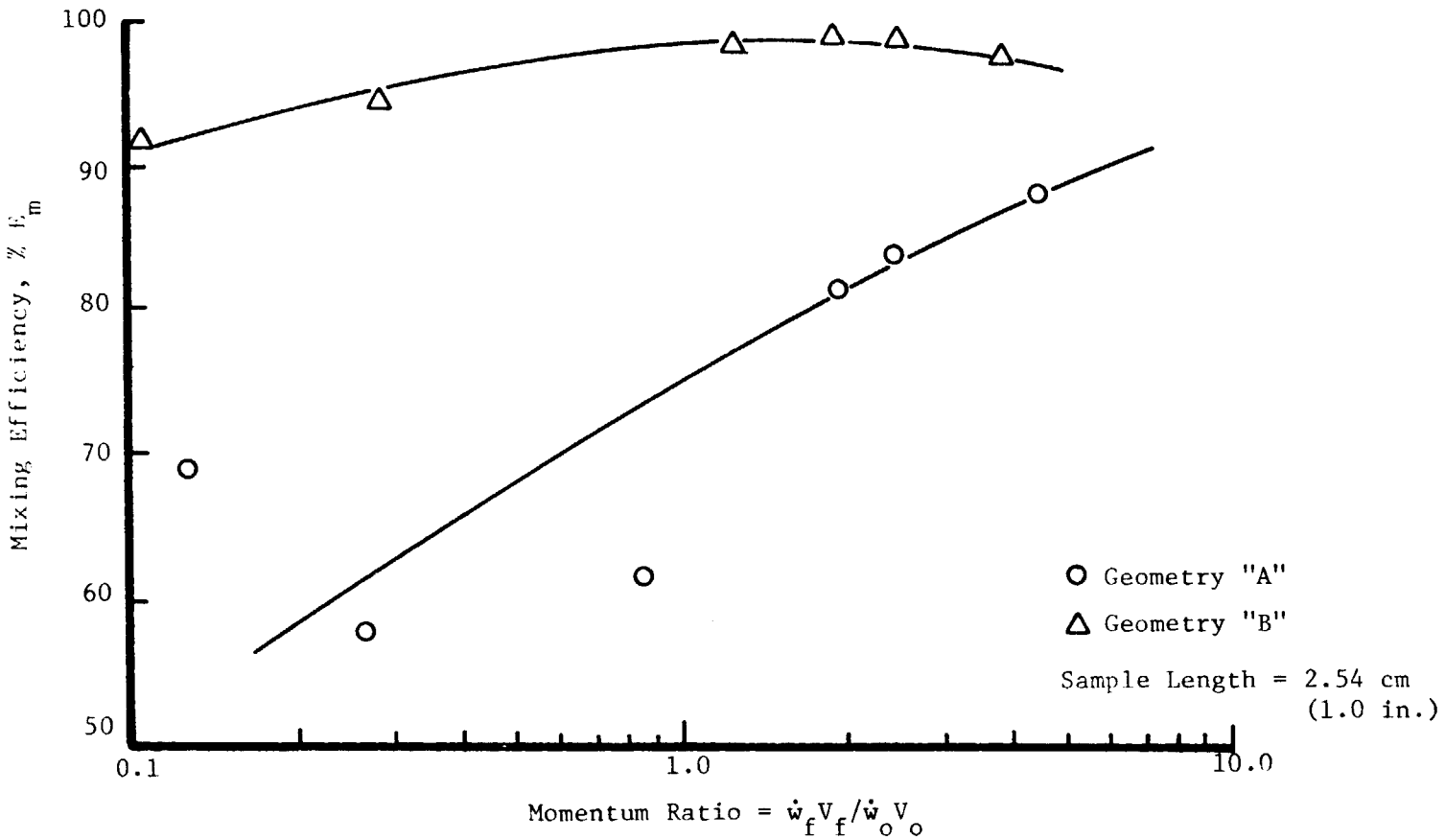

Figure 2. Effect of Momentum Ratio on Premix Impinging Element Mixing Efficiency

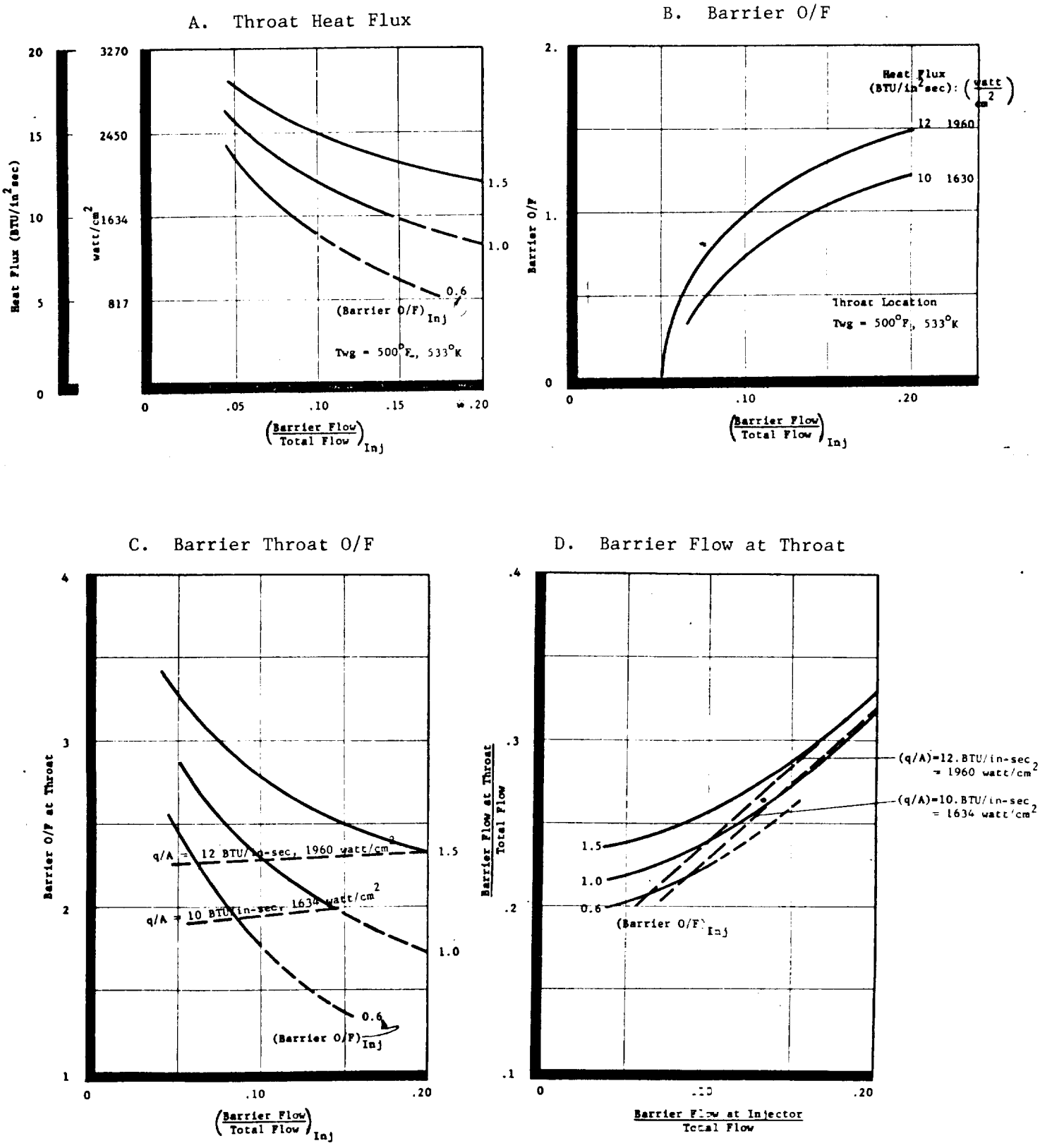

Figure 3. Results of Barrier Cooling Analysis

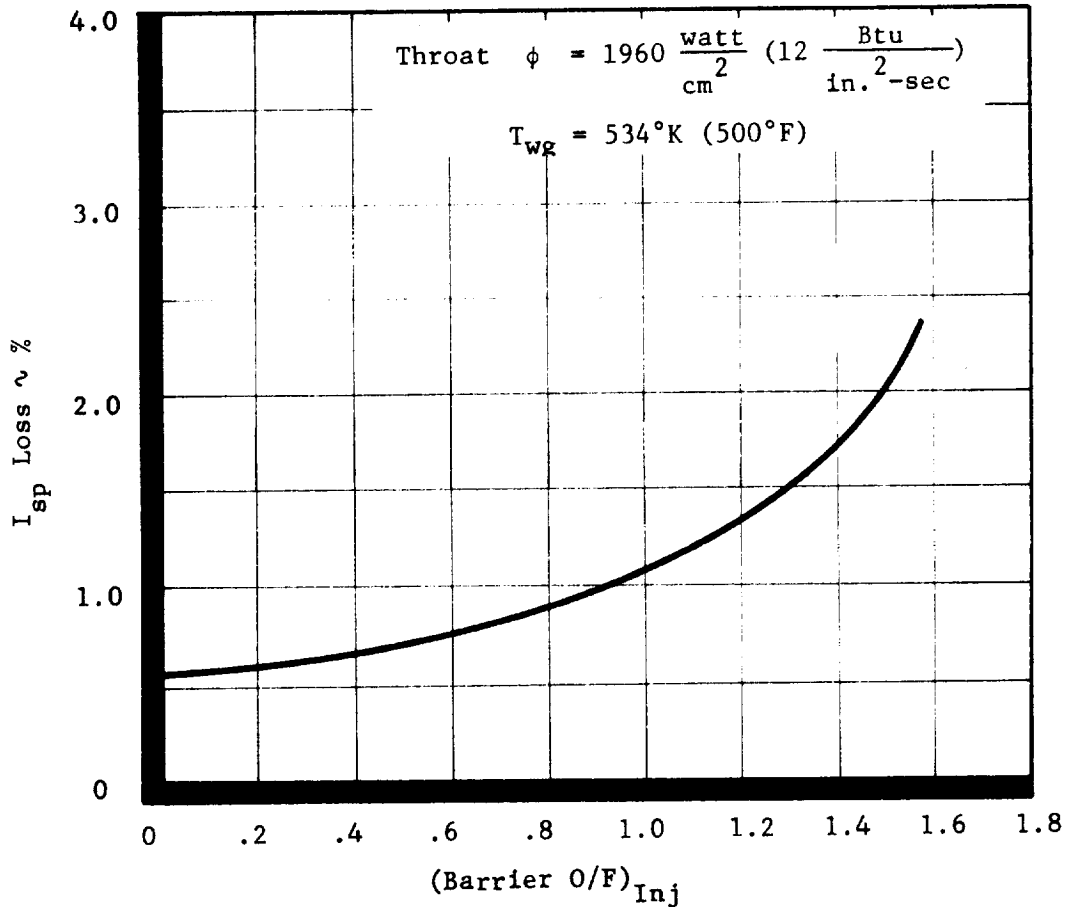

Figure 4. Vacuum I_{sp} Loss for a Barrier Cooled Design

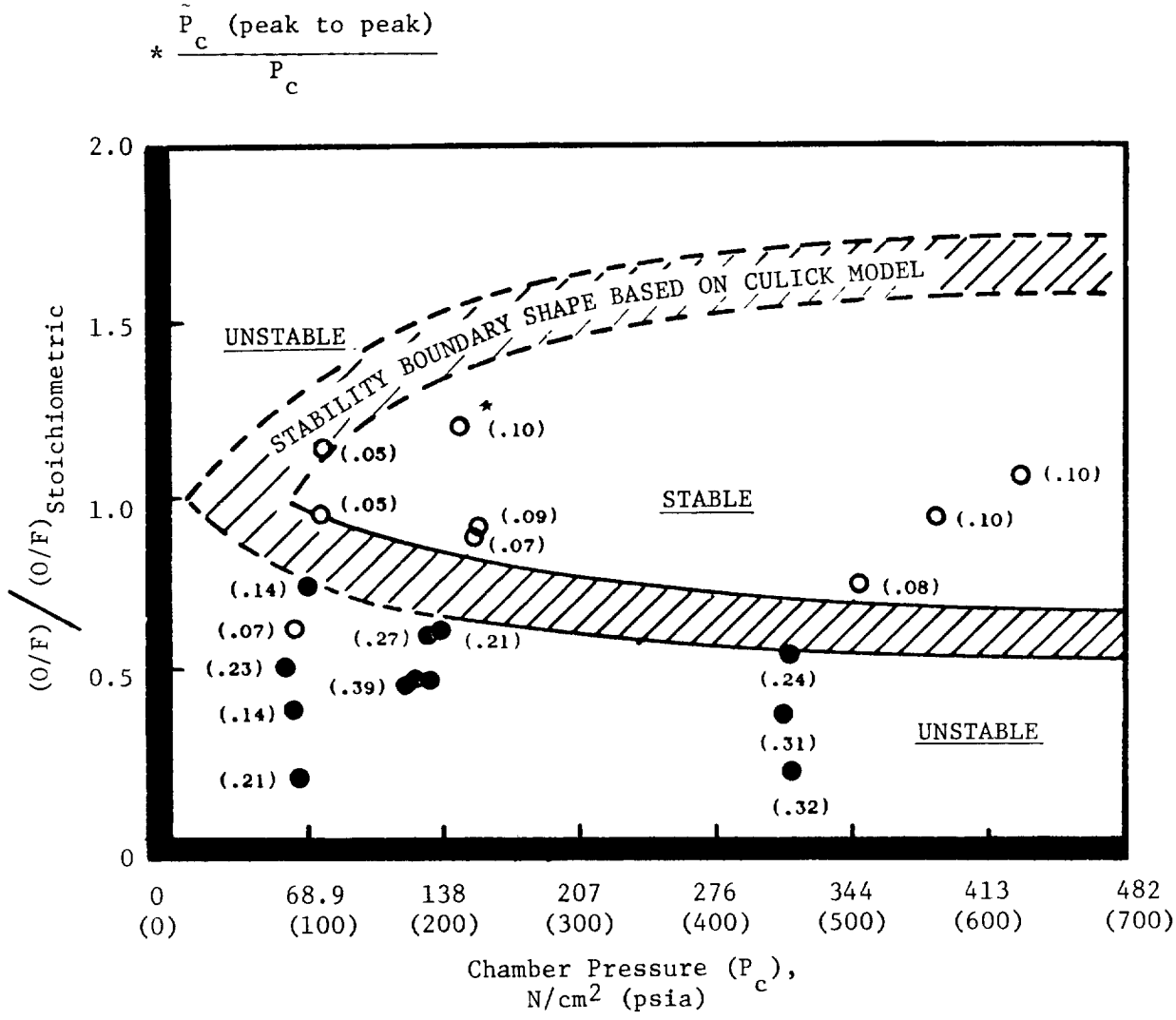

Figure 5. 4.448 N (1000 lbf) Thrust H_2/O_2 Stability Map

SHEAR

	F/E, N/E (lbf/E)	A_o/A_f 0.50	1.0	2.0
Coaxial	13.35 (3)	X	X	X
	66.75 (15)		X	
	222.50 (50)	X	X	X
Increased Shear (2 Times Shear Area of Coaxial)	13.35 (3)	X	X	X
	66.75 (15)		X	
	222.50 (50)	X	X	X
Swirl Coaxial (Tangential Velocity Equal 0.5 x Axial Velocity)	13.35 (3)			X
	66.75 (15)		X	
	222.50 (50)	X		
Swirl Coaxial (Tangential Velocity Equal 1.0 x Axial Velocity)	13.35 (3)	X	X	X
	66.75 (15)		X	
	222.50 (50)	X	X	X

PREMIX

	F/E, N/E (lbf/E)	A_o/A_f 0.50	1.0	2.0
Triplet (Fuel Slot Width Equal to Ox Dia)	13.35 (3)	X	X	X
	66.75 (15)		X	
	222.50 (50)	X	X	X
Triplet (Fuel Slot Width Equal to 0.66 Ox Dia)	13.35 (3)			X
	66.75 (15)		X	
	222.50 (50)	X		
Triplet (Fuel Slot Width Equal to 0.33 Ox Dia)	13.35 (3)	X	X	X
	66.75 (15)		X	
	222.50 (50)	X	X	X
Pentad (Fuel Slot Width Equal to Ox Dia)	13.35 (3)			X
	66.75 (15)		X	
	222.50 (50)	X		
Pentad (Fuel Slot Width Equal to 0.33 Ox Dia)	13.35 (3)	X	X	X
	66.75 (15)		X	
	222.50 (50)	X	X	X

EXTERNAL IMPINGING

	F/E, N/E (lbf/E)	A_o/A_f 0.50	1.0	2.0
$\pi/4$ rad (45°) Impingement Angle	13.35 (3)			X
	66.75 (15)		X	
	222.50 (50)	X		
$\pi/3$ rad (60°) Impingement Angle	13.35 (3)	X	X	X
	66.75 (15)		X	
	222.50 (50)	X	X	X
$\pi/2$ rad (90°) Impingement Angle	13.35 (3)			X
	66.75 (15)		X	
	222.50 (50)	X		

MICRO-ORIFICE

	F/E, N/E (lbf/E)	A_o/A_f 0.50	1.0	2.0
Sheet	13.35 (3)		X	
	66.75 (15)		X	
	222.50 (50)		X	
Like Doublet	13.35 (3)		X	
	66.75 (15)	X	X	X
	222.50 (50)		X	
Spacing Varied	66.75 (15)		X	
	66.75 (15)		X	

Figure 6. Element Types Selected for Cold Flow Evaluation

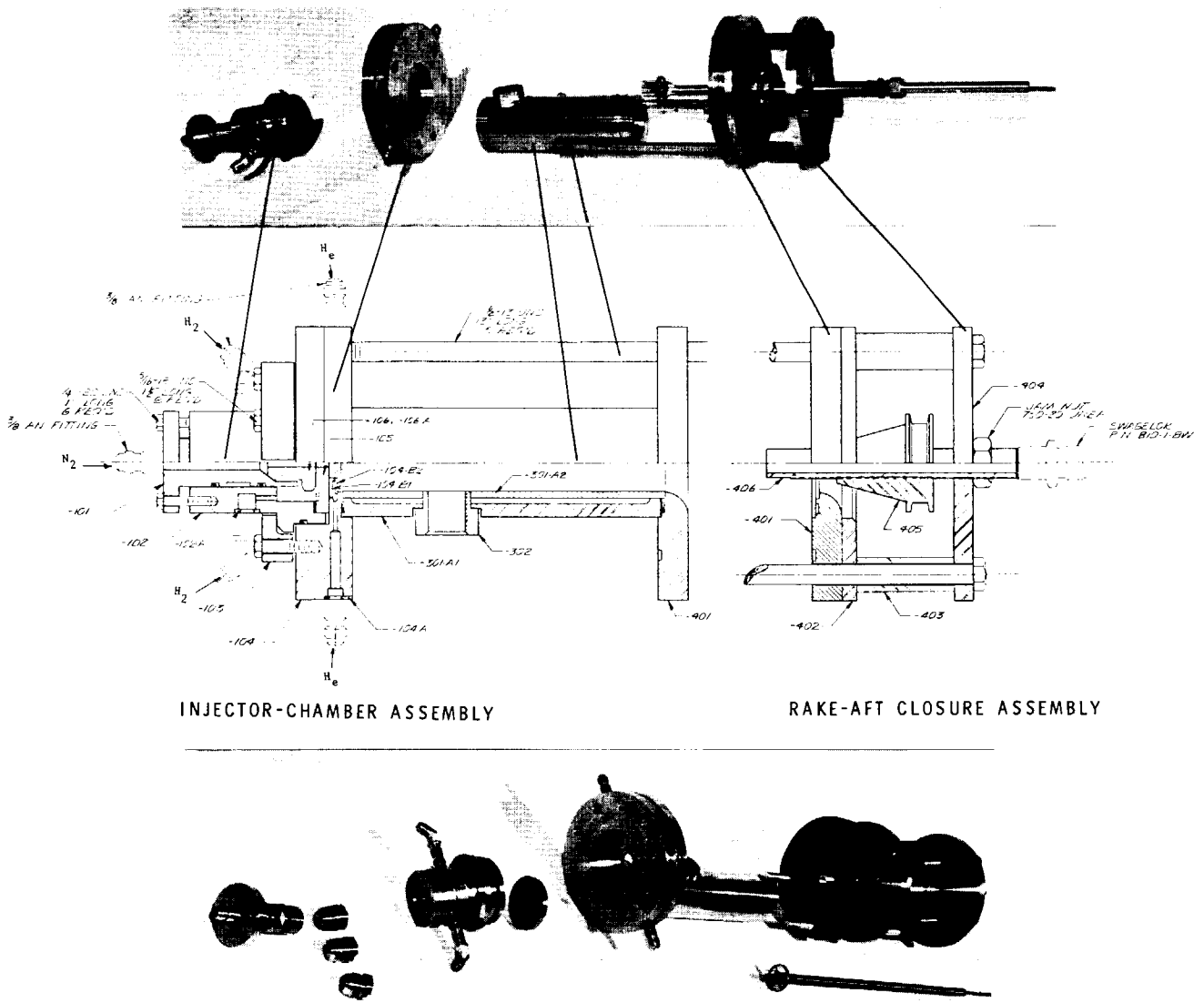

Figure 7. Single Element Cold Flow Assembly

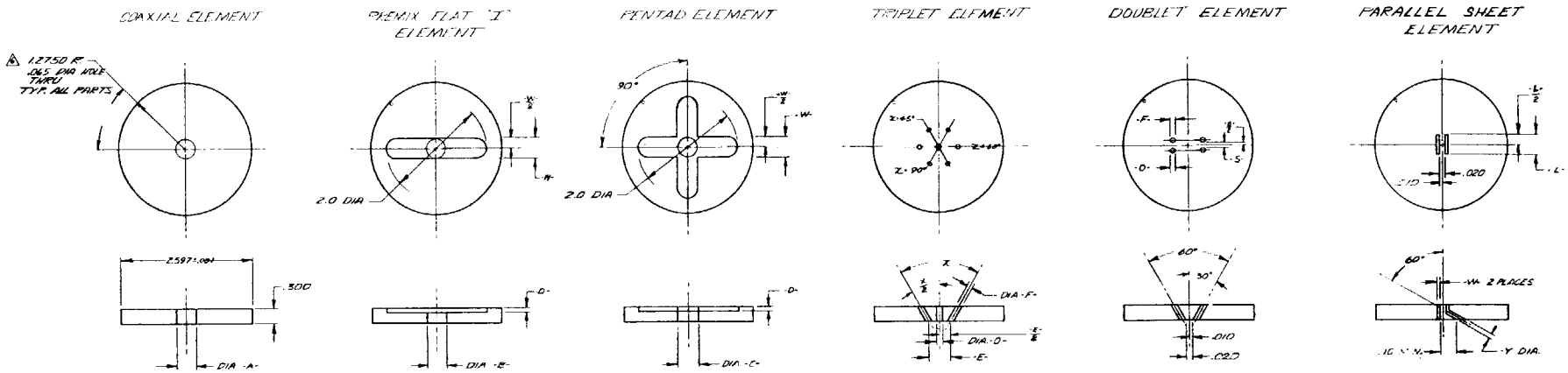

COAX ELEMENTS

S/N	DIA 'A'
3C-0.5	.094
3C-1.0	.104
3C-2.0	.122
15C-1.0	.212
50C-0.5	.364
50C-1.0	.406
50C-2.0	.484

PREMIX FLAT I ELEMENTS

S/N	DIA 'B'	DEPTH 'D'	WIDTH 'W'
3F1-0.5	.0635	.012	.064
3F1-1.0	.0635	.025	.064
3F1-2.0	.0635	.050	.064
15F1-1.0	.144	.056	.143
50F1-0.5	.261	.051	.262
50F1-1.0	.261	.103	.262
50F1-2.0	.261	.206	.262
3F1-66-2.0	.0635	.076	.0427
15F166-1.0	.144	.084	.098
50F166-0.5	.261	.077	.176
3F133-0.5	.0635	.051	.0214
3F133-1.0	.0635	.075	.0214
3F133-2.0	.0635	.150	.0214
15F133-1.0	.144	.170	.0475
50F133-0.5	.261	.154	.0825

PENTAD ELEMENTS

S/N	DIA 'C'	DEPTH 'D'	WIDTH 'W'
3P-2.0	.0635	.025	.064
15P-1.0	.144	.028	.143
50P-0.5	.261	.026	.262
3P33-0.5	.0635	.016	.0214
3P33-1.0	.0635	.037	.0214
3P33-2.0	.0635	.075	.0214
15P33-1.0	.144	.085	.0475
50P33-0.5	.261	.072	.176
50P33-1.0	.261	.154	.0825

TRIPLET ELEMENTS

S/N	DIA. 'B'	DIA. 'F'	'E'
*3T-0.5	.0635	.0320	.149
3T-1.0	.0635	.0453	.167
3T-2.0	.0635	.0635	.195
15T-1.0	.144	.0995	.325
50T-0.5	.261	.1298	.487
*50T-1.0	.261	.181	.558
50T-2.0	.261	.261	.672

* 60° ONLY, BOTH SETS OF HOLES IN ONE PLATE

DOUBLET ELEMENTS

S/N	DIA 'D'	DIA 'F'	'S'
3D-1.0	.045	.045	.050
15D-0.5	.0995	.0709	.100
15D-1.0	.0995	.0995	.100
15D-2.0	.0995	.144	.100
50D-1.0	.181	.181	.100
15D-1.0	.0995	.0995	.050
15D-1.0	.0995	.0995	.200

PARALLEL SHEET ELEMENTS

S/N	'W'	'L'	Y
3PS-1.0	.0188	.188	.0310
15PS-1.0	.0400	.400	.0492
50PS-1.0	.0732	.732	.090

COAX

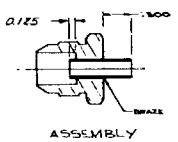

ASSEMBLY

S/N	"B" DIA	"C" DIA	"D" TUBE
3C	.625	.0886	.083 O.D. x .063 I.D.
15C	.625	.1610	5/32 O.D. x .144 I.D.
50C	.625	.3160	5/16 O.D. x .263 I.D.

TRIPLET

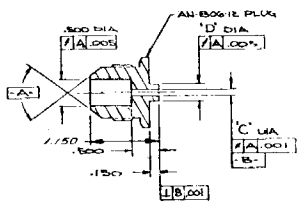

S/N	"C" DIA	"D" DIA
3T	.0995	.300
15T	.1496	.400
50T	.2992	.500

PARALLEL SHEET ELE.
S/N 3PS, 15PS, & 50PS

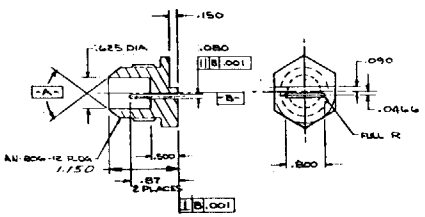

PREMIX FLAT I ELE. & PENTAD

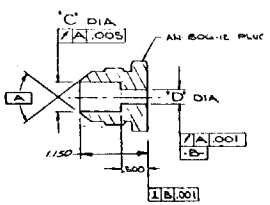

S/N	"C" DIA	"D" DIA
3 F.I. & P.	.187	.0635
15 F.I. & P.	.406	.1440
50 F.I. & P	.625	.2610

DOUBLET ELEMENTS
S/N 3D, 15D & 50D

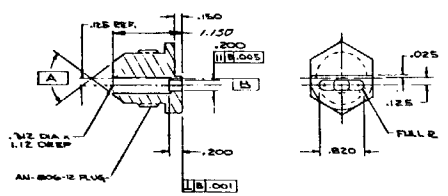

Figure 8. Single Element Cold Flow Designs

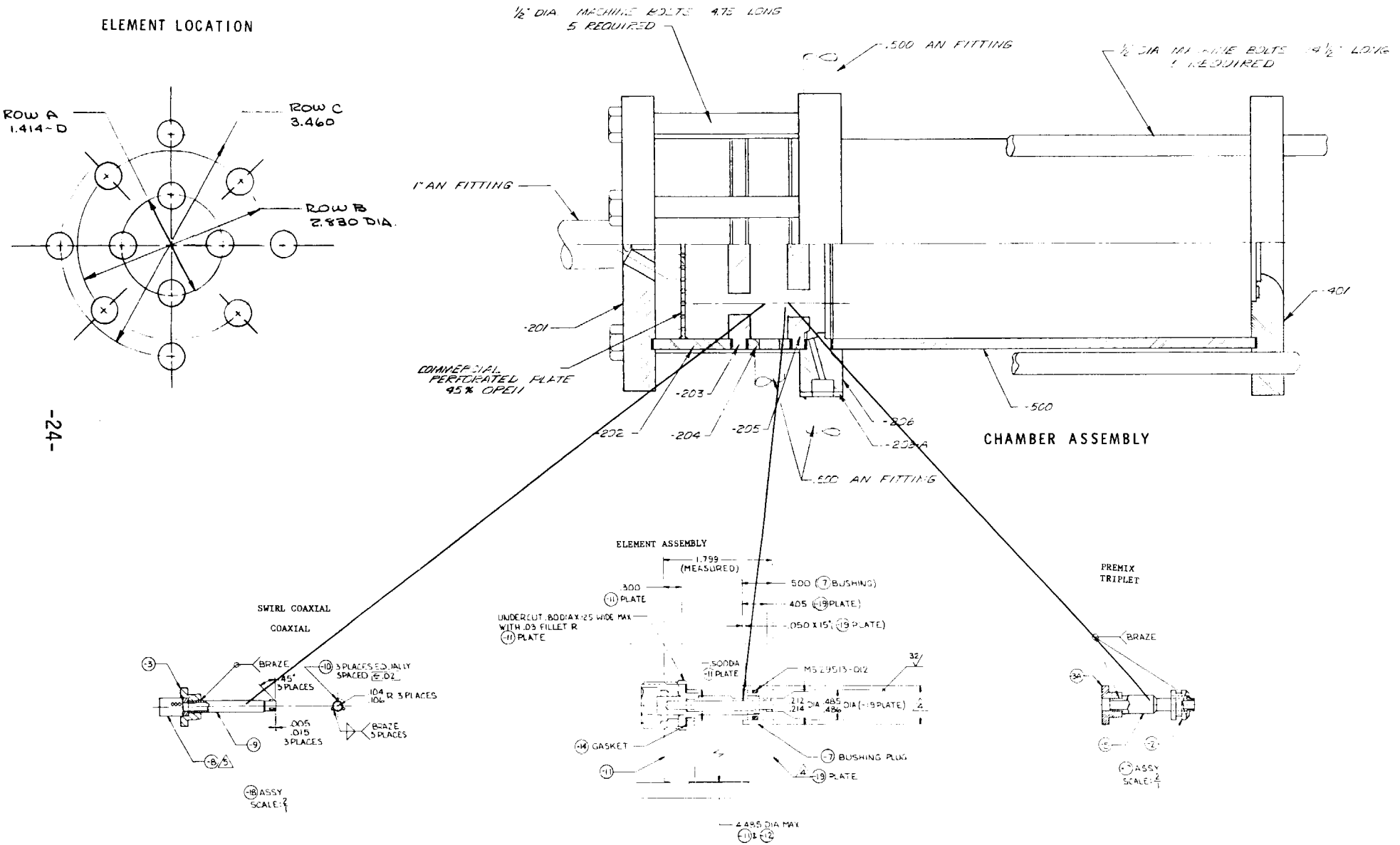

Figure 9. Multiple Element Cold Flow Assembly

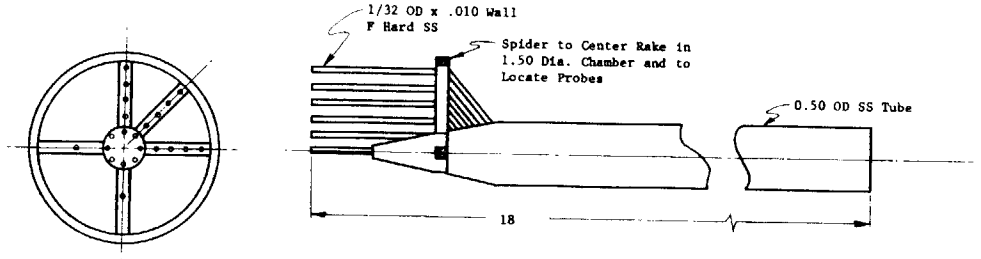

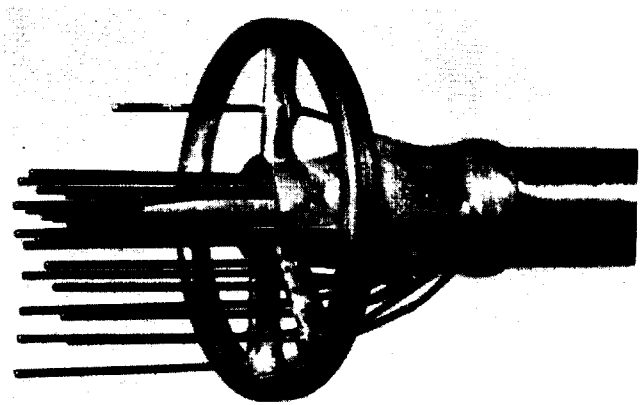

ELEMENT NO.	DIAMETER	ANGLE	TYPE	ELEMENT NO.	DIAMETER	ANGLE	TYPE
1	1.25	0°	Total	16	.75	45°	Total
2	1.00			17	.25	45	
3	.75			18	.25	225	
4	.50			19	.25	315	
5	.25			20	.25	135	Total
6	0.0	0°		21	.75	270	Static
7	.25	180		22	.75	180	
8	1.25	90		23	.75	45	Static
9	1.00						
10	.75						
11	.50						
12	.25	90					
13	.25	270					
14	1.25	45					
15	1.00	45	Total				

NOTE: All length dimensions in inches

Figure 10. Sampling Rake

IV. COLD FLOW MODELING

A. SINGLE ELEMENT COLD FLOW

Using the methods described in Appendix B some 223 single element cold flow tests were conducted and analyzed. The data from these tests is summarized in Table III, Table IV and in Figures 11 through 24. Table III, Single Element Cold Flow Test Summary is a tabulation of the injection element design parameters, test operating parameters, injection parameters and calculated mixing efficiencies (E_m). Table IV is a summary of element design and operating effects on mixing efficiency. The figures present both mixing efficiencies and compatibility data at the chamber wall as a function of thrust/element, (F/E), length, element area ratio (A_f/A_o) and mixture ratio. Compatibility at the chamber wall is indicated by the measured local mixture ratio at the edge of the flow field $(O/F)_{wall}$ divided by the overall nominal mixture ratio $(O/F)_{nominal}$. The open symbols represent the most oxidizer-rich composition measured at the flow field boundary, the closed symbols represent most fuel-rich composition and the half-open symbols represent the average boundary composition.

Figure 11 is a summary graph of E_m for all injectors as a function of L/D, F/E, A_f/A_o and O/F. The effect of sample position on L/D, where D is the oxidizer orifice diameter or equivalent diameter if the element is non-circular, is shown in Figure 11 for the area ratio one elements. The characteristics of the elements are as expected, increasing E_m with increasing length. The swirl coaxial, premix pentad, and triplet elements group together at high mixing efficiencies, while the coaxial element has the lowest element E_m. The remaining elements group between the extremes of the shear coaxial and the swirl coaxial elements. When these elements are compared on a thrust/element basis, the same effects are noted i.e., the premix designs and the swirl coaxial element are high mixing rate elements while the shear coaxial is a low mixing rate element. With the exception of the swirl coaxial element, the data trends are in the expected direction, reduced mixing with larger elements. The swirl coaxial element E_m is maximum at 89 N/Element (20 lb/element). It appears that the fuel annulus size and radial oxidizer momentum are related. It is interesting to note that the parallel sheet element at low F/E 3 lbf (13 Newtons) approaches the mixing efficiency of the best elements. For small thrust/element injectors (such as HIPERTHIN), these data indicate that the parallel sheet element is an excellent element concept.

Area ratio influences for the basic element concepts are illustrated in Figure 11 as well. Both shear mixing elements, the coaxial and increased shear element, decrease in performance as fuel to oxidizer orifice area ratio is increased. It should be noted that the area ratio was varied by changing only the fuel geometry; the oxidizer diameter was held constant. Decreasing area ratio is in the direction of both smaller fuel annulus widths and higher velocity ratios or delta velocities; effects which analytically are predicted to lead toward increased mixing efficiency.

TABLE III
SINGLE ELEMENT COLD FLOW TEST SUMMARY

Test No. (Units)	Run No.	Basic Elem.	Variation	F/E N (lb_f)	A_f/A_o	T_o °R (°K)	T_f °R (°K)	ΔP_{OJ} psi (N/cm^2)	ΔP_{FJ} psi (N/cm^2)	$\dot{W}_f V_f / \dot{W}_o V_o$	Normal Ax. Mom.	V_f/V_o	L/D	O/F	$\bar{R}$	$(O/F)_I$	E_m	η_m	%C*
1	6	Co-Ax	Shear	66.7 (15)	0.99	518 (288)	540 (300)	6 41 (4.42)	7.02 (4.84)	0.94	0.00	3.72	3	3.97	.211	3.77	47.8	58.0	85.79
2	5					517 (287)	541 (301)	5.72 (3.94)	6.33 (4.36)	0.94	0.00	3.73	7	3.96	.500	4.06	72.1	62.9	96.83
3	7					519 (288)	542 (301)	6 34 (4.37)	6.78 (4.67)	0.95	0.00	3.74	15	3.94	.500	4.63	96.5	94.3	99.95
4	8					517 (287)	542 (301)	6.33 (4.36)	6.93 (4.78)	0.95	0.00	3.75	30	3.94	.750	4.20	97.9	96.3	99.95
5	9					504 (280)	530 (294)	5.27 (3.63)	14.11 (9.73)	3.65	0.00	7.35	7	2.01	.362	2.43	82.4	75.7	98.43
6	10					500 (278)	529 (294)	14.88 (10.26)	1.72 (1.19)	0.35	0.00	2.29	7	6.49	.275	6.74	55.4	52.0	93.66
7	11		(1)			230 (128)	371.7 (207)	7.29 (5.03)	1.64 (1.13)	1.30	0.00	5.44	7	4.19	.625	4.38	79.9	69.0	98.19
8	13		High Swirler			519 (288)	541 (301)	26.50 (18.27)	3.85 (2.65)	0.92	0.00	3.68	3	3.99	.538	2.95	92.5	87.4	99.59
9	12					514 (286)	541 (301)	26.52 (18.28)	3.99 (2.75)	0.92	0.00	3.68	7	4.02	.330	2.81	98.2	97.1	99.98
10	14					515 (286)	542 (301)	25.96 (17.90)	3.21 (2.21)	0.92	0.00	3.69	15	4.01	.50 to .75	3.30	98.5	97.6	99.99
11	15					516 (287)	542 (301)	26.13 (18.02)	3.31 (2.28)	0.92	0.00	3.69	30	4.01	.750	3.19	99.9	99.8	100.00
12	16					518 (288)	543 (302)	20.06 (13.83)	10.58 (7.29)	3.17	0.00	6.84	7	2.16	.412	3.15	95.6	92.9	99.93
13	17					510 (283)	541 (301)	35.07 (24.18)	-0.14 (.09)	0.35	0.00	2.30	7	6.49	.325	7.67	96.9	95.5	100.01
14	18		(1)			207.5 (116)	348.8 (194)	8.48 (5.85)	0.58 (.39)	1.49	0.00	5.93	7	3.99	.325	7.24	95.1	95.4	100.08
15.2	20		Low Swirler			513 (285)	531 (295)	15.21 (10.48)	4.44 (3.06)	0.93	0.00	3.68	7	3.96	.334	5.13	94.3	91.2	99.83
16	22		Increased Shear		0.88	509 (282)	529 (294)	13.84 (9.54)	17.20 (11.86)	1.04	0.00	4.12	3	3.98	.444	3.88	73.3	68.6	96.61
17	21					512 (284)	530 (294)	13.45 (9.27)	16.93 (11.67)	1.04	0.00	4.12	7	3.97	.361	4.20	83.1	75.4	99.05
18	23					509 (283)	529 (294)	13.15 (9.07)	16.81 (11.59)	1.03	0.00	4.11	15	3.99	.439	3.08	98.1	96.7	99.96
19	24					507 (282)	528 (293)	13.55 (9.34)	17.04 (11.75)	1.03	0.00	4.12	30	3.99	.500	5.00	99.4	99.0	100.00
20.0	27										0.00		7		Data Not Available				
20.1	28		(2) . 1/2 W_{He}			501 (278)	528 (293)	9.39 (6.47)	48.30 (33.30)	4.11	0.00	8.27	7	2.01	.290	2.77	98.0	97.1	99.96
20.2	29		(2). 0 W_{He}			502 (279)	527 (293)	10.48 (7.22)	50.11 (34.55)	4.13	0.00	8.27	7	2.00	.136	4.39	95.1	95.5	99.81
21	25					500 (278)	529 (294)	17.25 (11.89)	6.93 (4.78)	0.24	0.00	2.00	7	8.35	.462	6.26	80.2	73.6	99.90
22	26					207.2 (115)	361.7 (201)	2.76 (1.90)	4.84 (3.34)	1.75	0.00	6.94	7	3.97	.281	5.85	86.9	80.4	99.29
23	30		Shear	13.3 (3)	0.49	536 (298)	537 (298)	11.63 (8.02)	41.32 (28.49)	1.76	0.00	7.08	7	4.01	.448	3.96	89.7	85.9	100.17

TABLE III

SINGLE ELEMENT COLD FLOW TEST SUMMARY

Test No. (Units)	Run No.	Basic Elem.	Variation	F/E N (lb_f)	A_f/A_o	T_o °R °K	T_f °R °K	ΔP_{OJ} psi (N/cm^2)	ΔP_{FJ} psi (N/cm^2)	$\dot{W}_f V_f / \dot{W}_o V_o$	Normal Ax. Mom.	V_f/V_o	L/D	O/F	$\bar{R}$	$(O/F)_1$	E_m	η_m	%C*
24	31	Co-Ax	Shear	13.3 (3)	0.49	533 (296)	540 (300)	11.10 (7.65)	41.66 (28.72)	1.80	0.00	7.18	15	4.00	.264	4.50	95.8	93.4	99.90
25	32					532 (296)	543 (302)	8.48 (5.85)	112.3 (77.43)	7.27	0.00	14.51	15	2.00	.250	2.70	95.2	91.7	99.75
26	33		(1)			532 (296)	537 (298)	14.22 (9.80)	20.25 (13.96)	0.79	0.00	4.77	15	6.01	.185	6.96	92.0	93.3	100.69
27	34		High Swirler			529 (295)	537 (298)	21.10 (14.55)	44.54 (30.71)	1.77	0.31	7.14	15	4.04	.444	4.47	96.4	93.5	99.93
28	35					530 (294)	542 (301)	14.06 (9.69)	114.4 (78.88)	7.25	0.094	14.50	15	2.00	.362	2.70	96.5	93.6	99.87
29	36					529 (294)	538 (299)	23.62 (16.28)	20.94 (14.44)	0.79	0.51	4.79	15	6.02	.239	6.50	96.2	94.5	100.02
31	37	Premix Triplet		66.7 (15)	0.98	514 (286)	527 (293)	44.62 (30.76)	40.82 (28.15)	0.92	0.92	3.66	3	3.97	.519	4.55	87.7	83.9	100.23
32	38					509	522 (290)	44.20 (30.47)	39.97 (27.56)	0.93	0.93	3.67	7	3.96	.672	4.42	94.0	89.8	100.06
33	39					514 (286)	525 (292)	43.70 (30.13)	39.65 (27.34)	0.94	0.94	3.69	15	3.93	.463	4.41	98.3	97.6	99.98
34	40					514 (285)	526 (292)	43.29 (29.85)	39.78 (27.43)	0.93	0.93	3.67	30	3.96	.375	4.66	99.0	98.9	99.99
35	41					513 (285)	520 (289)	52.91 (36.48)	54.58 (37.63)	2.59	2.59	6.09	7	2.36	.750	2.62	88.4	82.3	98.43
36	42					502 (279)	523 (291)	36.22 (24.97)	28.26 (19.48)	0.38	0.38	2.38	7	6.22	.595	7.48	96.3	93.4	99.83
37	44					234.6 (131)	310.7 (173)	18.78 (12.95)	12.75 (8.79)	1.15	1.15	4.64	7	4.05	.250	7.98	90.1	88.2	100.43
38	45			222 (50)	0.50	522 (290)	493 (274)	40.56 (27.97)	54.84 (37.81)	1.69	1.69	6.68	7	3.94	.625	5.72	89.9	81.4	99.33
39	46		(3)			520 (289)	495 (275)	41.57 (28.66)	55.00 (37.92)	1.74	1.74	6.79	3	3.91	.657	5.49	89.0	81.9	98.17
40	47		67%	13.3 (3)	2.05	537 (298)	532 (296)	23.92 (16.49)	11.24 (7.75)	0.42	0.42	1.67	15	4.02	.219	4.61	95.6	94.0	99.99
41	49		34%		0.69	536 (298)	532 (296)	48.93 (33.74)	53.48 (36.87)	1.27	1.27	5.04	7	3.98	.625	5.22	95.2	91.8	101.65
42	48					536 (298)	533 (296)	49.38 (34.05)	53.59 (36.95)	1.27	1.27	5.05	15	3.98	.214	4.94	98.6	97.3	100.06
43	50					537 (298)	528 (293)	68.88 (47.49)	57.65 (39.75)	4.93	4.93	9.90	15	2.01	.234	2.54	97.7	96.6	99.97
44	51					525 (292)	520 (289)	38.84 (26.78)	49.66 (34.24)	0.55	0.55	3.33	15	6.01	.249	6.71	96.9	94.6	100.07
44.6	52					518 (288)	516 (287)	40.86 (28.17)	114.07 (78.67)	0.57	0.57	3.39	15	5.94	.229	6.82	97.0	94.9	100.17
44.4	53					521 (289)	515 (286)	50.20 (34.61)	109.38 (75.43)	1.24	1.24	4.98	15	4.01	.195	5.15	99.0	98.4	100.02
44.2	54					526 (289)	513 (285)	70.39 (48.53)	96.43 (66.49)	4.93	4.93	9.87	15	2.00	.202	2.60	98.3	97.4	99.96
45	55	Premix	32%	222 (50)	0.48	511 (284)	478 (266)	40.21 (27.72)	60.30 (41.58)	1.77	1.77	6.97	3	3.93	.650	5.42	91.4	85.4	99.10
46	56	Pentad		13.3 (3)	2.02	520 (289)	517 (287)	46.26 (31.90)	29.86 (20.59)	0.43	0.43	1.72	15	3.98	.375	4.68	96.6	93.8	100.07

TABLE III

SINGLE ELEMENT GOLD FLOW TEST SUMMARY

Test No. (Units)	Run No.	Basic Elem.	Variation	F/E N (lb_f)	A_f/A_o	T_o °R (°K)	T_f °R (°K)	ΔP_{OJ} psi (N/cm^2)	ΔP_{FJ} psi (N/cm^2)	$\dot{W}_f V_f / \dot{W}_o V_o$	Normal Ax. Mom.	V_f/V_o	L/D	O/F	$\bar{R}$	$(O/F)_I$	E_m	η_m	%C*
		Premix																	
47	57	Pentad		13.3 (3)	2.02	523 (291)	516 (287)	47.56 (32.79)	30.90 (21.31)	0.43	0.43	1.71	7	3.99	.625	4.81	91.0	85.4	100.80
48	58		34%		0.43	522 (290)	518 (288)	45.84 (31.61)	29.86 (20.59)	2.00	2.00	7.99	15	4.00	.213	5.42	98.6	98.1	99.97
48.2	59					529 (294)	516 (287)	64.31 (44.34)	39.52 (27.24)	7.91	7.91	15.76	15	1.99	.250	2.48	97.1	95.2	100.00
48.6	60					525 (292)	514 (286)	42.01 (28.97)	28.05 (19.34)	0.74	4.82	4.82	15	6.55	.514	8.45	97.0	94.8	100.00
50	62	Doublet			1.00	532 (296)	524 (291)				.58	6.88	15	1.99	.631	2.30	93.0	87.5	99.7
49	63					531 (295)	523 (291)				.58	3.42	15	4.00	.451	4.90	91.5	87.3	99.83
51	61												15		(No Data)				
One Test 51.4	64		0°	66.7 (15)	0.51								7						
One Test 51.5	65		90° C.W.			532 (296)	512 (284)	17.83 (12.29)	32.98 (22.74)	1.63	0.58	6.56	7	4.02	.750	5.06	81.4	73.2	97.27
52	87	Co-Ax	Shear	13.3 (3)	0.99	534 (297)	539 (299)	11.66 (8.04)			0.00		15	3.81	.750	4.77	77.5	67.9	100.44
53	88					533 (296)	542 (301)	12.14 (8.37)			0.00		7	3.94	.75	5.39	56.0	41.2	100.44
54	89		(1)			198 (110)	181 (101)	-.26 (-.18)			0.00		15	4.00	.190	4.92	84.8	76.1	98.4
55	91		High Swirler			459 (255)	487 (271)	24.03 (16.57)					15	3.97	.225	5.10	91.4	90.1	100.07
56	92					501 (278)	531 (295)	25.11 (17.31)					7	3.97	.500	4.24	87.3	79.0	101.33
57	90					200 (111)	180 (100)	2.72 (1.88)					15	3.98	.271	5.05	95.3	93.4	100.03
58	93		Increased Shear		1.59	531 (295)	535 (297)	17.66 (12.18)			0.00		7	3.94	.750	4.03	70.5	58.4	98.51
59	94					530 (294)	538 (299)	18.04 (12.44)			0.00		15	3.95	.688	4.21	81.4	72.0	99.35
60	84	Co-Ax	Shear	222 (50)	0.50	491 (273)	520 (289)	8.06 (5.56)			0		7	3.81	.750	3.52	73.1	66.2	96.6
61	83					490.6 (272)	521 (289)	8.16 (5.63)			0		3	3.81	.7293	5.60	63.4	59.5	95.07
62	85		(1) High Swirler			497 (276)	520 (289)	29.20 (20.13)					7	3.76	.750	5.39	95.8	92.0	99.9
63	86		(1) Low Swirler			506 (281)	521 (289)	14.9 (10.27)					7	3.78	.375	4.38	94.0	88.9	99.71
		Premix																	
65	66	Pentad	67%	222 (50)	0.95	532 (296)	497 (276)	41.24 (28.43)	34.56 (23.83)	0.88	0.88	3.48	7	3.94	.727	6.65	91.5	84.6	99.55
65.1	67					530 (294)	498 (277)	42.07 (29.01)	34.91 (24.07)	0.88	0.88	3.49	3	3.95	.375	4.54	87.3	83.6	97.90
66	68		32%			539 (299)	497 (276)	41.07 (28.32)	39.76 (27.41)	0.87	0.87	3.43	3	3.94	.375	6.24	91.6	86.9	99.33
67	70					497.6 (277)	399.9 (222)	39.47 (27.21)	36.87 (25.42)	0.74	0.74	2.95	3	3.99	.744	5.16	91.4	86.5	99.64

TABLE III

Sheet 4 of 9

SINGLE ELEMENT COLD FLOW TEST SUMMARY

Test No. (Units)	Run No.	Basic Elem.	Variation	F/E N (lb_f)	A_f/A_o	T_o °R (°K)	T_f °R (°K)	ΔP_{OJ} psi (N/cm^2)	ΔP_{FJ} psi (N/cm^2)	$\dot{W}_f V_f / \dot{W}_o V_o$	Normal Ax. Mom.	V_f/V_o	L/D	O/F	$\bar{R}$	$(O/F)_I$	E_m	η_m	% C*
68.0	71	Parallel Sheet	0°	222 (50)	1.00	491 (273)	527 (293)	49.33 (34.01)	10.28 (7.09)	1.01	0	3.89	3						
68.1	72		90° C.W.										3	3.84	.397	7.94	63.4	55.0	92.73
69.0	73		0°			491 (273)	526 (292)	50.67 (34.94)	9.82 (6.77)	1.01	0	3.88	7	3.83	.750	5.68	86.3	77.3	98.98
69.1	74		90° C.W.										7						
70.0	75		0°			491 (273)	524 (291)	51.14 (35.26)	9.48 (6.53)	1.00	0	3.86	15	3.85	.619	6.44	96.0	92.7	99.95
70.1	76		90° C.W.										15						
71.0	77		0°			491 (273)	526 (292)						3	2.50	.483	4.60	61.0	53.8	91.01
71.1	78		90° C.W.										3						
72.0	79		90° C.W.			485 (269)	525 (292)						3	5.77	.750	8.54	72.9	65.7	95.93
72.1	80		0°										3						
73.0	81		0°			366 (203)	430 (239)						3	3.88	.315	6.92	71.8	63.8	94.91
73.1	82		90° C.W.										3						
74	215		0°	13.3 (3)		507 (282)	523 (291)	14.11 (9.73)	9.48 (6.53)	.90	0	3.59	7	3.99	.375	4.34	92.2	89.9	100.18
9.74	216		90° C.W.										7						
9.75	217		90° C.W.			512 (284)	526 (292)	11.22 (7.74)	22.46 (15.48)	2.96	0	6.51	7	2.20	.375	3.26	90.8	88.3	99.37
75	218		0°										7						
76	219		0°			509 (283)	522 (290)	14.90 (10.27)	4.26 (2.93)	0.41	0	2.41	7	5.92	.500	5.91	94.4	91.6	100.07
9.76	220		90° C.W.										7						
77.6	161	Doublet .200" Spacing (.508 cm)	90° C.C.W.	66.7 (15)	1.00	502 (279)	526 (292)	16.94 (11.68)	4.23 (2.91)	.36	58	2.28	7	6.38	.750	8.06	84.7	76.9	99.14
77.5	162		0°										7						
77.3	163		0°			503 (279)	525 (292)	9.95 (6.86)	18.05 (12.44)	3.69	.58	7.32	7	1.98	.750	3.39	78.2	69.6	94.94
77.4	164		90° C.C.W.										7						
77.2	165		90° C.C.W.			498 (277)	525 (292)	13.40 (9.24)	6.93 (4.77)	.94	.58	3.70	7	3.96	.75	5.23	80.4	69.8	98.4
77.1	166	.200" Spacing (.508 cm)	0°										7						
78.1	139	Doublet - .100" Spacing (.254cm)	0°	66.7 (15)	1.00	509 (283)	525 (292)	10.81 (7.45)	6.66 (4.59)	.88	.58	3.56	3.1	4.03	.624	5.29	70.7	61.3	95.38
78.2	140		90° C.C.W.										3.1						
79.1	141		0°			508 (282)	525 (292)	9.99 (6.89)	8.47 (5.84)	.92	.58	3.64	7	3.95	.750	5.05	85.5	76.0	98.85
79.2	142		90° C.C.W.										7						
80.1	143		0°			507 (282)	525 (292)	10.18 (7.02)	7.35 (5.06)	.92	.58	3.64	15	3.95	.750	4.75	95.5	91.6	99.88
80.2	144		90° C.C.W.										15						

TABLE III

SINGLE ELEMENT COLD FLOW TEST SUMMARY

Test No. (Units)	Run No.	Basic Elem.	Variation	F/E N (lb_f)	A_f/A_o	T_o °R / °K	T_f °R / °K	ΔP_{OJ} psi (N/cm^2)	ΔP_{FJ} psi (N/cm^2)	$\dot{W}_f V_f / \dot{W}_o V_o$	Normal Ax. Mom.	V_f/V_o	L/D	O/F	$\bar{R}$	$(O/F)_I$	E_m	η_m	% C*
			(.254 cm)																
81.1	145	Doublet	.100" Spacing 0°	66.7 (15)	1.00	506 (281)	525 (292)	10.35 (7.14)	9.32 (6.43)	.92	.58	3.64	30	3.96	.750	4.55	97.8	95.7	99.98
81.2	146		90° C.C.W.										30						
82.11	147		0°										7						
82.12	148		0°			512 (284)	525 (292)	7.20 (4.96)	21.66 (14.93)	3.67	.58	7.23	7	1.97	.25	3.35	82.6	72.3	97.52
82.2	149		90° C.C.W.																
83.2	150		90° C.C.W.			501 (278)	525 (292)	13.61 (9.38)	5.68 (3.91)	.36	.58	2.29	7	6.36	.75	7.52	86.5	79.2	99.75
83.1	151		0°										7						
84.11	152		0°			Missing Cold Test - Not Recorded on Tape @ Aerophysics Lab							7						
84.12	153		0°										7						
84.13	154		0°										7						
			(.127 cm)																
85.1	155		.050" Spacing 0°			506 (281)	525 (292)	12.89 (8.89)	11.40 (7.86)	.92	.58	3.65	7	3.96	.75	5.09	82.0	71.8	98.42
85.2	156		90° C.C.W.										7						
85.4	157		90° C.C.W.			506 (281)	525 (292)	9.86 (6.80)	30.80 (21.23)	3.68	.58	7.29	7	1.98	.375	3.32	82.3	72.8	97.85
85.3	158		0°										7						
85.5	159		0°			497 (276)	525 (292)	16.04 (11.06)	5.50 (3.79)	.36	.58	2.29	7	6.41	.541	8.29	85.6	78.2	100.02
85.6	160		90° C.C.W.										7						
		Premix																	
86	95	Triplet		13.7 (3)	1.01	538 (299)	541 (301)	48.60 (33.51)	45.18 (31.15)	0.88	0.88	3.49	15	3.97	.565	4.93	97.9	96.1	100.14
87	96					210.8 (117)	182.0 (101)	18.81 (12.97)	22.09 (15.23)	0.73	0.73	2.95	15	4.03	.25 to .75	7.0	≈72	≈64	≈96
														Note: Test 87 Distribution is Approximate & is Result of 2 phase ox. dist.					
88	99		34%(3)		1.01	533 (296)	544 (302)	73.15 (51.82)	37.95 (26.17)	0.89	0.89	3.53	15	3.98	.249	4.58	98.1	97.4	99.96
89	100		67%(3)	66.7 (15)	0.99	517 (287)	535 (297)	41.91 (28.90)	36.22 (24.97)	0.95	0.95	3.73	7	3.91	.604	4.48	95.3	91.7	99.92
90	101					510 (283)	531 (295)	43.74 (30.16)	37.99 (26.19)	0.94	0.94	3.70	3	3.96	.517	4.16	90.2	87.2	100.38
91	104			222 (50)	1.01	480 (267)	518 (288)	34.94 (24.09)	31.33 (21.60)	0.98	0.98	3.82	3	3.89	.556	5.09	85.1	80.6	99.48
92	106					395.6 (220)	423.4 (235)	27.45 (18.93)	23.57 (16.25)	0.98	0.98	3.79	3	3.89	.357	5.62	84.2	81.3	99.33
93	171		67%(3)		0.51	490 (272)	530 (294)	34.28 (23.64)	43.45 (29.96)	2.06	2.06	7.82	3	3.80	.611	5.49	89.6	85.1	99.79
94	105				1.01	482 (268)	518 (288)	34.27 (23.63)	30.80 (21.30)	1.03	1.03	3.91	7	3.79	.481	4.56	97.1	95.9	99.96
		Premix																	
95	103	Pentad		66.7 (15)	0.98	503 (279)	528 (293)	37.99 (26.19)	34.79 (23.99)	0.95	0.95	3.76	7	3.95	.575	4.70	92.6	88.8	99.79
96	102					513 (285)	533 (296)	38.65 (26.65)	35.55 (24.51)	0.94	0.94	3.72	3	3.96	.506	4.20	90.3	87.5	100.26

TABLE III

SINGLE ELEMENT COLD FLOW TEST SUMMARY

Test No. (Units)	Run No.	Basic Elem.	Variation	F/E N (lb_f)	A_f/A_o	T_o °R (°K)	T_f °R (°K)	ΔP_{OJ} psi (N/cm^2)	ΔP_{FJ} psi (N/cm^2)	$\dot{W}_f V_f / \dot{W}_o V_o$	Normal Ax. Mom.	V_f/V_o	L/D	O/F	$\bar{R}$	$(O/F)_I$	ζ_m	η_m	%C*
97	98	Premix Pentad	34%(3)	13.7 (3)	1.00	522 (290)	539 (299)	50.94 (35.12)	45.33 (37.46)	0.91	0.91	3.61	15	3.98	.290	4.69	98.6	97.9	100.01
98	97	↓	↓	↓	↓	204.5 (114)	177.0 (98)	3.76 (2.59)	0.90 (.62)	0.72	0.72	2.95	15	4.08	.15 to .75	60 to 80	85 to 91	80 to 88	102 to 106
						Test 98 Data Indicates Two Phase Oxidizer Injection Distribution; Mixing Efficiency Data Probably Meaningless													
99	107	Co-Ax	Shear		2.01	524 (291)	531 (295)	12.33 (8.50)	1.47 (1.01)	.45	0.00	1.77	15	3.96	.575	4.18	72.0	66.1	96.32
100	109		Low Swirler			521 (289)	526 (292)	16.19 (11.16)	1.59 (1.09)	.44	.28	1.76	15	3.98	.625	4.35	87.7	81.2	99.73
101	108		High Swirler			524 (291)	529 (294)	19.10 (13.17)	1.70 (1.17)	.44	.59	1.76	15	3.97	.625	4.31	91.6	86.8	99.89
102	110		Increased Shear		2.87	520 (289)	525 (292)	17.14 (11.82)	2.16 (1.49)	0.32	0.00	1.25	15	3 90	.417	3.94	86.1	79.4	99.41
103	111		Shear	222 (50)	0.99	483 (268)	519 (288)	7.03 (4.85)	5.56 (3.83)	1.03	0.00	3.93	7	3.82	.658	4.41	74.0	67.7	96.12
104	112					481 (267)	518 (288)	7.30 (5.03)	5.83 (4.01)	1.02	0.00	3.92	3	3.84	.633	5.49	49.5	49.0	85.98
105	113					395.5 (220)	425.5 (237)	7.05 (4.86)	5.21 (3.59)	1.00	0.00	3.89	3	3.87	.726	4.96	50.9	51.7	87.25
106	116		High Swirler			479 (266)	515 (286)	25.20 (17.38)	8.13 (5.61)	1.01		3.90	7	3.85	.750	4.10	94.3	90.0	99.78
107	115					479 (266)	515 (286)	26.43 (18.22)	8.03 (5.53)	0.98		3.83	3	3.92	.750	5.44	94.5	89.8	99.87
108	114					396.5 (221)	428.5 (238)	21.53 (14.84)	5.61 (3.86)	1.08		4.05	3	3.74	.660	6.04	93.2	87.8	99.67
109	117		Increased Shear		1.10	480 (267)	525 (292)	11.55 (7.96)	8.58 (5.91)	0.98	0.00	3.68	7	3.77	.745	6.12	82.0	76.6	98.36
110	118	↓	↓	↓	↓								3	(No Data Available)					
111	122	Triplet	(4) 60° Imp.	66.7 (15)	0.96	500 (278)	524 (291)	11.12 (7.68)	4.84 (3.34)	0.96	0.26	3.83	3	3.98	.358	4.61	65.0	62.7	94.12
112	123					497 (276)	522 (290)	10.79 (7.44)	4.65 (3.21)	0.97	0.26	3.85	7	3.97	.678	3.37	82.4	72.6	98.58
113	124					495 (275)	522 (290)	10.87 (7.49)	4.78 (3.30)	0.96	0.26	3.84	15	3.99	.716	4.59	95.0	90.8	99.93
114	125					496 (276)	522 (290)	10.48 (7.23)	4.61 (3.17)	0.96	0.26	3.83	30	3.99	.375 to .750	4.80	98.9	98.2	99.99
115	126					503 (279)	522 (290)	7.80 (5.38)	10.08 (6.95)	3.80	0.44	7.57	7	1.99	.631	2.34	86.2	78.4	98.84
116	127					487 (271)	519 (288)	13.56 (9.35)	2.95 (2.03)	0.38	0.14	2.41	7	6.42	.314	6.68	77.3	69.6	99.02
117	128					279.1 (155)	289.9 (161)	6.46 (4.45)	2.70 (1.86)	1.14	0.29	4.15	7	3.64	.643	4.41	78.1	67.5	98.31
118	136		45° Imp.			488 (271)	516 (287)	10.33 (7.12)	8.23 (5.67)	0.97	0.20	3.85	7	3.99	.750	3.55	57.9	49.3	93.59
119	134					488 (271)	513 (285)	10.40 (7.17)	8.70 (5.99)	0.98	0.20	3.87	3	3.96	.375	9.01	59.1	65.7	94.42
120	135	↓	↓	↓	↓	483 (268)	514 (286)	12.90 (8.89)	4.90 (3.38)	0.37	0.11	2.40	3	6.44	.688	6.30	46.8	43.9	93.49

TABLE III

SINGLE ELEMENT COLD FLOW TEST SUMMARY

Test No. (Units)	Run No.	Basic Elem.	Variation	F/E N (lb_f)	A_f/A_o	T_o °R (°K)	T_f °R (°K)	ΔP_{OJ} Psi (N/cm^2)	ΔP_{FJ} psi (N/cm^2)	$\dot{W}_f V_f / \dot{W}_o V_o$	Normal Ax. Mom.	V_f/V_o	L/D	O/F	$\bar{R}$	$(O/F)_I$	E_m	η_m	% C*
121	133	Triplet[4]	45° Imp.	66.7 (15)	0.96	497 (276)	515 (286)	7.39 (5.10)	20.23 (13.95)	3.81	0.32	7.57	3	1.99	.750	2.83	63.4	50.7	90.29
122	129		90° Imp.			495 (275)	518 (288)	9.92 (6.84)	10.99 (7.58)	0.97	0.41	3.84	7	3.96	.439	4.30	97.6	95.9	99.92
123	130					492 (273)	516 (287)	9.97 (6.87)	10.76 (7.42)	0.98	0.41	3.86	3	3.95	.307	4.49	91.7	89.8	99.03
124	132					485 (269)	514 (286)	11.96 (8.25)	6.35 (4.37)	0.38	0.21	2.41	3	6.38	.375	8.84	73.7	70.5	99.98
125	131					496 (276)	515 (286)	7.69 (5.30)	23.59 (16.27)	3.85	0.73	7.62	3	1.98	.350	2.20	73.4	62.4	95.54
126	175		60° Imp.	13.3 (3)	1.02	515 (286)	530 (294)	10.29 (7.09)	6.92 (4.77)	0.89	0.25	3.54	15	3.98	.252	4.58	97.9	97.2	99.94
127	176					197 (109)	(Cold Propellant Test - 2 Phase Ox)						15	4.03	(Date Not Applicable)				
1.01270	177					503 (279)	530 (294)	10.38 (7.16)	18.89 (13.02)	2.51	0.40	6.02	15	2.40	.316	2.98	92.2	88.4	99.55
128	172				0.51								15		(No Data Available)				
129	173					521 (289)	533 (296)	5.47 (3.77)	105.07 (72.45)	7.17	0.50	14.18	15	1.98	.299	2.27	97.8	97.0	99.99
130	174	Premix				519 (288)	531 (295)	9.84 (6.78)	20.05 (13.82)	.79	.23	4.69	15	5.96	.266	6.95	93.2	90.2	99.59
131	121	Triplet			2.02	519 (288)	531 (295)	38.59 (26.61)	27.03 (18.64)	0.45	0.45	1.77	15	3.98	.630	4.64	95.6	92.3	100.01
132	168			222 (50)		486 (270)	530 (294)	35.77 (24.66)	27.30 (18.82)	0.51	.51	1.97	3	3.83	.486	4.73	88.9	83.5	99.43
133	167					492 (273)	525 (292)	54.41 (37.52)	51.94 (35.81)	1.95	1.95	3.79	3	1.94	.331	2.68	89.2	85.2	99.46
134	169					485 (269)	530 (294)	27.66 (19.07)	16.67 (11.49)	.23	.23	1.31	3	5.77	.720	6.50	84.0	74.8	99.00
135	119	Premix Triplet[3]	34%	13.3 (3)	2.02	529 (294)	534 (297)	40.52 (27.94)	32.67 (22.53)	0.46	0.46	1.78	15	3.90	.278	4.32	98.9	98.2	99.97
136	120	Premix Pentad[3]	34%			520 (289)	531 (295)	47.30 (32.61)	36.57 (25.22)	0.44	0.44	1.76	15	3.99	.249	4.73	99.1	98.4	100.04
137	170			222 (50)	0.51	489 (272)	530 (294)	35.30 (24.34)	60.77 (41.90)	2.02	2.02	7.74	3	3.84	.682	5.36	90.0	85.7	98.52
139	214	Triplet	45° Imp.		0.50	483 (268)	507 (282)	10.60 (7.31)	22.91 (15.80)	2.03	.27	7.73	4.9	3.81	.621	4.81	91.0	86.1	99.30
140	204		60° Imp.			479 (266)	512 (284)	9.03 (6.23)					3	3.83	.240	3.88	83.4	81.1	97.06
240	205					482 (268)	512 (284)	9.02 (6.22)	25.05 (17.27)	2.03	.37	7.78	7	3.84	.594	4.64	96.2	93.0	99.87
340	206					479 (266)	512 (284)	8.97 (6.20)	24.50 (16.89)	2.01	.37	7.77	4.9	3.86	.435	4.49	90.8	85.7	99.21
141	211		90° Imp.			481 (267)	530 (294)	7.37 (5.08)	38.07 (26.25)	4.99	.78	12.44	4.9	2.49	.393	3.48	83.8	76.2	97.87
142	210					484 (269)	530 (294)	9.56 (6.59)	22.40 (15.44)	2.13	.60	8.10	4.9	3.80	.427	5.22	84.0	75.9	97.70
143	212					477 (265)	530 (294)	9.90 (6.82)	14.66 (10.11)	1.34	.49	6.46	4.9	4.83	.441	6.96	85.2	77.3	98.37

TABLE III

SINGLE ELEMENT COLD FLOW TEST SUMMARY

Test No. (Units)	Run No.	Basic Elem.	Variation	F/E N (lb_f)	A_f/A_o	T_o °R / °K	T_f °R / °K	ΔP_{OJ} psi (N/cm^2)	ΔP_{FJ} psi (N/cm^2)	$\dot{W}_f V_f / \dot{W}_o V_o$	Normal Ax. Mom.	V_f/V_o	L/D	O/F	R	$(O/F)_I$	E_m	η_m	% C*
144	213	Triplet[4]	60° Imp.	222 (50)	0.96	481 (267)	508 (282)	9.82 (6.77)	6.36 (4.38)	1.06	.28	4.01	4.9	3.80	.585	4.57	97.2	95.7	99.97
146	207				2.00	480 (267)	511 (284)	9.55 (6.58)	3.81 (2.63)	.50	.17	1.92	4.9	3.86	.697	4.78	93.2	88.3	99.83
147	208					481 (267)	509 (283)	7.93 (5.47)	8.45 (5.83)	1.33	.31	3.13	4.9	2.35	.715	3.21	92.3	86.5	98.93
148	209					476 (264)	510 (283)	10.50 (7.24)	1.31 (.90)	.22	.092	1.28	4.9	5.83	.653	6.72	78.6	69.6	98.48
149	178	Triplet	60° Imp.	13.3 (3)	2.00	505 (281)	530 (294)	7.67 (5.29)	2.10 (1.45)	.47	.13	1.86	15	3.93	.270	4.93	94.2	92.1	99.99
151	223					511 (284)	523 (291)	13.23 (9.12)	1.04 (.72)	.46	.16	1.80	7	3.95	.250	4.70	83.3	79.3	98.74
152	222					512 (284)	526 (292)	10.55 (7.27)	2.69 (1.85)	1.46	.32	3.23	7	2.21	.367	2.57	95.1	91.7	99.75
153	221					508 (282)	521 (289)	13.64 (9.40)	?	.20	.086	1.20	7	5.96	.500	6.90	75.0	73.7	101.91
154	192	Co-Ax	Shear	222 (50)	1.98								16.5		(No Data)				
254	193					480 (267)	513 (285)	8.96 (6.18)	3.09 (2.13)	0.49	0.00	1.93	3	3.90	.750	4.50	41.2	42.0	80.01
354	194		$(1/2\ \dot{W}_{He})^{(2)}$			481 (267)	514 (286)	9.23 (6.36)	3.39 (2.33)	0.50	0.00	1.95	3	3.86	.750	4.84	49.1	47.7	83.14
454	195		$(0\ \dot{W}_{He})^{(2)}$			482 (268)	513 (285)	9.22 (6.36)	3.29 (2.27)	.51	0.00	1.95	3	3.84	.375	3.77	41.8	49.6	77.62
155	196					483 (268)	512 (284)	7.07 (4.87)	5.02 (3.46)	1.23	0.00	3.03	3	2.46	.750	3.21	42.9	40.8	81.10
156	197					479 (266)	512 (284)	9.70 (6.69)	1.51 (1.04)	.22	0.00	1.29	3	5.83	.750	5.55	47.8	44.5	83.41
157	199		High Swirler			482 (268)	510 (283)	23.74 (16.37)	2.85 (1.97)	.51	.56	1.94	3	3.84	.576	4.49	94.9	91.5	99.81
158	198					491 (273)	512 (284)	18.36 (12.66)	4.71 (3.24)	1.14	.37	2.89	3	2.54	.750	1.85	39.1	39.4	85.53
159	200					481 (267)	511 (284)	25.61 (17.66)	1.29 (.89)	.22	.73	1.29	3	5.78	.750	7.11	94.1	89.8	99.96
160	201		Increased Shear		2.12	490 (272)	510 (283)	6.10 (4.20)	4.46 (3.08)	0.94	0.00	2.53	3	2.70	.750	3.91	56.8	49.9	87.99
260	202					482 (267)	510 (283)	9.63 (6.64)	5.20 (3.58)	0.46	0.00	1.78	3	3.90	.500 to .750	6.27	48.7	45.8	86.44
360	203					483 (268)	510 (283)	8.29 (5.72)	1.59 (1.09)	0.23	0.00	1.27	3	5.44	.750	8.02	44.5	45.3	85.31
161	179	Premix Triplet[3]	33%	66.7 (15)	0.99	510 (283)	530 (294)	40.32 (27.80)	37.51 (25.86)	.94	.94	3.70	3	3.93	.500	4.54	93.3	90.0	100.54
162	180					506 (281)	530 (294)	36.71 (25.31)	34.38 (23.72)	.93	.93	3.70	7	3.96	.750	4.28	93.8	88.8	100.09
163	181					507 (282)	530 (294)	36.66 (25.28)	34.26 (23.65)	.93	.93	3.70	15	3.96	.250	3.82	94.9	90.6	99.78
164	182					509 (283)	530 (294)	36.52 (25.18)	33.91 (23.37)	.93	.93	3.68	30	3.96	.750	5.04	95.3	91.1	99.81

TABLE III

SINGLE ELEMENT COLD FLOW TEST SUMMARY

Test No. (Units)	Run No.	Basic Elem.	Variation	F/E N (lb_f)	A_f/A_o	T_o °R / °K	T_o °R / °K	ΔP_{OJ} psi (N/cm^2)	ΔP_{FJ} psi (N/cm^2)	$\dot{W}_f V_f / \dot{W}_o V_o$	Normal Ax. Mom.	V_f/V_o	L/D	O/F	$\bar{R}$	$(O/F)_I$	E_m	η_m	% C*
165	183	Premix Triplet	(3) 33%	66.7 (15)	0.99	515 (286)	530 (294)	56.37 (38.87)	68.35 (47.16)	3.70	3.70	7.30	7	1.97	.749	2.26	92.4	86.5	99.64
965	184	↓	↓	↓	↓	510 (283)	530 (294)	56.95 (39.27)	69.27 (47.76)	3.68	3.68	3.68	3	1.99	.750	1.99	88.8	83.5	95 43
166	185	↓	↓	↓	↓	496 (276)	530 (294)	32.77 (22.59)	25.28 (17.43)	.36	.36	2.33	3	6.44	.250	6.13	96.6	95.2	99.34
168	191	Premix Pentad	33%	↓	↓	502 (279)	530 (294)	38.94 (26.85)	36.09 (24.88)	.94	.94	3.73	30	3.96	.750	5.70	94.0	89.9	99.78
														(Lower Limit: only 3 wide O/F Points Avg'd. $P_D \neq 0$)					
169	189	↓	↓	↓	↓	501 (278)	530 (294)	39.24 (27.06)	36.28 (25.01)	.94	.94	3.73	7	3.97	.625	4.77	93.0	91.7	99.87
170	190	↓	↓	↓	↓	502 (279)	530 (294)	38.82 (26.77)	35.92 (24.77)	.95	.95	3.74	15	3.95	.750	4.51	98.1	96.6	99.99
171	188	↓	↓	↓	↓	499 (277)	530 (294)	40.33 (27.81)	38.00 (26.20)	.95	.95	3.75	3	3.97	.595	4.21	92.3	88.3	100.30
172	187	↓	↓	↓	↓	506 (281)	530 (294)	58.92 (40.63)	65.85 (45.40)	3.73	3.73	7.40	3	1.98	.375	1.98	93.1	89.5	97.98
173	186	↓	↓	↓	↓	506 (281)	530 (294)	32.56 (22.45)	26.19 (18.06)	.36	.36	2.31	3	6.35	.250	7.57	91.3	89.5	101.35

(1) High and low swirler have tangential to axial velocity components (V_T/V_A) = 1 and .5, respectively.

(2) These tests were conducted with decreased H_e bleed flow.

(3) % Designation signifies fuel slot width to oxidizer orifice dia. W_g/D_o.

(4) Impingement angle is total included angle.

TABLE IV

SUMMARY OF DESIGN AND OPERATING EFFECTS ON MIXING EFFICIENCY

E_m Influence

	Coax	Swirler	Increased Shear	Premix	Doublet	Parallel	Triplet
Increasing F/E	D	M	D	D	D	D	D
Increasing A_f/A_o	D	M	D	M	I	NT	M
Increasing L/D	I	I	I	I	I	I	I
Increasing O/F	D	O	D	M	I	I	M
Increasing Prop. Temp.	D	I	D	I	NT	D	NT
Increasing Spacing	NA	NA	NA	NA	M	NT	NA
Increasing Impingement Angle	NA	NA	NA	NA	NT	NA	M
Increasing Orifice Width	NA	NA	NA	M	NT	NT	NT
Increasing Swirl	NA	I	NA	NT	NA	NA	NA

I Indicates increasing E_m

D Indicates decreasing E_m

M Indicates a maximum or minimum in E_m

O Indicates no influence

NT Not tested

NA Not Applicable

The swirl coaxial and premix designs are insensitive to area ratio influences, an effect that was somewhat surprising for the premix case. Cold flow testing by ALRC on an element design similar to the premix triplet design revealed that mixing efficiency was significantly impacted by orifice geometry changes; see Reference 10 for these data. Although the single-element injectors of both these series were similar, two important geometry differences are evident. The mixing cup length of the element tested on this program was significantly longer than that of Reference 10. For this program, cup depths ranged from 1.15 to 4.75 L/D, where L is the cup depth and D is the oxidizer hole diameter. For the program of Reference 10, the ratio, on the same basis, was 0.1. The increased mixing cup depth forces mixing and therefore attenuates the effects of area ratio and mixture ratio (momentum ratio) variations. In addition this program only investigated rectangular fuel slots while the data of Ref. 10 was obtained with a fuel slot geometry that was similar to a capital "I" in cross section.

Referring again to Figure 11, note the very sensitive external impinging triplet orifice area ratio influences, where the element optimized at an A_f/A_o of 1.25. This element type, in general, is sensitive to most geometry and hydraulic variations and a designer must pay particular attention to the design parameters in order to obtain an optimum design.

The effect of mixture ratio on E_m is illustrated in Figure 11 as well. Again, the swirl coaxial and premix designs are relatively insensitive to this influence, while the shear coaxial element decreases in efficiency as a function of increasing mixture ratio (less ΔV). The remaining elements were found to be insensitive to variations in mixture ratio.

Detailed parametric curves of data obtained from the coaxial family of elements are illustrated in Figures 12 through 15. Included in this family are the coaxial, increased shear coaxial, and swirl coaxial elements. Figure 12 compares these elements on a length basis (L/D) (D is the oxidizer tube diameter), a mixture ratio basis, and a propellant temperature basis. The effect of increased shear area and swirl is to increase mixing efficiency. Increased surface area does promote increased mixing as illustrated by the increased shear element E_m data. Radial transport of oxidizer by swirling forces mixing when compared to simple coaxial mixing element. When compared on a mixture ratio basis, the swirl coaxial shows no influence and the shear and increased shear coaxial exhibit decreasing efficiency with increasing mixture ratio. This effect is due to a decreased ΔV influence. The effect of lower propellant temperature on E_m is shown in Figure 12 as well. With the exception of the swirler data, E_m increases with decreasing temperature. This trend is contrary to hot-fire data generated with 1500 lbf thrusters on Contract NAS 3-14352, (Ref. 11), which indicated a slight reduction in performance when tested with cold propellants. The contrary temperature effect noted in hot testing may be influenced by the combustion influence on the mixing/reaction process.

The effects of area ratio (or fuel annulus width) for these elements are illustrated in Figure 13 as a function of thrust/element. In general, decreasing fuel to oxidizer orifice area ratio is in the direction of increased E_m for the three coaxial type elements; again indicating the influence of ΔV. The swirl coaxial data in Figure 13 indicate an optimum in thrust size at approximately 67 Newtons/element (15 lbf/element). This indicates that the radial component of momentum and the physical size are related, or that there is a fuel momentum to oxidizer radial momentum ratio which produces optimum mixing. The effect of swirl magnitude for various area ratio elements is illustrated in Figure 14. These data indicate that large changes in mixing efficiency can be obtained with a rather moderate amount of oxidizer radial momentum, $V_t/V_a = 0.5$).

The compatibility characteristics of the three shear elements are indicated in Figure 15, where the coaxial and swirl coaxial elements are compared in Figure 15a. In the near zone (close to the injector face) the coaxial element is fuel rich as compared to the swirler. This effect was noted in combustion testing of full-scale hardware in Contract NAS 3-14354 where the near zone heat flux using a swirler element was higher than the equivalent coaxial element, Ref. 12. Combustion data generated during this contract, discussed in a later section, also supports this observation. As a function of A_f/A_O, the coaxial element becomes more fuel-rich with increasing area ratio (see Figure 15c). This fuel rich boundary is reflected in the low E_m data for this element, which was previously discussed. It is interesting to note however that as the E_m improves (lower A_f/A_O) the compatibility decreases. In general, this characteristic is universal, i.e., those elements that exhibit high potential compatibility do so at the expense of a low mixing rate.

An equivalent data set for the premix designs is illustrated in Figures 16 through 18. With the exception of length, shown on Figure 16, premix elements are relatively insensitive to design and operating variables. For all variables investigated, resulting E_m was approximately 90% or higher. Referring to Figures 16 and 17, note a decrease in E_m with increasing thrust/element for both the pentad and triplet; a slight decrease in E_m with temperature and a small effect of mixture ratio on E_m. However, all these influences are minor, which indicates that premix elements can run over a wide range of engine conditions without suffering a serious performance penalty. As discussed earlier, however, the fact that they are insensitive is somewhat surprising and can be attributed to the fact that the mixing cup depths used on this program attenuate the expected response to variations in design and operating conditions.

The premix element compatibility variations, illustrated in Figure 18, are not negligible as demonstrated by the large differences in maximum and minimum local O/F. This condition indicated a potential chamber wall streaking problem. Note, for the premix triplet, Figure 18b, that increasing the element width ratio tended to stratify the flow field. This

can be explained by considering the geometry of the injector pattern. For a narrow fuel slot width, the available fuel momentum is concentrated on the center of the oxidizer stream, penetrating the bulk of the oxidizer resulting in a homogenous flow field. As the penetration is reduced by broadening the fuel slot, the fuel momentum is insufficient at the center of the oxidizer stream. The net effect is to form a flow field edge condition that is alternately fuel and oxidizer rich at $\pi/2$ rad (90°) intervals. The pentad element does not appear to streak as readily because the available momentum of any one fuel stream is only half of the equivalent premix triplet element. In no case did the pentad completely penetrate the oxidizer stream and, in general, always tended to result in unmixed flow rather than completely penetrate and mix with the oxidizer. The streaking characteristics of the A_f/A_o = 1.0 triplet element can be attenuated by reducing the total fuel momentum with larger fuel orifice area, as illustrated in Figure 18c.

Data similar to those presented earlier for the premix and shear designs are found for the like doublet element in Figures 19 and 20. Particular attention should be directed at Figure 19 where the element spacing effects are parametrically illustrated. These data indicate that an optimum is found at a fuel to oxidizer spacing of approximately 0.25 cm (0.1 in.). Element spacing lower than the optimum have lower mixing efficiency because the primary fans interact strongly forming secondary fans. These fans are nonhomogenous in nature, with fuel on one side of the fan and oxidizer on the other. When the doublet spacing is larger than the optimum value, complete mixing is prevented because the elements are too far apart. Compatibility of this element, as shown in Figure 20 was not good since large circumferential variations in O/F or streaks were measured. This result was caused by testing a single pair of oxidizer and fuel elements. Multi-element injectors should attenuate some of this unmixed flow.

Data for the parallel sheet elements are found in Figures 21 and 22. Mixing efficiency as a function of length, thrust/element, and propellant temperature is shown in Figure 21, compatibility in Figure 22. Like the other elements investigated, mixing efficiency increases with length and decreases with F/E. As a function of O/F, the data indicates an increase in mixing efficiency, contrary to the trend of the similar coaxial element. Compatibility effects are similar to those observed with the doublet element: wide O/F variations with $(O/F)_{wall}$ depending on which side the element is probed. Again, some attenuation of this effect would be expected in a multiple element configuration.

The external impinging F-O-F triplet data are depicted in Figures 23 and 24. In general, this element configuration is very sensitive to all operating and geometry variables. Figure 23 displays mixing efficiencies for various impingement angles and area ratios as a function of thrust/element. At the 67 N (15 lbf) level, the extreme sensitivity of mixing efficiency with impingement angle is noted. One also notes that area ratio influences are optimized in the 1.0 to 1.25 A_f/A_o range. Referring to Figure 23b note that

the A_f/A_o = 1.0 mixing efficiency increases dramatically with impingement angle. Inspection of the detailed flow field reveals that, as the radial momentum component is increased by increasing the impingement angle, increased penetration of the axial oxidizer jet occurs, thus yielding a more homogenous flow field. However, for the area ratio = 0.50 data, a contrary trend is noted. In this case, overpenetration is achieved and increasing the impingement angle only amplifies the excess penetration of the fuel. Mixing was also determined to be a strong function of mixture ratio coupled with impingement angle as shown in Figure 23d. On the fuel-rich side of the optimum, overpenetration occurred; on the oxidizer-rich side, under-penetration occurred.

In general, the compatibility of this element was expected to be poor. Figure 24 indicates the degree and magnitude of the potential compatibility problem for the overpenetrated oxidizer jet. The entire flow field boundary is higher in O/F than the nominal with a large composition variance in the circumferential direction.

B. MULTIPLE ELEMENT COLD FLOW

As an integral part of the cold flow program, three prototype injection elements were flowed in a multiple element test configuration (four elements). The intent of this testing was to generate information that would allow evaluation of interelement mixing effects. The three injection elements were 67 Newton (15 lbf) thrust shear coaxial, swirl coaxial, and premix triplet configurations. These elements are illustrated in Figure 9. They are arranged in a square injection matrix as shown in that figure. Testing was conducted as outlined in Appendix B and was essentially identical to the technique used in single element testing. The reduced data and test conditions are tabulated by test number in Table V. The first sixteen tests were conducted with the shear coaxial element, tests 17 to 32 were with the swirl coaxial, and the remainder of the tests were with the premix triplet element. Included in this table are both the single element and multiple element mixing efficiencies.

The single element and multiple element data for the shear coaxial element are compared in Figure 25. The data in this figure represent identical test points for both the single and multiple element testing. Inspection of Figure 25b, c, and d indicates that a dramatic increase in mixing efficiency occurred when multiple elements were used. However, two observations run counter to this conclusion. The first is shown in Figure 25 where the data show that element spacing influenced E_m only slightly during the multiple element testing. In fact, as the element-to-element distance is increased (from Row A to Row C), the apparent multiple element mixing efficiency increased. If element proximity tends to increase mixing, then an increase in element-to-element distance should decrease the relative mixing efficiency - an effect not noted. The second observation was that a large amount of recirculation occurred between the elements. Flow apparently was coming from the far downstream region. In this region, the flow is well mixed which, when recirculated to the near field and sampled, would produce an apparent increase in mixing efficiency.

TABLE V

GAS/GAS MULTIPLE ELEMENT COLD FLOW DATA SUMMARY

Test	Element	O/F	L/D	Row	$E_{m_{ME}}$	$E_{m_{SE}}$	$N_{m_{ME}}$	$N_{m_{SE}}$
1	Shear Coax	4	3	A	86.9	47.8	78.4	58.0
2		4	7	A	93.0	72.1	86.9	62.9
3		4	15	A	95.4	96.5	91.3	94.3
4		2	3	A	87.5		79.6	
5		6	3	A	81.3		72.7	
6		2	7	A	95.7	82.4	91.9	75.7
7		6	7	A	90.1	55.4	82.9	52.0
8		2	15	A	97.0		94.3	
9		6	15	A	95.8		92.0	
10		6	7	C	95.6	55.4	92.0	52.0
11		6	7	C				
12		2	7	C	96.7	82.4	93.8	75.7
13		2	7	C				
14		4	7	B	93.2	72.1	87.5	62.9
15		4	7	B				
16	Shear Coax	4	7	A	93.2	72.1	87.6	62.9
17	Swirl Coax	4	3	A	95.0	92.5	90.6	87.4
18		4	7	A	95.3	98.2	91.2	97.1
19		4	15	A	96.0	98.5	92.6	97.6
20		2	3	A	97.3		94.8	
21		6	3	A	97.1		94.5	
22		2	7	A	95.1	95.6	90.7	92.9
23		6	7	A	97.6	96.9	95.5	95.5
24		2	15	A	95.5		91.6	
25		6	15	A	97.1		94.4	
26		6	7	C	96.1	96.9	92.8	95.5
27		6	7	C				
28		2	7	C	88.7	95.6	81.6	92.9
29		2	7	C				
30	Swirl Coax	4	7	B	95.0	98.2	90.7	97.1

Test	Element	O/F	L/D	Row	$E_{m_{ME}}$	$E_{m_{SE}}$	$N_{m_{ME}}$	$N_{m_{SE}}$
31	Swirl Coax	4	7	B				
32	Swirl Coax	4	7	A	98.1	98.2	96.3	97.1
33	Premix Trip.	4	3	A	97.7	87.7	95.5	83.9
34		4	7	A	96.9	94.0	94.1	89.8
35		4	15	A	98.3	98.3	96.8	97.6
36		2	3	A	96.3		92.9	
37		6	3	A	94.6		89.9	
38		2	7	A	95.5	88.4	91.7	82.3
39		6	7	A	97.2	96.3	94.8	93.4
40		2	15	A	97.5		95.2	
41		6	15	A	97.6		95.6	
42		6	7	C	95.3	96.3	91.4	93.4
43		6	7	C				
44		2	7	C	96.0	88.4	92.6	82.3
45		2	7	C				
46		4	7	B	98.0	94.0	96.2	89.8
47		4	7	B				
48		4	7	A	98.0	94.0	96.2	89.8
49		2	3	A				
50(1)		4	3	A	97.2	87.7	94.6	83.9
51(1)	Premix Trip.	6	3	A	95.1		90.7	

* Not Run

(1) Tangential Fuel Slots

Some insight into this recirculation mechanism was gained by looking at the element centerline oxidizer concentration data. This was done by inputting, the multiple element design parameters and operating conditions into the single element cold flow mixing computer program. It was found that the single element model provided an excellent prediction of the multiple element fuel and oxidizer element centerline mass fraction composition (mixture ratio) and axial mixing distributions. This implied that multiple element mixing rates were much closer to the single element mixing rates than the higher experimental E_m's indicated.

In addition, it was noticed that the multiple element test integrated mass factors were significantly higher than unity, indicating gross recirculation occurring between the multiple elements. To adjust the data for this influence, it was assumed that the recirculation gases flowing between the elements would come from downstream and consist of essentially uniformly mixed gases (E_m = 100%). Then by the definition of E_m, the corrected E_m is:

$$E_m, \text{ ME} = 100 \left\{ 1 - \sum_{i=1}^{n} \frac{\dot{w}_i}{\dot{w}_t} \left[\frac{O/F - O/F_i}{O/F\ (1+O/F_i)} \right] - \sum_{j=n}^{n} \left[\frac{\dot{w}_j}{\dot{w}_t} \quad \frac{O/F_j - O/F}{1 + O/F_j} \right] \right\} \quad (3)$$

it can be shown that the corrected

$$E_m, \text{ ME} = 100 - \frac{\dot{w}_{int}}{\dot{w}_{inj}} \left[100 - E_m, \text{ ME, Meas} \right] \quad (4)$$

Results from this data re-evaluation for the multiple shear coaxial elements test are summarized in Table VI. The measured multiple element mixing efficiencies are shown for each of the test conditions evaluated. The "mass integration" column in Table VI Σ_{mass}, represents the ratio of the integrated mass flowrate over the entire flow field divided by the injected mass flowrates. This factor is approximately 4 except for two tests. Thus, a constant factor of 4 was used as the mass integration factor for all tests to determine the corrected multiple element mixing efficiency. Where the data is available, the comparable single element mixing efficiency (E_m, SE) also is tabulated in Table VI. A comparison of both raw and corrected multiple element vs single element E_m's are shown graphically in Figure 26. The E_m, ME vs E_m, SE is the data previously mentioned in Table V and Figure 25. When corrected for the mass integration (recirculation) factor the multiple element mixing efficiency is comparable to the single element data. Thus, it was concluded that when recirculation effects are compensated for there is no significant effect of multiple element interactions in comparison to single element mixing.

TABLE VI

MULTIPLE SHEAR CO-AX ELEMENT COLD FLOW SUMMARY
BASED ON RECIRCULATED DOWNSTREAM GASES

O/F	L/D	Row	$E_{m,\ ME}$	$\sum$ Mass	$4(100-E_{m,\ ME})$	Corrected $E_{m,\ ME}$	$E_{m,\ SE}$
2	3	A	87.53	3.99	49.9	50.1	-
2	7	A	95.68	3.47	17.3	82.7	82.4
2	7	C	96.67	9.60	13.3	86.7	82.4
2	15	A	96.97	3.15	12.1	87.9	-
4	3	A	86.88	4.43	52.4	47.6	47.8
4	7	A	92.95	4.43	28.2	71.8	72.1
4	7	A	93.15	3.56	27.4	72.6	72.1
4	7	B	93.18	7.78	27.3	72.7	72.1
4	15	A	95.40	3.92	18.4	81.6	96.5
6	3	A	81.31	3.65	74.8	25.2	-
6	7	A	90.09	3.41	39.7	60.3	55.4
6	7	C	95.17	12.46	19.3	80.7	55.4
6	15	A	95.77	4.39	16.9	83.1	-
6	15	A	96.03	3.13	15.9	84.1	-

$$\text{Corrected } E_{m,\ ME} = 100 - 4\ (100 - E_{m,\ ME})$$

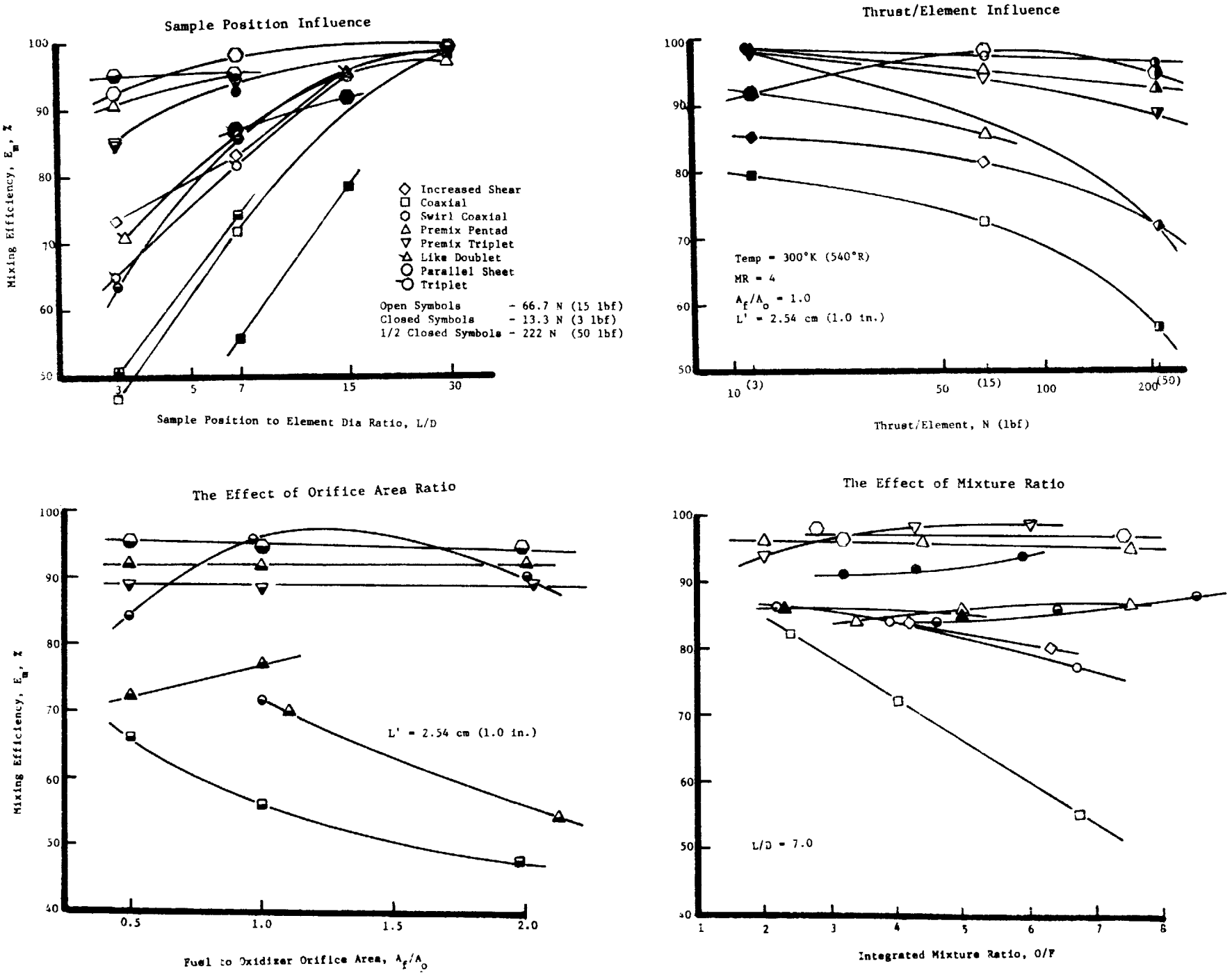

Figure 11. Effect of Design Parameters on Em

The Effect of Temperature on Mixing Efficiency

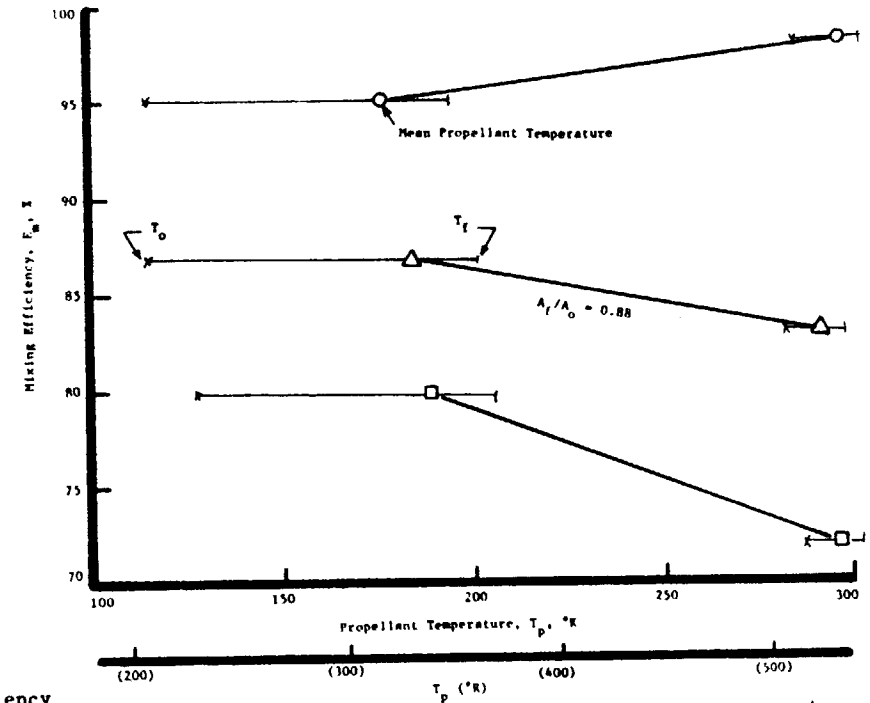

Defined by $\bar{T} \left[\dot{w}_o C_{p_o} T_{ox} + \dot{w}_f C_{p_f} T_f\right] / \left[\dot{w}_o C_{p_o} + \dot{w}_f C_{p_f}\right]$

□ Coaxial
△ Increased Shear
○ V_T/V_A = 1.0 Swirl Coaxial
● V_T/V_A = 0.5 Swirl Coaxial

Effect of Length on Mixing Efficiency

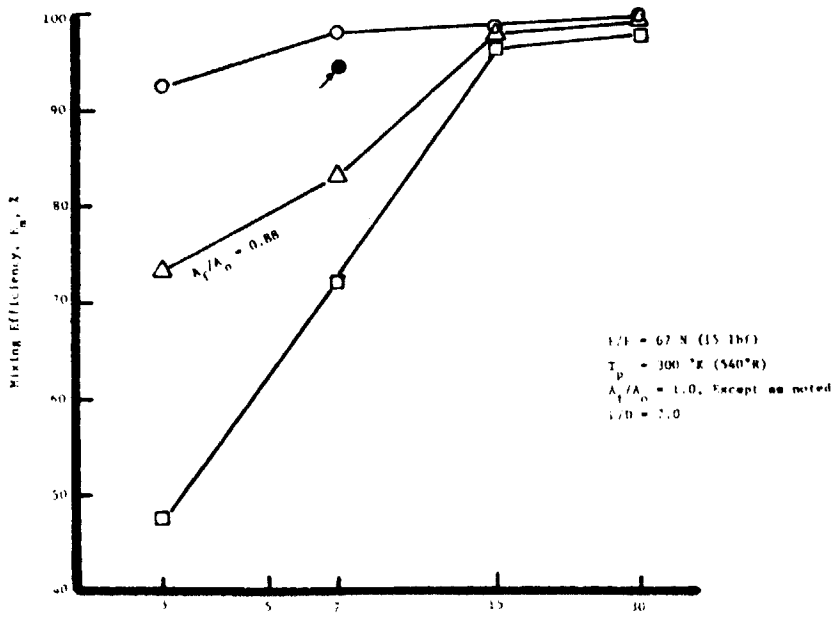

Effect of Mixture Ratio on Mixing Efficiency

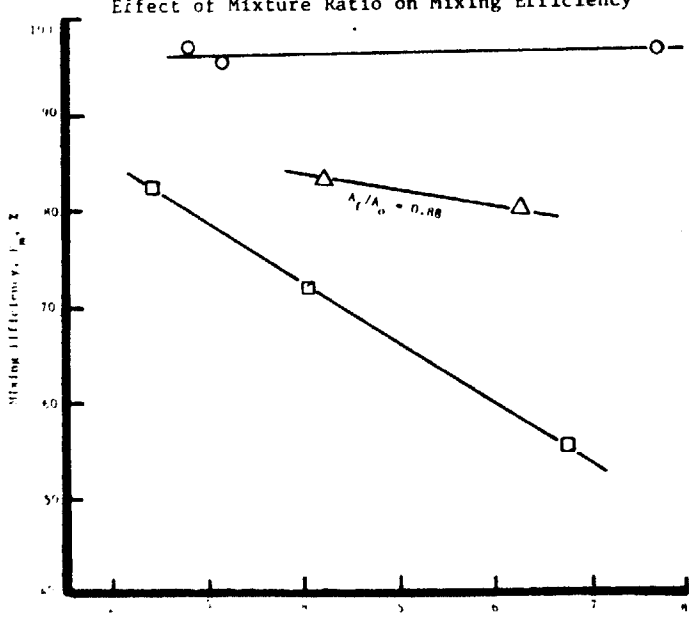

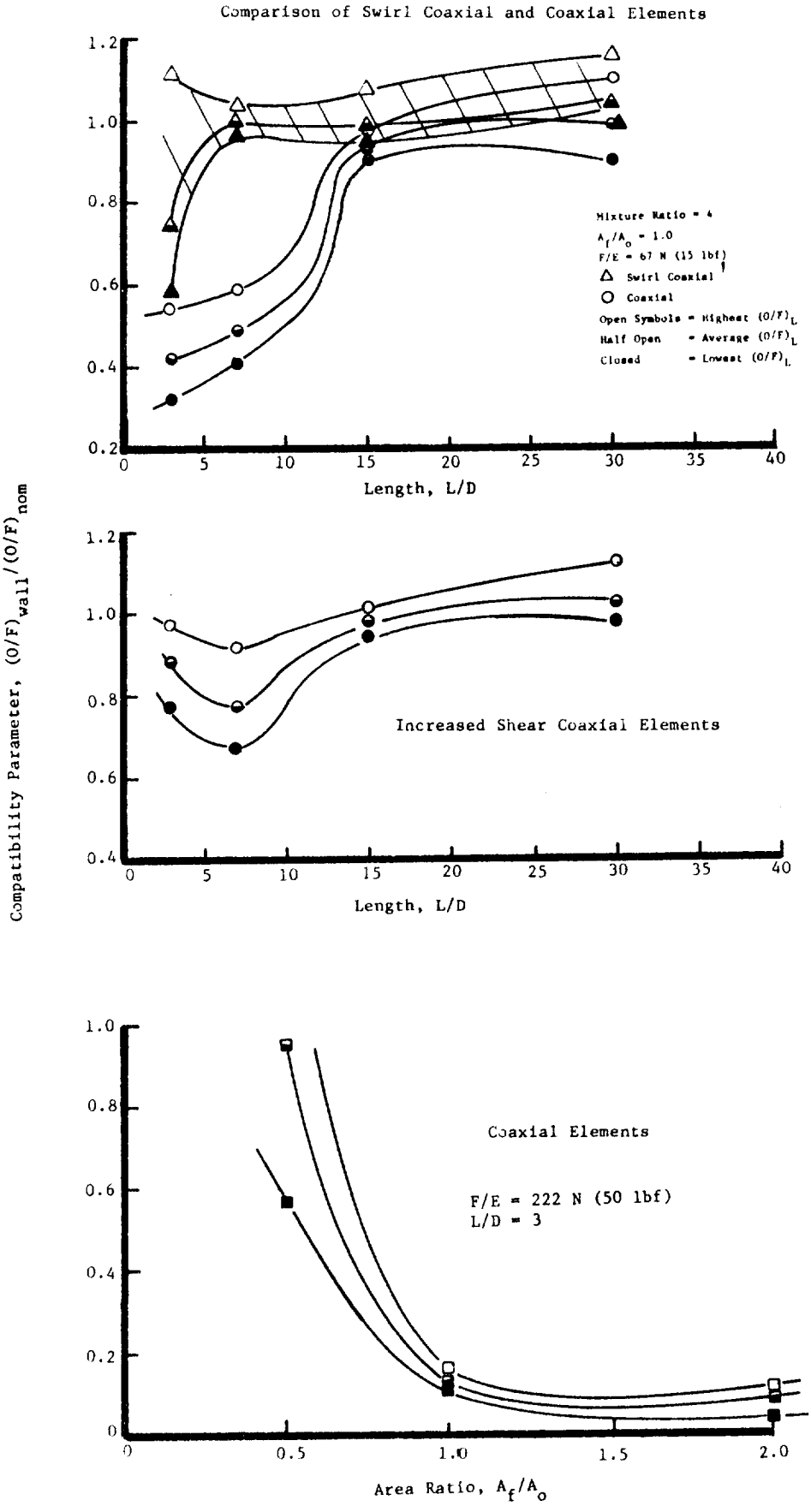

Figure 15. Compatibility Characteristics of Shear Mixing Elements

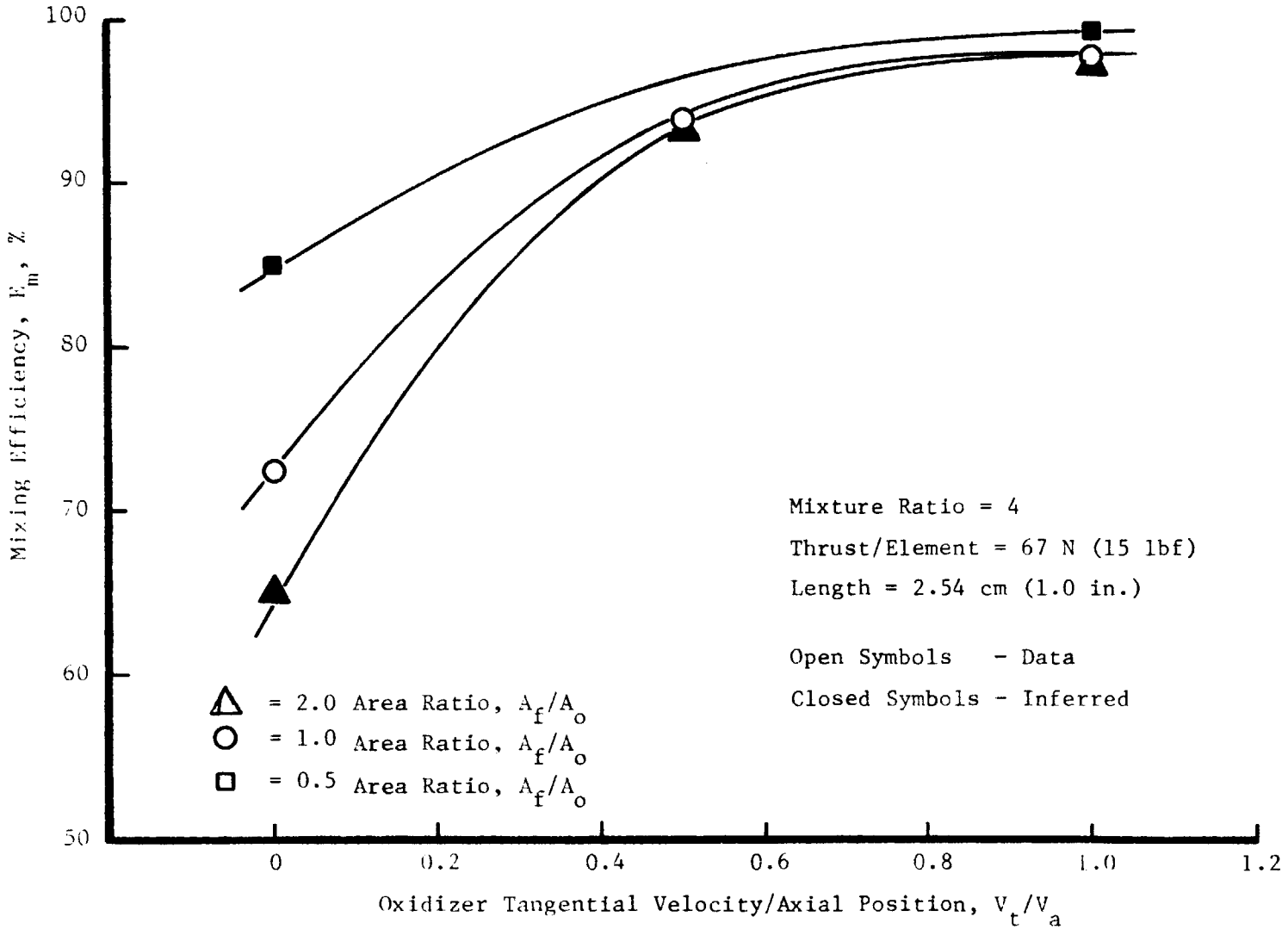

Figure 14. The Effect of Oxidizer Swirl on Mixing Efficiency

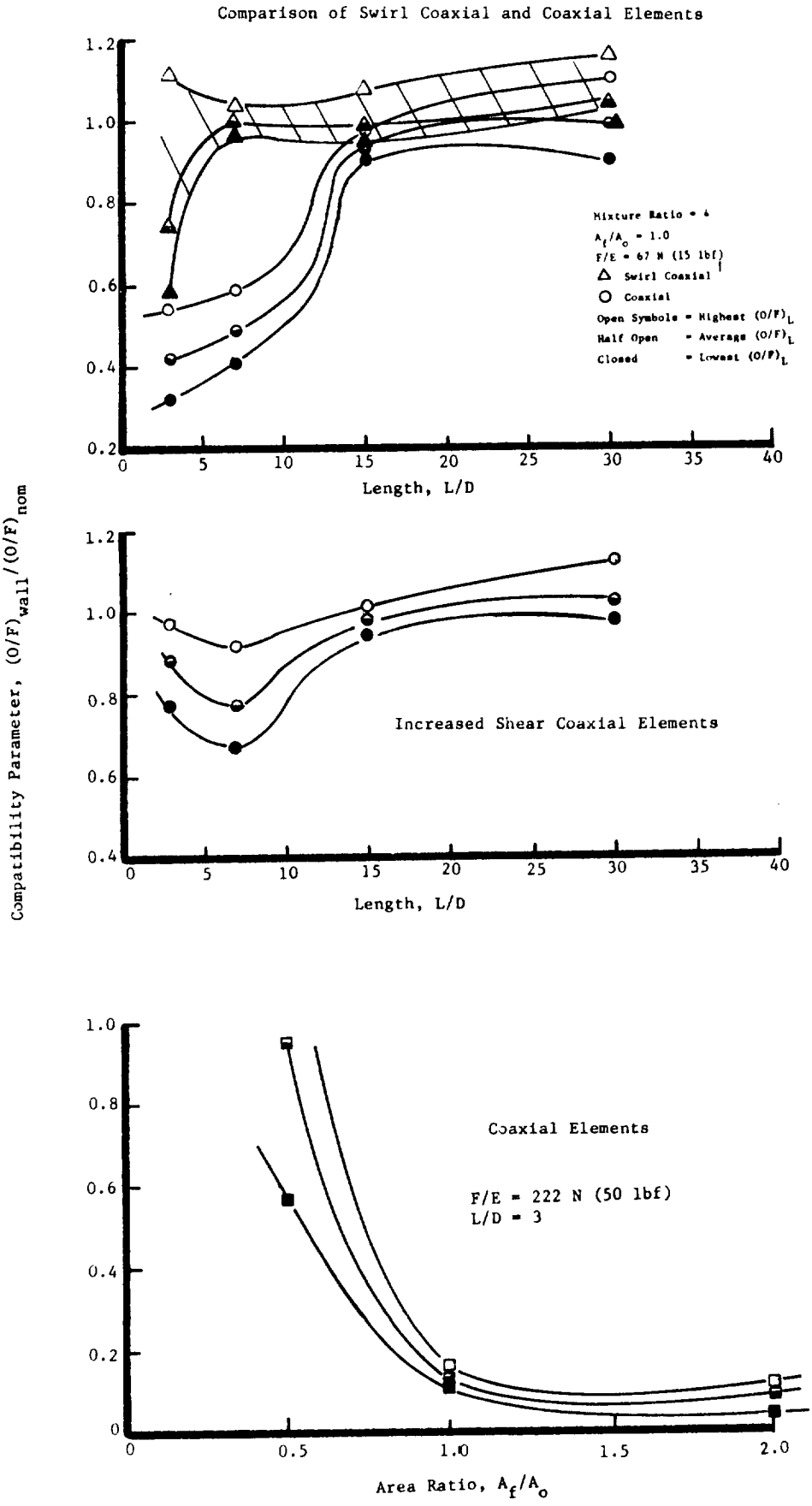

Figure 15. Compatibility Characteristics of Shear Mixing Elements

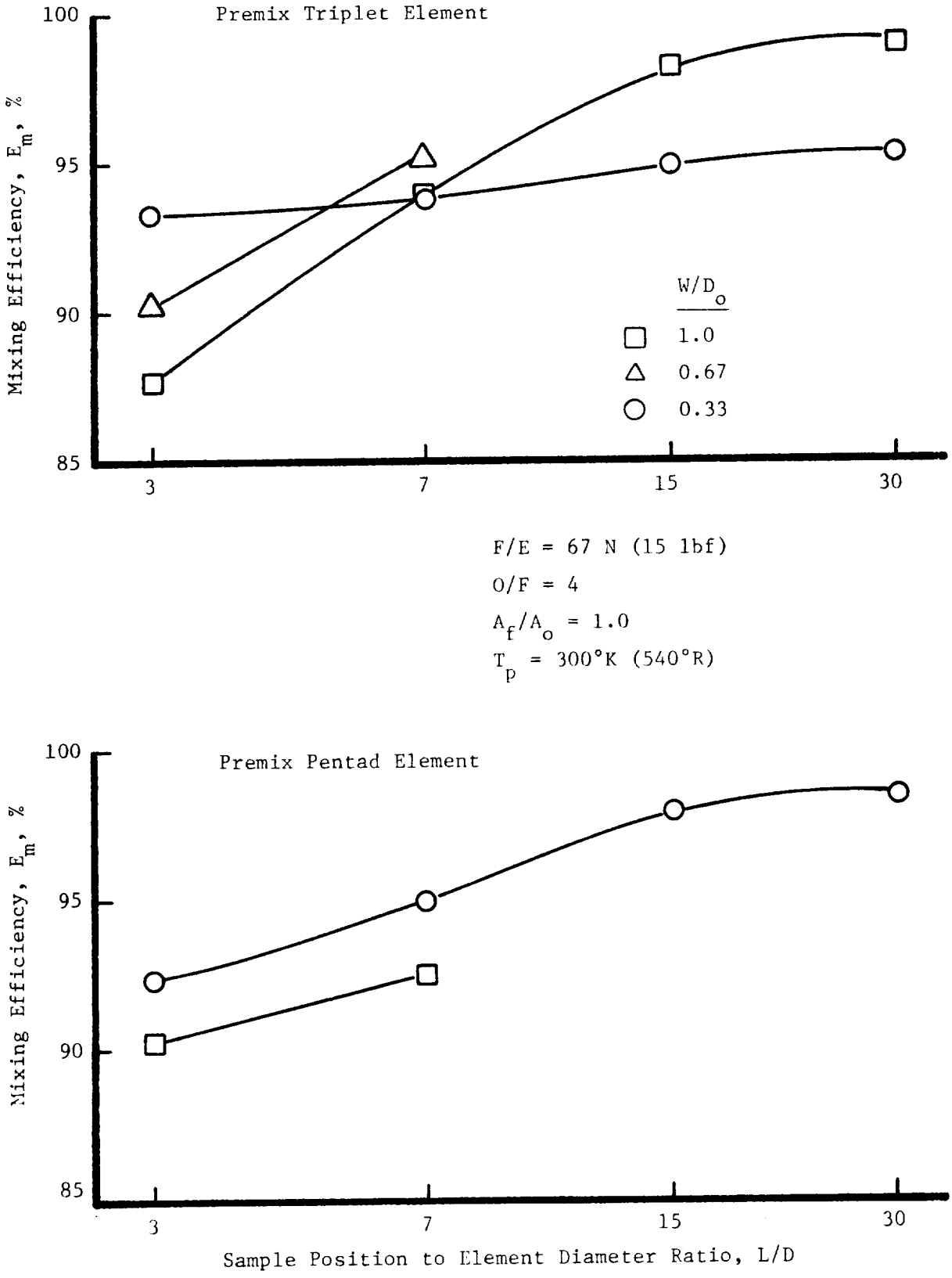

Figure 16. The Effect of Length on Mixing Efficiency for Premix Elements

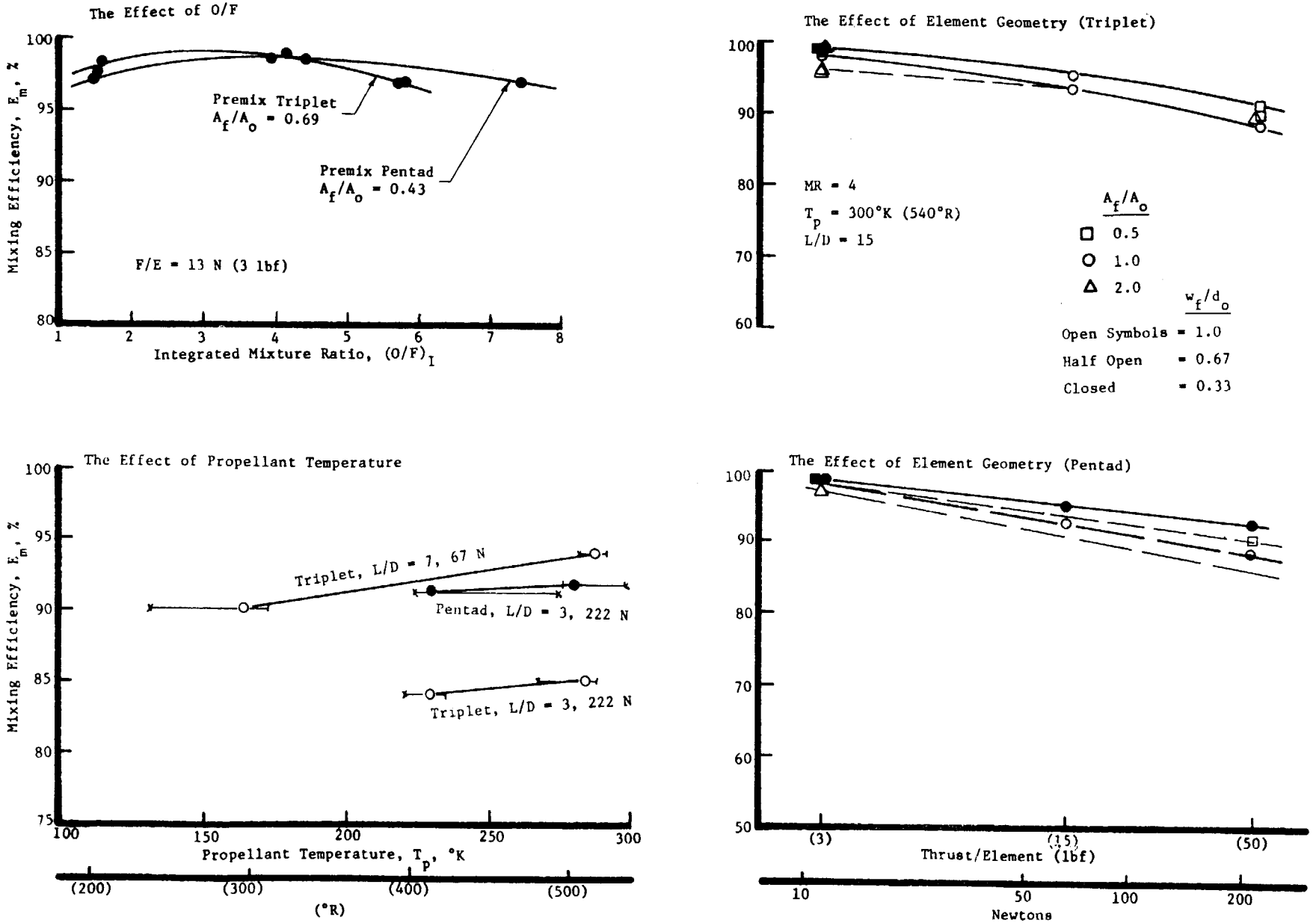

Figure 17. The Parametric Influence of Various Design Variables on the Mixing Efficiency on Premix Triplet and Pentad Elements

The Effect of Length on Compatibility

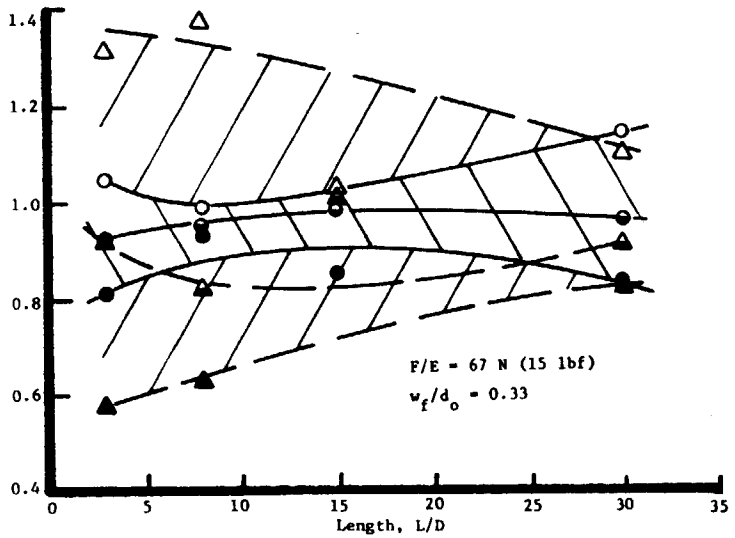

The Effect of Element Area Ratio on Compatibility

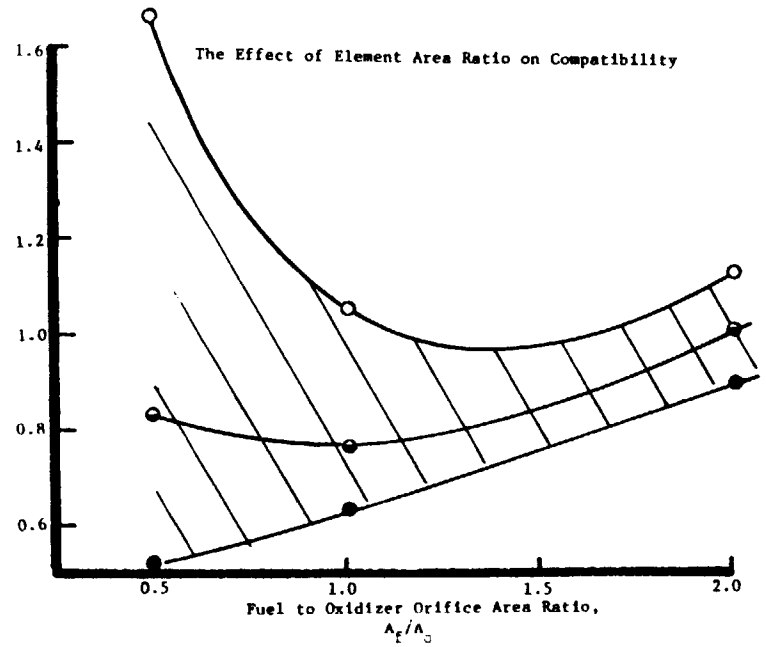

The Effect of Orifice Geometry on Compatibility

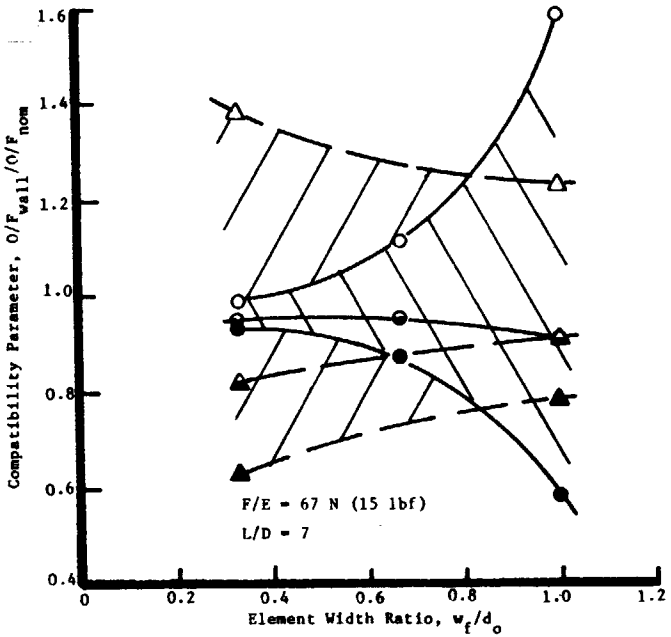

Mixture Ratio = 4

A_f/A_o = 1.0

T_p = 300°K (540°R)

○ Triplet

△ Pentad

Open Symbols = Higheat $(O/F)_t$

Half Open = Average $(O/F)_t$

Closed = Lowest $(O/F)_t$

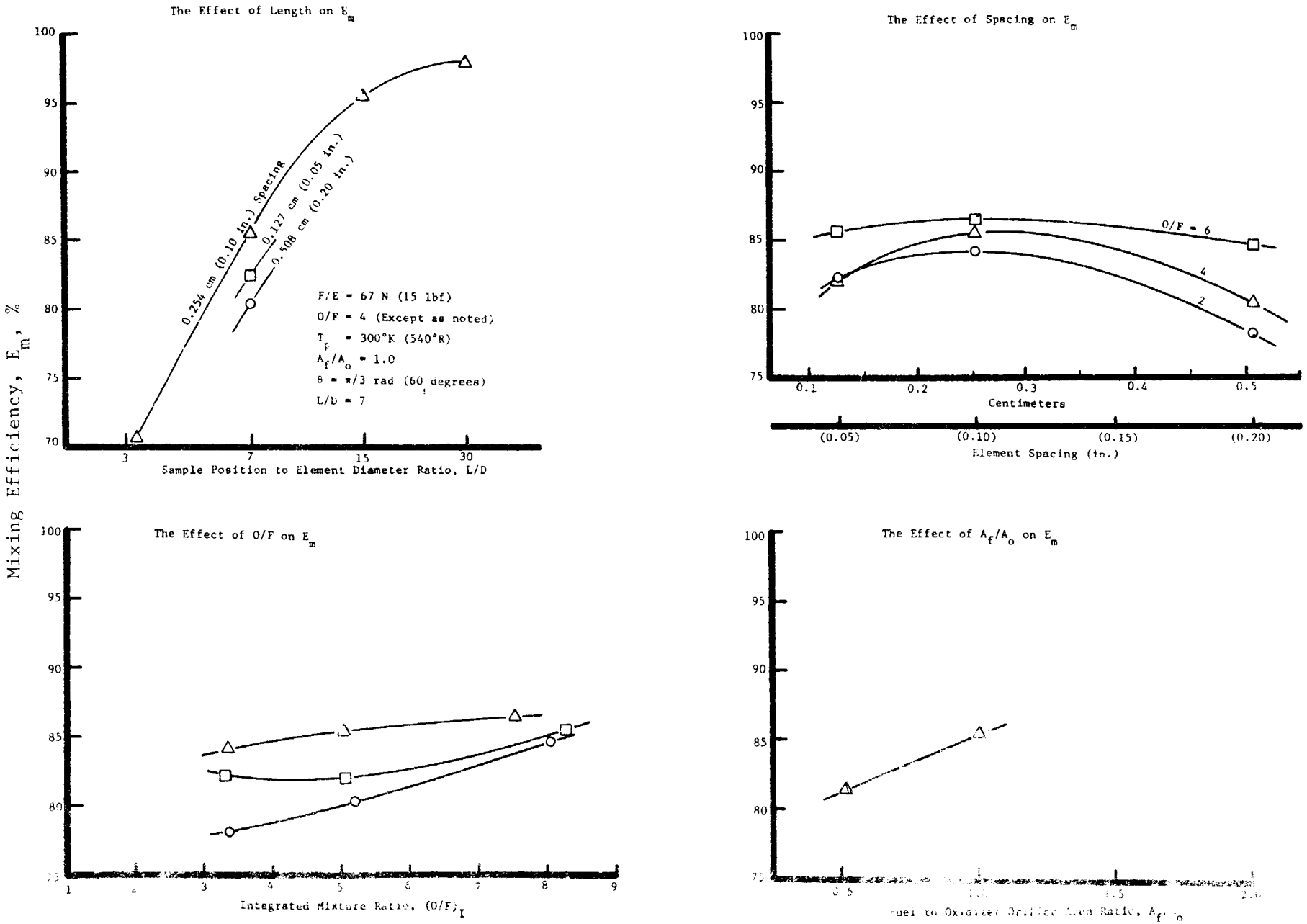

Figure 19. Doublet Element Mixing Efficiency

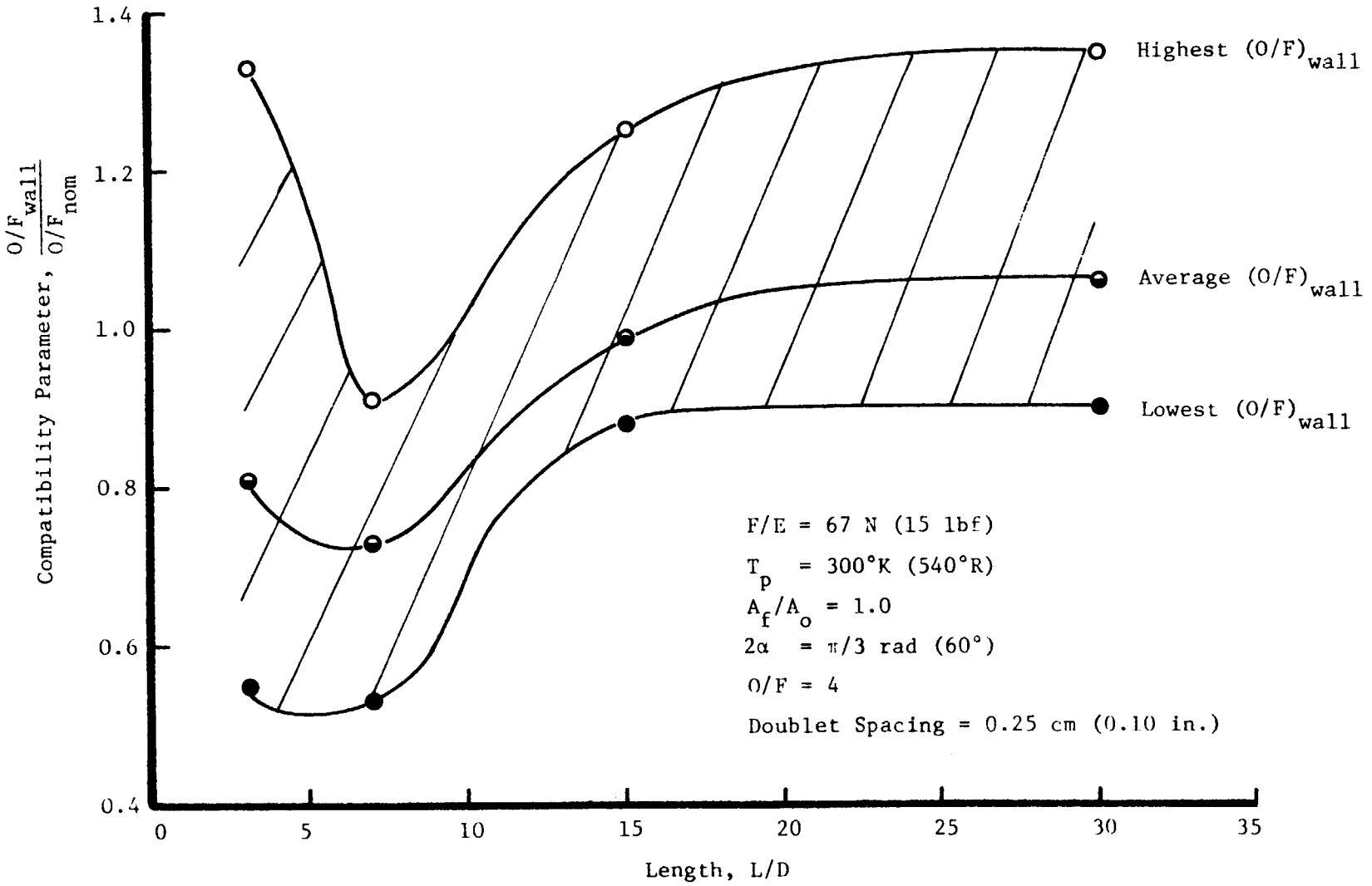

Figure 20. Compatibility of a Like Doublet

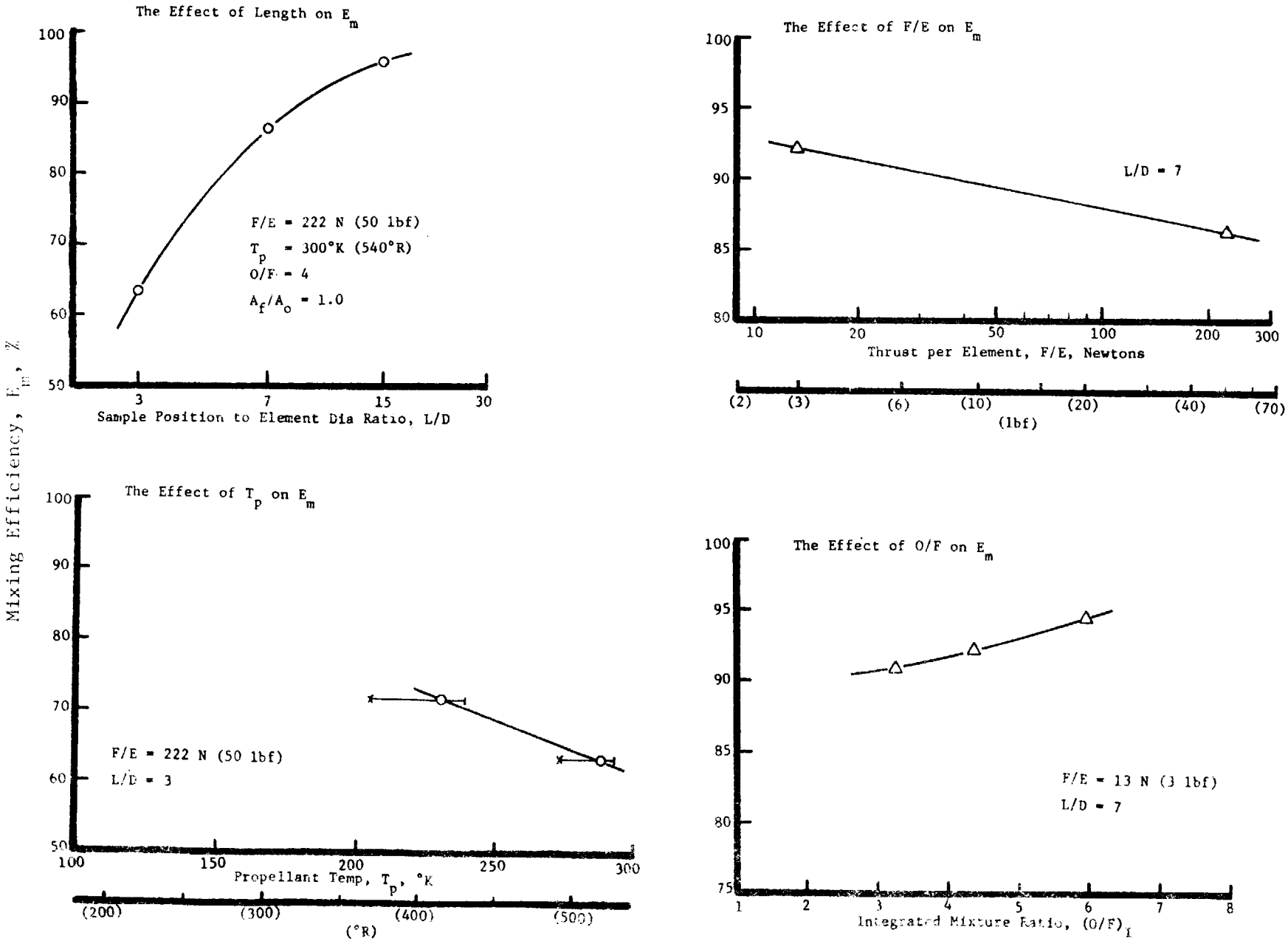

Figure 21. Parallel Sheet Element Mixing Efficiency for Various Test Conditions

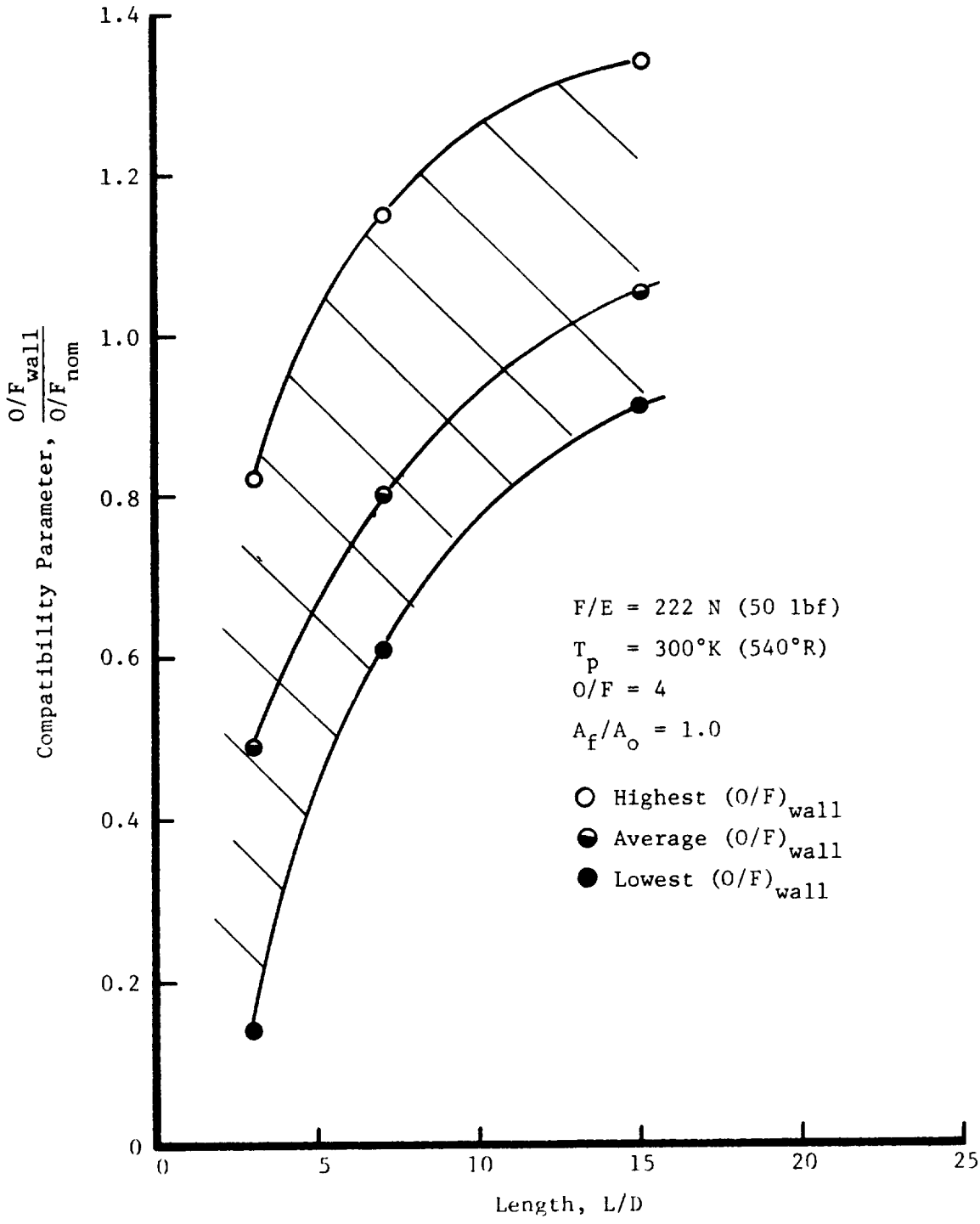

Figure 22. Compatibility of Parallel Sheet Element

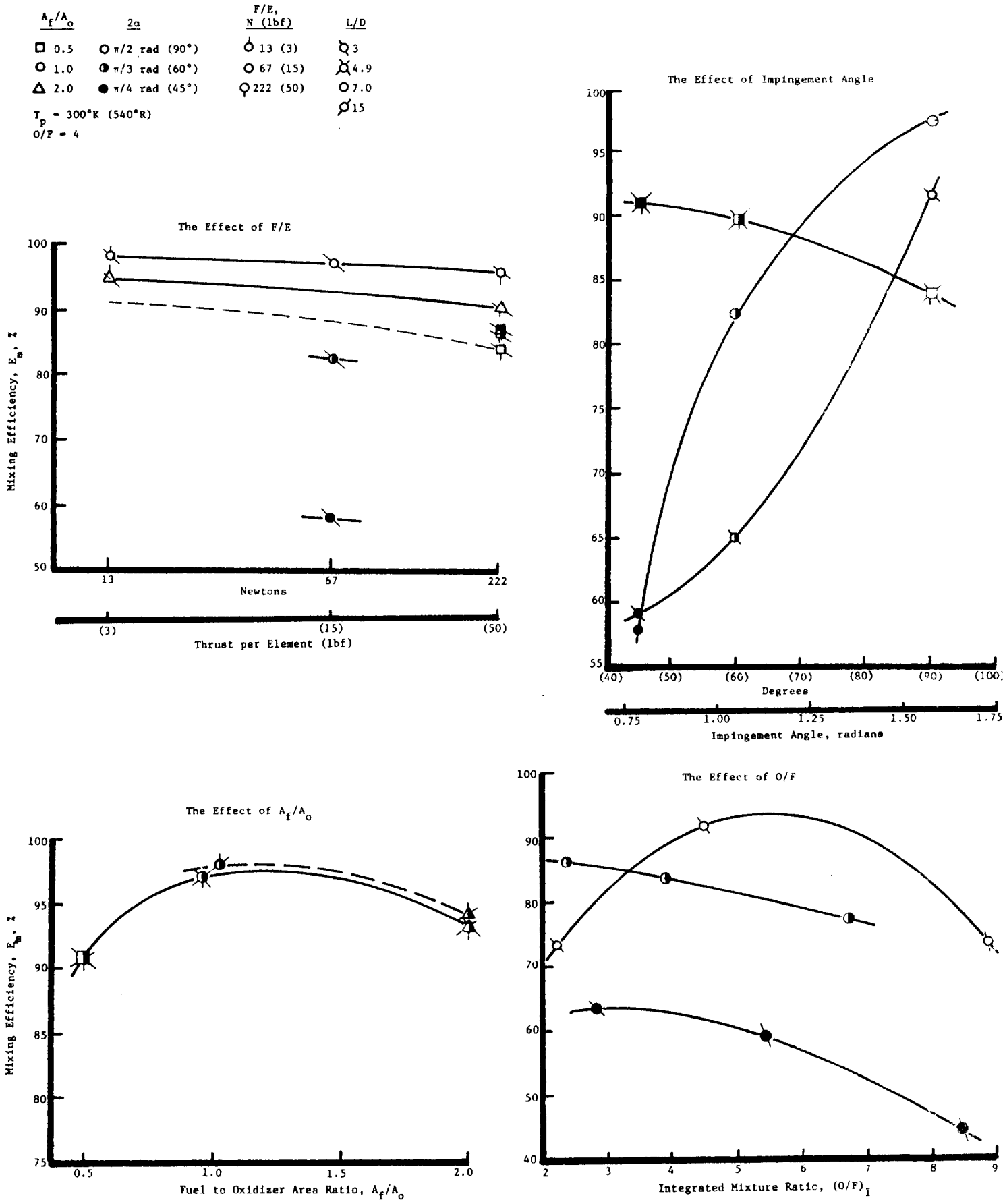

Figure 23. F-O-F Triplet Mixing Efficiencies as a Function of Test Conditions

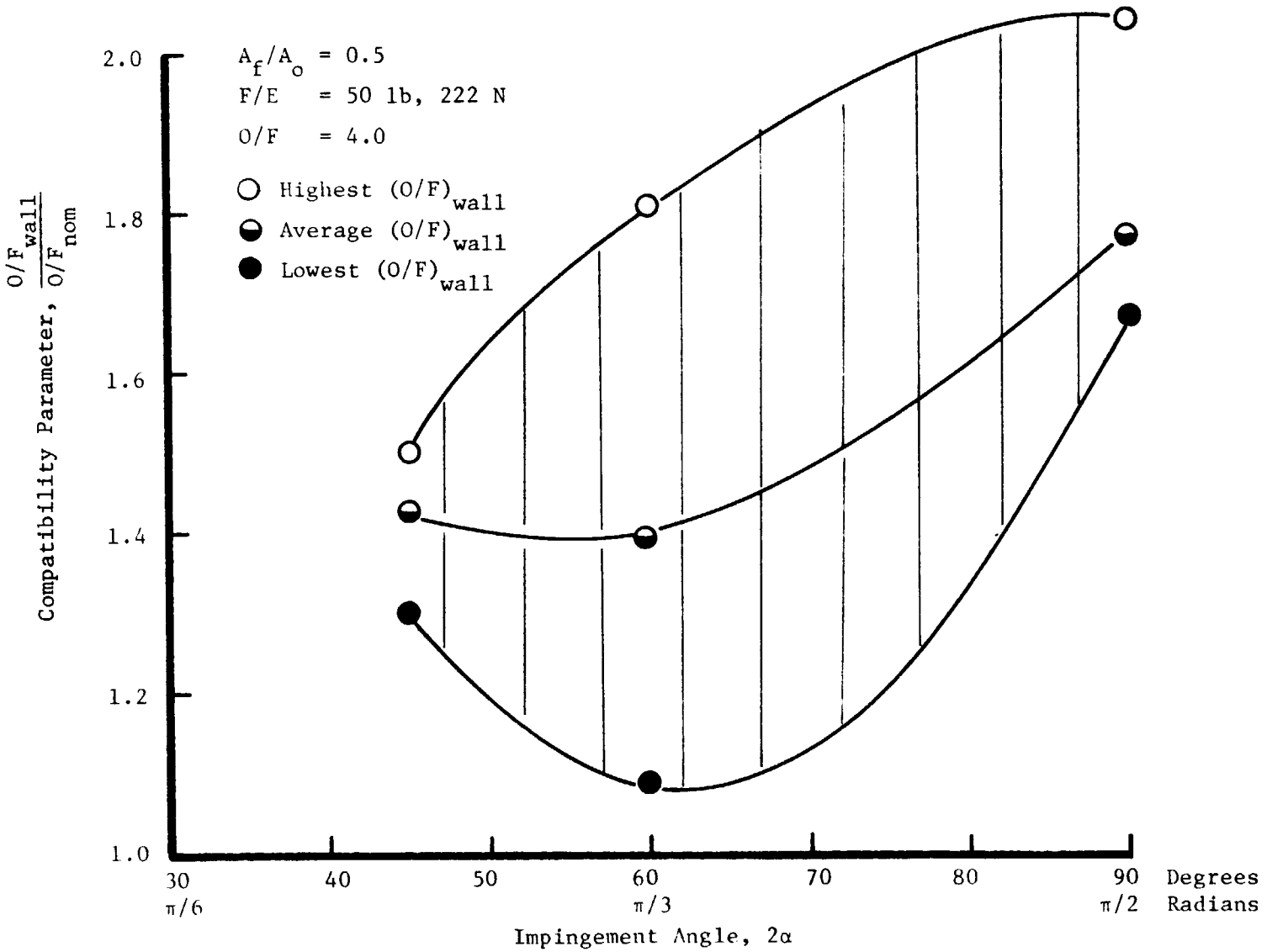

Figure 24. Triplet Element Compatibility Characteristics

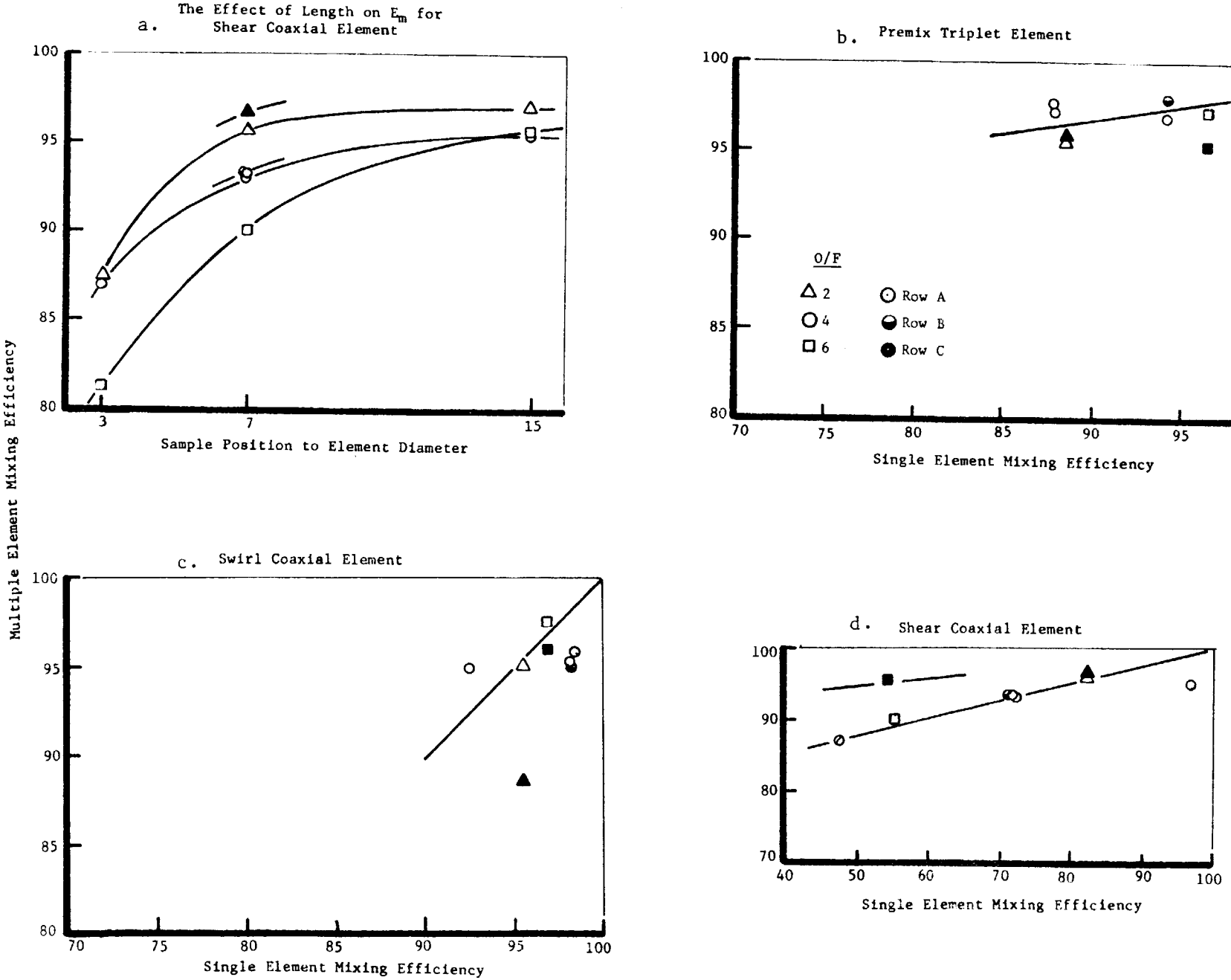

Figure 25. The Comparison of Multiple Element to Single Element Mixing Efficiency

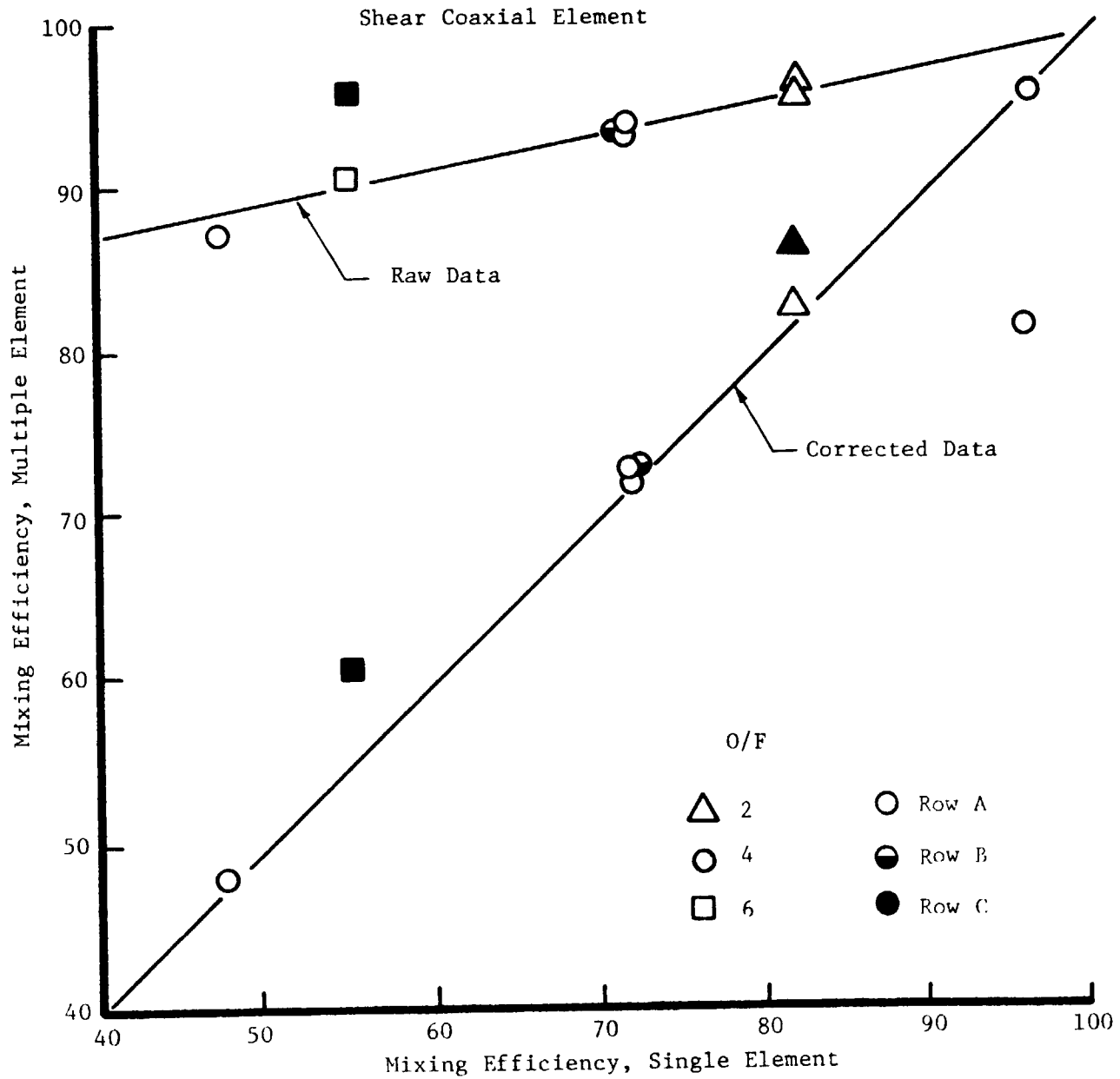

Figure 26. The Comparison of Multiple Element to Single Element Mixing Efficiency

V. HOT FLOW MODELING

It is ALRC's belief that cold flow testing alone does not completely describe the mixing process under combustion conditions. Chemical reaction does impact adversely the mixing profiles generated in cold flow testing. In Reference 10, this impact was described both analytically and empirically for a conventional shear coaxial element. In general, the combustion adversely biased the mixture ratio profiles, i.e., mixing profiles measured in cold flow were displaced downstream axially by combustion. As part of this program, the effects of combustion were studied for a high mixing efficiency element, the swirler coaxial element.

The intent of this portion of the program was not to model the combustion process, but rather to gain phenomenological information that would broaden the insight into the combustion process. In order to accomplish this end, a limited test program was designed that was structured to look at the differences between "identical" combusting and noncombusting flow fields. This testing was conducted with the cold flow swirler element at ambient pressure maintaining Mach number similarity in both the injector and chamber.

The data generated was local mixture ratio distributed axially and radially through the chamber. Both hot and cold flow gas flow fields were generated with identical hardware and flow conditions. The only difference between these tests was that in one case the H_2/O_2 propellants were burning and in the other case they were not. The hot flow hardware was the same hardware used during the cold flow program.

This hot fire testing was conducted in a steam-cooled chamber* and utilized a double-walled, hot H_2 cooled probe to withdraw the gas sample. The sample was routed into the mass spectrometer via copper steam-heated tubing. The resulting data conclusively indicated a combustion mixture ratio profile substantially different than the cold flow profile. These data are presented in Figure 27 as a function of the probe radial and axial distance. This figure indicates that the cold flow mixture ratio gradients had essentially dissipated at the first axial position, indicative of the desirable mixing qualities of the swirl coaxial element. Comparing the hot flow profiles with the cold flow profiles at the same length, it is apparent that the mixture ratio profiles are steeper (greater deviations from uniformity) and persist to 18.2 cm (7.17 in.). This data comparison substantiates that the combustion does adversely affect the mixing. These data are plotted in a different format in Figure 28 where three mixing zones are postulated.

*Particular care must be taken in this type of testing to ensure that the combustion products (H_2O) do not condense anywhere in the system. Thus, all components were heated to over 250°F during testing using either steam or heated hydrogen.

1. The near zone where high mass transfer rates of reactants exist and combustion is initiated.

2. An intermediate zone where the large density gradients due to combustion products displace the oxidizer inward and the fuel outward.

3. A region where the continued rotation of the oxidizer-rich core promotes additional radial diffusion of the oxidizer-rich products into the fuel-rich outer stream tubes.

Based on this data the scaleability of the cold flow data directly to combustion conditions must be questioned. In later sections of this report the effects of combustion are again investigated and a relationship is determined that corrects the cold flow data to compensate for hot fire conditions.

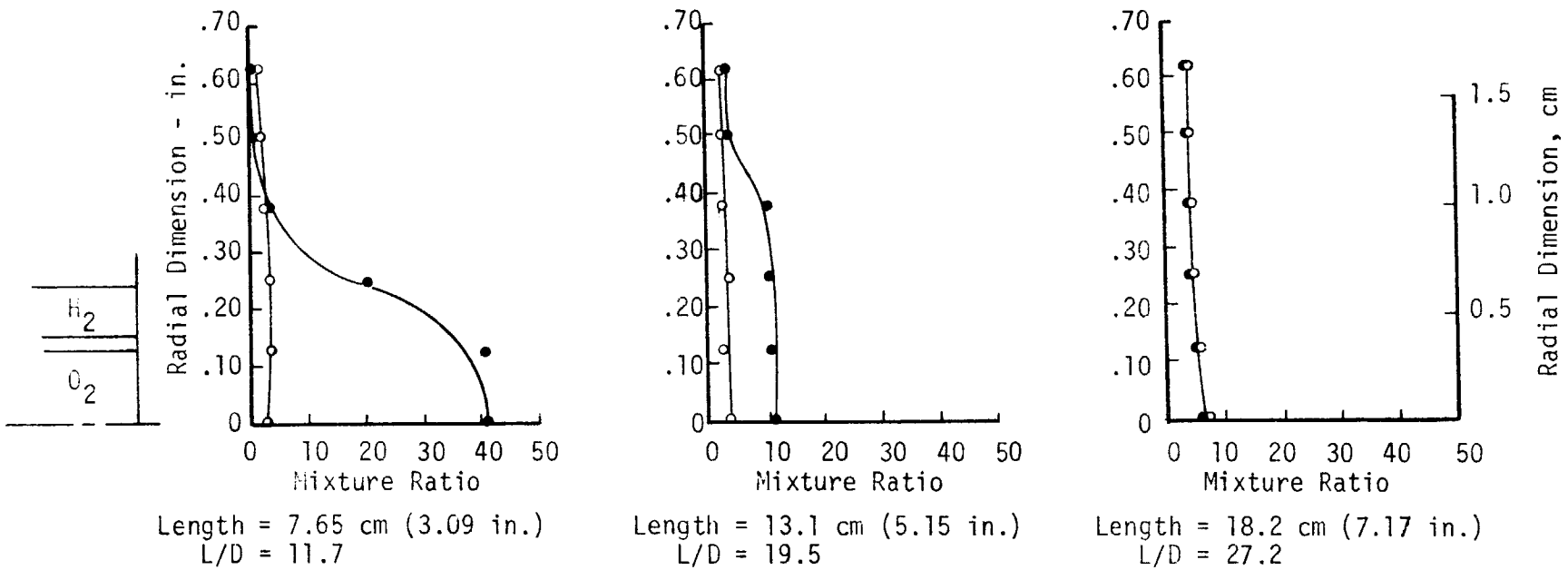

Overall Mixture Ratio (O/F) = 4
Chamber Pressure = One Atmosphere

Closed Symbols Hot Flow
Open Symbols Cold Flow

Figure 27. The Comparison of Hot and Cold Mixture Ratio Profiles for a Swirl Coaxial Element

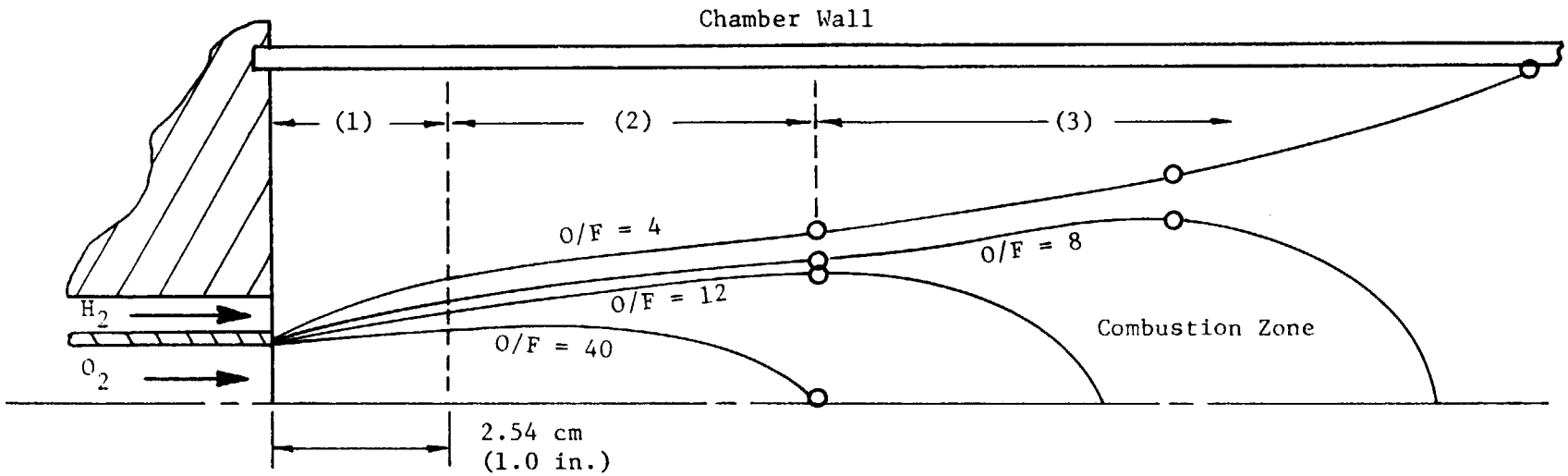

(1) Region of high diffusion rates of reactants of combustion products; combustion initiation.

(2) Region of high diffusion rates of combustion products; probable collapse of oxidizer-rich hollow cone.

(3) Continued rotation of oxidizer-rich core promotes additional radial diffusion.

Figure 28. Schematic of Swirl Element Combustion Process

VI. SINGLE ELEMENT INJECTOR EVALUATION

A. TEST ARTICLES

Based on the cold flow work described previously, four 222N (50 lb_f) single element injector configurations were selected as being potentially high performing or having good compatibility characteristics. These injectors were:

1. Coaxial element
2. Swirler coaxial elements
3. Premix element
4. F-O-F triplet elements

The injectors are illustrated in Figure 29 together with the salient design parameters. The coaxial and swirl coaxial units were the same hardware used during the cold flow program, both high (V_t/V_a = 1.0) and low (V_t/V_a = 0.5) swirl velocity elements were investigated. The only difference between these elements and the cold flow elements was a seal surface added to the hot fire injectors. The premix and triplet injectors were also fabricated from the same components used during cold flow with the exception that new faces were manufactured from OFHC copper rather than the stainless steel used for cold flow.

Three 222N (50-lbf)-thrust chambers were built to interface with the cold flow injector assembly shown in Figure 7. These chambers together with the pertinent physical dimensions are illustrated in Figure 30. Two chambers were 5.1 cm (2.0 in.) long with a 2.5 and 3.5 contraction ratio, A_c/A_t, and referred to as the -1 and -3 configurations, respectively. The third chamber was 14 cm (5.5 in.) long with a 2.5 contraction (the -2 configuration). All the chambers had an exit area ratio, A_e/A_t = 1.75. They were copper heat sink in type and were designed to have a 2-sec test duration and provide adequate thermal response to obtain heat flux data. Twelve thermocouples were buried at approximately mid-wall depth. The thermocouples were located 1.72 cm (0.5 in.) apart axially and in three rows, $\pi/4$ rad (45°) apart circumferentially. Provision was made for a spark type igniter to be located in the chamber wall. The two P_c taps were located near the injector face and at the entrance to the convergent section of the nozzle.

B. TEST FACILITY AND PROCEDURES

The uni-element testing was conducted in the Physics Laboratory, Test Bay 1; a bay that has been used extensively for H_2/O_2 ignition and uni-element combustion research. The facilities in Test Bay 1 include gaseous hydrogen and gaseous oxygen feed systems of 0.154 m^3 (5.5 ft^3) capacity each, an alternate hydrogen and oxygen feed system of smaller capacity, and complete

instrumentation and process control capabilities. These systems are enclosed within insulated cylinders which provided temperature conditioned propellants. The propellants were conditioned by a LN_2 spray over the vessels for subambient tests. Figure 31 is a schematic flow diagram of the propellant feed systems.

For ambient propellant temperature tests, system gas regulators were used for setting the supply pressure to critical flow nozzles. For the temperature conditioned tests, the feed systems were operated in a blowdown mode, and critical flow nozzles were selected to provide the required flow at feed system average pressure.

System pressures and thrust were measured using a six-wire measurement system utilizing strain gage pressure or force transducers. The transducers have 350 Ohm strain gages in a fully active four arm bridge configuration. Typical transducers employed in this system are the Taber Model 206 pressure transducer or the BLH Model U3XXA load cell.

C. SINGLE ELEMENT TEST RESULTS

The following paragraphs summarize the resulting performance, heat transfer and stability data from the 76 single element tests. Data is presented that was obtained using the techniques described in Appendices C and D. Performance data is listed in Table VII and VIII in English and SI Units respectively, and is plotted in Figure 32 through 35. Heat transfer information is plotted in Figure 36 through 42 and stability data is presented in Table IX and plotted in Figure 43.

1. Performance

A summary of the single element hot fire test series performance is presented in Tables VII and VIII and illustrated in Figure 32 through 35. Identified for each data point are the applicable test conditions, the measured and theoretical performance values, specific impulse performance losses, and calculated performance efficiencies. Included under the test conditions are the test number, injector and chamber identification, the data period, and the chamber pressure, mixture ratio, and the oxygen and hydrogen manifold temperature. Some of the ERE data were computed to be over 100% for the triplet element. This inaccuracy is believed to be caused primarily by the very large boundary layer heat loss calculated for these small copper heat sink chambers. Under some test conditions, heat losses were as high as 13% of delivered I_{sp}. Also accuracy of measuring thrust values in the 222 N (50 lbf) range is difficult to achieve, although the thrust cell was quoted to be calibrated within $\pm$ 0.5% thrust accuracy. These two effects combined limit the accuracy of the single element data to be no better than 3% on an absolute basis. However, when comparing element performance data for different elements at a given test condition, the ΔERE values should be accurate within <1%.

TABLE VII

AEROJET LIQUID ROCKET COMPANY

G A S - G A S T E C H N O L O G Y P R O G R A M

SINGLE ELEMENT HOT FIRE TEST SERIES PERFORMANCE SUMMARY

IN

ENGLISH UNITS

TEST CONDITIONS								PERFORMANCE					EFFICIENCIES		
TEST NO.	INJ	CHR	DATA PERIOD	PC (PSIA)	O/F	TO2 (R)	TH2 (R)	ISP(ODE) (LBF-SEC/LBM)	ISP(M)	C*(ODE)	C*(PC-1) (FT/SEC)	C*(PC-2)	C*(E)	ISP --	C*PC-1 (PERCENT)	EFF --
0C-17-103	S*	-3	2.3-2.5	264.	3.84	505.	514.	364.3	265.5	8238.	6718.	6885.	6557.	78.4	81.6	81.7
0C-17-104	S	-3	2.3-2.5	283.	1.95	508.	516.	368.3	305.8	8329.	7235.	7476.	7020.	83.0	86.9	86.0
0C-17-105B	S	-3	2.3-2.5	268.	5.87	501.	511.	340.5	278.4	7681.	6607.	6797.	6389.	81.8	86.0	85.4
0C-17-106	S	-3	2.3-2.5	252.	7.71	499.	509.	317.1	268.3	7150.	6353.	6523.	6154.	84.6	88.9	88.8
0C-17-107	S	-3	2.2-2.4	295.	.99	509.	513.	348.4	313.2	7878.	7352.	7703.	7185.	89.9	93.3	93.0
0C-17-109	S	-3	1.7-1.9	442.	3.96	498.	513.	364.0	284.0	8232.	6723.	6873.	6522.	78.0	81.7	80.8
0C-17-110	S	-3	2.7-2.9	87.	4.01	507.	511.	360.9	278.3	8157.	6557.	6754.	6395.	77.1	80.4	82.0
0C-17-112	S	-1	2.2-2.4	275.	5.91	503.	512.	340.8	284.3	7673.	6853.	7275.	6525.	83.4	89.3	87.1
0C-17-113	S	-1	2.2-2.4	283.	1.99	506.	514.	369.3	300.7	8340.	7142.	7573.	6902.	81.4	85.6	84.3
0C-17-114	S	-1	3.2-3.4	89.	6.03	502.	505.	335.1	277.8	7542.	6657.	7104.	6390.	82.9	88.3	88.4
0C-17-115	C	-1	2.3-2.5	240.	3.99	493.	502.	363.4	237.7	8201.	5863.	6172.	5457.	65.4	71.5	67.6
0C-17-116	C	-1	3.8-4.0	274.	2.03	496.	506.	369.7	273.3	8349.	6731.	7157.	6272.	73.9	80.6	75.8
0C-17-117	C	-1	3.6-3.8	217.	5.93	492.	504.	339.4	213.4	7642.	5266.	5507.	4896.	62.9	68.9	65.0
0C-17-118	C	-1	5.0-5.2	69.	6.23	498.	502.	331.8	211.4	7470.	5133.	5379.	4860.	63.7	68.7	66.5
0C-17-119	C	-1	8.3-8.5	93.	1.94	498.	503.	368.8	279.7	8328.	6784.	7253.	6420.	75.8	81.5	77.9
0C-17-120	C	-1	3.6-3.8	447.	1.96	490.	505.	369.2	270.7	8338.	6657.	7049.	6212.	73.3	79.8	75.1
0C-17-121	C	-1	3.6-3.8	374.	3.84	489.	507.	365.5	234.3	8251.	5766.	6050.	5379.	64.1	69.9	65.9
0C-17-122	C	-2	3.6-3.8	315.	3.90	496.	505.	362.7	325.1	8232.	7955.	8271.	7472.	89.6	96.6	97.2
0C-17-123	C	-2	3.6-3.8	302.	2.03	501.	507.	367.9	310.3	8348.	7557.	7938.	7122.	84.3	90.5	90.0
0C-17-124	C	-2	3.6-3.8	302.	6.01	495.	505.	337.9	301.7	7653.	7406.	7639.	6924.	89.3	96.8	97.6
0C-17-125	C	-2	5.0-5.2	96.	6.00	499.	503.	333.6	294.0	7556.	7231.	7481.	6762.	88.1	95.7	99.6
0C-17-126	C	-3	4.0-4.2	207.	5.99	486.	499.	336.8	206.1	7619.	4985.	5070.	4727.	61.2	65.4	63.3
0C-17-127	C	-3	4.0-4.2	194.	7.74	489.	502.	314.6	197.7	7114.	4783.	4875.	4533.	62.8	67.2	65.1
0C-17-128	C	-3	8.3-8.5	73.	4.06	500.	506.	359.3	225.6	8140.	5417.	5522.	5182.	62.8	66.6	65.7
0C-17-129	C	-3	4.0-4.2	222.	3.94	494.	507.	362.2	230.4	8208.	5510.	5645.	5290.	63.6	67.1	65.8
0C-17-130	C	-3	3.8-4.0	251.	1.98	500.	511.	367.9	263.4	8338.	6271.	6360.	6043.	71.6	75.2	73.7
0C-17-131	C	-3	3.8-4.0	369.	3.91	488.	511.	363.3	234.1	8236.	5609.	5727.	5373.	64.4	68.1	66.3
0C-17-132	C	-3	1.3-1.4	300.	.99	503.	512.	347.6	310.3	7877.	7445.	7702.	7119.	89.3	94.5	91.9
0C-17-132	C	-3	1.5-1.6	266.	.99	504.	512.	347.7	296.4	7877.	7100.	7222.	6799.	85.3	90.1	87.8
0C-17-132	C	-3	2.3-2.4	286.	.99	504.	512.	347.7	295.3	7878.	7112.	7154.	6774.	84.9	90.3	87.5
0C-17-132	C	-3	2.8-2.9	297.	.99	503.	512.	347.7	308.2	7877.	7388.	7609.	7070.	88.7	93.8	91.3
0C-17-132	C	-3	4.1-4.2	285.	.99	503.	511.	347.7	297.4	7878.	7071.	7110.	6821.	85.5	89.8	88.1
0C-17-134	P	-3	1.1-1.3	311.	3.90	507.	512.	364.0	331.2	8232.	7877.	7822.	7612.	91.0	95.7	97.0
0C-17-135	P	-3	1.1-1.3	291.	6.01	504.	512.	339.0	300.7	7648.	7161.	7155.	6900.	88.7	93.6	94.1
0C-17-136	P	-3	.6- .9	258.	7.63	506.	516.	318.0	275.3	7173.	6623.	6499.	6314.	86.5	92.3	91.9
0C-17-139	P	-3	1.1-1.3	325.	2.05	512.	518.	369.4	340.8	8354.	8069.	7811.	7825.	92.3	96.6	98.4
0C-17-140	P	-3	1.1-1.3	522.	3.97	509.	518.	364.0	334.5	8232.	7966.	7896.	7686.	91.9	96.8	97.2
0C-17-141	P	-3	1.1-1.3	103.	4.02	513.	515.	361.0	320.9	8160.	7624.	7621.	7378.	88.9	93.4	97.3
0C-17-143	P	-3	1.1-1.3	302.	.99	521.	531.	348.5	325.8	7881.	7654.	7100.	7475.	93.5	97.1	99.2
0C-17-144	P	-2	1.1-1.3	303.	3.93	511.	518.	364.0	324.0	8224.	7604.	7870.	7445.	89.0	92.5	99.3
0C-17-145	P	-2	1.1-1.3	304.	2.03	514.	0.	369.4	327.8	8349.	7636.	7626.	7525.	88.7	91.5	99.3
0C-17-146	P	-2	1.1-1.3	291.	6.01	510.	518.	339.3	306.6	7648.	7229.	7521.	7035.	90.3	94.5	99.1

TABLE VII (cont.)

TEST NO.	INJ	CHB	TEST CONDITIONS DATA PERIOD	PC (PSIA)	O/F	TO2 (R)	TH2 (R)	PERFORMANCE ISP(ODE) (LBF-SEC/LBM)	ISP(M)	C*(ODE) (FT/SEC)	C*(PC-1)	C*(PC-2)	C*(F)	EFFICIENCIES ISP	C*PC-1 (PERCENT)	ERE
OC-17-147	P	-2	1.1-1.3	98.	4.12	517.	520.	360.2	313.2	8132.	7285.	7577.	7200.	87.0	89.6	100.8
OC-17-148	P	-1	1.1-1.3	317.	3.94	511.	518.	363.7	324.1	8224.	7884.	8012.	7448.	89.1	95.9	94.3
OC-17-149	P	-1	1.1-1.3	329.	2.06	512.	520.	369.5	336.2	8356.	8159.	8026.	7719.	91.0	97.6	96.7
OC-17-150	P	-1	1.1-1.3	524.	3.90	511.	520.	364.6	329.8	8245.	8085.	8209.	7577.	90.5	98.1	95.3
OC-17-151	P	-1	1.1-1.3	290.	5.99	514.	523.	339.2	294.7	7652.	7192.	7370.	6762.	86.9	94.0	91.7
OC-17-152	P	-1	1.1-1.3	103.	4.14	517.	520.	359.7	313.5	8128.	7587.	7749.	7208.	87.1	93.3	94.6
OC-17-153	P	-3	1.1-1.3	91.	6.08	516.	520.	333.3	287.0	7528.	6802.	6807.	6600.	86.1	90.4	94.0
OC-17-154	P	-3	1.1-1.3	105.	1.96	517.	521.	368.0	333.8	8331.	7869.	7644.	7665.	90.7	94.5	99.0
OC-17-155	MS	-3	1.9-2.1	284.	3.89	517.	525.	363.5	303.7	8229.	7210.	7422.	6977.	83.5	87.6	87.2
OC-17-156	MS	-3	1.9-2.1	299.	2.02	518.	527.	368.7	315.2	8346.	7507.	7762.	7235.	85.5	89.9	88.4
OC-17-157	MS	-3	1.9-2.1	275.	5.93	514.	524.	339.3	288.0	7665.	6854.	7030.	6610.	84.9	89.4	88.9
OC-17-158	MS	-2	1.9-2.1	271.	5.94	514.	525.	339.2	287.9	7662.	6859.	7342.	6607.	84.9	89.5	93.3
OC-17-159	MS	-2	1.9-2.1	304.	3.92	516.	524.	363.4	324.4	8226.	7761.	8241.	7456.	89.3	94.3	97.8
OC-17-160	MS	-2	1.9-2.1	307.	2.00	516.	526.	368.6	329.5	8343.	7861.	8481.	7565.	89.4	94.2	96.3
OC-17-162B	MS	-3	1.7-1.9	297.	3.89	379.	346.	359.7	288.3	8138.	6884.	7060.	6622.	80.1	84.6	83.2
OC-17-162B	MS	-3	2.2-2.3	277.	3.92	378.	342.	359.3	270.7	8128.	6457.	6563.	6217.	75.3	79.4	78.3
OC-17-163	P	-3	1.6-1.8	325.	3.72	386.	339.	361.0	325.7	8169.	7734.	7771.	7484.	90.2	94.7	95.7
OC-17-164	C	-3	2.4-2.6	221.	3.93	369.	364.	359.3	223.1	8131.	5407.	5505.	5122.	62.1	66.5	64.3
OC-18-101	T1	3	1.0-1.3	262.	3.86	540.	542.	359.1	256.2	8154.	6765.	6867.	5885.	71.4	83.0	74.6
OC-18-102	T1	3	1.0-1.3	312.	2.00	535.	537.	363.9	337.2	8262.	8213.	8459.	7742.	92.7	99.4	97.5
OC-18-103	T1	3	1.0-1.3	84.	4.08	529.	531.	355.1	262.4	8059.	6425.	6506.	6030.	73.9	79.7	78.7
OC-18-104	T1	3	1.0-1.3	233.	5.94	532.	533.	334.1	243.5	7572.	5966.	6069.	5587.	72.9	78.8	76.2
OC-18-105	T2	3	1.0-1.3	233.	5.92	536.	535.	334.4	241.7	7578.	5939.	5961.	5545.	72.3	78.4	75.7
OC-18-106	T2	3	1.0-1.3	83.	4.15	534.	534.	354.3	258.4	8040.	6327.	6465.	5938.	72.9	78.7	75.6
OC-18-107	T2	3	1.0-1.3	261.	3.92	536.	535.	358.5	272.9	8141.	6704.	7303.	6268.	76.1	82.4	79.6
OC-18-108	T2	3	1.0-1.3	319.	2.00	535.	535.	363.9	339.5	8261.	8253.	8420.	7795.	93.3	99.9	98.3
OC-18-109	T3	3	1.0-1.3	305.	3.88	538.	538.	359.1	321.9	8155.	7897.	7878.	7398.	89.6	96.8	94.9
OC-18-110	T3	3	1.0-1.3	323.	1.93	540.	540.	363.2	345.3	8245.	8405.	8627.	7928.	95.1	101.9	100.4
OC-18-111	T3	3	1.0-1.3	99.	4.11	537.	540.	355.0	305.6	8056.	7486.	7580.	7027.	86.1	92.9	92.9
OC-18-112	T3	3	1.0-1.3	255.	5.77	541.	541.	336.7	269.4	7631.	6595.	6638.	6183.	80.0	86.4	84.0
OC-18-113	T3	2	1.0-1.3	266.	5.87	538.	537.	337.1	303.4	7614.	7359.	7554.	6964.	90.0	96.7	97.7
OC-18-114	T3	2	1.0-1.3	98.	4.10	537.	538.	356.3	316.3	8059.	7502.	7833.	7272.	88.8	93.1	103.6
OC-18-115	T3	2	1.2-1.4	300.	3.92	539.	539.	360.0	327.3	8147.	7736.	8139.	7522.	90.9	95.0	102.1
OC-18-116	T3	2	1.0-1.3	300.	1.98	539.	540.	364.8	333.3	8258.	7814.	8360.	7652.	91.4	94.6	102.4

INJECTOR TYPE

S	.5 V_T/V_A Swirler
C	Coaxial
P	Premix
MS	1 V_T/V_A Swirler
T1	-1 Triplet
T2	-2 Triplet
T3	-3 Triplet

TABLE VIII

AEROJET LIQUID ROCKET COMPANY

G A S - G A S T E C H N O L O G Y P R O G R A M

SINGLE ELEMENT HOT FIRE TEST SERIES PERFORMANCE SUMMARY

IN

S.I. UNITS

TEST CONDITIONS								PERFORMANCE						EFFICIENCIES		
TEST NO.	INJ	CHB	DATA PERIOD	PC (N/SQCM)	O/F	TO2 (K)	TH2 (K)	ISP(ODE) (N-SEC/KG)	ISP(M)	C*(ODE) (M/SEC)	C*(PC-1)	C*(PC-2)	C*(F)	ISP --	C*PC-1 (PERCENT)	ERE --
OC-17-103	S*	-3	2.3-2.5	182.	3.84	281.	286.	3573.	2799.	2511.	2048.	2099.	1999.	78.4	81.6	81.7
OC-17-104	S	-3	2.3-2.5	195.	1.95	282.	287.	3612.	2999.	2539.	2205.	2279.	2140.	83.0	86.9	86.0
OC-17-105B	S	-3	2.3-2.5	185.	5.87	278.	284.	3339.	2730.	2341.	2014.	2072.	1948.	81.8	86.0	85.4
OC-17-106	S	-3	2.3-2.5	173.	7.71	277.	283.	3109.	2631.	2179.	1936.	1988.	1876.	84.6	88.9	88.8
OC-17-107	S	-3	2.2-2.4	203.	.99	283.	285.	3417.	3071.	2401.	2241.	2348.	2190.	89.9	93.3	93.0
OC-17-109	S	-3	1.7-1.9	305.	3.96	277.	285.	3570.	2785.	2509.	2049.	2095.	1988.	78.0	81.7	80.8
OC-17-110	S	-3	2.7-2.9	60.	4.01	282.	284.	3539.	2729.	2486.	1999.	2059.	1949.	77.1	80.4	82.0
OC-17-112	S	-1	2.2-2.4	189.	5.91	280.	284.	3342.	2788.	2339.	2089.	2217.	1989.	83.4	89.3	87.1
OC-17-113	S	-1	2.2-2.4	195.	1.99	281.	285.	3621.	2949.	2542.	2177.	2308.	2104.	81.4	85.6	84.3
OC-17-114	S	-1	3.2-3.4	61.	6.03	279.	280.	3286.	2724.	2299.	2029.	2165.	1948.	82.9	88.3	88.4
OC-17-115	C	-1	2.3-2.5	165.	3.99	274.	279.	3563.	2330.	2500.	1787.	1881.	1663.	65.4	71.5	67.6
OC-17-116	C	-1	3.8-4.0	189.	2.03	276.	281.	3626.	2680.	2545.	2052.	2181.	1912.	73.9	80.6	75.8
OC-17-117	C	-1	3.6-3.8	149.	5.93	273.	280.	3328.	2093.	2329.	1605.	1678.	1492.	62.9	68.9	65.0
OC-17-118	C	-1	5.0-5.2	48.	6.23	277.	279.	3253.	2073.	2277.	1564.	1640.	1481.	63.7	68.7	66.5
OC-17-119	C	-1	8.3-8.5	64.	1.94	277.	280.	3616.	2742.	2538.	2068.	2211.	1957.	75.8	81.5	77.9
OC-17-120	C	-1	3.6-3.8	308.	1.98	272.	280.	3621.	2655.	2541.	2029.	2148.	1893.	73.3	79.8	75.1
OC-17-121	C	-1	3.6-3.8	258.	3.84	272.	281.	3584.	2298.	2515.	1758.	1844.	1640.	64.1	69.9	65.9
OC-17-122	C	-2	3.6-3.8	217.	3.90	276.	281.	3556.	3188.	2509.	2425.	2521.	2277.	89.6	96.6	97.2
OC-17-123	C	-2	3.6-3.8	208.	2.03	278.	281.	3608.	3043.	2544.	2303.	2419.	2171.	84.3	90.5	90.0
OC-17-124	C	-2	3.6-3.8	208.	6.01	275.	281.	3313.	2959.	2333.	2257.	2328.	2110.	89.3	96.8	97.6
OC-17-125	C	-2	5.0-5.2	66.	6.00	277.	279.	3271.	2883.	2303.	2204.	2280.	2061.	88.1	95.7	99.6
OC-17-126	C	-3	4.0-4.2	143.	5.99	270.	277.	3303.	2021.	2322.	1519.	1545.	1441.	61.2	65.4	63.3
OC-17-127	C	-3	4.0-4.2	134.	7.74	272.	279.	3085.	1939.	2168.	1458.	1486.	1382.	62.8	67.2	65.1
OC-17-128	C	-3	8.3-8.5	50.	4.06	278.	281.	3523.	2213.	2481.	1651.	1683.	1579.	62.8	66.6	65.7
OC-17-129	C	-3	4.0-4.2	153.	3.94	274.	281.	3551.	2259.	2502.	1680.	1721.	1612.	63.6	67.1	65.8
OC-17-130	C	-3	3.8-4.0	173.	1.98	278.	284.	3607.	2583.	2541.	1911.	1939.	1842.	71.6	75.2	73.7
OC-17-131	C	-3	3.8-4.0	254.	3.91	271.	284.	3563.	2295.	2510.	1710.	1746.	1638.	64.4	68.1	66.3
OC-17-132	C	-3	1.3-1.4	207.	.99	280.	284.	3409.	3043.	2401.	2269.	2347.	2170.	89.3	94.5	91.9
OC-17-132	C	-3	1.5-1.6	197.	.99	280.	284.	3409.	2907.	2401.	2164.	2201.	2072.	85.3	90.1	87.8
OC-17-132	C	-3	2.3-2.4	197.	.99	280.	284.	3409.	2896.	2401.	2168.	2180.	2065.	84.9	90.3	87.5
OC-17-132	C	-3	2.8-2.9	205.	.99	280.	284.	3409.	3022.	2401.	2252.	2319.	2155.	88.7	93.8	91.3
OC-17-132	C	-3	4.1-4.2	196.	.99	280.	284.	3409.	2916.	2401.	2155.	2167.	2079.	85.5	89.8	88.1
OC-17-134	P	-3	1.1-1.3	215.	3.90	282.	284.	3570.	3248.	2509.	2401.	2384.	2320.	91.0	95.7	97.0
OC-17-135	P	-3	1.1-1.3	201.	6.01	280.	285.	3324.	2949.	2331.	2183.	2181.	2103.	88.7	93.6	94.1
OC-17-136	P	-3	.8- .9	178.	7.63	281.	286.	3119.	2699.	2186.	2019.	1981.	1924.	86.5	92.3	91.9
OC-17-139	P	-3	1.1-1.3	224.	2.05	284.	288.	3622.	3342.	2546.	2459.	2381.	2385.	92.3	96.6	98.4
OC-17-140	P	-3	1.1-1.3	360.	3.97	283.	288.	3570.	3280.	2509.	2428.	2407.	2343.	91.9	96.8	97.2
OC-17-141	P	-3	1.1-1.3	71.	4.02	285.	286.	3540.	3147.	2487.	2324.	2323.	2249.	88.9	93.4	97.3
OC-17-143	P	-3	1.1-1.3	208.	.99	289.	295.	3418.	3195.	2402.	2333.	2164.	2278.	93.5	97.1	99.2
OC-17-144	P	-2	1.1-1.3	209.	3.93	284.	288.	3569.	3177.	2507.	2318.	2399.	2269.	89.0	92.5	99.3
OC-17-145	P	-2	1.1-1.3	210.	2.03	285.	0.	3623.	3214.	2545.	2328.	2324.	2294.	88.7	91.5	99.3
OC-17-146	P	-2	1.1-1.3	201.	6.01	283.	288.	3327.	3006.	2331.	2203.	2292.	2144.	90.3	94.5	99.1

TABLE VIII (cont.)

TEST NO.	INJ	CHB	TEST CONDITIONS: DATA PERIOD	PC (N/SQCM)	O/F	TO2 (K)	TH2 (K)	PERFORMANCE: ISP(ODE) (N-SEC/KG)	ISP(M) (N-SEC/KG)	C*(ODE) (M/SEC)	C*(PC-1) (M/SEC)	C*(PC-2) (M/SEC)	C*(F) (M/SEC)	EFFICIENCIES: ISP --	C*PC-1 (PERCENT)	FRE --
OC-17-147	P	-2	1.1-1.3	68.	4.12	287.	289.	3532.	3071.	2479.	2220.	2309.	2195.	87.0	89.6	100.8
OC-17-146	P	-1	1.1-1.3	218.	3.94	284.	288.	3566.	3178.	2507.	2403.	2442.	2270.	89.1	95.9	94.3
OC-17-149	P	-1	1.1-1.3	227.	2.06	285.	289.	3623.	3297.	2547.	2487.	2446.	2353.	91.0	97.6	96.7
OC-17-150	P	-1	1.1-1.3	361.	3.90	284.	289.	3575.	3234.	2513.	2464.	2502.	2310.	90.5	98.1	95.3
OC-17-151	P	-1	1.1-1.3	200.	5.99	286.	290.	3326.	2889.	2332.	2192.	2246.	2061.	86.9	94.0	91.7
OC-17-152	P	-1	1.1-1.3	71.	4.14	287.	289.	3527.	3074.	2477.	2313.	2362.	2197.	87.1	93.3	94.6
OC-17-153	P	-3	1.1-1.3	63.	6.08	287.	289.	3268.	2814.	2295.	2073.	2075.	2012.	86.1	90.4	94.0
OC-17-154	P	-3	1.1-1.3	73.	1.96	287.	289.	3609.	3273.	2539.	2399.	2330.	2336.	90.7	94.5	99.0
OC-17-155	MS	-3	1.9-2.1	196.	3.89	287.	292.	3565.	2978.	2508.	2198.	2262.	2127.	83.5	87.6	87.2
OC-17-156	MS	-3	1.9-2.1	206.	2.02	288.	293.	3615.	3091.	2544.	2288.	2366.	2205.	85.5	89.9	88.4
OC-17-157	MS	-3	1.9-2.1	190.	5.93	286.	291.	3327.	2825.	2336.	2089.	2143.	2015.	84.9	89.4	88.9
OC-17-158	MS	-2	1.9-2.1	187.	5.94	286.	291.	3326.	2823.	2335.	2091.	2238.	2014.	84.9	89.5	93.3
OC-17-159	MS	-2	1.9-2.1	210.	3.92	287.	291.	3564.	3181.	2507.	2365.	2512.	2272.	89.3	94.3	97.8
OC-17-160	MS	-2	1.9-2.1	211.	2.00	286.	292.	3614.	3231.	2543.	2396.	2585.	2306.	89.4	94.2	96.3
OC-17-162B	MS	-3	1.7-1.9	205.	3.89	210.	192.	3527.	2827.	2480.	2098.	2152.	2018.	80.1	84.6	83.2
OC-17-162B	MS	-3	2.2-2.3	191.	3.92	210.	190.	3524.	2654.	2478.	1968.	2001.	1895.	75.3	79.4	78.3
OC-17-163	P	-3	1.6-1.8	224.	3.72	214.	188.	3540.	3194.	2490.	2357.	2369.	2281.	90.2	94.7	95.7
OC-17-164	C	-3	2.4-2.6	152.	3.93	205.	202.	3523.	2188.	2478.	1648.	1678.	1561.	62.1	66.5	64.3
OC-18-101	T1	3	1.0-1.3	180.	3.86	300.	301.	3521.	2512.	2485.	2062.	2093.	1794.	71.4	83.0	74.6
OC-18-102	T1	3	1.0-1.3	215.	2.00	297.	298.	3569.	3307.	2518.	2503.	2578.	2360.	92.7	99.4	97.5
OC-18-103	T1	3	1.0-1.3	58.	4.08	294.	295.	3482.	2573.	2456.	1958.	1983.	1838.	73.9	79.7	78.7
OC-18-104	T1	3	1.0-1.3	161.	5.94	295.	296.	3276.	2388.	2308.	1818.	1850.	1703.	72.9	78.8	76.2
OC-18-105	T2	3	1.0-1.3	160.	5.92	298.	297.	3279.	2370.	2310.	1810.	1817.	1690.	72.3	78.4	75.7
OC-18-106	T2	3	1.0-1.3	57.	4.15	296.	297.	3474.	2534.	2451.	1929.	1970.	1810.	72.9	78.7	75.6
OC-18-107	T2	3	1.0-1.3	180.	3.92	298.	297.	3516.	2676.	2481.	2044.	2226.	1910.	76.1	82.4	79.6
OC-18-108	T2	3	1.0-1.3	220.	2.00	297.	297.	3568.	3329.	2518.	2515.	2567.	2376.	93.3	99.9	98.3
OC-18-109	T3	3	1.0-1.3	210.	3.88	299.	299.	3522.	3157.	2486.	2407.	2401.	2255.	89.6	96.8	94.9
OC-18-110	T3	3	1.0-1.3	223.	1.93	300.	300.	3561.	3386.	2513.	2562.	2629.	2417.	95.1	101.9	100.4
OC-18-111	T3	3	1.0-1.3	68.	4.11	298.	300.	3481.	2997.	2455.	2282.	2310.	2142.	86.1	92.9	92.9
OC-18-112	T3	3	1.0-1.3	176.	5.77	301.	301.	3301.	2642.	2326.	2010.	2023.	1885.	80.0	86.4	84.0
OC-18-113	T3	2	1.0-1.3	197.	5.87	299.	299.	3306.	2975.	2321.	2243.	2302.	2123.	90.0	96.7	97.7
OC-18-114	T3	2	1.0-1.3	68.	4.10	298.	299.	3494.	3101.	2456.	2287.	2387.	2217.	88.8	93.1	103.6
OC-18-115	T3	2	1.2-1.4	207.	3.92	299.	299.	3530.	3210.	2483.	2358.	2481.	2293.	90.9	95.0	102.1
OC-18-116	T3	2	1.0-1.3	207.	1.98	300.	300.	3577.	3268.	2517.	2382.	2548.	2332.	91.4	94.6	102.4

INJECTOR TYPE

S	.5 V_T/V_A Swirler
C	Coaxial
P	Premix
MS	1 V_T/V_A Swirler
T1	-1 Triplet
T2	-2 Triplet
T3	-3 Triplet

TABLE IX

STABILITY DATA
FOR SINGLE ELEMENT INJECTORS

Test No.	Injector Type	Chamber	MR	P_c, psia	P_c (N/cm^2)	$(\Delta P/P_c)_{ox}$	$(\Delta P/P_c)_{fuel}$	(1) Stability Freq. Hz
103	Swirler	-3	3.83	264	182	0.059	0.119	US 1050
104	(V_t/V_a=0.5)		1.94	283	195	0.026	0.227	US 1050
105B			5.86	268	185	0.037	0.040	S
106			7.70	252	173	0.044	0.023	S
107			0.99	295	203	0.005	0.438	US 1050
109			3.96	442	305	0.057	0.110	--
110			4.01	87	60	0.057	0.098	US 1050
112		-1	5.90	275	189	0.129	0.037	S
113			1.99	283	195	0.188	0.256	US 1500
114			6.03	89	61	0.034	0.031	S
115	Coaxial		3.98	240	165	0.008	0.098	S
116			2.03	274	189	0.005	0.200	MS 750
117			5.93	217	149	0.019	0.062	S
118			6.23	69	48	0.026	0.056	S
119			1.94	93	64	0.005	0.208	MS 750
120			1.98	447	308	0.004	0.207	MS 750
121			3.89	374	258	0.009	0.103	S
122		-2	3.90	315	217	0.007	0.057	MS 600
123			2.03	302	208	0.005	0.199	US 750
124			6.01	302	208	0.014	0.032	S
125			6.00	96	66	0.015	0.028	S
126		-3	5.99	207	143	0.023	0.078	S
127			7.73	194	134	0.031	0.061	S
128			4.05	73	50	0.030	0.137	MS 750
129			3.93	222	153	0.031	0.137	MS 900
130			1.98	251	173	0.028	0.318	US 900
131			3.91	369	254	0.027	0.133	MS 750
132			0.99	300	207	0.003	0.437	US 800
134			3.90	311	215	0.226	0.288	S
135	Premix		6.01	291	201	0.182	0.208	S
138			7.63	258	178	0.181	0.194	S
139			2.05	325	224	0.410	0.581	S
140			3.97	522	360	0.227	0.291	S
141			4.02	103	71	0.217	0.278	S
143			0.99	302	208	0.707	1.159	S
144		-2	3.93	303	209	0.226	0.291	S
145			2.03	304	210	0.438	0.625	S
146			6.01	291	201	0.166	0.1906	S
147			4.12	98	68	0.221	0.279	S
148		-1	3.94	317	218	0.221	0.283	S
149			2.06	329	229	0.398	0.569	S
150			3.90	524	361	0.218	0.283	S
151			5.99	290	200	0.176	0.203	S
152			4.14	103	71	0.213	0.270	S
153		-3	6.08	91	63	0.185	0.208	S
154			1.96	105	73	0.420	0.600	S
155	High		3.89	284	196	0.077	0.077	MS 700
156	Swirler		2.02	299	206	0.055	0.191	MS 1100
157	(V_t/V_a=1.0)		5.93	275	190	0.099	0.042	S
158		-2	5.93	271	187	0.100	0.048	S
159			3.92	304	210	0.065	0.064	S
160			2.00	307	211	0.043	0.161	MS 1100
101	-1 Triplet	-3	3.86	262	180	0.273	0.083	US 3500
102			2.00	312	215	0.122	0.128	S
103			4.08	84	58	0.314	0.084	US 3500
104			5.94	233	161	0.395	0.072	US 3500
105	-2 Triplet		5.92	233	160	0.414	0.073	US 3500
106			4.15	83	57	0.354	0.077	US 3500
107			3.92	261	180	0.271	0.078	US 3500
108			2.00	319	220	0.116	0.137	S
109	-3 Triplet		3.88	305	210	0.197	0.255	S
110			1.93	323	223	0.098	0.594	S
111			4.11	99	68	0.224	0.254	S
112			5.77	255	176	0.324	0.154	S
113		-2	5.87	286	197	0.247	0.141	S
114			4.10	98	68	0.178	0.232	S
115			3.92	300	207	-		S
116	Triplet	-2	1.98	300	207	0.114	0.644	S

(1) US = Unstable
S = Stable
MS = Marginally stable

Figure 32 shows the variation of energy release efficiency with mixture ratio for the five injector elements tested and the two 5.08 cm (2.0-in.) long combustion chambers (-1 and -3). These data show that the F-O-F triplet element is the highest performing at low mixture ratios, while the premix injector is the highest consistent performing element over the total mixture ratio range. The high swirler coaxial element, the low velocity swirler element and the conventional coaxial element are in order of decreasing performance. The effect of mixture ratio and contraction ratio on ERE is also shown to be a function of the injector element design. The premix triplet element ERE increases with decreasing mixture ratio over the entire test mixture ratio range from 8 to 1. The swirler coaxial element, on the other hand, reaches a minimum ERE near the nominal design mixture ratio of 4 and increases from this value for either increasing or decreasing mixture ratio. The coaxial element achieves maximum ERE at a mixture ratio of 1 and decreases significantly ($\sim$25%) with increasing mixture ratio to a minimum value at a mixture ratio of 6. Further increases in mixture ratio result in slightly ($\sim$2%) higher energy release efficiency.

The detailed F-O-F triplet performance is illustrated in Figure 33. Energy release efficiencies for the three injectors and two chambers are represented as a function of mixture ratio. Two characteristics are apparent from the data in Figure 33: (1) all injectors are higher performing at low mixture ratios; (2) the low area ratio element (A_f/A_O = 1.0) is substantially higher performing than either of the A_f/A_O = 2 elements. Both the above trends indicate that this element is sensitive to fuel momentum; i.e., there must be sufficient fuel momentum to penetrate the oxidizer jet to effect complete propellant mixing.

A correlation of these data as a function of momentum ratio is depicted in Figure 33 as well. The stable data from all the injectors correlate well with the mixing parameter, MP.

$$MP \equiv \frac{\dot{w}_O \, V_O}{\dot{w}_f \, V_f \sin \alpha} \tag{4}$$

Referring to Figure 33a, note that the mixing parameter maximizes at a value of 0.5 in the short chambers and is flat up to a value of 2 in the long chambers. However, the value of 0.5 is not realistic for practical engine systems, since low values of the mixing parameter are in the direction of high fuel pressure drop. An O_2/H_2 engine operating at mixture ratio 4.0 with an oxidizer pressure drop of 10% of chamber pressure would have a sonic fuel injection velocity if a MP of 0.5 were maintained. Depending on the particular injector design, the fuel pressure drop would be on the order of the chamber pressure, a value too high to be realistically considered for practical engine systems. Since the mixing parameter tends to be rather flat over the range of 0.5 to 2 for the longer chamber, it is therefore not an

adverse compromise to relax the criterion of MP = 0.5 to a value somewhat higher. The performance penalty should not be large, and the fuel pressure drop is more consistent with practical injector design practice.

The effect of chamber contraction ratio on ERE is seen in Figure 32 to be a function of the injector design. For the premix triplet element, ERE increases with increasing contraction ratio. This is caused by the increased chamber stay time resulting from the larger L* (6.1 vs 4.8) cm. The ERE of the coaxial element is, on the other hand, higher for the lower contraction ratio. In this case, it appears that the lower contraction ratio enhances the coaxial mixing process by maintaining a higher absolute ΔV for mixing so as to overpower the effect of the decreased chamber stay time.

The chamber axial length (L') has a significant influence on the energy release efficiency. The ERE obtained with four of the injector elements and the 14 cm (5.5 in.) long chamber is shown in Figure 34a. At this chamber length, all four injector elements have ERE's greater than 95%. The effect of chamber length is, however, a function of the injector design as shown in Figure 34a. The ERE of the premix element, increases only slightly from about 96% to 99% as the chamber length increases from 5.08 to 14 cm (2 to 5.5 in.). The swirl coaxial element ERE increases from 88 to 98%, the coaxial element ERE increases from approximately 67 to 97%, while the F-O-F triplet injector increases from 93 to 100% over the same range. The chamber characteristic length (L*) has a similar effect on ERE as shown in Figure 34b. The L* was varied by contraction ratio or length changes as noted. These data also indicate that characteristic length or stay time is the primary variable that influences the premix element performance, while physical chamber length is the first order influence on the coaxial element performance.

The effect of chamber pressure and propellant temperature on the experimental ERE is presented in Figure 35a for various injector element/chamber configurations and overall mixture ratio. Over the range of chamber pressures investigated (45.6 to 341 N/cm^2) 70 to 500 psia, little variation in ERE with P_c is noted except for the triplet element. Its ERE increased over 2% when P_c was raised from 68 N/cm^2 (100 psia) to 200 N/cm^2 (300 psia).

The propellant temperature shown on Figure 35 is a mass weighted average of the fuel and oxidizer manifold temperatures, i.e.,

$$T_p = \left(\frac{1}{O/F + 1} \right) T_f + \left(\frac{O/F}{(O/F + 1)} \right) T_o \qquad (5)$$

The fuel and oxidizer temperatures were always within 28°K (50°R) of each other and generally were within a few degrees of being the same. In all cases the ERE increased with increasing propellant temperature. The premix triplet element exhibited the smallest performance change with propellant temperature, increasing 1.0% per 55.5°K (100°R). The coaxial element ERE increased 1.25%

per 55.5°K (100°R) while the high velocity swirler element increased 2.7% per 55.5°K (100°R). Combustion stability variations experienced with the high velocity swirler may have influenced the performance variation of this element over the tested propellant temperature range.

2. Heat Transfer

The detailed calculational techniques are discussed in Appendix D. The primary concern of this program was to understand injector related heat transfer effects. The data is presented in the form of a heat flux ratio, where the local heat flux expr is nominalized by the heat flux calculated from a conventional turbulent heat transfer correlation: $\phi nom = 0.026\ k/D\ R_c^{0.8}\ Pr^{0.4}\ (T_o - T_w)$. Values of one or higher indicate local heat fluxes that are higher than nominal and values less than one indicate values of relatively low heat flux.

The design point data for all the injectors is shown in Figure 36. This data shows that near zone heat fluxes (in the first 1.27 cm, (0.5 in.) of chamber length) can vary by an order of magnitude depending on injector type. The swirler injector have ϕ expr/ϕ_{nom} ratios of 0.2 in the near zone while the premix injector demonstrated heat flux ratios of over 2. The conclusion from this data is that the single biggest variable that influences the chamber wall heat flux is the element type.

The specific results for each element type are discussed in the following paragraphs and are illustrated in Figures 37 through 43.

a. Coaxial Element Axial Heat Transfer Characteristics (19 Tests)

The coaxial element data are shown in Figure 37. These data group together reasonably well and a rather gradual increase in heat flux with axial distance is indicated. The heat fluxes are generally low and, in most cases, are less than one half of the nominal values. Notable effects indicated by the data are:

(1) Contraction Ratio Effect

Contraction ratio does not appear to exert a large influence; however, there is a slight tendency toward higher heat flux ratios in the 3.5 contraction ratio chamber (-3 chamber).

(2) Chamber Length Effects

A rather sharp increase in heat flux is indicated at 4.44 cm (1.75 in.) axial distance in the long 2.5 contraction ratio chamber (-2 chamber) but not in the short one (-1 chamber). This behavior is unexplained, but it could be an indication that the film cooling effect of the fuel annulus deteriorates at about 4.44 cm (1.75-in.).

(3) Mixture Ratio Effect

Relatively high heat flux ratios (up to 0.85) are indicated by the O/F = 1 data obtained at 205 N/cm^2 (300 psia) chamber pressure in the -3 chamber. This could be largely due to the high mixing rate and thus performance of this element at the very low MR operating point.

(4) Chamber Pressure Effect

Chamber pressure effects on the heat flux ratio are generally very small. The only notable P_c influence exists at 4.44 cm (1.75 in.) axial distance in the -2 chamber.

(5) Propellant Temperature Effect

The propellant temperature influence appears small since the heat fluxes measured at O/F = 4, P_c = 205 N/cm^2 (300 psia) are about the same with and without cold propellants.

b. Swirl Coaxial Element (V_t/V_a = 0.5) Axial Heat Transfer Characteristics (7 Tests)

The low velocity (V_t/V_a = 0.5) swirl coaxial element data are shown on Figure 38. These data indicate a very low heat flux region exists within about 0.6 cm (0.25 in.) from the element face. The heat flux increases quite rapidly from this point and is about equal to the nominal value (+25% except for the P_c = 341 N/cm^2 (500 psia) test) beyond 3.17 cm (1.25 in.) axial distance.

(1) Contraction Ratio Effects

Contraction ratio effects appear small. About the same results were obtained at O/F = 5, P_c = 205 N/cm^2 (300 psia) with both the 2.5 and 3.5 contraction ratio chambers.

(2) Mixture Ratio Effects

O/F effects are irregular. The O/F = 2 and 8 data obtained at P_c = 205 N/cm^2 (300 psia) are about the same, whereas the O/F = 6, P_c = 205 N/cm^2 heat flux ratios are about 30% lower.

(3) Chamber Pressure Effects

The heat flux ratio is inversely related to P_c (decreases P_c). This is demonstrated by the O/F = 4, P_c = 68 N/cm^2 (100 psia) and 341 N/cm^2 (500 psia) data as well as the O/F = 6, P_c = 68 and 205 N/cm^2 data.

c. Swirl Coaxial Element (V_t/V_a = 1.0) Axial Heat Transfer Characteristics (7 Tests)

The high velocity swirl (V_t/V_a = 1.0) element heat transfer characteristics are similar to those of the V_t/V_a = 0.5 swirl element injector as shown on Figure 39. All testing was done at 205 N/cm^2 (300 psia) chamber pressure. The only significant difference between these data and the V_t/V_a = 0.5 swirl element data is the high heat flux ratios measured at O/F = 2 with the long, 2.5 contraction ratio chamber. This behavior is similar to that observed with the coaxial element in the long chamber. With this injector element, the use of cold propellants reduced the heat flux by about 25%.

d. Premix Element Axial Heat Transfer Characteristics (19 Tests)

Premix element data are shown in Figure 40. A wide range of results were obtained with this element as the calculated heat flux ratios range from 0.7 to 3.0. The heat transfer environment produced by the premix element is fundamentally different from the shear mixing elements and is similar to the F-O-F triplet elements, in that the heat flux decreased with axial distance except within the 2 cm (0.75-in.) long zone nearest the element. This indicates that the premix element produces much more rapid combustion than the coaxial or swirl coaxial elements.

(1) Contraction Ratio Effect

Two distinct types of heat flux distributions were obtained for the 3.5 and 2.5 contraction ratio chambers. The distribution drawn through the 205 N/cm^2 (300 psia) data in Figure 40a shows that the 3.5 contraction ratio heat flux ratios are generally higher and that the peak heat flux existed further downstream. The 2.5 contraction ratio distribution shows a nearly uniform decrease in heat flux with axial distance (Figure 40b and c).

(2) Chamber Length Effect

No effect of chamber length is indicated since the -1 and -2 chamber data agree reasonably well for the range of O/F and P_c values tested (Figure 40b and c).

(3) Mixture Ratio Effect

Mixture ratio effects are very significant with the premix element, especially in the 3.5 contraction ratio chamber (Figure 40a). The data clearly show a decrease in heat flux ratio with increasing O/F. This characteristic appears related to the momentum of the fuel stream (injected perpendicular to the chamber axis in the premix element design) since the fuel injection velocity decreases as O/F increases. This causes a decrease in fuel penetration, resulting in more fuel at the outer edge of the jet.

(4) Chamber Pressure Effect

The indicated P_c effect is not great and irregular. At O/F = 4 (3.5 and 2.5 contraction ratio), the heat flux ratio tended to be inversely related to P_c; however, the dependency was weak as the variation was within + 15%. The opposite effect is indicated for mixture ratios of 2 and 6 as the 68 N/cm^2 (100 psia) data are slightly lower than the 205 N/cm^2 (300 psia) data (3.5 contraction ratio data).

(5) Propellant Temperature Effect

The use of cold propellants at O/F = 4 and P_c = 205 N/cm^2 (300 psia) test conditions reduced heat flux ratios by about 35%.

e. F-O-F Triplet Axial Heat Flux Characteristics (16 Tests)

Axial heat flux distributions for the B row (the location of this row is shown in Figure 42) of thermocouples are shown in Figure 41 for each injector type in terms of the experimental to nominal heat flux ratio. The results show that the heat transfer characteristics of the 60° and 90° impingement angle injector designs are quite similar, thereby indicating that the impingement angle has a small effect on wall heat flux. With both injectors relatively high heat fluxes were measured at O/F = 2; where the heat flux ratios range from 0.9 to 1.5. This O/F trend is consistent with the premix results discussed previously. The axial heat transfer distribution with the 60° and 90° impingement angle injectors is considered normal at O/F = 4 to 6; the heat flux increases fairly regularly with axial distance and the heat flux ratio is in the 0.2 to 0.8 range. A tendency toward a heat flux peak at 1.0 cm (0.75 in.) axial distance is apparent in the 68.6 N/cm^2 (100 psia) chamber data. A quite different axial characteristic is indicated by the O/F = 2 data as the peak heat flux occurs near the injector face and the heat flux decreases with axial distance downstream of this point. The O/F = 2, P_c = 205 N/cm^2 (300 psia) data for the 60° impingement angle injector has a characteristic almost identical to the previously mentioned premix element; however, the external triplet element heat fluxes are about 60% lower than the previous data.

Generally, higher heat fluxes were measured with the A_f/A_o = 1 injector element. Heat flux ratios as high as 2.0 were indicated as shown in Figure 41. Data were obtained with both the 2.5 and 3.5 contraction ratio chamber designs with this element. The heat flux ratios in both chambers are about the same at axial distances of 4.45 cm (1.75 in.) or more from the injector face but significantly lower in the 2.5 contraction ratio chamber nearer the injector face.

Axial and circumferential heat flux distributions are given for each injector at O/F = 4, P_c = 206 N/cm^2 (300 psia) operating conditions in Figure 42. This graph shows that the A_f/A_o = 1 injector heat fluxes are consistently the highest, but also the most uniform in both the longitudinal and circumferential directions. The A_f/A_o = 2 injector designs are classical "streakers" in that the heat flux along Row C are about 100% higher than the heat fluxes along Rows A and B.

Referring again to Figure 42 it is interesting to note that the high heat flux values associated with the A_f/A_o = 1 injector are consistent with the high performance of this injector as noted earlier. This correlation is consistent with a good mixing element, i.e., high heat fluxes and a small data spread. The data from the A_f/A_o = 2 injectors have a contrary characteristic that is again consistent with the performance data, i.e., low average heat fluxes with low performance injectors. In addition, these injectors indicated a chamber hot streak in an area rotated 90° from the plane of the fuel holes. These streaks are the result of the poor mixing characteristics of the injection elements. The fuel momentum of these injectors is not high enough to penetrate the central oxidizer jet. As a result, the propellant is incompletely mixed and a near-stoichiometric zone is formed locally at the wall. This condition results in the streak noted in Figure 42. It would be expected that a full scale injector with A_f/A_o = 2 elements would behave in a similar manner, i.e., lower performance, lower average heat flux with locally high values.

3. Single Element Stability

Unstable combustion was encountered during some of the single element tests. The test-by-test stability characteristics are listed in Table IX. The premix element exhibited stable operation for all test conditions. The swirler and coaxial elements were, on the other hand, stable only at mixture ratios of approximately 6 or greater, while the triplet injector exhibited low frequency instabilities at high mixture ratio operating points and low fuel side pressure drops. This data is plotted in Figure 43 as a function of oxidizer and fuel circuit $\Delta P/P_c$. At lower mixture ratios, both elements were either marginally stable or unstable. The frequency of instability varied from 700 to 1100 Hz for the swirler element and 600 to 900 Hz for the coaxial element.

The combustion instability undoubtedly influenced the energy release efficiency as noted during Tests 132 (coaxial element) and 162B (swirler element). During both these tests, the combustion stability varied with attendant performance changes. During Test 132, the combustion would shift back and forth from a moderately stable condition to an unstable condition (800 Hz) and the energy release efficiency would shift from 93.5% during stable operation to 89.9% during unstable operation. Similarly, during Test 162B (a cold propellant test), combustion occurred in two modes: marginally

stable and unstable (1000 to 1200 Hz). During the stable mode, the energy release efficiency was approximately 83.5% while, during the unstable mode, the energy release efficiency was 78.7%.

The triplet instability at 3500 Hz was evident at mixture ratios of four and above for both $A_f/A_o = 2$ injectors. At mixture ratio two, these injectors were stable. With the high fuel pressure drop injector ($A_f/A_o = 1$), the injector was stable over the entire operating range. The triplet data are plotted as a function of $(\Delta P/P_c)_o$ vs $(\Delta P/P_c)_f$ in Figure 43. All injectors were stable at $(\Delta P/P_c)_f$ ratios in excess of 10%. No oxidizer circuit ΔP related instability was noted for values of $(\Delta P/P_c)_o$ as low as 10%. Based on these data, both circuits should be held to $\Delta P/P_c$ ratios higher than 10% of P_c as a good design criterion. The coaxial and swirler data indicated a reverse influence on the fuel side, i.e., high values of $\Delta P/P_c$ were unstable while low values of $\Delta P/P_c$ were stable as indicated in Figure 43.

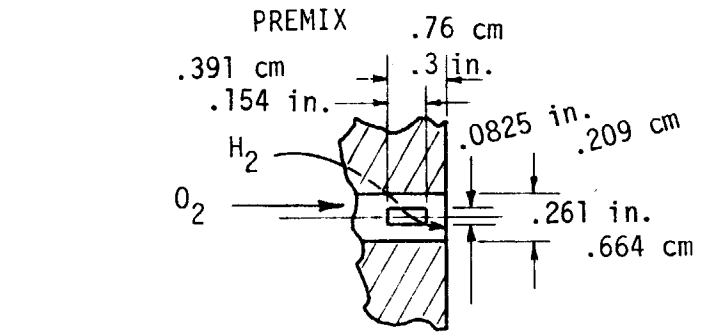

Thrust = 222 Newtons, (50 lb_f)

A_f/A_o = .5

Fuel Slot Width/Oxidizer Diam. = 33%

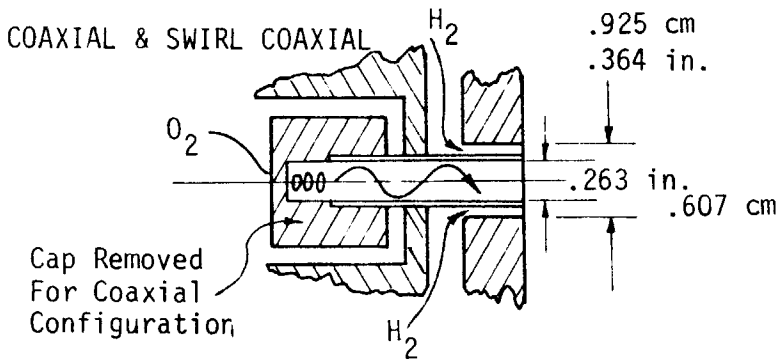

Thrust = 222 Newtons, (50 lb_f)

A_f/A_o = .5

Swirl: $\frac{V_{Tangential}}{V_{Axial}}$ = 0.5 & 1.0

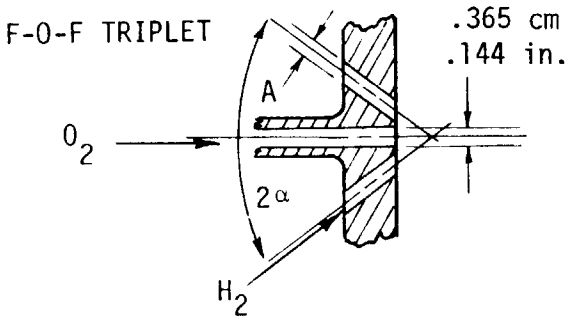

Thrust = 222 Newtons, (50 lb_f)

Configuration	A_f/A_o	2α	A Dia. cm/in	
-1	2.0	90	.365	.144
-2	2.0	60	.365	.144
-3	1.0	60	.253	.0995

FIGURE 29. HOT FIRE SINGLE ELEMENT DESIGN PARAMETERS

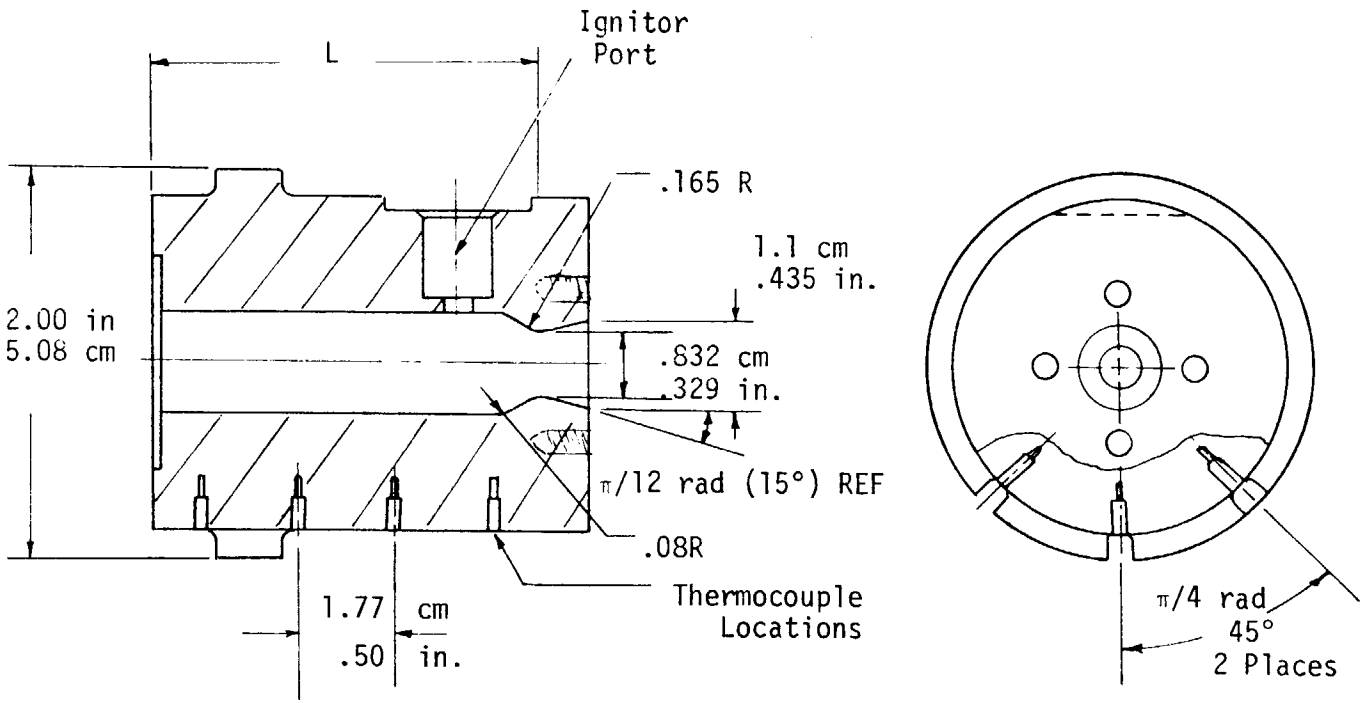

Chamber Design	D_c cm/in	L cm/in	CR
-1	1.32/.52	5.07/2.0	2.5
-2	1.32/.52	14.0/5.5	2.5
-3	1.56/.615	5.08/2.0	3.5

FIGURE 30. SINGLE ELEMENT THRUST CHAMBER

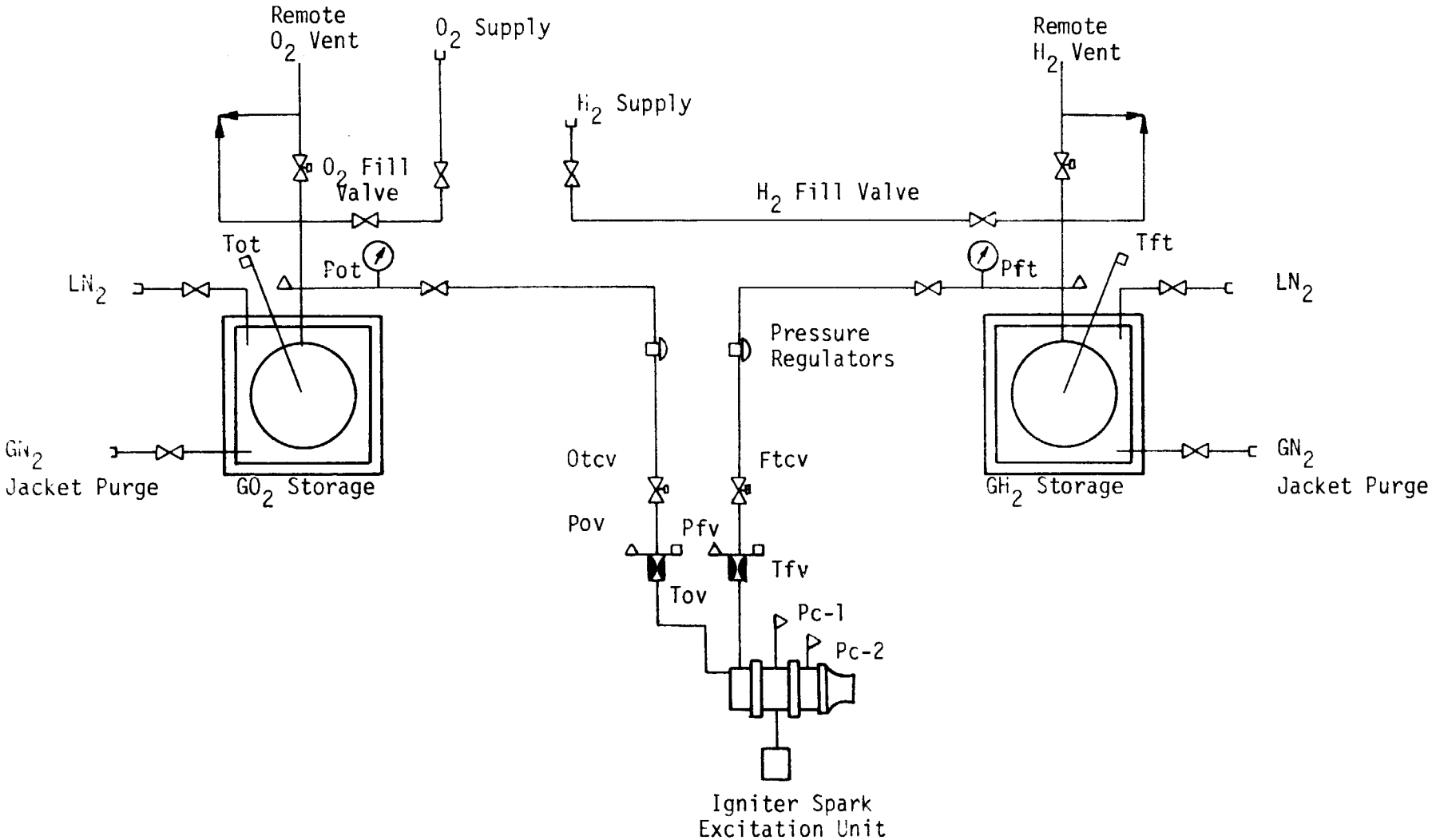

FIGURE 31 SINGLE ELEMENT TEST BAY SCHEMATIC

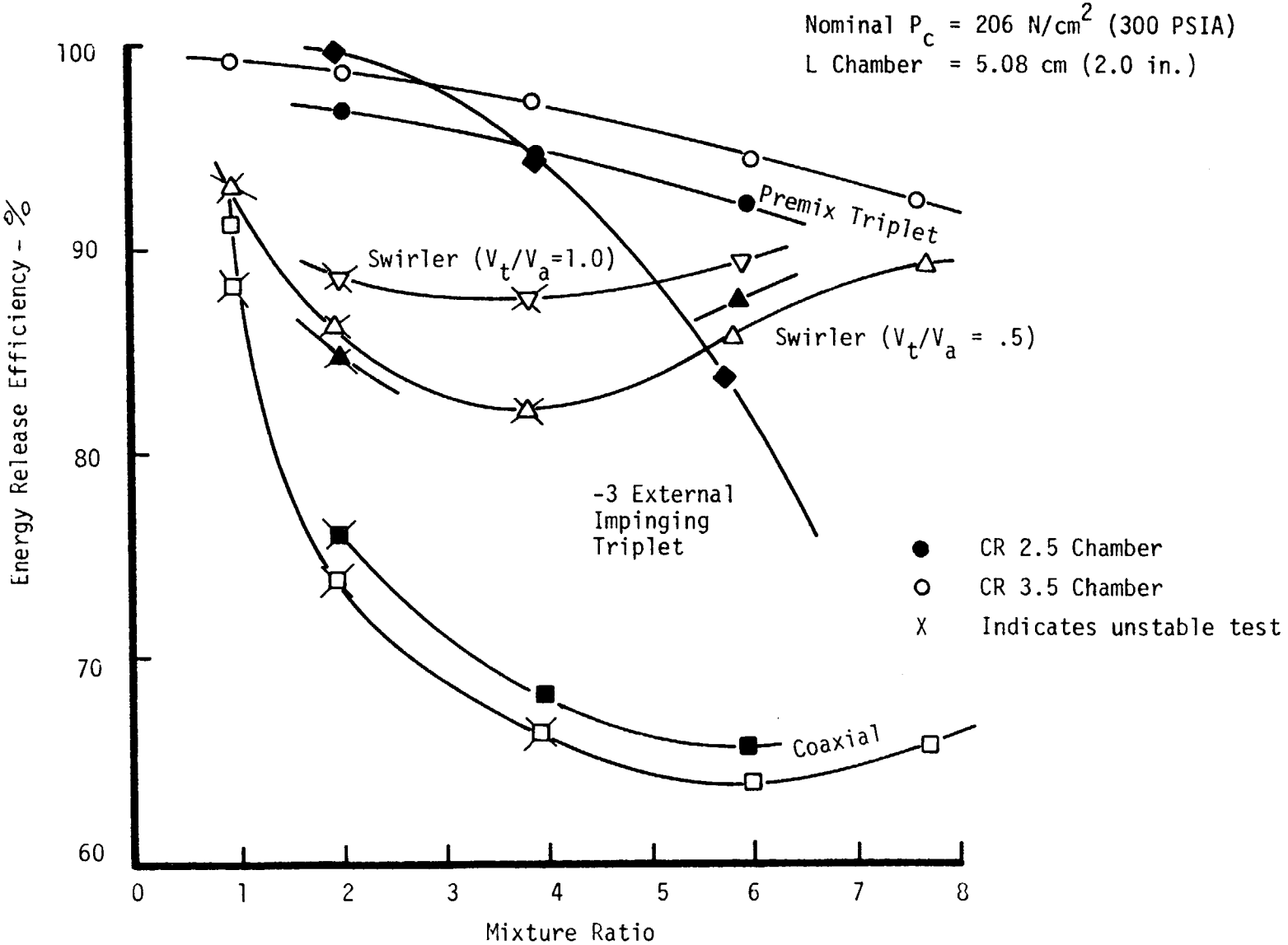

FIGURE 32. SINGLE ELEMENT PERFORMANCE

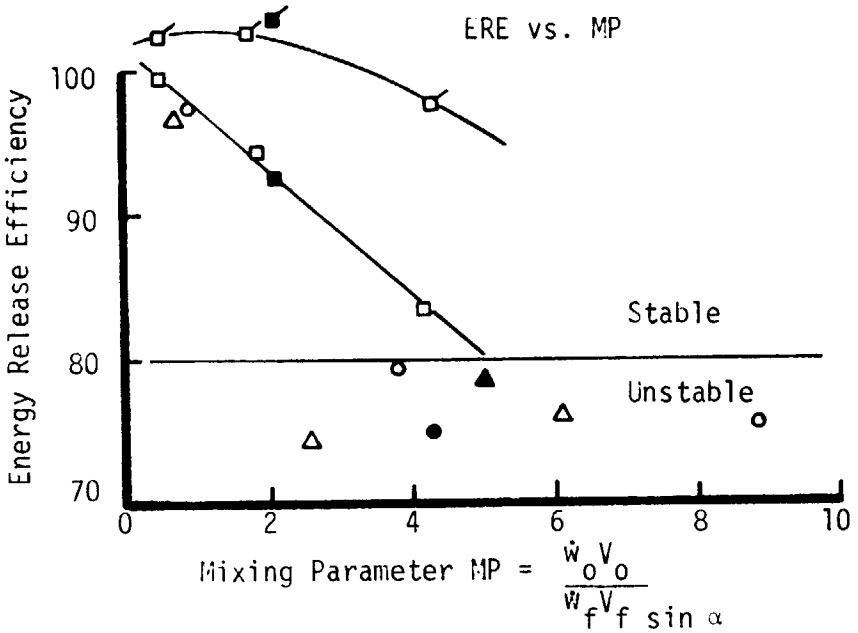

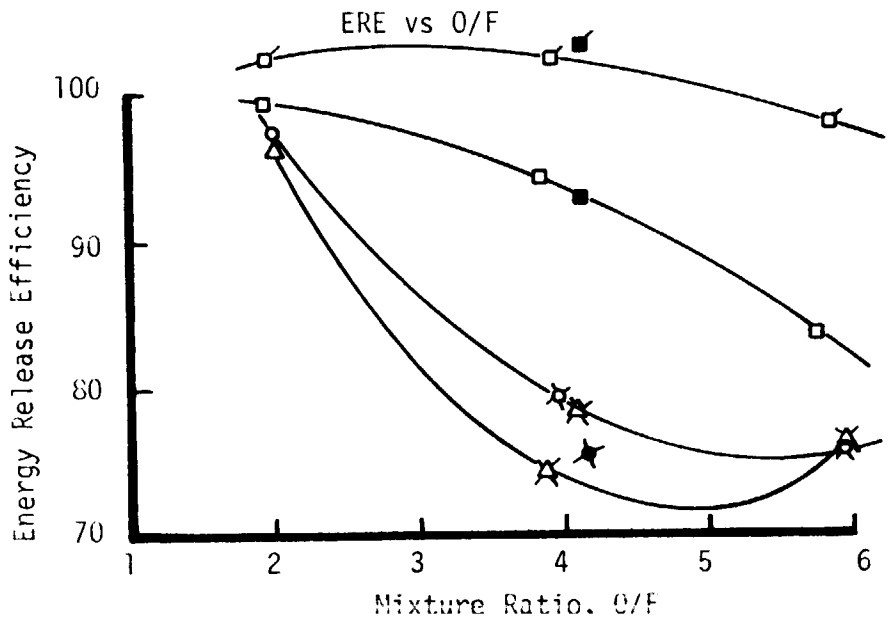

Symbol	Chamber Length cm(in)	Impingement Angle, 2α Radian (Degrees)	Area Ratio A_f/A_o	Cham. Press. N/cm² (PSIA)	Trip. Config.
△	5.1 (2)	π/2 (90)	2	206 (300)	-2
○	5.1 (2)	π/3 (60)	2	206 (300)	-1
□	5.1 (2)	π/3 (60)	1	206 (300)	-3
□	14 (5.5)	/3 (60)	1	206 (300)	-3
■	5.1 (2)	/3 (60)	1	69 (100)	-3
⌑	Unstable at 3500 Hz				

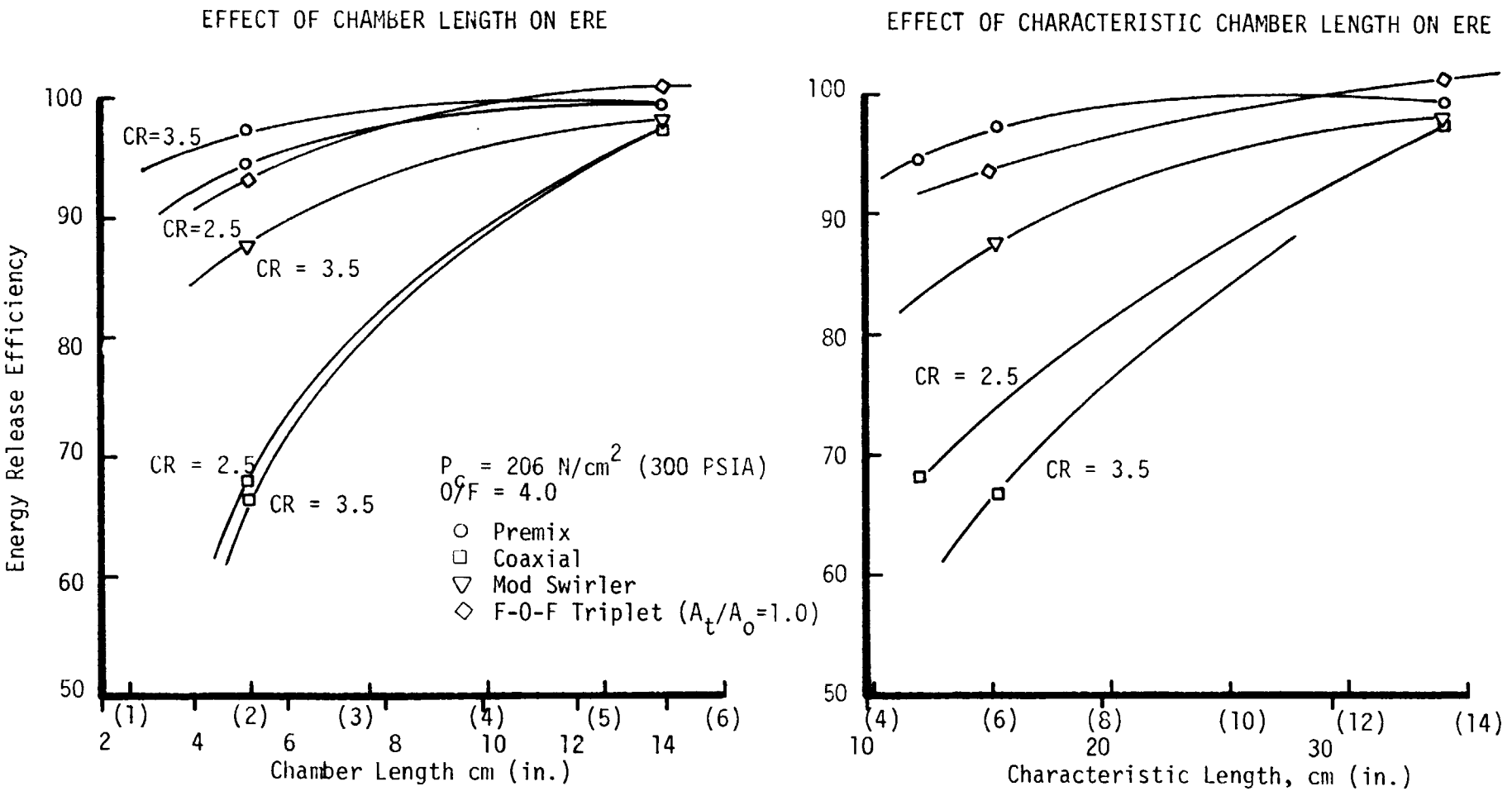

FIGURE 34. EFFECT OF CHAMBER VARIABLES ON SINGLE ELEMENT PERFORMANCE

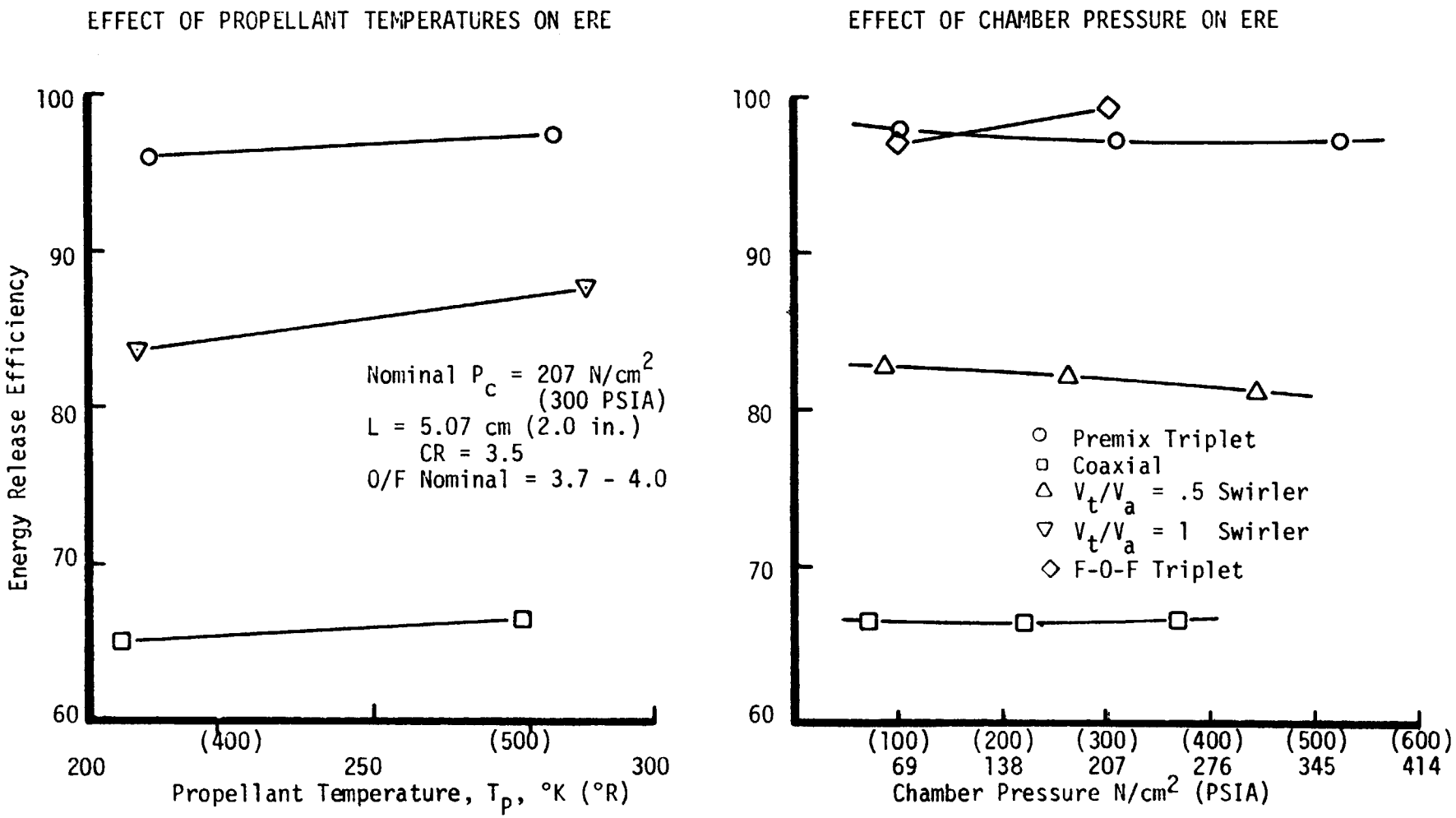

FIGURE 35. THE EFFECT OF T_p AND P_c ON ERE

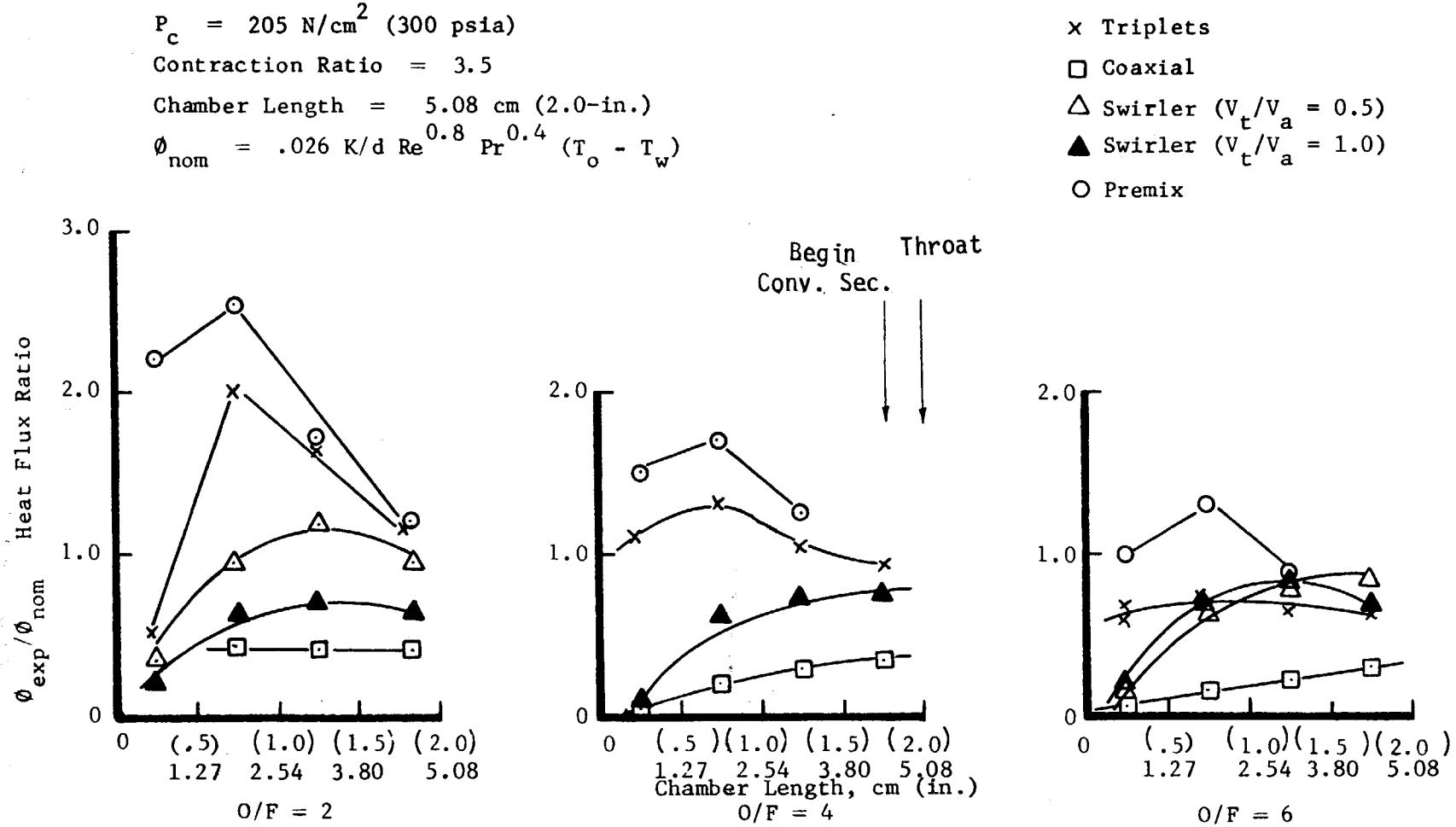

FIGURE 36. SINGLE ELEMENT HEAT TRANSFER CHARACTERISTICS FOR VARIOUS ELEMENTS

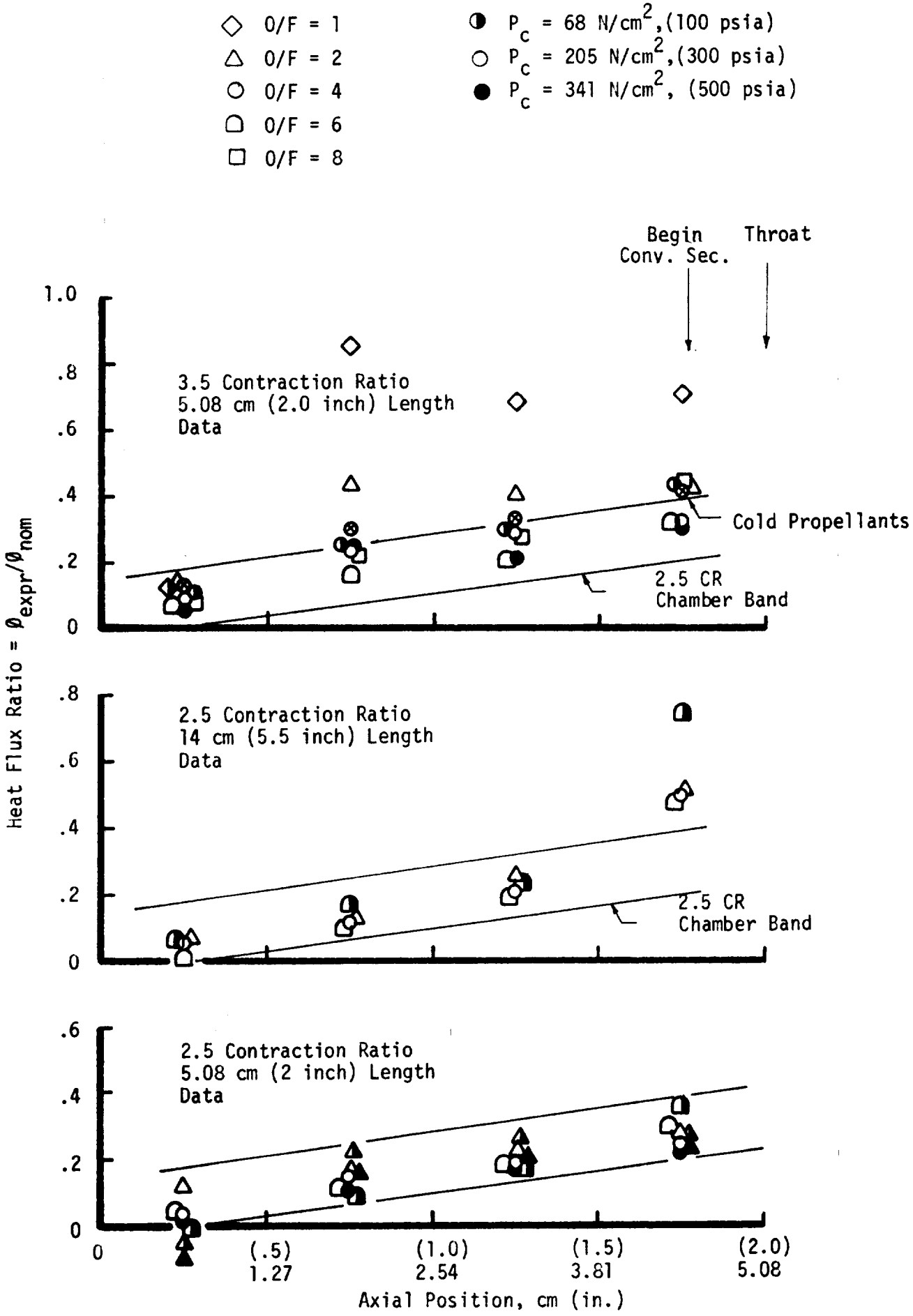

FIGURE 37. COAXIAL ELEMENT HEAT FLUX IN VARIOUS CHAMBERS

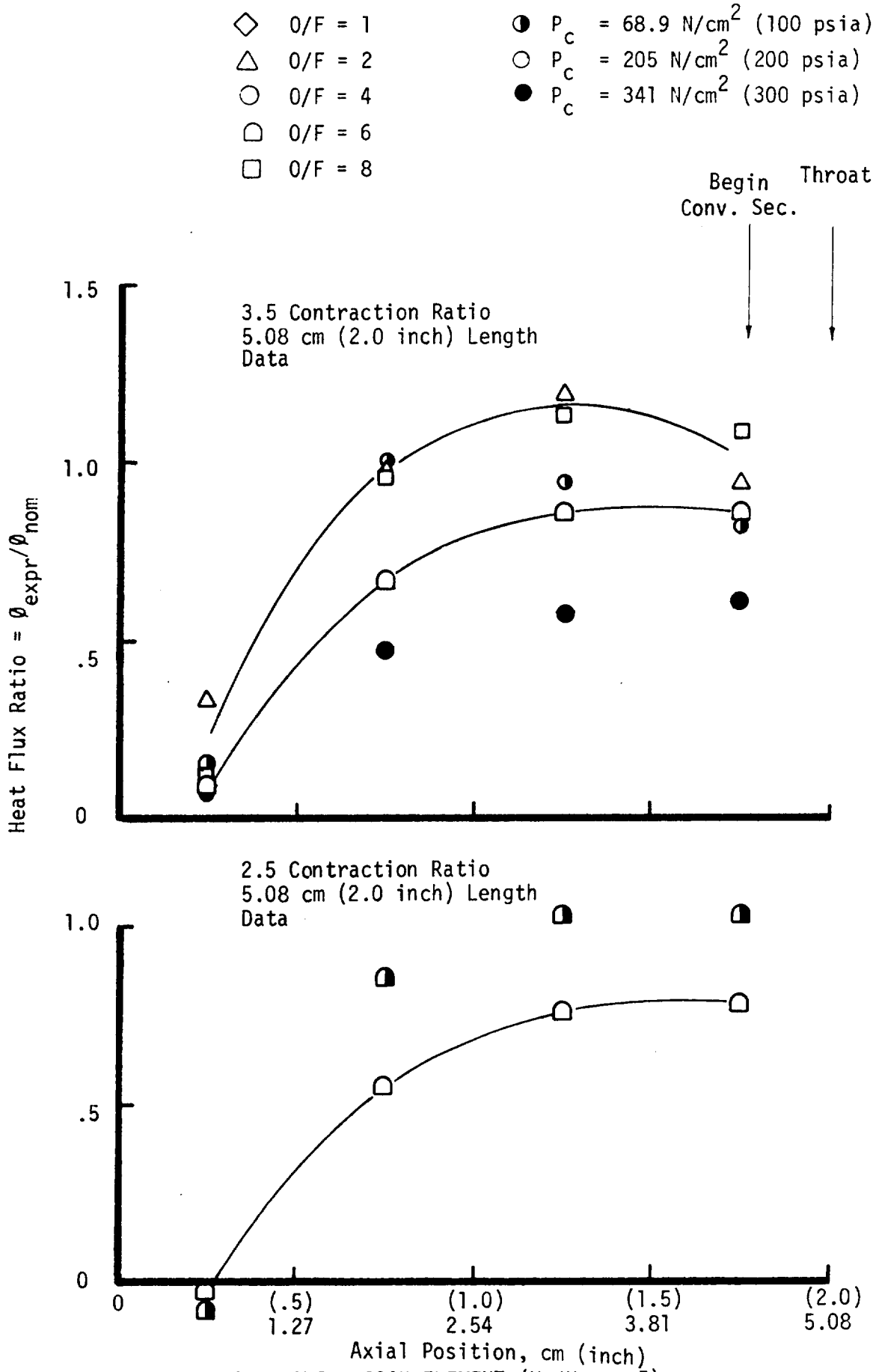

FIGURE 38. SWIRL COAX ELEMENT (V_t/V_a = .5) HEAT TRANSFER CHARACTERISTICS

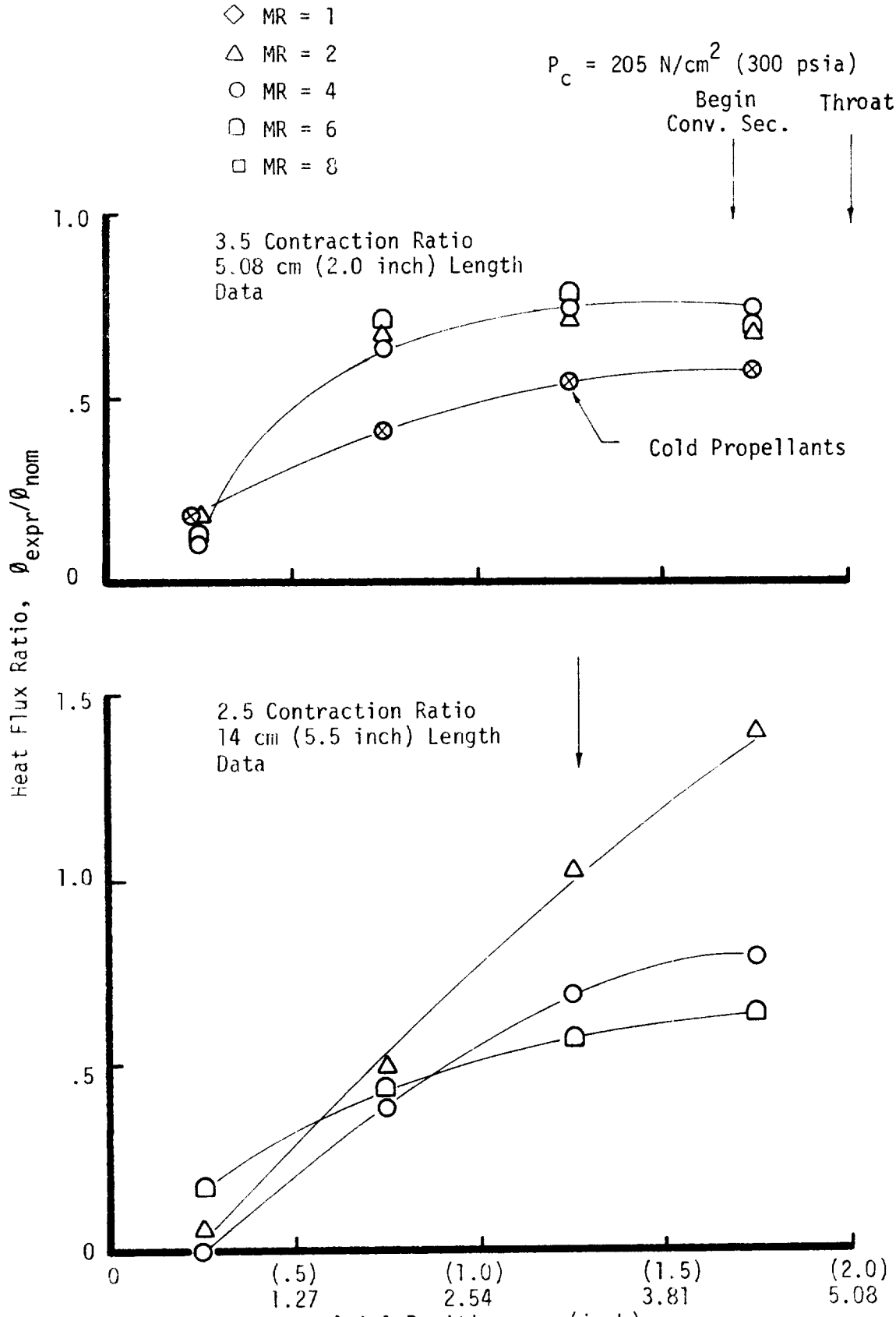

FIGURE 39. SWIRL COAXIAL ELEMENT (V_t/V_a = 1) HEAT TRANSFER CHARACTERISTICS

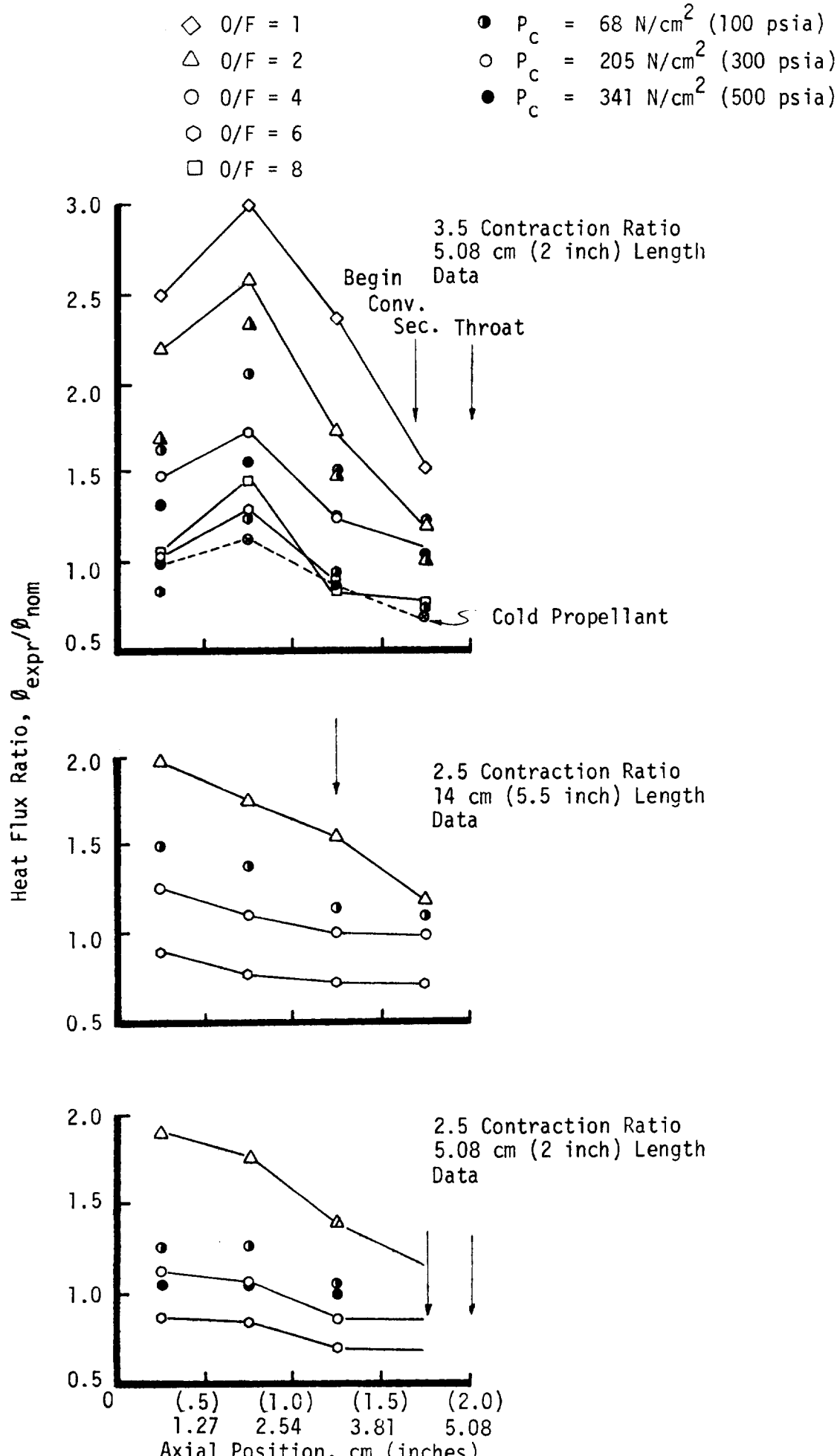

Figure 40. PREMIX ELEMENT HEAT TRANSFER CHARACTERISTICS IN VARIOUS CHAMBERS

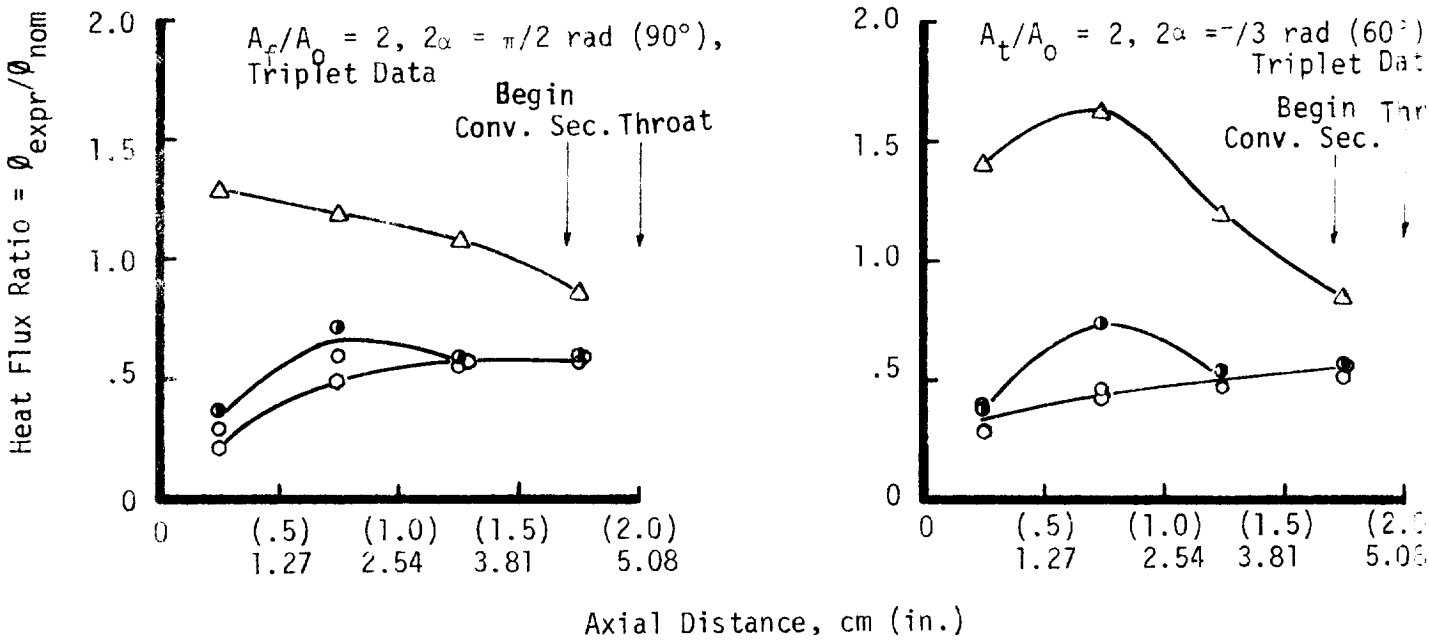

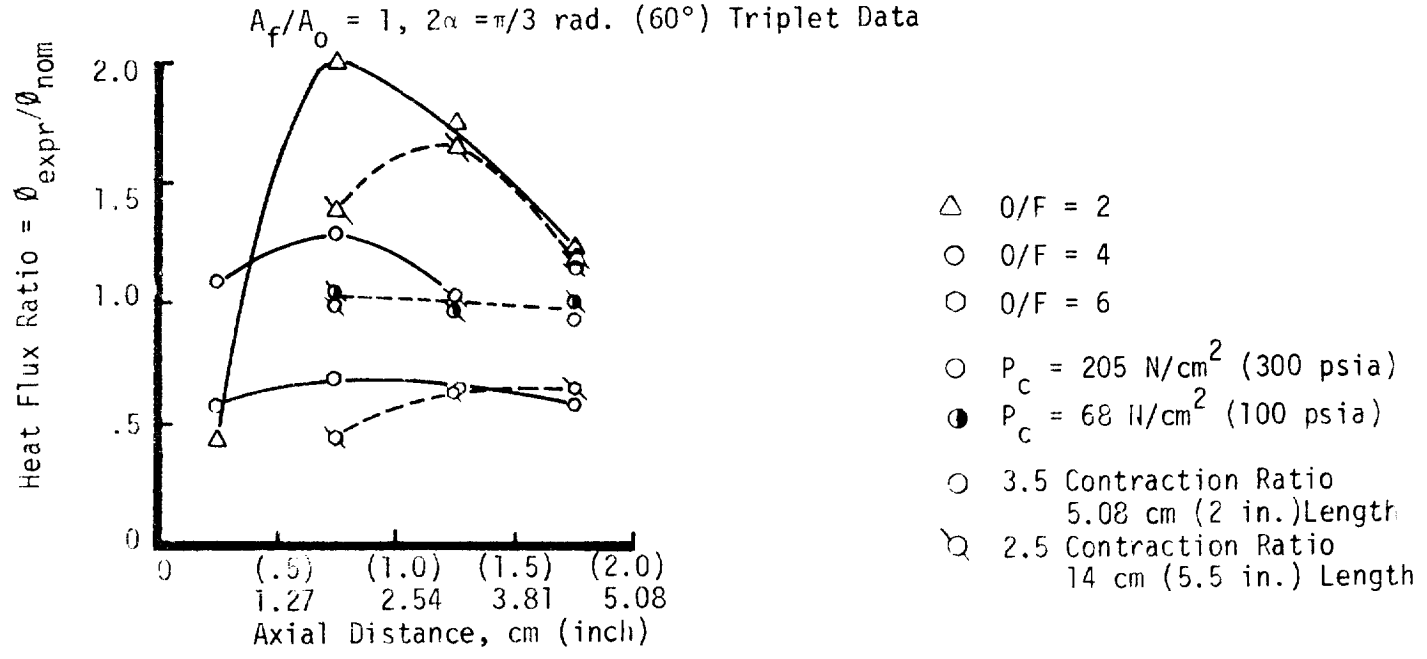

FIGURE 41. TRIPLET ELEMENT HEAT TRANSFER CHARACTERISTICS

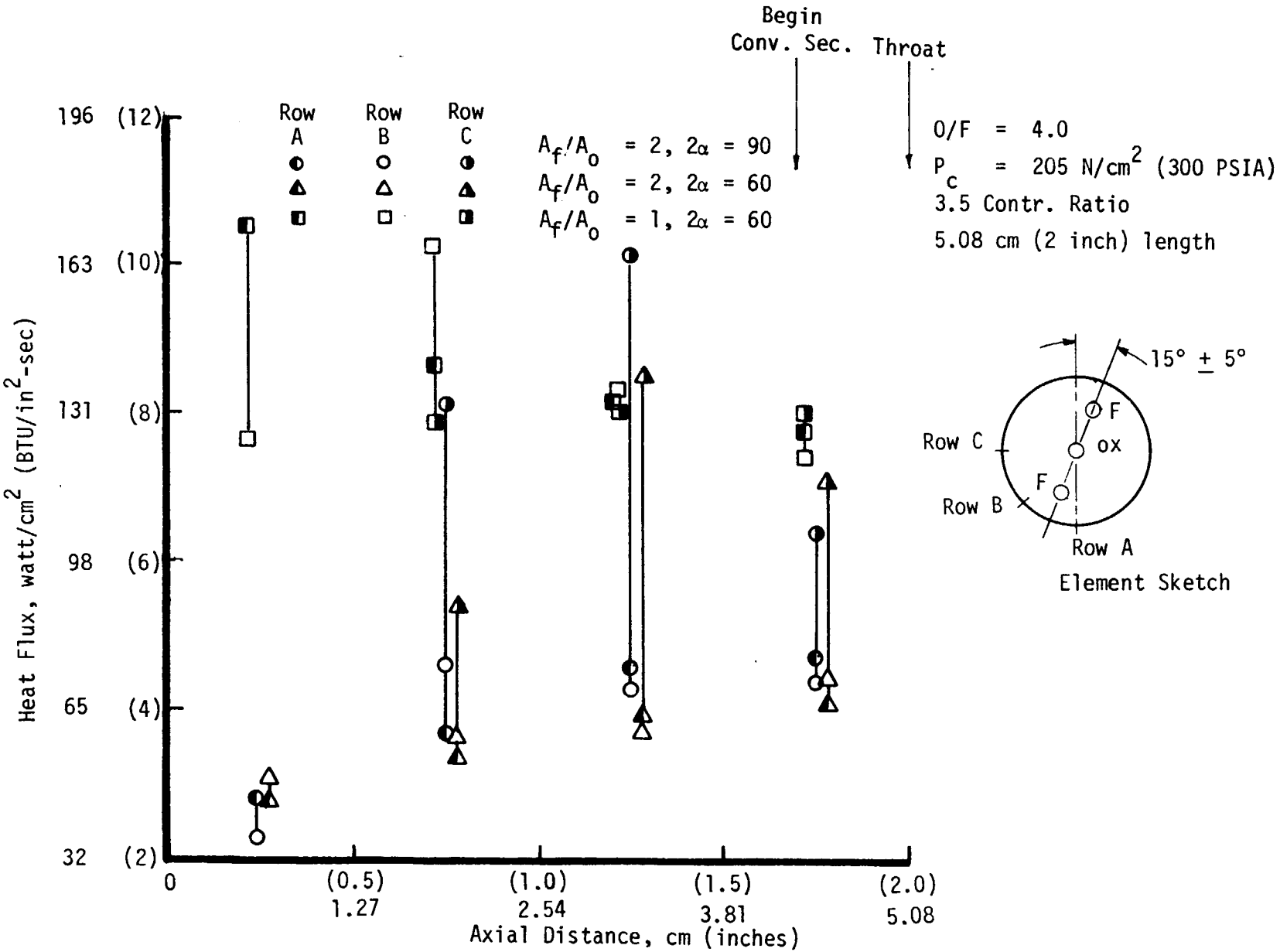

FIGURE 42. TRIPLET AXIAL AND CIRCUMFERENTIAL HEAT FLUX DISTRIBUTION FOR O/F = 4 AND CHAMBER PRESSURE (205 N/cm² (300 PSIA))

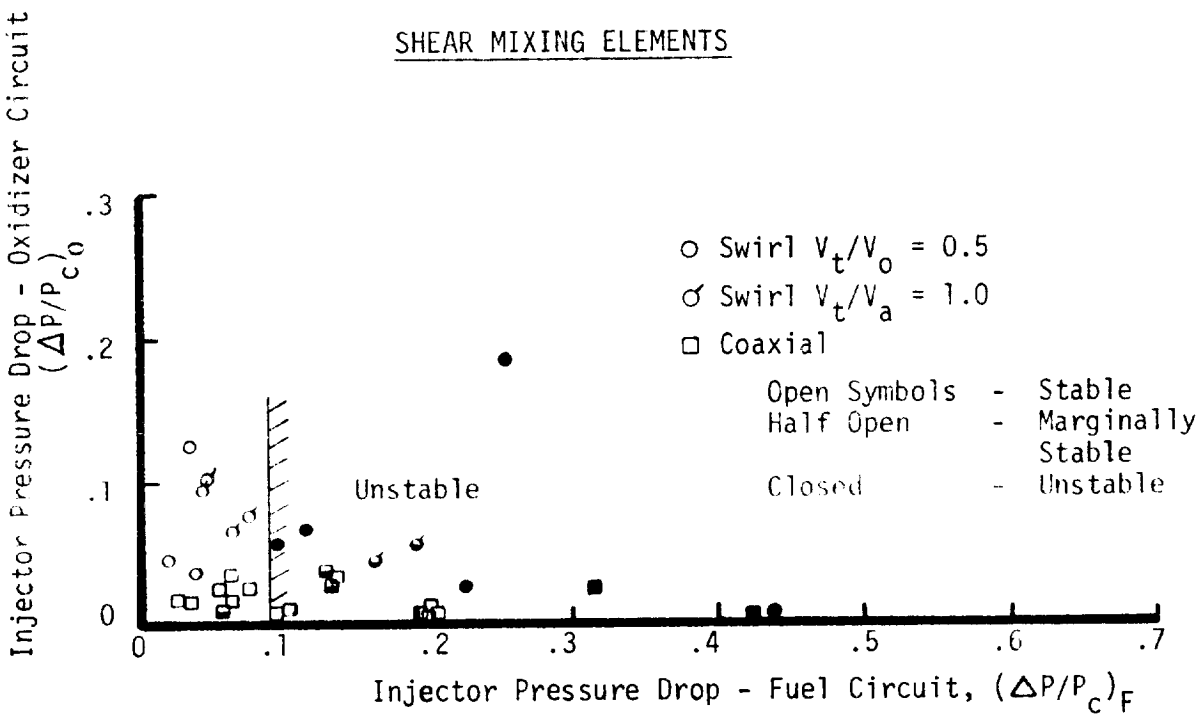

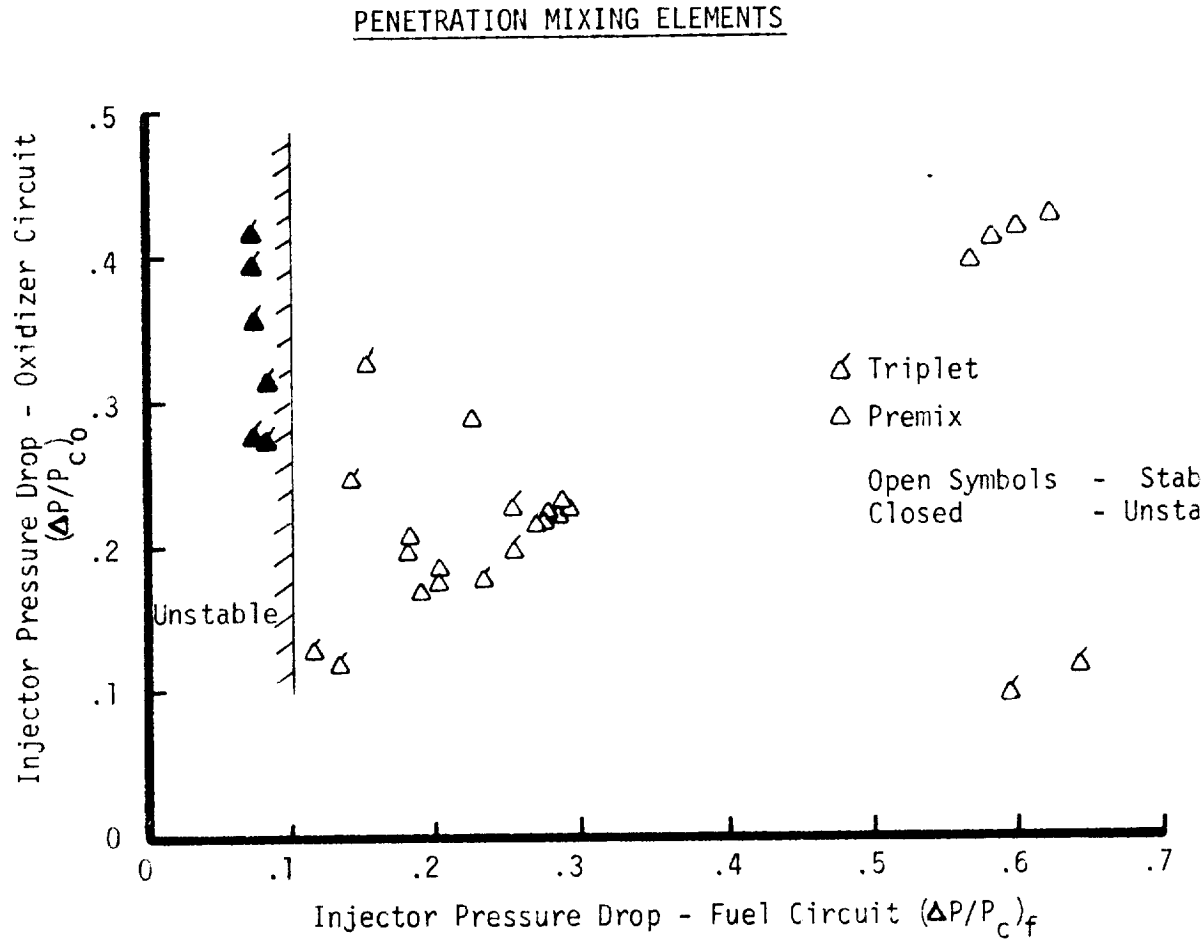

FIGURE 43. LOW FREQUENCY STABILITY CHARACTERISTICS OF GASEOUS INJECTOR ELEMENT

VII FULL SCALE INJECTOR EVALUATION

As a part of this program full scale test series was conducted (at the 6200 N (1500 lb) thrust level) with injectors that were optimized based on cold flow and single element testing. The intent of this testing was to investigate performance, heat transfer and stability with full scale prototype hardware under conditions representative of auxiliary propulsion systems, APS, for the Space Shuttle. This testing was accomplished with three basic injectors; a deep-cup premix, a F-O-F triplet and two zoned (barrier cooled) F-O-F triplet injectors. The results of this testing are briefly summarized below.

Performance efficiencies approaching 100% ERE were achieved in 7.62 cm (3.0 inches) long chambers using both the premix and triplet element injector patterns. The zoned injectors were lower performing due to barrier cooling related mixture ratio maldistribution effects and due to the core mixture ratio shift which caused the core elements to operate off of their uniform mixture ratio peak operating point for which they were originally designed. Future barrier cooled injectors should be designed so both barrier and core elements are optimized at their respective barrier and core mixture ratios to minimize the latter effect. High injector-end chamber heat fluxes were recorded for both the triplet and premix injectors. Injector face thermal data indicated the need for active cooling of the face. All three injectors resulted in at least one case of high frequence instability, indicating the need for damping devices such as resonators and/or baffles.

A. DESCRIPTION OF TEST ARTICLES

1. Injectors

a. Deep Cup Premix Injector

The premix injector designed for this program is conceptually similar to that injector successfully demonstrated on Contract NAS3-14354, Ref. 12. For this program, the basic injector body and manifolding designs were retained. Only the injection element design was changed. A sketch of the element is shown in Figure 44 and it is referred to as the deep cup premix element concept. This injector was designed to satisfy the following conditions:

Number of Elements	36
Oxidizer Dia.	.60 cm (.237 in.)
Fuel Slot Geometry	.201 x .356 cm (.079 x .140 in.)
Pressure Drop	41 N/cm^2 (60 psi)
Injection Velocity	330 m/sec (1080 fps)

The oxygen enters the mixing cup through a cylindrically etched passage formed of 14 nickel platelets. Fuel is directed radially into the oxygen through a rectangular passage etched through the same platelets. At the base of the fuel drop-through-passage, 6% of the fuel is diverted into the face cooling circuit. A set of three platelets redistributes this fuel over the injector face, where it is injected axially into the combustion chamber through 384 orifices.

The deep cup premix concept developed on this program utilizes confined mixing of the O_2/H_2 propellants prior to injection into the chamber. This is accomplished by impinging two fuel streams on a central oxidizer stream in a mixing cup recessed into the injector face. The basic design is similar to the injector that has been demonstrated successfully by ALRC on the APS program (Contract NAS3-14354) Ref. 12. This design differs in that the mixing cup depth is an order of magnitude deeper than the APS design (0.764 cm deep vs. 0.076 cm deep).

This design modification was a result of comparing the cold flow and hot firing test performance on this and the APS program. The APS single element cold flow data for the premix element with a rectangular fuel channel and a shallow cup depth indicated a strong relationship between E_m and momentum ratio and a relatively low mixing effectiveness. This strong functional relationship was not noted in the experimental data from this program and the performance level was considerably higher for the deep cup design. Also the single element hot fire data obtained on this program indicated that the confined mixing imposed by the deep cup increases propellant mixing, since the ERE was nearly 100% in a 5.08 cm (2.0 in.) long chamber. The injector assembly and platelets are shown in Figure 45. The injector is shown at an intermediate step in the fabrication process. The body, platelet stack, and individual platelets are depicted. Oxygen enters the injector through a 3.8 cm (1.5 in.) diameter stainless steel tube and is distributed through the injector body with the aid of sheet metal distribution plates. The oxygen enters the face through 36 tubes brazed to the injector body and face. Fuel enters the face platelet stack through 36 holes drilled through the face plate. The injection platelet stack shown schematically in Figure 44 is bonded to the face plate, completing the injector assembly.

The 14 Nickel 200 platelets immediately joined to the face plate are the fuel injection platelets, a detail of which is shown in Figure 45. The "dumb-bell" shaped passages form the fuel geometry of the premix element. Oxygen enters the element through the 36 tubes joined to the face plate, and flows into a cylindrical cavity formed by the 14 injection platelets. The fuel is injected into the same cavity and intimate mixing of the H_2 and O_2 is accomplished. After the propellants are mixed, the gas proceeds through the cup plate shown in Figure 45. The function of this plate is to provide increased constrained mixing time as well as diverting approximately 6% of the fuel into the face cooling circuit.

The face cooling circuit was comprised of a three-platelet stack. The first platelet (the coolant inlet platelet shown in Figure 45) was located just below the cup plate, where further H_2 coolant metering was accomplished by the 72 0.061 cm (0.024 in.) diameter holes. After the coolant passes through this platelet, it was distributed over the injector face by the distribution platelet illustrated in Figure 45. The fuel leaving the inlet platelet entered the rectangular passages of the distribution platelets and flowed over the surface of the injector face, serving to both regeneratively cool the face and feed the face bleed holes. The last platelet labeled face in Figure 45 provided the means to inject both the fuel coolant and premixed gases into the combustion chamber.

b. F-O-F Triplet Injector

Based on cold flow data presented earlier an injector composed of an array of external impinging F-O-F triplet elements had the potential to be high performing. Also, this element was extremely sensitive to design and operating point variables such as relative orifice area and

impingement angle. This information was insufficient to design a full-scale injector since the effects of combustion were not known but were suspected to be important. The experience gained in the single element testing program with elements similar to the prototype full scale injection elements, clearly indicated that the combustion process did modify the cold flow characteristics. This data was then used in conjunctions with the cold flow data to complete the full scale injector design. An injector was designed based on the design criteria discussed in Section VIII, which resulted in the following parameters.

Number of elements	72	
Oxidizer element diameter	0.283 cm	(0.112 in.)
Fuel element diameter	0.1325 cm	(0.0521 in.)
Impingement angle	$\pi/3$ rad.	60°
Oxidizer injection velocity	86 m/sec	(281 ft/sec)
Fuel injection velocity	895 m/sec	(2940 ft/sec)

The triplet injector assembly is shown in Figure 46 together with details of the injector face. The basic injector body was manufactured from a surplus premix injector from a previous program. Oxygen entered the injector via a 3.81 cm (1.5 in.) diameter stainless steel tube and was distributed throughout the injector body with the aid of sheet metal distribution plates. The oxygen was routed to the injection elements through 72 tubes brazed to the injector body and face plate. Fuel entered the injector through a manifold around the oxygen tubes. The hydrogen passed between the tubes and entered the elements via holes drilled through the face plate. Up to this point the triplet injector and the premix injector were virtually identical except that the premix injector was composed to 36 oxidizer tubes rather than 72 for the triplet.

Figure 46 shows the injector element. It was machined into a 0.47 cm (0.185 in.) thick copper plate that contains additional fuel injection orifices, the oxidizer injection orifices and the face coolant metering orifices. This plate was bonded to the injector body such that the oxidizer tubes were aligned with the oxidizer injection orifices and the fuel galleries were aligned with the holes through the body plate. This plate serves the dual function of directing both propellants into the chamber. Immediately below the face plate was a set of three platelets that comprised the face cooling circuit when bonded to the injection plate. These platelets were made of 1/4 hard nickel 200 and were 0.0254 cm (0.010 in.) thick. The first platelet, the coolant metering plate, controlled the amount of GH_2 directed into the coolant circuit (7% of the total fuel flow). Fuel exited this plate and was directed into the distribution platelet. Fuel entered each shaped passage of this platelet and was distributed throughout the injector face. Covering these passages was the last platelet in the stack, which injected the coolant into the combustion chamber through 460 0.038 cm (0.015 in.) diameter holes.

c. Zoned Injectors

The third full scale injector was a zoned injector, designed to produce an environment of lower temperature barrier gases composed of fuel rich combustion products. This was achieved by tailoring the triplet injector described earlier to produce a low mixture ratio barrier at the chamber wall by modifying the element design. The zoned injector was manufactured from the triplet injector by first removing the triplet face and then bonding a zoned face and cooling circuit onto the triplet body. Two different injector patterns were tested, the -1 and -2 injectors. These injectors differed in the values of the barrier mixture ratio and mass flow. The -2 injector was made from the -1 injector element by increasing the diameter of the oxidizer injection elements in the outer row. A detail drawing of the injection elements and pattern is illustrated in Figure 47.

The flow distribution in the core and barrier circuits of the -1 and -2 injectors were determined empirically, by cold flowing the injector with GN_2. The individual orifice flow rates were measured with a rotameter type flow meter, with the injector flowing GN_2 at the design Mach No. The barrier mixture ratios and flow rates were then computed and are plotted in Figure 48a. At an overall mixture ratio of 4.0, the -1 injector flowed 35.6% of the total injector flow in the barrier at an O/F of 2.93 while the remaining flow is in the core at an O/F ratio of 4.9. The -2 injector (with increased diameter oxidizer orifices) at an overall O/F ratio of 4.0 flowed 39.2% of the toal injector flow through the barrier circuit at a mixture ratio of 3.3 while the remaining flow was directed through the core at an O/F of 4.6.

The zoned injector cooling concept results in a performance loss due to off design mixture ratio operation of the barrier and core circuits. The specific impulse loss was computed by assuming that the combustion zone was comprised of two streamtubes operating at the respective core and barrier mixture ratios and mass fluxes. The streamtubes were assumed to expand one dimensionally through the full engine area ratio without mixing. This analysis was completed by calculating an overall specific impulse consistent with the sum of the mass weighed specific impulse of the individual streamtubes. The results of this analysis are illustrated in Figure 48b. The specific impulse loss for these injectors at an overall mixture ratio of 4.0 is 0.8% and 0.5% of one-dimensional kinetic specific impulse ($I_{sp\ ODK}$) for the -1 and -2 injectors, respectively. Additional performance loss was expected because the elements were operating away from the optimum injection momentum ratio as discussed in Section VIII.

2. Chambers

The injectors were tested in the heat sink copper chambers illustrated in Figure 49. These chambers had provision for high frequency instrumentation, two static pressure ports and inner wall, C-A thermocouples located both between and in line with the injection elements. In addition a port was provided for a 2 grain RDX charge for stability evaluation.

Two chambers (-1 and -2) and a L* section were fabricated. The -2 chamber differed from the -1 chamber in that the throat diameter was larger resulting in a smaller contraction ratio. Provision for increasing chamber length from 7.62 cm (3.0 in.) to 13.9 cm (5.47 in.) was provided by a cylindrical copper section also instrumented with flush-mounted thermocouples and both high and low frequency response pressure transducers. The salient chamber design parameters are listed in the following table.

	-1 Chamber	-2 Chamber	L* Section
Length - cm (in.)	7.62 (3.0)	7.62 (3.0)	6.27 (2.47)
Throat Diameter cm (in.)	4.87 (1.92)	6.27 (2.47)	
Chamber Diameter cm (in.)	8.94 (3.52)	8.94 (3.52)	8.94 (3.52)
Contraction Ratio	3.4	2.02	
L* cm (in.)	13.5 (5.32)	8.37 (3.29)	39 (15.3)(1)
Area Ratio	2.97	2.97	

B. TEST FACILITIES AND PROCEDURES

Physics Laboratory Test Bay 6 was selected for the full-scale tests. The Bay 6 flow and instrumentation schematic together with the test hardware installed in the bay are shown in Figure 50. This bay is equipped with complete gaseous hydrogen/gaseous oxygen feed systems with sufficient capacity to run 6600 N (1500-lbf) engines for 10-sec duration. The facilities include a spherical heat sink hydrogen conditioning vessel that was used for the temperature conditioned propellant tests. Oxygen was temperature conditioned by flowing LN_2 through a small packed bed. The O_2 then was chilled by transfer of heat within the bed.

The mass flow rates were measured with critical flow venturis. Both ambient and propellant temperature conditioned tests used gas regulators for setting the supply pressure to critical flow nozzles. These nozzles provide reliable and accurate flow rate data while maintaining a constant flow rate to the engine independent of downstream perturbations. System pressures and thrust were measured using a six-wire measurement system utilizing strain gage pressure or force transducers. The transducers have 350 Ohm strain gauges in a fully active four-arm bridge configuration.

C. FULL SCALE TEST RESULTS

Fifty four full scale injectors tests were completed. The test series for the premix, triplet and zoned triplet injectors involved 21, 19 and 14 tests, respectively. A detailed list of test parameters, test configuration and test results is found in Tables X and XI. Table X is in English Units and Table XI S.I. units. The following paragraphs summarize the performance, heat transfer and stability results from this series of tests. The techniques used to yield these results are discussed in Appendices C and D.

(1) With -1 Chamber

TABLE X

TEST DATA FOR
DEEP CUP PREMIX INJECTOR

Test No.	Date	Duration sec.	Chamber	P_{c1} psia	P_{c2} psia	$F_{avg_{vac}}$ lbf	T_o °F	T_f °F	T_{f_I} °F	$\dot{W}_o$ lbm/sec	$\dot{W}_f$ lbm/sec	MR_{inj}	$\dot{W}_{f_{ign}}$ lbm/sec	MROA	A_e/A_t	$\dot{W}_T$ lbm/sec	C* ft/sec	$I_{s_{vac}}$ lbf-sec/lbm	$I_{s_{vac_{theo}}}$ lbf-sec/lbm	$\%\eta I_s$
2K-11-101	8-29-72	0.45	-1	290.7	291.5	1251	97.4	94.0	95.2	2.61	0.678	3.85	0.0094	3.80	2.94	3.29	8194	379.4	396.2	95.7
102	8-30-72	1.15	-1	296.3	292.8	1285	89.4	83.2	84.0	2.726	0.667	4.09	0.0096	4.03	2.94	3.40	8093	377.7	394.6	95.7
103	8-30-72	1.45	-1	304.5	294.6	1322	101.3	88.0	94.9	2.304	1.139	2.02	0.0094	2.00	2.94	3.45	8197	382.9	397.0	96.4
104	8-30-72	1.11	-1	277.0	273.4	1203	100.1	88.0	94.6	2.826	0.486	5.84	0.0093	5.71	2.94	3.38	7620	355.4	374.0	95.0
105	8-31-72	2.10	-1	103.8	100.2	459	96.0	80.3	91.5	0.780	0.384	2.03	0.0094	1.98	2.94	1.17	8221	391.2	396.7	98.6
106	8-31-72	2.10	-1	115.5	111.8	501	103.5	86.2	93.3	0.924	0.368	2.51	0.0093	2.45	2.94	1.30	8249	385.0	399.6	96.3
107	8-31-72	2.10	-1	110.4	108.1	487	103.4	82.2	93.2	1.116	0.217	5.14	0.0094	4.93	2.94	1.34	7643	362.8	382.8	94.6
108	8-31-72	2.10	-1	103.9	103.8	458	108.2	84.8	96.3	1.201	0.162	7.39	0.0094	6.99	2.94	1.37	7048	333.6	354.6	94.1
134	10-11-72	0.89	-1	290.5	280.4	1280	73	72	58	1.774	1.754	1.01	0.0095	1.01	2.94	3.53	7648	361.8	373.3	96.9
135	10-11-72	1.17	-1+L*	308.8	318.0	1360	57	42	56	2.470	1.093	2.26	0.0096	2.24	2.94	3.57	8050	380.7	398.7	95.5
136	10-11-72	1.26	-1+L*	305.8	309.2	1334	57	52	57	2.823	0.679	4.16	0.0097	4.10	2.94	3.51	8110	379.9	394.0	96.4
137	10-11-72	1.55	-1+L*	295.4	296.3	1292	55	52	58	3.134	0.4939	6.32	0.0095	6.20	2.94	3.63	7560	355.0	369.4	96.1
138	10-11-72	1.56	-2	179.5	166.8	1323	64	67	64	2.389	1.108	2.16	0.0095	2.14	2.43	3.50	7859	377.3	389.3	96.9
139	10-11-72	1.57	-2	179.5	171.8	1293	64	53	64	2.833	0.6864	4.13	0.0095	4.07	2.43	3.52	7809	366.4	383.4	95.6
140	10-11-72	1.52	-2	165.4	161.0	1190	64	52	65	3.093	0.4662	6.59	0.0095	6.46	2.43	3.54	7155	335.4	353.3	94.9
141	10-13-72	1.59	-1	309.2	304.9	1329	57	58	57	2.799	0.6763	4.14	0.0096	4.08	2.94	3.48	8263	381.4	394.2	96.8
142	10-13-72	1.58	-1	266.3	263.3	1150	61	50	63	3.176	0.371	8.57	0.0094	8.35	2.94	3.55	6974	323.5	341.5	94.7
143	10-13-72	0.65	-1	526.8	511.0	2242	73	56	73	4.644	1.234	3.76	0.0093	3.74	2.94	5.88	8334	380.8	397.2	95.9
144	10-13-72	0.76	-1	473.6	470.1	2030	79	53	76	4.939	0.831	5.94	0.0093	5.88	2.94	5.77	7632	351.2	373.6	94.0
154	10-19-72	0.78	-1	527.9	515.9	2235	70	74	65	3.880	1.952	1.93	0.0096	1.88	2.95	5.84	8416	382.6	396.7	96.4
155	10-20-72	0.77	-1	291.2	288.5	1230	-107	-112	58	2.673	0.664	4.03	0.0096	3.97	2.95	3.34	7936	367.5	390.6	94.1

TEST DATA FOR
TRIPLET INJECTOR

111	9-13-72	0.68	-1	301.6	304.6	1308	86.7	65.3	77.8	2.720	.689	3.95	.0093	3.91	2.94	3.41	8217	382.6	395.3	96.8
112	9-13-72	0.75	-1	306.4	304.8	1322	98.1	69.8	83.2	2.304	1.099	2.10	.0093	2.08	2.94	3.41	8363	387.4	397.6	97.4
113	9-13-72	0.75	-1	285.2	286.7	1251	98.1	65.9	86.7	2.948	.501	5.88	.0092	5.78	2.94	3.45	7681	361.7	374.9	96.5
114	9-14-72	0.72	-1	110.2	109.2	476	89.7	72.9	84.9	.825	.392	2.10	.0092	2.06	2.94	1.22	8370	388.5	397.4	97.8
115	9-14-72	0.74	-1	105.4	104.7	461	91.2	71.2	85.8	.945	.244	3.87	.0093	3.73	2.94	1.19	8192	385.1	395.6	97.3
116	9-14-72	0.73	-1	98.2	98.4	434	91.0	74.0	85.4	1.002	.180	5.57	.0095	5.29	2.94	1.19	7677	364.6	377.7	96.5
117	9-15-72	0.73	-1+L*	295.5	296.0	1286	95.0	75.5	86.6	2.677	.675	3.96	.0093	3.91	2.94	3.36	8187	382.6	395.4	96.8
118	9-15-72	0.74	-1+L*	305.2	302.7	1320	95.3	72.9	86.9	2.297	1.096	2.10	.0095	2.08	2.94	3.40	8354	388.0	397.6	97.6
119	9-15-72	0.74	-1+L*	296.8	299.0	1313	96.1	70.0	86.8	3.167	.497	6.37	.0092	6.26	2.94	3.67	7525	357.5	368.4	97.0
120	9-18-72	0.74	-2	168.0	171.0	1220	80.5	63.2	70.9	3.023	.495	6.11	.0094	5.99	2.43	3.52	7342	345.9	359.5	96.2
121	9-18-72	0.75	-2	189.1	188.3	1370	80.3	67.2	71.0	2.514	1.101	2.28	.0096	2.26	2.43	3.62	8043	378.0	389.8	97.0
122	9-18-72	0.74	-2	171.8	173.6	1246	80.8	58.0	70.8	2.657	.686	3.87	.0093	3.82	2.43	3.35	7900	371.7	385.8	96.3
123	9-18-72	0.87	-1	304.7	308.3	1231	82.3	66.7	74.1	2.755	.676	4.06	.0094	4.02	2.94	3.44	8248	384.0	394.7	97.2
124	9-19-72	0.88	-1	266.8	267.4	1166	78.7	61.8	73.7	3.124	.389	8.03	.0094	7.84	2.94	3.52	7054	331.0	347.6	95.2
127	9-20-72	0.75	-1	519.6	519.7	2240	90.6	61.7	84.0	4.532	1.232	3.68	.0097	3.65	2.94	5.77	8381	388.0	397.7	97.6
128	9-20-72	0.70	-1	472.0	475.0	2056	90.4	65.3	85.5	4.863	.797	6.10	.0094	6.03	2.94	5.66	7754	362.6	373.7	97.0
131	9-22-72	0.88	-1	307.3	313.1	1317	-98.4	-129.7	73.8	2.734	.712	3.84	.0098	3.79	2.94	3.45	8282	381.2	392.1	97.2
132	9-25-72	0.87	-1	515.7	513.1	2219	67.0	9.7	75.6	3.680	2.107	1.75	.0094	1.74	2.96	5.79	8157	382.8	393.6	97.2
133	9-25-72	0.87	-1	292.2	290.2	1298	78.4	8.0	74.6	1.761	1.844	0.95	.0096	0.95	2.96	3.61	7407	359.1	370.	97.1

TABLE X

TEST DATA FOR
-1 ZONED INJECTOR

Test No.	Date	Duration Sec.	Chamber	P_{c1} psia	P_{c2} psia	$F_{avg_{vac}}$ lbf	T_o °F	T_f °F	T_{f_I} °F	$\dot{W}_o$ lbm/sec	$\dot{W}_f$ lbm/sec	MR_{inj}	$\dot{W}_{f_{ign}}$	MROA	A_e/A_t	$\dot{W}_T$ lbm/sec	C* ft/sec	$I_{s_{vac}}$ lbf-sec/lbm	$I_{s_{vac_{theo}}}$ lbf-sec/lbm	$\%\eta I_s$
2K-11-147	10-18-72	0.70	-1	295.9	295.4	1251	84	64	78	2.772	.673	4.12	0.0094	4.06	2.95	3.45	7978	362.1	394.4	91.8
148	10-18-72	1.01	-1	283.4	282.4	1222	79	59	78	3.037	.477	6.37	0.0093	6.24	2.95	3.52	7492	346.9	368.7	94.0
149	10-18-72	1.31	-1	299.8	297.8	1267	79	67	76	2.765	.667	4.15	0.0094	4.09	2.95	3.44	8113	368.2	394.1	93.4
150	10-18-72	0.66	-1	307.5	306.3	1302	88	67	71	2.362	1.114	2.12	0.0096	2.10	2.95	3.48	8216	373.5	397.7	93.9
151	10-18-72	1.30	-1	108.8	107.6	458	86	62	71	.993	.2505	3.97	0.0097	3.82	2.95	1.25	8086	365.5	394.9	92.7
152B	10-18-72	0.80	-1	527.4	525.3	2225	78	62	72	4.670	1.231	3.79	0.0095	3.76	2.95	5.91	8310	376.4	397.1	94.8

TEST DATA FOR
-2 ZONED INJECTOR

2K-11-157	10-23-72	1.12	-1	106.7	105.9	450	76	36	72	.948	.251	3.78	0.0095	3.64	2.95	1.20	8052	372.4	396.2	94.0
158	10-23-72	1.29	-1	264.4	263.4	1110	78	34	73	3.04	.388	7.84	0.0095	7.65	2.95	3.43	7013	322.8	350.0	92.2
159	10-24-72	1.28	-1	316.3	314.8	1323	54	20	55	2.860	.710	4.03	0.0097	3.97	2.95	3.57	8059	369.6	395.	93.5
160	10-24-72	1.28	-1	315.7	314.3	1321	61	26	66	2.853	.704	4.05	0.0097	4.00	2.95	3.56	8073	370.4	394.9	93.8
161	10-24-72	1.28	-1	291.5	290.4	1216	66	24	71	3.056	.479	6.38	0.0095	6.26	2.95	3.54	7500	343.1	368.6	93.1
162	10-24-72	1.28	-1	323.8	322.8	1360	73	39	73	2.416	1.160	2.08	0.0096	2.07	2.95	3.58	8236	379.3	397.4	95.4
163	10-24-72	1.28	-1	301.3	297.5	1282	82	33	74	1.751	1.789	.98	0.0094	.98	2.95	3.55	7735	360.9	372.3	96.9
164	10-24-72	1.28	-1	535.7	533.5	2181	83	21	75	4.583	1.273	3.60	0.0097	3.57	2.95	5.86	8329	371.8	398.1	93.4

Chamber	CR	L*	L' in.
-1	3.38	5.32	3.0
-1+L*	3.38	14.36	5.47
-2	2.03	3.29	3.0

TABLE XI

TEST DATA FOR
DEEP CUP PREMIX INJECTOR

Test No.	Date	Duration sec.	Chamber	P_{c1} N/cm^2	P_{c2} N/cm^2	$F_{avg_{vac}}$ N	T_o °K	T_f °K	T_{f_I} °K	$\dot{W}_o$ Kg/sec	$\dot{W}_f$ Kg/sec	MR_{inj}	$\dot{W}_{f_{ign}}$ Kg/sec	MROA	A_e/A_t	$\dot{W}_T$ Kg/sec	C* M/sec	$I_{s_{vac}}$ M/sec	$I_{s_{vac_{theo}}}$ M/sec	%I_s
2K-11-101	8-29-72	0.45	-1	200.2	200.8	5564.7	309.7	307.8	308.4	1.18	.31	3.85	.0043	3.80	2.94	1.49	3308	3722	3886	95.7
102	8-30-72	1.15	-1	204.1	201.7	5715.9	305.2	301.8	302.2	1.24	.30	4.09		4.03	2.94	1.54	3267	3705	3871	95.7
103	8-30-72	1.45	-1	209.8	202.9	5880.5	311.8	304.4	308.3	1.05	.52	2.02		2.00	2.94	1.56	3309	3756	3894	96.4
104	8-30-72	1.11	-1	190.8	188.3	5351.2	311.2	304.4	308.3	1.28	.22	5.84		5.71	2.94	1.53	3076	3486	3669	95.0
105	8-31-72	2.10	-1	71.5	69.0	2041.7	308.9	300.0	306.7	.35	.17	2.03		1.98	2.94	.53	3319	3837	3891	98.6
106	8-31-72	2.10	-1	79.5	77.0	2228.5	313.1	303.3	307.2	.42	.16	2.51		2.45	2.94	.59	3330	3777	3920	96.3
107	8-31-72	2.10	-1	76.0	74.4	2166.2	313.0	301.1	307.2	.51	.10	5.14		4.93	2.94	.61	3086	3559	3755	94.6
108	8-31-72	2.10	-1	71.5	71.5	2037.2	316.7	302.8	308.9	.54	.07	7.39		6.99	2.94	.62	2845	3272	3478	94.1
134	10-11-72	0.89	-1	200.1	193.1	5693.7	296.1	295.6	288.0	.80	.80	1.01		1.01	2.94	1.60	3088	3549	3662	96.9
135	10-11-72	1.17	-1+L*	212.7	219.1	6049.5	287.2	278.8	286.7	1.12	.50	2.26		2.24	2.94	1.62	3250	3734	3911	95.5
136	10-11-72	1.26	-1+L*	210.6	213.0	5933.9	287.2	284.4	287.2	1.28	.31	4.16		4.10	2.94	1.59	3274	3726	3865	96.4
137	10-11-72	1.55	-1+L*	203.5	204.1	5747.1	286.1	284.4	287.8	1.42	.22	6.32		6.20	2.94	1.65	3052	3482	3623	96.1
138	10-11-72	1.56	-2	123.6	114.9	5884.9	291.1	292.8	291.1	1.08	.50	2.16		2.14	2.43	1.59	3173	3701	3819	96.9
139	10-11-72	1.57	-2	123.6	118.3	5751.5	291.1	285.0	291.1	1.29	.31	4.13		4.07	2.43	1.60	3153	3594	3761	95.6
140	10-11-72	1.52	-2	113.9	110.9	5293.3	291.1	284.4	291.7	1.40	.21	6.59		6.46	2.43	1.61	2889	3290	3466	94.9
141	10-13-72	1.59	-1	213.0	210.0	5911.6	287.2	287.8	287.2	1.26	.31	4.14		4.08	2.94	1.58	3336	3741	3867	96.8
142	10-13-72	1.58	-1	183.4	181.4	5115.4	289.4	283.3	290.5	1.44	.17	8.57		8.35	2.94	1.61	2816	3173	3350	94.7
143	10-13-72	0.65	-1	362.9	352.0	9972.9	296.1	286.7	296.1	2.11	.56	3.76		3.74	2.94	2.66	3365	3735	3896	95.9
144	10-13-72	0.76	-1	326.3	323.8	9029.8	299.4	285.0	297.8	2.24	.38	5.94		5.88	2.94	2.62	3081	3445	3665	94.0
154	10-19-72	0.78	-1	363.7	355.4	9941.7	294.4	296.7	291.7	1.76	.89	1.99		1.98	2.95	2.65	3398	3753	3891	96.4
155	10-20-72	0.77	-1	200.6	198.7	5471.3	196.1	193.3	287.8	1.21	.30	4.03	.0043	3.97	2.95	1.52	3204	3605	3831	94.1

-101-

TEST DATA FOR
TRIPLET INJECTOR

111	9-13-72	0.68	-1	207.8	209.8	5818.2	303.7	291.8	298.9	1.23	.31	3.95	.0043	3.91	2.94	1.55	3318	3753	3878	96.8
112	9-13-72	0.75	-1	211.1	210.0	5880.5	310.1	294.4	301.7	1.05	.50	2.10		2.08	2.94	1.55	3376	3800	3900	97.4
113	9-13-72	0.75	-1	196.5	197.5	5564.7	310.1	292.2	303.9	1.34	.23	5.88		5.78	2.94	1.56	3101	3548	3677	96.5
114	9-14-72	0.72	-1	75.9	75.2	2117.3	305.4	296.1	302.8	.37	.18	2.10		2.06	2.94	.55	3379	3811	3898	97.8
115	9-14-72	0.74	-1	72.6	72.1	2051.0	306.2	256.1	303.3	.43	.11	3.87		3.73	2.94	.54	3307	3777	3880	97.3
116	9-14-72	0.73	-1	67.6	67.7	1931.0	306.1	296.7	302.8	.45	.08	5.57		5.29	2.94	.54	3099	3576	3705	96.5
117	9-15-72	0.73	-1+L*	203.5	204.0	5720.4	308.3	297.8	303.9	1.21	.31	3.96		3.91	2.94	1.52	3305	3753	3879	96.8
118	9-15-72	0.74	-1+L*	210.2	209.0	5871.6	308.5	296.1	303.9	1.04	.50	2.10		2.08	2.94	1.54	3373	3806	3900	97.6
119	9-15-72	0.74	-1+L*	204.4	206.0	5840.5	308.9	294.4	303.9	1.44	.23	6.37		6.26	2.94	1.66	3038	3507	3614	97.0
120	9-18-72	0.74	-2	115.7	118.0	5427.0	300.3	290.6	295.0	1.37	.22	6.11		5.99	2.43	1.60	2964	3393	3526	96.2
121	9-18-72	0.75	-2	130.2	130.0	6094.0	300.2	292.8	295.0	1.14	.50	2.28		2.26	2.43	1.64	3247	3708	3824	97.0
122	9-18-72	0.74	-2	118.3	120.0	5542.0	300.4	287.8	295.0	1.21	.31	3.87		3.82	2.43	1.52	3190	3646	3784	96.3
123	9-18-72	0.87	-1	209.9	212.4	5476.0	301.3	292.8	296.7	1.25	.31	4.06		4.02	2.94	1.56	3330	3767	3872	97.2
124	9-19-72	0.88	-1	183.8	184.2	5187.0	299.3	290.0	296.7	1.42	.18	8.03		7.84	2.94	1.59	2848	3247	3410	95.2
127	9-20-72	0.75	-1	358.0	358.0	9964.0	305.9	290.0	302.2	2.06	.56	3.68		3.65	2.94	2.62	3384	3806	3901	97.6
128	9-20-72	0.70	-1	325.2	327.2	9145.5	305.8	291.7	303.3,	2.21	.36	6.10		6.03	2.94	2.57	3131	3557	3666	97.0
131	9-22-72	0.88	-1	211.7	215.7	5858.3	200.9	183.3	296.7	1.24	.32	3.84		3.79	2.94	1.56	3344	3739	3846	97.2
132	9-25-72	0.87	-1	355.3	353.5	9871.0	292.8	260.9	297.8	1.67	.96	1.75		1.74	2.96	2.63	3293	3755	3861	97.2
133	9-25-72	0.87	-1	201.3	199.9	5774.8	299.1	260.0	297.2	.80	.84	0.95	.0043	0.95	2.96	1.64	2990	3522	3629	97.1

TABLE XI (cont.)

TEST DATA FOR
-1 ZONED INJECTOR

Test No.	Date	Duration sec.	Chamber	P_{c1} N/cm^2	P_{c2} N/cm^2	$F_{avg_{vac}}$ N	T_o °K	T_f °K	T_{f_I} °K	$\dot{W}_o$ Kg/sec	$\dot{W}_f$ Kg/sec	MR_{inj}	$\dot{W}_{f_{ign}}$ Kg/sec	MROA	A_e/A_t	$\dot{W}_T$ Kg/sec	C* M/sec	$I_{s_{vac}}$ M/sec	$I_{s_{vac_{theo}}}$ M/sec	% I_s
2K-11-147	10-18-72	0.70	-1	203.6	203.5	5564.7	302.2	291.1	298.9	1.26	.31	4.12	.0043	4.06	2.95	1.56	3221	3552	3869	91.8
148	10-18-72	1.01	-1	195.2	194.5	5435.7	299.4	288.3	298.9	1.38	.22	6.37	↓	6.24	2.95	1.60	3025	3403	3617	94.0
149	10-18-72	1.31	-1	206.5	205.1	5635.8	299.4	292.8	297.8	1.25	.30	4.15	↓	4.09	2.95	1.56	3276	3612	3866	93.4
150	10-18-72	0.66	-1	211.8	211.0	5791.5	304.4	292.8	295.0	1.07	.51	2.12	↓	2.10	2.95	1.58	3317	3664	3901	93.9
151	10-18-72	1.30	-1	74.9	74.1	2037.2	303.3	290.0	295.1	.45	.11	3.97	↓	3.82	2.95	.57	3265	3585	3874	92.7
152B	10-18-72	0.80	-1	363.3	361.9	9897.2	298.9	290.0	295.7	2.12	.56	3.79	.0043	3.76	2.95	2.68	3355	3692	3895	94.8

TEST DATA FOR
-2 ZONED INJECTOR

2K-11-157	10-23-72	1.12	-1	73.5	72.9	2001.6	297.8	275.6	295.6	.43	.11	3.78	.0043	3.64	2.95	.54	3251	3653	3886	94.0
158	10-23-72	1.29	-1	182.1	181.4	4937.5	298.9	274.4	296.1	1.37	.18	7.84	↓	7.65	2.95	1.55	2831	3166	3433	92.2
159	10-24-72	1.28	-1	217.9	216.8	5884.9	285.6	266.7	286.1	1.30	.32	4.03	↓	3.97	2.95	1.62	3254	3625	3875	93.5
160	10-24-72	1.28	-1	217.5	216.5	5876.0	289.4	270.0	292.2	1.29	.32	4.05	↓	4.00	2.95	1.61	3259	3633	3874	93.8
161	10-24-72	1.28	-1	200.8	20.2	5409.0	292.2	268.8	256.1	1.39	.22	6.38	↓	6.26	2.95	1.61	3028	3365	3616	93.1
162	10-24-72	1.28	-1	223.0	222.4	6049.5	296.1	277.2	296.1	1.10	.53	2.08	↓	2.07	2.95	1.62	3325	3721	3898	95.4
163	10-24-72	1.28	-1	207.5	204.9	5702.6	301.1	273.9	296.7	.79	.81	.98	↓	.98	2.95	1.61	3123	3540	3652	96.9
164	10-24-72	1.28	-1	369.0	367.5	9701.5	301.7	267.2	297.2	2.08	.58	3.60	.0043	3.57	2.95	2.66	3363	3647	3905	93.4

Chamber	CR	L* cm	L' cm
-1	3.38	13.51	7.62
-1+L*	3.38	36.47	13.89
-2	2.03	8.36	7.62

1. Performance

A summary of the full scale performance data is presented in Tables XII and XIII in English and S. I. units, respectively, and is plotted in Figures 51 through 53. The performance is listed in the following table for the four injectors at the nominal design point (206.7 N/cm^2 (300 psia) chamber pressure, O/F = 4, 7.62 cm (3 in.) chamber length).

Injector Delivered Performance Comparison

Injector	Energy Release Efficiency - %
Triplet	100
Premix	98.4
-2 Zoned	96.8
-1 Zoned	96.2

The energy release efficiencies for both the triplet and premix injectors are very high in a very short chamber. The achievement of this performance level underscores the value of conducting single element cold flow and combustion testing.

Triplet Injector Performance

The triplet performance was the highest recorded. In chambers of 7.6 cm (3.0 in.) length the performance of this injector was 100% ERE, as shown in Figures 51 and 52. The data groups very closely and with the exception of mixture ratio, no single parameter appears to affect the performance level of the injector. The highest performance occurs at the mixture ratio four, design point. This is consistent with the design parameter MP generated from the single element testing and discussed in Section VI. The full-scale triplet data is replotted in terms of this design parameter in Figure 53, which is a curve fit of the test data. This figure indicates an optimum performance in the range of MP = 0.75 a value consistent with what was predicted based on cold flow and single element testing. One deleterious aspect of this design point is that it leads to very high pressure drop fuel elements or very low pressure drop oxidizer elements. The observed drop in performance on both sides of the optimum can be explained on the basis of the cold flow work accomplished earlier in the program where it was apparent that at low values of MP the fuel momentum completely penetrated and split the oxidizer jet. At high MP values, the low fuel momentum jet failed to penetrate the oxidizer but merely surrounded the oxidizer jet which resulted in unmixed flow. At the design point, optimum penetration is achieved and a well mixed homogenous fan is formed.

The triplet ERE as a function of chamber geometry is found in Figure 52. Performance is not a strong function of chamber length especially at O/F = 4. This fact is not surprising considering the high overall performance in the short chamber. In fact, it is probable that good performance could be obtained in a 5.08 cm (2 in.) long chamber. Contraction ratio influences were insignificant.

TABLE XII
AEROJET LIQUID ROCKET COMPANY

G A S - G A S T E C H N O L O G Y P R O G R A M

MULTI-ELEMENT HOT FIRE TEST SERIES PERFORMANCE SUMMARY

****** DEEP CUP PREMIX INJECTOR ******

ENGLISH UNITS (SEE TABLE NOMENCLATURE LIST)

TEST No.	PC-1	O/F	TO	TF	ISP(ODE)	C*(ODE)	ISP(M)	C*(PC-1)	C*(PC-2)	C*(F)	%ISP	%C*(PC-1)	ERE
101	295.9	3.8	557.	554.	396.4	8250.	379.4	8340.	8363.	8110.	95.7	101.1	98.5
102	303.6	4.0	549.	543.	394.7	8203.	377.7	8237.	8085.	8064.	95.7	100.4	98.5
103	310.3	2.0	561.	548.	397.0	8362.	382.9	8354.	8082.	8258.	96.4	99.9	98.8
104	281.9	5.8	560.	548.	374.4	7701.	355.4	7753.	7653.	7514.	94.9	100.7	98.0
105*	105.3	2.0	556.	540.	396.7	8357.	391.2	8379.	8088.	8455.	98.6	100.3	99.5
106	117.7	2.4	563.	546.	399.6	8396.	385.0	8404.	8135.	8296.	96.4	100.1	99.2
107	112.3	4.9	563.	542.	382.6	7890.	362.8	7778.	7616.	7744.	94.8	98.6	99.1
108	105.7	7.0	568.	545.	354.7	7272.	333.6	7171.	7164.	7068.	94.1	98.6	98.8
134	296.4	1.8	533.	532.	373.4	7910.	361.8	7804.	7532.	7840.	96.9	98.7	99.1
135	314.6	2.2	517.	502.	398.9	8387.	380.7	8202.	8447.	8200.	95.4	97.8	97.8
136	311.2	4.1	517.	512.	394.1	8187.	379.9	8254.	8346.	8107.	96.4	100.8	99.2
137	300.6	6.2	515.	512.	369.6	7597.	355.0	7692.	7716.	7496.	96.1	101.3	99.1
138	190.0	2.1	524.	527.	389.1	8379.	377.3	8320.	7731.	8314.	97.0	99.3	99.3
139	189.4	4.1	524.	513.	383.6	8163.	366.4	8242.	7888.	8007.	95.5	101.0	98.5
140	174.4	6.5	524.	512.	353.3	7460.	335.4	7545.	7344.	7275.	94.9	101.1	98.1
141	314.7	4.1	517.	518.	394.3	8192.	381.4	8410.	8293.	8141.	96.7	102.7	99.6
142	271.0	4.4	521.	510.	341.2	6996.	323.5	7096.	7016.	6811.	94.8	101.4	97.8
143	536.2	3.7	533.	516.	397.4	8274.	380.8	8483.	8229.	8133.	95.8	102.5	98.3
144	481.9	5.9	539.	513.	375.6	7730.	351.2	7766.	7708.	7417.	93.5	100.5	96.2
154	538.0	2.0	530.	534.	396.7	8357.	382.6	8577.	8382.	8249.	96.4	102.6	98.6
155	296.4	4.0	553.	548.	390.6	8125.	367.5	8077.	8002.	7856.	94.1	99.4	96.9

TABLE XII (cont.)
********* TRIPLET INJECTOR **********

ENGLISH UNITS (SEE TABLE NOMENCLATURE LIST)

TEST NO.	PC-1	O/F	TO	TF	ISP(ODE)	C*(ODE)	ISP(M)	C*(PC-1)	C*(PC-2)	C*(F)	%ISP	%C*(PC-1)	ERE
111	307.0	3.9	547.	525.	395.6	8228.	382.6	8363.	8446.	8174.	96.7	101.6	99.5
112	312.2	2.1	558.	530.	397.7	8372.	387.4	8523.	8478.	8354.	97.4	101.8	99.8
113	290.2	5.6	553.	526.	375.2	7718.	361.7	7816.	7857.	7648.	96.4	101.3	99.5
114*	112.3	2.1	550.	533.	397.5	8369.	388.5	8530.	8452.	8394.	97.7	101.9	100.2
115*	107.3	3.7	551.	531.	395.6	8227.	385.1	8339.	8283.	8261.	97.3	101.4	99.6
116*	99.9	5.3	551.	534.	377.9	7779.	364.6	7812.	7828.	7769.	96.5	100.4	98.9
117	300.8	3.9	555.	535.	395.6	8228.	382.6	8333.	8347.	8174.	96.7	101.3	99.5
118	311.0	2.1	555.	533.	397.7	8372.	388.0	8513.	8444.	8367.	97.6	101.7	100.0
119	302.9	0.3	556.	530.	368.8	7580.	357.5	7657.	7713.	7546.	96.9	101.0	100.0
120	277.2	6.0	540.	523.	359.5	7597.	345.9	7743.	7881.	7508.	96.2	101.9	99.4
121	280.1	2.3	540.	527.	389.7	8389.	378.0	8513.	8477.	8325.	97.0	101.5	99.4
122	181.4	3.8	541.	518.	385.8	8221.	371.7	8340.	8428.	8130.	96.4	101.5	99.3
123	310.1	4.0	542.	527.	394.7	8205.	384.0	8394.	8494.	8199.	97.3	102.3	100.1
124	271.5	7.8	539.	522.	347.9	7136.	331.0	7177.	7193.	6969.	95.1	100.6	98.1
127	525.9	3.7	551.	522.	397.9	8289.	388.0	8531.	8533.	8290.	97.5	102.9	100.0
128	480.5	6.0	550.	525.	373.7	7686.	362.6	7890.	7940.	7654.	97.0	102.6	99.8
131	312.8	3.8	362.	330.	392.1	8160.	381.2	8430.	8589.	8150.	97.2	103.3	100.1
132	525.7	1.7	527.	470.	393.7	8310.	382.6	8316.	8274.	8270.	97.2	100.1	99.4
133	296.2	1.0	538.	468.	370.9	7859.	359.1	7559.	7507.	7782.	96.8	96.2	99.0

********* -1 ZONED INJECTOR **********

ENGLISH UNITS (SEE TABLE NOMENCLATURE LIST)

TEST NO.	PC-1	O/F	TO	TF	ISP(ODE)	C*(ODE)	ISP(M)	C*(PC-1)	C*(PC-2)	C*(F)	%ISP	%C*(PC-1)	ERE
147	301.2	4.1	544.	524.	394.4	8196.	362.1	8120.	8106.	7731.	91.8	99.1	94.6
148	288.4	6.2	539.	519.	369.0	7585.	346.9	7623.	7596.	7325.	94.0	100.5	97.0
149	305.1	4.1	539.	527.	394.2	8189.	368.2	8257.	8202.	7860.	93.4	100.8	96.2
150	313.4	2.1	548.	527.	397.9	8374.	373.5	8373.	8340.	8055.	93.9	100.0	96.2
151	110.7	3.8	546.	522.	394.9	8206.	365.5	8230.	8140.	7841.	92.6	100.3	96.4
152b	536.5	3.8	538.	522.	397.3	8270.	376.4	8459.	8425.	8039.	94.8	102.3	97.3

TABLE XII (cont.)

********* -2 ZONED INJECTOR **********

ENGLISH UNITS (SEE TABLE NOMENCLATURE LIST)

TEST NO.	PC-1	O/F	TO	TF	ISP(ODE)	C*(ODE)	ISP(M)	C*(PC-1)	C*(PC-2)	C*(F)	%ISP	%C*(PC-1)	ERE
157	108.6	3.6	536.	496.	396.2	8247.	372.4	8197.	8135.	7993.	94.0	99.4	97.7
158	269.0	7.7	538.	494.	350.4	7189.	322.8	7136.	7109.	6800.	92.1	99.3	95.1
159	321.9	4.0	514.	480.	395.1	8215.	369.6	8202.	8163.	7895.	93.5	99.8	96.3
160	321.3	4.0	521.	486.	394.9	8209.	370.4	8216.	8180.	7911.	93.8	100.1	96.6
161	296.6	6.3	526.	484.	368.8	7580.	343.1	7631.	7602.	7246.	93.0	100.7	96.1
162	330.0	2.1	533.	499.	397.6	8371.	379.3	8393.	8367.	8180.	95.4	100.3	97.7
163	307.5	1.0	542.	493.	372.2	7885.	360.9	7893.	7793.	7824.	97.0	100.1	99.2
164	545.3	3.6	543.	461.	398.3	8301.	371.8	8479.	8444.	7951.	93.4	102.1	95.8

NOMENCLATURE LIST FOR PERFORMANCE SUMMARY

PARAMETER	DEFINITION	S.I. UNITS	ENGLISH UNITS
PC-1	CHAMBER PRESSURE	N/SQ.CM	PSIA
O/F	MIXTURE RATIO	KG/KG	LBM/LBM
TO	OXYGEN TEMPERATURE	DEG. K	DEG. R
TF	HYDROGEN TEMPERATURE	DEG. K	DEG. R
ISP(ODE)	ONE-DIM. EQUIL. SPECIFIC IMPULSE	N-SEC/KG	LBF-SEC/LBM
C*(ODE)	ONE-DIM. EQUIL. CHARACTERISTIC VELOCITY	M/SEC	FT/SEC
ISP(M)	MEASURED VACUUM SPECIFIC IMPULSE	N-SEC/KG	LBF-SEC/LBM
C*(PC-1)	MEASURED CHARACTERISTIC VELOCITY (PC-1)	M/SEC	FT/SEC
C*(PC-2)	MEASURED CHARACTERISTIC VELOCITY (PC-2)	M/SEC	FT/SEC
C*(F)	CORRECTED CSTAR BASED ON THRUST	M/SEC	FT/SEC
%ISP	SPECIFIC IMPULSE EFFICIENCY	%	%
%C*(PC-1)	MEASURED CSTAR EFFICIENCY BASED ON PC-1	%	%
ERE	ENERGY RELEASE EFFICIENCY	%	%

NOTE - TESTS IN WHICH NOZZLE FLOW SEPARATION IS SUSPECTED ARE NOTED WITH AN * AFTER THE TEST NO. IN THESE CASES THE ERE HAS BEEN COMPUTED ON THE BASIS OF THE MEASURED CSTAR AND THE OBSERVED RELATIONSHIP BETWEEN ERE AND CSTAR FOR THE FULL FLOW TESTS

TABLE XIII
AEROJET LIQUID ROCKET COMPANY

G A S - G A S T E C H N O L O G Y P R O G R A M

MULTI-ELEMENT HOT FIRE TEST SERIES PERFORMANCE SUMMARY

****** DEEP CUP PREMIX INJECTOR ******

S.I. UNITS (SEE TABLE NOMENCLATURE LIST)

TEST NO.	PC-1	O/F	TO	TF	ISP(ODE)	C*(ODE)	ISP(M)	C*(PC-1)	C*(PC-2)	C*(F)	%ISP	%C*(PC-1)	EFF
101	204.0	3.8	310.	308.	3887.	2514.	3720.4	2542.	2549.	2472.	95.7	101.1	98.5
102	209.3	4.0	305.	302.	3870.	2500.	3703.7	2511.	2464.	2458.	95.7	100.4	98.5
103	213.9	2.0	312.	304.	3893.	2549.	3754.7	2546.	2463.	2517.	96.4	99.9	98.8
104	194.3	5.3	311.	304.	3671.	2347.	3485.1	2363.	2333.	2290.	94.9	100.7	98.0
105*	72.9	2.0	309.	300.	3890.	2547.	3836.1	2554.	2465.	2577.	98.6	100.3	99.5
106	81.1	2.4	313.	303.	3918.	2559.	3775.3	2561.	2479.	2529.	96.4	100.1	99.2
107	77.4	4.9	313.	301.	3752.	2405.	3557.6	2371.	2321.	2360.	94.8	98.6	99.1
108	72.9	7.0	316.	303.	3478.	2216.	3271.3	2186.	2184.	2154.	94.1	98.6	98.8
134	204.4	1.0	296.	296.	3662.	2411.	3547.8	2379.	2296.	2390.	96.9	98.7	99.1
135	216.9	2.2	287.	279.	3912.	2556.	3733.1	2500.	2575.	2499.	95.4	97.8	97.8
136	214.6	4.1	287.	284.	3865.	2495.	3725.3	2516.	2544.	2471.	96.4	100.8	99.2
137	207.2	6.2	286.	284.	3624.	2315.	3481.1	2345.	2352.	2285.	96.1	101.3	99.1
138	131.0	2.1	291.	293.	3815.	2554.	3699.8	2536.	2356.	2534.	97.0	99.3	99.3
139	130.6	4.1	291.	285.	3761.	2488.	3592.9	2512.	2404.	2440.	95.5	101.0	98.5
140	120.2	6.5	291.	284.	3465.	2274.	3288.9	2300.	2239.	2217.	94.9	101.1	98.1
141	216.9	4.1	287.	288.	3866.	2497.	3740.0	2563.	2528.	2481.	96.7	102.7	99.6
142	186.8	8.4	289.	283.	3346.	2132.	3172.2	2163.	2138.	2076.	94.8	101.4	97.8
143	369.7	3.7	296.	287.	3897.	2522.	3734.1	2586.	2508.	2479.	95.8	102.5	98.3
144	332.2	5.9	299.	285.	3683.	2356.	3443.9	2367.	2349.	2261.	93.5	100.5	96.2
154	370.9	2.0	294.	297.	3890.	2547.	3751.8	2614.	2555.	2514.	96.4	102.6	98.6
155	204.3	4.0	196.	193.	3831.	2477.	3603.7	2462.	2439.	2395.	94.1	99.4	96.9

TABLE XIII (cont.)

********* TRIPLET INJECTOR **********

S.I. UNITS (SEE TABLE NOMENCLATURE LIST)

TEST NO.	PC-1	O/F	TO	TF	ISP(ODE)	C*(ODE)	ISP(M)	C*(PC-1)	C*(PC-2)	C*(F)	%ISP	%C*(PC-1)	ERE
111	211.6	3.9	304.	292.	3879.	2508.	3751.8	2549.	2574.	2491.	96.7	101.6	99.5
112	215.3	4.1	310.	294.	3900.	2552.	3798.8	2598.	2594.	2546.	97.4	101.8	99.8
113	200.1	3.8	310.	292.	3879.	2353.	3546.8	2382.	2395.	2331.	96.4	101.3	99.5
114*	77.4	2.1	305.	296.	3898.	2551.	3809.6	2600.	2576.	2559.	97.7	101.9	100.2
115*	74.9	3.7	306.	295.	3879.	2508.	3776.3	2542.	2525.	2518.	97.3	101.4	99.6
116*	66.9	5.3	306.	297.	3705.	2371.	3575.3	2381.	2386.	2368.	96.5	100.4	98.9
117	207.3	3.9	303.	297.	3879.	2508.	3751.8	2540.	2544.	2491.	96.7	101.3	99.5
118	214.4	4.1	308.	296.	3900.	2552.	3804.7	2595.	2574.	2550.	97.6	101.7	100.0
119	206.2	3.5	309.	294.	3616.	2310.	3505.6	2334.	2351.	2300.	96.9	101.0	100.0
120	122.1	8.0	300.	291.	3526.	2316.	3391.9	2360.	2402.	2289.	96.2	101.9	99.4
121	138.0	2.3	300.	293.	3822.	2557.	3706.7	2595.	2584.	2537.	97.0	101.5	99.4
122	125.9	3.6	300.	288.	3783.	2506.	3644.9	2542.	2569.	2478.	96.4	101.5	99.3
123	213.3	4.0	301.	293.	3871.	2501.	3765.5	2559.	2589.	2499.	97.3	102.3	100.1
124	187.1	7.6	299.	290.	3412.	2175.	3245.8	2188.	2193.	2124.	95.1	100.6	98.1
127	364.6	3.7	306.	290.	3901.	2526.	3804.7	2600.	2601.	2527.	97.5	102.9	100.0
128	331.1	6.0	306.	292.	3665.	2343.	3555.7	2405.	2420.	2333.	97.0	102.6	99.8
131	215.6	3.8	201.	183.	3845.	2487.	3738.0	2569.	2618.	2484.	97.2	103.3	100.1
132	362.4	1.7	293.	261.	3861.	2533.	3753.7	2535.	2522.	2521.	97.2	100.1	99.4
133	205.6	1.0	299.	260.	3637.	2395.	3521.3	2304.	2288.	2372.	96.8	96.2	99.0

********* -1 ZONED INJECTOR **********

S.I. UNITS (SEE TABLE NOMENCLATURE LIST)

TEST NO.	PC-1	O/F	TO	TF	ISP(ODE)	C*(ODE)	ISP(M)	C*(PC-1)	C*(PC-2)	C*(F)	%ISP	%C*(PC-1)	ERE
147	267.5	4.1	302.	291.	3868.	2498.	3550.6	2475.	2471.	2356.	91.8	99.1	94.6
148	198.9	4.2	299.	288.	3619.	2312.	3401.7	2324.	2315.	2233.	94.0	100.5	97.0
149	210.3	4.1	299.	293.	3866.	2496.	3610.6	2517.	2500.	2396.	93.4	100.8	96.2
150	216.9	4.1	304.	293.	3902.	2552.	3662.5	2552.	2542.	2455.	93.9	100.0	96.2
151	76.3	3.8	303.	290.	3873.	2501.	3584.1	2509.	2481.	2390.	92.6	100.3	96.4
152	370.1	3.8	299.	290.	3895.	2521.	3691.0	2578.	2568.	2450.	94.8	102.3	97.3

TABLE XIII (cont.)

********* -2 ZONED INJECTOR **********

S.I. UNITS (SEE TABLE NOMENCLATURE LIST)

TEST NO.	PC-1	O/F	TO	TF	ISP(ODE)	C*(ODE)	ISP(M)	C*(PC-1)	C*(PC-2)	C*(F)	%ISP	%C*(PC-1)	ERE
157	74.9	3.6	298.	276.	3886.	2514.	3651.8	2496.	2480.	2436.	94.0	99.4	97.7
158	135.5	7.7	299.	274.	3436.	2191.	3165.4	2175.	2167.	2073.	92.1	99.3	95.1
159	221.9	4.0	286.	267.	3875.	2504.	3624.3	2500.	2488.	2406.	93.5	99.8	96.3
160	221.5	4.0	289.	270.	3872.	2502.	3632.1	2504.	2493.	2411.	93.8	100.1	96.6
161	204.5	6.3	292.	269.	3616.	2310.	3364.4	2326.	2317.	2209.	93.0	100.7	96.1
162	227.5	2.1	296.	277.	3899.	2551.	3719.4	2556.	2550.	2493.	95.4	100.3	97.7
163	212.0	1.0	301.	274.	3650.	2403.	3539.0	2406.	2375.	2385.	97.0	100.1	99.2
164	376.0	5.6	302.	267.	3905.	2530.	3645.9	2584.	2574.	2423.	93.4	102.1	95.8

NOMENCLATURE LIST FOR PERFORMANCE SUMMARY

PARAMETER	DEFINITION	S.I. UNITS	ENGLISH UNITS
PC-1	CHAMBER PRESSURE	N/SQ.CM	PSIA
O/F	MIXTURE RATIO	KG/KG	LBM/LBM
TO	OXYGEN TEMPERATURE	DEG. K	DEG. R
TF	HYDROGEN TEMPERATURE	DEG. K	DEG. R
ISP(ODE)	ONE-DIM. EQUIL. SPECIFIC IMPULSE	N-SEC/KG	LBF-SEC/LBM
C*(ODE)	ONE-DIM. EQUIL. CHARACTERISTIC VELOCITY	M/SEC	FT/SEC
ISP(M)	MEASURED VACUUM SPECIFIC IMPULSE	N-SEC/KG	LBF-SEC/LBM
C*(PC-1)	MEASURED CHARACTERISTIC VELOCITY (PC-1)	M/SEC	FT/SEC
C*(PC-2)	MEASURED CHARACTERISTIC VELOCITY (PC-2)	M/SEC	FT/SEC
C*(F)	CORRECTED CSTAR BASED ON THRUST	M/SEC	FT/SEC
%ISP	SPECIFIC IMPULSE EFFICIENCY	%	%
%C*(PC-1)	MEASURED CSTAR EFFICIENCY BASED ON PC-1	%	%
ERE	ENERGY RELEASE EFFICIENCY	%	%

NOTE - TESTS IN WHICH NOZZLE FLOW SEPARATION IS SUSPECTED ARE NOTED WITH AN * AFTER THE TEST NO. IN THESE CASES THE ERE HAS BEEN COMPUTED ON THE BASIS OF THE MEASURED CSTAR AND THE OBSERVED RELATIONSHIP BETWEEN ERE AND CSTAR FOR THE FULL FLOW TESTS

Premix Injector Performance

The premix performance data is plotted as a function of mixture ratio in Figures 51 and 52. These figures indicate that ERE is relatively insensitive to O/F changes. ERE was over 98% across a mixture ratio range extending from 1 to 8. This characteristic was observed in both the single element combustion and cold flow testing. Insensitivity to mixture ratio is an advantage from an engine system standpoint. Shown in Figure 51 are the influences of P_c and propellant temperature. Lowering P_c is in the direction of slightly increased performance [approximately 0.1% ERE per 68 N/cm^2 (100 psia)] and lowering temperature is in the direction of lower performance [approximately 1% ERE/55°K (100°R)]. The effect of chamber geometry is illustrated in Figure 52. As shown in this figure varying contraction ratio did not influence the performance. Increasing the chamber length from 7.6 to 13.9 cm (3.0 to 5.5 in.) resulted in changes in performance that were small enough to be within the data scatter (±1%).

Zoned Injector Performance

The ERE of the zoned triplet injectors is presented in Figure 51. These injectors deliver substantially less performance than either the triplet or premix injectors. The low performance of the zoned triplet injector when compared to the triplet injector is due to two effects: (1) the mixture ratio distribution loss due to zone cooling and (2) the off-optimum element design dictated by the barrier concept. As discussed earlier in this report, 0.8 and 0.5 percent I_{sp} loss can be attributed to mixture ratio maldistribution for the -1 and -2 zoned injectors, respectively. If one accounts for this loss, the remaining difference between the zoned triplet and triplet injectors must be attributed to injector element design.

Referring to Figure 53, where the triplet element ERE as a function of the mixing parameter is displayed, note the design point mixing parameter values for the core and barrier circuits of both zoned injectors. Both circiuts were composed of triplet elements removed from the optimum of a F-O-F triplet element design. This departure from an optimum design is forced because the barrier flow split is controlled by injection element area. Without a complicated injector manifold (i.e., separate barrier and core circuits) an overall optimum element can not be obtained. Therefore, in any engine that uses F-O-F triplet elements, performance losses will result from both the effects of barrier coolant (mixture ratio distribution) and non-optimum element design. Based on this concept and the work presented in Section III on film vs varrier cooling, it would appear that film rather than barrier cooling would be a better design approach. In general, any GO_2/GH_2 injector-chamber that is comprised of injection elements that are mixture ratio sensitive, should be cooled with a film rather than a barrier.

2. Heat Transfer

a. Chamber Heat Flux

The full scale chamber heat transfer was evaluated in a manner similar to the single element data. This approach is discussed in Appendix D and it relies on a ratio of measured experimental heat flux nominalized by the nominal heat flux based on conventional turbulent heat transfer correlations (Bartz). This nominalization accounts for differences in P_C, O/F, and chamber diameter. The direction of this ratio away from one therefore is a measure of the injector related influences on chamber heat flux.

The data for the various injectors is plotted in Figures 54 through 63 and is discussed in the following paragraphs. All four injectors are summarized in Figure 54 for the nominal test conditions (O/F = 4, P_C = 205 N/cm^2, (300 psia) -1 chamber).

The experimental chamber heat fluxes for the triplet and premix injectors when compared to the predicted heat flux (as defined by the simplified Bartz relation) were high in the injector end of the chamber, decaying to one at the throat. This trend and the values of the heat flux ratio is nearly identical to the data from the single elements. The chamber heat flux using the zoned triplet injectors was a factor of three less than the triplet injector near the face. This decrease in heat flux is not entirely due to the effects of zoning. It is in part generated by the inefficient injection elements of the barrier circuit. These elements, because they are not well mixed, do not release heat equivalent to an optimum triplet element. Therefore, the measured flux levels reflect a depression generated by both the barrier cooling and decreased energy release.

(1) Premix Injector Data

Heat flux ratios calculated from the premix injector data are plotted in Figures 55, 56 and 57. Figure 55 shows the -1 chamber data for P_C = 68 N/cm^2 (100 psia) (O/F = 2, 5, 7) and P_C = 206 N/cm^2 (300 psia) (O/F = 1, 2, 4, 8). Figure 56 shows the -1 chamber data for P_C = 344 N/cm^2 (500 psia) (O/F = 2, 4, 6) and the -2 chamber data (P_C = 119 N/cm^2 (175 psia) and O/F = 2, 4, 6). Figure 57 shows the premix data obtained with the L* section positioned between the injector and the -1 chamber.

The premix data indicate that mixture ratio does not influence significantly the thrust chamber heat flux. Also chamber pressure does not appear to influence the heat flux ratio distributions. This is demonstrated on the bottom graph of Figure 55 where the band drawn for the 68 (100 psia) and 344 N/cm^2 (500 psia) chamber pressure data matches the 206 N/cm^2 (300 psia) data. There is a slight tendency for the -2 chamber (CR = 2.0) heat flux ratios to be less than the -1 chamber (CR = 3.4) values (bottom graph of Figure 56).

A distinct pattern of heat transfer characteristics is evident in the premix injector/short chamber data (Figures 55 and 56): (1) Heat fluxes are somewhat above nominal near the injector face (heat flux ratio = 1.1 to 2.0); (2) The heat flux ratio increases quite sharply downstream of the injector and a peak ratio of 2.0 to 2.9 occurs at 1.9 cm (0.75 in.) axial distance; (3) The heat flux ratio decreases from this point until it is 1.0 or slightly less (heat flux about nominal) at the throat; (4) The heat flux remains at a nominal level in the divergent nozzle section to an area ratio of 2.3.

The data from tests using the -1 chamber and the L* section is shown in Figure 57. These data demonstrate that the high heat flux ratios observed in the cylindrical section of the shorter chambers are a function of distance from the injector face. With the L* section in place, heat fluxes in the -1 chamber cylindrical are near nominal and the high heat flux ratios exist upstream in the L* section. Apparently the -1+L* cylindrical length is sufficiently long that a near fully developed boundary layer exists at the downstream end, since the throat data are slightly lower than the short chamber data.

(2) Triplet Injector Data

Chamber heat flux ratios obtained from triplet injector tests are plotted in Figures 58, 59, and 60 in the same format used for the premix data. Figure 58: -1 chamber results, P_c = 68 N/cm^2 (100 psia) O/F = 2, 4, 5) and P_c = 206 N/cm^2 (300 psia) (O/F = 1, 2, 4, 6). Figure 59: -1 chamber results for P_c = 344 N/cm^2 (500 psia) (O/F = 2, 4, 6), and -2 chamber results for P_c = 119 N/cm^2 (175 psia) (O/F = 2, 4, 6). Triplet data for the -1+L* chamber configuration are shown in Figure 60.

Over most of the mixture ratio range tested, the O/F effects are similar to those noted for the premix injector; slight, irregular changes in heat flux ratio are produced by changes in O/F. However, a fairly regular low O/F effect is evident in the triplet data as the heat fluxes tended to be lower than nominal at the lower O/F values. This occurred at O/F = 1, P_c = 206 N/cm^2 (300 Psia) (bottom graph, Figure 58) and at O/F = 2, P_c = 344 N/cm^2 (500 psia) (top graph, Figure 59). This reduction in heat flux may be a film cooling like effect produced by the outer impinging fuel elements when excess amounts of fuel and high fuel injection momentum create a fuel rich zone adjacent to the wall.

Some P_c effects are evident in the triplet data. The heat flux ratio 0.634 cm (0.25 in.) from the injector face tends to decrease with increasing P_c (Figure 59). Heat fluxes in the -1 chamber were slightly higher than the -2 chamber values at comparable MR and P_c conditions.

Heat flux ratios calculated from the triplet injector/-1+L* test data, shown in Figure 60, are similar to the premix injector. The somewhat lower heat flux ratio calculated from the -1+L* data

nearest the injector face may be due to the use of the 1D data reduction model for the L* section (see Appendix D).

(3) Zone-1 Injector Data

Data for the Zone-1 triplet injector are plotted on Figure 61. The top graph of Figure 61 shows that the effect of converting the triplet injector to the Zone-1 triplet design was to produce a pronounced decrease in heat flux ratio in the cylindrical chamber region (compare with top graph, Figure 58). The nominal heat flux decrease due to the decrease in O/F along the wall is only 10 - 25%, but the data show that the actual decrease ranged from 15% to 60% at 1.9 cm (0.75 in.) axial distance. The largest effect was at O/F = 4 and the smallest effect was at O/F = 2. Heat fluxes downstream of the cylindrical section were about the same as the triplet. Chamber pressure effects are small except that streaking at the throat occurred at 344 N/cm^2 (500 psia) chamber pressure (bottom graph, Figure 61). This streaking was probably due to the non-optimum element design of this injector.

(4) Zone-2 Injector Data

The Zone-2 triplet injector heat flux ratios are plotted on Figure 62. Comparison of the P_c = 206 N/cm^2 (300 psia) data (top graph) to the triplet results (top graph, Figure 58) reveals that the Zone-2 triplet injector also produced lower heat fluxes in the cylindrical region. However, very pronounced streaking occurred downstream of the cylindrical length, and the Row B heat fluxes were higher than the triplet injector heat fluxes in the convergent region; again the result of non-optimum element design. The low heat fluxes observed at O/F = 1 with the triplet injector did not occur with the Zone-2 injector. No P_c effect is apparent in the Zone-2 data since the P_c = 68 N/cm^2 (100 psia) and 344 N/cm^2 (500 psia) data compare reasonable well with the 206 N/cm^2 (300 psia) data band (bottom graph, Figure 62).

(5) Generalized Correlation of the Data

The chamber throat heat transfer data are compared to traditional turbulent and laminar boundary layer correlations in the graph shown as Figure 63. The graph shows the St $Pr^{0.6}$ parameter as a function of throat Reynolds number. This is the approach utilized in the Reference 13 study of relaminarization. The turbulent equation shown on Figure 63 is the equation used to calculate nominal heat flux values. Data from the ALRC APS thruster program (Reference 12) are also shown in Figure 63. For the purposes of Figure 63 only, the MR = 4, 6, and 8 heat flux ratios were divided by correction factors which adjust the data to a nominal heat flux based on enthalpy driving potential rather than temperature driving potential. This was done so as to be consistent with the Reference 13 approach. The correction factors used were: 1.1 for O/F = 4, 1.4 for O/F = 6, 1.5 for O/F = 1.8.

The data indicate a tendency toward laminar boundary layer behavior at Reynolds numbers below 5 x 10^5 (about the same transition point noted for the APS data). At higher Re values, the data generally agree with the turbulent equation although a slightly lower coefficient (0.023 instead of 0.026) is indicated. The trend toward laminarization is more gradual than indicated by the APS results.

A few of the data appear unusually low as they compare well with the laminar correlation at Reynolds numbers in excess of 10^6. These data are the Zone-2 row B throat values for P_c = 206 N/cm^2 (300), O/F = 1 and 8; the Zone-2 row B value for P_c = 68 N/cm^2 100, O/F = 4, and the triplet value for P_c = 206 N/cm^2 (300, O/F = 1). It is not clear why these four data points are so low, combustion streaking effects may be a factor in these data.

b. Injector Face Heat Transfer

The face temperatures of all the injectors are listed in Table XIV. Tests 101 - 109, 134 - 144, 154 and 155 are with the premix injector. The thermocouple locations can be referenced to the injector face by referring to Figure 45 of this report. This data indicates a dependence of face temperature on chamber pressure i.e., low chamber pressures result in lower face temperatures. It is also apparent that the face temperatures are hotter than would be desired with a long cycle life injector. They are as high as 844°K (1060°F).

The triplet data are shown in Tests 111 - 133. The locations of these thermocouples can be determined by referring to Figure 46 of this report. The data presented in Table XIV is not entirely representative of the actual face temperature as the locations of TJ-1 and TJ-2 were in a very cool portion of the face. In fact, the visual appearance of the injector face indicated temperatures in excess of 925°K (1200°F), a value too high for long cycle life injectors.

The zoned injector data is included in Tests 147 - 152B and 157 - 164. This injector was designed and manufactured with increased cooling capability when compared to the triplet injector. The injector was constructed with a face bleed circuit designed to flow 13% of engine fuel flow. The triplet, by comparison had a design bleed flow of 6% of the total fuel. Inspection of this data indicated temperatures as hot as 1084°K, (1491°F) at the O/F = 2 run condition. Mixture ratios on either side of O/F = 2 were in the direction of lower temperature. Again face temperatures are too high for long cycle life applications. By visual comparison, however, the effects of increased coolant did reduce the overall face temperature, although local hot spots were still present.

TABLE XIV

INJECTOR FACE TEMPERATURE

Test No.	P_c (PSIA)	P_c N/Cm^2	O/F	TJ-1		TJ-2		TJ-3		TJ-4		TJ-5		TJ-6		Injector Type
				°F	°K	°F	°K	°F	°K	°F	°K	°F	°K	°F	°K	
2K-11-101	290.7	198	3.80													
-102	298.3	203	4.03	1160	900					959	788	1060	844	1057	842	Premix
-103	304.5	208	2.01	1137	887					930	772	1090	861	963	791	Premix
-104	277.0	189	5.84	1188	916					905	758	993	807	998	809	Premix
-105	103.8	71	1.98	896	753					714	652	832	718	779	688	Premix
-106	115.5	79	2.45	928	771					748	671	869	738	828	716	Premix
-107	110.4	75	4.93	999	811					666	626	817	709	813	707	Premix
-108	103.9	71	6.99	926	770					611	595	770	683	750	672	Premix
-109	424.1	290	4.08	1248	949					906	759	978	799	980	800	Premix
-111	301.6	206	3.91	185	358	550	561									Triplet
-112	306.4	209	2.08	113	318	275	408									Triplet
-113	285.2	195	5.78	242	390	586	581									Triplet
-114	110.2	75	2.06	347	448	173	352									Triplet
-115	105.4	72	3.73	432	496	269	405									Triplet
-116	98.2	67	5.29	483	523	352	436									Triplet
-117	295.5	202	3.91	299	422	165	347									Triplet
-118	305.2	208	2.08	242	390	138	332									Triplet
-119	296.8	203	6.26	413	485	245	392									Triplet
-120	168.0	114	5.99	347	448	205	369									Triplet
-121	189.1	129	2.26	383	468	129	327									Triplet
-122	171.8	117	3.82	342	446	162	346									Triplet
-123	304.7	208	4.02	739	666	219	377									Triplet
-124	266.8	182.2	7.84	405	481	239	388									Triplet
-125	267.1	182	1.00	686	637	114	319									Triplet
-126	458.3	313	2.13	272	407	116	320									Triplet
-127	519.6	355	3.65	-		138	332									Triplet
-128	472.0	322	6.03	-		234	386									Triplet
-131	307.3	210	3.79	-		56	287									Triplet
-132	515.7	352	1.74	402	479	50	283									Triplet
-133	292.2	200	0.95	476	520	55	287									Triplet
-134	290.5	198.8	1.01	472	518	564	569	967	793	530	550					Premix
-135	308.8	211.4	2.26	591	584	879	744	976	798	788	693					Premix
-136	305.8	209.3	4.16	696	642	987	804	1054	841	947	782					Premix

TABLE XIV (cont.)

INJECTOR FACE TEMPERATURE

Test No.	P_c (PSIA)	P_c N/Cm^2	O/F	TJ-1		TJ-2		TJ-3		TJ-4		TJ-5		TJ-6		Injector Type
				°F	°K	°F	°K	°F	°K	°F	°K	°F	°K	°F	°K	
2K-11-137	295.4	282.2	6.32	748	671	978	799	1070	850	1001	812					Premix
-138	179.5	122.9	2.16	601	589	905	758	1015	819	817	709					Premix
-139	179.5	122.9	4.13	707	648	1045	836	1132	884	1003	813					Premix
-140	165.4	113.2	6.59	747	670	1037	832	1080	855	1006	814					Premix
-141	309.2	211.6	4.14	721	656	1046	837	1197	920	1096	864					Premix
-142	266.3	182.3	8.57	770	603	1003	813	1066	848	945	780					Premix
-143	526.8	360.6	3.76	535	553	1059	844	1186	914	985	803					Premix
-144	473.6	324.2	5.94	514	541	895	753	1034	830	832	718					Premix
-154	527.9	361.3	1.99	637	609	777	687	932	773							Premix
-155	291.2	199.3	4.03	447	503	788	693	786	692							Premix
-147	295.9	202.5	4.12					630	605	1167	904					-1 Zoned
-148	283.4	194.0	6.37					712	651	556	564					-1 Zoned
-149	299.8	205.2	4.15					621	600	1263	957					-1 Zoned
-150	307.5	210.5	2.12					1370	1016	1367	1015					-1 Zoned
-151	108.9	74.5	3.97					637	609	1166	903					-1 Zoned
-152B	527.4	361.0	3.79					615	597	615	597					-1 Zoned
-157	106.7	73.0	3.78					633	607	1156	898					-2 Zoned
-158	264.4	181.0	7.84					600	589	588	582					-2 Zoned
-159	316.3	216.5	4.03					439	499	1297	976					-2 Zoned
-160	315.7	216.1	4.05					421	489	1299	977					-2 Zoned
-161	291.5	199.5	6.38					416	486	1174	908					-2 Zoned
-162	323.8	221.6	2.08					855	730	1491	1084					-2 Zoned
-163	301.3	206.2	.98					426	492	1163	902					-2 Zoned
-164	535.7	366.7	3.60					548	560	1492	1084					-2 Zoned

3. Stability

The stability data for this program are listed in Table XV by run number. The relevant run conditions and the stability conditions including frequencies and amplitudes of unstable tests are included. As it was beyond the scope of this program to attempt to formulate a generalized stability model for gas-gas combustion, the data presented are intended to be used for further development of existing analytical models.* To permit full utilization of this data, a complete description of the engine system is given in Figure 64 with the relevant engine flow parameters.

A summary of the data reveals the following stability characteristics:

(1) The triplet injector exhibited unstable combustion in the first radial and third tangential mode at mixture ratios near four. At mixture ratios two and six the injector was stable.

(2) Using the premix injector, two tests with unstable combustion were observed at mixture ratio of four. All the remaining tests were stable. This instability appeared to couple with the first tangential mode of the chamber.

(3) The -1 zoned injector produced unstable combustion at a mixture ratio of six which coupled with the first tangential mode of the chamber. The remaining -1 and -2 tests were stable.

Since at least one case of high frequency instability was noted with each injector, stability damping devices probably would be needed on a production engine. A designer could incorporate either a resonator or face mounted baffles in any injector design.

*Recently emerging gas/gas combustion stability models are underwork at NASA Lewis Research Center. Dr. R. J. Priem using this data was able to successfully correlate at least a part of this data. This model will be published by LeRC as a NASA TN in the near future. This document title is listed in Reference 20.

TABLE XV

GAS/GAS INJECTOR STABILITY DATA

Premix Injector

Test	Chamber Contraction Ratio	L* In.	L* CM	Chamber Pressure Psia	Chamber Pressure N/CM^2	$W_{\emptyset}$ lbm/sec	$W_{\emptyset}$ Kg/sec	W_f lbm/sec	W_f kg/sec	ΔP_{ox} PSI	ΔP_{ox} N/CM^2	ΔP_{Fuel} PSI	ΔP_{Fuel} N/CM^2	Freq. HZ	Peak to Peak Amp. PSI	Peak to Peak Amp. N/CM^2	Comments
2K-11-101	3.38	5.32	13.51	291	201	2.61	1.184	0.678	0.307	82.7	57.0	104	71.7				Stable
102	3.38	5.32	13.51	296	204	2.726	1.236	0.667	0.302	81.0	55.8	99.3	68.5				
103	3.38	5.32	13.51	305	210	2.304	1.045	1.139	0.517	132	91.0	204	141				
104	3.38	5.32	13.51	277	191	2.826	1.282	0.486	0.220	69.5	48.0	68.9	47.5				
105	3.38	5.32	13.51	104	71.7	0.780	0.354	0.384	1.174	43.6	30.1	65.8	45.4				
106	3.38	5.32	13.51	116	80.0	0.924	0.419	0.368	0.167	42.5	29.3	61.0	42.1				
107	3.38	5.32	13.51	110	75.8	1.116	0.506	0.217	0.0984	28.9	19.9	30.8	21.2				
108	3.38	5.32	13.51	104	71.7	1.201	0.545	0.162	0.0735	26.0	17.9	23.8	16.4				
134	3.38	5.32	13.51	291	201	1.774	0.805	1.754	0.795	199	137	364	251				
135	3.38	16.65	34.67	309	213	2.470	1.120	1.093	0.496	136	93.8	198	137				Stable
136	3.38	13.65	34.67	306	211	2.823	1.280	0.679	0.308	91.9	63.4	110	76.1	12,000	15	10.3	Noisy
137	3.38	13.65	34.67	295	203	3.134	1.421	0.496	0.225	76.5	52.7	75.3	51.9				Stable
138	2.03	3.29	8.36	180	124	2.389	1.083	1.108	0.502	207	143	285	197				Stable
139	2.03	3.29	8.36	180	124	2.833	1.285	0.686	0.311	141	97.2	165	114				Noisy
140	2.03	3.29	8.36	165	114	3.093	1.782	0.466	0.211	112	77.2	110	75.8				Stable
141*	3.38	5.32	13.51	309	213	2.799	1.269	0.676	0.307	91.2	62.9	110	75.8	12,600	135	93.1	Bomb Test; Test Unstable for Total Duration
142	3.38	5.32	13.51	266	183	3.176	1.440	0.371	0.168	67.3	46.4	55.3	38.1				Stable
143	3.38	5.32	13.51	527	363	4.644	2.106	1.234	0.560	163	112	207	143	12,800	142	97.9	Unstable
144	3.38	5.32	13.51	474	327	4.939	2.240	0.831	0.377	121	83.4	127	87.6				
154	3.38	5.32	13.51	528	364	3.880	1.760	1.952	0.885	237	163	362	250				
155	3.38	5.32	13.51	291	201	2.673	1.212	0.664	0.301	71.7	49.4	86.7	59.8				

* Bomb 2 grain RDX

TABLE XV (cont.)
GAS/GAS INJECTOR STABILITY DATA

Triplet Injector

Test	Chamber Contraction Ratio	L* In.	L* CM	Chamber Pressure Psia	Chamber Pressure N/CM^2	W_ϕ lbm/sec	W_ϕ Kg/sec	W_f lbm/sec	W_f Kg/sec	ΔP_{ox} PSI	ΔP_{ox} N/CM^2	ΔP_{Fuel} PSI	ΔP_{Fuel} N/CM^2	Freq. HZ	Peak to Peak Amp. PSI	Peak to Peak Amp. N/CM^2	Comments
2K-11-111	3.38	5.32	13.51	302	208	2.720	1.234	0.689	0.312	65.8	45.4	141	97.2	26,000	28.2	19.4	Noisy
112	3.38	5.32	13.51	306	211	2.304	1.045	1.099	0.498	43.9	30.3	332	229				Stable
113	3.38	5.32	13.51	285	196	2.948	1.337	0.501	0.227	78.5	54.1	81.4	56.1				Stable
114	3.38	5.32	13.51	110	76	0.825	0.374	0.392	0.1778	14.9	10.3	119	82.0				
115	3.38	5.32	13.51	105	72	0.945	0.429	0.244	0.1107	22.8	15.7	50.2	34.6	24,000	95	65.2	Unstable for short time in middle of run.
116	3.38	5.32	13.51	98	67.5	1.002	0.454	0.180	0.0816	28.3	19.5	30.6	21.1				Stable
117	3.38	13.65	34.67	296	204	2.677	1.214	0.675	0.306	64.1	44.2	140	96.5				↓
118	3.38	13.65	34.67	305	210	2.297	1.042	1.096	0.497	41.3	28.5	331	228				
119	3.38	13.65	34.67	297	204	3.167	1.436	0.497	0.225	87.9	60.6	78.8	55.0				
120	2.03	3.29	8.36	168	116	3.023	1.371	0.495	0.224	150	103	132	91.0				
121	2.03	3.29	8.36	189	130	2.514	1.140	1.101	0.499	86.1	59.4	453	312				Stable
122	2.03	3.29	8.36	172	118	2.657	1.205	0.686	0.311	113	77.9	229	158				
123*	3.38	5.32	13.51	305	210	2.755	1.249	0.676	0.307	64.8	44.7	141	97.2	19,000 24,000	64 30	44.1 20.7	Unstable Before Bomb. Unstable After Bomb.
124	3.38	5.32	13.51	267	184	3.124	1.417	0.389	0.1764	91.3	62.9	53.5	36.9				
126	3.38	5.32	13.51	458	316	3.728	1.691	1.744	0.791	82.9	57.2	340	234	20,000	222	153	Unstable After 0.36 sec.
127	3.38	5.32	13.51	520	358	4.532	2.055	1.232	0.559	105	72.4	273	188	22,000	137	94	Unstable
128	3.38	5.32	13.51	472	326	4.863	2.205	0.797	0.361	125	86.2	131	90.3				
131	3.38	5.32	13.51	307	211	2.734	1.240	0.712	0.323	50.2	34.6	115	79.3	18,000	138	95.2	Unstable
132	3.38	5.32	13.51	516	356	3.680	1.669	2.107	0.956	59.7	41.2	-					
133	3.38	5.32	13.51	292	202	1.761	0.799	1.844	0.836	22.6	15.8	-					
									-1 Zoned Triplet								
147	3.38	5.32	13.51	296	204	2.772	1.257	0.673	0.305	162	112	65.5	45.2				
148	3.38	5.32	13.51	283	195	3.037	1.377	0.477	0.216	210	145	46.5	32.1	12,000	205	141	Unstable
149*	3.38	5.32	13.51	300	207	2.765	1.254	0.667	0.302	165	114	63.1	43.5				Stable Test; 312 PSI Peak to Peak @ Bomb, Attenuating to tare amplitude in 0.08 sec.
150	3.38	5.32	13.51	308	212	2.362	1.071	1.114	0.505	137	94	182	125				
151	3.38	5.32	13.51	109	75.2	0.993	.450	0.251	0.114	62.4	43.0	23.1	15.9				
152B	3.38	5.32	13.51	527	363	4.670	2.118	1.231	0.558	267	184	127	87.6				
									-2 Zoned Triplet								
157	3.38	5.32	13.51	107	73.8	0.948	0.430	0.251	0.114	55.3	38.1	24.2	16.7				
158	3.38	5.32	13.51	264	182	3.040	1.379	0.388	0.176	208	143.	21.9	15.1				
159	3.38	5.32	13.51	316	218	2.860	1.297	0.710	0.322	157	108	64.2	44.3				
160*	3.38	5.32	13.51	316	218	2.853	1.294	0.704	0.319	159	110	64.0	44.1				Stable Test; 78 PSI Peak to Peak @ Bomb attenuating to tare amplitude in .08 sec.
161	3.38	5.32	13.51	292	201	3.056	1.386	0.479	0.217	191	132	30.9	21.3				
162	3.38	5.32	13.51	324	223	2.416	1.096	1.160	0.526	134	92.4	181	125				
163	3.38	5.32	13.51	301	208	1.751	0.794	1.789	0.811	68.3	47.1	393	271				
164	3.38	5.32	13.51	536	370	4.583	2.078	1.273	0.577	244	168	128	88.3				

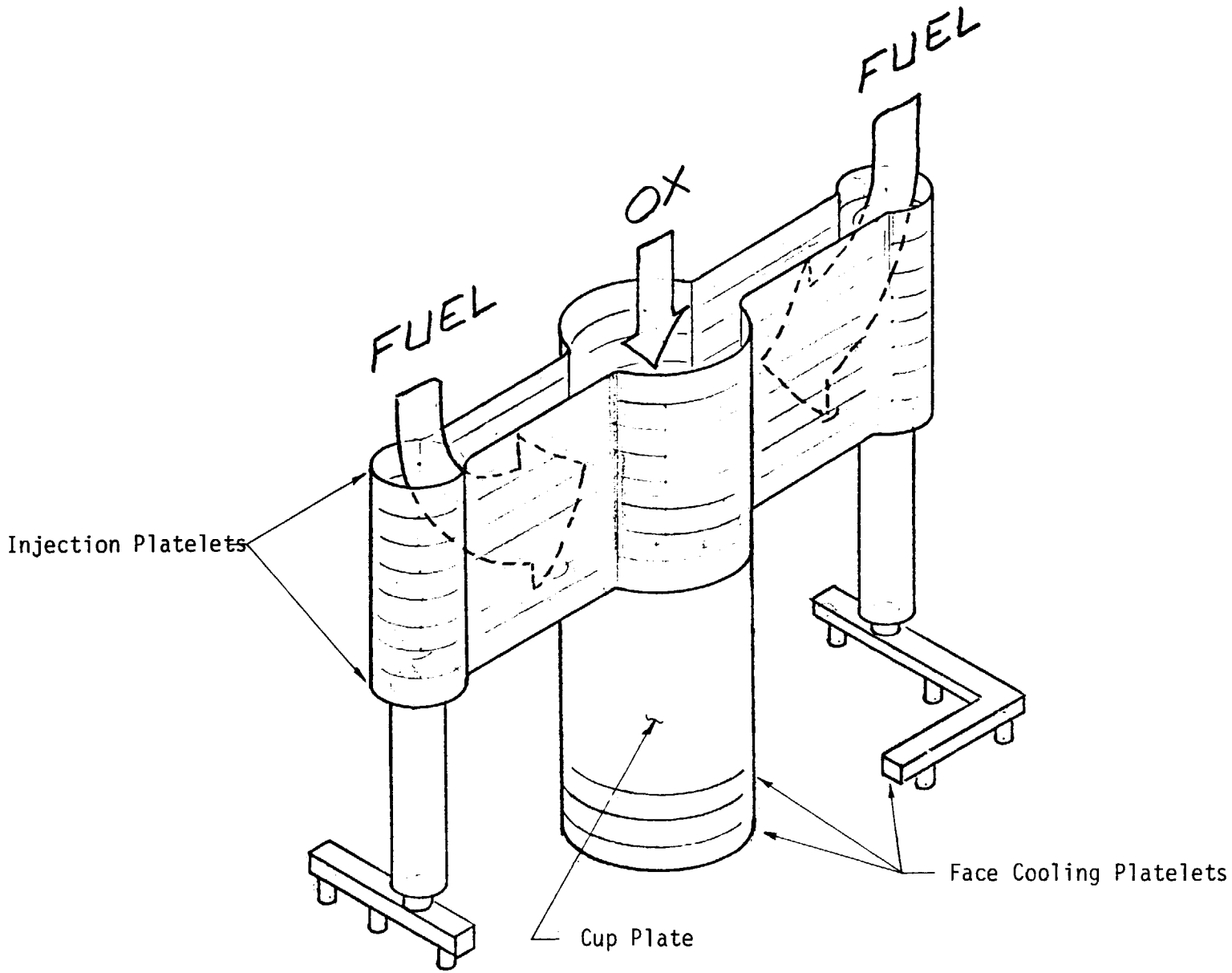

FIGURE 44. DEEP CUP PREMIX ELEMENT SCHEMATIC

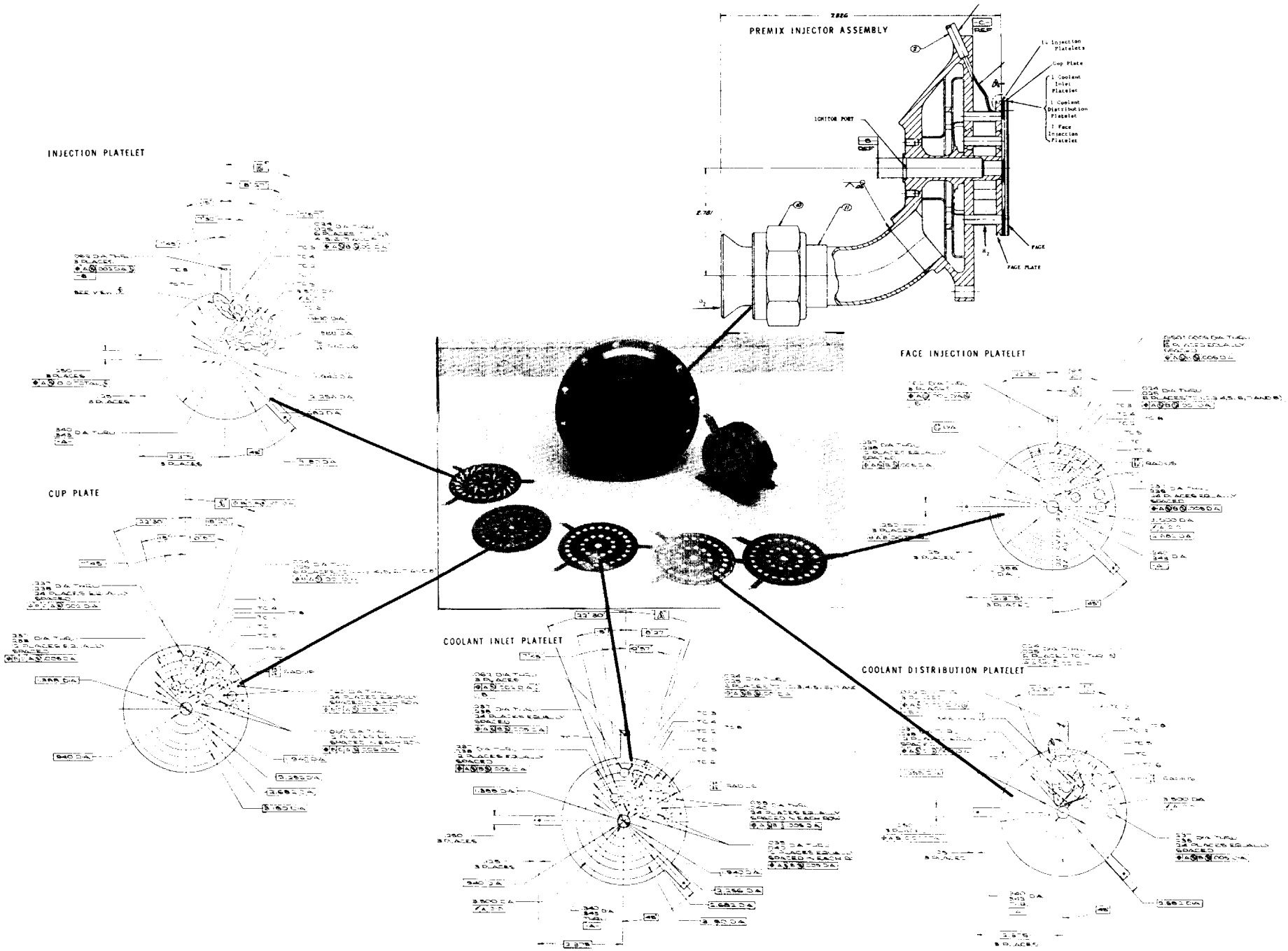

Figure 45. Premix Injector

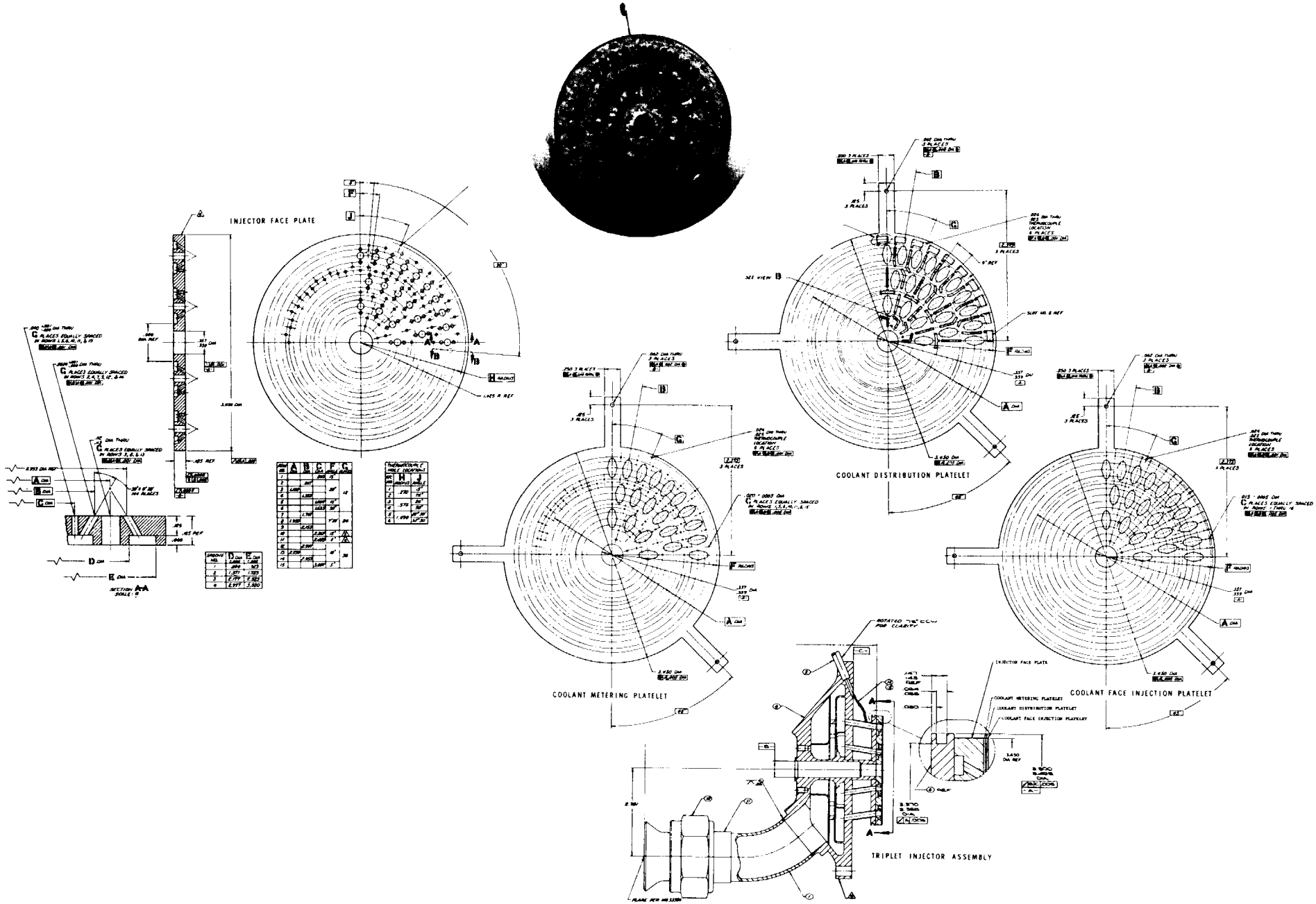

Figure 46. Triplet Injector

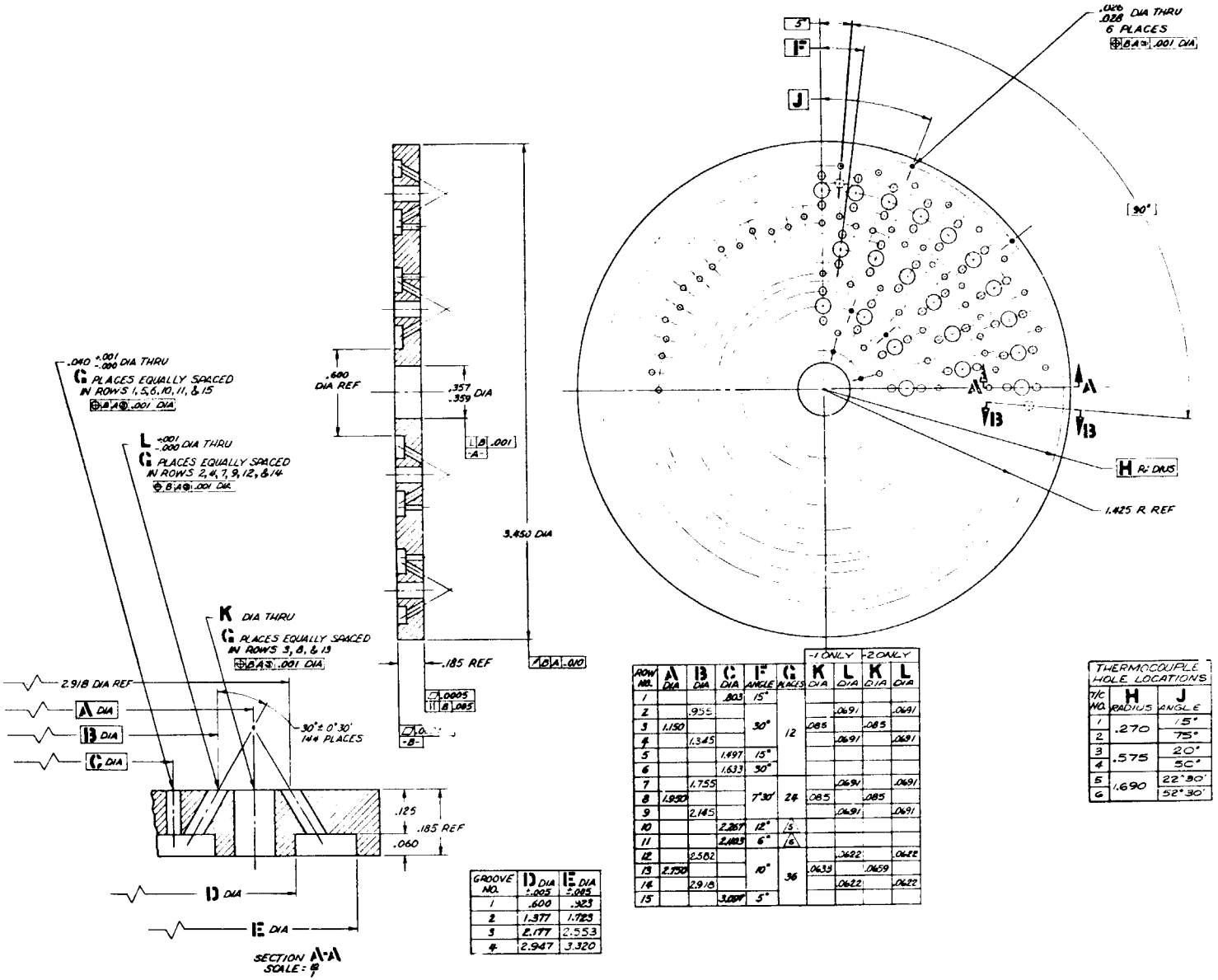

GROOVE NO.	D DIA +.005	E DIA ±.005
1	.600	.323
2	1.377	1.729
3	2.177	2.553
4	2.947	3.320

ROW NO.	A DIA	B DIA	C DIA	F ANGLE	G PLACES	-1 ONLY K DIA	-1 ONLY L DIA	-2 ONLY K DIA	-2 ONLY L DIA
1			.803	15°					
2		.955		30°	12		.0691		.0691
3	1.150					.085		.085	
4		1.345					.0691		.0691
5			1.497	15°					
6			1.633	30°					
7		1.755					.0691		.0691
8	1.950			7°30'	24	.085		.085	
9		2.145					.0691		.0691
10			2.287	12°	15				
11			2.483	6°	18				
12		2.582					.0622		.0622
13	2.750			10°	36	.0639		.0659	
14		2.918					.0622		.0622
15			3.089	5°					

T/C NO.	H RADIUS	J ANGLE
1	.270	15°
2		75°
3	.575	20°
4		50°
5	1.690	22°30'
6		52°30'

THERMOCOUPLE HOLE LOCATIONS

Figure 47. Zoned Injector

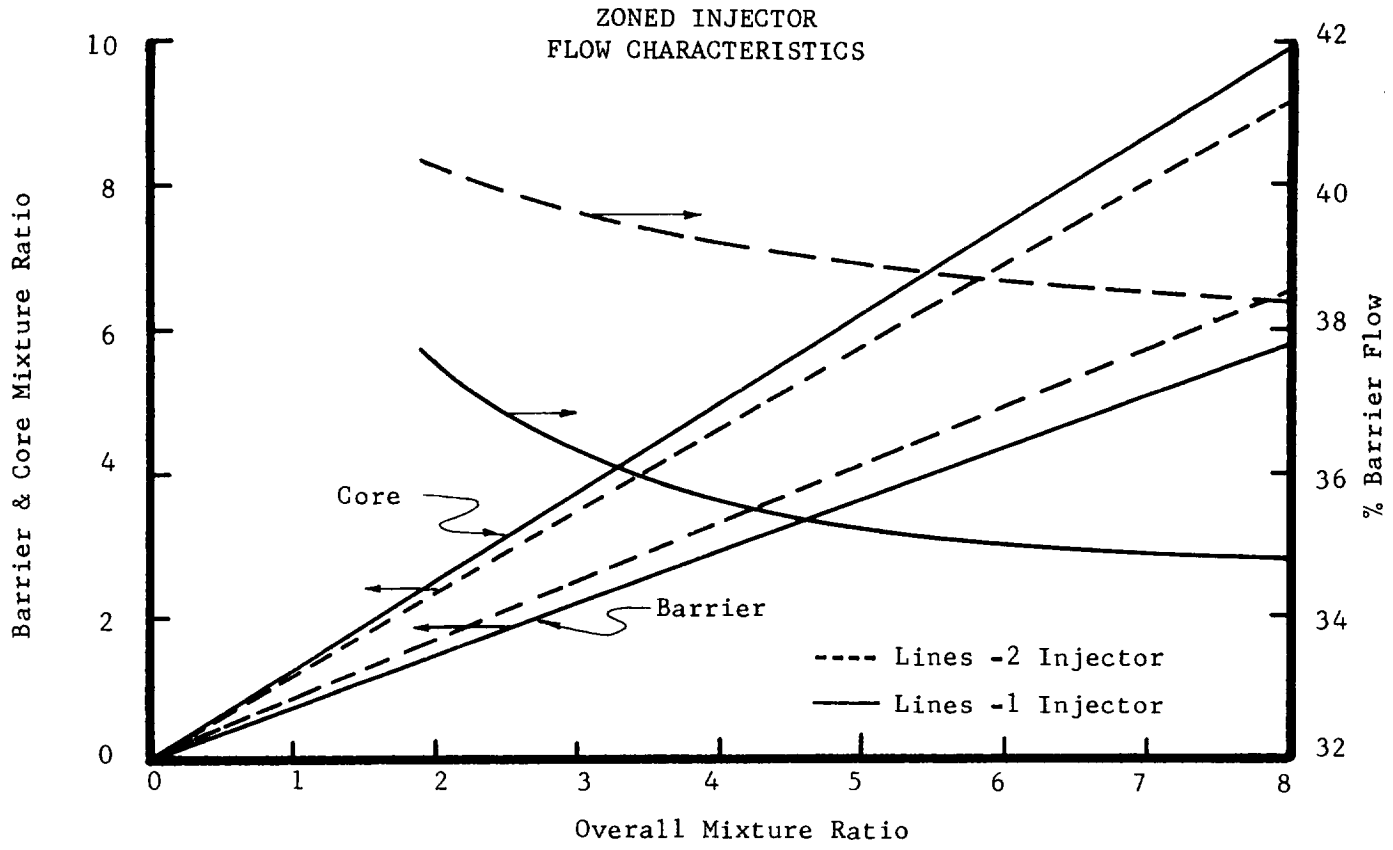

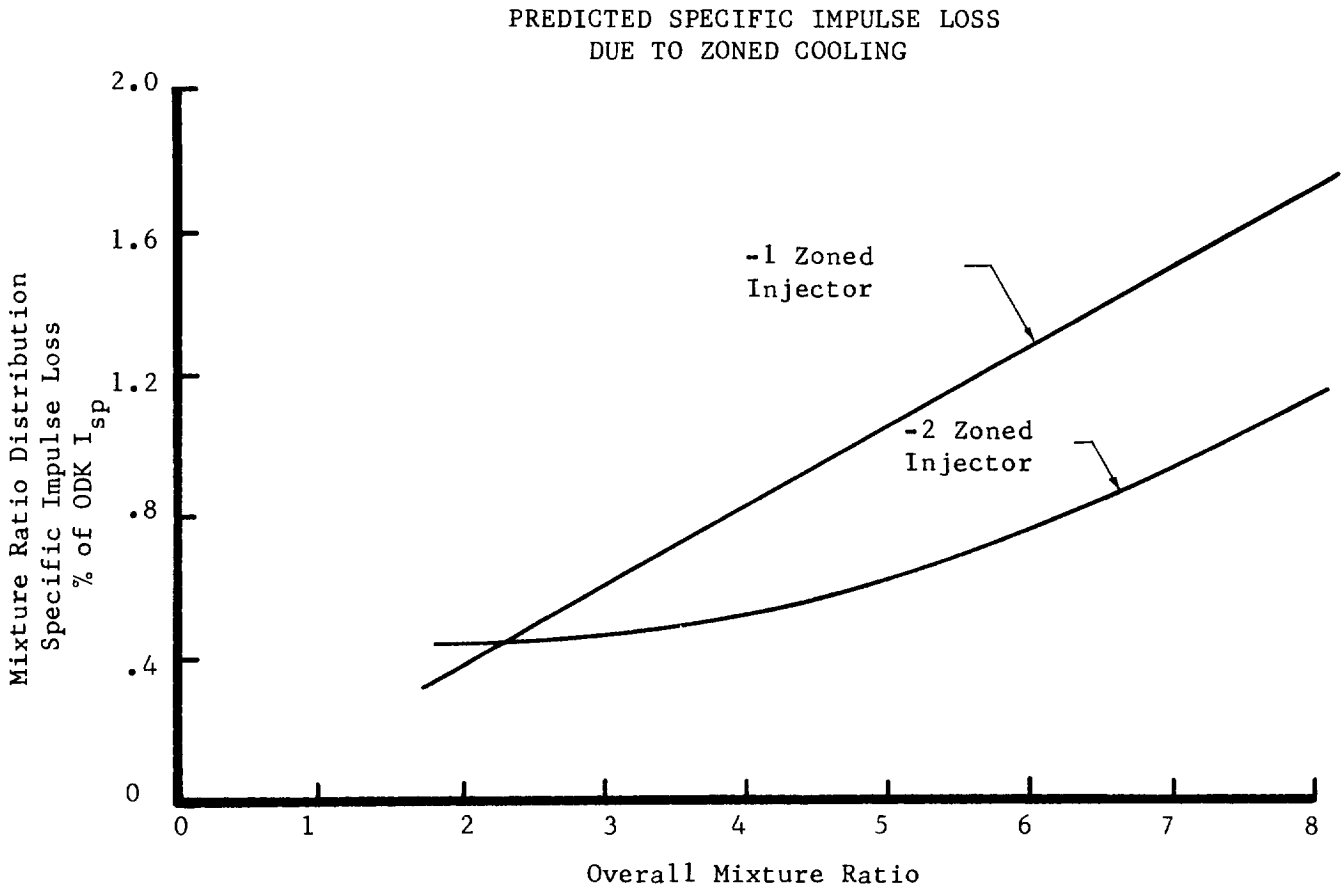

FIGURE 48. BARRIER INJECTOR CHARACTERISTICS

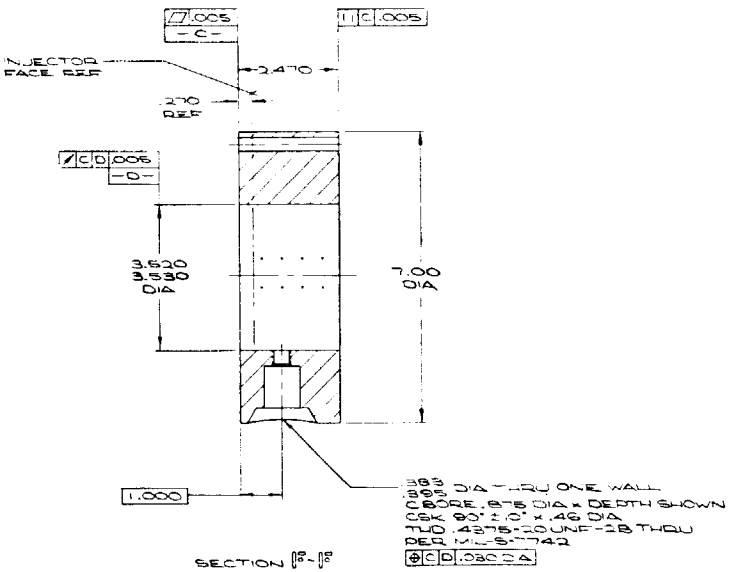

CHAMBER L* SECTION

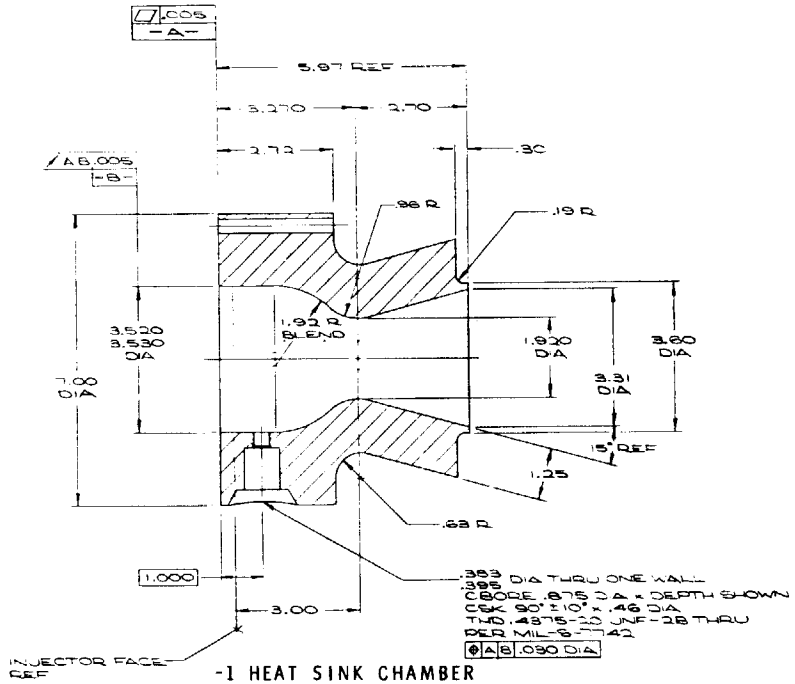

-1 HEAT SINK CHAMBER

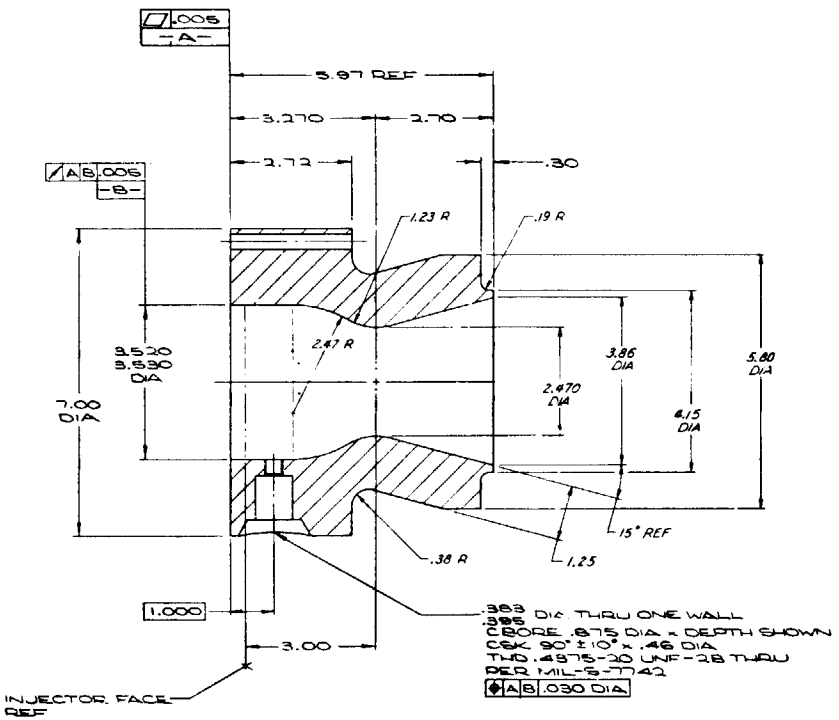

-2 HEAT SINK CHAMBER

Figure 49. Full Scale Chambers

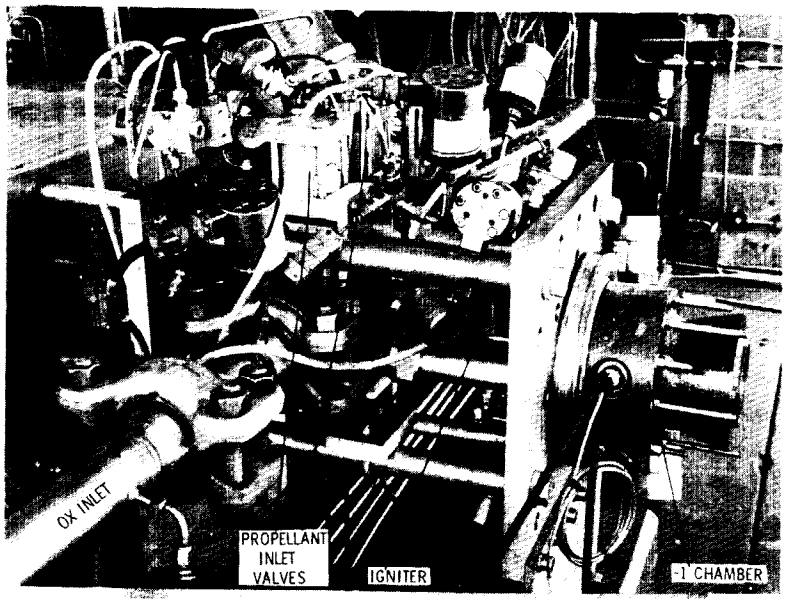

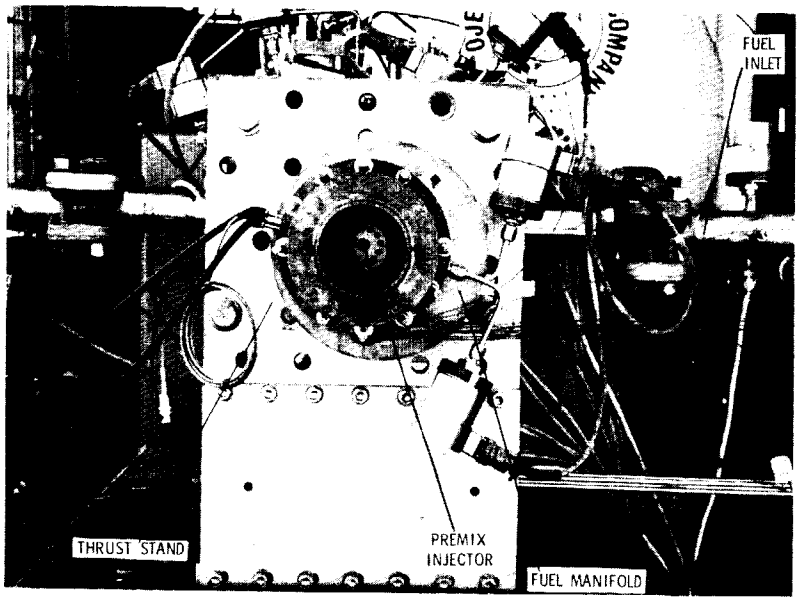

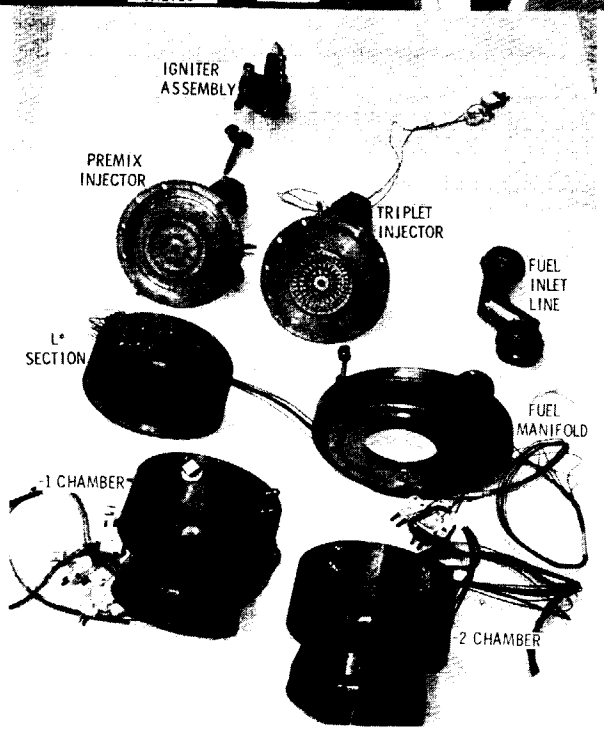

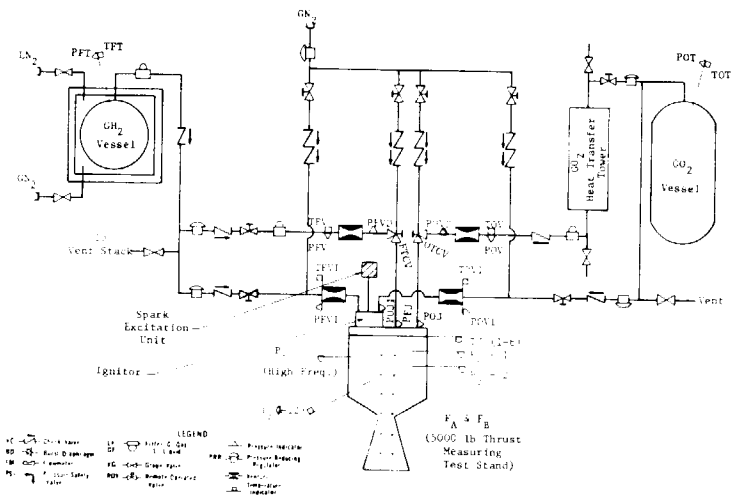

Figure 50. Full Scale Test Hardware and Assembly

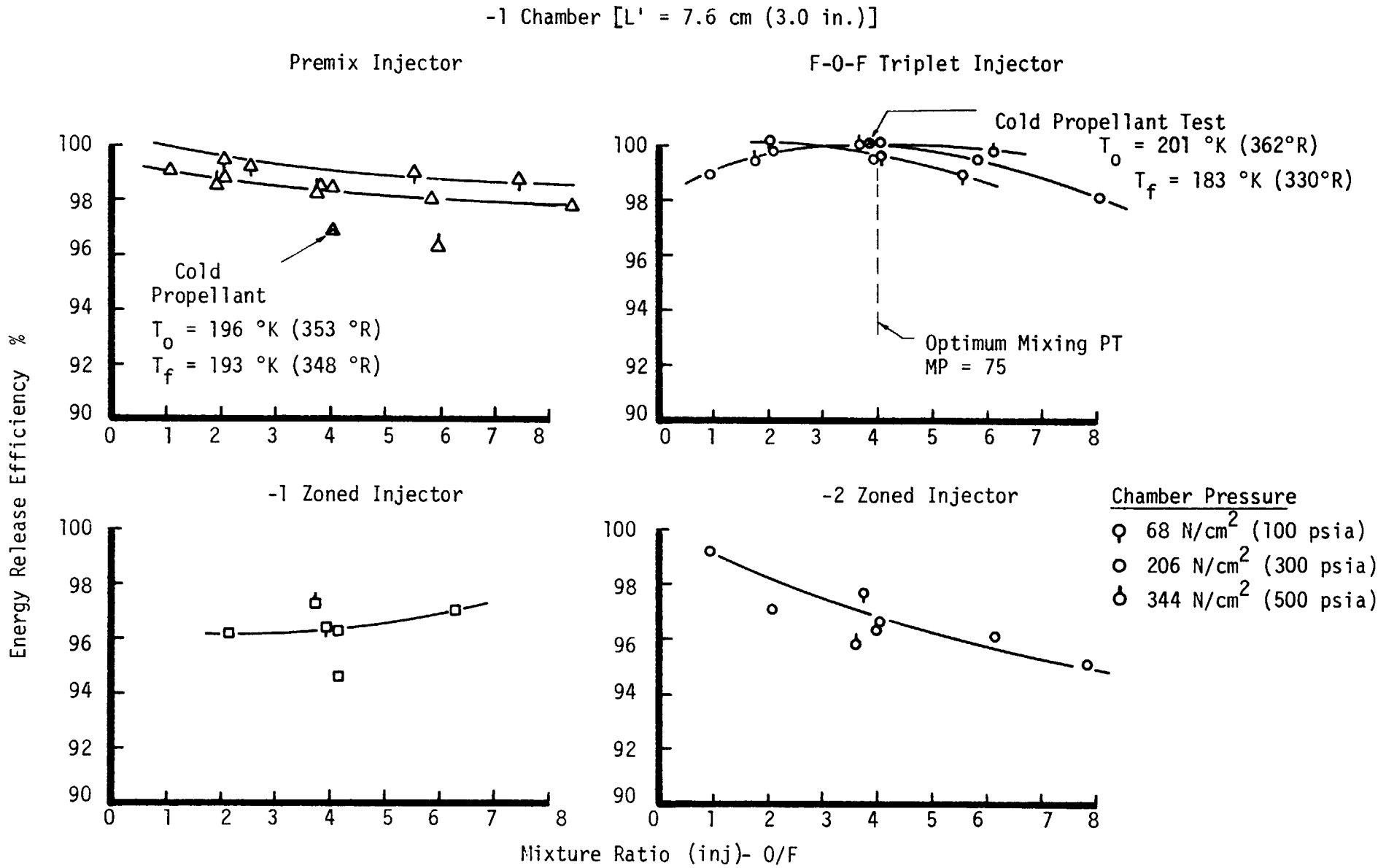

FIGURE 51. EFFECTS OF MIXTURE RATIO AND CHAMBER PRESSURE ON FULL SCALE PERFORMANCE

P_c = 206 N/cm^2 (300 psia)
T_P = Ambient

		CR	L'		L*	
			cm	(in)	cm	(in)
o	-1 Chamber	3.4	7.6	(3.0)	13.5	(5.3)
♁	-2 Chamber	2.0	7.6	(3.0)	8.4	(3.3)
♀	-1+L* Chamber	3.4	13.9	(5.5)	39.0	(15.3)

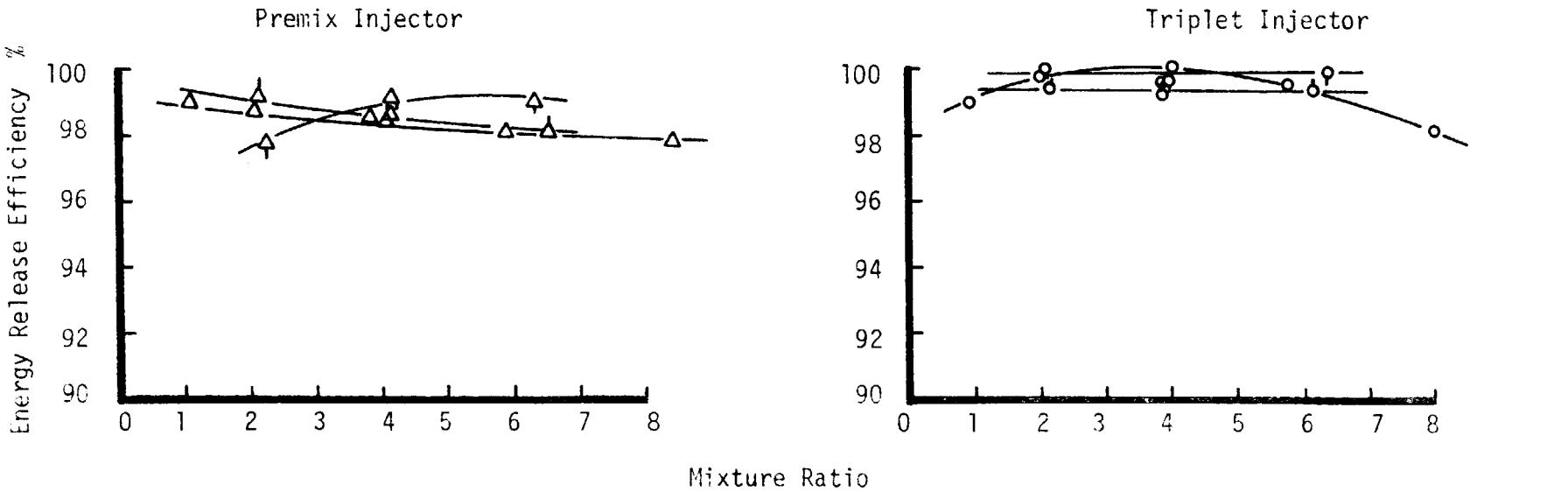

FIGURE 52. EFFECT OF CHAMBER GEOMETRY ON FULL SCALE PERFORMANCE

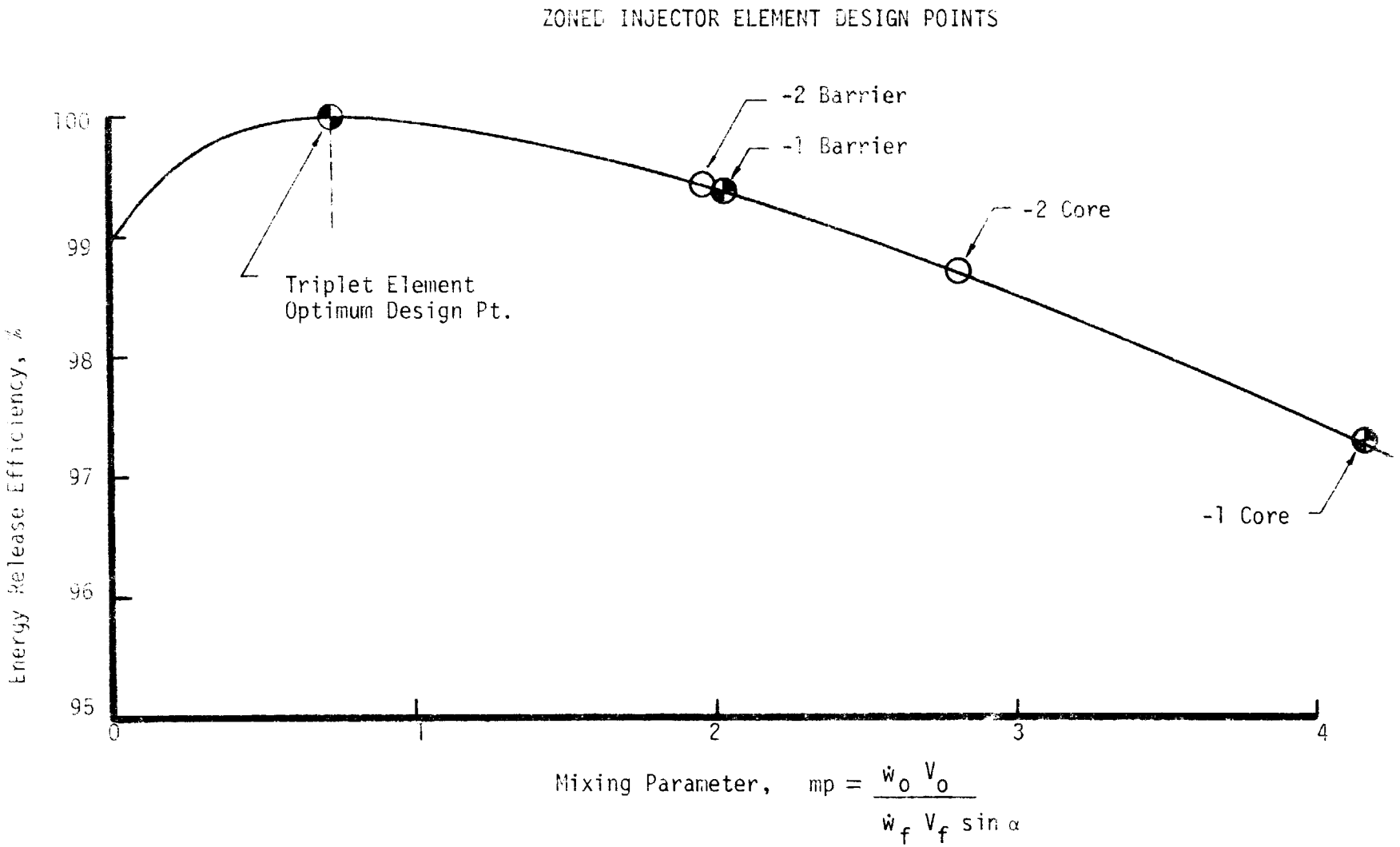

FIGURE 53. THE EFFECT OF MIXING PARAMETER ON TRIPLET ELEMENT PERFORMANCE

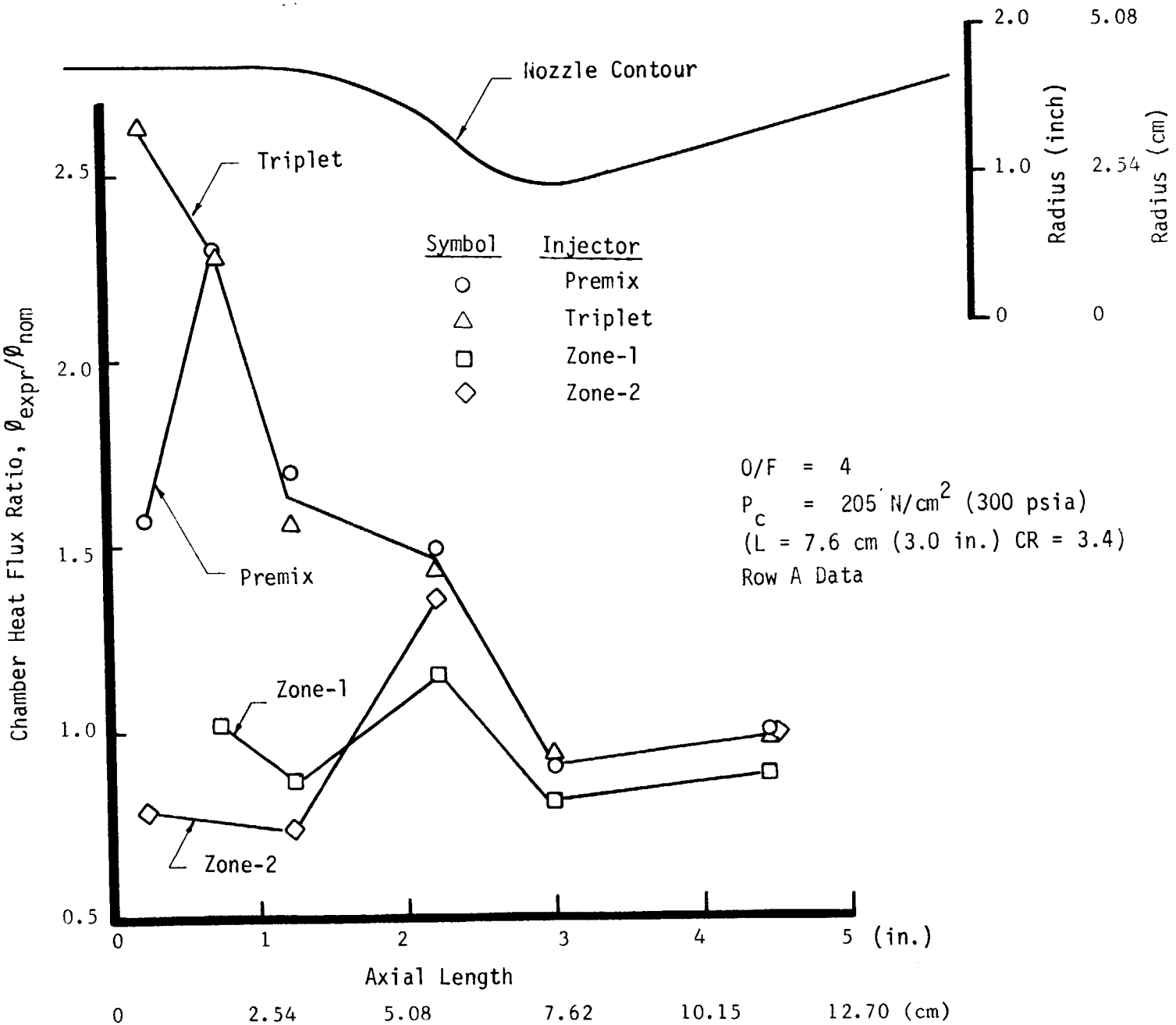

FIGURE 54. HEAT FLUX FOR THE FULL SCALE INJECTORS

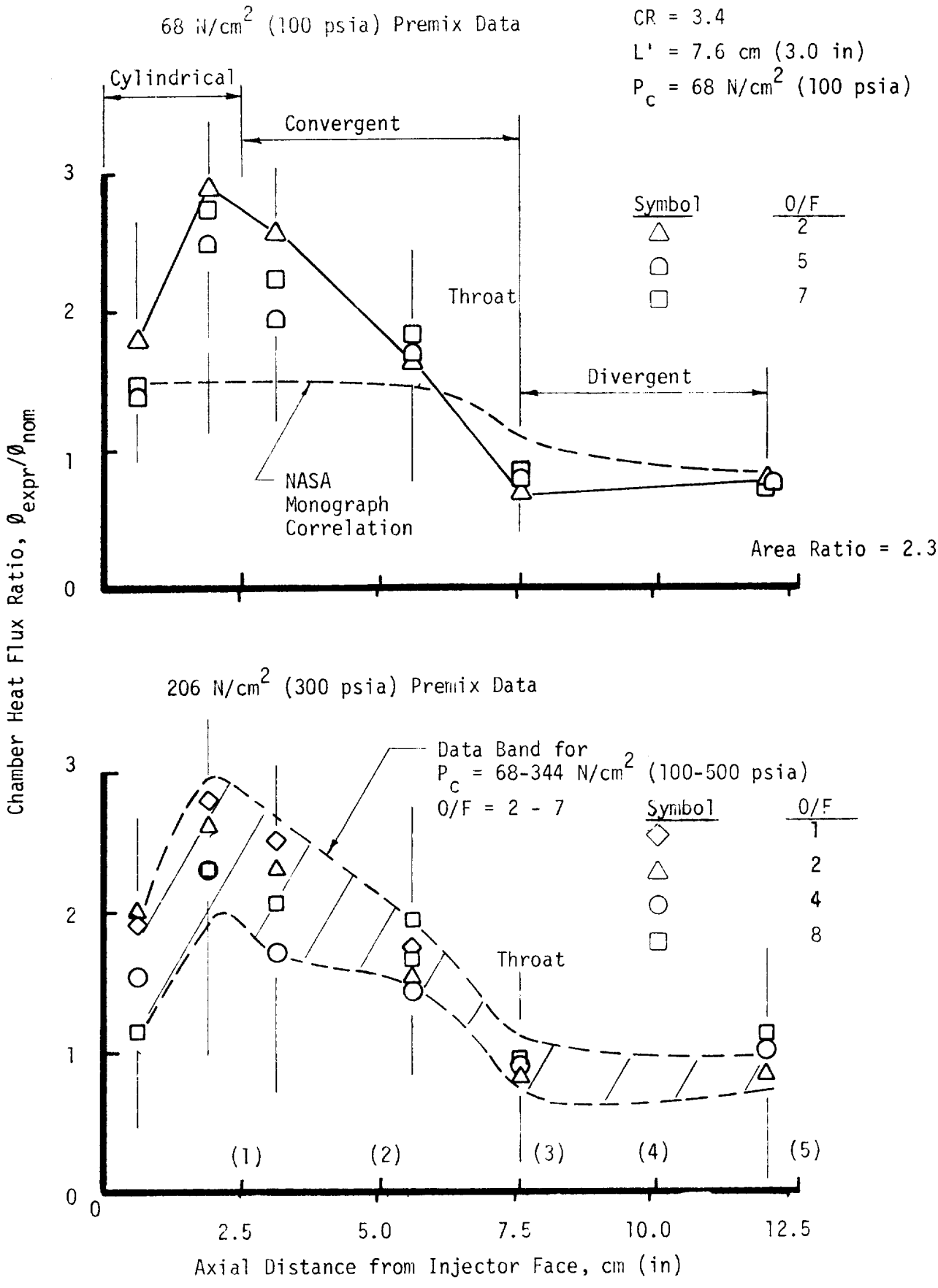

FIGURE 55. PREMIX-CHAMBER HEAT FLUX DATA (-1 CHAMBER)

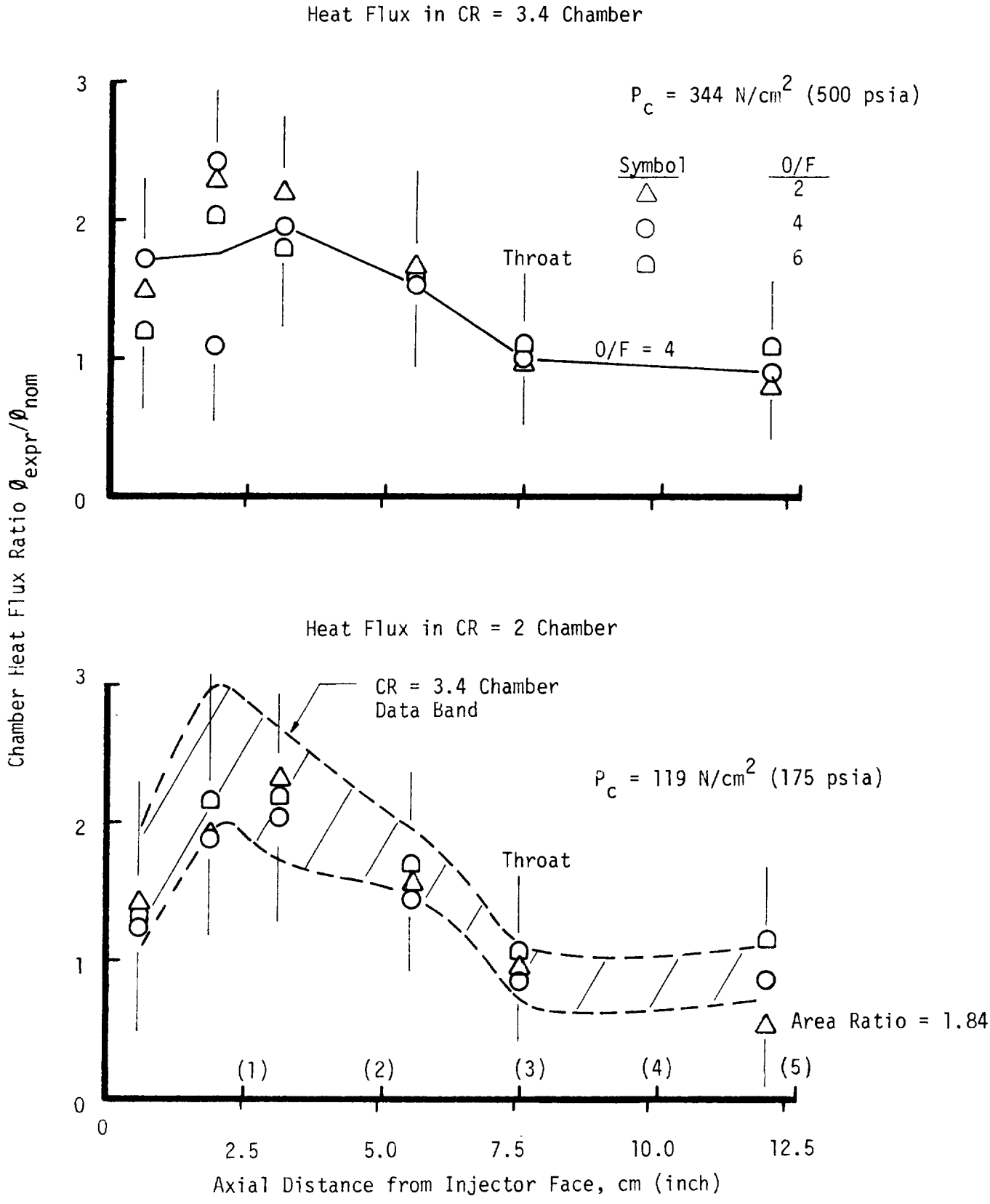

FIGURE 56. PREMIX CHAMBER HEAT FLUX USING L = 7.6 cm (3.0 in) CHAMBERS

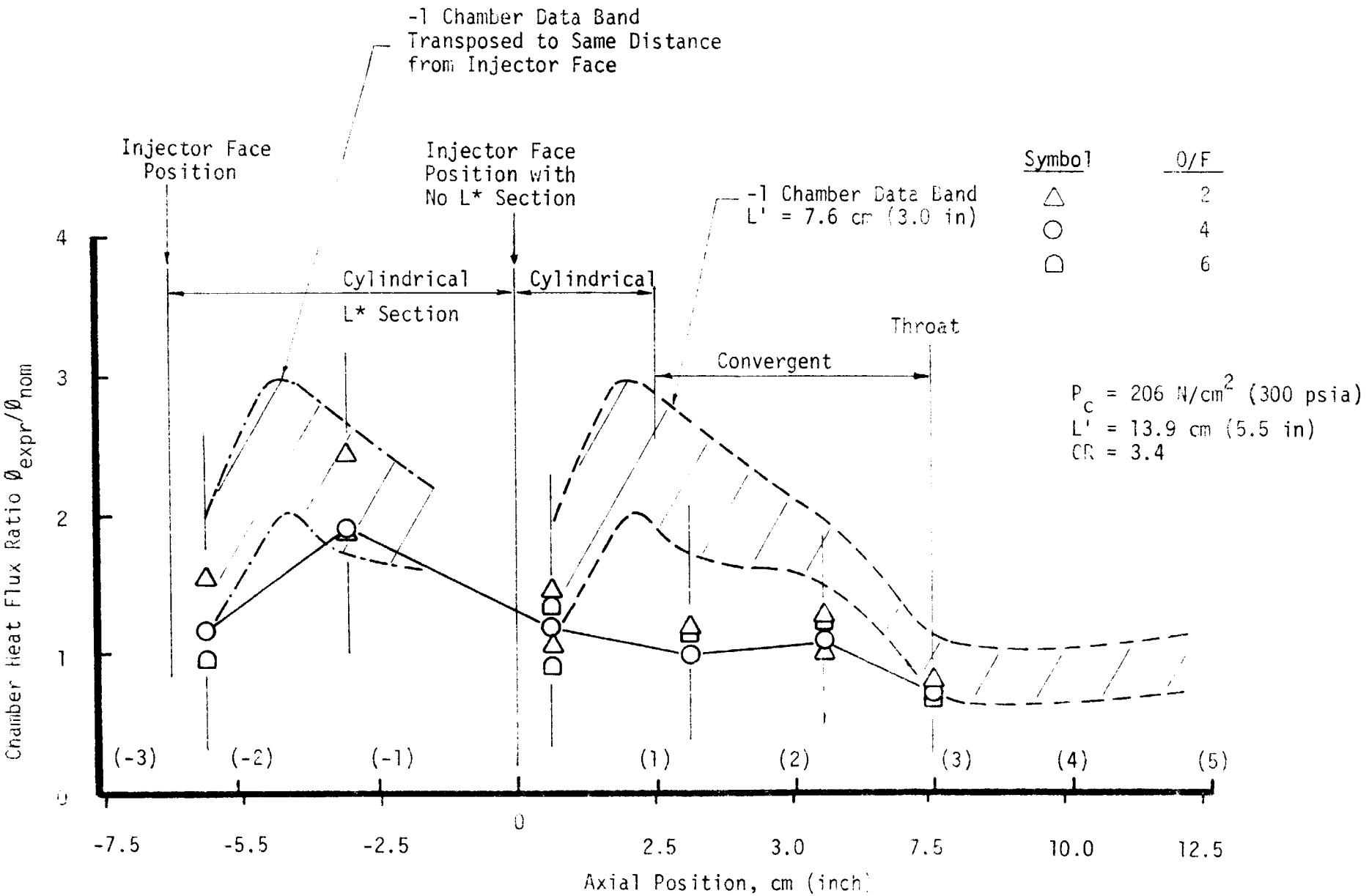

FIGURE 57. PREMIX CHAMBER HEAT FLUX FOR -1 + L* CHAMBER

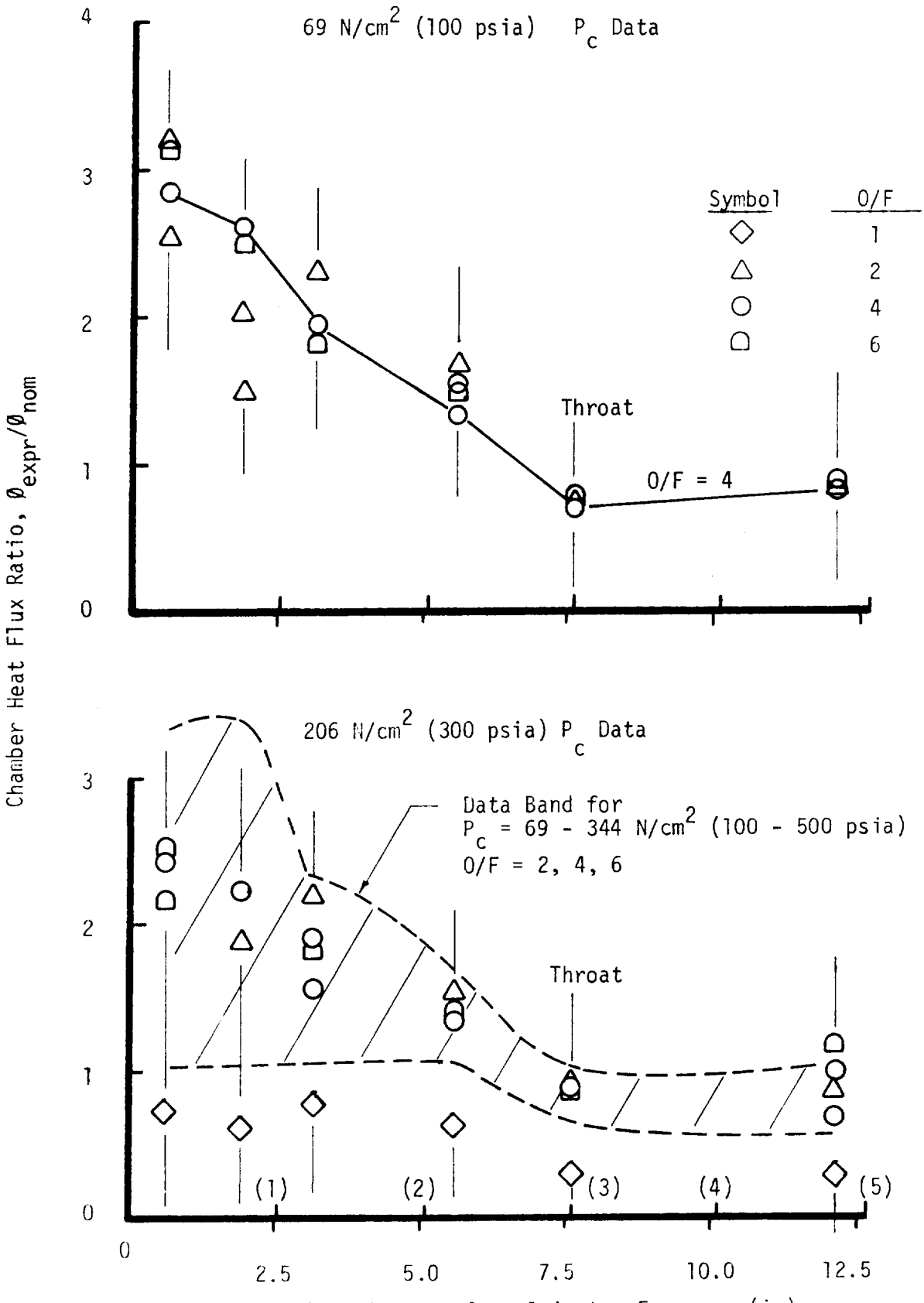

FIGURE 58. TRIPLET CHAMBER HEAT FLUX IN THE CR 3.4, 7.6 L CHAMBER

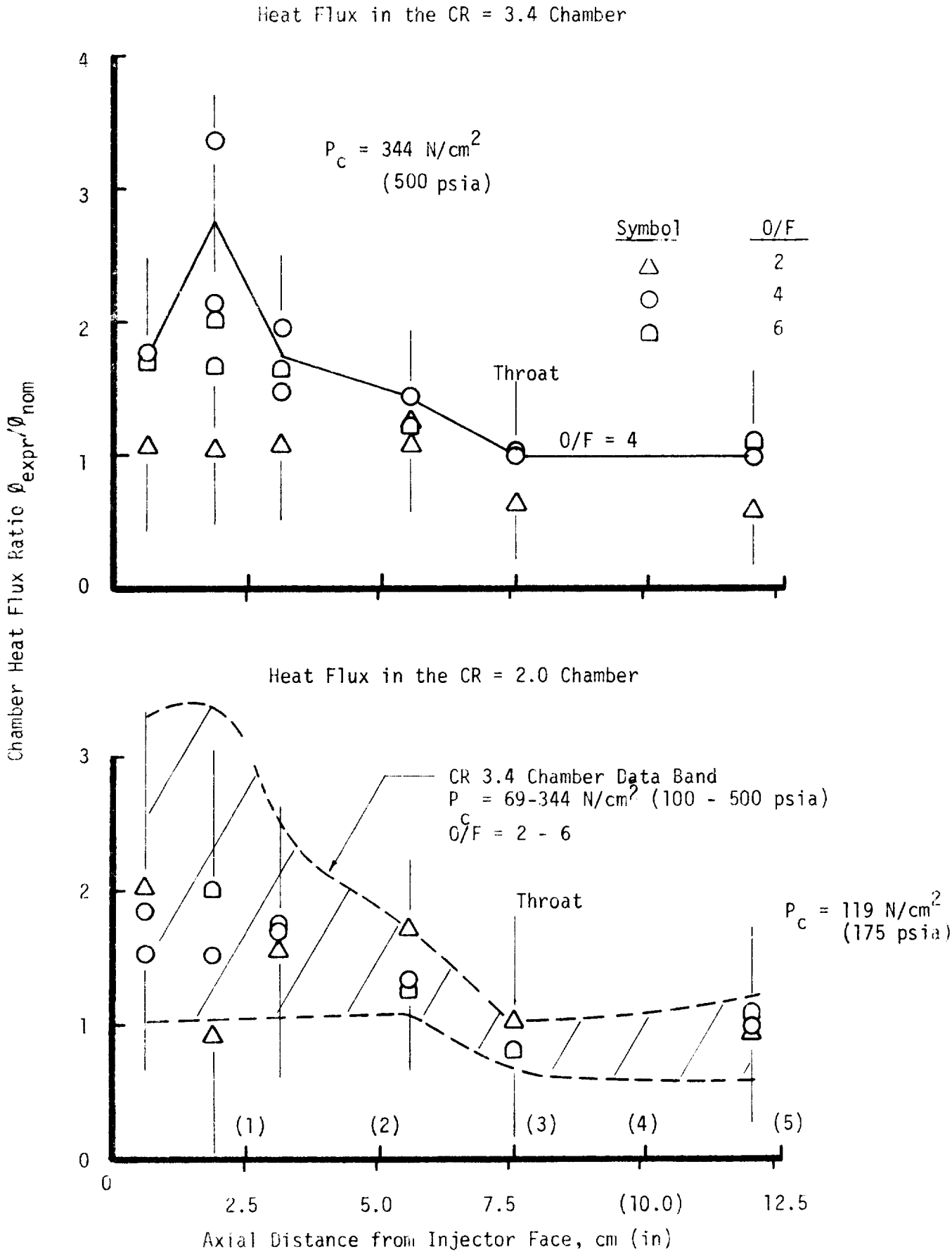

FIGURE 59. TRIPLET CHAMBER HEAT FLUX USING L = 7.6 cm (3.0 in) CHAMBER

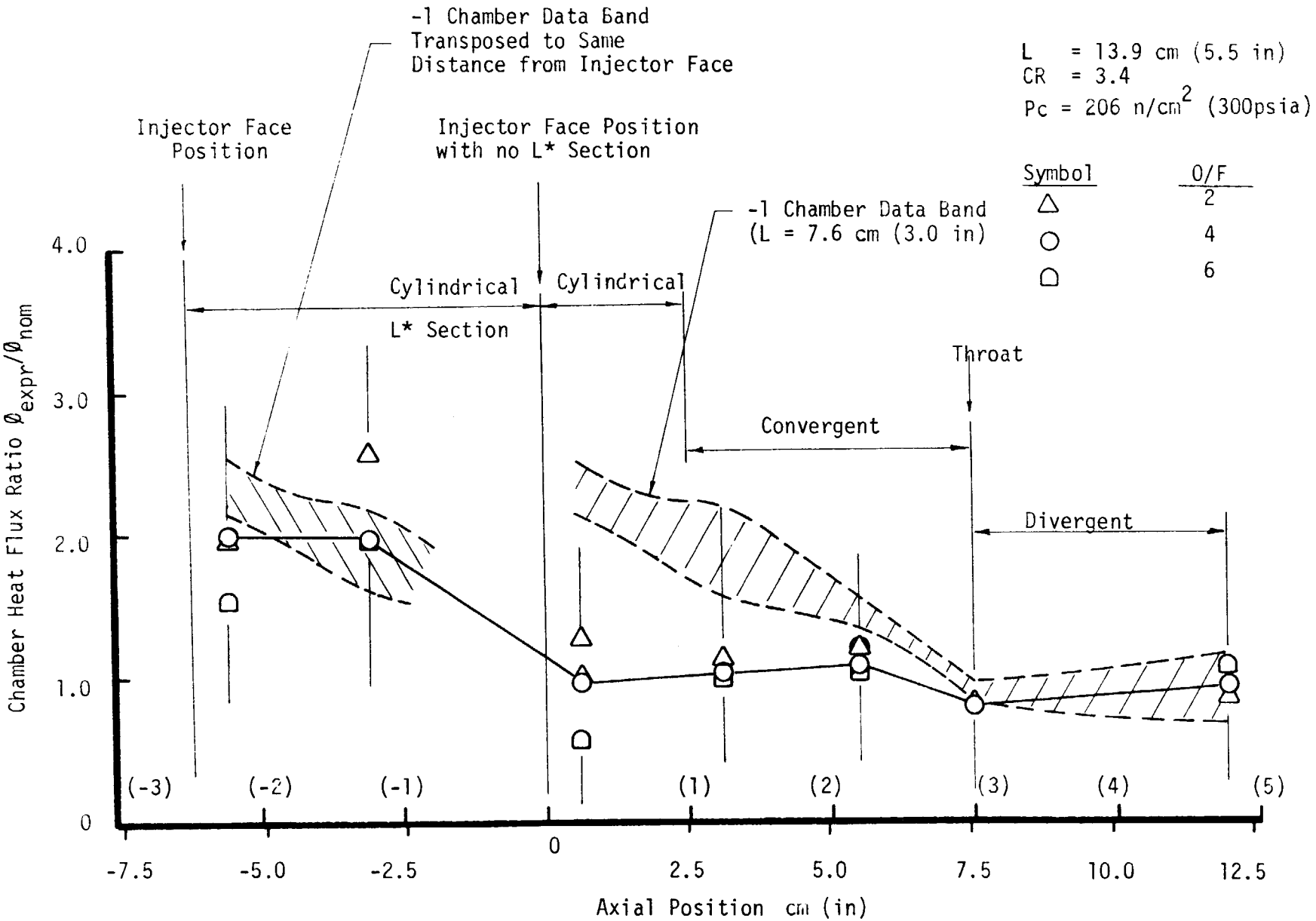

FIGURE 60. TRIPLET CHAMBER HEAT FLUX FOR -1+L* CHAMBER

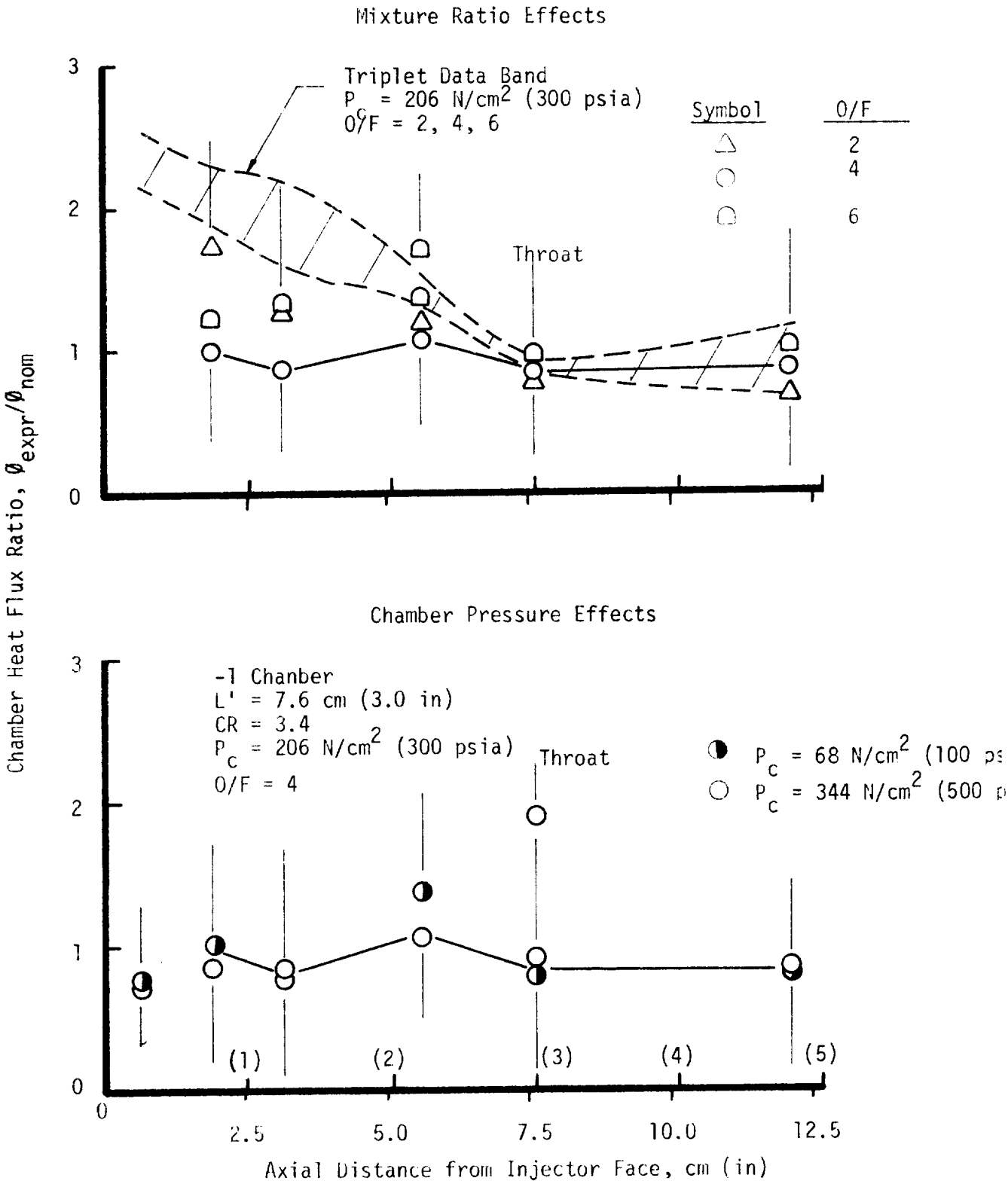

FIGURE 61. ZONE-1 TRIPLET CHAMBER HEAT FLUX

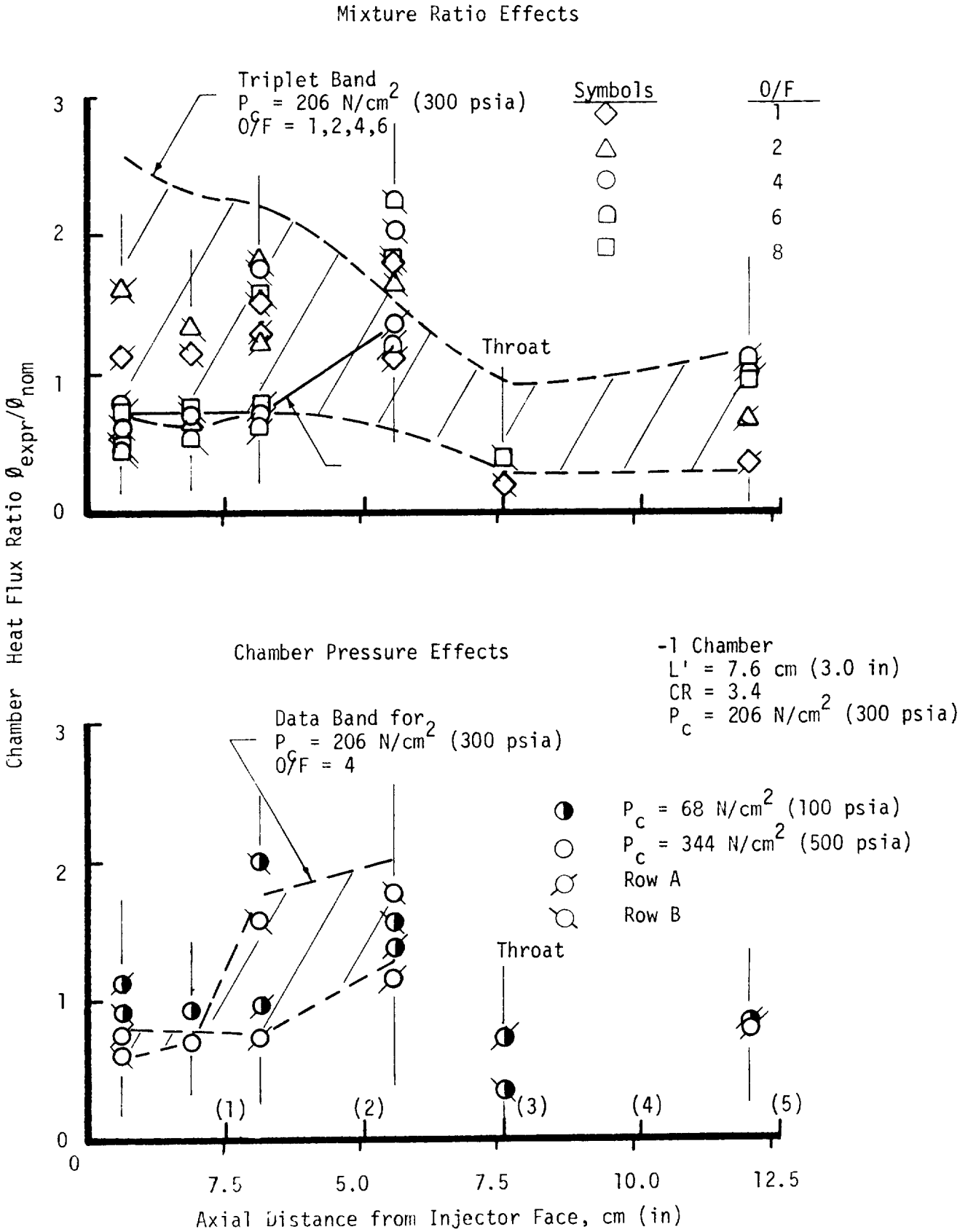

FIGURE 62. ZONE-2 TRIPLET CHAMBER HEAT FLUX

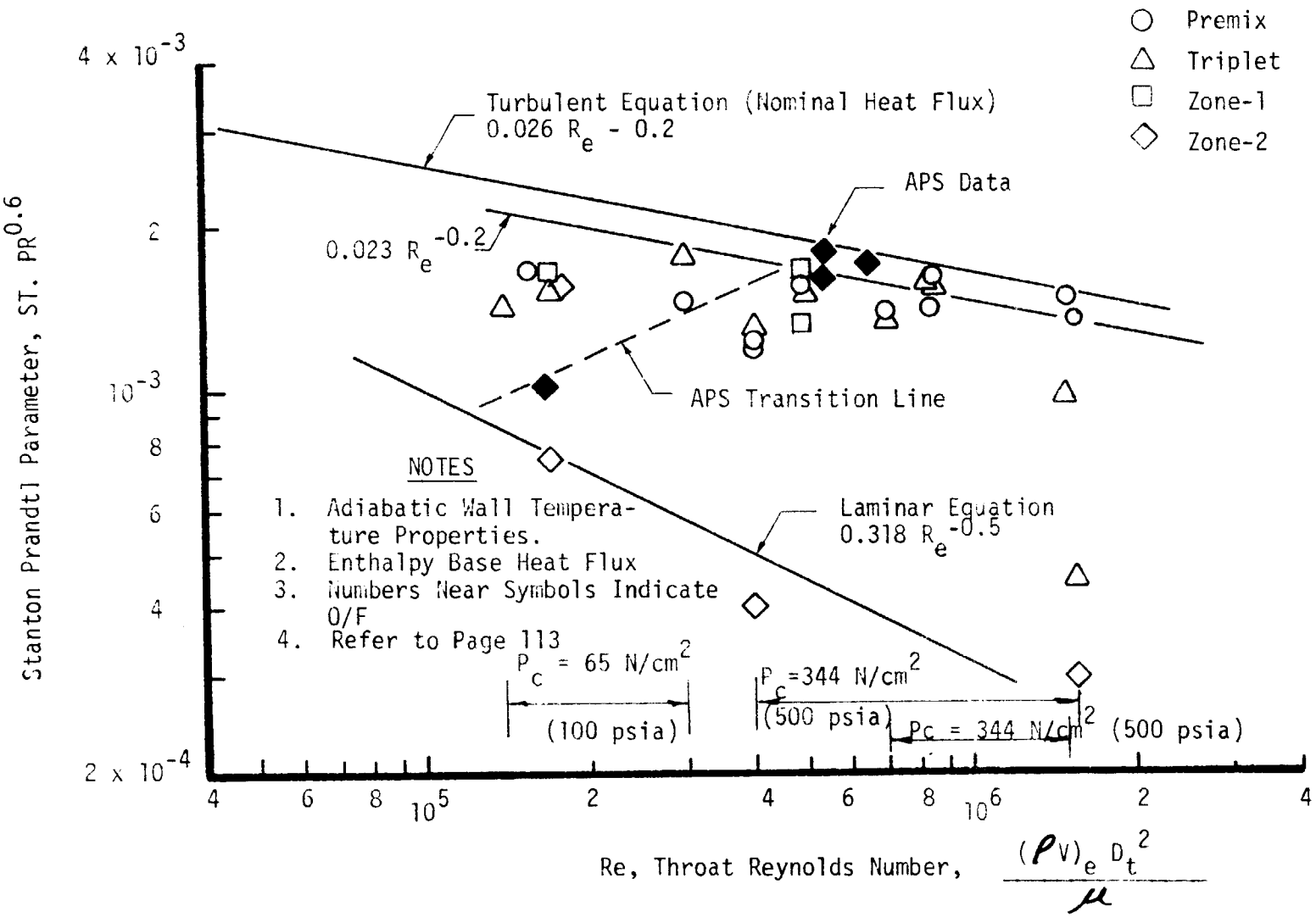

FIGURE 63. THROAT HEAT TRANSFER CHARACTERISTICS

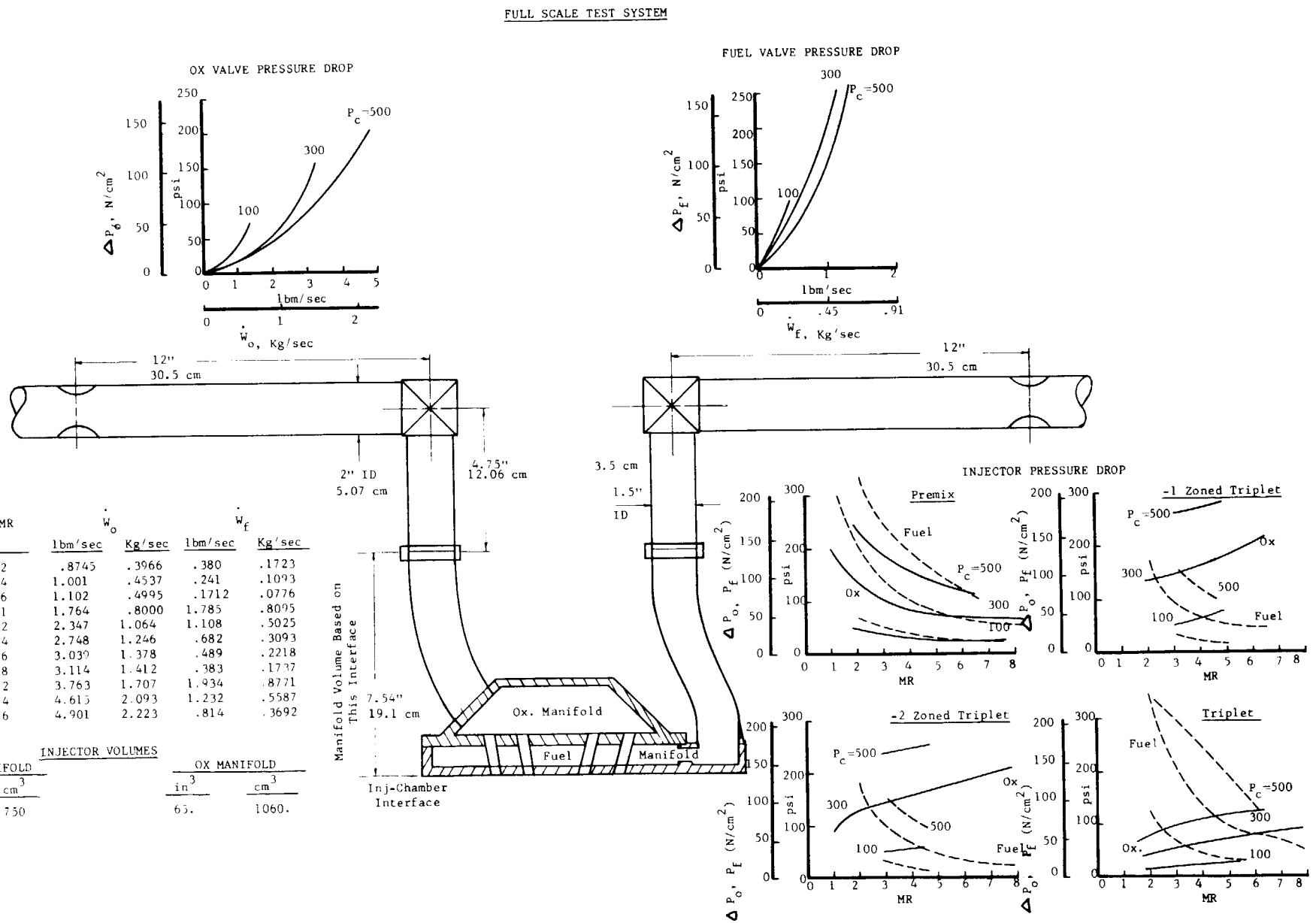

P_c PSIA	P_c N/cm^2	MR	$\dot{W}_o$ lbm/sec	$\dot{W}_o$ Kg/sec	$\dot{W}_f$ lbm/sec	$\dot{W}_f$ Kg/sec
100	68.9	2	.8745	.3966	.380	.1723
		4	1.001	.4537	.241	.1093
		6	1.102	.4995	.1712	.0776
		1	1.764	.8000	1.785	.8095
300	207	2	2.347	1.064	1.108	.5025
		4	2.748	1.246	.682	.3093
		6	3.039	1.378	.489	.2218
		8	3.114	1.412	.383	.1737
500	345	2	3.763	1.707	1.934	.8771
		4	4.615	2.093	1.232	.5587
		6	4.901	2.223	.814	.3692

INJECTOR VOLUMES

FUEL MANIFOLD in^3	FUEL MANIFOLD cm^3	OX MANIFOLD in^3	OX MANIFOLD cm^3
46.	750	65.	1060.

Figure 64. Test System Parameters Applicable to Stability Analysis

VIII. DATA EVALUATION

A. INTRODUCTION - METHODS OF APPROACH

The objective of this task was to synthesize analytical models that were based upon the experimental data of this program. The resulting design equations and curves were prepared to provide an injector designer with a technique to estimate performance and chamber heat flux for prototype injectors. This work culminated in the procedures contained in the Design Handbook. The intent of the modeling work was to bring together all aspects of the performance and heat transfer problem and unify the data within the structure of a firmly based analytical formation. It became clear early in the program that these aims could best be served by two fundamentally different approaches to the mixing/combustion problem: (1) one based entirely on empiricism tempered by physical fundamentals and (2) one based on an analytical approach tuned with empirical data.

The first approach has as its advantage ease of computation and accuracy. Its disadvantage is that it is tied exclusively to specific injection element and test conditions and can not be extrapolated beyond the tested envelope with confidence. The second approach is more complex, but it has modeled the first order mixing/combustion mechanisms. Thus it is general in nature and can handle most design problems. However, approximation had to be incorporated to make the model practical which reduces the accuracy of the model as a prediction tool.

The empirical approach is based on correlation of the cold flow data, leading to design equations that predict mixing efficiency (E_m). These equations are modified (where data was available) by appropriate constants to account for combustion influences. The basic combustion influence was treated by an "equivalent-length" function. This equivalent cold flow length is the technique by which the cold flow based equations can be scaled to equivalent combustion conditions. Energy release efficiency is obtained by scaling E_m by an empirically determined function that relates the two parameters. In addition to the performance aspects of the model, chamber wall heat flux data was correlated. This correlation estimates the local flux in the forward end of the chamber as a function of injection momentum ratio.

The analytical approach results in much the same information except that it is not element-specific. The details of the analytical modeling are found in Appendix A. In this section a generalized approach is discussed that simplifies the rather tedious computational procedures implicit in the analytical model for clarity in presentation of the concept. The discussion in this section is a result of correlations formed by using the analytical model. These correlations result in four non-dimensional parameters that characterize the mixing process for both axisymmetric and two dimensional jets. By appropriately selecting and/or calculating the various parameters contained

within this correlation virtually any element or test condition can be analyzed. Combustion is treated via an analytical technique that considers the thermochemical impact of combustion in conjunction with the mixing process. In addition, chamber heat flux can be predicted based on computation of outer-edge combustion gas properties.

The following paragraphs describe the details of both approaches. The empirical approach is discussed first followed by a synopsis of the analytical approach.

B. DISCUSSION OF RESULTS - EMPIRICAL APPROACH

The objective of this section is to document the work that resulted in the design equations and plots presented in the Design Handbook. The approach taken here was empirically based as opposed to analytical approach described in the next section. Basic design equations were formulated by correlation of the cold flow data with the relevant data from the single element hot fire series. The effects of combustion were treated by empirically determining a functional relationship between cold flow length and combustion length. This functional relationship was unique for each element type, and allows the design equations based on cold flow data to be scaled to a combustion environment. In order to predict combustion performance, it was also necessary to determine a relationship between mixing efficiency and combustion efficiency. In addition, the single element and full scale injector heat flux data were correlated as a function of momentum ratio; resulting in a technique that estimates the characteristic heat flux for various elements. The following paragraphs describe the details of the cold flow correlation; the functional relationship between E_m and combustion efficiency; the determination of an equivalent cold flow length, and the correlation of the heat flux data.

1. Cold Flow Data and Correlations

The cold flow data discussed earlier in Section IV, were used to form correlations between E_m and various operating and design variables. These correlations were intended to organize the data into an easily used format that accounted for the effect of the primary variables on E_m. In general, this aim was realized. Single element data was correlated with an equation that is of the following general form.

$$E_m = K\ f\ (L/D_o,\ O/F,\ D_o/D_f,\ A_f/A_o) \qquad (6)$$

where K is a function of the particular variables plotted vs K in Figures 65 through 69 for each element type.

The technique used to correlate the data was similar for each element type. Each variable of the cold flow data was investigated to ascertain its particular influences on E_m. The variables were then grouped and

plotted point by point versus experimental E_m. If second order influences then become evident, a new variable grouping was synthetized that accounted for the observed influence and the resulting data were replotted again point by point versus experimental E_m. This process was continued until the experimental data grouped within $\pm$ 5% or better. The experimental E_m versus the variable-grouping then defined a unique relationship between E_m and the variable-group. This relationship was then put into equation form by defining a new variable (K) that was a function of the relevant physical parameters and resulted in Equation 6. The single element and full-scale combustion performance data was then investigated to see if the equations would predict the absolute values and trends of the combustion performance data. In general, the combustion did influence the mixing process resulting in modifications of the cold flow equations. These modifications were constants that were applied to the cold flow equations to account for combustion influences. The resulting equations, therefore, were formulated such that one constant was used for the cold flow correlation and another constant was used for the combustion correlation. The following paragraphs describe the results of this work for each element type.

Coaxial Element

The coaxial element and increased shear element data is correlated in Figure 65. Referring to Figure 65, note that the equation:

$$E_m = 100 - 26.2 \ln \left(\frac{K_c}{L/D_{eq}}\right) \tag{7}$$

where K_c is a variable plotted in Figure 65, correlates the experimental data to within $\pm$ 5% over the entire ranges of design and operating variables tested. Inspection of the above equation and the relationship with $\left(\frac{V_f-V_o}{V_o}\right)$ reveals the following information:

- E_m is related inversely to L/D_o. (Long chambers and small diameter elements are in the direction of high performance.)

- E_m is related to $\frac{V_f-V_o}{V_o}$ with high $\frac{V_f-V_o}{V_o}$ in the direction of high performance. At zero V_f-V_o K_c is a maximum (minimum E_m). K_c becomes asymtotic to a value of 10 at about 10 $\frac{V_f-V_o}{V_o}$.

  The maximum K_c was not precisely defined by the experimental data of this program as there were no tests conducted with $\frac{V_f-V_o}{V_o}$ less than 0.27. However, the fundamental physics of

turbulent mixing, dating back to Prandtl's mixing length hypothesis, is believed to be modeled by a criterion that mixing is minimum at $V_f - V_o = 0$. Therefore, the K_c curve was defined with a zero slope at $V_f - V_o = 0$, which was used to extrapolate K_c from $\frac{V_f - V_o}{V_o} = 0.27$ to $\frac{V_f - V_o}{V_o} = 0$.

- The effects of an increased shear area oxidizer tube can be accounted for by use of the oxidizer hydraulic diameter D_H. Increased shear area (smaller hydraulic diameter) when compared to an equivalent area circular element (D_{eq}) is in the direction of increased performance. This correlation treats increased shear as a multiplier to the basic $V_f - V_o / V_o$ relationship. That is, the addition of added diffusion surface area has the same effect as increasing the relative velocity. In practice however, increased shear designs are difficult to fabricate and a better design choice would be to increase the relative velocity between the propellants.

Swirler Elements

The relevant design parameters and curves necessary to estimate the E_m of a swirler (oxidizer swirl) coaxial element are found in Figure 66. It must be noted that this is an equation valid for a swirl element with a tangential to axial velocity ratio of 1 only. The equation correlates the bulk of the swirler cold flow data to ± 2%.

$$E_m = 100 - C \ln \left(\frac{K_s}{L/D_o}\right) \qquad (8)$$

Other values of swirl must be scaled using the empirical relationship defined in the upper right hand portion of Figure 66. Because the swirler element is such an efficient mixing element*, the E_m data generated during this program was all over 90%; a fact which limited the extent of the correlation. However, the single element combustion data discussed in Section V was as useful as the cold flow data. By backing out E_m from ERE, the combustion data was used to supply some of the information necessary to complete this correlation. The cold flow data was correlated with the constant "C" in the correlation equation equal to 2.7. However, using the 2.7 value to predict performance resulted in consistent overpredictions. A better combustion correlation was obtained using C = 5. Therefore, C = 2.7 should be used for cold flow mixing analysis and C = 5 should be used for the combustion problem. In addition to the above the following information is relevant.

*In cold flow only - combustion influences the mixing of this element more adversely than any other element tested.

- E_m is a function of L/D_o. Again, long chamber lengths and small element sizes are in the direction of high performance.

- The degree of swirl does influence the resulting mixing performance. The curve shown in Figure 66 is a crossplot of the data shown in Section IV. E_m for values of V_t/V_a less than one were computed by applying this factor to the E_m calculated through use of the swirler equation.

- Inspection of the variable, K_s reveals a maximum (min E_m) at a $V_f\text{-}V_o/V_o$ equal to ten. It can be reasoned that values to the left of the maximum are controlled by swirl and to the right of the maximum by shear mechanisms. Since the total swirl component is directly related to the amount of oxidizer the mixing process is controlled by the oxidizer flow rate. Low values of $V_f\text{-}V_o/V_o$ are generated by high oxidizer flow rates and thus swirl controls the mixing process. At high values of $V_f\text{-}V_o/V_o$ less of the total flow is swirling, (less oxidizer), however, the relative shear is increased and becomes the controlling parameter.

Premix Elements

The relevant design correlating parameters and auxiliary curves for both the premix triplet and pentad elements are found in Figure 67. The design equation is

$$E_m = \frac{100 - K_p \ln\left(\frac{21}{L/D_o}\right)}{1 + 3\left(0.07\ W/D_o - 0.02\right)/(L/D_o)} \qquad (9)$$

This equation correlates both the premix triplet and pentad cold flow data to within + 4% E_m using the cold flow K_p curve. Applying the cold flow K_p to the single element combustion data overpredicted the performance at low fuel flow rates (high mixture ratio). A K_p for combustion was found by applying the above equation to the single element hot fire data. Figure 67 shows the influence to be large (high K_p) at low $\frac{\dot{w}_f V_f}{\dot{w}_o V_o}$ and becomes identical to the cold flow at high values of momentum ratio. Because these elements were premixed i.e., mixing occurs before combustion, it was expected that there would be very little combustion influence. However, a combustion influence can be reasoned to be a function of the bulk velocity in the mixing cup. As the H_2 flow rate is reduced bulk velocity of the gases through the mixing cup is reduced increasing the likelihood that some combustion could take place inside the cup. Visual inspection of both the full scale and single element injectors did reveal that some combustion occurred locally inside the cup, which evidently modified the mixing process. Therefore the combustion K_p should be used for the combustion problem while the cold flow K_p should be used for cold flow predictions.

The design parameters and plots reveal the following additional information.

- E_m is sensitive to L/D_o. Long chamber lengths and small oxidizer (mixing cup) diameters are in the direction of higher E_m.

- An optimum design is achieved at a $\frac{\dot{w}_f V_f}{\dot{w}_o V_o}$ equal to three.

- The width of the fuel injection orifice (w) is an important mixing process variable. When the fuel slot is narrow with respect to the oxidizer dia ($0.33\ W/D_o$ in Figure 67), the injected fuel penetrates the oxidizer and produces a well mixed product. When the fuel slot is wide with respect to the oxidizer diameter, the fuel jet is split by the oxidizer forming a striated stream that is fuel rich on the periphery and oxidizer rich in the core.

F-O-F Triplet Element

The relevant design parameters and curves are found in Figure 68 for the F-O-F triplet element. The design equation is as follows.

$$E_m = 100 - K_t \ln [9.5/(L/D_o)] \qquad (10)$$

This equation, together with the appropriate K_t, correlates the data to within $\pm$ 5%. Referring to Figure 68 note that a combustion influence constant "C" is applied to the momentum ratio to obtain K_t. The data plotted in Figure 68 was generated with "C" equal to one and is based on cold flow data only. However, as with the other elements discussed previously, combustion effects influenced the correlation. Based on the single element and full scale data, an optimum performance was obtained at $\dot{w}_o V_o/\dot{w}_f V_f \sin \alpha = 0.75$; a value significantly below the value of two obtained in cold flow. A possible reason for this shift might be that the burning was occurring at the propellant impingement interface. The resulting change in temperature and density formed a hot gas barrier between the propellants analogous to the situation created by the liquid-liquid "blow apart" phenomenon found with hypergolic propellants. In order to penetrate this barrier, relatively more fuel momentum was required resulting in an optimum at a fuel momentum higher than the equivalent cold flow situation. C = 2.3 correlates the combustion data, while C = 1 correlates the cold flow data.

In addition to the combustion effects the design parameters and plots reveal the following additional information.

- Performance increases with length and decreases with element size as with every other element. However, the length here should be based on distance from the impingement point, not from the face. This distance was used to correlate the data.

- The F-O-F triplet element has a well defined optimum at a $(\dot{w}_o V_o)/w_f V_f \sin \alpha = 2$ for the cold flow situation and 0.75 for the combustion case. Higher fuel momentum over penetrates the oxidizer jet resulting in a fan that is fuel-rich in the center and oxidizer-rich on the periphery. High oxidizer momentum results in the reverse situation - oxidizer in the center and fuel on the outside.

- Impingement angle affects mixing in that it defines the component of fuel momentum that is directed at the oxidizer jet. Increasing the impingement angle increases the fuel momentum available for mixing the propellants.

Like Doublet

The like doublet relevant design parameters and plots are found in Figure 69. The design equation is as follows.

$$E_m = \left(K_d - \frac{100}{(L/D_{eq})^{1.08}}\right) \Bigg/ \left[\frac{0.07}{L/D_{eq}}\left(\frac{.36\ \dot{W}_f V_f}{\dot{W}_o V_o}\right)^{0.77} (A_o/A_f)^{1.44} + 0.99\right] \quad (11)$$

where:

$$D_{eq} = 1.44\ D_o$$

It should be noted that no combustion data was generated with this element and the correlation is based entirely on cold flow data. Considering the effects noted before it is likely that combustion would modify the mixing process. The following conclusions can be made.

- Length and element size were the single most important variables affecting the mixing process.

- Inspecting the K_d curve, a weak optimum in mixing efficiency (high K_d implies high mixing efficiency) occurs at an element spacing (S/D_o) of one. Element spaced either further or nearer than one oxidizer diameter, tend to result in lower mixing efficiencies. Large fuel to oxidizer spacing allows the propellants to dissipate before they mix. Small spacing does not produce better mixing because of interaction of the individual oxidizer and fuel fans. That is, the secondary impingement of the fans produces striated flow that effectively blocks further mixing.

- Small momentum ratio and area ratio influences were noted. High values of fuel momentum and small fuel areas were in the direction of increased mixing efficiency.

2. The Relationship Between Combustion Efficiency and E_m

The work presented previously predicts E_m for various elements as a function of the injection , flow, design and operating variables. Although E_m is a measure (and a very sensitive one) of an elements ability to produce a well mixed stream, it does not in itself predict performance, i.e., it is not combustion efficiency. In order to predict performance it was necessary to determine a functional relationship between E_m and combustion efficiency.

If the local properties of a gas flow field can be determined either experimentally or analytically, combustion efficiency can be calculated. A flow field can be subdivided into streamtubes each of which has an associated mixture ratio and flow rate. A combustion efficiency for the total flow field can be computed by summing the mass weighted contribution of each stream tube and dividing by combustion efficiency based on overall properties.

$$\eta_c = \frac{\sum_{ii=1}^{nn} \dot{W}_{ii} \, C^*_{ii}}{\dot{W}_t \, C^*_a} \qquad (12)$$

This calculation was performed for every cold flow data point tested in this program (see Table III).

A calculation of η_c is based on the local flow properties and E_m as well is based on the same local properties (i.e., local mass flux and O/F). It follows therefore that a functional relationship exists between E_m and η_c. Plotting the values of E_m against the corresponding values of η_c (found in Table III) should define this relationship. This data is found in Figure 70 and a functional relationship does exist. The two following items are restrictions to this relationship:

a. This relationship is valid only for the H_2/O_2 propellant combination. Other propellant combinations could result in a function much different than that represented in Figure 70. This difference stems from the relationship of C* with mixture ratio. H_2/O_2 propellants have the characteristic of a flat C* vs O/F curve while some propellants have a steeper functional relationship between these parameters. The insensitivity of H_2/O_2 to mixture ratio distribution is demonstrated by the fact that an E_m of 70% results in a combustion efficiency of 96.2%. Other propellant combinations at the same E_m level may exhibit a lower combustion efficiency for an equivalent E_m.

b. The distribution of mass and mixture ratio through the flow field is similar for each element and test condition; i.e., the same proportions of oxidizer rich and fuel rich streamtubes are found in each element streamtube. For the axisymmetric elements i.e., (the coaxial, swirl coaxial and increased shear coaxial) this relationship is quite valid. In general, the center of the flow field is oxidizer rich and progressively becomes more fuel rich towards the edge. As can be seen from Figure 70, the axisymmetric element data spread is less than the total spread of all the data and is more tightly grouped around the line identified as O/F = 4 on Figure 70. The external impinging elements, however, can not be said to have similar flow fields regardless of O/F. For instance, depending on the relative fuel to oxidizer momentum ratio the centers of the flow field can vary between very oxidizer rich and very fuel rich. Fortunately this characteristic was experimentally determined as is shown on Figure 70 for the curves identified as O/F = 6 and O/F = 2. This data indicates that the impinging element data tend to group above and below the O/F = 4 curve, established from the coaxial data, for mixture ratios of 6 and 2 respectively. The curve in Figure 70 therefore is the functional relationship that allows the designer to convert E_m to combustion efficiency. The data spread is such that this technique will yield a combustion efficiency that is usually accurate to within $\pm$ 2%.

3. Discussion of Combustion Influences

The preceding discussion and data evaluation has been based to a large extent on element mixing data obtained during the cold flow experiments. It was noted in that discussion that combustion influenced the cold flow mixing, resulting in the need for modification of the correlations based on cold flow data alone. In order to explain this effect, the fundamental differences between cold flow and combustion must be addressed. This is done from an empirical standpoint in the following paragraphs and from a more rigorous analytical standpoint in the following section and Appendix A.

The combustion process results in an overall flow field that appears to be "stretched" in length.* That is, when comparing identical tests, O/F and mass profiles that have decayed to a uniform value in cold flow, still exhibit considerable nonuniformity under combustion conditions at the same length. Therefore, cold flow correlations based on a cold flow length when used to predict combustion performance would seriously overpredict that performance. It was necessary therefore, to develop a functional relationship between cold flow and combustion.

Chamber length or combustion length is a parameter that can be scaled i.e., there exists a function that will transform combustion length to an equivalent cold flow length. Neglecting the influence of combustion on

*See Section V where the results of identical combusting and noncombusting testing was discussed.

the basic mixing process and considering only the differences between cold flow and hot flow; results in the conclusion that the change in density between the two processes is the single biggest difference. The effect of combustion is to increase the temperature, decrease the density, and for confined flow increase the flow field velocity when compared to the equivalent cold flow case.

The last effect is the key to generating a stretching function. It implies that the common parameter between cold flow and combustion flow is stay time; i.e., a relationship between cold flow length and hot flow length can be equated on an equal time basis.

$$\int_0^t dt = \int_0^{L_{cold}} \frac{dL}{V} \tag{13}$$

$$\int_0^t dt = \int_0^{L_{comb}} \frac{dL}{V} \tag{14}$$

Equating time and noting that in cold flow the field velocity is a constant results in the following expression.

$$\left(\frac{\ell}{V}\right)_{cold} = \int_0^{L_{comb}} \frac{dL}{V} \tag{15}$$

Evaluation of the integral in Equation (15) requires a knowledge of how the hot flow velocity varies as a function of chamber length. The evaluated integral then defines the cold flow length as a function of the combustion length and the respective field velocities of the cold and hot gases.

The key to evaluating the integral was knowledge of how hot gas velocity varies with length. A priori this information was not available. However, a number of reasonable relationships were postulated and various solutions of the above equation were found that related equivalent cold flow length to hot flow length. The validity of any one solution was determined by comparison of combustion efficiency calculated from the empirical equations at an equivalent cold flow length to the actual combustion efficiency at its nominal length. If any one solution provided a good correlation it was deemed a valid solution.

Shown in the following sketch are 3 possible ways that velocity can vary with length.

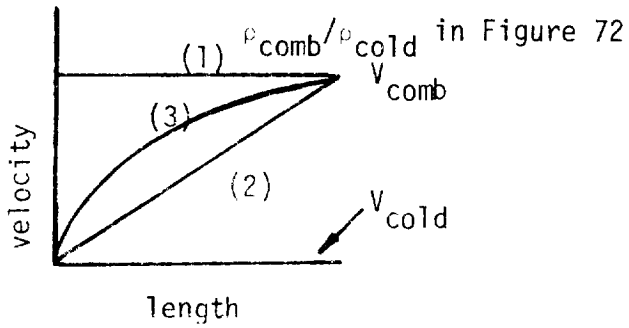

(1) V_{comb} = constant

(2) $V_{comb} = K_1 L + V_{cold}$

(3) $V_{comb} = K_2/e\ K_3 L + V_{comb}$

The first solution V_{comb} = constant, assumes a step function change in density from cold reactants to combustion products at the injector face. This solution is one that is a limit solution (i.e., it is the maximum deviation from the cold flow situation). The second solution assumes a linear distribution of temperature (velocity) with axial distance, and the third solution assumes an exponential increase of temperature with distance. The equivalent cold flow length was determined by substituting for velocity in the right-hand side of Equation 15, each of the three possible velocity-length relationships described above and integrating the equation between zero and L_{comb}. The constants in the various velocity relationships were evaluated by assuming that $V = V_{comb}$ at $L = L_{comb}$ and $V = V_{cold}$ at $L = 0$. The resulting solutions expressed L_{cold} as a function of L_{comb}, and the results are shown in Figure 71 for the 3 assumed velocity-length relationships.

Inspection of these results reveal that a factor as large as 3.7 in length exists between hot fire and cold flow conditions. This means that if a combustion chamber is 37 cm long, the combustion efficiency predicted from cold flow correlation should be based on a 10 cm length.

In order to test this model, combustion efficiencies were computed using the correlations of the previous section. These computations were done at various cold flow lengths for the test conditions and element types of the single element testing. The cold flow length equation that best matched the experimental observed combustion efficiency was then a functional equivalent of the hot fire length. These relationships are illustrated in Figure 72 for the single element F-O-F triplet, swirler, premix and coaxial elements. Also included in this figure is the analytical solution of V_{comb} = constant from Figure 71.

The V_{comb} = constant solution results in the maximum predicted change of cold flow length with hot fire length. Referring to Figure 72, note that without exception experimentally measured combustion efficiency is lower than the values analytically predicted by the V_{comb} = constant limit correlation. Thus the combustion chamber length must be significantly longer than that predicted by V_{comb} = constant analytical model.

Two reasons for this deviation can be offered; and their relative importance is a function of the element type. The first is that combustion does affect the mixing process and, as can be seen from Figure 72, affects it to varying degrees depending on the element type. The elements least affected by the combustion process lie closest to the analytically predicted line based on V_{comb} = constant. This element is the premix which is not affected for obvious reasons; the bulk of the mixing is accomplished before combustion can take place. The swirler element and triplet elements, however, depend on a mixing mechanism that is highly concentrated near the injector face. If combustion interfers with these processes, then the mixing is dramatically reduced and as a result longer chambers will be required to effect mixing by turbulent diffusion. The data of Figure 72 indicates that this is the case. The coaxial element is only slightly affected for the second reason, i.e., the mixing process is so distributed over the length of the chamber that the combustion does not have much impact on the mixing rate. The above discussion indicates nothing about the absolute mixing efficiency in a given length. Even though the triplet element is sensitive to combustion effects it is still a higher performing element in a given length than the coaxial element.

The fact that each element type results in a different combustion pattern is unfortunate for it precludes the existence of a universal stretching function. The designer must therefore use the empirical function of Figure 72 to estimate the cold flow length appropriate for use in the performance correlations. For element types different from those tested the designer must use judgement or refer to the generalized prediction techniques discussed in the following section (VIII,C, Analytical Model).

4. Empirical Heat Transfer Correlations

Heat flux at the injector end of the chamber was found to be very sensitive to injector type and operating conditions during this program. In fact, chamber heat flux near the injector was observed to vary an order of magnitude depending on which injection element was used. The following paragraphs describe how these effects were modeled.

A relevant chamber heat transfer parameter for design purposes is the ratio of experimental heat flux at the injector end to nominal heat flux based on conventional turbulent heat transfer correlations. The nominalization parameter accounts for all combustion parameters (P_c, O/F, chamber dia) that are related to the chemistry and thermodynamics of the combustion process. The deviation of this parameter away from one is a measure of how the injector affects the chamber heat transfer. Values of the heat flux ratio higher than one indicates local heat fluxes higher than would be predicted based on conventional turbulent heat transfer correlations alone. Values of the heat flux ratio lower than one indicate a benign environment due to a relatively low heat flux.

The relationship between the heat flux ratio and momentum ratio at the head end of the chamber, 1.9 cm, (0.75 in.) is shown in Figure 73 for coaxial, swirl coaxial, premix and triplet elements. The bands shown in Figure 73 includes all the data from both the full scale and single element testing. The values of the heat flux ratio illustrated in this figure should be used to estimate local values of heat flux at the injector end of the chamber. Heat flux ratios for axial positions between the injector and throat can be estimated by interpolation. As can be seen from the data of Sections VI and VII the heat flux ratio tends towards one at the throat independent of injector type and varies reasonably linearly with length between X = 1.9 cm and the throat plane. The heat flux ratio at any length can be estimated using the following equation.

$$\left(\frac{\phi_{est}}{\phi_{nom}}\right)_x = \left(\frac{\phi_{est}}{\phi_{nom}}\right)_h \left(1 - \frac{X}{L_{comb}}\right) + \frac{X}{L_{comb}} \qquad (16)$$

Inspection of Figure 73 reveals heat flux ratios over three for the triplet and premix elements at momentum ratios of 0.2 - 0.4. It is important to note that all the elements tend to have a functional relationship between heat flux and momentum ratio that is similar to that already discussed for combustion performance. The triplet element for instance has a maximum heat flux at the identical momentum ratio that the correlation equations and experimental data would predict optimum performance (see Figure 68). In addition the shape of the local heat flux curve is similar to the analogous performance curve. The premix and coaxial element curves indicate the same relationships; i.e., high local heat fluxes at injection conditions that favor high performance. The significance of the above is that an injector designer can expect high heat flux with high performing injectors, or conversely designing for low wall heat flux will be in the direction of low performance.

5. Empirical Model ERE Prediction

In order to test the validity of the empirical model, it was used to predict the performance of the single element injectors of this program and the full scale injector data of this and other relevant APS sized thrusters.

The model was used as detailed in the Design Handbook and outlined below in the following procedure. Chamber lengths were converted to equivalent cold flow lengths via Figure 1 of the Design Handbook. Mixing efficiencies were computed using the specific equations and related curves for each element. ERE was determined from the empirical relationship between ERE and E_m (Figure 70).

Predicted vs actual ERE for the single element data is shown in Figure 74. This correlation groups all the data to within ± 5%. Reflected in this ± 5% accuracy is the inherent inaccuracy of the single element data. Because of the small size and large heat losses, the measured energy release efficiency is probably only accurate to ± 3%. It can therefore be reasoned that the accuracy of the empirical model may be better than ± 5%.

A better indication of the accuracy of the model is shown in Table XVI. This table compares the experimental performance of various H_2/O_2 engines with the model predictions. The predictions were based on the nominal design point of the particular engine. With the exception of the TRW engine the nominal design point was O/F = 4, P_c = 207 N/cm^2. The TRW engine prediction was based on an overall O/F of 5.3. The two, zoned injector predictions were based on a mass weighted prediction of the barrier and core streamtubes. As can be seen by refering to the table the model predicts the performance to within ± 1.4% total scatter. It is also significant that the model predicts the rank of the injector performance accurately. That is, it predicts the highest performance for the injector that was highest performing and predicts lowest performance for the injector that was lowest performing.

The fact is especially encouraging considering the different variety of injectors included in the list. There are four triplets (all at different element design points*; two coaxial injectors, one designed by ALRC and one designed by Rocketdyne; and two premix injectors both designed at ALRC but with different element design points. Using this model, the injector designer has a powerful tool for predicting GO_2/GH_2 performance.

C. DISCUSSION OF RESULTS - ANALYTICAL APPROACH

1. Introduction

The preceding section has described the empirical approach to data correlation. In addition, a parallel effort was carried on throughout the program utilizing a more general analytical approach. The advantage of the latter is that it identifies design and operating parameter interactions and their influences on mixing rate which can not be accounted for using an empirical approach alone. The physical insight of the mixing and combustion processes provided by the analytical model permits extension and extrapolation of the data acquired on this program to untested future design requirements.

*The TRW O-F-O triplet injector was not modeled by the empirical correlation. The model is based on F-O-F elements rather than O-F-O elements. An accurate performance prediction for this element was obtained by using fuel properties in the design equations where oxidizer properties are indicated and vice versa.

TABLE XVI

COMPARISON OF EMPIRICAL PERFORMANCE

PREDICTION TO MEASURED DATA

INJECTOR ELEMENT TYPE	CONTRACT	CHAMBER LENGTH (IN) CM	NUMBER OF ELEMENTS	PREDICTED ERE	ACTUAL ERE	RANK PRE	RANK ACT
O-F-O Triplet	NAS 3-14347	(6) 15.2	144	99.6	100	1	1
Coaxial (CT-A)	NAS 3-14352	(5) 12.7	54	97.2	96	6	6
Coaxial	NAS 3-14354	(5.5)14	42	98.4	97	5	5
Premix	NAS 3-14354	(5.5)14	72	98.9	98.5	3	3
F-O-F Triplet	NAS 3-14379	(3) 7.6	72	99.4	100	1	2
Premix	NAS 3-14379	(3) 7.6	36	98.7	98.4	4	4
-1 Zoned (F-O-F Triplet)	NAS 3-14379	(3) 7.6	72	95.1	96.2	8	8
-2 Zoned (F-O-F Triplet)	NAS 3-14379	(3) 7.6	72	95.6	96.8	7	7

A description of the analytical model formulation requires a lengthy discussion and is therefore documented separately in Appendix A. This section summarizes how the analytical model was used to correlate the experimental data. The methodology to use the analytical model to analyze or design future gaseous injectors is covered in the Design Handbook.

Based on the preliminary data correlations from the cold flow portion of the program, the analytical model was initiated by postulating probable physical mechanisms that might explain the observed data behavior. The selection of pertinent process variables were ascertained by an approximate mathematical mixing model formulation described in Appendix A and was based on such considerations as the momentum and continuity equations, Newton's laws of motion, equation of state for idealized perfect gases, boundary layer equations, potential flow equation, etc. This step of the analysis was the most critical and most important step in the analytical data correlation. The mathematical analysis model suggested probable groups of primary design variables and their interactions. Absolute quantitative predictability was not initially considered a primary objective. The latter was achieved empirically by appropriate curve fitting of experimental data vs predicted analytical trends.

It was recognized that modeling of fundamental mixing processes was necessary to obtain meaningful scaling criteria that could be extrapolated to untested design variables. In addition, it was recognized that basic differences between cold flow vs hot flow, single element hot fire and multiple element hot fire mixing processes exist. Only by recognizing and properly accounting for differences in the fundamental mixing processes was it possible to accurately extrapolate to and predict hot fire mixing characteristics. It was for this reason that the emphasis had been placed on modeling and correlating mixing processes, rather than correlating injection element design parameters as was done in the empirical approach.

The concept behind the model is basically simple. The model consists of defining the characteristic potential flow element dimension from the functional relationship of design parameter interactions. A boundary layer approximation is then defined and integrated to analytically predict an axial dynamic pressure decay rate which is used to predict mass diffusion profiles. The model yields considerable understanding of the mixing mechanism, sheds physical insight upon experimental data and is suggestive of design modifications required for element optimization. However, it is hindered by the difficulty that the design parameter interaction differs according to element type as summarized in subsection 2 of Appendix A.

2. Description of Generalized Analytical Model

Specific cold flow and hot fire mixing models were developed during the program for each element type tested which successfully correlated all types of test data which was experimentally generated on this contract.

However, to attempt to disseminate this detailed knowledge contained in six different cold flow and four additional combustion mixing models would be impractical. Therefore, based on the objective of reducing this vast body of knowledge into a practical form usable to the average design engineer, a simpler generalized approach was taken. This should encourage greater usage because of its relative simplicity and yet maintain its generality, while sacrificing some absolute accuracy. This approach was only possible because certain groups of non-dimensional design parameters were common to all elements and had a consistently predictable impact on the model solution.

Cross correlations of the results from the specific element models led to the development of only two sets of non-dimensional mixing correlation parameters. B_a for axi-symmetric elements and B_t for two dimensional elements. This generalized model has successfully correlated chemical composition mixing rates, O/F; mixing efficiency, E_m; performance efficiencies, % C* and % ERE; and chamber wall heat flux, Q/A, for both cold flow and combustion operation test data generated with every element type evaluated on this contract. The choice of correlation parameters was selected on the basis of maximizing its physical significance for the benefit of the designer. Those parameters having maximum significance on performance improvement are visibly identified. A conscious effort has been made to minimize the "black box" syndrome often encountered in analytical models. Even if the designer does not immediately satisfy all of his technical objectives on his very first design attempt, at least the direction of change required and the quantitative magnitude of change will be identified for the desired improvement by inspection of the numerical values of his B_a or B_t parameters.

Two versions of non-dimensional mixing correlation parameters, B_a and B_t, have been defined to characterize axi-symmetric and two dimensional elements, respectively. The general form of these B parameters are shown below for both the fuel and oxidizer jets emanating from their respective source in any given injector element concept.

$$B_{ao} = \frac{(L/D_{ho}) \left(\frac{4\ (O/F)}{MW_o/MW_f} \right)^{0.45} f\ [\text{Elem. Type}]}{\left[C_{do}\ (1 + Da_o) \right]^{0.625} \left(\frac{Re_{do}}{10^5} \right)^{0.25} \left(\frac{Pd_o}{Pd_{eq}} \right)^{F_o}} \tag{17}$$

$$B_{af} = \frac{L/D_{hf}\ \ f\ [\text{Elem. Type}]}{\left[\frac{4\ (O/F)}{MW_o/MW_f} \right]^{0.13} \left[C_{df}\ (1 + Da_f) \right]^{0.625} \left(\frac{Re_{df}}{10^5} \right)^{0.25} \left(\frac{Pd_f}{Pd_{eq}} \right)^{F_f}} \tag{18}$$

$$B_{to} = \frac{(L/D_{ho}) \left[\frac{4\ (O/F)}{MW_o/MW_f}\right]^{0.66} f\ [\text{Elem. Type}]}{\left[C_{do}\ (1 + Da_o)\right]^{1.25} \left(\frac{Re_{do}}{10^5}\right)^{0.25} \left(\frac{Pd_o}{Pd_{eq}}\right)^{F_o}} \tag{19}$$

$$B_{tf} = \frac{(L/D_{hf})\ f\ [\text{Elem. Type}]}{\left(0.8 + 0.2\ \frac{4\ (O/F)}{MW_o/MW_f}\right) \left[C_{d_f}\ (1 + Da_f)\right]^{1.25} \left(\frac{Re_{df}}{10^5}\right)^{0.25} \left(\frac{Pd_f}{Pd_{eq}}\right)^{F_f}} \tag{20}$$

Physically speaking, these parameters represent a generalized element L/D ratio. It has repeatedly been shown for all element types that L/D is the single most important parameter for correlating mixing efficiency; all elements tested show improved performance at longer L/D's.

An identification of specific element design parameters (type, size, hydraulic characteristics), propellant physical properties (viscosity, density, molecular weight, temperature, combustion characteristics) and engine operating conditions (mixture ratio, injection ΔP's, chamber pressure) uniquely define discrete numerical values of B_a or B_t for both fuel and oxidizer elements. This information is sufficient to completely define everything of interest about the gas mixing distribution. The generalized solution permits bypassing all of the intermediate computation steps required by the various specific element models.

To calculate the local oxidizer composition evaluate either Equation (17) or (19). For that numerical value of the correlation parameter, B, on the abscissa of Figure 75 find the local oxidizer-rich mixing ratio η; on the ordinate, using the appropriate curve (axisymetrical or two dimensional). Then the local oxidizer rich stream tube mixture ratio is as follows:

$$O/F_j = \frac{O/F}{\eta_j} \tag{21}$$

Similarly the local fuel composition can be determined by using either Equation (18) or (20) with Figure 75 to find η_i on the ordinate for the appropriate numerical value of the correlation parameter, B, on the abscissa. Then calculate the local fuel rich mixture ratio.

$$O/F_i = \eta_i \times (O/F) \tag{22}$$

To satisfy the overall continuity relationship, the mass fractions contained in the fuel rich and oxidizer rich stream tubes are uniquely defined so that the overall mixture ratio is the design engine O/F. This can be done by defining an intermediate parameter

$$U = \eta_j \frac{(1 - \eta_i)}{(1 - \eta_j)} \tag{23}$$

from which it is possible to define the oxidizer rich stream tube mass fraction and fuel rich stream tube mass fractions by Equations (24) and (25), respectively.

$$X_j = \frac{U}{1 + U} \left[\frac{1 + (O/F)_j}{1 + (O/F)}\right] \tag{24}$$

$$X_i = 1 - X_j \tag{25}$$

The local streamtube mixture ratios and mass fractions then enable mixing efficiency and performance efficiency predictions as follows;

$$E_m = 100 \left\{1 - X_j \left[\frac{(O/F)_j - (O/F)}{1 + (O/F)_j}\right] - X_i \left[\frac{(O/F) - (O/F)_i}{(O/F)\,[1 + (O/F)_i]}\right]\right\} \tag{26}$$

$$\eta_m = 100\,[X_j \cdot \eta_j + X_i \cdot \eta_i] \tag{27}$$

$$\%C^* = \frac{X_j \cdot C^*\,(O/F)_j + X_i \cdot C^*\,(O/F)_i}{C^*\,(O/F)} \tag{28}$$

$$\%ERE = \frac{X_j \cdot I_{sp}\,(O/F)_j + X_i \cdot I_{sp}\,(O/F)_i}{I_{sp}\,(O/F)} \tag{29}$$

The term E_m as defined in Equation 26 is a two streamtube version of the Rupe mixing efficiency parameter (Ref. 1). Although E_m is a widely used single value parameter which is useful for relative ranking of element mixing efficiencies, detailed information about the specific mass distribution is required to ascertain a quantitative performance efficiency prediction. For example, if low nozzle area ratio sea level combustion efficiency data (%C* or %ERE) were available, the corresponding mixing distribution and hot fire E_m would still remain unknown; and it would be impossible to analytically extrapolate the sea level performance to high area ratio vacuum performance.

To circumvent the above shortcoming in E_m, the mass weighted mixing parameter, η_m, defined in Equation (27) is proposed. The term η_m is likewise a single valued function between 0 to 1.0 like E_m, but it can be used directly to estimate performance efficiency. First of all, assume $\eta_j = \eta_i = \eta_m$. Then using Equations (21) through (25), the oxidizer rich and fuel rich mixture ratios and respective stream tube mass fractions can be calculated. Thus, if experimental hot fire %C* and %ERE are available, η_m can be estimated empirically using Equations (28) and (29) through parametric variation. Then using this empirically inferred value of η_m, the vacuum performance can be analytically extrapolated to any desired nozzle exit area ratio by using the appropriate C* or I_{sp} vs O/F characteristics.

The above discussion, encompassing Equations (17) through (29), is a summary of the generalized analytical procedure. A brief description of two of the terms in Equations (17) through (20) which are unique to this model will be described, i.e., D_{af} or D_{ao} and f [Elem. Type]. The remaining terms in Equations (17) through (20) are standard parameters defined in the nomenclature list.

D_{af} or D_{ao} are symbols for the combustion influence parameter. The combustion influence parameter was developed to relate the chemistry and thermodynamics of the combustion process to parameters that controlled the mixing process. The detailed development of this parameter is discussed in Appendix A. For cold flow the combustion influence parameter has a numerical value of zero. For the GO_2/GH_2 propellants tested on this program the combustion influence parameter varied from 0 to 10 as shown in Figure 76. If hot-fire performance and/or chamber heat flux values are required, then the combustion influence parameters (Da_f and Da_o) must be included in the calculation. For combustion performance problems several iterations may be required until the calculated combustion influence parameter converges upon the assumed value used in the equations for obtaining the parameter B as defined in Equations (17) through (20). This process is demonstrated in the sample problem in the Design Handbook.

The second design correlation factor identified in the mixing correlation Equations (17 through 20) is dependent upon element type. This term designated "f [Elem. Type]" has a value of unity for shear mixing elements without transverse injection momentum component such as showerhead or shear coaxial elements. The physical significance of this term is the ratio of the characteristic jet or fan dimension at the injector face plane to a downstream location. The mathematical derivation of this parameter is described in Subsections 2 and 4 of Appendix A. In addition, penetration mixing elements such as the premix or external impinging triplets are characterized by an initial composition at the injector face plane which has been already pre-mixed to some degree as described in Equations (A-64) through (A-73) in Appendix A. The initial premix composition significantly enhances mixing efficiency. For penetration mixing elements the adjustment for impingement

mixing is accounted for by determining an apparent L/D increase for an analogous shear mixing element. In addition, the swirler co-axial element in a combustion environment requires special consideration as described in Subsection 8 of Appendix A.

3. Analytical Data Correlation

A correlation of analytically predicted cold flow E_m's vs experimental test E_m's are shown for various element families in Figures 77 and 78. These elements were tested over the following ranges.

Parameter	Nominal	Range
F/E - newtons (lb_f)	67 (15)	13 - 222 (3 - 50)
O/F	4	2 - 6
A_f/A_o	1	0.5 - 2.0
L/D	7	3 - 30
T_p - °K (°R)	300 (540)	110 - 300 (200 - 540)
α - Radians (degrees)	$\pi/3$ (60)	$\pi/4$ - $\pi/2$ (45 - 90)

Of these tests, experimental data from the smallest 13 newton (3 lb_f) thrust element is least accurate. That is because all elements used the same measurement rake resulting in relatively coarser (fewer probe measurements) sampling with the smallest element. Furthermore, due to the large quantity of test data, both experimental data reduction and mathematical model analysis had to be highly automated. For example, element C_d's were analytically estimated and input on the basis of orifice Reynold's number, L/D, and assumed entry conditions. Only a few random tests were selected to compare predicted injection dynamic heads against experimental injector ΔP's to verify actual test C_d's. A more detailed input data selection could vary predicted E_m's by a few percent. On some tests (see Table III) the integrated O/F differed from the injected O/F which may indicate some inaccuracy in the experimental E_m. For some elements at short L/D's where the gradients are steep, the maximum fuel or oxidizer rich zones did not coincide with a probe position resulting in the loss of a high mass flux region between the probe positions. Thus, some disparity between the calculated and experimental data could not be avoided.

The analytical predictions are in reasonably good agreement with the experimental data attesting to the validity of the generalized analytical model. The analytical model is not only limited to its ability to predict absolute E_m. Even more important is its ability to identify significant design

variables for a given type element and their interactions thus providing the designer an analytical means for optimizing his design or extrapolating previous test data to future design requirements. The physical insight which the mathematical model sheds on experimental data trends is likewise invaluable.

By incorporating the combustion influence parameter into the generalized mixing parameters, B_a and B_t, the experimental single element hot fire mixing performance data were predicted. As analytically predicted by the approximate mathematical model, combustion effects significantly impeded the mixing process and degraded performance compared to analogous cold flow conditions.

The correlations for the single element hot fire test data using the generalized analytical model are shown in Figure 79. For the latter tests the cold flow GN_2 properties (MW_o, ρ_o, μ_o) were replaced by hot fire GO_2 properties. Otherwise, the only difference between cold flow and hot fire model calculations was the inclusion of the combustion influence parameter, Da_f and Da_o to account for combustion effects. Satisfactory correlations between predicted and experimental test energy release efficiencies were obtained for the shear coaxial, premix, and external impinging F-O-F triplets elements.

The swirler coaxial element data were correctly predicted in their relative performance order (lowest to highest) but somewhat off on exact magnitude. The reason for this is as follows. As explained in Section 5 of Appendix A, the swirler coaxial element is characterized in a combustion environment with a collapsed oxidizer cone beyond which it is necessary to evaluate its mixing rate by axisymmetric shear characteristics. A specific swirler coaxial combustion model was developed consistent with actual physically occurring mechanisms. The specific model predictions quantitatively agreed with experimental data in both magnitude and trend. Use of the modifications required to develop the generalized model, however, resulted in the loss of accuracy noted. The recommended procedure for utilizing the generalized combustion correlation to describe the swirler coaxial element is described in Subsection 8 of Appendix A.

In addition, the generalized hot fire swirler coaxial element predictions shown in Figure 79 were based upon using only five axial analysis stations (corresponding to the four measured thermocouple stations and the nozzle throat plane) for the 5.1 cm (2-in.) chamber length tests and eight axial analysis stations for the 14 cm (5.5-in.) chamber length tests. This coarse grid results in a bias which accounts for the consistent performance underprediction. An alternative procedure would be to use a comparable coarse grid swirler calculation technique but adjust the anticipated performance efficiency higher by using the empirical dependence between "predicted" and experimental performance shown in Figure 79 for all hot fire swirler elements.

4. Generalized Chamber Wall Heat Flux Correlation

The analytical compatibility model described in the Design Handbook provides heat flux predictions in the absence of experimental data. Although the predicted absolute heat flux values are not as accurate as the performance mixing predictions, the model predicts relative trends and identifies the approximate heat flux magnitude within approximately $\pm$ 30 to 50%.

The heat flux is calculated based on the properties of either the oxidizer or fuel rich streamtubes using the following relationship.

$$\phi_{ij} = \frac{0.026}{D_c^{0.2}} \frac{\mu^{0.2} C_P}{P_r^{0.6}} \left(\frac{\dot{w}_t}{A} \right)^{0.8} (T_{gas} - T_{wall}) \qquad (30)$$

The designer must visually examine his injector pattern layout to identify the local wall mixture ratio. For example, if annular fuel coaxial elements are used the wall mixture ratio will be fuel rich. Hence the wall heat flux will be more closely approximated by using ϕ_i. If external impinging F-O-F triplets are used, the wall O/F will depend upon element orientation next to the wall and whether the fuel underpenetrates or over-penetrates the oxidizer jet. In the event of like doublets, predicted wall heat flux will depend upon whether a fuel doublet or oxidizer doublet is nearest the wall. Figures 80 and 81 show correlations of predicted vs measured heat flux ratios for the various injectors tested on this program.

The external impinging F-O-F triplet single element hot fire tests were underpenetrated above O/F = 2.0 resulting in a generally fuel rich boundary around two sides in line with the fuel orifices. However, two oxidizer rich lobes are squeezed out perpendicular to the fuel rich spray regions and somewhere in between, nominal O/F zones occur. Analytically, one would predict widely varying heat flux ratios around the periphery of a single hot fire F-O-F triplet element. This thermal streaking tendency is verified by the measured heat fluxes experimentally measured around the single element F-O-F triplet as shown in Figure 81. The predicted minimum/maximum heat flux extremes predicted by the analytical heat flux model corresponding to fuel-rich, oxidizer-rich, and nominal O/F stream tubes is in good agreement with experimentally measured thermal flux variations.

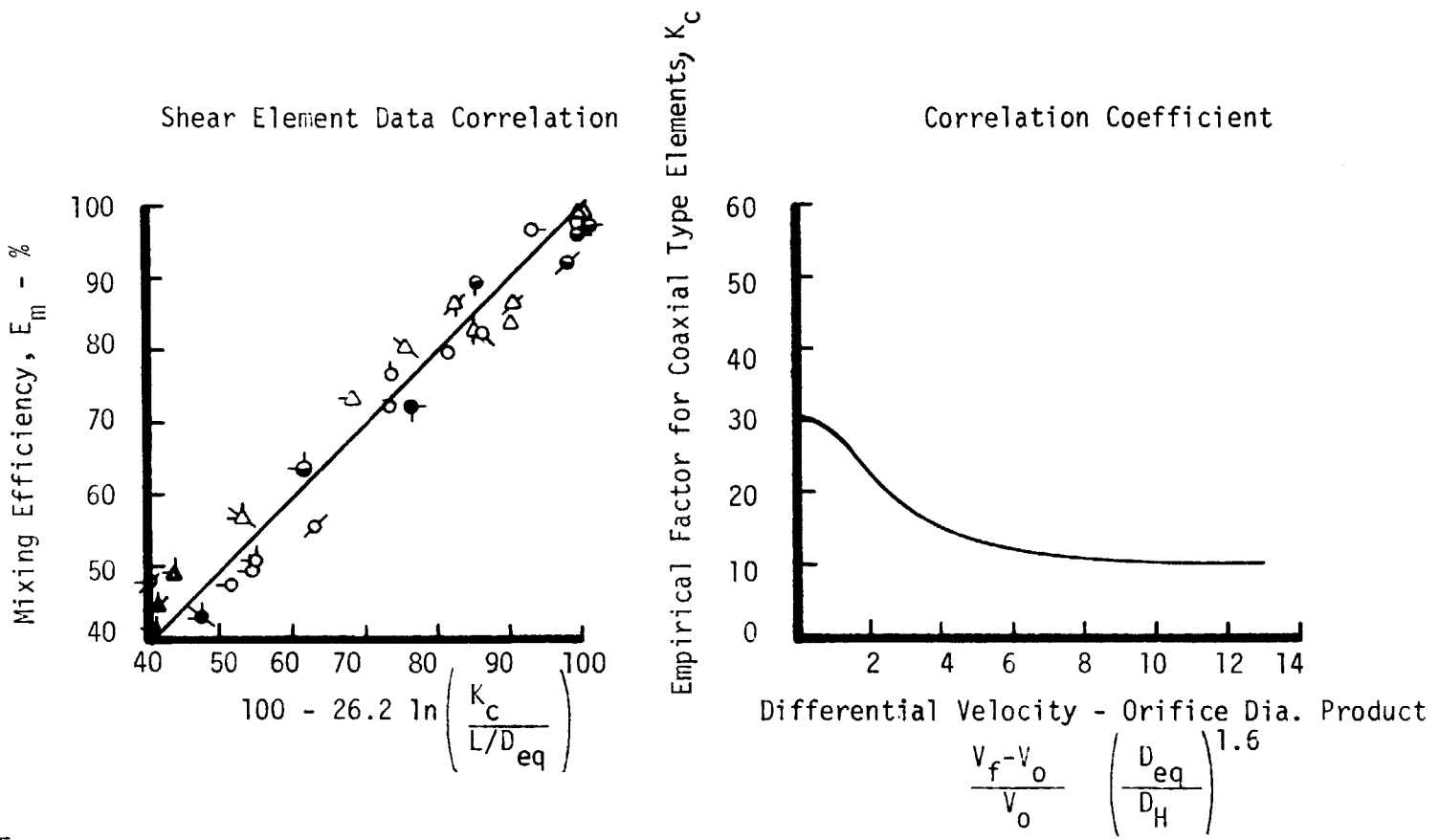

FIGURE 65. COAXIAL AND INCREASED SHEAR COAXIAL DESIGN CORRELATIONS

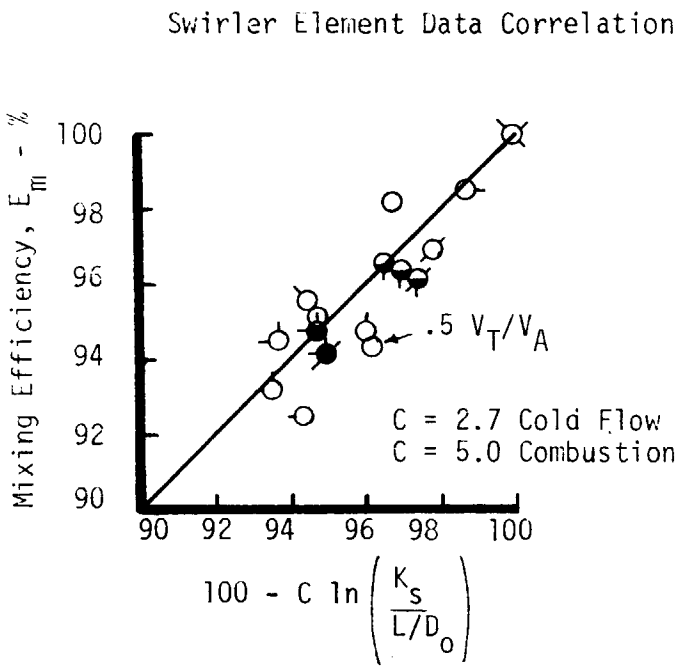

SYMBOLS

N	F/E	(lb_f)	A_f/A_o	L/D_o	O/F
13	⚲	3	.5 ◒	3 ⚲	2 ⚤
68	○	15	1.0 ○	7 ○	4 ○
224	⚲	50	2.0 ●	15 ⚲	6 ⚤
				30 ⚤	

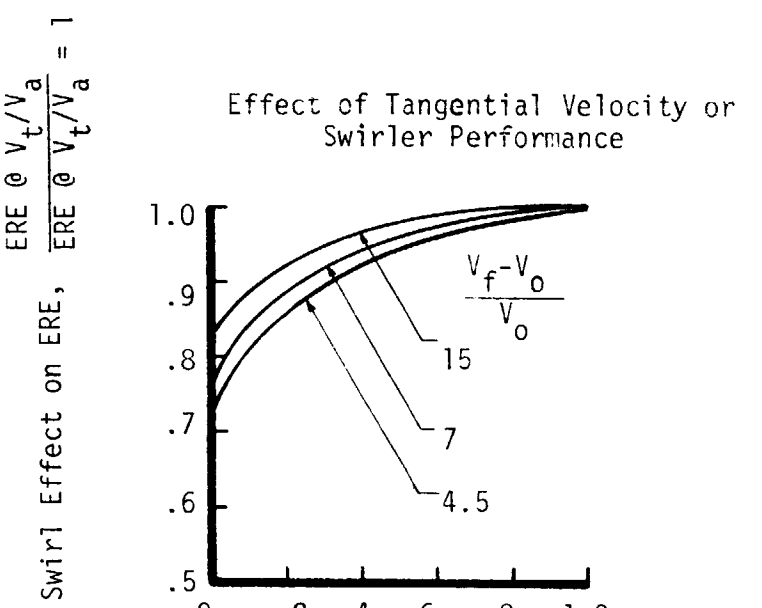

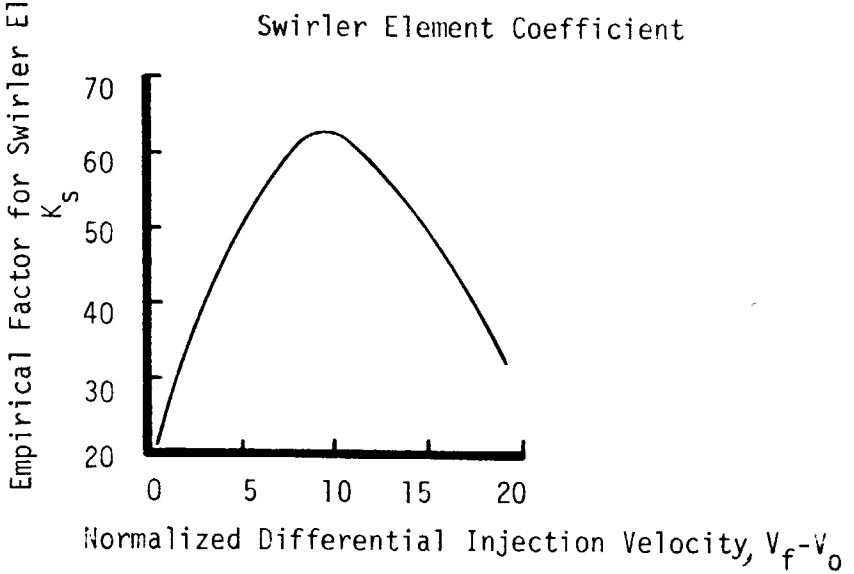

FIGURE 66. SWIRLER DESIGN CORRELATIONS

Premix Element Data Correlation

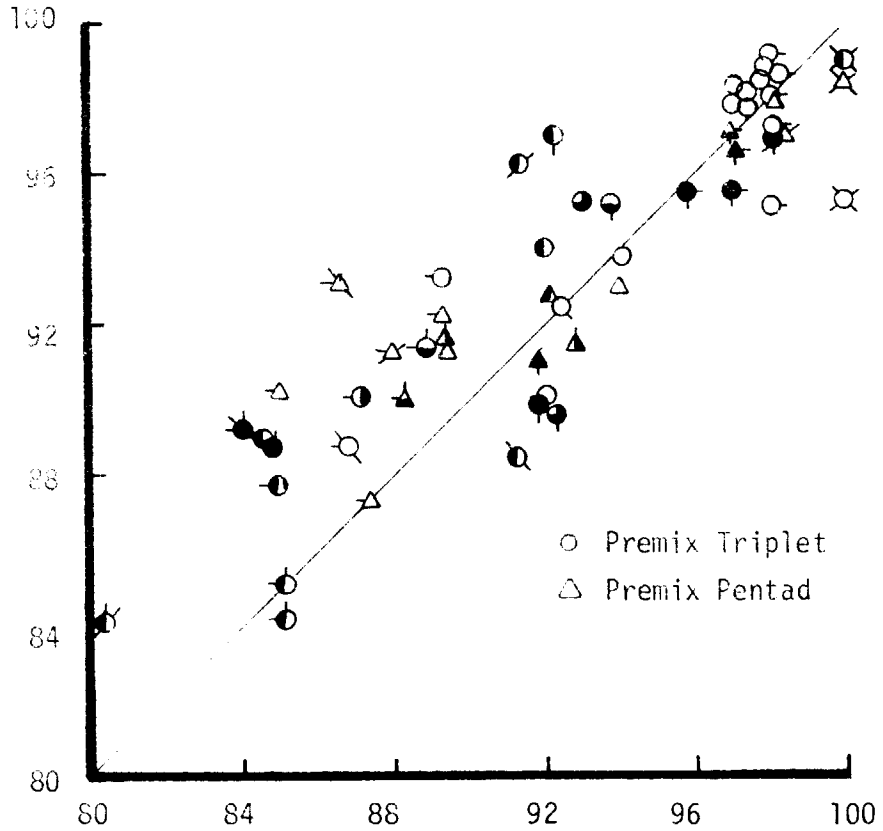

$$\frac{100 - K_p \ln\left(\frac{21}{L/D_o}\right)}{1 + 3\,(.07\ W/D_o - .02)/\,(L/D_o)}$$

N	F/E (lb_f)	A_f/A_o	L/D_o	O/F	W/D_{ox}
13 ♀	3	.5 ◒	3 ⊖	2 ♀	.33 ○
68 ♂	15	1.0 ○	7 ○	4 ○	.67 ◑
224 ♂	50	2.0 ●	15 ♀	6 ♂	1.0 ◐
			30 ♂		

Correlation Coefficient

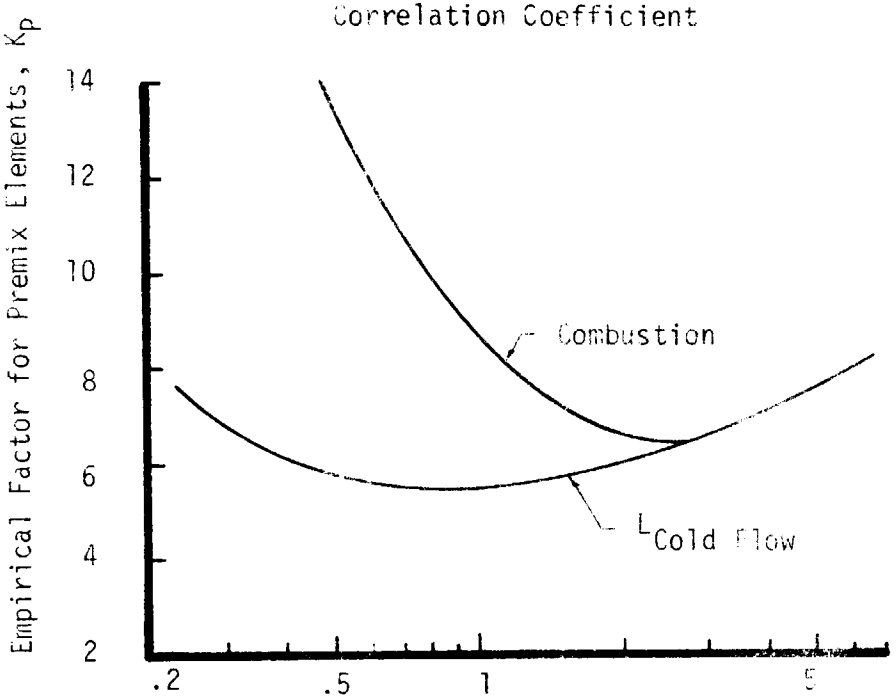

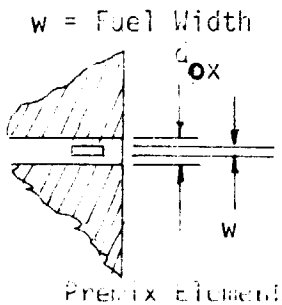

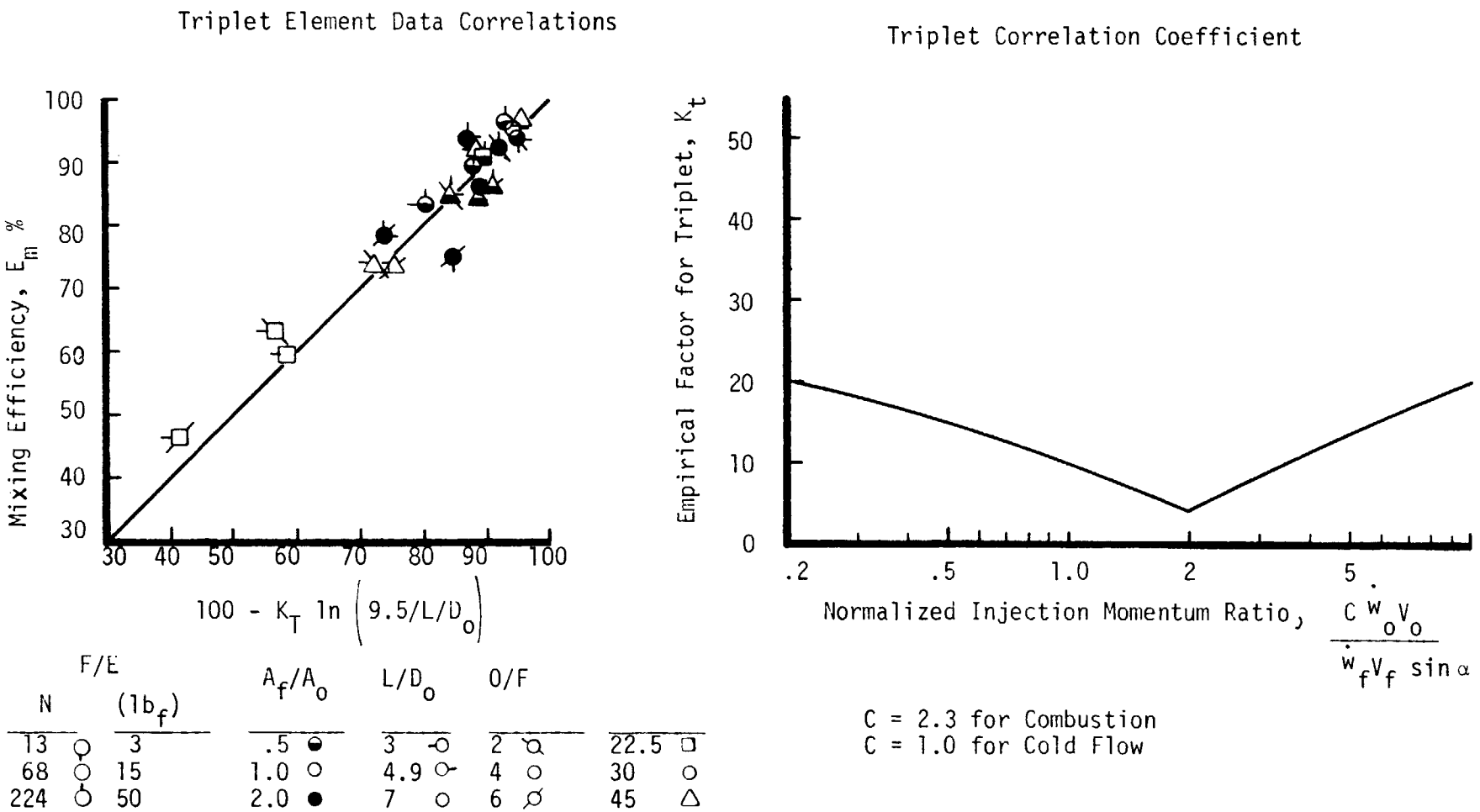

FIGURE 68. TRIPLET ELEMENT DESIGN CORRELATIONS

Doublet Element Data Correlation

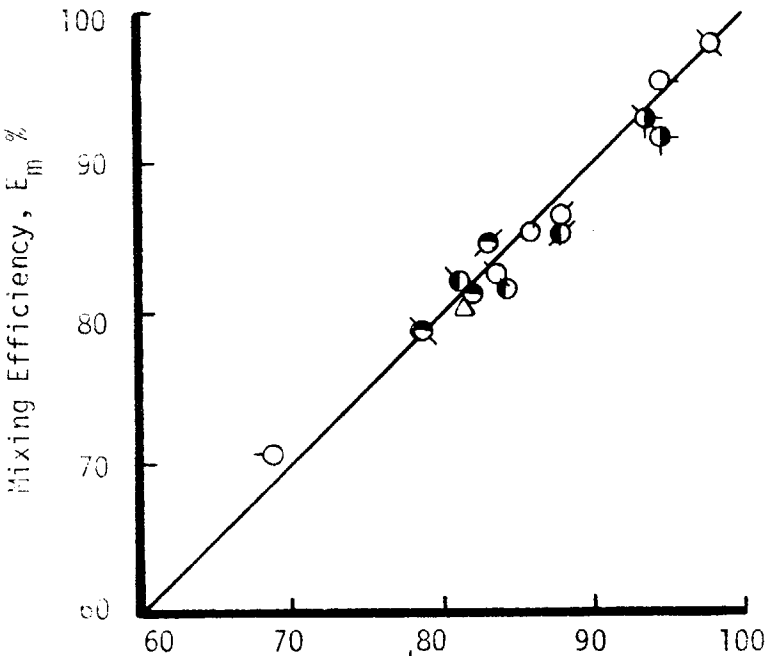

$$\left[k_D - \frac{100}{(L/D_{eq})^{1.08}}\right] \Bigg/ \left[\frac{.07}{L/D_{eq}} \left(\frac{.36\ \dot{w}_f V_f}{\dot{w}_o V_o}\right)^{.77} \left(\frac{A_o}{A_f}\right)^{1.44} + .99\right]$$

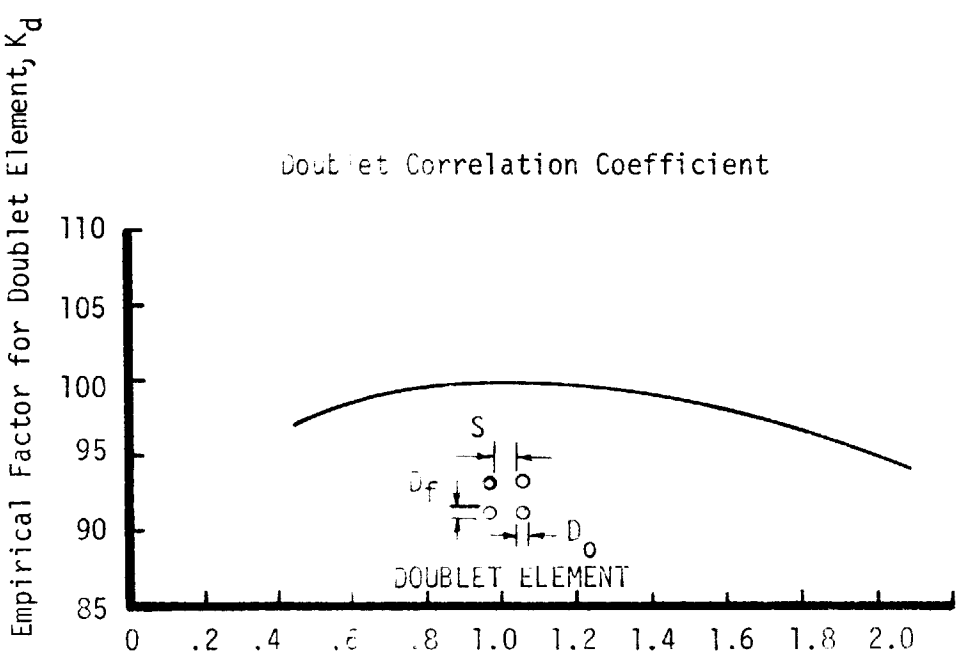

Doublet Correlation Coefficient

$$D_{eq} = 1.44\ D_o$$

N	F/E (lb_f)	A_f/A_o	L/D_{eq}	O/F	S/D_o
13	(3)	.5 △	3	2	.5
68	(15)	1.0 ○	7 ○	4 ○	1.11
			15	6	1.00 ○
			30		2.00

FIGURE 60 - LIKE DOUBLET DESIGN CORRELATION

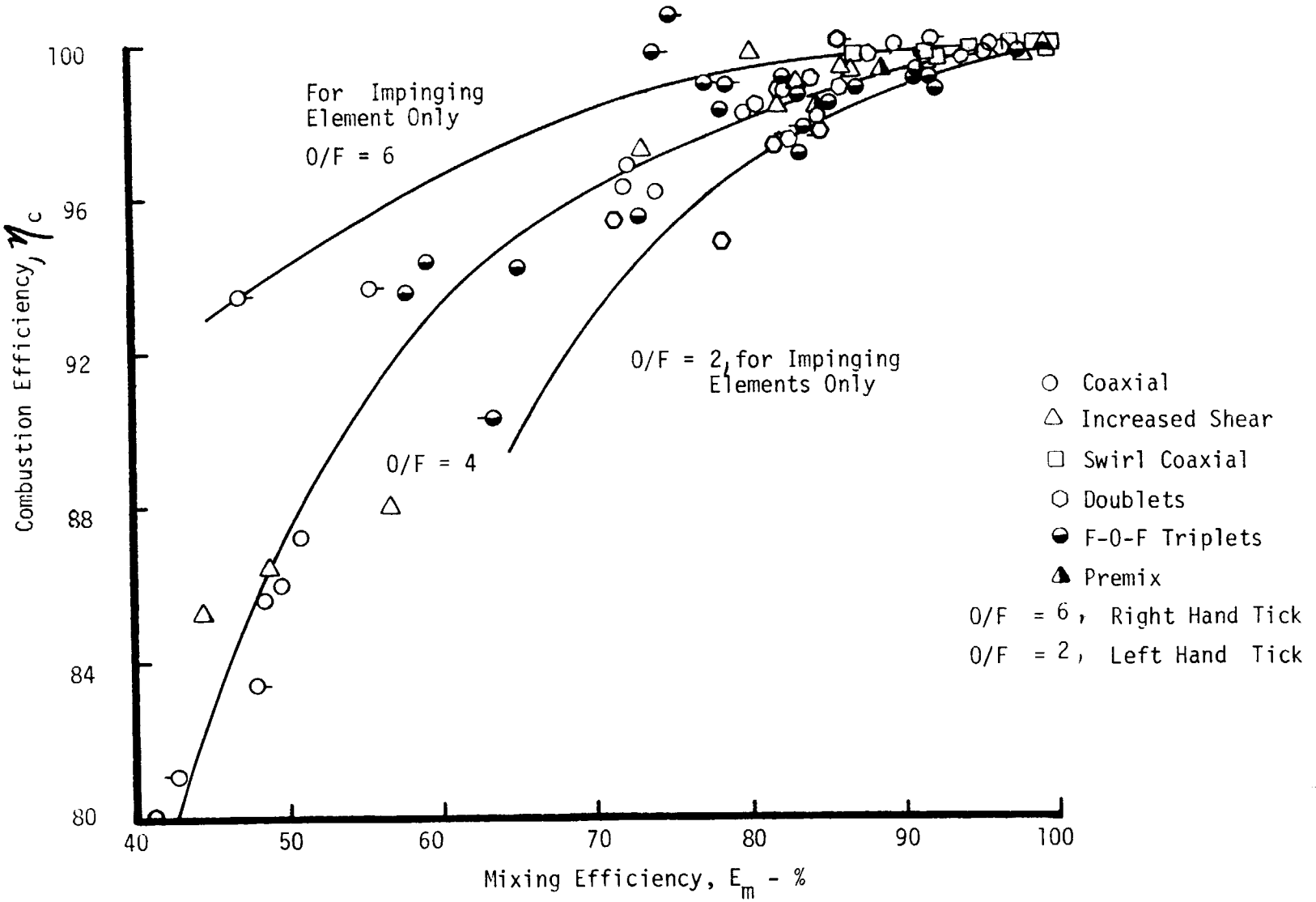

FIGURE 70. THE RELATIONSHIP BETWEEN H_2/O_2 η_c AND E_M

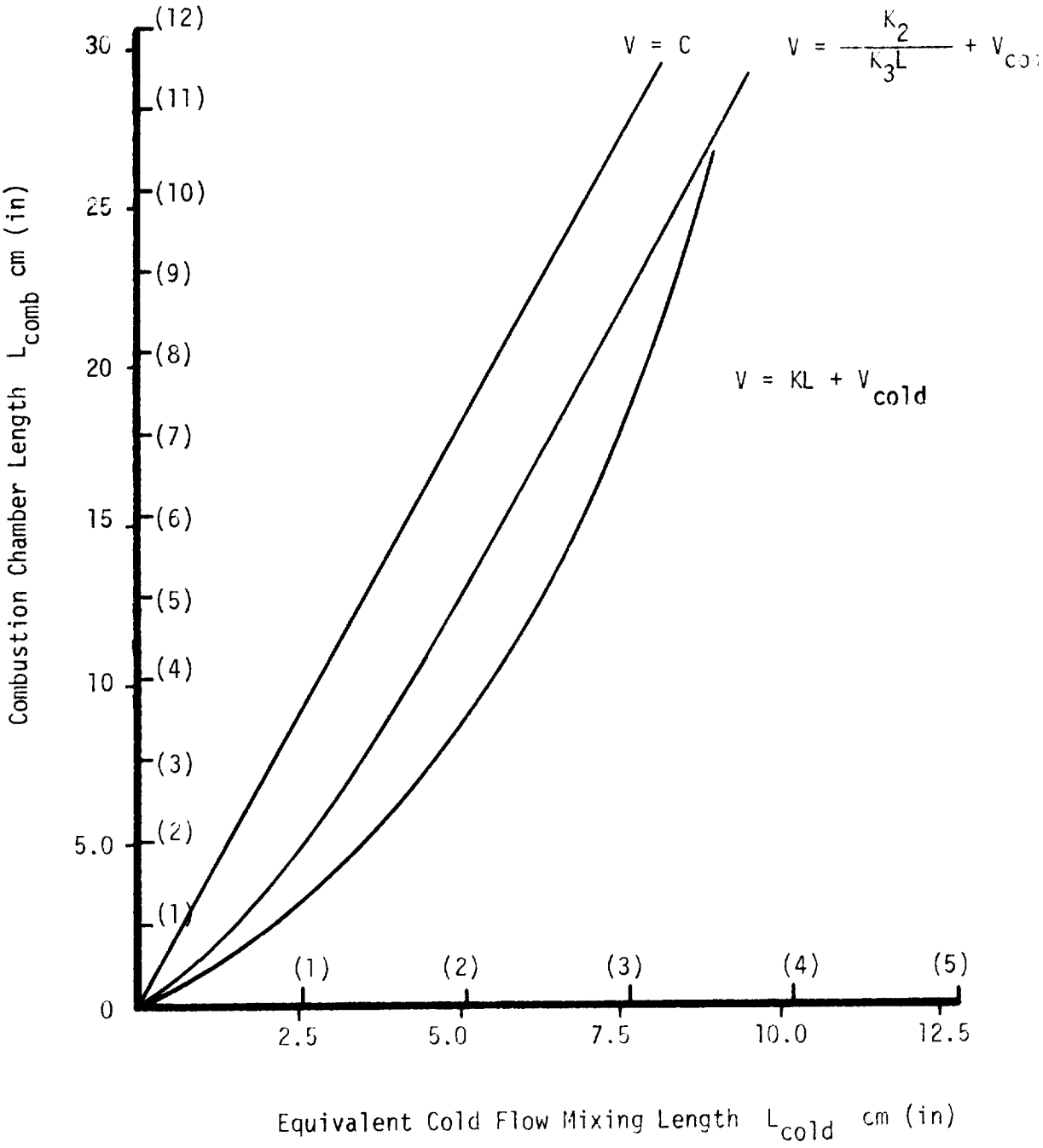

FIGURE 71. ANALYTICAL RELATIONSHIP BETWEEN COLD AND HOT FIRE LENGTHS

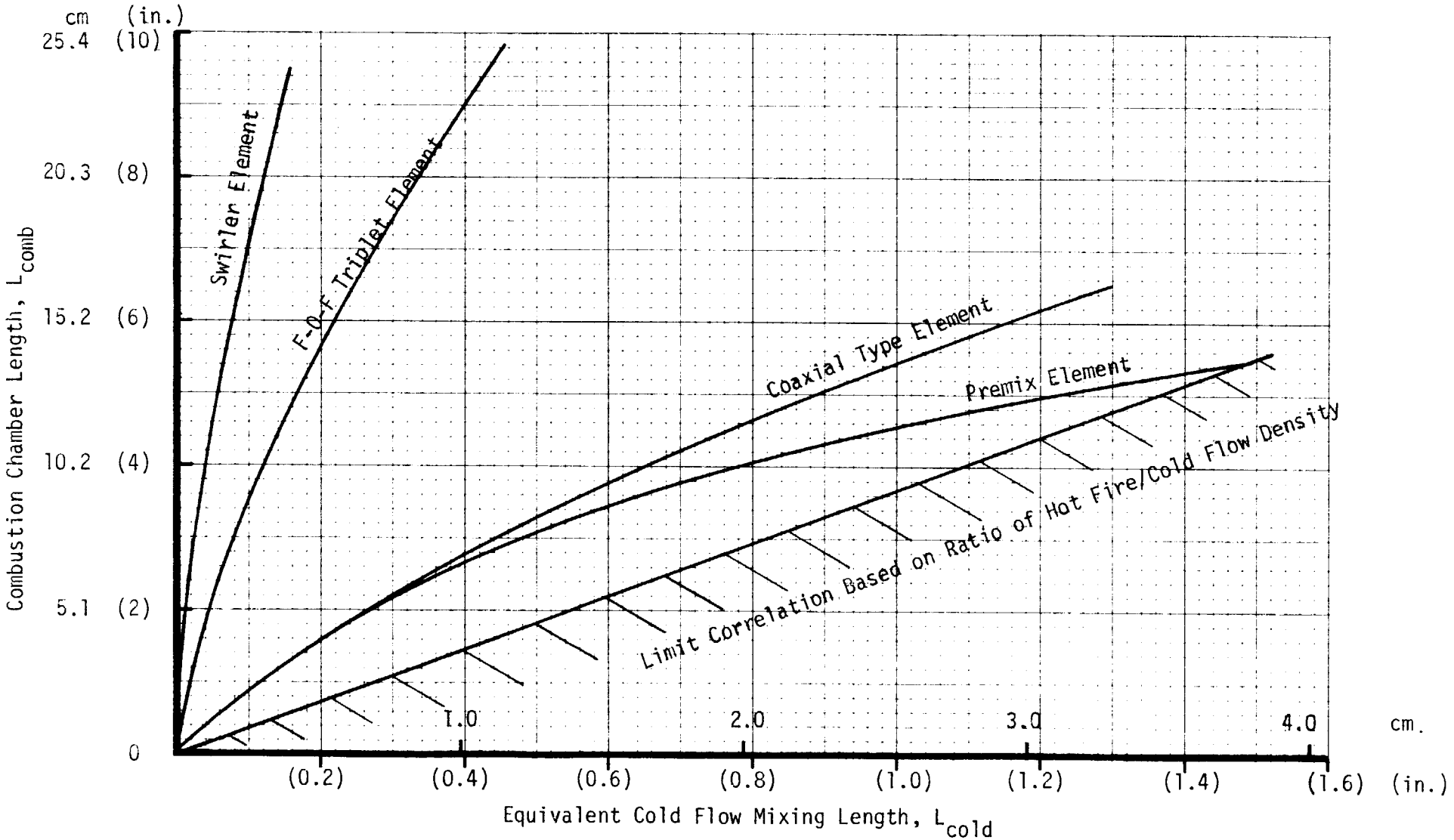

FIGURE 72. RELATIONSHIP BETWEEN CHAMBER LENGTH AND COLD FLOW MIXING LENGTH

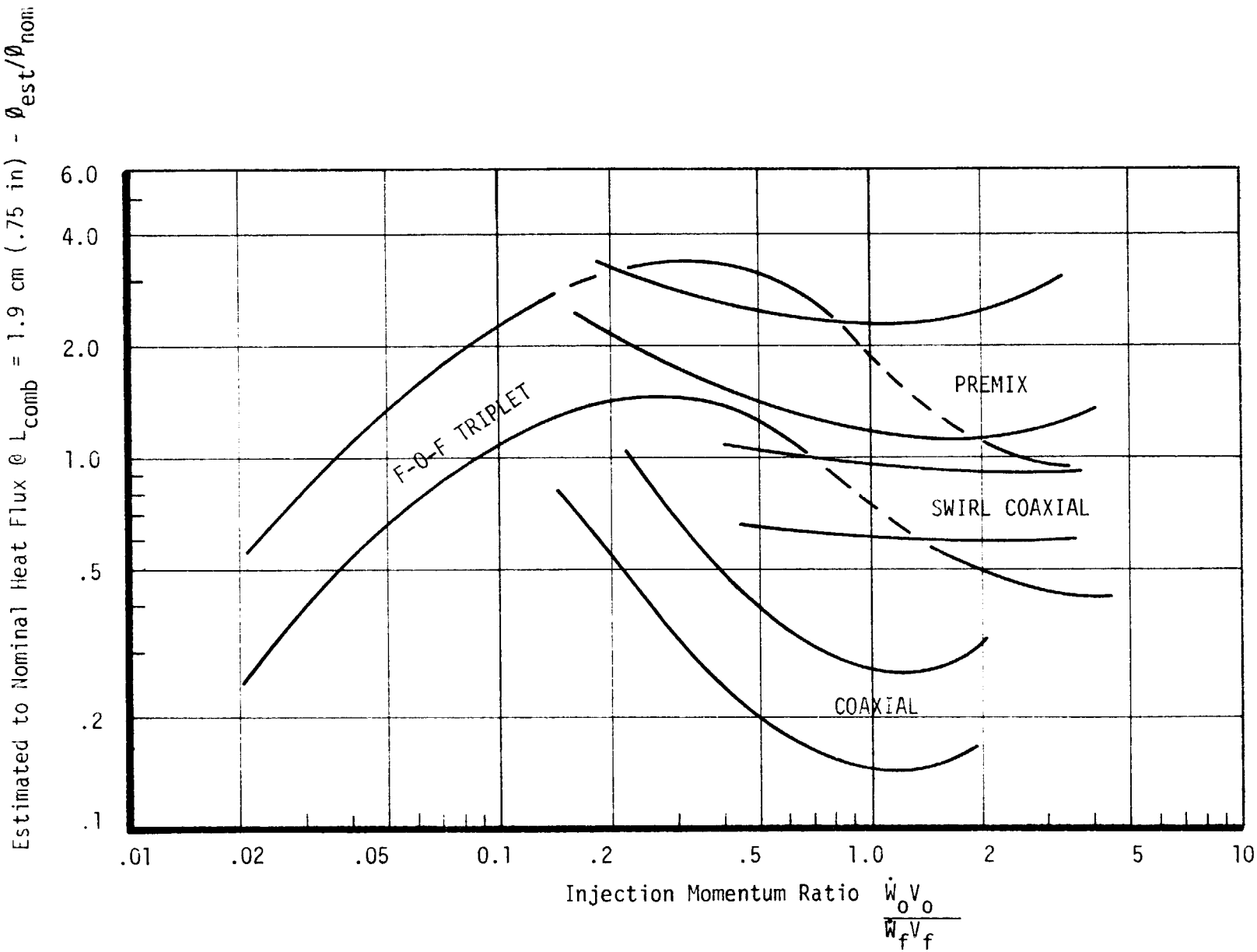

FIGURE 73. CHAMBER HEAT FLUX CHARACTERISTICS OF GASEOUS INJECTOR ELEMENTS

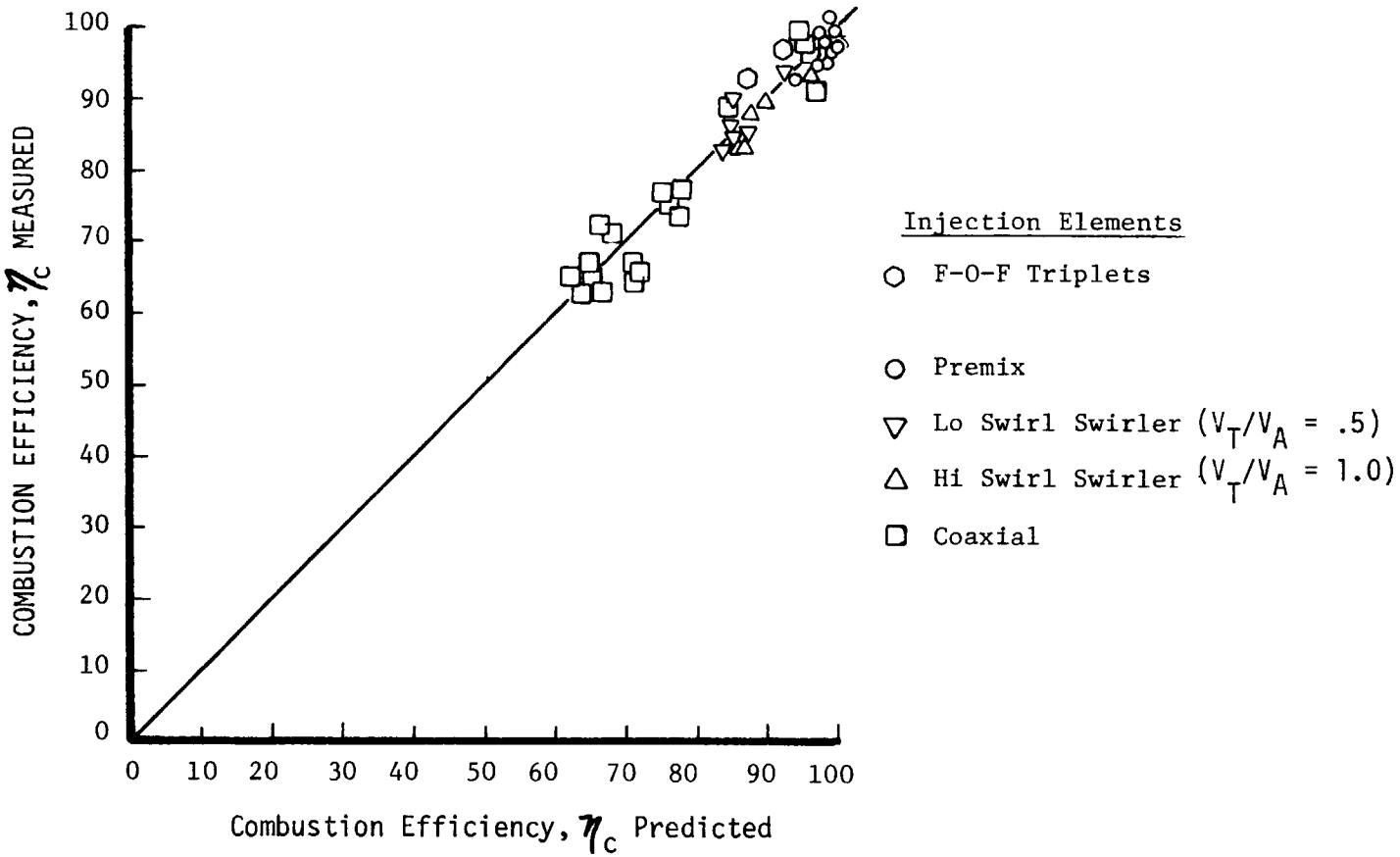

FIGURE 74. PREDICTED VS. MEASURED ENERGY RELEASE EFFICIENCY

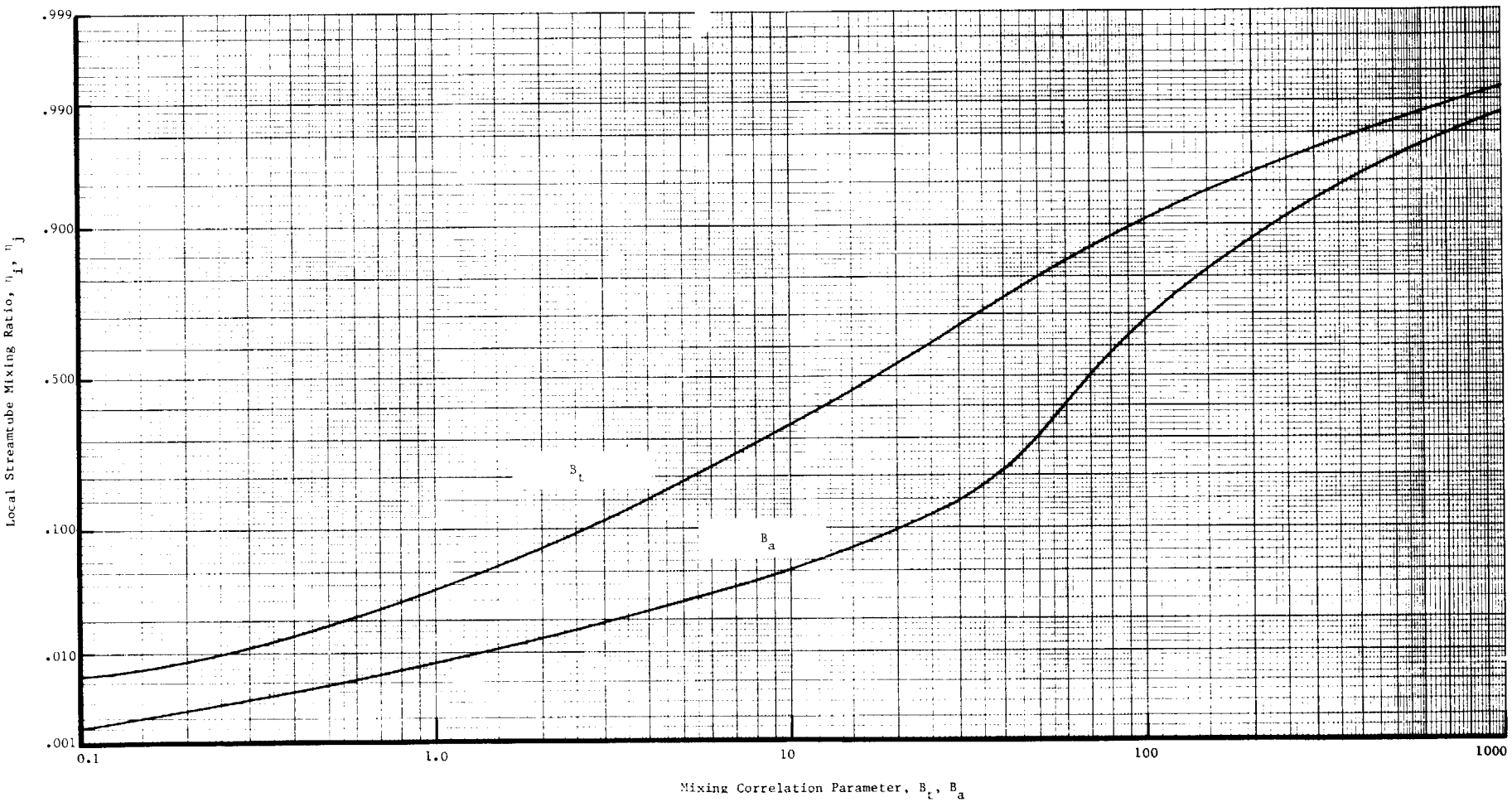

FIGURE 75. GENERALIZED MIXING CORRELATION CHART

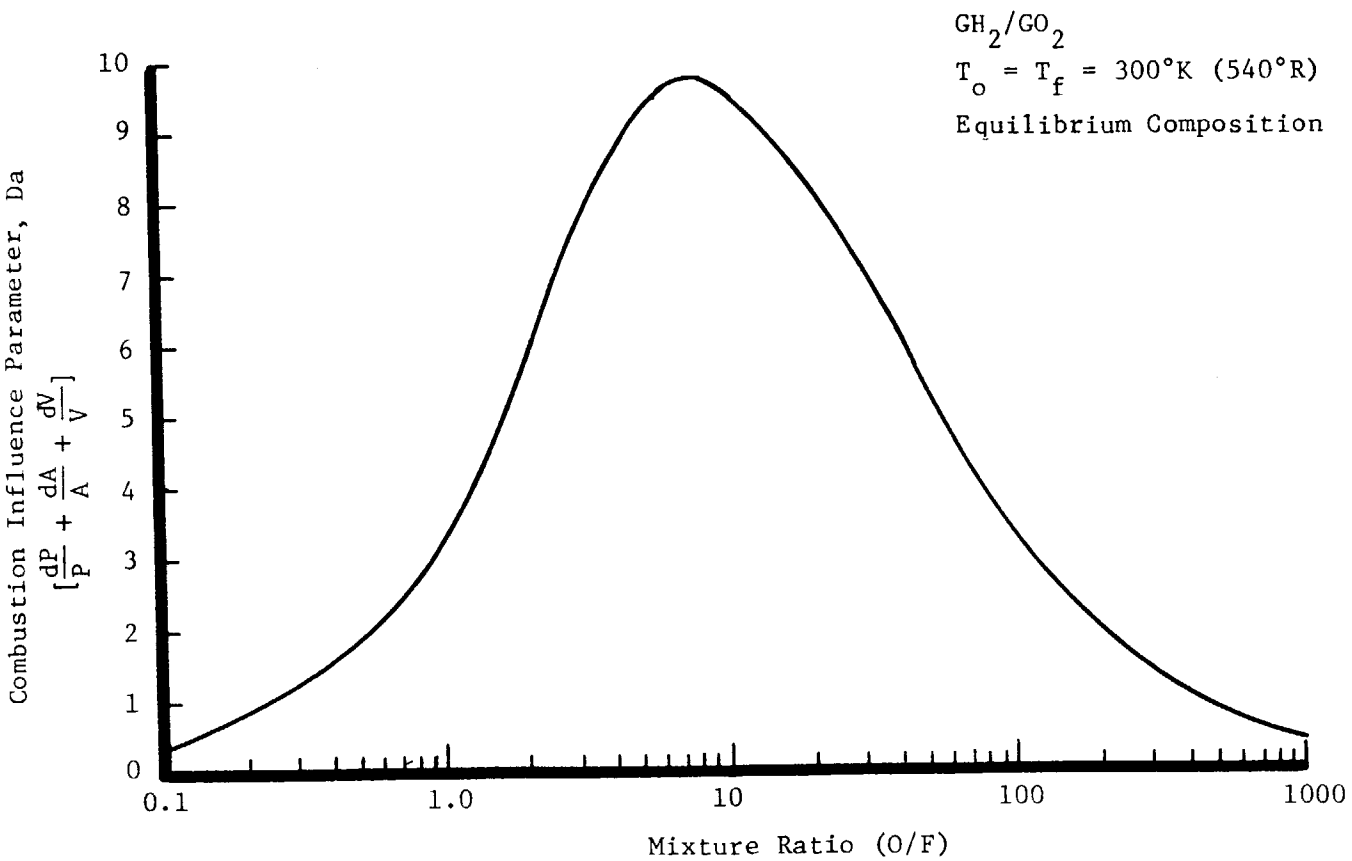

FIGURE 76. COMBUSTION INFLUENCE PARAMETER VS. MIXTURE RATIO GO_2/GH_2

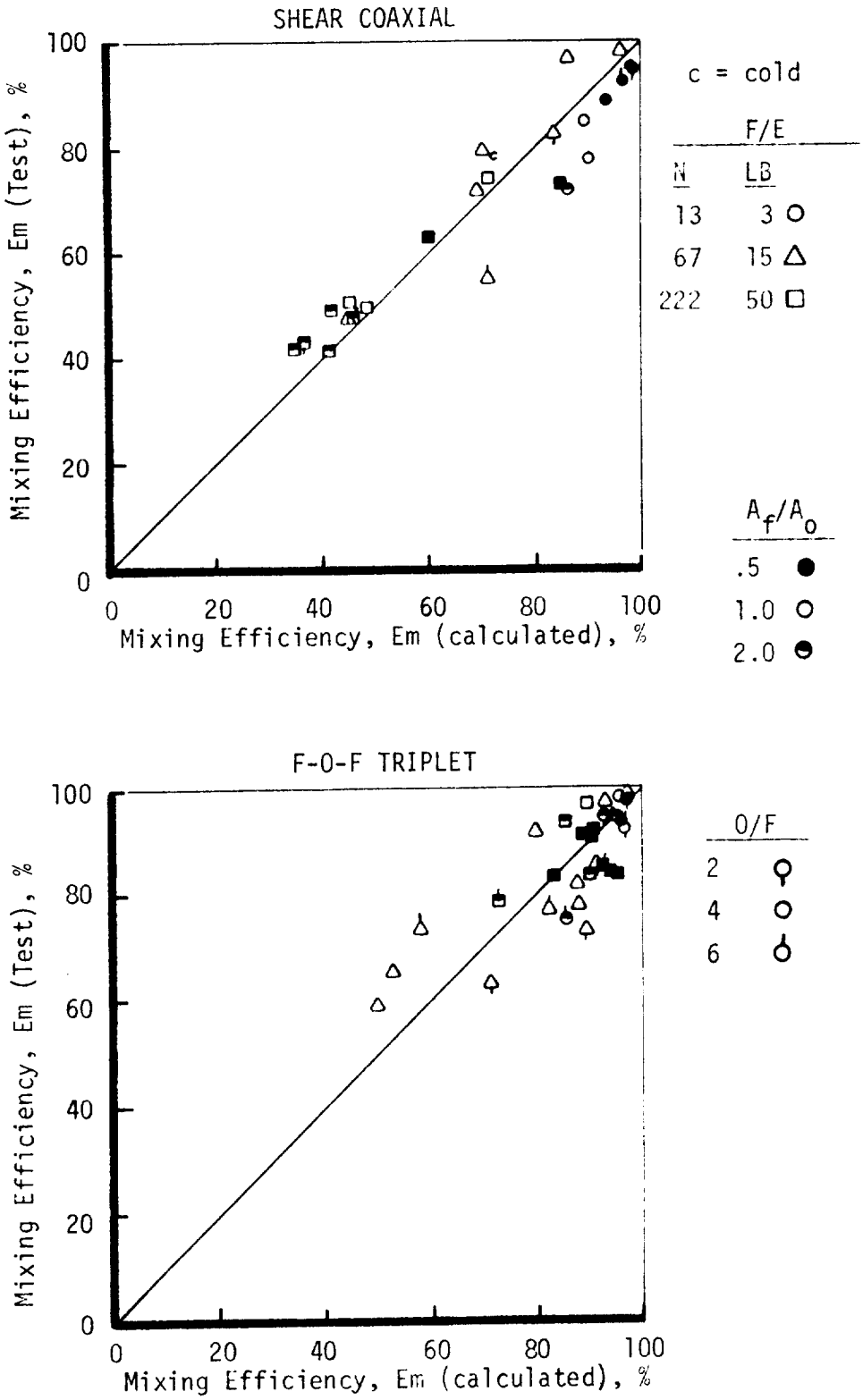

FIGURE 77. CORRELATION OF ANALYTICAL MODEL WITH SINGLE ELEMENT COLD FLOW DATA - COAXIAL AND TRIPLET

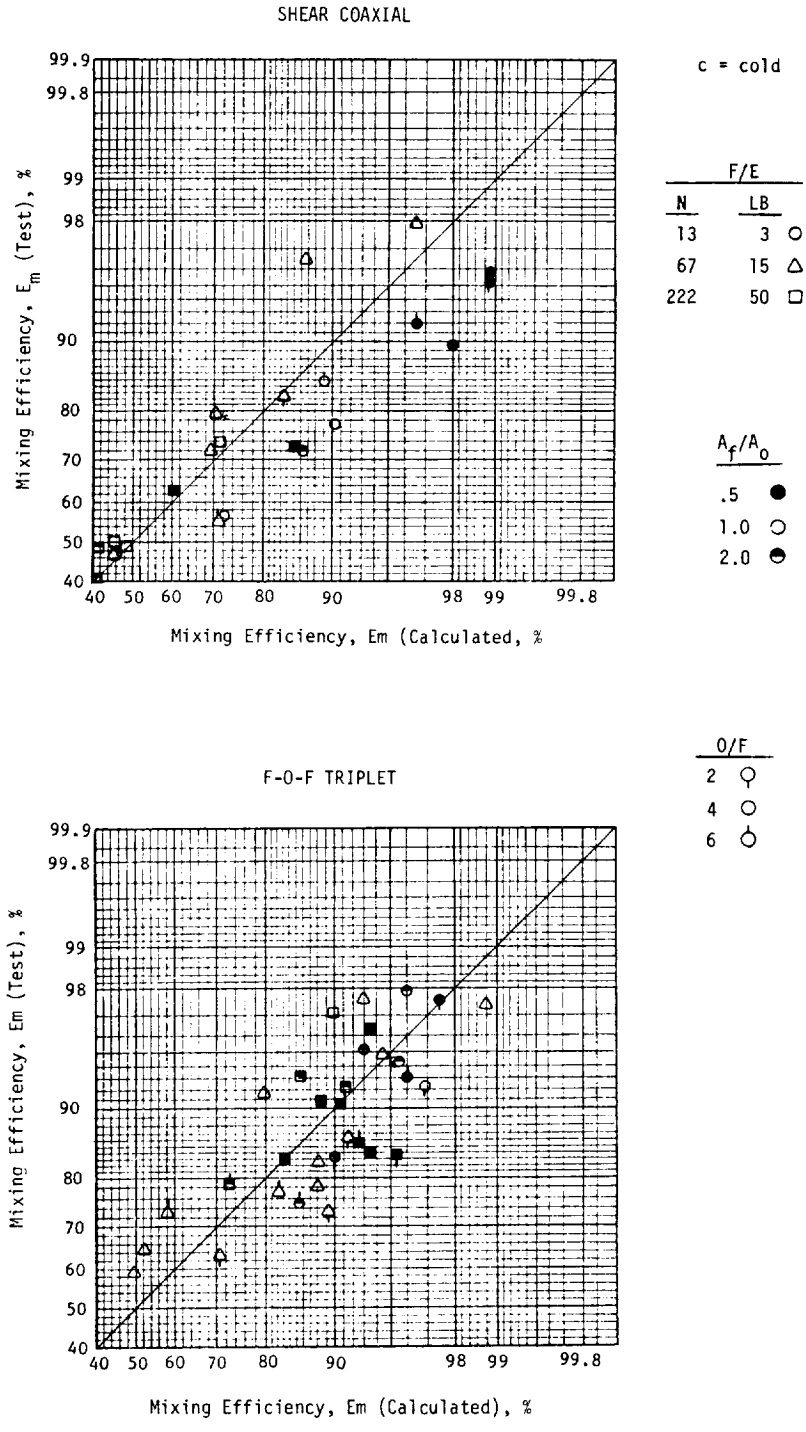

FIGURE 77.b CORRELATION OF ANALYTICAL MODEL WITH SINGLE ELEMENT COLD FLOW DATA - COAXIAL AND TRIPLET

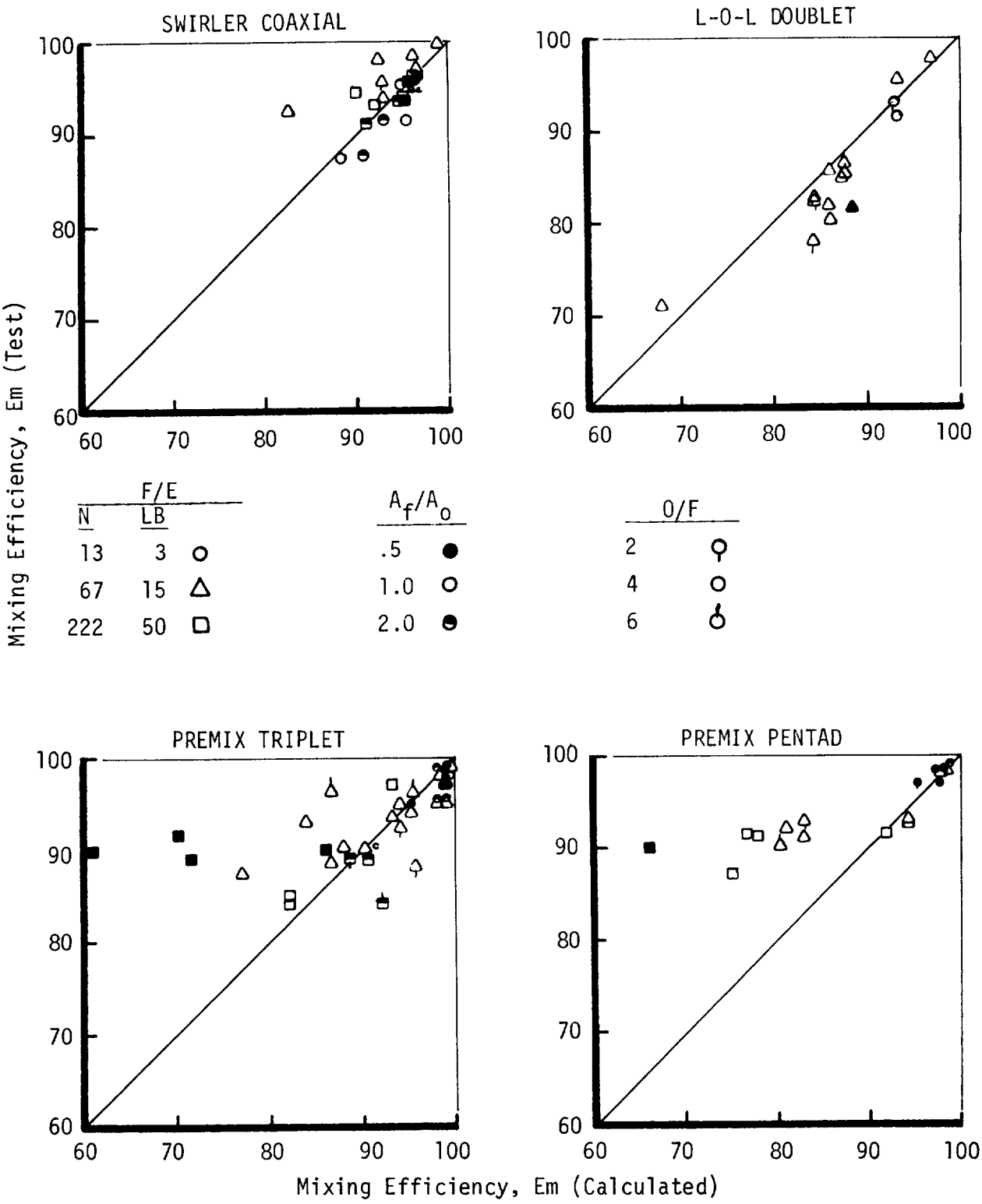

FIGURE 78. CORRELATION OF ANALYTICAL MODEL WITH SINGLE ELEMENT DATA - SWIRL, DOUBLET AND PREMIX

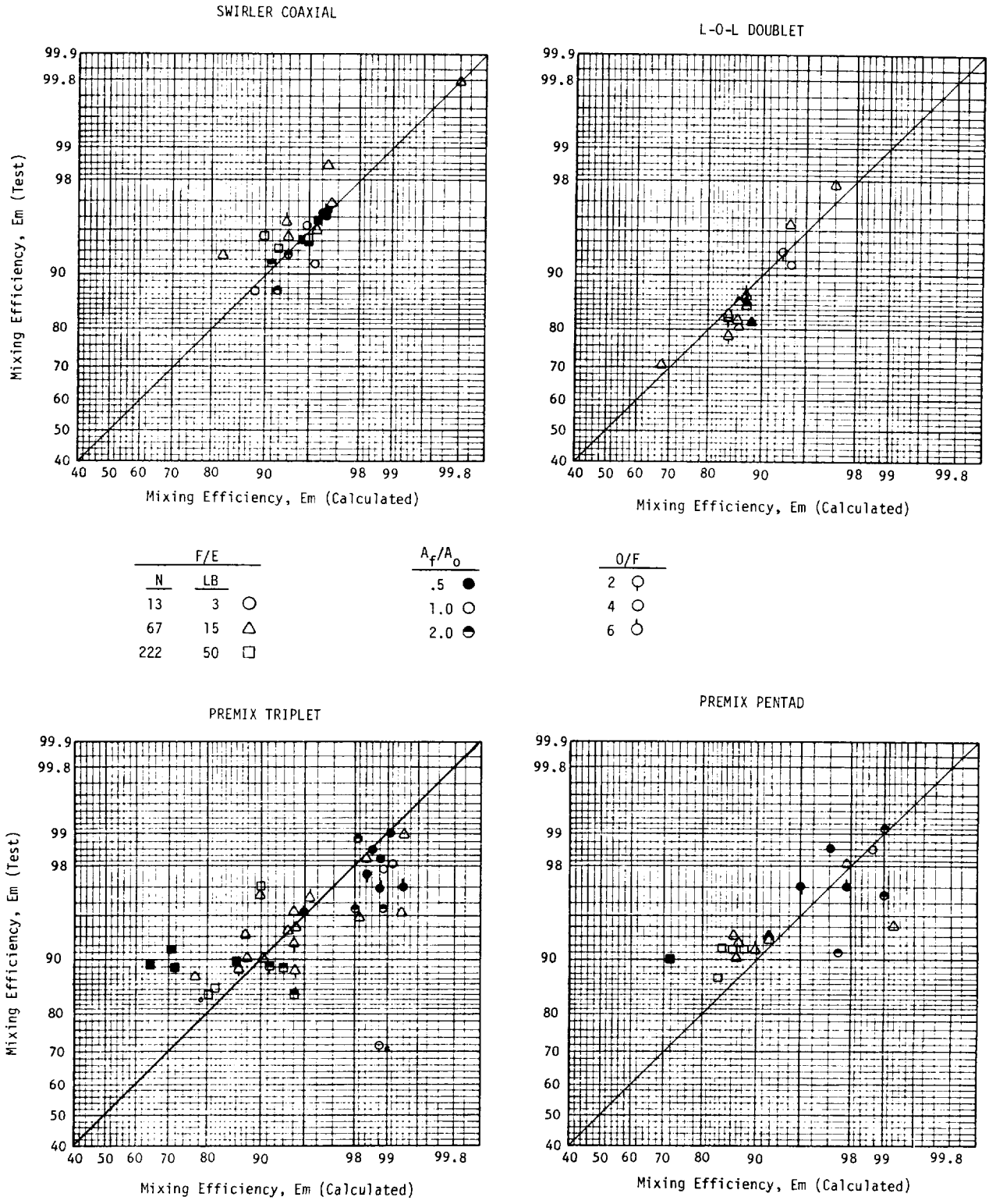

FIGURE 78.b CORRELATION OF ANALYTICAL MODEL WITH SINGLE ELEMENT DATA - SWIRL, DOUBLET AND PREMIX

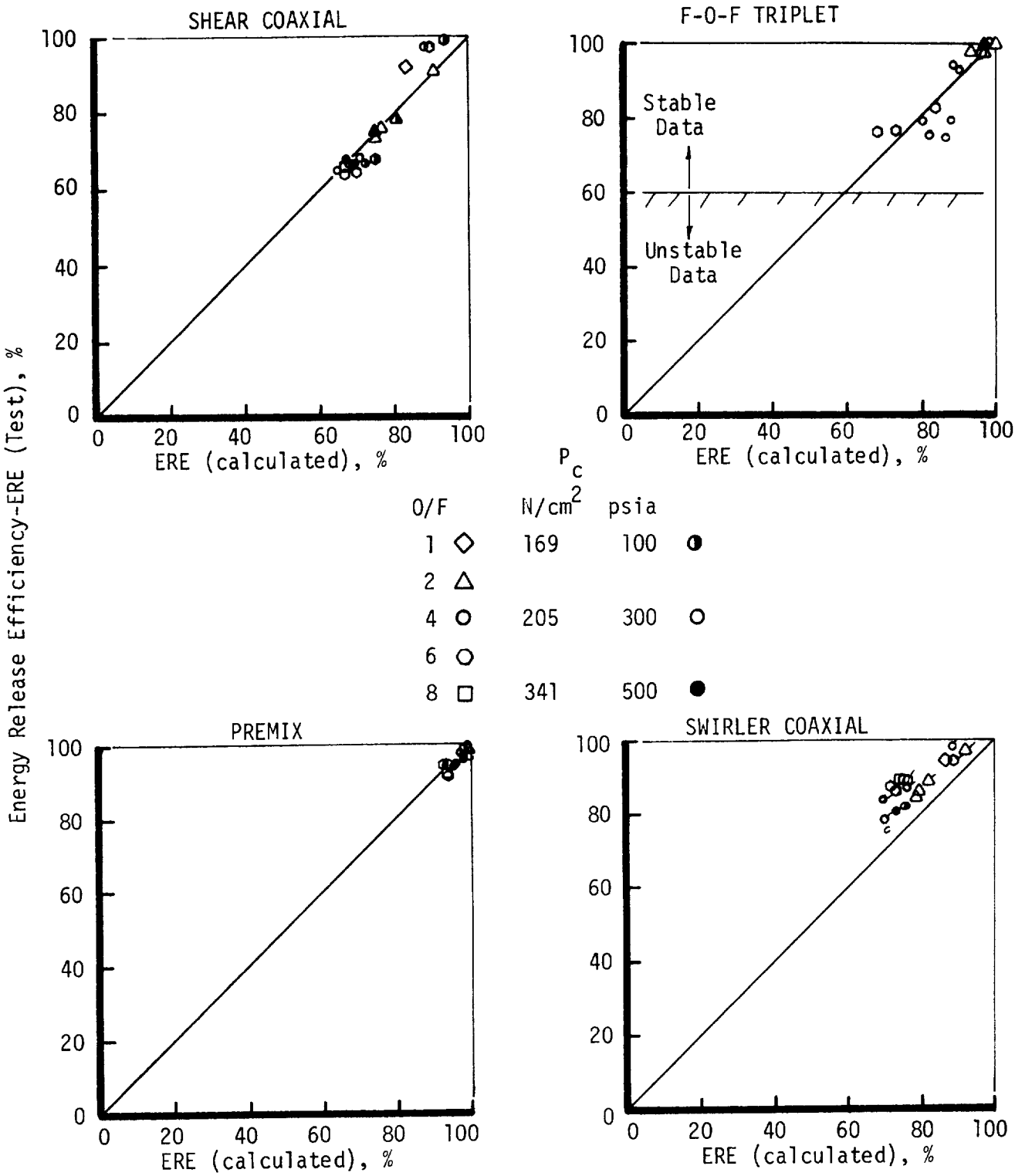

FIGURE 79. CORRELATION OF ANALYTICAL MODEL WITH SINGLE ELEMENT COMBUSTION DATA

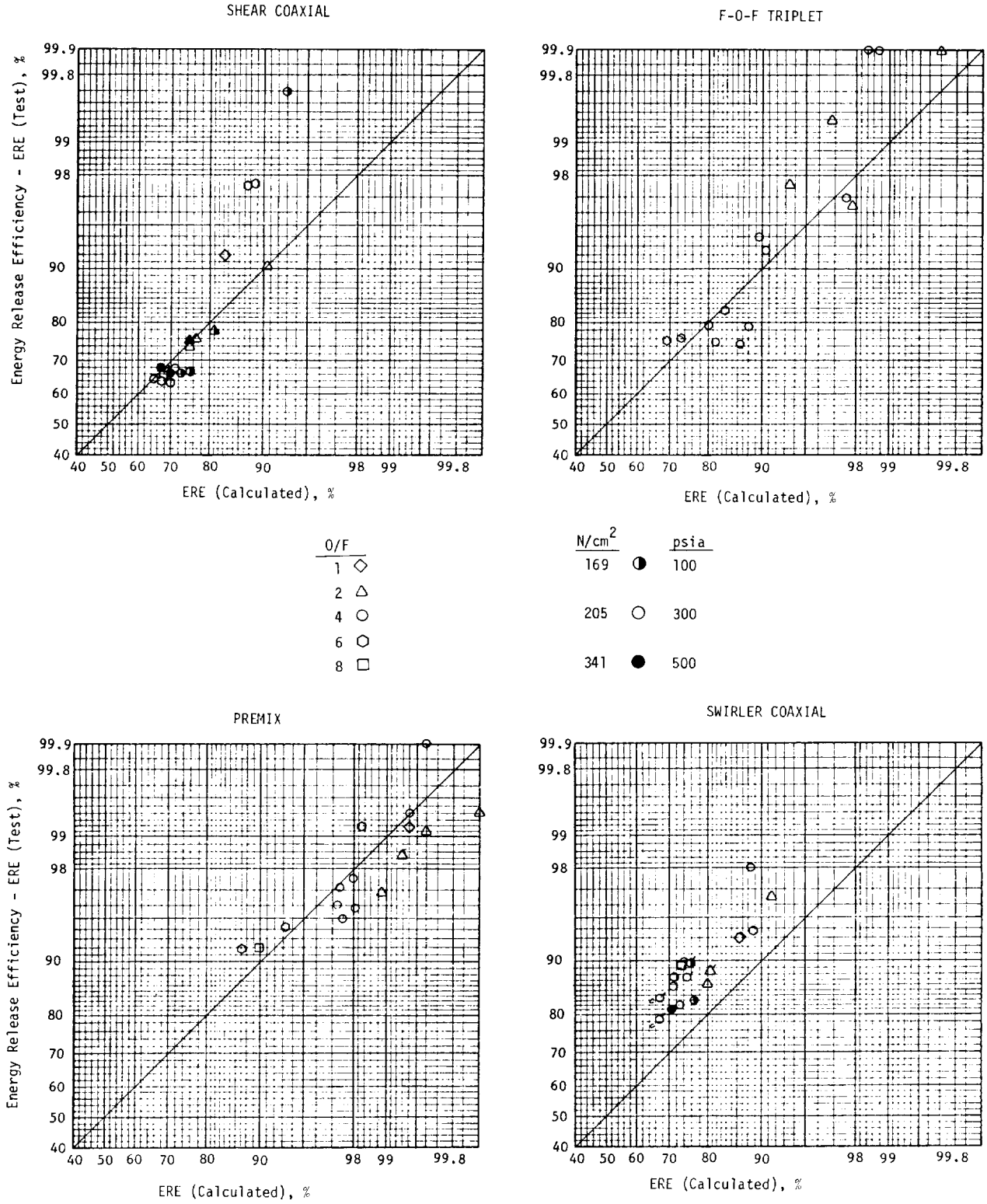

FIGURE 79.b CORRELATION OF ANALYTICAL MODEL WITH SINGLE ELEMENT COMBUSTION DATA

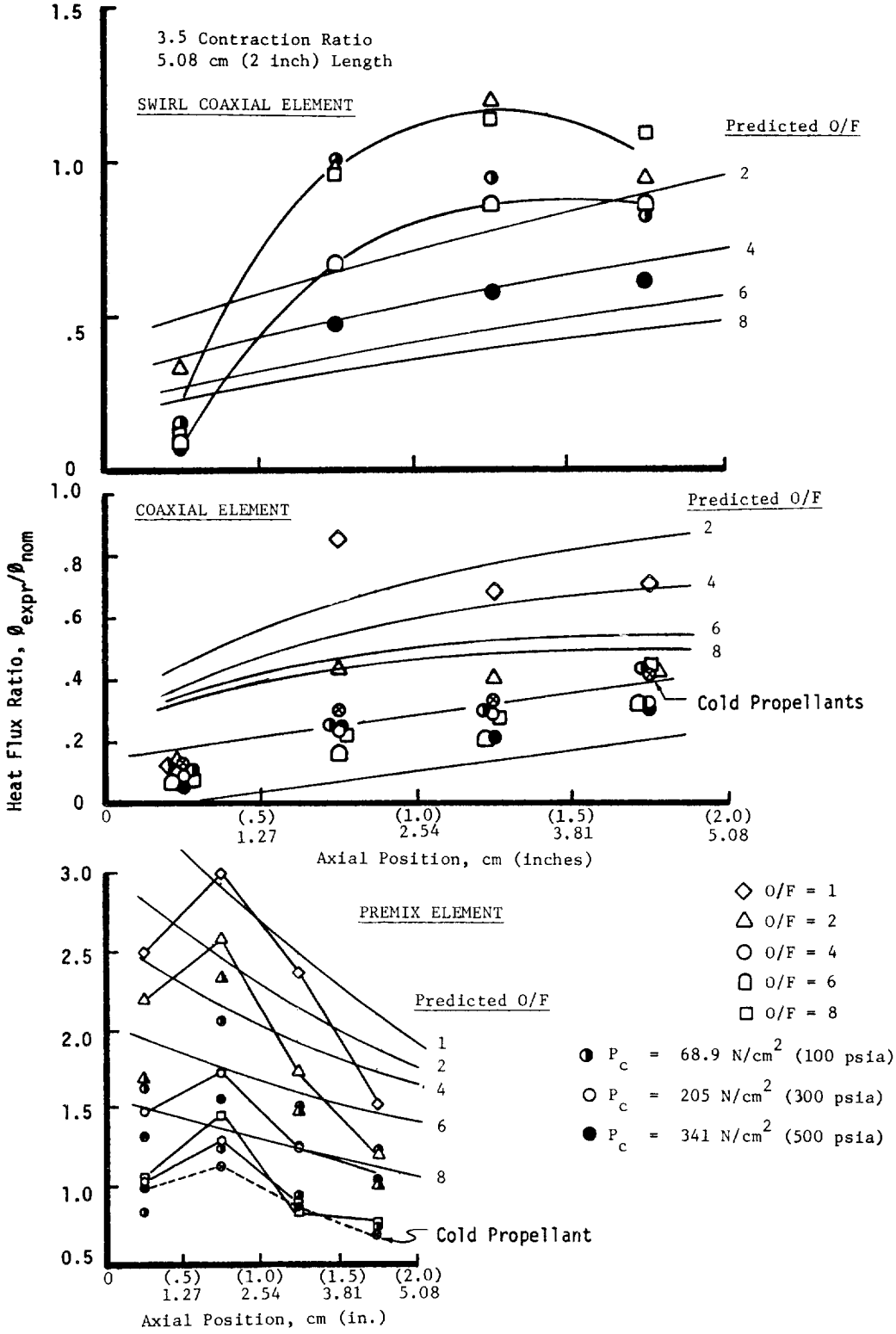

Figure 80. Correlation between Predicted and Measured Heat Flux

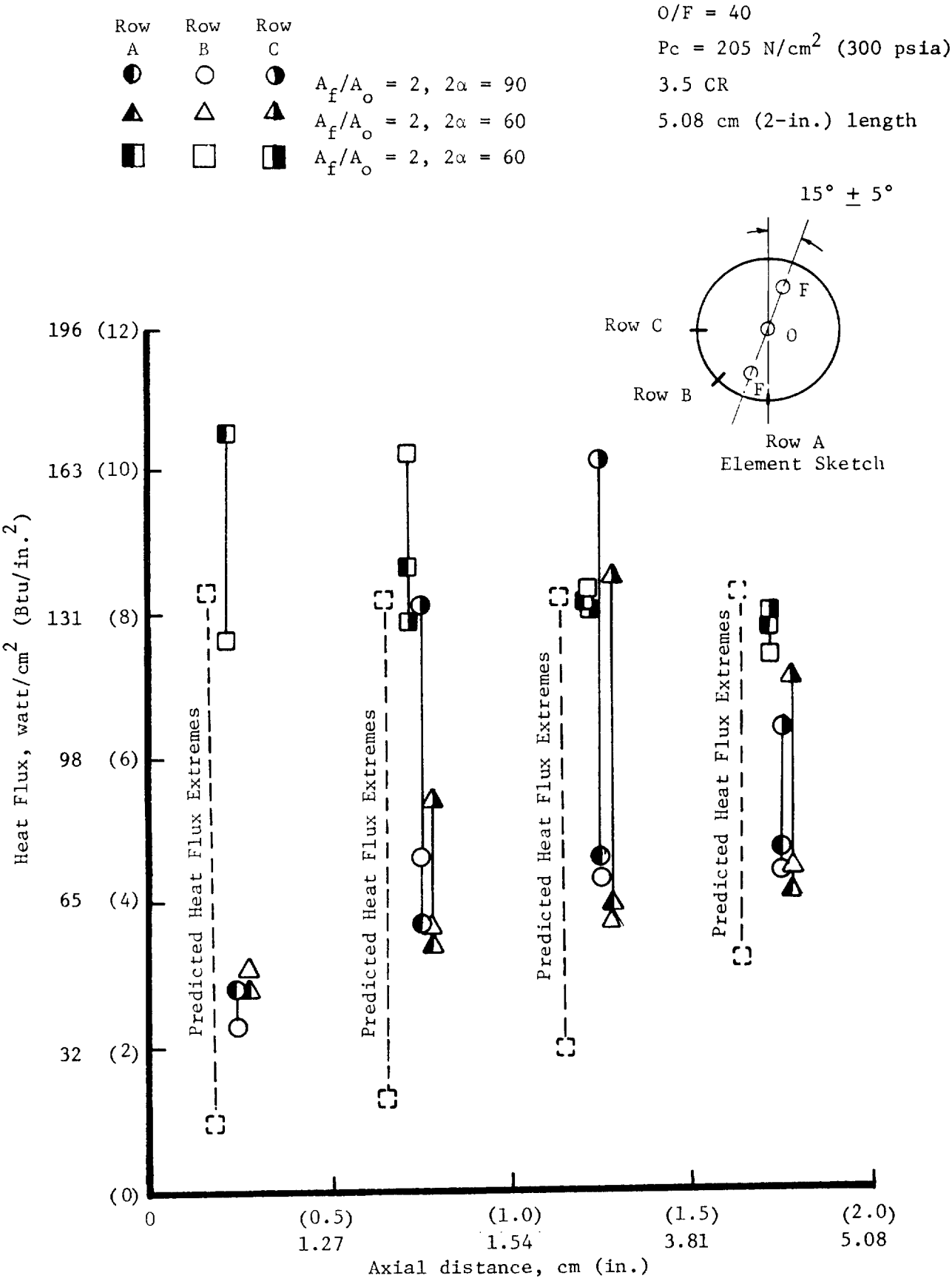

Figure 81. Correlation between Predicted and Measured Heat Flux-Triplet

IX. CONCLUSIONS

The objective of this program was to develop an injector/chamber combustion technology base for gaseous hydrogen-gaseous oxygen rocket engines. The end product of this program was a design handbook that summarized the resulting information into models that characterize performance and compatibility. These objectives were accomplished by: (1) empirically determining the mixing characteristics of a number of elements in a comprehensive cold flow test program. (2) empirically determining the effects of combustion by comparing the mixing characteristics of a swirler element in a combustion and non-combustion environment. (3) conducting an extensive series of single element rocket tests to determine the performance characteristics and chamber heat flux of selected elements. (4) designing and testing four full scale injectors to obtain multielement performance and chamber heat flux information and (5) utilizing the data from (1), (2), (3) and (4) to synthesize models that relate performance and chamber heat flux to the design variables of the injector/chamber.

The major conclusions from this program were:

1. Energy release efficiencies of 100% and 98.4% were demonstrated with F-O-F triplet and premix injectors, respectively, in chambers 7.62 cm (3 in.) long at nominal operating conditions.

2. Chamber heat flux is highly dependent on injection element type with injector-end wall fluxes as much as three times that predicted by conventional turbulent heat transfer correlations.

3. High performance GO_2/GH_2 injectors can be unstable at high frequencies and provision for damping devices should be incorporated into the injector and/or chamber design.

4. The zoned or barrier cooling concept results in a high performance penalty in comparison to GH_2 film cooling to effect a chamber wall temperature and heat flux consistent with long life thrusters.

5. Mixing characteristics can not be modeled from cold flow data alone; combustion is a first order effect on the mixing process.

6. Two models were developed that allow an injector designer to a priori estimate the performance and chamber heat flux characteristics of potential injector concepts.

APPENDIX A

ANALYTICAL MIXING MODEL DESCRIPTION

This appendix describes the analytical mixing model which was developed to predict the influence of design and operating variables upon gaseous cold flow and combustion mixing rates. To facilitate cross reference, the appendix is subdivided into eight headings. The first section below describes the inter-relationships of the remainder of the model.

1. Physical Basis for Analytical Model

One of the first significant discoveries which occurred while analyzing the cold flow data was the observation that those injection element types which rapidly dissipated their injection dynamic heads tended to be high performing (rapid mixers). From this it was apparent that if the axial rate of dynamic head dissipation could be analytically predicted, it might be possible to analytically predict mixing rates. ALRC had previously predicted dynamic head decay rates by integrating the element potential flow velocity profile modified for viscous boundary layer effects. The methods for calculating element potential flow characteristic dimensions are developed in subsection 2 and the boundary layer approximation in subsection 3 of this appendix. Some element types are characterized by decreasing potential flow spray fan thicknesses. These elements, however, are limited in their spreading rate at a critical length to diameter, $(L/D)^*$, described in subsection 4. Combustion effects and chemical species change on mixing rate are analytically developed in subsection 5. Subsection 6 utilizes a shear coaxial element for illustration and mathematically predicts its mixing rate based on the above calculated parameters. The mathematical mixing model is then extended to describe all other element types tested on this program in subsection 7. Finally, subsection 8 describes the special treatment required for analysis of swirl coaxial elements.

2. Potential Flow Characteristics of Several Conventional Gaseous Injection Elements

A primary requirement of the analytical mixing model is a quantitative description of the characteristic element fan or jet dimension as a function of element design parameters and injector operating conditions. This subsection summarizes characteristic fans for several conventional injection elements which were tested on this and other program or which may be of interest for future gaseous injection element designs. ALRC had developed extensive injection models to parametrically predict element potential flow dimensions as a function of variable design and operating parameters on other programs. Liquid spray models had been developed at ALRC to analytically predict and correlate experimental atomized drop sizes with significant element design and operating parameters. These liquid element spray models were modified to describe gas injection element flow fields. The results of these modifications are described below.

Shear Coaxial Element

The parallel stream shear coaxial element has been used extensively with the O_2/H_2 propellant combination on numerous programs. It is mathematically characterized by a central oxidizer jet having a circular diameter.

$$D_o = \left[\frac{4\ A_o}{\pi}\right]^{1/2} \tag{A-1}$$

where:

D_o = oxidizer jet diameter

A_o = orifice area of a single oxidizer element

The oxidizer jet is surrounded by a concentric fuel annulus having inner diameter D_{f1}, and outer diameter, D_{f2}. The fuel jet is characterized by its hydraulic diameter:

$$D_{hf} = D_{f2} - D_{f1} \tag{A-2}$$

Both oxidizer and fuel potential flow characteristic dimensions remain constant as a function of increasing axial length.

Increased Shear Coaxial Element

A minor variation of the shear coaxial element is the increased shear element. The increased shear element is achieved by convoluting the oxidizer jet so that it is non-circular. Thus for the same oxidizer orifice area (indicative of constant thrust/element) its wetted perimeter is greater than the circular shear coaxial element, resulting in a smaller hydraulic diameter. Similarly, the fuel wetted perimeter across which turbulent mixing occurs is also increased resulting in reduced fuel hydraulic diameter.

Both oxidizer and fuel hydraulic diameters are calculated using the standard equation.

$$D_h = \frac{4\ (\text{Area})}{\text{Wetted Perimeter}} \tag{A-3}$$

Swirler Coaxial Element

The swirler coaxial element is characterized by a tangential oxidizer injection velocity component. The tangential velocity may either be imparted by a hydraulic swirler or a mechanical swirler.

Three important characteristic design parameters of the swirler coaxial element are its oxidizer diameter, D_o; discharge coefficient, C_{do}; and oxidizer spray cone angle, θ_o. Due to the tangential velocity component, the oxidizer stream adheres to the oxidizer element wall resulting in an

annular oxidizer jet at the injector face characterized by the oxidizer element discharge coefficient. The oxidizer jet hydraulic diameter at the injector face can be calculated from the continuity equation:

$$D_{ho\ (L\ =\ 0)} = [1 - \sqrt{1 - C_{do}}]\ D_o \tag{A-4}$$

The oxidizer sheet thickness at the injector face is one-half the above hydraulic diameter.

$$t_{o\ (L\ =\ 0)} = \left(\frac{1 - \sqrt{1 - C_{do}}}{2}\right)\ D_o \tag{A-5}$$

The tangential velocity component results in a hollow oxidizer cone of angle, θ_o, in the absence of fuel injection. Because of the annular axial fuel injection momentum impinging on the oxidizer cone, the resultant bipropellant cone angle is reduced. The resultant spray cone angle, ϕ, can be calculated as follows from the momentum equation.

$$\phi = \tan^{-1}\left(\frac{\dot{w}_o\ V_o \sin \theta_o}{\dot{w}_f\ V_f + \dot{w}_o\ V_o \cos \theta_o}\right) \tag{A-6}$$

It is readily evident that the bipropellant cone angle depends upon the element O/F and design A_f/A_o ratios, as well as the oxidizer spray cone angle.

Because of the divergence of the spray cone, momentum and continuity considerations dictate that the oxidizer potential flow thickness diminishes with increasing displacement from the injector face as shown below.

$$\frac{t_{o\ (L)}}{D_o} = \frac{C_{do}}{4\ [1 + 2\ (L/D_o)\ \tan \phi]} \tag{A-7}$$

Similarly, the fuel potential spray fan thickness can be shown to vary as follows.

$$\frac{t_{f\ (L)}}{D_{f2}} = \frac{C_{df}\ \left[1 - \left(\frac{D_{f1}}{D_{f2}}\right)^2\right]}{4\ \left[1 + 2\ \frac{L}{D_{f2}}\ \tan \phi\right]} \tag{A-8}$$

Equations (A-4) through (A-8) above can then be used to provide the necessary input for the analytical swirler mixing model.

Parallel Sheet or Showerhead Element

The showerhead injection element is the simplest to fabricate and analyze. It merely consists of axial injection orifices. In the case of

circular showerhead elements the circular orifice diameter is the characteristic potential flow dimension.

$$D = \sqrt{\frac{4\ (\text{Area})}{\pi}} \qquad \text{(A-9)}$$

For non-circular parallel sheet elements the hydraulic diameter is the characteristic dimension and can be calculated from Equation (A-3) above. In any case the showerhead element has a constant characteristic potential flow dimension for any axial length.

Like on Like Doublet

The like on like doublet element incorporates both impingement and shear principles. The impingement momentum is mathematically characterized to describe a gaseous potential flow fan similar to a conventional liquid propellant spray fan. A like doublet is mathematically characterized by equal stream diameters, equal density, equal injection velocity, and equal momentums from the opposing orifices. Thus, the impingement fan is symmetrical.

Consider a like-on-like doublet having stream diameter, D_o; discharge coefficient, C_d; injection velocity, V_o; impingement half-angle, α; propellant density, ρ; and viscosity, μ. The axial component of stream injection velocity is ($V_o \cos \alpha$). The component of injection velocity normal to the plane of impingement is ($V_o \sin \alpha$). This component is locally stagnated at the point of impingement on the stream axis, but from energy conservation must result in a component ($V_o \sin \alpha$) flowing radially outward from the impingement point in the impingement plane. The axial component of injection velocity ($V_o \cos \alpha$) is conserved at the outer fan boundary envelope after impingement, from axial momentum considerations.

This impingement process corresponds to a constant radial ($V_o \sin \alpha$) velocity source traveling in a constant axial ($V_o \cos \alpha$) velocity coordinate system. Thus, solving for the resultant fan propagation angle

$$\phi = \sin^{-1} (\tan \alpha) \qquad \text{(A-10)}$$

defines the shape of the fan envelope.

From continuity relationships

$$\dot{w}_t = 2\rho\ C_d\ (\tfrac{\pi}{4} D_o^2)\ \ V_o = 2\rho\ (L \tan \phi) \cdot t\ V_o \cos \alpha \qquad \text{(A-11)}$$

where:

$\dot{w}_t$ = total flow rate from both orifices
L = axial fan location from point of impingement
t = fan thickness at axial location, L

Therefore, the like double fan thickness decreases with increasing displacement from the impingement point as

$$\frac{t(L)}{D_o} = \frac{\pi C_d}{4\ (L/D)\ \tan\ \phi\ \cos\ \alpha} \qquad \text{(A-12)}$$

Thus, in principle the like on like doublet is similar to the swirler coaxial element described previously from the standpoint that its characteristic potential flow spray dimension decreases with increasing L/D from the injector face. The local fan thickness can also be functionally related to the orifice diameter, discharge coefficient, and impingement angle as shown in Equation (A-12).

External Impinging F-O-F Triplet

The triplet element is characterized by both impinging fan potential flow and boundary layer shear principles. The fuel/oxidizer orifice diameter ratio is an important parameter for unlike impinging element designs. Except for the $A_f/A_o = 2.0$ design which has equal fuel and oxidizer diameters, the other F-O-F triplet designs tested result in partial oxidizer mis-impingement because of the smaller fuel diameter. The fraction of oxidizer which does not impinge with the fuel is calculated below.

$$Om = \frac{\beta - \sin\ \beta}{\pi} \qquad \text{(A-13)}$$

where:

$$\beta = \pi - 2\ \sin^{-1}\ [D_f/D_o] \qquad \text{(A-14)}$$

The two misaligned oxidizer lobes are each approximated by an equivalent showerhead orifice of apparent diameter, D_o'.

$$D_o' = D_o \sqrt{\frac{\beta - \sin\ \beta}{2\pi}} \qquad \text{(A-15)}$$

The next step in the F-O-F triplet element analysis is to evaluate the relative fuel penetration distance into the oxidizer jet to determine whether the F-O-F triplet should be approximated with an oxidizer rich core between two fuel rich fans or a single fuel rich core with a split oxidizer fan.

From the momentum equation considerations the F-O-F triplet fan propagation angle normal to the impingement plane can be mathematically shown to be

$$\phi = \sin^{-1}\left[\frac{\dot{w}_f\ V_f\ \sin\ \alpha_f}{(\dot{w}_f\ V_f\ \cos\ \alpha_f) + \dot{w}_o\ V_o\ (1 - Om)}\right] \qquad \text{(A-16)}$$

In the case of underpenetrated jets ($Y < 0.5\ D_o$) from continuity equation formulations the fuel potential fan thickness can be calculated as indicated below.

$$\frac{t_f\ (L)}{D_f} = \frac{\pi\ C_{df}}{8\ (L/D)_f \cos\ \alpha_f \tan\ \phi} \qquad \text{(A-17)}$$

Similarly, the oxidizer fan thickness can be calculated by the following equation.

$$\frac{t_o\ (L)}{D_o} = \frac{\pi\ C_{do}\ (1 - Om)}{8\ (L/D_o) \tan\ \phi} \qquad \text{(A-18)}$$

If the fuel injection momentum over penetrates the oxidizer jet ($Y > 0.5\ D_o$), the comparable fuel and oxidizer spray fan thicknesses are indicated by Equations (A-19) and A-20), respectively.

$$\frac{t_f\ (L)}{D_f} = \frac{\pi\ C_{df}}{4\ (L/D)_f \cos\ \alpha_f \tan\ \phi} \qquad \text{(A-19)}$$

$$\frac{t_o\ (L)}{D_o} = \frac{\pi\ C_{do}\ (1 - Om)}{16\ (L/D_o) \tan\ \phi} \qquad \text{(A-20)}$$

Deep Cup Premix Elements

The premix elements evaluated on this program consisted of a circular axial oxidizer jet with either two (triplet) or four (pentad) rectangular fuel jets injected normally into the oxidizer stream. The premixing cup consisted of a circular cross section identical in area to the oxidizer jet and a moderate (approximately 1 to 5) cup L/D ratio. The deep cup provides constraints for the premix gases and directs the gas jet in a nearly circular axial jet. For the premix injection element it was assumed that the mixing cup diameter is the characteristic potential flow dimension for both fuel and oxidizer jets.

$$D_f = D_o = \left[\frac{4\ A_{cup}}{\pi}\right]^{1/2} \qquad \text{(A-21)}$$

Unlike the other impinging elements such as the like doublets, swirler coaxial, or F-O-F triplet, the characteristic potential flow dimension does not diminish with increasing L/D from the injector face. In the event that shallow cup ($L/D < 1$ or $A_{cup} >> A_o$) premix injectors are evaluated in the future, its characteristics could be expected to behave more like the external F-O-F triplet (or pentad) model described previously with $\alpha_f = \pi/2$ radians.

Other Element Types

Based upon the above illustrated analysis concepts utilizing the injection momentum and continuity considerations, it is possible to synthesize

potential flow models for any conceivable injection element type based upon the physical insight of the injection process. For example the unlike doublet (which was not evaluated on this program) can be synthesized with only minor modification of the like doublet and F-O-F triplet element models.

3. Boundary Layer Approximation to Predict Axial Velocity Head Decay Rate

ALRC had previously developed a mathematical model describing liquid injection element hydraulics in reference 14. In this analytical hydraulic model, potential flow characteristics and approximate viscous boundary layer solutions had been combined to describe many diverse hydraulic phenomena including axial static pressure distributions.

To reiterate the analytical objective, it was not the intent to develop a mathematically rigorous gas mixing model. It was only intended to utilize an approximate mathematical model to identify significant design variables and their interactions which could then be used to correlate the experimental data for numerical accuracy. Consistent with this limited objective, Figure 82 schematically illustrates the basic concept underlying the mathematical assumptions.

The injection velocity profile at the injector face plane is assumed to be described by potential flow. It is readily recognized that a finite velocity profile exists at the injection plane depending upon feed system design parameters, but the uniform velocity approximation greatly simplifies the mathematical solution. During cold flow testing, the gases within the combustion chamber are relatively quiescent. Therefore, the high injection velocity gases from the injection element are decelerated by viscous drag. Strictly speaking the viscous boundary layer equations should be solved in cylindrical co-ordinates for the jet with increasing radial and axial static pressure gradients simultaneously with the momentum and continuity equations. Because of its mathematical complexity it was more practicle to solve the problem using boundary layer approximations to identify the general form of the solutions and use the empirical data to fine tune the model for numerical accuracy. For the gas injection elements evaluated on this program the Reynolds numbers were on the order of 10^5; indicative of turbulent boundary layer characteristics. For simplicity the velocity boundary layer growth rate as a function of axial distance was approximated from the flat plate solution.

$$\delta = \frac{0.375\ L}{Re_L^{0.2}} \qquad \text{(A-22)}$$

For convenience the above equation was transformed to the following representation.

$$\frac{\delta}{R_o} = \frac{0.75\ (L/D)^{0.8}}{Re_d^{0.2}} \qquad \text{(A-23)}$$

To be exact, the injection velocity profile should have been integrated to simultaneously satisfy the momentum and continuity equations with appropriate boundary conditions. However, for mathematical simplicity, the assumption was made that the initial potential flow diameter is reduced radially inward at the same rate that the boundary layer grows radially outward. Then a reduced oxidizer potential flow boundary coefficient, C_b, can be defined by

$$C_b = (\sqrt{C_{do}} - \delta_o/R_o)^2 \tag{A-24}$$

Similarly, an increased oxidizer boundary layer contraction coefficient, C_c, can be defined by

$$C_c = (\sqrt{C_{do}} + \delta_o/R_o)^2$$

Next, it was approximated that the local oxidizer velocity profile in the boundary layer varies linearly from V_{oJ} at C_b to zero velocity at C_c as shown schematically in Figure 82. The momentum transfer (dynamic head dissipation) rate can now be calculated by integrating the dynamic head throughout the local velocity profile.

$$Pd(L) = \frac{1}{C_c \pi R_o^2} \left\{ \int_0^{R_o\sqrt{C_b}} (1/2\ \rho_o\ V_{oJ}^2)\ 2\pi r dr + \int_{R_o\sqrt{C_b}}^{R_o\sqrt{C_c}} 1/2\ \rho_o\ V_{oJ}^2 \left[1 - \left(\frac{r/R_o - \sqrt{C_b}}{\sqrt{C_c} - \sqrt{C_b}}\right)\right]^2 2\pi r dr \right\} \tag{A-26}$$

Integration of Equation (A-26) results in the following solution.

$$\frac{Pd(L)}{Pd_o} = \frac{C_b}{C_c} + \frac{\left[\frac{1}{6} - \frac{C_b}{C_c} + 4/3\left(\frac{C_b}{C_c}\right)^{3/2} - 1/2\ \frac{C_b}{C_c}^2\right]}{\left(1 - \sqrt{\frac{C_b}{C_c}}\right)^2} \tag{A-27}$$

The dynamic head dissipation rate in the near zone can be adequately approximated by neglecting the second term in the right handmember of Equation (A-27). This makes the mathematical solution computationally tractable for manual calculation.

$$\frac{Pd(L)}{Pd_o} \approx \frac{C_b}{C_c} = \frac{\left[\sqrt{C_{do}} - \delta_o/R_o\right]^2}{\left[\sqrt{C_{do}} + \delta_o/R_o\right]^2} \qquad \text{(A-28)}$$

The above derivation has been limited to an axi-symmetric element such as the oxidizer circuit of a shear coaxial element.

For a two dimensional element such as the coax annular fuel jet, a parallel derviation is as follows. From subsection 2 it was shown that the fuel hydraulic diameter for a shear coax is

$$D_{hf} = D_{f2} - D_{f1} \qquad \text{(A-29)}$$

where:

D_{f2} = outer fuel annulus diameter

D_{f1} = inner fuel annulus diameter

and the fuel gap thickness

$$t_f = 1/2\ (D_{f2} - D_{f1}) \qquad \text{(A-30)}$$

Equation (A-22) can then be transformed as follows.

$$\frac{\delta}{t_f} = \frac{0.75\ (L/D_{hf})^{0.8}}{Re_{D_{hf}}^{0.2}} \qquad \text{(A-31)}$$

The comparable definitions of the two dimensional boundary and contraction coefficients are indicated in Equations (A-32) and (A-33), respectively.

$$C_b = C_{df} - 2\ (\delta_f/t_f) \qquad \text{(A-32)}$$

$$C_c = C_{df} + 2\ (\delta_f/t_f) \qquad \text{(A-33)}$$

The dynamic head ratio associated with the two-dimensional annular fuel velocity profile described by Equations (A-32) and (A-33) was numerically integrated. The two dimensional solution is shown on Figures 83 and 84 along with the axi-symmetric solution.

4. Minimum Potential Flow Fan Characteristic

Of the element types evaluated on this program, the swirler coaxial element, like-on-like doublet, and external impinging F-O-F triplet result in fan spreading characteristics. A mathematical description of the jet spreading rate is developed in subsection 2.

Swirler Coaxial Element

The oxidizer spray fan thickness for the swirler is given as follows:

$$t_o(L) = \frac{C_{do} * D_o}{4\,[1 + 2\,(L/D_o)\tan\phi]} \qquad \text{(A-34)}$$

The velocity boundary layer thickness can be approximated as shown below.

$$\delta(L) = \frac{0.75\,(L/D_o)^{0.8}\,(D_o/D_{ho})^{0.8}}{Re_{D_{ho}}^{0.2}} \left[\frac{1 - \sqrt{1 - C_{do}}}{2}\right] D_o \qquad \text{(A-35)}$$

The critical $(L/D_o)^*$ can be solved by equating twice Equation (A-35) to Equation (A-34) and approximating with the quadratic solution.

$$2\tan\phi\,(L/D_o)^{1.8} + (L/D_o)^{0.8} - \frac{C_{do}}{3}\left(\frac{Re_{d_{ho}}}{1 - \sqrt{1 - C_{do}}}\right)^{0.2} = 0$$

$$(L/D_o)^* = \left\{ \frac{\left[1 + \frac{8}{3}\left(\frac{Re_{d_{Ho}}}{1 - \sqrt{1 - C_{do}}}\right)^{0.2} C_{do}\tan\phi\right]^{1/2} - 1}{4\tan\phi} \right\}^{1.111} \qquad \text{(A-36)}$$

Similarly, solving for the fuel side,

$$t_f(L) = \frac{C_{df}\,[1 - (D_{f1}/D_{f2})^2]\,D_{f2}}{4\,[1 + 2\,(L/D_{f2})\tan\phi]} \qquad \text{(A-37)}$$

$$\delta_f(L) = \frac{0.75\,(L/D_{f2})^{0.8}\left(\frac{D_{f2}}{D_{f2} - D_{f1}}\right)^{0.8}}{Re_{D_{hf}}^{0.2}} \left(\frac{D_{f2} - D_{f1}}{2}\right) \qquad \text{(A-38)}$$

$$2 \tan \phi \, (L/D_{f2})^{1.8} + (L/D_{f2})^{0.8} - \frac{C_{df}}{3} \left[1 + \frac{D_{f1}}{D_{f2}}\right] \left[1 - \frac{D_{f1}}{D_{f2}}\right]^{0.8} Re_{d\,hf}^{0.2} = 0$$

$$(L/D_{f2})^{*} = \left\{ \frac{\left[1 + \frac{8}{3} \left(1 + \frac{D_{f1}}{D_{f2}}\right) \left(1 - \frac{D_{f1}}{D_{f2}}\right)^{0.8} Re_{D_{Hf}}^{0.2} C_{df} \tan \phi \right]^{1/2} - 1}{4 \tan \phi} \right\}^{1.111} \tag{A-39}$$

If the local L/D's exceed the critical values indicated by Equations (A-36) and (A-39) for oxidizer or fuel, respectively; the oxidizer and fuel minimum fan thicknesses predicted by Equations (A-34) and (A-37), respectively, must be evaluated at the critical length.

Like-on-Like Doublet

A similar derivation can be developed for the like doublet.

$$t(L) = \frac{\pi C_d D}{4 (L/D) \tan \phi \cos \alpha} \tag{A-40}$$

$$\delta(L) = \frac{0.75 (L/D)^{0.8}}{Re_D^{0.2}} \left(\frac{D}{2}\right) \tag{A-41}$$

$$(L/D)^{*} = Re_D^{0.111} \left(\frac{\pi C_d}{3 \tan \phi \cos \alpha} \right)^{0.555} \tag{A-42}$$

External Impinging F-O-F Triplet

Prior to calculating critical $(L/D)^{*}$'s for the F-O-F triplet, it must first be determined whether we are analyzing under-penetrated or over-penetrated conditions.

If $Y < 0.5 D_o$

$$t_o(L) = \frac{\pi C_{do} (1 - Om) D_o}{8 (L/D_o) \tan \phi}$$

The oxidizer velocity boundary layer can be calculated from Equation (A-41) above. Solving for the above set of equations,

$$(L/D_o)^* = Re_{do}^{0.111} \left[\frac{\pi C_{do} (1 - Om)}{6 \tan \phi}\right]^{0.555} \quad \text{(A-43)}$$

The corresponding fuel side equations are (A-41) and A-44) shown below.

$$t_f(L) = \frac{\pi C_{df} D_f}{8 (L/D_f) \cos \alpha_f \tan \phi} \quad \text{(A-44)}$$

$$\text{from which} \quad (L/D_f)^* = Re_{D_f}^{0.111} \left(\frac{\pi C_{df}}{6 \cos \alpha_f \tan \phi}\right)^{0.555} \quad \text{(A-45)}$$

On the other hand it can be shown that if $Y > 0.5\ D_o$, Equations (A-46) and (A-47) replaces (A-43) and (A-45), respectively.

$$(L/D_o)^* = Re_{d_o}^{0.111} \left[\frac{\pi C_{do} (1 - Om)}{12 \tan \phi}\right]^{0.555} \quad \text{(A-46)}$$

$$(L/D_f)^* = Re_{d_f}^{0.111} \left[\frac{\pi C_{df}}{3 \cos \alpha_f \tan \phi}\right]^{0.555} \quad \text{(A-47)}$$

5. Hot Fire Mixing Model Derivation

Prior to this program, ALRC had recognized that combustion effects significantly impeded the mixing process. Elements which developed 90-100% cold flow E_m within approximately 2.54 cm (1 in.) from the injector face were observed to deliver only about 70% E_m or less under combustion environments with approximately 12.7 cm (5 in.) chambers.

In recognition of this limitation a series of one atmosphere chamber pressure combustion tests designated herein as hot flow tests utilizing GH_2/GO_2 (without gaseous helium) propellants was conducted with the low velocity swirler coaxial element (see Section V). Other nominal element design parameters were F/E = 222 Newtons (50 lb_f), A_f/A_o = 0.5, O/F = 4, and T_p = 300°K (540°R). Mass spectrometer data were obtained at six radial locations at each of three axial stations to obtain local chemical composition data both with and without combustion. As expected on the basis of previous observations radical differences were noted in the mixture ratio profile with and without combustion. In support of this hot flow test data analysis, a general combustion model was formulated to describe the effects of combustion on the gas dynamics of the diffusion/mixing process. This portion of the analysis is general and applicable to any element type or propellant combination tested. Results of this general model were then extended to apply to the GH_2/GO_2 propellant combination and in particular to the swirler coaxial

element which was hot flow tested. It was thereupon found that the mathematical cold flow model previously derived for non-chemical reacting elements must be modified as indicated herein to account for combustion effects on the mixing process.

General Combustion Model Formulation

The continuity equation can be written and differentiated as follows:

$$\dot{w}_t = \rho A V \tag{A-48}$$

$$\frac{d\dot{w}_t}{\dot{w}_t} = \frac{d\rho}{\rho} + \frac{dA}{A} + \frac{dV}{V} \tag{A-49}$$

From the principle of conservation of total mass, $d\dot{w}_t = 0$. Therefore, from Equation (A-49),

$$\frac{d\rho}{\rho} = -\left[\frac{dA}{A} + \frac{dV}{V}\right] \tag{A-50}$$

The equation of state for a mixture of assumed perfect gas approximation can be written and differentiated as follows:

$$P = \rho \frac{Ro}{MW} T \tag{A-51}$$

$$\frac{dP}{P} = \frac{d\rho}{\rho} - \frac{dMW}{MW} + \frac{dT}{T} \tag{A-52}$$

Equations (A-50) and (A-52) can be combined and transposed into the following form.

$$\frac{dP}{P} + \frac{dA}{A} + \frac{dV}{V} = \frac{dT}{T} - \frac{dMW}{MW} \tag{A-53}$$

The right hand member of Equation (A-53) characterizes the combustion effect of a gaseous propellant stream. The left hand member describes the gas dynamic result acting upon the reacting stream. Equation (A-53) is a basic derivation which is applicable to any element type and any gaseous propellant combination. (To be applicable to a liquid or solid propellant mixture, additional terms are required to account for the intermediate phase change.)

The physical significance of the right hand member is as follows. If the combustion stoichiometry is such that the mole-weighted molecular weight of the product gas mixture is lighter than the mole weighted reactant gas mixture, its contribution is positive, and vice versa. This chemical effect is

a relatively small contribution in comparison with the thermodynamic effect reflected in the temperature term. All reactions of interest for rocket engines depend on propellant systems whose product gas (combustion flame) temperature is approximately one order of magnitude higher than the incoming reactant gas temperature. Therefore, the summation of the right hand member of Equation (A-53) is always positive and generally between 3 to 30 and depends only upon the propellant combination and O/F.

The physical significance of the left hand member is as follows. If combustion were to occur at constant volume, $dA = dV = 0$ and the static pressure would have to rise proportional to the chemical effect characterized by the right member. On the other hand, near the injector face plane the total propellant orifice area is considerably smaller than the chamber cross-sectional area. From the momentum equation $dV = 0$, and if $dP \simeq 0$ then the gas flow area must increase; $dA > 0$. If low contraction ratio chambers are used it is probable that at some point the hot gas cross section may fill the entire combustor flow area. Beyond that point no recirculation exists, $dA = 0$ and $dV > 0$ due to flow acceleration dictated by the continuity equation. From the subsonic compressible flow equations, the increase in gas velocity must result in a reduction in static pressure, $dP < 0$. Even if chemical reaction is completed (right hand member of Equation (A-53) equal to zero), in the throat convergent section ($dA < 0$) the gas velocity must accelerate ($dV > 0$) and the static pressure must decrease ($dP < 0$). Incidentally, if the right hand member of Equation (A-53) is set equal to zero, the trivial solution which results, characterizes non-reacting cold flow conditions. If, in addition, $dP = 0$, the solution is characteristic of a free jet diffusion.

In spite of the gross simpliciations made in the derivation of Equation (A-53), it is obvious that many additional real conditions of gaseous propellant systems can be described by Equation (A-53) depending upon the assumptions made concerning applicable boundary constraints. The inter-relationships of chemical reaction, heat release, static pressure, flow area, and velocity are linked through Equation (A-53). The necessary limiting assumptions and simplifications can only be readily obvious by considering the real physical mechanism under analytical consideration, i.e., Equation (A-53) is a mechanistic equation.

Application of Hot Flow Model to Swirler Coaxial Element Using GH_2/GO_2 Propellants

The following simplified stoichiometry is suggested to describe GH_2/GO_2 combustion at an overall O/F = 4.0.

$$4\ H_2 + O_2 \rightarrow 2\ H_2O + 2H_2 \qquad \text{(A-54)}$$

A numerical example is presented that illustrates the combustion effect on the right hand member of Equation (A-53). In this example the reactants are characterized by the subscript 1 and the products by the subscript 2. Assume initial reactant temperatures are at 300°K (540°R).

$$MW_1 = [n_{H_2}\ MW_{H_2} + n_{O_2}\ MW_{O_2}] / (n_{H_2} + n_{O_2})$$

$$MW_1 = (4 \times 2 + 1 \times 32) / (4 + 1) = 8$$

$$MW_2 = [n_{H_2O}\ MW_{H_2O} + n_{H_2}\ MW_{H_2}] / (n_{H_2O} + n_{H_2})$$

$$MW_2 = [2 \times 18 + 2 \times 2] / (2 + 2) = 10$$

$$T_1 = 300°K = 540°R$$

$$T_2 = 3020°K = 5436°R$$

$$\frac{dMW}{MW} = \frac{MW_2 - MW_1}{MW_1} = \frac{10 - 8}{8} = +0.25$$

$$\frac{dT}{T} = \frac{T_2 - T_1}{T_1} = \frac{3020 - 300}{300} \quad \text{or} \quad \frac{5436 - 540}{540} = +9.07$$

Therefore:

$$\frac{dT}{T} - \frac{dMW}{MW} = 9.07 - 0.25 = +8.82$$

From which

$$\frac{dP}{P_1} + \frac{dA}{A_1} + \frac{dV}{V_1} = +8.82 \ (@\ O/F = 4)$$

Similarly the right hand member of Equation (A-53) was evaluated in an identical manner at a multitude of other mixture ratio points ranging from O/F = 0.1 to 1000. The numerical results are shown on Figure 76 of the main text. At O/F = 0 (pure H_2) and O/F = ∞ (pure O_2), the limits correspond to non-reacting cold flow and the right hand member vanishes. Figure 76 shows the right hand member varies from approximately 0 to 10. It is not surprising to find that the peak occurs at the stoichiometric O/F. Thus incipient combustion effects will always tend to separate the unreacted fuel from the unreacted oxidizer to impede the mixing process. The method of incorporating the above calculated reaction data into the earlier cold flow mixing model is described in Section VIII of the main text.

It has been shown that the non-reacting cold flow swirler coaxial model incorporates a diverging hollow cone oxidizer jet with an annular fuel stream. The initial injection momentums define the resultant hydraulic cone divergence angle. Incipient combustion must initially occur along this fuel-oxidizer interface. Viscous boundary layer drag initially decelerates a

small portion of the fuel and oxidizer causing initial species diffusion from the potential core. This causes minute concentrations of oxidizer and fuel to diffuse into each other forming a near stoichiometric boundary separating the two. Due to the momentum equation and in spite of the viscous boundary layer drag, dV is negligible very close to the injector face plane. Empirically it is known that gases cannot sustain high shear forces or radial pressure gradients and dP/P_1 is on the order of 1% or less and is negligible. Therefore the energy release must be accounted for almost entirely by an increase in the injection gas stream area.

As an initial approximation, the combustion effects on the Reynolds number were neglected since the calculated boundary layer thickness is only weakly dependent to the 2/10-th power of the Reynolds number. On the other hand, the heat release was assumed to have a first order effect on the potential flow gas stream characteristic dimension. Heat addition to and area increase of the hollow oxidizer cone relative to its resultant hydraulic momentum angle show that the rate of oxidizer flow area increase is greater than the rate of cone divergence causing the hollow oxidizer cone to collapse into a solid cylindrical jet within a short distance from the injector face. Thus at any given L/D from the injector face, the hot flow boundary layer thickness is comparable to the corresponding cold flow boundary layer thickness; but the hot flow potential flow stream characteristic dimension is considerably larger than the cold flow dimension. This results in a very slow rate of decrease in the hot flow boundary coefficient (C_b). Likewise, the local dynamic head to injection dynamic head ratio ($\rho V^2/\rho V^2$), decreases very slowly accounting for the slow rate at which the initial injection concentration approaches the equilibrium design value. In addition to the above features, the hollow oxidizer cone collapse reduces the wetted perimeter on which diffusion occurs from both inner and outer surfaces of the hollow oxidizer annulus to only the outer surface of the collapsed cylindrical surface. This increases the hydraulic diameter, reduces effective L/D and further retards turbulent mixing with combustion.

A high oxidizer swirl cone angle and low oxidizer discharge coefficient can delay the swirl cone collapse. This in turn improves performance. Downstream of the collapse point the mixing rate is similar to the shear coaxial element. However, within the distance from the injector face plane to the initial swirl cone collapse point, the swirler coaxial element achieves a much higher mixing efficiency than a shear coaxial within the same length. Thus, it is necessary to calculate the longer equivalent chamber length which would have been required by a shear coaxial element to achieve the same mixing distribution as the swirler coaxial element at its collapse point. This length differential quantitatively represents the advantage of the swirler over the shear coaxial in a combustion environment.

6. Shear Coaxial Element Mixing Model

Having established the above mathematical preliminaries, it is now possible to analytically predict and verify with experimental data the mixing rate for a shear coaxial element.

Two fundamental types of cold flow data were measured at various transverse probe positions and variable axial stations on this program. A mass spectrometer measured the local mole fraction chemical compositions of H_2 (fuel), N_2 (oxygen simulant), and H_e (base bleed). From this data it was possible to determine the local mixture ratio profile. Pitot tube measurements of local dynamic pressure heads were also obtained to determine local mass flux at each probe position.

For shear coaxial elements the oxidizer injection dynamic head at the injector face plane is essentially equal to the oxidizer injector manifold pressure to P_c differential. At the injector face plane it is known that the initial cold flow oxidizer mole fraction must be 100% N_2 and that $E_m = 0$. Far downstream when the gas is assumed uniformly mixed ($E_m = 100\%$), and the local dynamic head is negligible, the equilibrium N_2 mole fraction can be calculated as follows.

$$x_{N_2,\ eql} = \frac{\dfrac{\dot{w}_{N_2}}{MW_{N_2}}}{\dfrac{\dot{w}_{N_2}}{MW_{N_2}} + \dfrac{\dot{w}_{H_2}}{MW_{H_2}} + \dfrac{\dot{w}_{H_e}}{MW_{H_e}}} \qquad \text{(A-55)}$$

Figure 85 shows the experimental relationship between the measured dynamic head ratio vs the measured N_2 mole fraction on the element axis. It was noted from Figure 85 that the empirical rate of change of species mole fraction from its 100% pure initial value to its asymptotic equilibrium value was directly proportional to the rate of change in local element dynamic head, starting from its initial injection value to its asymptotic uniform negligible value. The above relationship indicated that the empirical mass diffusion rate is directly proportional to the momentum transfer rate. Based on the above data, it became clear turbulent diffusion is a force initiated mechanism which can be characterized better by Newton's equation of motion rather than by the molecular diffusion equation modified with a turbulent eddy viscosity. The driving force responsible for turbulent mixing is the radial pressure gradient potential. The dynamic pressure dissipation rate was analytically predicted by integrating the velocity head across the potential flow characteristic dimension described in subsection 2 of this appendix modified for the boundary layer calculated from subsection 3. Thus, it was postulated that if it were analytically possible to predict the axial rate of dynamic pressure dissipation that by inferrence it would also be possible to predict the mass diffusion and mixing rate.

The analytically predicted axial profile of oxidizer local dynamic head using the numerical solution from Figures 83 and 84 is plotted on Figure 86 vs L/D for the 67 Newton (15 lbf) shear coaxial element. The experimental oxidizer dynamic head measured on the element axis probe is shown for comparison. Figure 86 shows that, in spite of the many gross mathematical approximations which were made, the calculated dynamic head decay rate based on a viscous boundary layer mechanism closely approximates the experimental trend. The predicted fuel dynamic head profile is also shown on Figure 86. It is obvious that the calculated fuel dynamic head dissipation rate occurs considerably faster than for the oxidizer.

The experimental dynamic pressure downstream of the fuel annulus was not available for direct comparison with the analysis. This is because the midpoint of the fuel annulus occurs on a 0.092-in. radius and the nearest experimental probes are on a 0.125-in. radius. Near the injector face where the gradients are steep, the 0.033-in. radial mismatch is significant in comparison with the fuel annulus dimension (t_f = 0.028 in.). Nevertheless, for lack of better data, the eight probes on the 0.125-in. radius were averaged as a measured lower limit of the fuel dynamic head. The correlations indicated in Figure 86 show that it is possible to analytically predict either axi-symmetric or two dimensional jet dynamic head dissipation rates based on a consideration of design parameters.

The above dissipation rates have been treated independently as if each were acting alone. In reality, the two solutions must be coupled and the interaction of one must be considered on the other. The above equations are only valid upstream of the point where the oxidizer and fuel boundary layers initially come into contact. Downstream of this point, the two jets combine to act as one. The contribution of each to the resultant jet must be proportional to their respective mole fractions since mixing occurs on a molecular basis. Since the rapid mixing zone near the injector face is controlled by Newton's equations of motion, the primary normalizing parameter must be the injection dynamic head since this provides the mixing potential. Therefore, define an equivalent injection dynamic head, Pd_{eq} which is the overall result of the separate fuel and oxidizer contributions.

$$Pd_{eq} = \frac{\frac{\dot{w}_o}{MW_o} \times Pd_o + \frac{\dot{w}_f}{MW_f} \times Pd_f}{\frac{\dot{w}_o}{MW_o} + \frac{\dot{w}_f}{MW_f}} \qquad \text{(A-56)}$$

The above relationship can be simplified to

$$Pd_{eq} = \frac{Pd_o + \frac{MW_o/MW_f}{O/F} \times Pd_f}{1 + \frac{MW_o/MW_f}{O/F}} \quad \text{(A-57)}$$

It is then possible to analytically predict the axial mole fraction decay rate of both fuel and oxidizer as indicated below.

$$x_o(L) = x_{o,\,eql} + \frac{Pd(L)}{Pd_o} \left(\frac{Pd_o}{Pd_{eq}}\right)^{F_o} (x_{o\ initial} - x_{o,\,equilibrium}) \quad \text{(A-58)}$$

$$x_f(L) = x_{f,\,eql} + \frac{Pd(L)}{Pd_f} \left(\frac{Pd_f}{Pd_{eq}}\right)^{F_f} [x_{f\ initial} - x_{f,\,equilibrium}] \quad \text{(A-59)}$$

In general the cold flow interaction exponent (F) represents the ratio of the common fuel-oxidizer wetted perimeter available for interpropellant mixing divided by the total fuel or oxidizer wetted perimeter available for diffusion and shear mixing.

$$F = \frac{\text{Bi Propellant Interaction Area}}{\text{Total Wetted Perimeter}} \quad \text{(A-60)}$$

For example, the shear coaxial element has $F_o = 1.0$ because the oxidizer jet is completely surrounded by the fuel annulus; but $F_f = 0.5$ because bipropellant interaction only occurs on the inside surface of the fuel annulus.

The analytically predicted oxidizer mole fraction decay rate for a shear coaxial element using Equations (A-1), (A-2), (A-8), (A-57), and (A-58) is plotted on Figure 87. The experimentally measured maximum oxidizer mole fraction which occurs on the coaxial element axis is plotted for comparison. Again, the mathematically predicted N_2 composition profile provides an adequate first order approximation to the measured local compositions. Likewise, the calculated fuel mole fraction profile is plotted on Figure 87, and the 0.125-in. radius probe measured compositions were averaged and plotted with the full realization that the actual maximum fuel mole fraction might be somewhat higher than shown.

It should be remembered that, near the injector face, the radial dynamic head gradient and species gradient are very steep. A deviation as small as one probe diameter from perfect concentricity between the element centerline and the probe measurement position could significantly influence the measured data. Thus, it is probable that the real (unmeasured) data may actually be in better agreement with the analytical prediction than the experimentally measured data shown in Figures 86 and 87. Therefore, it can

be concluded that the viscous boundary layer solutions provide an acceptable theoretical model of the shear coaxial mixing rate as a function of length.

The experimental shear coaxial mixing data in Figures 12 and 13 indicate high performance at low A_f/A_o or low O/F. Both cases result in low Pd_o/Pd_f ratio. From Equations (A-57) and (A-58) these influences are quantitatively predicted. Figure 88 shows a correlation of experimental E_m's vs the aforementioned oxidizer diffusion parameter prediction. In the range from 0 to 30 L/D at nominal (4.0) O/F and 2.0 to 6.5 O/F at L/D = 7, a nearly linear correlation is obtained verifying the validity of the approximate mathematical mixing model.

The analytical development described thus far has utilized the shear coaxial element as an example because many O_2/H_2 injectors have been developed using coaxial injectors. Another reason is that two basically different analytical solutions result for axi-symmetric and two dimensional mixing characteristics and the shear coaxial incorporates both characteristics for oxidizer and fuel respectively. The fact that axi-symmetric and two dimensional mixing characteristics differ has been experimentally verified by empirical turbulent eddy viscosity correlations which notethat two different empirical correlation constants are required.

7. Other Element Mixing Models

The model derived to this point is valid for those element types whose potential flow characteristic dimensions remain constant with increasing axial length. For a summary of elements that satisfy this condition review subsection 2.

Another series of element families exist whose transverse injection momentum components cause diverging fans whose characteristic potential flow thickness initially decrease inversely proportional to increasing L/D.

$$\frac{t(L)}{D(0)} \propto \frac{K_1}{L/D} \qquad \text{(A-61)}$$

or

$$\frac{t(L)}{D(0)} \propto \frac{K_2}{1 + K_3\ (L/D)} \qquad \text{(A-62)}$$

where:

$t(L)$ = characteristic potential flow dimension at length, L

$D(0)$ = characteristic potential flow dimension at the injector face plane

K_i = appropriate design constants defined in subsection 2

Again, see subsection 2, to determine which elements satisfy this behavior. These latter element types dissipate their injection dynamic heads at a considerably faster rate with L/D because not only do their velocity boundary layer thickness increase proportional to $(L/D)^{0.8}$, but their characteristic potential flow dimension from which δ is subtracted to define C_b (Equations (A-4) and (A-12)) decreases.

The characteristic potential flow dimension of these diverging fans do not decrease in thickness indefinitely with increasing (L/D), however. A critical $(L/D)^*$ exists for each element which characterizes its minimum allowable potential flow spray fan thickness. This critical $(L/D)^*$ occurs when the increasing velocity boundary layer thicknesses from both sides of the spray fan just equals the local potential flow thickness.

$$2 \times \delta \left[@ (L/D)^*\right] = t \left(@ (L/D)^*\right] \qquad \text{(A-63)}$$

Specific application of this criterion to the various applicable elements is derived mathematically in subsection 4. The physical significance of $(L/D)^*$ is as follows. The normal component of injection momentum causes the spray fan to spread perpendicular to the orifice plane. Lateral spreading of the spray fan causes the fan to become thinner from momentum and continuity considerations (see subsection 2). At the critical $(L/D)^*$ when Equation (A-63) is satisfied the radial component of the injection momentum has been dissipated by viscous drag with the chamber recirculation gases and further radial fan spreading ceases. Thus $(L/D)^*$ represents the asymptotic limit beyond which the potential flow fan geometry essentially remains constant.

The equations introduced thus far in conjunction with those from subsections 2 and 4 are sufficient to predict the axial mole fraction decay rate of any shear mixing family of elements. The shear mixing elements include shear coaxial, increased shear coaxial, swirler coaxial, like-on-like doublets, and parallel sheet (showerhead) elements. The shear mixing elements are characterized by having their initial fuel mole fraction start with 100% H_2 and whose initial oxidizer mole fractions are 100% N_2 or O_2. On the other hand, the penetration mixing elements (premix and external impinging F-O-F triplets) start with an initial concentration already premixed to some degree very near the injector face plane even with zero boundary layer growth and diffusion. The degree of premix effectiveness depends upon the design parameters as described below.

In spite of the difference in numbers of fuel orifices per element, the premix triplets and pentads can be characterized similarly. The primary design parameter of the premix element was discovered to be its cup ΔP. In the designs tested on this program the mixing cup area was equal to the oxidizer area; and the fuel area varied between 0.5 to 2.0 times the oxidizer area. The measured cup ΔP was averaged between the fuel and oxidizer injector ΔP's less their respective injection dynamic heads entering the mixing cup.

$$\Delta P_{cup} = \frac{1}{2}\left[(P_{fJ} - P_c - Pd_f) + (P_{oJ} - P_c - Pd_o)\right] \quad \text{(A-64)}$$

The initial premix oxidizer and fuel concentrations at the mixing cup exit were calculated from Equations (A-65) and (A-66) below.

$$x_o(0) = x_{o,\,eql} + \frac{Pd_o}{Pd_o + \Delta P_{cup}} \left(1.000 - x_{o,\,eql}\right) \quad \text{(A-65)}$$

$$x_f(0) = x_{f,\,eql} + \frac{Pd_f}{Pd_f + \Delta P_{cup}} \left(1.000 - x_{f,\,eql}\right) \quad \text{(A-66)}$$

Notice the similarity between Equations (A-65) and (A-66) with Equations (A-58) and (A-59), respectively. Again, the similarities are based upon the premise that turbulent mixing is governed by Newton's equation of motion and pressure potentials. The initial concentrations at the injector face plane predicted by Equations (A-65) and (A-66) are then utilized in Equations (A-58) and (A-59) to determine local concentrations as a function of chamber length.

In general, the cup ΔP calculated by Equation (A-64) is maximized at low O/F which increased the total number of gas moles at constant weight flowrate because of lower fuel molecular weight; or at constant O/F, cup ΔP increases at low A_f/A_o ratios because higher fuel injection momentum normal to the axial oxidizer jet decreases cup discharge coefficient.

The initial premix composition of the F-O-F triplet element depends upon the fuel penetration ratio into the oxidizer jet. For two fuel impinging diametrically opposed on a single oxidizer, a penetration ratio of one-half is optimum and results in highest performance.

In reference 15 it was found from empirical penetration studies that

$$\frac{Y}{D_f} = K_p \frac{V_f \sin \alpha_f}{V_o} \left(\frac{\rho_f}{\rho_o}\right)^{1/2} \quad \text{(A-67)}$$

where:

Y = fuel penetration distance into oxidizer stream

K_p = empirical penetration coefficient

The investigators in Reference 15 found $K_p = 2.5$ for gas/liquids and $K_p = 3.2$ for GHe/GN_2.

Based upon the experimental test data from the current program, Equation (A-67) above was transformed to the following form for single element F-O-F triplet cold flow tests.

$$\frac{Y}{D_o} = 0.62 \sin \alpha_f \frac{D_f}{D_o} \left(\frac{1/2\ \rho_f\ V_f^2}{1/2\ \rho_o\ V_o^2} \right)^{0.1} \quad \text{(A-68)}$$

For underpenetrated jets ($Y < 0.5\ D_o$) the initial oxidizer and fuel premix concentrations can be approximated as follows.

$$x_o(0) = 1.000 - \left[\frac{Y/D_o}{0.5} \quad (1 - Om) \right] \left[\frac{1}{1 + \frac{(O/F)_p}{MW_o/MW_f}} \right] \quad \text{(A-69)}$$

and $$x_f(0) = \frac{1}{1 + \frac{(O/F)_p}{MW_o/MW_f}} \quad \text{(A-70)}$$

where $$(O/F)_p = \frac{(Y/D_o)}{0.50} \quad (1 - Om)\ (O/F) \quad \text{(A-71)}$$

For over-penetrated jets ($Y \geq 0.5\ D_o$) the initial concentrations are calculated below.

$$x_o(0) = \frac{\frac{(O/F)_p}{MW_o/MW_f}}{1 + \frac{(O/F)_p}{MW_o/MW_f}} \quad \text{(A-72)}$$

$$x_f(0) = \frac{1}{1 + \frac{(O/F)_p}{MW_o/MW_f}} \quad \text{(A-73)}$$

The above equations can then be used as applicable to predict the initial concentrations to be used in Equations (A-58) and (A-59) for external impinging F-O-F triplets.

As part of the data correlation analysis, specific mixing models were developed for each family of elements which were cold flow tested. Element design parameters and test operating conditions were then input into the analytical mixing computer model to predict local dynamic heads, mole fractions, mixture ratio distributions, E_m, η_m, C* efficiency, energy release efficiency (ERE), and other hydraulic parameters for each test point summarized in Table III.

Although the details contained in each specific element model are too numerous to itemize, a cursory description of the basic equations will be summarized below to provide the reader with an understanding behind the model formulation concept. It was felt that to include all the details of each element model formulation would become so complex that it would discourage the reader from attempting to utilize the models for design or analysis purposes. In Section VIII of the main text, the solutions from these individual models are condensed into a generalized analysis technique which is applicable to any of these elements and in simple enough form to encourage its use as a universal gas/gas Design Calculation Procedure.

For each element and test point, the following parameters were given or assumed as model inputs. For sake of brevity where both fuel and oxidizer parameters are applicable the propellant subscripts will be deleted and the equation will only be written once with the understanding that in the model, oxidizer and fuel were accounted for separately. The input parameters were propellant temperature, T_p; molecular weight, MW; pressures, P; weight flow rates, $\dot{w}$; base bleed mass fraction, $\dot{w}_{He}/(\dot{w}_o + \dot{w}_f + \dot{w}_{He})$; orifice areas, A; discharge coefficients, C_d; viscosities, μ; interaction exponents, F, and axial length, L.

The first step was to calculate propellant gas density.

$$\rho = \frac{P\ (MW)}{R_o\ T_p} \tag{A-74}$$

Injection velocities and injection dynamic heads were calculated next.

$$V = \frac{\dot{w}}{\rho A\ C_d} \tag{A-75}$$

$$Pd = 1/2\ \rho\ V^2 \tag{A-76}$$

The hydraulic diameters at the injector face, L/D_h, and one dimensional Reynolds numbers based on diameter were calculated next.

$$D_h = \frac{4\ (\text{Area})}{\text{Wetted Perimeter}} \quad \text{and } L/D_h \tag{A-77}$$

$$Re_{d_h} = \frac{\rho\ (C_d\ V)\ D_h}{\mu} \tag{A-78}$$

Equilibrium mole fractions and equivalent dynamic heads were previously defined in Equations (A-55) and (A-57). Equations (A-23) and (A-31), based on injector face potential flow properties, were used to calculate the velocity boundary layer thicknesses for axi-symmetric or two dimensional element characteristics.

For divergent fan two dimensional elements, if $L/D_h \leq (L/D)^*$ use L/D_h; if $L/D_h > (L/D)^*$ use $(L/D)^*$ to calculate t(L) at $(L/D)^*$ (see subsections 2 and 4). For two dimensional characteristics

$$\frac{C_b}{C_d} = \frac{t(L) - 2\delta}{t(L)} \tag{A-79}$$

If $C_b > 0$ find axi-symmetric dynamic head ratio from Equation (A-28) or Figure 82 and two dimensional dynamic head ratio from Figure 83. If $C_b < 0$ find dynamic head ratios from Figure 84.

For penetration mixing elements, the initial premix mole concentrations are defined in the front of this subsection. For all shear mixing elements the initial mole concentration is 100%. Equations (A-58) and (A-59) can then predict the oxidizer rich and fuel rich mole fractions for any element and any cold flow test.

$$O/F_j = \frac{x_o(L)\,[1 - x_{o,\,eql}]}{x_{f,\,eql}\,[1 - x_o(L)]} \cdot \frac{MW_o}{MW_f} \tag{A-80}$$

$$O/F_i = \frac{x_{o,\,eql}\,[1 - x_f(L)]}{x_f(L)\,[1 - x_{f,\,eql}]} \cdot \frac{MW_o}{MW_f} \tag{A-81}$$

Further, define the following parameters

$$\eta_j = \frac{O/F}{(O/F)_j} \leq 1.0 \tag{A-82}$$

$$\eta_i = \frac{(O/F)_i}{O/F} \leq 1.0 \tag{A-83}$$

$$U = \eta_j \frac{(1 - \eta_i)}{(1 - \eta_j)} \tag{A-84}$$

From which the mass fractions in stream tubes i and j can be calculated so that the overall O/F is nominal.

$$x_j = \frac{U}{(1 + U)} \frac{[1 + (O/F)_j]}{[1 + (O/F)]} \tag{A-85}$$

$$x_i = 1 - x_j \tag{A-86}$$

Based upon the above calculations the following performance parameters can be predicted.

$$E_m = 100 \left\{ 1 - x_j \left[\frac{(O/F)_j - (O/F)}{1 + (O/F)_j} \right] - x_i \left[\frac{(O/F) - (O/F)_i}{(O/F)\,[1 + (O/F)_i]} \right] \right\} \quad \text{(A-87)}$$

$$\eta_m = 100\,[x_j \cdot \eta_j + x_i \cdot \eta_i] \quad \text{(A-88)}$$

$$\%C^* = \frac{x_j \cdot C^*\,(O/F)_j + x_i \cdot C^*\,(O/F)_i}{C^*\,(O/F)} \quad \text{(A-89)}$$

$$\%ERE = \frac{x_j \cdot I_{sp}\,(O/F)_j + x_i \cdot I_{sp}\,(O/F)_i}{I_{sp}\,(O/F)} \quad \text{(A-90)}$$

8. Generalized Treatment of Swirler Coaxial Element with Combustion Effects

Section VIII,C in the text described the synthesis of the specific element mixing models detailed herein into a simpler generalized mixing correlation procedure. In a combustion environment, the swirler coaxial element requires special treatment in the generalized model. The following procedure utilizing the generalized charts is recommended. Evaluate the hollow cone swirler for hot fire conditions using small increments of axial step sizes. Calculate the axial length at which the hollow cone collapses.

$$L_{collapse} = \left[\frac{1 - \sqrt{C_{do}\,(1 + Da_o)}}{2 \tan \phi} \right] \left[\frac{4\,A_o}{\pi} \right]^{1/2} \quad \text{(A-91)}$$

Notice that Da_o in Equation (A-91) is a function of L. To assure numerical accuracy it is recommended that at least ten points be evaluated between the injector face plane and the collapse point and evaluate the oxidizer composition at the collapse point. Then parametrically analyze a similar shear coaxial design as a function of L and define a transition length, L-Prime, at which the shear coaxial oxidizer composition is identical to the swirler composition at the collapse point. Again, at least ten intermediate points from the injector face to L-Prime are recommended for numerical accuracy. Finally, use the hollow cone swirler combustion profile from the injector face to the collapse point and the shear coaxial solution evaluated at a pseudo-length defined by Equation (A-92).

$$L_{Apparent\ Shear} = L_{Physical\ Swirler} + [(L\text{-Prime}) - L_{Collapse}] \quad \text{(A-92)}$$

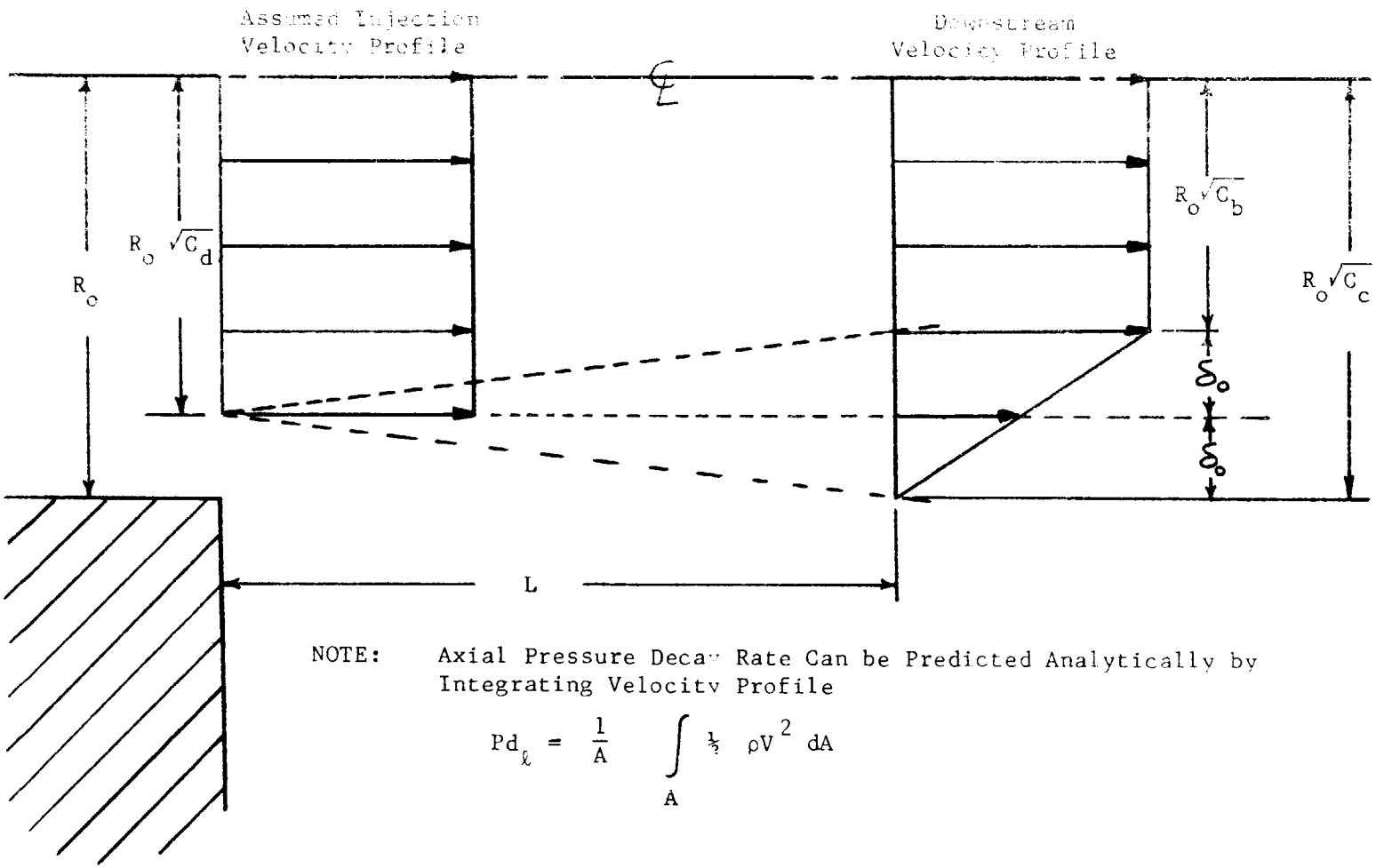

NOTE: Axial Pressure Decay Rate Can be Predicted Analytically by Integrating Velocity Profile

$$Pd_{\ell} = \frac{1}{A} \int_A \tfrac{1}{2} \rho V^2 \, dA$$

FIGURE 82. SCHEMATIC VELOCITY DECAY PROFILE FOR SHEAR MIXING

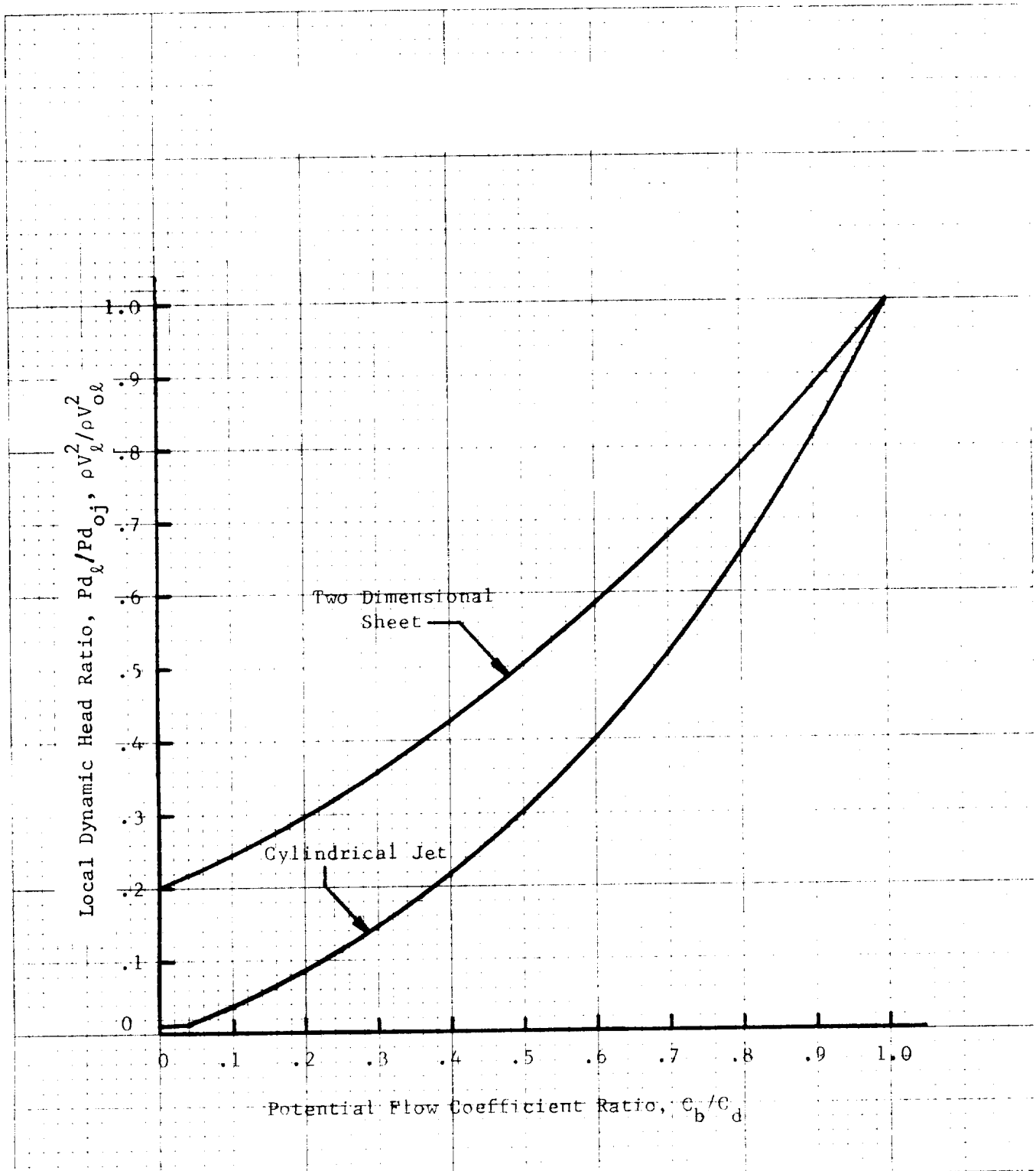

FIGURE 83. THE EFFECT OF BOUNDARY LAYER POTENTIAL FLOW RATIO UPON THE DYNAMIC HEAD RATIO

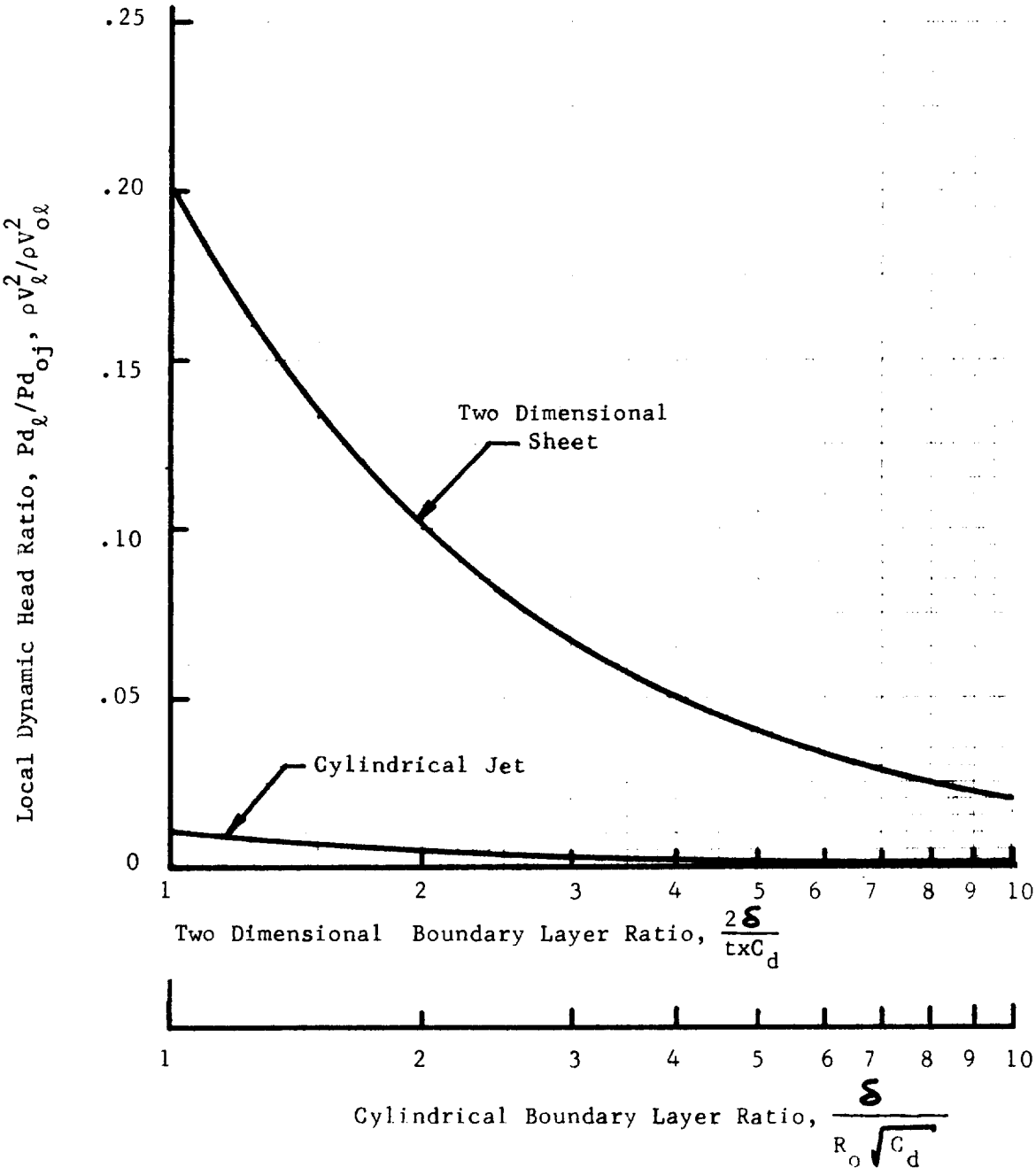

FIGURE 84. LOCAL DYNAMIC HEAD RATIO FOR FULLY DEVELOPED BOUNDARY LAYER FLOW

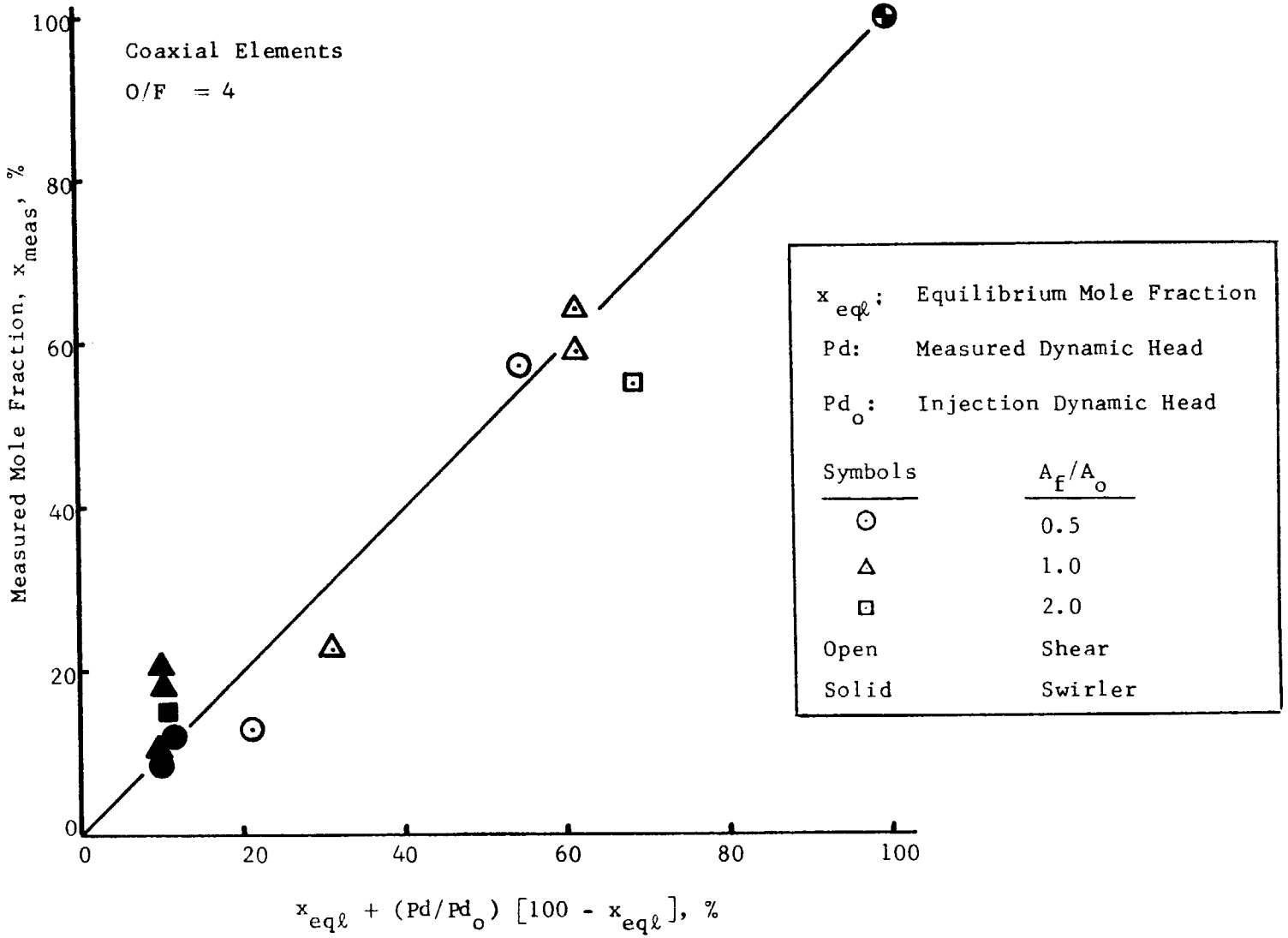

FIGURE 85. EXPERIMENTAL RELATIONSHIP BETWEEN PRESSURE DECAY AND MASS DIFFUSION

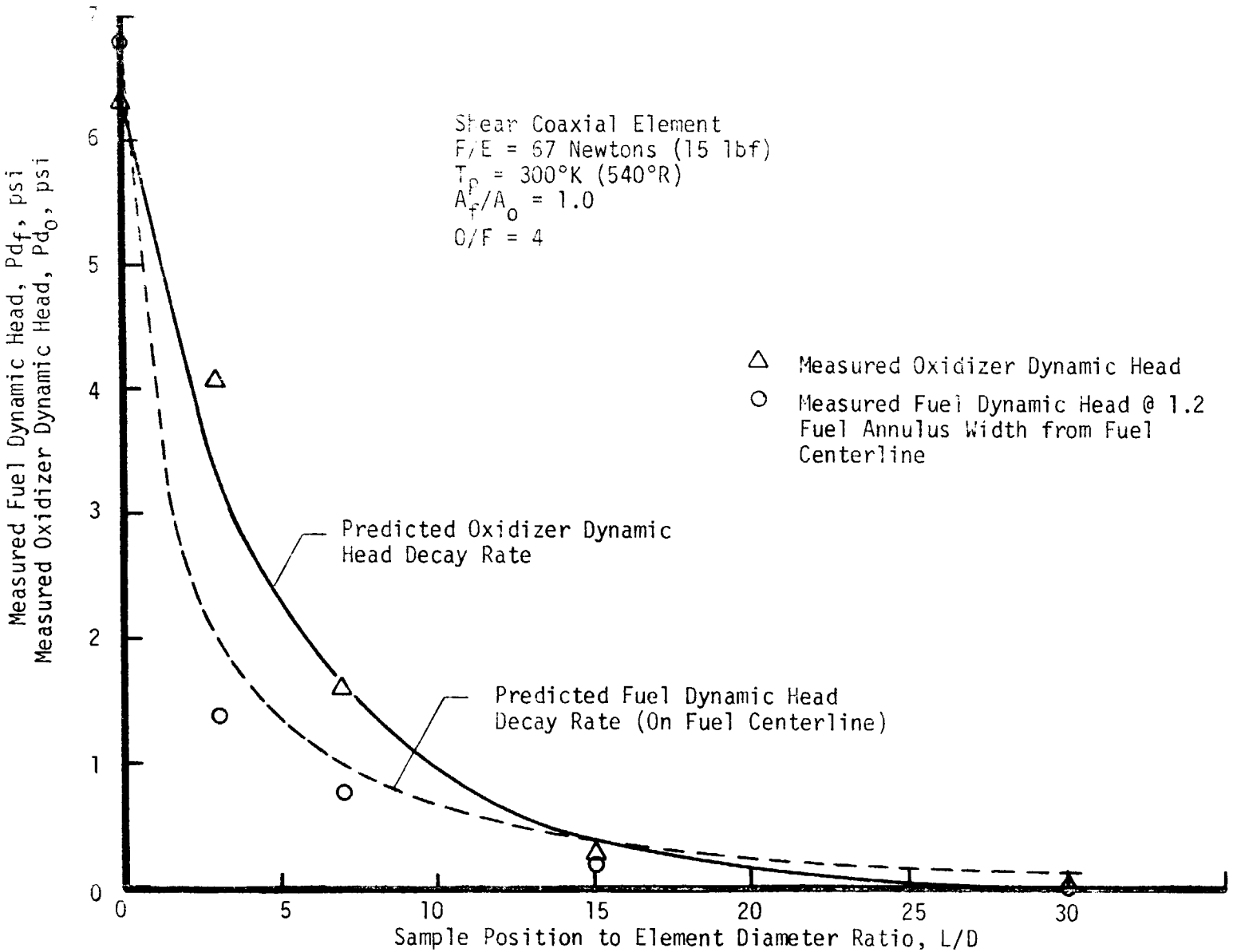

FIGURE 86. DYNAMIC HEAD DECAY

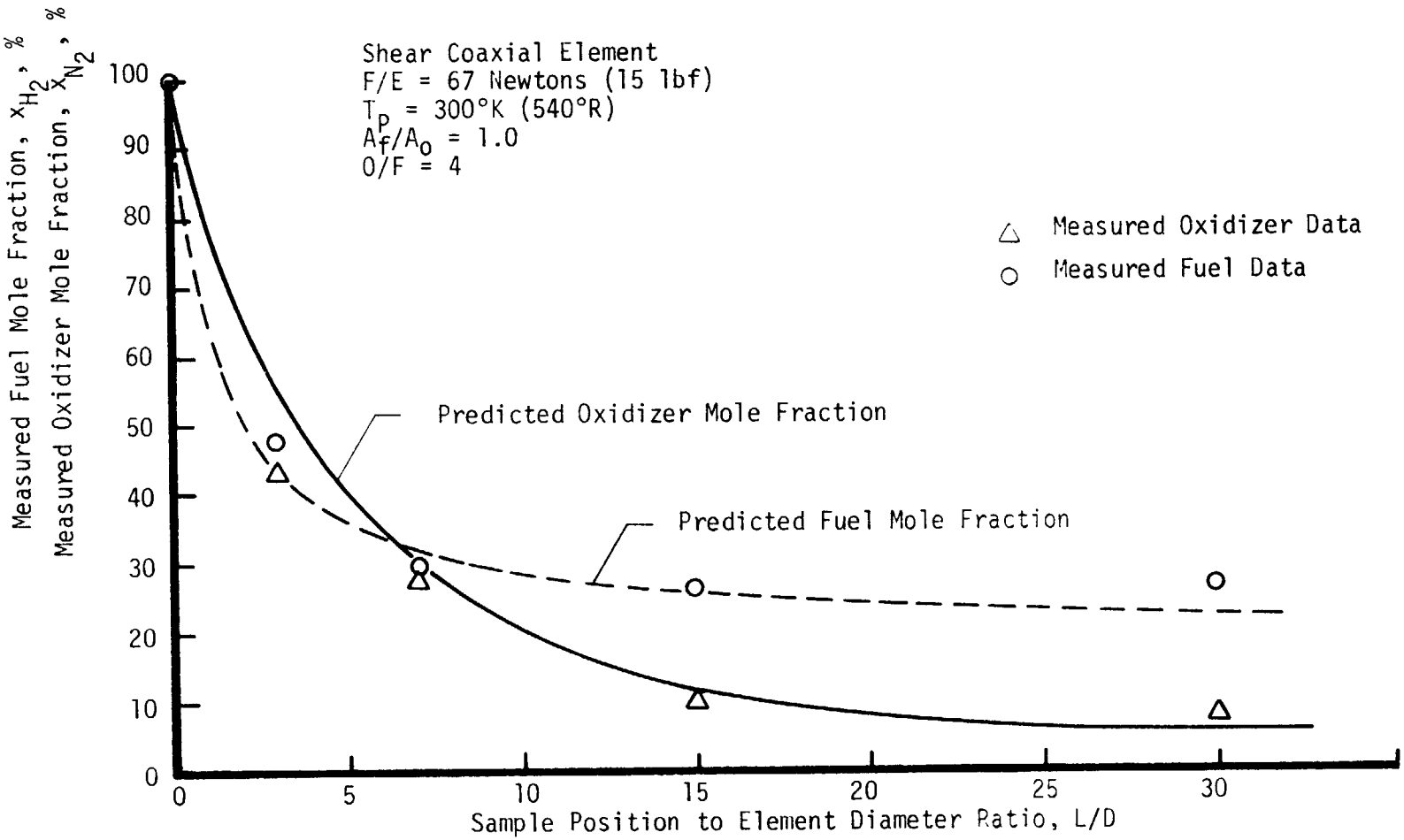

FIGURE 87. MOLE FRACTION DECAY

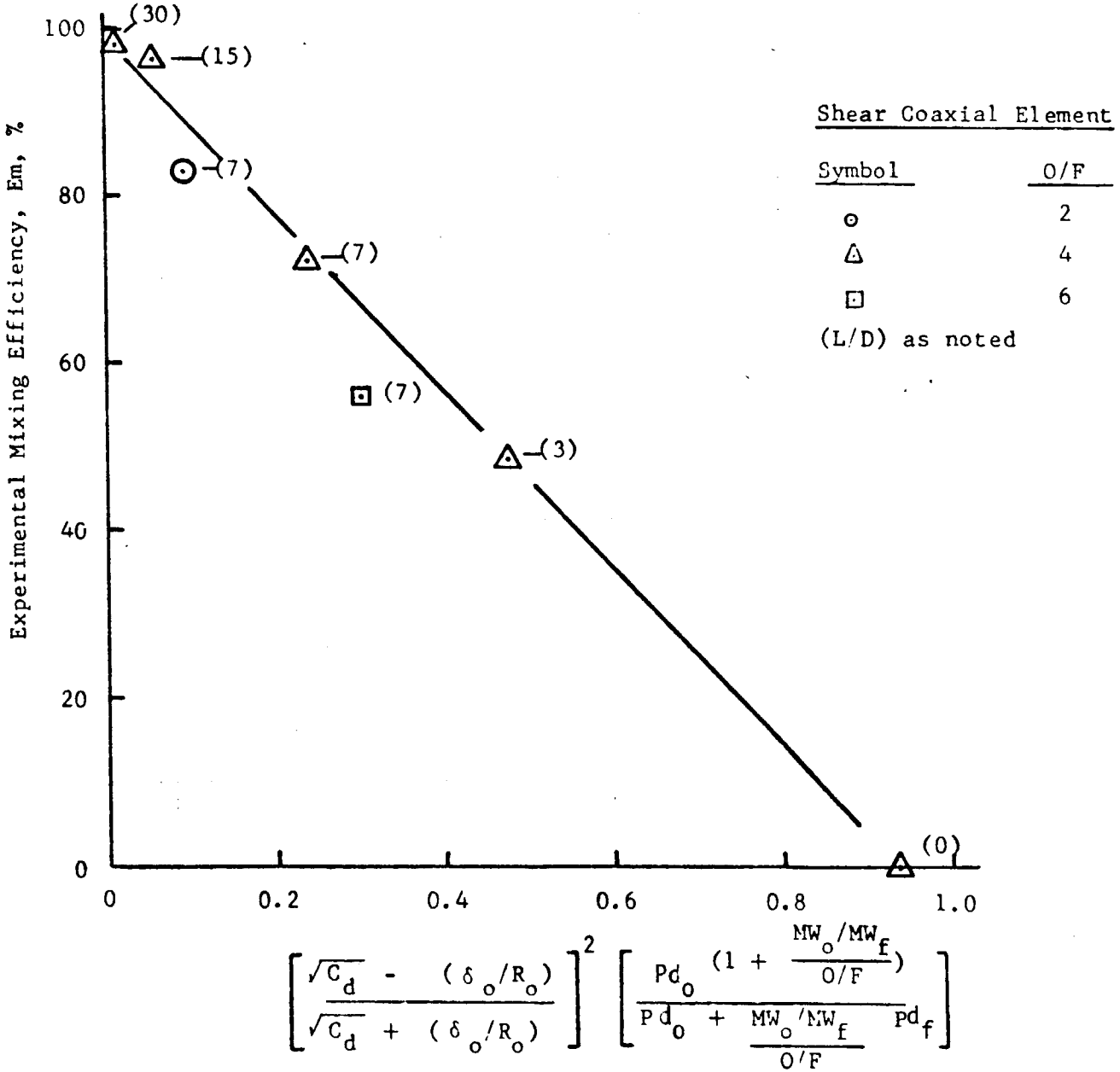

FIGURE 88. ANALYTICAL CORRELATION OF EXPERIMENTAL DATA

APPENDIX B

COLD FLOW TEST AND DATA CORRELATION PROCEDURES

1. Cold Flow Facility and Test Procedures

The basic means of generating mixing information is to measure discrete species and mass concentrations throughout the injector element gas flow field. A parameter termed, E_m, relates these discrete measurements to a single number which indicates deviations from uniform mixture ratio. Any measuring technique must therefore be assessed by its ability to accurately measure local mixture ratio and mass flux.

The cold flow test setup shown schematically and pictorially in Figure 89 consists of a twenty element probe and a gas supply and flow metering system for accurate control of mass flow rate. The flow tests were conducted using hydrogen for fuel and nitrogen as an oxygen simulant. The need to scale different molecular weight propellants was avoided by using nitrogen as an oxygen simulant during the cold flow tests, and ignition of the exhaust gases was precluded. The cold flow hardware was used also for single element hot fire testing.

Gas samples are taken with the twenty element probe which can be traversed axially and radially throughout the complete mixing zone. The rake shown in detail in Figure 10 has 20 total pressure and 3 static probes to yield mass flux data. The individual probes are arranged so that by rotating the rake, fine sampling of the flow field can be obtained at any radial and circumferential location. Composition samples were sequentially drawn through the total pressure probes and routed to the mass spectrometer via a 24 position valve.

The individual gas samples were obtained with the sampling system that connected the total pressure tube of each probe to one of the 24 input ports of a 24-position single-throw selector valve (Scaniswitch, Mod W1261, qualified for 500 psia operation). The single output of this valve was connected to the input of the mass spectrometer. Operational experience with the mass spectrometer indicated that the time constant for the system is on the order of three seconds. Therefore, the sample selector switch was triggered every three seconds by a remotely controlled rotary stepping solenoid; and a complete scan of the injector flow field was accomplished in about 160 sec. The output of the mass spectrograph consisted of four continuous analog signals which were related to preset atomic mass numbers. Any four atomic mass numbers (AMU) may be selected, but for this testing AMU's of 2, 4, and 28 -- corresponding to hydrogen, helium, nitrogen -- were preset. The hydrogen and nitrogen concentrations gave mixture ratio data. Helium was used to prevent gross face recirculation.

Measurement of local pressure ratio and total pressure was required to determine local mass flux. To obtain the necessary precision for mass flux resolution, both total pressure and the difference between total and static pressures had to be measured. Therefore, in addition to the sample being connected to the mass spectrograph, the sample had to be monitored for both static

and total pressure. This was accomplished by connecting the output of the first Scaniswitch to the home channel of a Scanivalve. The Scanivalve, an integral 48-position valve and pressure transducer, permits very precise repeatable data by making up to 48 pressure measurements on the same transducer. For this testing the Scanivalve used a ± 2 psi differential transducer, providing less than 1% full-scale error (± 0.02 psi) and capable of withstanding 500 psi overload in either direction.

The static pressure taps of the pressure rake are connected to the low side of the Scanivalve differential pressure transducer. To obtain a pressure reading, a solenoid valve was closed, thus putting total pressure on one side of the differential transducer and static on the other. A separate pressure transducer was used to obtain total pressure. As a system check, a third transducer measured the absolute static pressure.

A high-accuracy digital data acquisition system was used to record data during these tests. It provided an on-line digital printout of test data in engineering units as well as a digital magnetic tape for detailed computer data reduction. The system has the required accuracy (± 0.01% four significant figures) at reasonable sampling rates. The accuracy requirement was very important, considering the relatively low velocity flow field and thus small differences in total and static pressure. The data acquisition system operated at up to 40 channels per second, with 30 channels of input.

During flow test the propellants were set at a desired flow rate and mixture ratio. When the flow rates stabilized, chamber pressure was set using a remotely operated throat pintle. When chamber pressure was set, the automatic rake scan was started. At the end of the complete rake scan -- which required about 120 sec -- the gas flow was stopped, the system purged, and the rake repositioned. Marker voltages were recorded that indicated Scanivalve, Scaniswitch, and isolation valve position. Sufficient scans of the data system were made to assure that steady-state pressure and concentration data are obtained.

The same setup and procedures as described above were used in both the single element and multiple element cold flow testing. To permit use of the same rake for the multiple element testing, it was mounted off the centerline of the chamber, centered on one of the elements. Rotation of the aft closure relative to the injector permitted mapping the complete injector face.

2. Cold Flow Data Acquisition and Reduction

The initial step in reduction of a typical cold flow test was to create an Engineering Unit File (EUF) from the raw signal received by the digital acquisition system. The full data acquisition process is outlined in Figure 90. The EUF computed and created a master tape that contained the following information.

a. Local sample pressure

b. Local sample composition

c. Rake sample position

d. System flow parameters

This program adjusted the data for tare values of pressure, composition and flow rate. Pressure data sampling was adjusted for transducer zero shift which was monitored continuously during the test. Composition data as recorded on the EUF was corrected by two factors: (1) the raw mass spectrometer peak voltage reading (for a particular species) was reduced according to the average voltage residual recorded during the time in which pressure data were being sampled. That is, the mass spectrometer transmitted a small voltage reading (on the order of ten percent of a typical steady-state peak height sample) when it was not actually sampling gas, which was subtracted from regular composition voltage values; (2) the second correction involved adjusting the mole fraction data to maintain consistency with a known composition calibration gas, which was continuously sampled by the mass spectrometer. Essentially, the calibration gas was utilized to calculate the constants K_1, K_2, and K_3 in the following equation. The equation is derived from the fact that the partial pressure of a particular species is proportional to its mole fraction in a gaseous mixture.

$$x_1 = \frac{K_1 \cdot P_{H1}}{K_1 \cdot P_{H1} + K_2 \cdot P_{H2} + K_3 \cdot P_{H3}} \qquad \text{(B-1)}$$

where:

x_1 = mole fraction of species one

P_{H1} = mass spectrometer peak height voltage for species one

P_{H2} = mass spectrometer peak height voltage for species two

P_{H3} = mass spectrometer peak height voltage for species three

When both of the adjustments have been made, the composition data for each rake position were entered in the EUF summary table.

System parameters such as weight flows, pressures and temperatures were averaged over the time period. All data was then stored on tape where it served as input to the analysis program Datnal. Following tape storage of the engineering unit file summary block, the data analysis program acquired the EUF data and computed the key test analysis parameters. It first calculated parametric test data based on system information and computed 24 non-dimensional parameters such as injection velocity momentum ratio, velocity ratio and delta velocity. These variables were based on the run conditions and injector geometry of the particular test.

Measured ΔP and static pressure matrices were computed. A complete flow and composition matrix was constructed by assuming flow field symmetry. Thus the data in the nonmeasured quadrants was constructed from the data in the measured quadrant. For some elements (doublets and parallel sheets) symmetry was based on a 180° section of the flow field ratherthan a 90° section. Figure 10 of the main report shows the rake element locations. Probe 1 lies on the zero-degree boundary, while probe 8 lies on the ninety-degree boundary. The measured total pressure matrix was calculated by adding corresponding terms of the delta pressure and static pressure matrices.

The local mixture ratio matrix was calculated with the equation shown below, from the mole fraction data obtained from the EUF program.

$$(O/F)_1 = \frac{(MF_{N2})_1 \times MW_{N2}}{(MF_{H2})_1 \times MW_{H2}} \qquad \text{(B-2)}$$

Local total mass fluxes were calculated based on subsonic compressible flow equations, where the gaseous mixture properties (ratio of specific heats, molecular weight) used to solve the equation were calculated based on the mole fraction data input from the EUF program. In essence, local properties were obtained for the flowing mixture based on mass or mole weighting local nitrogen, hydrogen, and helium properties.

The analysis of the engineering unit data was accomplished in a program termed DATNAL. After the local mass flux and mixture ratio matrices have been established from the EUF program, DATNAL was used to characterize the total chamber flow field. The total, fuel, and oxidizer local mass flux matrices were integrated over the entire chamber. The integrated mixture ratio through any radial location was calculated by dividing the integrated oxidizer flow rate by the integrated fuel flow rate. Typically, integrated flow rates do not equal measured flow rates when the entire chamber flow field is examined. Most tests were characterized by integrated flow rates that were higher than the measured value. The reason was suspected to be chamber recirculation zones. To characterize all cold flow tests on a common basis, key analysis parameters were typically compared at the radial location, $\bar{R}$. $\bar{R}$ is the radial location at which the integrated mass flow rate (oxidizer and fuel) equals the measured flow rate. If the flow field integrates low, $\bar{R}$ is equated to the chamber wall radius (0.75 in.).

The analysis parameters E_m, η_m and percent c* were computed. E_m is the mixing coefficient, defined by the equation below.

$$E_m = 100 \left[1 - \sum_{o}^{n} \frac{A_i M_{t1}}{\dot{w}_o} \left(\frac{\dot{w}_o}{\dot{w}_t} \frac{M_{o1}}{M_{t1}} \right) - \sum_{n}^{\bar{n}+n} \frac{A_1 M_{t1}}{\dot{w}_f} \left(\frac{\dot{w}_o}{\dot{w}_t} - \frac{M_{o1}}{M_{t1}} \right) \right] \qquad \text{(B-3)}$$

E_m is the central parameter in cold flow element modeling. It was calculated for the six flow regions formed by considering each rake probe radial location to be the outside flow streamline. E_m was also calculated at $\bar{R}$ by interpolating between the E_m values at the bounding radial positions. The $\bar{R}$ E_m was the value which was usually utilized in intra- and inter-element correlative analysis.

η_m is a mass-weighted mixture ratio distribution term defined by the following equation:

$$\eta_m = 100 \left[\sum_{o}^{n} \left(\frac{\dot{w}_i}{\dot{w}_t} \right) \times \frac{(O/F)_i}{(O/F)_o} + \sum_{n}^{\bar{n}} \left(\frac{\dot{w}_j}{\dot{w}_t} \right) \frac{(O/F)_o}{(O/F)_j} \right] \qquad \text{(B-4)}$$

Effectively, η_m indicates the mass-weighted deviation from nominal mixture ratio. η_m is calculated through the same flow field boundaries as E_m. Percent nominal c* was the final analysis parameter calculated in DATNAL. It was determined by calculating a local c* matrix based on local values of O/F. The local c* distribution was mass-weighted, integrated and divided by the total integrated mass flow rate to produce a c* value characteristic of a particular test. Percent nominal c* was found by dividing test c* by nominal c* at the flow field integrated mixture ratio. Percent c* was calculated for the same regions and at $\bar{R}$ in similar manner to E_m and η_m.

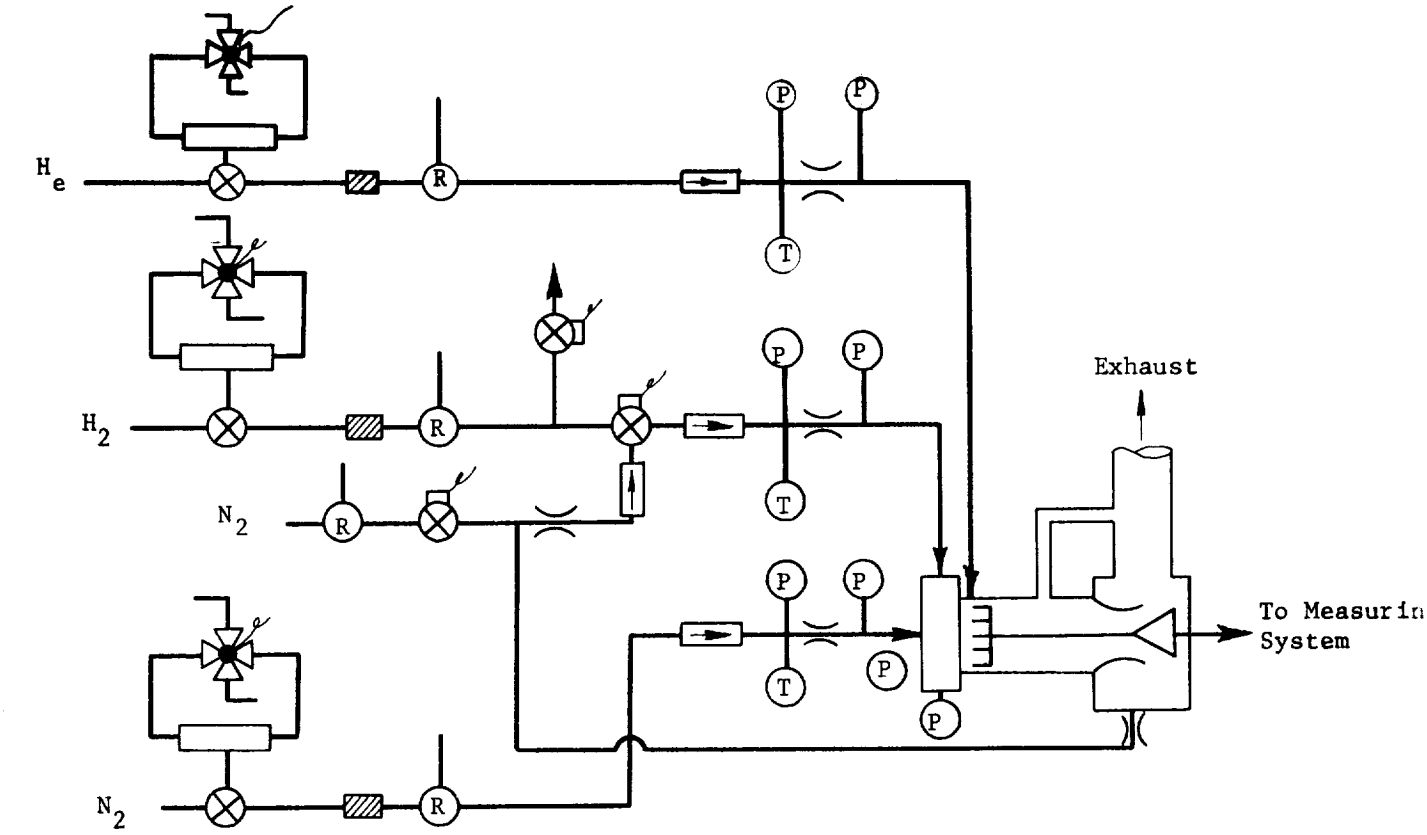

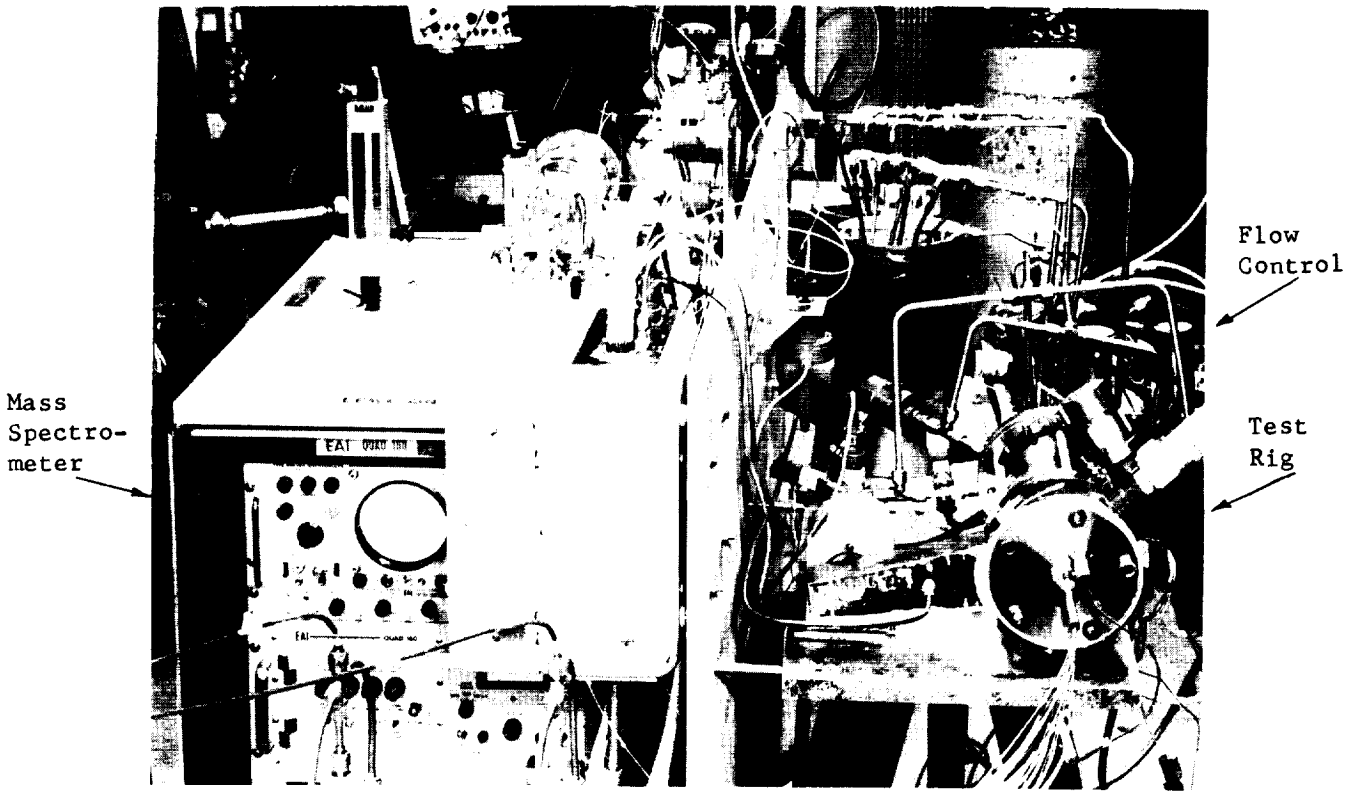

Figure 89. Cold Flow Facility

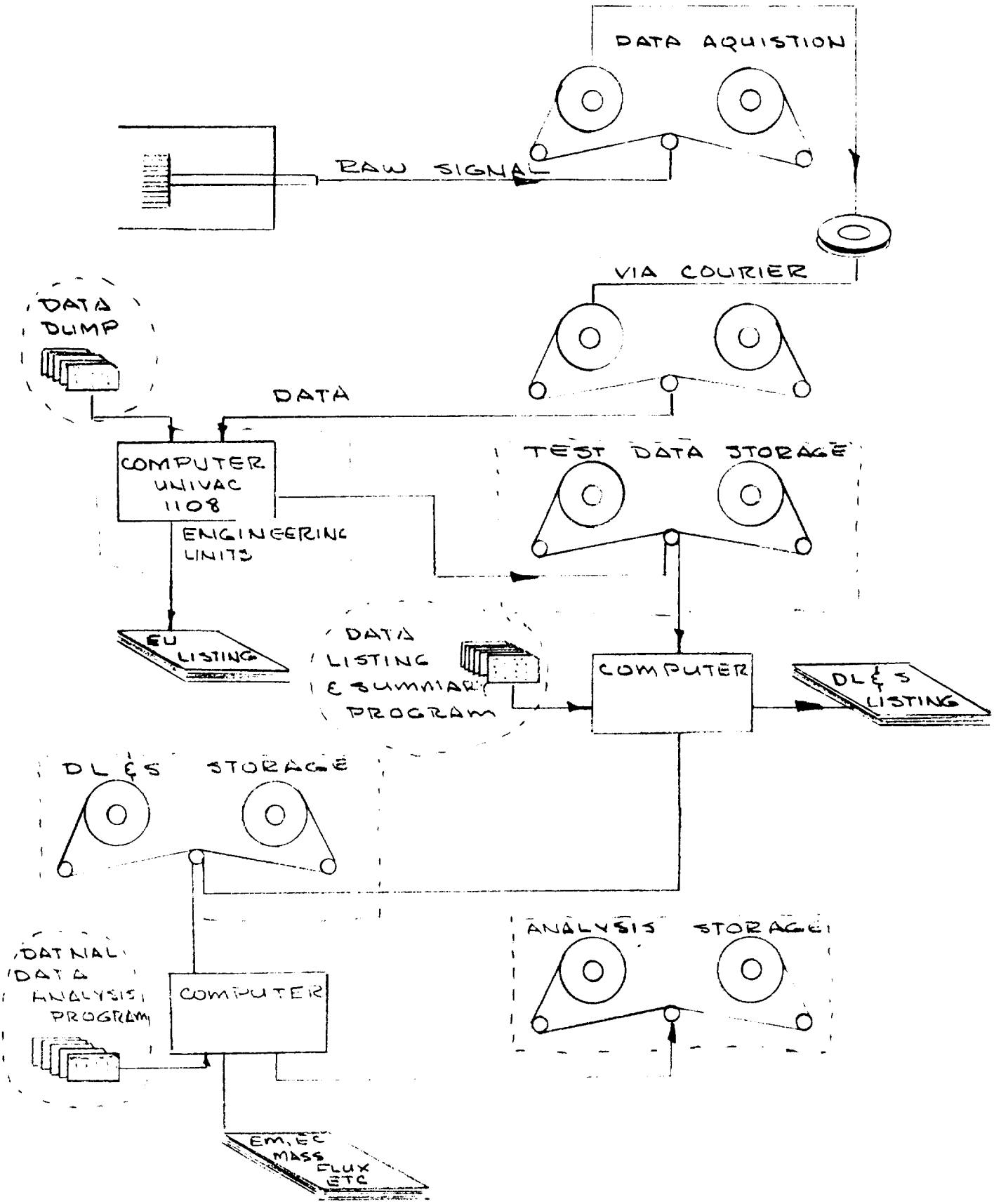

FIGURE 90. DATA ACQUISITION-REDUCTION-ANALYSIS SYSTEM

APPENDIX C

PERFORMANCE EVALUATION TECHNIQUES

Summaries of the single element and multi-element hot fire test series performance are presented in Tables VII, VIII, XII and XIII of the main report. Included in these tables for each test are the test conditions (P_C, O/F, and propellant temperatures), the one-dimensional equilibrium specific impulse and characteristic velocity for the test conditions, the delivered vacuum specific impulse, the delivered characteristic velocity based on P_C-1, P_C-2, and thrust, and the delivered I_{sp}, C* (P_C-1), and energy release efficiencies. The techniques used to calculate the various performance parameters are described herein.

The chamber pressure values reported in the performance have been corrected to stagnation conditions, i.e.

$$P_c\text{-}1 = (P_c\text{-}1)_{meas} \; (P_t/P) \tag{C-1}$$

$$P_c\text{-}2 = (P_c\text{-}2)_{meas} \; (P_t/P) \tag{C-2}$$

where:

$$(P_t/P) = \left(1 + \frac{\gamma-1}{2} M^2\right)^{\gamma/(\gamma-1)} \tag{C-3}$$

$$\gamma = f\,(O/F) \tag{C-4}$$

$$M = f\,(\gamma, \varepsilon_c) \tag{C-5}$$

The chamber pressure calculated in the above manner is equivalent to the throat stagnation pressure providing that no additional momentum pressure loss occurs within the combustion chamber between the P_C tap location and the nozzle throat and that parallel flow conditions exist at the pressure tap location. The P_C-1 pressure tap is located on the combustion chamber wall immediately upstream of the contraction section, while the P_C-2 tap is located on the chamber wall an inch or more upstream of the P_C-1 tap. In reality, the P_C-1 static pressure is probably increased by the subsonic deceleration caused by the flow turning at the inlet to the contraction section. In addition, both the P_C-1 and P_C-2 static pressure measurements should be corrected (lowered) for losses due to heat addition and friction downstream of the pressure tap location. The exact pressure correction, however, is a function of the gas properties, chamber contour, tap location, and the energy release profile established by the injection and mixing process. The derivation and calculation of these correction factors was beyond the scope of this effort. However, the thrust based C* and energy release efficiency (ERE) are not affected by these considerations.

The theoretical (ODE) specific impulse and characteristic velocity are computed using the ODE option of the JANNAF TDK computer program[16]. The calculations are made on the basis of one-dimensional flow assuming complete chemical equilibrium. For these calculations, the oxidizer was assumed to be

comprised of 99.398% O_2, 0.549% Ar, and 0.053% N_2 on a mass basis. The fuel was assumed to be comprised entirely of H_2. The effect of mixture ratio, chamber pressure, propellant temperature, and expansion area ratio were considered in evaluating the theoretical performance for each data point.

The delivered specific impulse (I_{spd}) is calculated from the ratio of the measured thrust corrected to vacuum conditions ($F + P_a A_e$) to the total propellant flow rate. The delivered characteristic velocity is calculated by two methods. In the first method, c* is calculated by the conventional chamber pressure basis, i.e.

$$c^* = P_c A_t g_c/\dot{w}_t$$

where P_c is the measured value (P_c-1 or P_c-2) corrected to stagnation conditions and A_t is based on the measured cold throat diameter. No corrections are applied for the nozzle throat discharge (two-dimensional) or boundary layer (displacement thickness) effects on c*. In the second method, the characteristic velocity is calculated on the basis of measured thrust and an analytical estimate of the delivered thrust coefficient (C_F). Thus, the thrust based c* is calculated as follows:

$$c^* (F) = I_{spd} g_c/C_{Fd}$$

where:

$$I_{spd} = F_{vac}/\dot{w}_t$$

$$C_{Fd} = C_{F\ (ODK)}{}^* (\eta_{DIV} - \Delta F_{BL}/F_{vac})$$

η_{DIV} = Divergence Efficiency

ΔF_{BL} = Boundary layer thrust decrement from the nozzle throat to the exit

The nozzle divergence efficiency (η_{DIV}) is evaluated using the charts from Appendix A of CPIA No. 178 (Ref. 17) while the boundary layer thrust decrement is evaluated using the turbulent boundary layer charts of Appendix B of CPIA No. 178. The thrust base c* is equivalent to the chamber pressure c* since no correction has been made for the chamber boundary layer and heat loss effects and the throat discharge coefficient effect.

The specific impulse efficiency is the percentage ratio of the delivered I_{sp} to the ODE I_{sp}. The c* efficiency is the percentage ratio of the delivered c* based on P_c-1 to the ODE c*. Finally, the energy release efficiency is computed as follows:

$$ERE = (1.0 - ERL/I_{sp\ (ODE)}) * 100$$

where:

$$ERL = I_{sp\ (ODE)} - I_{spd} - [\Delta I_{sp\ KL} + \Delta I_{sp\ DL} + \Delta I_{sp\ BL}]$$

$\Delta I_{sp\ KL}$ = Kinetic performance loss

$\Delta I_{sp\ DL}$ = Divergence performance loss

$\Delta I_{sp\ BL}$ = Boundary layer performance loss

The performance losses used to calculate the energy release loss (ERL) from the measured specific impulse were determined as follows:

The kinetic performance loss accounts for the performance degradation because of chemical recombination lag during the gas expansion process. It is calculated using the ODK option of the JANNAF Two Dimensional Kinetic Computer program. Reaction rates used for the kinetic calculations were those recommended by the JANNAF Liquid Rocket Performance Subcommittee (Ref. 18). The kinetic loss was computed as the difference between the ODE and ODK specific impulse at the test conditions under consideration, i.e.,

$$\Delta I_{sp\ KL} = I_{sp\ (ODE)} - I_{sp\ (ODK)}$$

Nozzle divergence loss is a measure of the performance which is lost due to non-axially directed momentum at the nozzle exit. The divergence efficiency used to calculate the I_{sp} performance loss was taken from Figure A-1 of CPIA No. 178. The performance loss is then computed as follows:

$$\Delta I_{sp\ DL} = [I_{spd}/\eta_{DIV}] - I_{spd}$$

The boundary layer loss (BLL), which accounts for the degradation in performance due to shear drag and heat transfer, was evaluated using the simplified design charts presented in Appendix B of CPIA No. 178. In the case of the single element test data where the heat loss was often substantial (0.5 to 12% of I_{sp}), an additional heat loss term was included in the boundary layer loss calculation. The shear drag effect was included using the simplified boundary charts assuming an adiabatic chamber wall. Next, the heat loss effect on performance was estimated by calculating the total heat transfer from

the chamber based on the heat flux data calculated from the thrust chamber thermocouple measurements*. The performance loss was calculated as follows:

$$\Delta I_{sp} = I_{sp}\ (ODK) \left(1 - \sqrt{\frac{T_o - \Delta T}{T_o}}\right)$$

where:

$$\Delta T = \Sigma Q / C_p\ \dot{w}_t$$

$$T_o = f\ (O/F)$$

$$C_p = f\ (O/F)$$

The total boundary layer loss is taken as the sum of the shear drag and heat flux components. The above procedure was used to calculate the boundary layer performance loss because it accounted for the test-to-test differences in heat transfer effects without expensive test-to-test TBL computer analysis. The procedure was checked for a few selected injector/chamber combinations and it was found that the boundary layer loss was within 5% of the boundary layer loss value calculated using the JANNAF TBL computer program analysis procedure.

---

* $\Sigma Q = \int q\ dA$, where q (heat flux - Btu/in.^{2}-sec) is evaluated from a curve fit of the 4 experimental values. Within the chamber contraction section the heat flux was assumed to be inversely proportional to the chamber diameter to the 1.8 power ($q \propto D^{-1.8}$). For the -2 chamber, in which the last thermocouple measurement is 3.75 inches from the nozzle throat, the heat flux in the chamber downstream of the last thermocouple was assumed to increase to the theoretical value i.e., $q_{theo} = DB * \dot{w}t\ (T_o - 500)D^{1.8}$. Since nearly 2/3's of the -2 chamber contained no thermal instrumentation, the heat flux and thus the resulting boundary layer performance loss for this configuration is much less certain than the B.L. losses calculated for the shorter -1 and -3 chambers.

APPENDIX D

HEAT TRANSFER EVALUATION TECHNIQUES

Single and multiple element thermal data was evaluated using the same basic methods. Local heat flux values were obtained and the ratio of local heat flux to nominal heat flux was computed.

Values of local heat flux in the case of the single element testing were obtained using a data reduction computer program written specifically for this test program. In essence this computer program performed a heat balance on an interior element of the chamber, accounting for heat transferred through the wall and heat conducted to or from adjacent elements. An internal surface heat flux transient was inferred based on the wall acting as a heat sink, with correlations for axial and circumferential conduction. A correction was also made for heat loss to a constant temperature sink or to an external mass such as a flange. Thus,

$$\text{Heat Flux} = (\text{Internal Surface Area})^{-1} (\text{Heat Storage Rate} + \text{Axial Heat Loss} + \text{Circumferential Heat Loss} + \text{Heat Loss to Sink}) \quad \text{(D-1)}$$

In the case of the full scale 6660 N, (1500 lb_f) hardware, a different heat flux technique was used. The local values of heat flux were obtained from the wall temperature measurements by inputting them as boundary conditions to transient conduction models for the chamber walls. These transient models were constructed within the framework of the SINDA computer program (Ref. 19). Two dimensional and one dimensional models were utilized. Heat flux values were calculated by assuming a linear temperature gradient between the gas-side surface and the first interior node (a distance of about 0.060 in.). The equation for experimental heat flux is given as Equation D-2.

$$\phi_{exp} = \frac{(G_{rad})\ \Delta T}{A_s} \quad \text{(D-2)}$$

ϕ_{exp} = experimental heat flux (Btu/sec $in.^2$)

$G_{rad} = \frac{2\ \pi R\ \Delta L K}{\Delta r}$ = conductance between surface node and first interior node

ΔT = Temperature difference between surface node and first interior node

A_s = Surface node area

R = Average radius between surface node and first interior node

ΔL = Axial length of nodes

Δr = Radial distance between surface node and first interior node

This approach for calculating heat flux has been employed in previous programs at ALRC; however, only one-dimensional conduction models were used previously. Two-dimensional conduction models were used as much as possible to analyze data from the -1 and -2 full scale chambers. It was found that heat fluxes calculated with the 2-D model were about 15% lower in the throat region than the 1-D values. Smaller differences were noted upstream and downstream of the throat.

The two-dimensional node network were determined for both the -1 and -2 chambers, while a one-dimensional model was used for the L* section data. While processing the data, the situation sometimes occurred where one of the surface temperatures was not measured. In these cases, the radial string of nodes attached to the missing surface node was eliminated from the analysis by assuming it was insulated from the adjacent node strings. This assumption probably produced less accurate heat flux values and in some cases produced a one-dimensional analysis.

Axial heat flux distributions and the effect of chamber geometry, O/F, P_c and propellant temperature on heat flux were evaluated in terms of the heat flux ratio defined below:

$$\text{Heat flux ratio} = \frac{\text{Measured heat flux}}{\text{Nominal heat flux}}$$

The nominal heat flux values were calculated from a turbulent flow correlation for heat transfer coefficient (Equation D-3) which was then used in Equation (D-4):

$$h_g = 0.026 \frac{k}{d} Re^{0.8} Pr^{0.4} \qquad \text{(D-3)}$$

where h_g is evaluated based on nominal combustion gas properties.

$$\text{Measured heat flux, } \phi = h_g (T_o - T_w) \qquad \text{(D-4)}$$

where:

T_o = theoretical combustion temperature

T_w = gas-side wall temperature 523K (960 R) (assumed to be representative)

Equation (D-3) is a correlation for heat transfer coefficient in fully developed turbulent pipe flow. This equation is commonly known to ALRC as the DB equation and can also be stated in the more familar form shown as Equation (D-5).

$$h_g = DB \frac{\dot{w}_t^{0.8}}{d^{1.8}}, \text{ Btu/in.}^2\text{-sec-°F} \qquad \text{(D-5)}$$

where:

DB = the DB factor given as output by the THERMOCAL computer program (includes all physical properties and the appropriate constants)

Experience at ALRC has shown that Equation (D-5) also yields reasonable predictions for heat flux within rocket thrust chambers. In actual design practice, the 0.026 correlation coefficient is often adjusted to account for contraction ratio and injector streaking effects. The 0.026 value was used in this study because of convenience and because it yields a representative heat flux value which is adequate for comparing the relative heat transfer characteristics of injector elements. Use of a heat flux ratio for comparing the element heat transfer characteristics is preferred to the use of heat flux alone because the ratio accounts for the known effects of mass flux and physical properties variations (O/F and P_c variations) in fully developed flow.

The heat flux ratio parameter, groups some of the data reasonably well, but does not yield a completely generalized correlation for injector element heat transfer characteristics. The ratio does characterize the relative severity of the heat transfer environment produced by each element and shows the effects of O/F and P_c variations over the above the effect normally expected due to overall changes in mass flux and gas physical properties. Axial distributions of the heat flux ratio were obtained for each injector element tested and are discussed in the main section of the report.

APPENDIX E

LIST OF ABBREVIATIONS AND SYMBOLS

A	Area, Alumel
APS	Auxiliary Propulsion System
Ar	Argon
a	constant in Rupe equation
B	Mixing correlation parameter
C	coefficient, chromel, constant, specific heat
C*	characteristic velocity
CR	contraction ratio
D′	apparent showerhead diameter
D	Diameter
Da	combustion influence parameter
d	differential
E	Efficiency, activation energy, element
ERE	energy release (combustion) efficiency
ERL	energy release loss
F	Fuel, thrust, interaction exponent
F-O-F	Two fuels impinging on ox (Triplet Element)
G	gaseous, conductance
g	gravitational constant
H	hydrogen
h	heat transfer coefficient
I	Impulse
J	Injector related
K	Empirical factor
k	thermal conductivity

L	length, liquid
L*	characteristic length
ln	natural logarithm
M	mass flux, Mach number
ME	multiple element
MP	mixing parameters
MW	molecular weight
N	nitrogen
n	number of moles
Om	Oxidizer misimpingement fraction
O	Oxygen
O/F	mixture ratio
O-F-O	Two oxidizers impinging on fuel (Triplet Element)
ODE	One-dimensional equilibrium
ODK	One-dimensional kinetic
P	Pressure
Pd	Dynamic pressure, = $\frac{\rho v^2}{2g}$
Pr	Prandtl number
Q	Energy Release Rate
R	gas constant, radius
r	radius
Re	Reynolds number
$\bar{R}$	Bounding radius in Em calculation
S	element spacing
SE	single element
St	Stanton number

T	Temperature
TBL	turbulant boundary layer
TJ	Injector face temperature
TDK	two-dimensional kinetic
t	time, thickness
U	mass distribution parameter
V	Velocity
W	premix fuel slot width
$\dot{w}$	flow rate
X	axial location, mass fraction
x	mole fraction
Y	penetration parameter
1D	one-dimensional
α	impingement half angle
β	non-dimensional parameter
γ	ratio of specific heats
Δ	differential
δ	boundary layer thickness
ϵ	area ratio
η	efficiency, mixing ratio
η	ERE at area ratio one
μ	viscosity
θ	oxidizer spray cone angle
π	3.1416
ρ	density
Σ	summations
ψ	heat flux, fan propagation angle, resultant spray cone angle

Subscripts

a	axial, average, axisymetric, ambient
c	chamber, coaxial, combustion
cold	refers to cold flow length
comb	refers to combustion chamber length
d	doublet, discharge, diameter
e	exit
eq	equivalent
eql	equilibrium
exp	experimental
f	fuel
g	gas or gas-side
h	hot, hydraulic
i	refers to fuel rich streamtube
ii	streamtubes
in	injector related, injected
int	integrated
j	refers to ox rich streamtube
l	local
m	mixing
n	number of fuel rich streamtubes, nominal
$\bar{n}$	number of oxidizer streamtubes, nominal
nn	number of streamtubes
nom	nominal

o	oxidizer, overall
ODK	one-dimensional kinetic
p	propellant, premix, at constant pressure
s	swirler
sp	specific
T	recirculation
tcv	thrust chamber valve
t	tangential, total, throat, triplet, tank, two-dimensional
v	venturi
wall	chamber wall properties
x	axial location

APPENDIX F

DISTRIBUTION LIST

APPENDIX F
DISTRIBUTION LIST
Contract NAS3-14379 NASA CR-121234

REPORT COPIES R	D	RECIPIENT	DESIGNEE
		National Aeronautics & Space Administration Lewis Research Center 21000 Brookpark Road Cleveland, Ohio 44135	
1		Attn: Contracting Officer, MS 500-313	
5		E. A. Burke, MS 500-205	
1		Technical Report Control Office, MS 5-5	
1		Technology Utilization Office, MS 3-I6	
2		AFSC Liaison Office, 501-3	
2		Library	
1		Office of Reliability & Quality Assurance, MS500-211	
1		J. W. Gregory, Chief, MS 500-203	
15		L. H. Gordon, Project Manager, MS 500-203	
1		N. T. Musial, MS500-113	
1		E. M. Krawczonek, MS 500-209	
1		J. P. Wanhainen, MS 500-203	
1		N. P. Hannum, MS 500-203	
1		R. J. Priem, MS 500-204	
1		J. M. Winter, MS 500-318	
1		Director, Shuttle Technology Office, RS Office of Aeronautics & Space Technology NASA Headquarters Washington, D. C. 20546	
2		Director Space Prop. and Power, RP Office of Aeronautics & Space Technology NASA Headquarters Washington, D. C. 20546	
1		Director, Launch Vehicles & Propulsion, SV Office of Space Science NASA Headquarters Washington, D. C. 20546	
1		Director, Materials & Structures Div., RW Office of Aeronautics & Space Technology NASA Headquarters Washington, D. C. 20546	
1		Director, Advanced Manned Missions, MT Office of Manned Space Flight NASA Headquarters Washington, D. C. 20546	

Report Copies R	D	Recipient	Designee
1		National Aeronautics & Space Administration Ames Research Center Moffett Field, California 94035 Attn: Library	Hans M. Mark Mission Analysis Division
1		National Aeronautics & Space Administration Flight Research Center P.O. Box 273 Edwards, California 93523 Attn: Library	
1		Director, Technology Utilization Division Office of Technology Utilization NASA Headquarters Washington, D.C. 20546	
1		Office of the Director of Defense Research & Engineering Washington, D.C. 20301 Attn: Office of Asst. Dir. (Chem. Technology)	
10		NASA Scientific and Technology Information Facility P.O. Box 33 College Park, Maryland 20740 Attn: NASA Representative	
1		Nation Aeronautics & Space Administration Goddard Space Flight Center Greenbelt, Maryland 20771 Attn: Library	Merland L. Moseson Code 620
1		National Aeroanutics & Space Administration John F. Kennedy Space Center Cocoa Beach, Florida 32931 Attn: Library	Dr. Kurt H. Debus
1		National Aeronautics & Space Administration Langley Research Center Langley Station Hampton, Virginia 23365 Attn: Library	E. Cortwright Director

Report Copies R	D	Recipient	Designee
1		National Aeronautics & Space Administration Manned Spacecraft Center Houston, Texas 77001 Attn: Library	J. G. Thiobodaux, Jr. Chief, Propulsion & Power Division
1		National Aeronautics & Space Administration George C. Marshall Space Flight Center Huntsville, Alabama 35912 Attn: Library	Hans G. Paul Leon J. Hastings James Thomas Dale Burrows I. G. Yates Clyde Nevins J. Blumrich
1		Jet Propulsion Laboratory 4800 Oak Grove Drive Pasadena, California 91103	Henry Burlage, Jr. Duane Dipprey R. Kushida
	1	Attn: Library	
1		Defense Documentation Center Cameron Station Building 5 5010 Duke Street Alexandria, Virginia 22314 Attn: TISIA	
1		RTD (RTNP) Bolling Air Force Base Washington, D.C. 20332	
1		Arnold Engineering Development Center Air Force Systems Command Tullahoma, Tennessee 37389 Attn: Library	Dr. H. K. Doetsch
1		Advanced Research Projects Agency Washington, D.C. 20525 Attn: Library	
1		Aeronautical Systems Division Air Force Systems Command Wright-Patterson Air Force Base Dayton, Ohio Attn: Library	D. L. Schmidt Code ARSCNC-2
1		Air Force Missile Test Center Patrick Air Force Base, Florida Attn: Library	L. J. Ullian

Report Copies R	D	Recipient	Designee
1		Air Force Systems Command Andrews Air Force Base Washington, D.C. 20332 Attn: Library	Capt. S. W. Bowen SCLT
1		Air Force Rocket Propulsion Laboratory (RPR) Edwards, California 93523 Attn: Library	
1		Air Force Rocket Propulsion Laboratory (RPM) Edwards, California 93523 Attn: Library	Donald Ross
1		Air Force FTC (FTAT-2) Edwards Air Force Base, California 93523 Attn: Library	
1		Air Force Office of Scientific Research Washington, D.C. 20333 Attn: Library	SREP, Dr. J. F. Masi
1		Space & Missile Systems Organization Air Force Unit Post Office Los Angeles, California 90045 Attn: Technical Data Center	
1		Office of Research Analyses (OAR) Holloman Air Force Base, New Mexico 88339 Attn: Library RRRD	
1		U.S. Air Force Washington, D.C. Attn: Library	Col. C. K. Stambaugh Code AFRST
1		Commanding Officer U.S. Army Research Office (Durham) Box CM, Duke Station Durham, North Carolina 27706 Attn: Library	
1		U.S. Army Missile Command Redstone Scientific Information Center Redstone Arsenal, Alabama 35808 Attn: Document Section	Dr. W. Wharton

Report Copies R	D	Recipient	Designee
1		Bureau of Naval Weapons Department of the Navy Washington, D.C. Attn: Library	J. Kay Code RTMS-41
1		Commander U.S. Naval Missile Center Point Mugu, California 93041 Attn: Technical Library	
1		Commander U.S. Naval Weapons Center China Lake, California 93557 Attn: Library	
1		Commanding Officer Naval Research Branch Office 1030 E. Green Street Pasadena, California 91101 Attn: Library	
1		Director (Code 6180) U.S. Naval Research Laboratory Washington, D.C. 20390 Attn: Library	H. W. Carhart J. M, Krafft
1		Picatinny Arsenal Dover, New Jersey 07801 Attn: Library	I. Forsten
1		Air Force Aero Propulsion Laboratory Research & Technology Division Air Force Systems Command United States Air Force Wright-Patterson AFB, Ohio 45433 Attn: APRP (Library)	R. Quigley C. M. Donaldson
1		Electronics Division Aerojet-General Corporation P.O. Box 296 Azusa, California 91703 Attn: Library	W. L. Rogers

Report Copies R	D	Recipient	Designee
1		Space Division Aerojet-General Corporation 9200 East Flair Drive El Monte, California 91734 Attn: Library	S. Machlawski
1		Aerojet Ordance and Manufacturing Aerojet-General Corporation 11711 South Woodruff Avenue Fullerton, California 90241 Attn: Library	
1	1	Rocketdyne, Division of Rockwell International 6633 Canoga Avenue Canoga Park, CA Attn: Library	D. Campbell A. Y. Falk R. J. Burick
1		Aeronutrionic Division of Philco Ford Corp. Ford Road Newport Beach, California 92663 Attn: Technical Information Department	Dr. L. H. Linder
1		Aerospace Corporation 2400 E. El Segundo Blvd. Los Angeles, California 90045 Attn: Library-Documents	J. G. Wilder
1		Arthur D. Little, Inc. 20 Acorn Park Cambridge, Massachusetts 02140 Attn: Library	A. C. Tobey
1		Astropower Laboratory McDonnel-Douglas Aircraft Company 2121 Paularino Newport Beach, California 92163 Attn: Library	
1		ARO, Incorporated Arnold Engineering Development Center Arnold AF Station, Tennessee 37389 Attn: Library	
1		Susquehanna Corporation Atlantic Research Division Shirley Highway & Edsall Road Alexandria, Virginia 22314 Attn: Library	

Report Copies R	D	Recipient	Designee
1		Beech Aircraft Corporation Boulder Facility Box 631 Boulder, Colorado Attn: Library	Douglas Pope
1		Bell Aerosystems, Inc. Box 1	T. Reinhardt W. M. Smith
	1	Buffalo, New York 14240 Attn: Library	J. M. Senneff
1		Instruments & Life Support Division Bendix Corporation P.O. Box 4508 Davenport, Iowa 52808 Attn: Library	W. M. Carlson
1		Boeing Company Space Division P.O. Box 868 Seattle, Washington 98124 Attn: Library	J. D. Alexander C. F. Tiffany
1		Chemical Propulsion Information Agency Applied Physics Laboratory 8621 Georgia Avenue Silver Spring, Marlyand 20910	Tom Reedy
1		Chrysler Corporation Missile Division P.O. Box 2628 Detroit, Michigan Attn: Library	John Gates
1		Chrysler Corporation Space Division P.O. Box 29200 New Orleans, Louisiana 70129 Attn: Librarian	
1		Curtiss-Wright Corporation Wright Aeronautical Division Woodridge, New Jersey Attn: Library	G. Kelley

Report Copies R	D	Recipient	Designee
1		University of Denver Denver Research Institute P.O. Box 10127 Denver, Colorado 80210 Attn: Security Office	
1		Fairchild Stratos Corporation Aircraft Missiles Division Hagerstown, Maryland Attn: Library	
1		Research Center Fairchild Hiller Corporation Germantown, Maryland Attn: Library	Ralph Hall
1		General Dynamics/Convair P.O. Box 1128 San Diego, California 92112 Attn: Library	Frank Dore
1		Missiles and Space Systems Center General Electric Company Valley Forge Space Technology Center P.O. Box 8555 Philadelphia, Pa. 19101 Attn: Library	A. Cohen F. Schultz
1		General Electric Company Flight Propulsion Lab. Department Cincinnati, Ohio Attn: Library	D. Suichu Leroy Smith
1		Grumman Aircraft Engineering Corporation Bethpage, Long Island, New York Attn: Library	Joseph Gavin
1		Hercules Powder Company Allegheny Ballistics Laboratory P.O. Box 210 Cumberland, Maryland 21501 Attn: Library	
1		IIT Research Institute Technology Center Chicago, Illinois 60616 Attn: Library	C. K. Hersh

Report Copies R	D	Recipient	Designee
1		Kidde Aer-Space Division Water Kidde & Company, Inc. 567 Main Street Belleville, N. J. 07109	R. J. Hanville
1		Ling-Temco-Vought Corporation P.O. Box 5907 Dallas, Texas 75222 Attn: Library	
1		Lockheed Missiles and Space Company P.O. Box 504 Sunnyvale, California 94087 Attn: Library	
1		Lockheed Propulsion Company P.O. Box 111 Redlands, California 92374 Attn: Library, Thackwell	H. L. Thackwell
1		Marquardt Corporation 16555 Saticoy Street Box 2013 - South Annex Van Nuys, California 91409	L. R. Bell Jr.
1		Denver Division Martin-Marietta Corporation P.O. Box 179 Denver, Colorado 80201 Attn: Library	Dr. Morganthaler F. R. Schwartzberg
1		Western Division McDonnell Douglas Astronautics 5301 Bolsa Ave. Huntington Beach, California 92647 Attn: Library	R. W. Hallet G. W. Burge P. Klevatt
1		McDonnell Douglas Aircraft Corporation P.O. Box 516 Lambert Field, Missouri 63166 Attn: Library	R. A. Herzmark
1		Space & Information Systems Division Rocketdyne International 12214 Lakewood Blvd. Downey, California Attn: Library	

Report Copies R	D	Recipient	Designee
1		Northrop Space Laboratories 3401 West Broadway Hawthorne, California Attn: Library	Dr. Wm. Howard
1		Purdue University Lafayette, Indiana 47907 Attn: Library (Technical)	Dr. Bruce Reese
1		Rocket Research Corporation Willow Road at 116th Street Redmond, Washington 98052 Attn: Library	F. McCullough, Jr.
1		Stanford Research Institute 333 Ravenswood Avenue Menlo Park California 94023 Attn: Library	Dr. Gerald Marksman
1		TRW Systems, Inc.	D. H. Lee
	1	1 Space Park	H. Burge
	1	Redondo Beach, California 90278 Attn: Tech. Lib. Doc. Acquisitions	W. A. Carter
1		United Aircraft Corporation Corporation Library 400 Main Street East Hartford, Connecticut 06108 Attn: Library	Dr. David Rix Erle Martin Frank Owen Wm. E. Taylor
1		United Aircraft Corporation Pratt & Whitney Division Florida Research & Development Center P.O. Box 2691 West Palm Beach, Florida 33402	R. J. Coar A. Masters Dr. Schmitke T. E. Bailey P. Mitchel
	1	Attn: Library	G. B. Cox
1		United Aircraft Corporation United Technology Center P.O. Box 358 Sunnyvale, California 94038 Attn: Library	Dr. David Altman
1		Garret Corporation AiResearch Division Phoenix, Arizona, 85036 Attn: Library	R. Bullock J. R. Erwin

REFERENCES

REFERENCES

1. Rupe, J. H., A Correlation Between the Dynamic Properties of a Pair of Impinging Streams and the Uniformity of Mixture Ratio Distribution in The Resulting Spray, Progress Report No. 20-209, Jet Propulsion Laboratory, Pasadena, California, 28 March 1956.

2. Elverum, G. W., Jr., and Morey, T. F., Criteria for Optimum Mixture Ratio Distribution Using Several Types of Impinging Stream Injector Elements, JPL Memo No. 30-5, 25 February 1959

3. Technical Documentary Report No. TR-65-107, Performance Characteristics of Compound A/Hydrazine Propellant Combinations, Rocketdyne, A Division of North American Aviation, Inc., Canoga Park, California, May 1965 (Conf.)

4. Riebling, R. W., "Criteria for Optimum Propellant Mixing in Impinging Jet Injection Elements," J. Spacecraft Rockets, Vol. 4, No. 6, June 1967, 817-819

5. Anon, Space Storable Propellant Performance Study, Final Report, NAS 3-11199, Report 7677, 24 November 1968

6. Anon, Advanced Rocket Aerospike Experimental Program, Interim Report, Vol. II (1 July 1967 to 31 May 1968), Report No. R7475, Rocketdyne Engineering

7. Ewen, R. L., Hydrogen Film/Conductive Cooling, ALRC Final Report NAS 3-14343, NASA CR-120926, Nov. 1972

8. Geode, P. J., Small-Amplitude Combustion Oscillations in the Gas Rocket, AFOSR Contracts 753-65, -66, Report No. TM-66-4, Jet Propulsion Center, Purdue University, June 1966.

9. Becker, H. A., Hottel, H. C., Williams, G. C., "Mixing and Flow in Ducted Turbulent Jets", 9th Symposium on Combustion, 1963.

10. Kors, D. L., Calhoon, D. F., Gaseous Oxygen/Gaseous Hydrogen Injector Element Modeling, AIAA Paper No. 71-674, June 14-18, 1971

11. Paster, R. D., Hydrogen Oxygen APS Engines (High Pressure), Contract NAS3-14352, Rocketdyne Report R8837-1, NASA CR 120805

12. Anon, Hydrogen-Oxygen Auxiliary Propulsion for the Space Shuttle, Vol. 1: High Pressure Thrusters, ALRC Report, NAS3-14354, NASA CR - 120895

13. Schoenman, L., and Block, P., "Laminar Boundary-Layer Heat Transfer in Low-Thrust-Rocket Nozzle," J. Spacecraft, Vol. 5, No. 9, 1082-1089, Dec. 68

14. Injector Orifice Study-Apollo Service Propulsion System, Final Report, Report 6925-F, Contract NAS9-6925, Aerojet-General Corp., 31 July 1968

15. Arbitt, H. A., Dickerson, R., Clapp, S. D., Nagai, C. K., Lithium-Fluorine Hydrogen Propellant Study, Final Report, NASA CR72325, Feb. 1968

16. Frey, H. M., and Nickerson, G. R., Two-Dimensional Kinetic Reference Program, Improved Version, Contract NAS9-10391, Dynamic Science, December 1970

17. Pieper, J. L., ICRPG Liquid Propellant Thrust Chamber Performance Evaluation Manual, Chemical Propulsion Information Agency, Report 178, Sept. 1968

18. CPIA No. 178 Addendum No. 1

19. SINDA Users Manual, TRW Systems Report 11207-6003-RO-001, NASA Contract 9-8289, Sept. 1970

20. Priem, R. J., and Yang, J. S., A Technique for Predicting High Frequency Stability Characteristics of Gaseous Propellant Combustors, NASA LeRC

TABLE OF CONTENTS

		Page
I.	Introduction	1
II.	Empirical Model	4
	A. Introduction	4
	B. Combustion Performance Prediction	4
	C. Heat Transfer Predictions	6
	D. Stability	8
	E. Sample Problem for Hot Fire Performance (Empirical Model)	8
III.	Analytical Model	26
	A. Introduction and General Procedure	26
	B. Description of Calculational Procedure	26
	C. Sample Problem for Hot Fire Performance	29
IV.	Symbols and Abbreviations	53
References		56

LIST OF FIGURES

		Page No.
1.	Relationship of Chamber Length and Cold Flow Mixing Length	12
2.	Coaxial and Increased Shear Coaxial Element Correlation	13
3.	Swirler Element Correlation	14
4.	Impinging Triplet (F-O-F) Element Correlation	15
5.	Premix Element Correlation	16
6.	Effect of Tangential Velocity on Swirler Performance	17
7.	Empirical Relationship Between Combustion Efficiency and Mixing Efficiency	18
8.	Chamber Heat Flux Characteristics of Gaseous Injector Elements at Injector End	19
9.	Low Frequency Stability Characteristics of Gaseous Injector Elements	20
10.	Test System Parameters Applicable to Stability Analysis	21
11.	Flow Chart and Source of Input Data - Analytical Model	37
12.	Generalized Mixing Correlation Chart	38
13.	Combustion Influence Parameter vs. Mixture Ratio - GO_2/GH_2	39
14.	$FLOX/CH_4$ Thermochemical Data	40
15.	Effect of Equilibrium Mole Fraction Ratio on Generalized Mixing Parameter	41

LIST OF TABLES

		Page No.
I	Gaseous Injection Element Characteristics	22
II	Mixing Efficiency Equations - Empirical Model	23
III	Gas/Gas Injector Stability Data	24
IV	Shear Co-Axial Element Equations - Analytical Model	42
V	Swirler Co-Axial Element Equations - Analytical Model	43
VI	Like Doublet Element Equations - Analytical Model	44
VII	Showerhead Element Equations - Analytical Model	45
VIII	Deep Cup Premix Element Equations - Analytical Model	46
IX	External Impinging F-O-F Triplet Element Equations - Analytical Model	48
X	Generalized Performance Equations - Analytical Model	51
XI	Generalized Chamber Heat Flux Equations	52

I. INTRODUCTION

The purpose of this guide is to present succinct design procedures for gaseous propellant injectors. Methods are presented for estimation of combustion efficiency, chamber heat flux and stability characteristics. Except for thermochemical data, which are readily available, the design guide contains all required procedural and empirical data for making preliminary design calculations. The design procedures are derived from a data base consisting of 405 cold flow and fire tests with six basic injector element types. Thus, the designer is assured reliable injector and chamber preliminary designs and associated performance characteristics.

The design procedures are based primarily on data from NASA Lewis Research Center Contract NAS 3-14379, Investigation of GH_2/GO_2 Combustion. However, industry wide data sources for gaseous propellant data were consulted and utilized in derivation of the design procedures and correlations.

The experimental portion of the subject contract was restricted in scope to tests using gaseous hydrogen/gaseous oxygen propellants under test conditions representative of auxiliary propulsion systems, APS, for the Space Shuttle. However, from the start, the motivation for this program was a recognition of the fact that no significant design procedures were available for injectors using propellants which are both in the gaseous state. Therefore, the intent during the development of design approaches on this contract has been to make them as applicable as possible to all gaseous propellant injectors.

It became apparent that this could be done most effectively by pursuing two approaches to gaseous injector modeling. The first approach had the objective of using the test data and correlating it directly with injector/chamber design parameters which are recognized from both theoretical and empirical standpoints as the controlling variables. This approach was defined as the Empirical Model and is located in SectionII of this document. It has the advantages of (1) inherently being the most accurate procedure for gaseous injectors which are to

be designed within the operating envelopes and using the same propellants as this program, and (2) simplicity in the calculation procedure itself. Both of these advantages accrue from the process used to develop the model, i.e., it was derived directly from the test data and only correlated with the sensitive design and operating parameters. However the Empirical Model has a corresponding disadvantage; it lacks generality since it stressed utilization of the test data and did not concentrate on quantifying the mechanistic causal relationships of the mixing combustion process itself. Therefore it should be used with caution when the desired propellant combination or operating envelopes differ significantly from those used on this program.

The second approach had the objective of understanding the mixing/combustion process to the maximum extent possible, using both available theoretical knowledge and new techniques suggested and developed from close observation of the test data. This approach was defined as the Analytical Model and is located in Section III of this document. It is somewhat more complex than the Empirical Model, but it has quantitatively characterized the mixing/combustion process for gaseous propellants so that it is general in nature and can handle all gaseous propellants and operating conditions. To make this procedure practical many second-order physical and mathematical influences had to be ignored. However, the procedure is based on sound principles and accurate modeling of the first order influences. It places at the disposal of the designer a preliminary design tool that is broadly applicable and should be particularly valuable in trade-off studies that need to consider both the influence of design parameters and propellan combinations. Further it provides the foundation that can later be calibrated, if required, in any particular region of interest encompassing gaseous propellant thrusters.

Both the Empirical Model and Analytical Model are described in detail in the main volume of the final report. This design handbook provides only the procedural steps, with most of the required information displayed in charts, graphs, and tables for clarity of presentation. The figures and tables applicable

to each methodology are located at the back of their respective sections. An example problem is included for each procedure, so that the reader can be assured that he is using the model correctly. The nomenclature is listed at the end of the handbook and comprises Section IV of this document.

II EMPIRICAL MODEL

A. Introduction

This portion of the Design Handbook is intended to provide a design approach for estimating combustion performance, chamber heat flux and stability of GH_2-GO_2 rocket engines based on empirical data correlations. The sources of data for the calculation procedures were from test series conducted over the following ranges of operating conditions:

Injector mixture ratio, O/F	1 to 8
Injector orifice area ratio, A_f/A_o	0.5 to 2
Chamber pressure, N/cm^2 (psia)	68 to 340 (100 to 500)
Propellant temperature, °K (°R)	167 to 333 (300 to 600)

The injector element types used to obtain these correlations and their basic characteristics are identified in Table 1. The accuracy of the combustion performance and chamber heat flux correlations are generally within the measurement accuracies of the test data used for the correlations (See Final Report). The stability characteristics are correlated with injector pressure drop for low frequency data, and the high frequency data is tabulated with corresponding design and operating conditions.

The performance correlation of this section of the Design Handbook should be used to determine combustion performance predictions only i.e., energy release efficiency, ERE. The mixing efficiency, E_m, correlations are different in some cases if the end product desired is a predicted cold flow E_m and not ERE. The cold flow E_m correlations and the reasons for their deviation from the corresponding hot fire values are contained in Reference 1. Section III, Analytical Model, includes calculational procedures which are applicable to obtaining both cold flow and hot fire E_m predictions.

B. Combustion Performance Prediction

The calculation procedure is structured such that it analyzes an engine point design and predicts a specific combustion performance efficiency.

II.B. Combustion Performance Prediction (cont.)

In general, a desired performance level must be found by iterations of the design variables, as shown in the following flow chart.

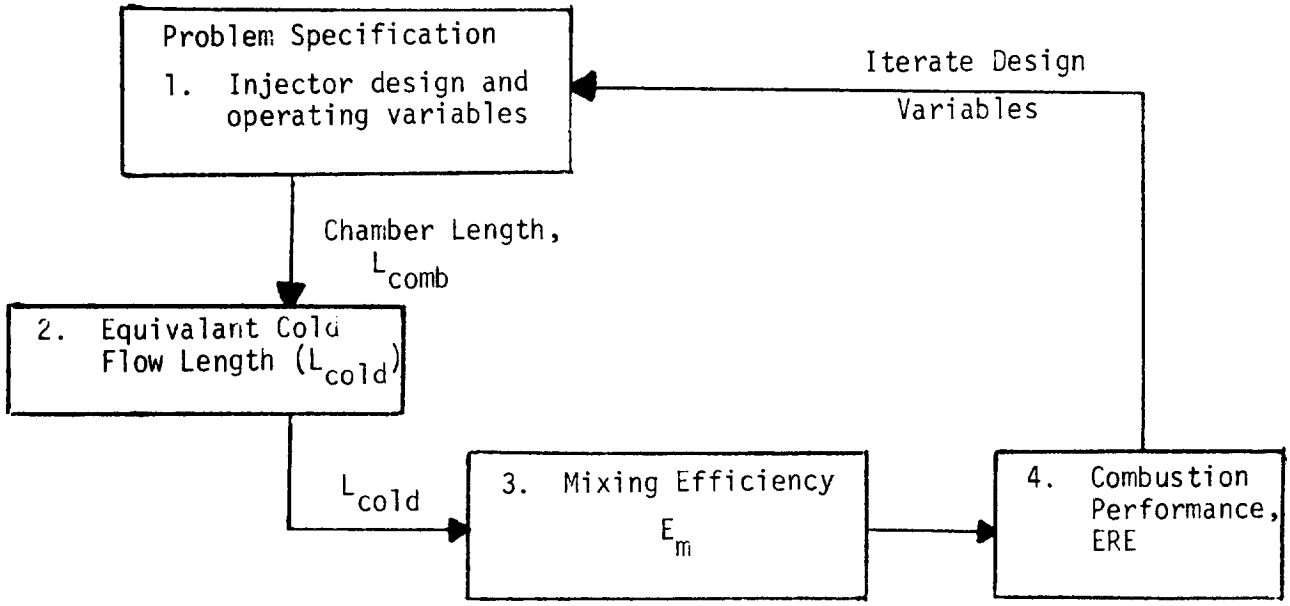

STEP NO.

1. To begin, a complete specification of the problem must be given. The following items must be either known, assumed or calculated:

(1) Chamber length
(2) Injection element type
(3) Mixture ratio
(4) Injection orifice area ratio
(5) O_2 and H_2 injection velocity
(6) Element size

2. Using Figure 1 and the known chamber length, determine an equivalent cold flow length. (For elements not shown on this curve, an engineering judgement will have to be used to select the most applicable generic curve depicted on Figure 1; e.g., for unlike impinging elements such as doublets, pentads, or

STEP NO.

quadlets, the triplet curve would be the most applicable).

3. Compute the mixing efficiency, E_m, using the equations and figures listed in Table II. E_m for elements that are not represented can be approximated by selecting the closest generic element type. For swirler elements with less than $V_t/V_a = 1.0$, combustion performance can be estimated by using the correlation displayed in Figure 6 for the effect of V_t/V_a on ERE.

4. Determine the energy release efficiency (ERE) by using Figure 7 which is the correlation between ERE and E_m. For the external impinging elements (F-O-F triplet), the mixture ratio dependent curves should be used. For all other elements, use the O/F = 4 curve.

An example problem, illustrating the use of this technique to calculate ERE is enclosed as the last subsection (II.E.) of the Empirical Model.

C. Heat Transfer Predictions:

This portion of the design guide provides estimates for the combustion chamber heat flux. Use Figure 8 where the estimated to nominal heat flux ratio, $\emptyset / \emptyset_{nom}$, is displayed as a function of oxidizer to fuel injection momentum ratio. This ratio is the estimated wall heat flux to the heat flux based on nominal properties of the combustion products.

The nominal heat flux, $\emptyset_{nom}$, is calculated from the following equation:

$$\emptyset_{nom} = 0.026 \; k/D \; Re^{.8} \; Pr^{.4} \; (T_{comb} - T_w)$$

where:

D	=	Local diameter	
Re	=	$\frac{(\rho U)_e D}{\mu}$	= Reynolds number based on diameter, overall mass flux, and gas properties at nominal O/F and P_c and adiabatic wall temperature.
Pr	=	$\frac{\mu C_p}{k}$	= Prandtl number of combustion gases based on nominal O/F and P_c and adiabatic wall temperature.
$(\rho U)_e$	=	Nozzle mass flux (one dimensional flow value)	
k, μ, C_p	=	Thermal conductivity, viscosity, and specific heat of combustion gases at nominal O/F and P_c and adiabatic wall temperature.	
T_{comb}	=	Theoretical combustion temperature	
T_w	=	Nominal design gas side wall temperature	

Calculate a nominal heat flux using the above equation or a similar technique. Then determine the chamber heat flux ratio, ϕ_{est}/ϕ_{nom} for the first 3.8 cm (1.5 in) from the injector face by referring to Figure 8 for a particular element and injection momentum ratio. The estimated value is the product of the heat flux ratio and the nominal heat flux:

$$\phi_{est} = \left(\frac{\phi_{est}}{\phi_{nom}}\right) \phi_{nom}$$

Estimated heat flux values at other chamber stations can be estimated using the experimental observation that the heat flux ratio tended to a value of one at throat plane independent of element type. The ϕ_{est}/ϕ_{nom} value at any station is determined by linearly scaling the head end ϕ_{est}/ϕ_{nom} as a function of injector to throat distance. The following equation can be used to calculate a heat flux ratio at any chamber length.

$$\left(\frac{\phi_{est}}{\phi_{nom}}\right)_x = \left(\frac{\phi_{est}}{\phi_{nom}}\right)_h \left[1 - \frac{X}{L_{comb}}\right] + \frac{X}{L_{comb}}$$

D. Stability

The injector designer should be aware that both low and high frequency instabilities can occur using GH_2-GO_2 propellants under the conditions specified at the start of this section. Low frequency stability criteria for momentum mixing and shear mixing elements are shown in Figure 9A and B. This data should be used as an approximate guide to stiffness requirements. The high frequency stability data listed in Table III in conjunction with the engine system schematic shown in Figure 10, constitutes a consistent set of data which can be used by the injector designer in conjunction with existing analytical models such as Reference 5.

E. Sample Problem for Hot Fire Performance (Empirical Model)

TASK: Predict the following:

Injector/chamber design required to achieve a ERE = 98%

GIVEN DESIGN REQUIREMENTS:

Oxidizer: GO_2
Fuel: GH_2

F_{vac} = 1,000 lb_f

P_c = 300 psia

O/F = 4.0

ϵ = 40:1

T_p = 540°R

Injector Allowable	ΔP
Oxid:	60 psi (max)
Fuel:	60 psi (max)

ASSUMED PRELIMINARY DESIGN PARAMETERS:

Element Type: Shear Co-Axial

L_{comb}: 5 in.

F/E: 50 lb_f

II.E. Sample Problem for Hot Fire Performance (Empirical Model) (cont.)

CALCULATIONS:

$$\text{Number of elements } N = \frac{F}{F/E} = \frac{1000}{50} = 20$$

and

$$I_{sp\ vac\ ode} = 453.5 \ \frac{lbf\text{-}sec}{lbm}$$ (Source: JANNAF One Dimensional Kinetic Program, Ref. 2)

$$\text{Fixed } I_{sp} \text{ Losses} = 15 \ \frac{lbf\text{-}sec}{lbm}$$ [assumed using JANNAF procedure Ref. 3)

$$\text{Perfect Injector } I_{sp} = 453.5 - 15 = 438.5 \ \frac{lbf\text{-}sec}{lbm}$$

The delivered Specific Impulse (I_{spd}) = ERE x 438.5 = .98 x 438.5 = 430 $\frac{lbf\text{-}s}{lbm}$

Solving for weight flows

$$\text{Total flow rate } (\dot{W}_T) = \frac{F}{I_{spd}} = \frac{1000}{430} = 2.33 \ \frac{lbm}{sec}$$

$$\text{Fuel flow rate } (\dot{W}_f) = \frac{\dot{W}_T}{1+O/F} = \frac{2.33}{5} = .467 \ \frac{lbm}{sec}$$

$$\text{Oxidizer flow rate } (\dot{W}_o) = \dot{W}_T - \dot{W}_f = 2.33 - .467 = 1.86 \ \frac{lbm}{sec}$$

Total pressure at injection inlet (P_o)

$$P_o = P_c + \Delta P$$

On oxidizer side use .10 P_c as a ΔP criteria.

II.E. Sample Problem for Hot Fire Performance (Empirical Model) (cont.)

$$\Delta P_o = .1\ P_c = .1 \times 300 = 30 \text{ psia}$$

On fuel side use all the available drop i.e., 60 psia.

$$\Delta P_f = 60 \text{ psia}$$

One should note that this value of ΔP_f is in the range of expected stability problems as shown in Figure 9 of this handbook.

and

$$\left(\frac{P_c}{P_{oT}}\right) = \frac{P_c}{P_c + \Delta P_o} = \frac{300}{330} = .910$$

$$\left(\frac{P_c}{P_{fT}}\right) = \frac{P_c}{P_c + \Delta P_f} = \frac{300}{360} = .834$$

From isentropic relationships the Mach numbers are:

$$\text{Mach No.}_{ox} = .37$$

$$\text{Mach No.}_{fuel} = .515$$

and solving for injection velocity:

$$V_f = .515\sqrt{\gamma gRT} = .515\sqrt{1.404 \times 32.2 \times 766.4 \times 540} = 2220 \text{ fps}$$

$$V_o = .37\sqrt{\gamma gRT} = .37\sqrt{1.395 \times 32.2 \times 48.3 \times 540} = 405 \text{ fps}$$

The ΔV ratio is:

$$\frac{V_f - V_o}{V_o} = \frac{2220 - 405}{405} = 4.5$$

and determining orifice injection area A_o

II.E. Sample Problem for Hot Fire Performance (Empirical Model) (cont.)

$$A_o = \frac{\dot{W}_o R_o T_o}{P_c V_o N} = \frac{1.86 \times 48.3 \times 540}{300 \times 405 \times 20} = .020 \text{ in}^2$$

and diameter (D_o)

$$D_o = \left(\frac{4 A_o}{\pi}\right)^{1/2} = \left(\frac{4 \times .020}{\pi}\right)^{1/2} = .160 \text{ in.}$$

From Figure 1 @ L_{comb} of 5, L_{cold} is:

$$L_{cold} = .88 \text{ in.}$$

and

$$L_{cold}/D_o = \frac{.88}{.160} = 5.5$$

and from Equation 1 of Table II the mixing efficiency E_m is calculated from the following expression:

$$E_m = 100 - 26.2 \ln \left[\frac{K_c}{(L_{cold}/D_{eq})_o}\right]$$

From Figure 2 determine K_c at $\frac{V_f - V_o}{V_o} (D_{eq_o}/DH_o)^{1.6} = 4.5$

$$K_c = 14.6$$

$$E_m = 100 - 26.2 \ln \left[\frac{14.6}{5.5}\right] = 74.4\%$$

and from Figure 7 the ERE is 97.6%. If this first try had not agreed with the ERE goal, the above procedure would have to be repeated, varying preliminary design parameters such as, F/E, L_{comb} or element type until agreement had been achieved.

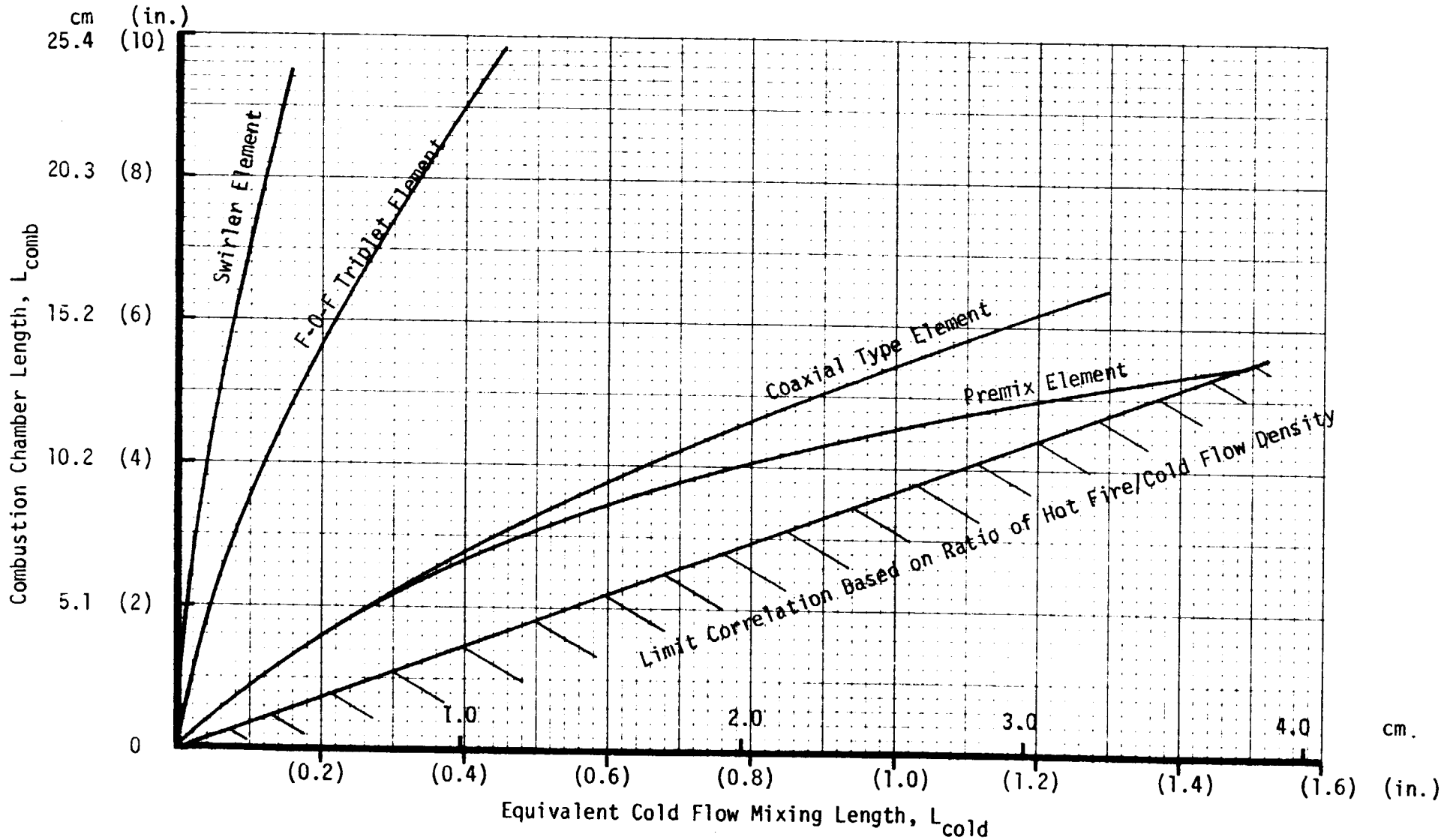

FIGURE 1. RELATIONSHIP BETWEEN CHAMBER LENGTH AND COLD FLOW MIXING LENGTH

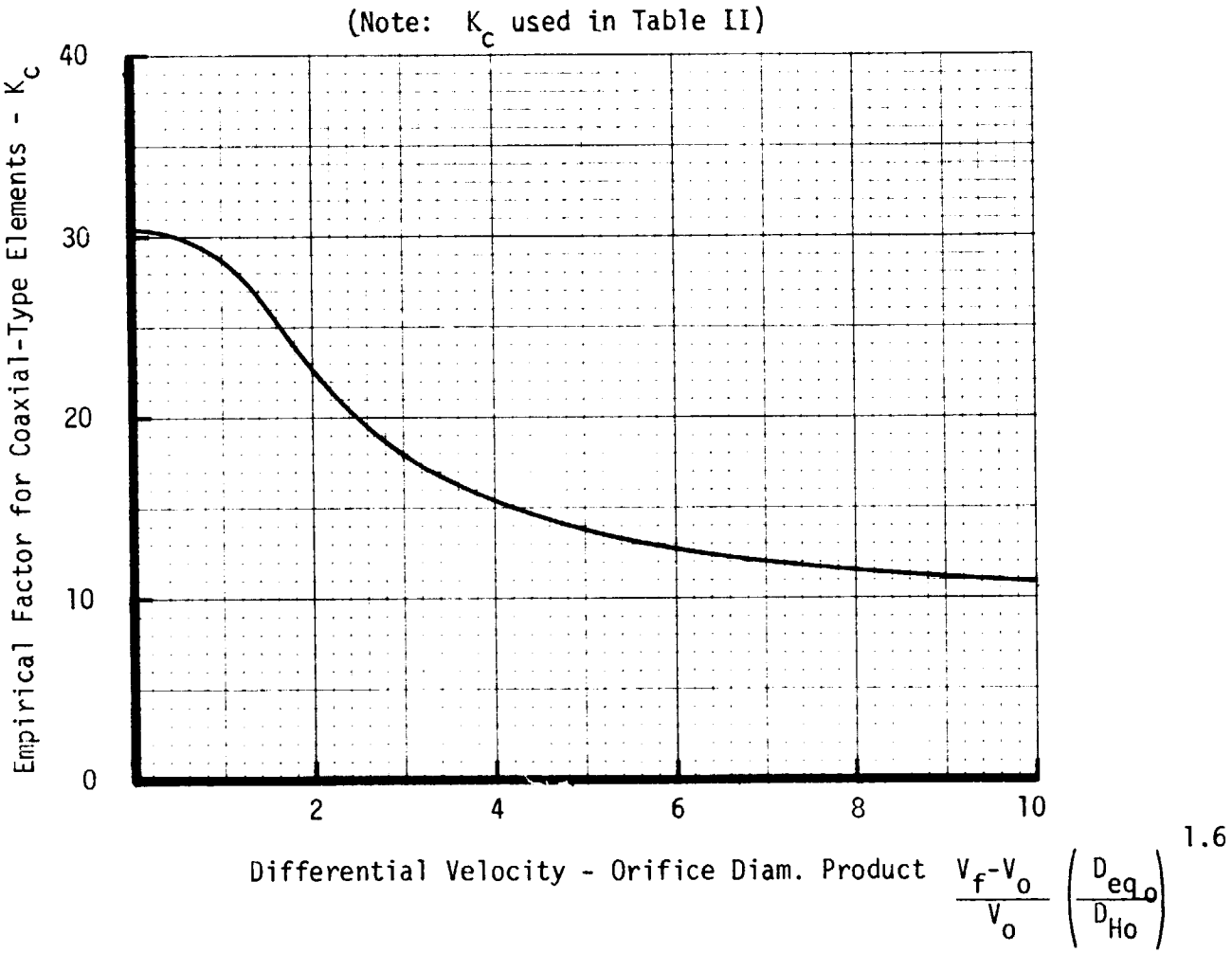

FIGURE 2. COAXIAL AND INCREASED SHEAR COAXIAL ELEMENT CORRELATION

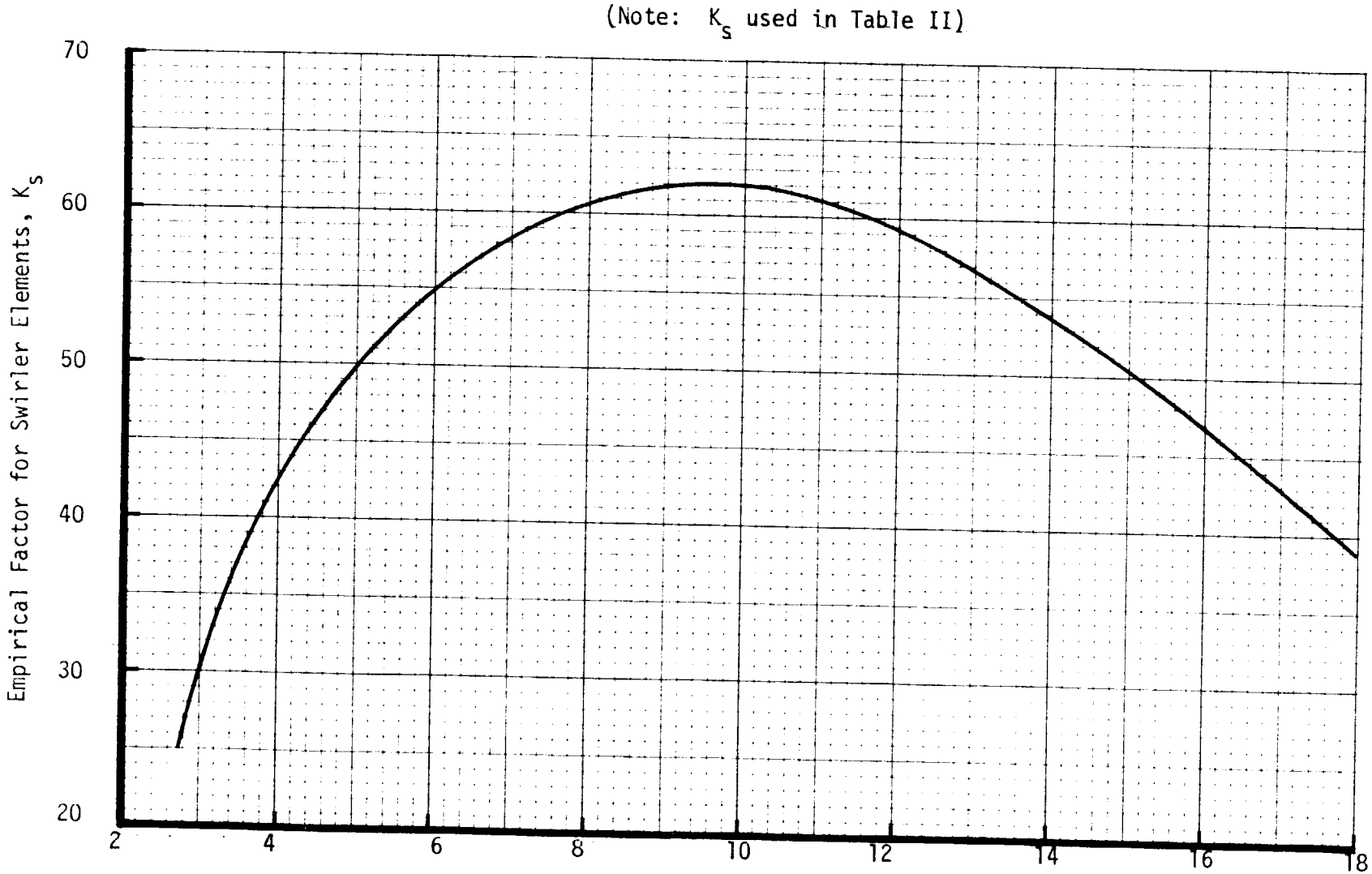

FIGURE 3. SWIRLER ELEMENT CORRELATION

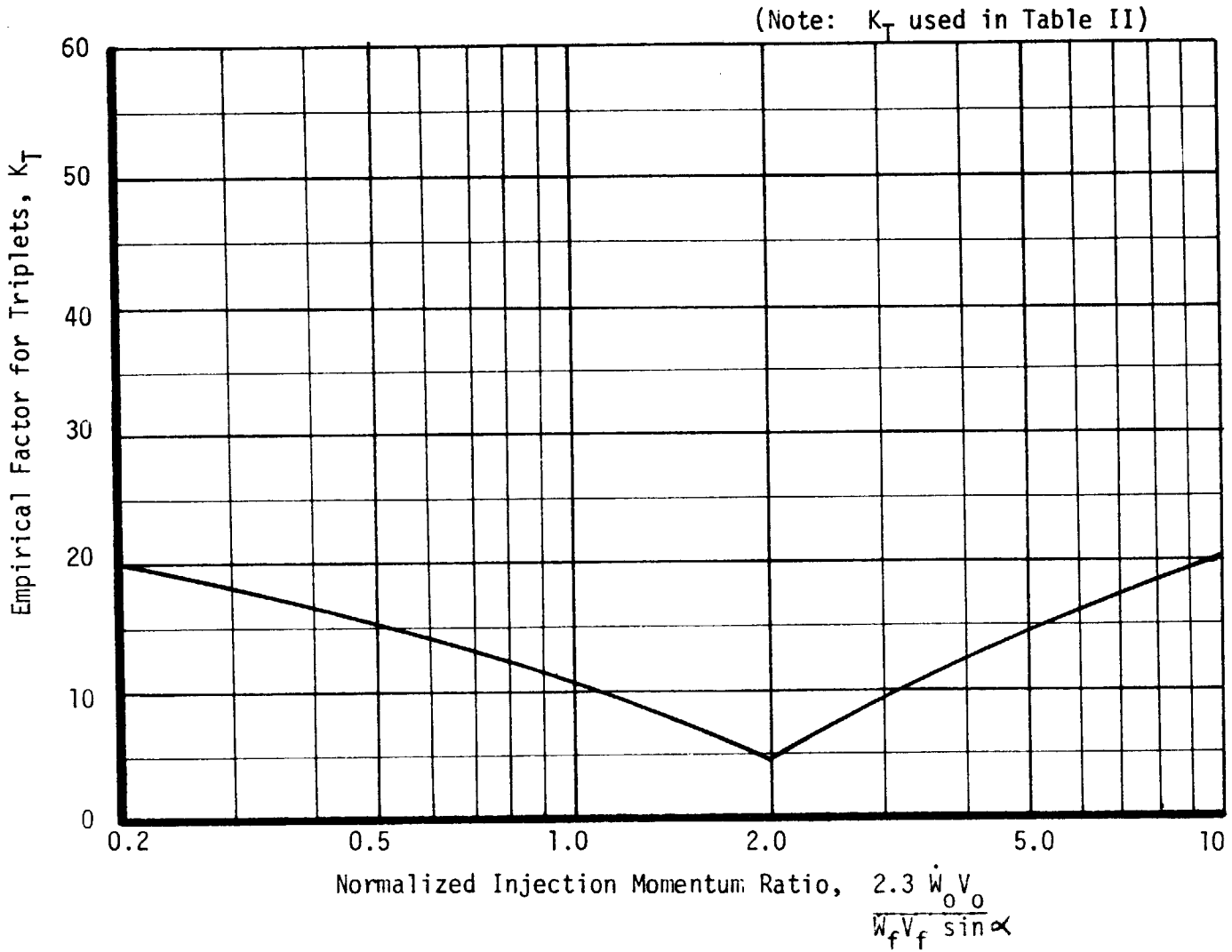
(Note: K_T used in Table II)
Empirical Factor for Triplets, K_T
60
50
40
30
20
10
0
0.2
0.5
1.0
2.0
5.0
10
Normalized Injection Momentum Ratio, $\frac{2.3\ \dot{W}_o V_o}{W_f V_f \sin\alpha}$

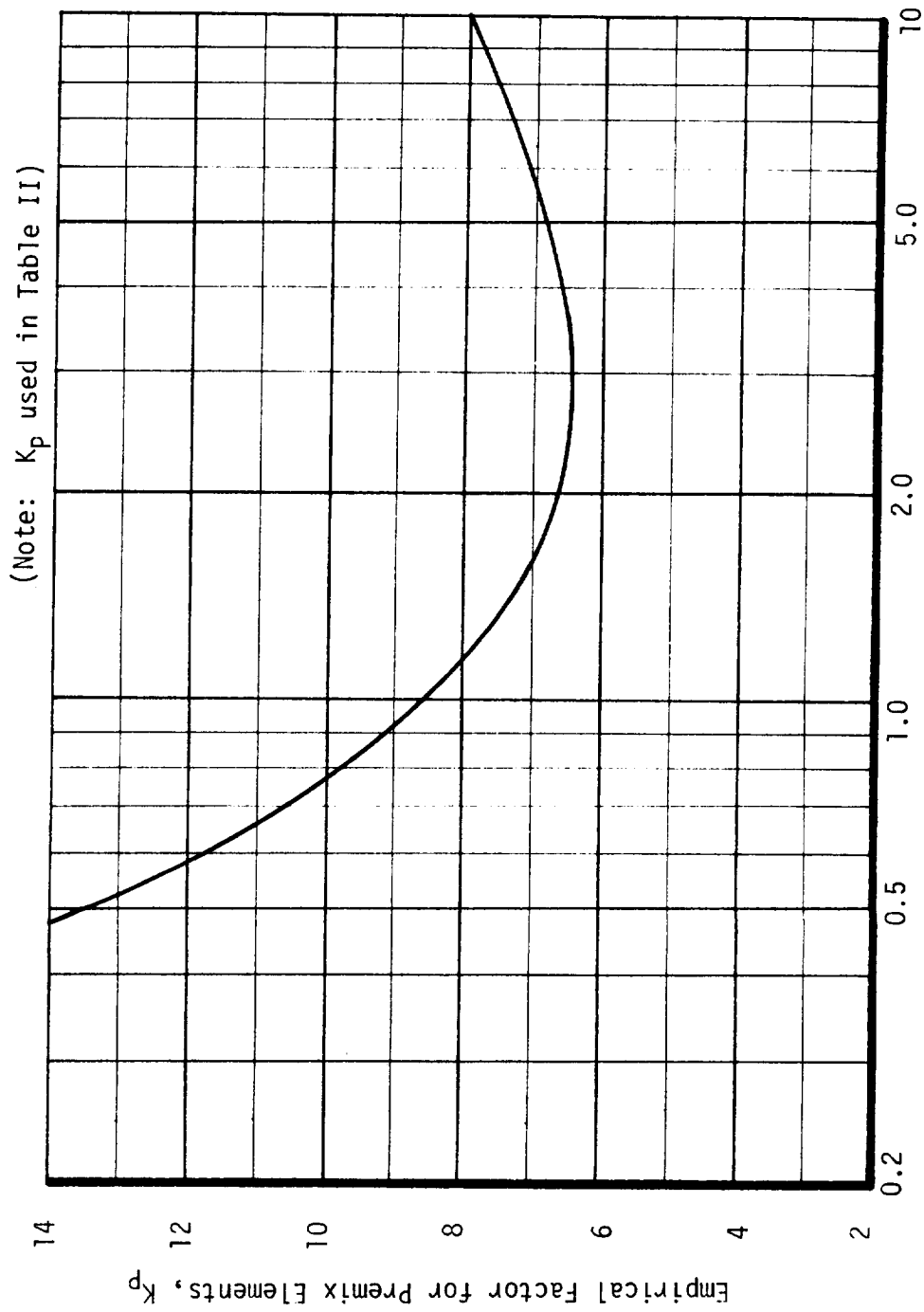

FIGURE 5. PREMIX ELEMENT CORRELATION

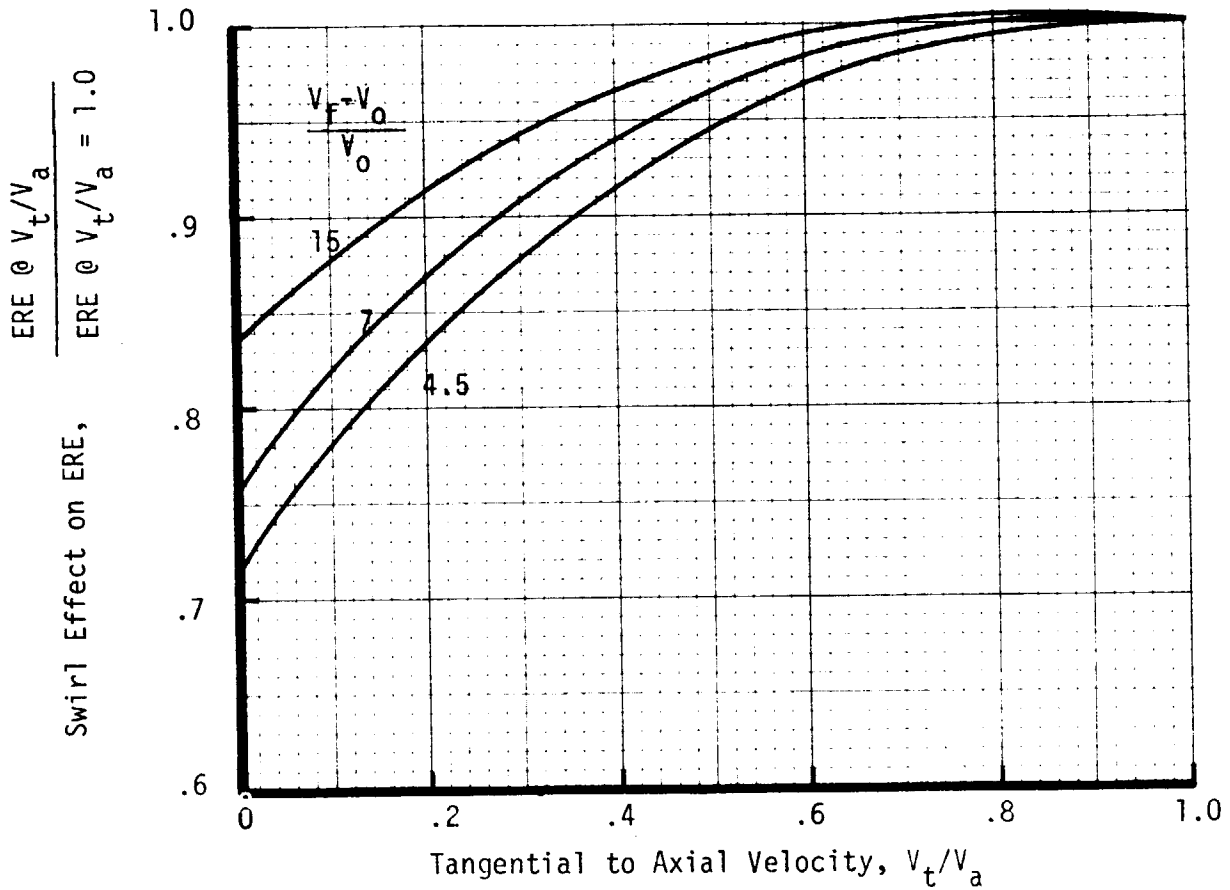

FIGURE 6. EFFECT OF TANGENTIAL VELOCITY ON SWIRLER PERFORMANCE

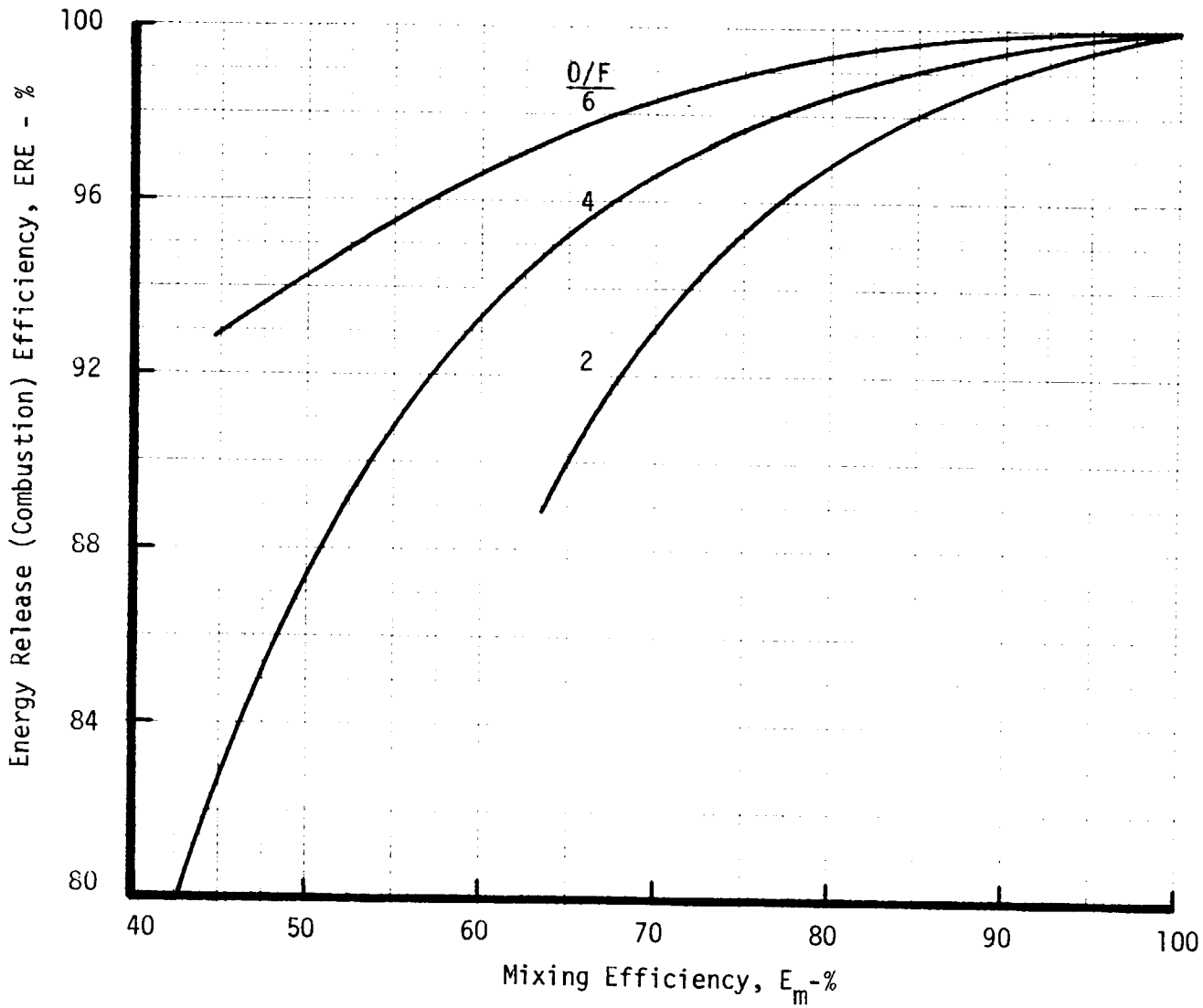

FIGURE 7. EMPIRICAL RELATIONSHIP BETWEEN COMBUSTION EFFICIENCY AND MIXING EFFICIENCY

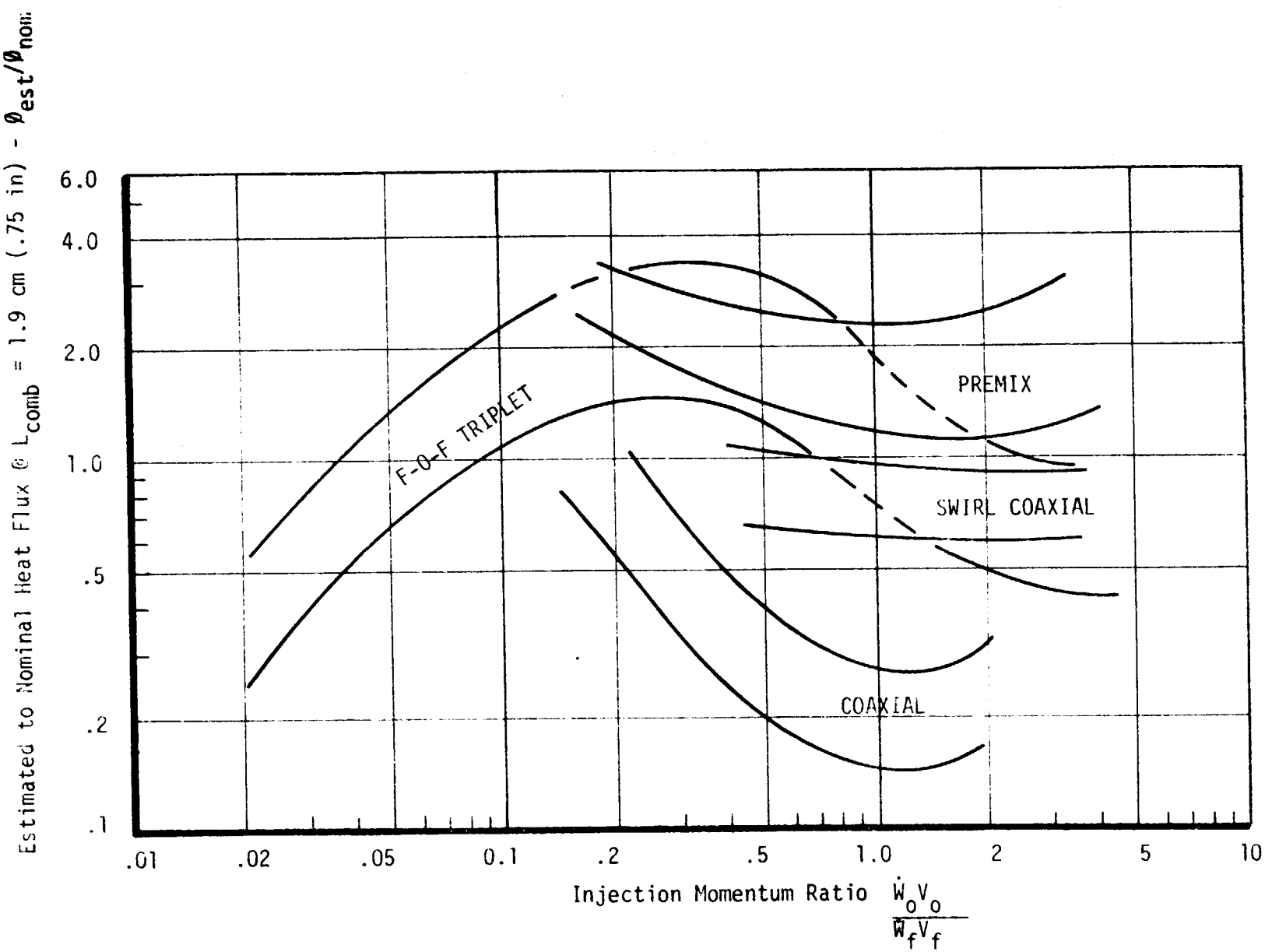

FIGURE 8 CHAMBER HEAT FLUX CHARACTERISTICS OF COAXIAL INJECTION ELEMENTS

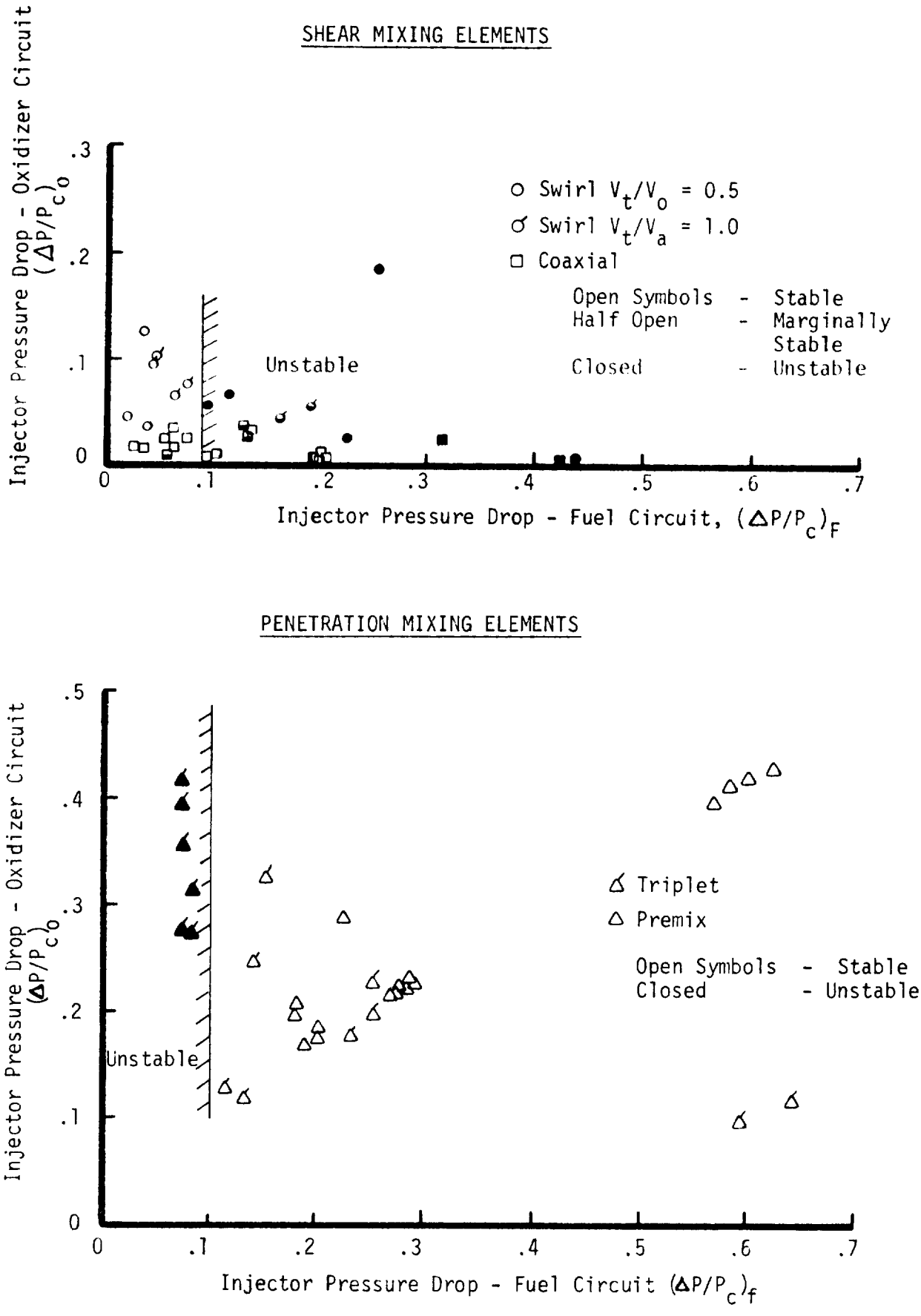

FIGURE 9. LOW FREQUENCY STABILITY CHARACTERISTICS OF GASEOUS INJECTOR ELEMENT

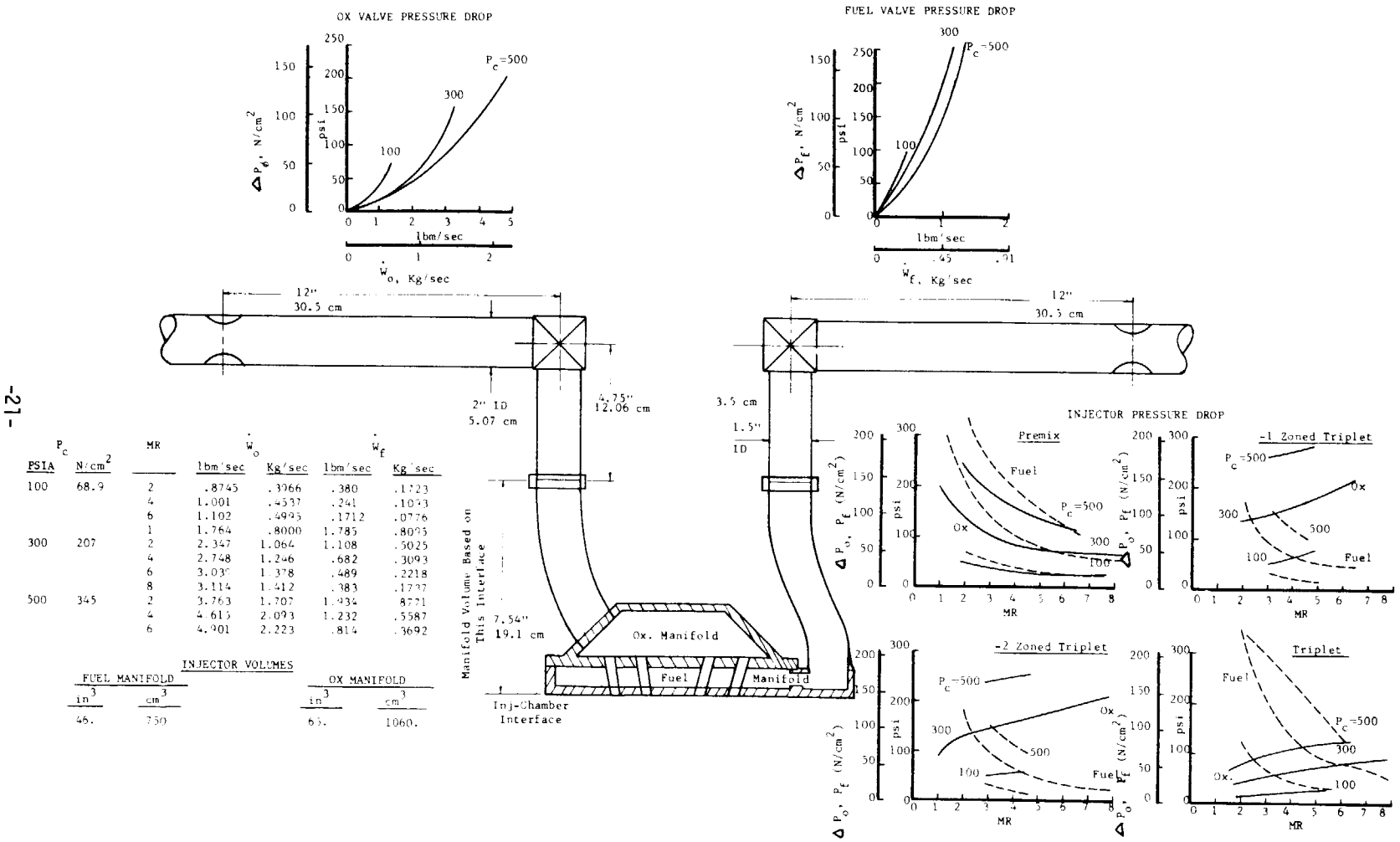

P_c PSIA	P_c N/cm^2	MR	$\dot{W}_o$ lbm/sec	$\dot{W}_o$ Kg/sec	$\dot{W}_f$ lbm/sec	$\dot{W}_f$ Kg/sec
100	68.9	2	.8745	.3966	.380	.1723
		4	1.001	.4537	.241	.1093
		6	1.102	.4995	.1712	.0776
		1	1.764	.8000	1.785	.8095
300	207	2	2.347	1.064	1.108	.5025
		4	2.748	1.246	.682	.3093
		6	3.039	1.378	.489	.2218
		8	3.114	1.412	.383	.1737
500	345	2	3.763	1.707	1.934	.8771
		4	4.615	2.093	1.232	.5587
		6	4.901	2.223	.814	.3692

INJECTOR VOLUMES

FUEL MANIFOLD in^3	FUEL MANIFOLD cm^3	OX MANIFOLD in^3	OX MANIFOLD cm^3
46.	750	65.	1060.

Figure 10. Test System Parameters Applicable to Stability Analysis

TABLE I GASEOUS INJECTION ELEMENT CHARACTERISTICS

ELEMENT TYPE	ELEMENT CONFIGURATION	COMBUSTION PERFORMANCE CHARACTERISTICS	CHAMBER HEAD-END HEAT FLUX CHARACTERISTICS	STABILITY CHARACTERISTICS
COAXIAL 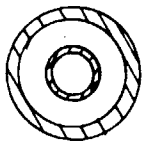	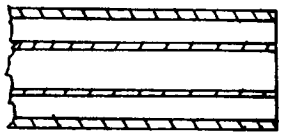	Low ERE, unless combined with long chamber or high ΔV	Low heat flux except at low $(\dot{M}V)_O / (\dot{M}V)_F$	Low freq. - unstable at $\Delta P_F/P_C \geq 0.1$ Hi Freq - Stable tendency.
INC. SHEAR 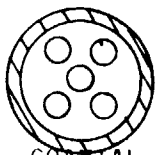	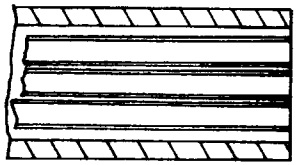	Slightly higher performance than coaxial.	Similar to coaxial.	(Not Determined)
COAXIAL SWIRLER 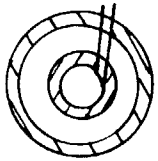	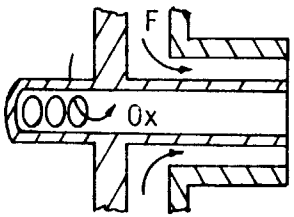	Mid-range performance.	Mid-range heat flux.	Low freq. - unstable at $\Delta P_F/P_C \geq 0.1$ High freq. - stable tendency.
IMPINGING  TRIPLET	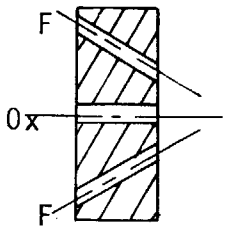	High performance at optimum $\dot{M}V_O/\dot{M}V_F$	Highly variable (Streaks); sensitive to $\dot{M}V_O/\dot{M}V_F$ and orientation	Low freq. - unstable at $\Delta P_F/P_C \leq 0.1$ High freq. - unstable tendency
PREMIX 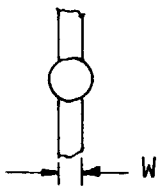	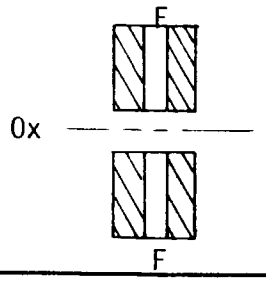	High performance; relatively insensitive to $\dot{M}V_O/\dot{M}V_F$ and geometry	High heat flux; relatively insensitive to $\dot{M}V_O/\dot{M}V_F$ and geometry	Low Freq. - Stable Hi. Freq. - stable tendency

TABLE II

MIXING EFFICIENCY EQUATIONS

Element Type	Equation	Constant Reference	Comments
Coaxial and Increased Shear Coaxial	$E_m = 100 - 26.2 \ln \left[\frac{K_c}{(L_{cold}/D_{eq_o})}\right]$	$K_c = f\left[\frac{V_f - V_o}{V_o}\left(\frac{D_{eq_o}}{D_{H_o}}\right)^{1.6}\right]$ (Figure 2)	$D_{eq_o} = \sqrt{\frac{4\,A_o}{\pi}}$ $D_{H_o} = \frac{4\,A_o}{WP}$
Swirler	$E_m = 100 - 5 \ln \left[\frac{K_s}{(L_{cold}/D_o)}\right]$	$K_s = f\left(\frac{V_f - V_o}{V_o}\right)$ (Figure 3)	Valid for V_{ot}/V_{oa} = 1.0; for other values See Figure 6
F-O-F Triplets	$E_m = 100 - K_T \ln \left[\frac{9.5}{(L_{cold}/D_o)}\right]$	$K_T = f\left(\frac{2.3\,\dot{W}_o\,V_o}{\dot{W}_f V_f \sin\alpha}\right)$ (Figure 4)	α = Impingement half angle
Premix	$E_m = \frac{100 - K_p \ln \left[\frac{21}{(L_{cold}/D_o)}\right]}{1 + \left[\frac{3}{(L_{cold}/D_o)}\right](.07\,W/D_o - .02)}$	$K_p = f\left(\frac{\dot{W}_f V_f}{\dot{W}_o V_o}\right)$ (Figure 5)	Valid for both pentads and triplets. Valid for cup depths of 2 ox diameters.

TABLE III

GAS/GAS INJECTOR STABILITY DATA

Premix Injector

Test	Chamber Contraction Ratio	L* In.	L* CM	Chamber Pressure Psia	Chamber Pressure N/CM^2	$W_\emptyset$ lbm/sec	$W_\emptyset$ Kg/sec	W_f lbm/sec	W_f kg/sec	ΔP_{ox} PSI	ΔP_{ox} N/CM^2	ΔP_{Fuel} PSI	ΔP_{Fuel} N/CM^2	Freq. HZ	Peak to Peak Amp. PSI	Peak to Peak Amp. N/CM^2	Comments
2K-11-101	3.38	5.32	13.51	291	201	2.61	1.184	0.678	0.307	82.7	57.0	104	71.7				Stable
102	3.38	5.32	13.51	296	204	2.726	1.236	0.667	0.302	81.0	55.8	99.3	68.5				
103	3.38	5.32	13.51	305	210	2.304	1.045	1.139	0.517	132	91.0	204	141				
104	3.38	5.32	13.51	277	191	2.826	1.282	0.486	0.220	69.5	48.0	68.9	47.5				
105	3.38	5.32	13.51	104	71.7	0.780	0.354	0.384	1.174	43.6	30.1	65.8	45.4				
106	3.38	5.32	13.51	116	80.0	0.924	0.419	0.368	0.167	42.5	29.3	61.0	42.1				
107	3.38	5.32	13.51	110	75.8	1.116	0.506	0.217	0.0984	28.9	19.9	30.8	21.2				
108	3.38	5.32	13.51	104	71.7	1.201	0.545	0.162	0.0735	26.0	17.9	23.8	16.4				
134	3.38	5.32	13.51	291	201	1.774	0.805	1.754	0.795	199	137	364	251				
135	3.38	16.65	34.67	309	213	2.470	1.120	1.093	0.496	136	93.8	198	137				Stable
136	3.38	13.65	34.67	306	211	2.823	1.280	0.679	0.308	91.9	63.4	110	76.1	12,000	15	10.3	Noisy
137	3.38	13.65	34.67	295	203	3.134	1.421	0.496	0.225	76.5	52.7	75.3	51.9				Stable
138	2.03	3.29	8.36	180	124	2.389	1.083	1.108	0.502	207	143	285	197				Stable
139	2.03	3.29	8.36	180	124	2.833	1.285	0.686	0.311	141	97.2	165	114				Noisy
140	2.03	3.29	8.36	165	114	3.093	1.782	0.466	0.211	112	77.2	110	75.8				Stable
141*	3.38	5.32	13.51	309	213	2.799	1.269	0.676	0.307	91.2	62.9	110	75.8	12,600	135	93.1	Bomb Test; Test Unstable for Total Duration
142	3.38	5.32	13.51	266	183	3.176	1.440	0.371	0.168	67.3	46.4	55.3	38.1				Stable
143	3.38	5.32	13.51	527	363	4.644	2.106	1.234	0.560	163	112	207	143	12,800	142	97.9	Unstable
144	3.38	5.32	13.51	474	327	4.939	2.240	0.831	0.377	121	83.4	127	87.6				
154	3.38	5.32	13.51	528	364	3.880	1.760	1.952	0.885	237	163	362	250				
155	3.38	5.32	13.51	291	201	2.673	1.212	0.664	0.301	71.7	49.4	86.7	59.8				

* Bomb 2 grain RDX

TABLE III (cont.)

Triplet Injector

Test	Chamber Contraction Ratio	L* In.	L* CM	Chamber Pressure Psia	Chamber Pressure N/CM^2	W_ϕ lbm/sec	W_ϕ Kg/sec	W_f lbm/sec	W_f Kg/sec	ΔP_{ox} PSI	ΔP_{ox} N/CM^2	ΔP_{Fuel} PSI	ΔP_{Fuel} N/CM^2	Freq. HZ	Peak to Peak Amp. PSI	Peak to Peak Amp. N/CM^2	Comments
2K-11-111	3.38	5.32	13.51	302	208	2.720	1.234	0.689	0.312	65.8	45.4	141	97.2	26,000	28.2	19.4	Noisy
112	3.38	5.32	13.51	306	211	2.304	1.045	1.099	0.498	43.9	30.3	332	229				Stable
113	3.38	5.32	13.51	285	196	2.948	1.337	0.501	0.227	78.5	54.1	81.4	56.1				Stable
114	3.38	5.32	13.51	110	76	0.825	0.374	0.392	0.1778	14.9	10.3	119	82.0				
115	3.38	5.32	13.51	105	72	0.945	0.429	0.244	0.1107	22.8	15.7	50.2	34.6	24,000	95	65.2	Unstable for short time in middle of run.
116	3.38	5.32	13.51	98	67.5	1.002	0.454	0.180	0.0816	28.3	19.5	30.6	21.1				
117	3.38	13.65	34.67	296	204	2.677	1.214	0.675	0.306	64.1	44.2	140	96.5				Stable
118	3.38	13.65	34.67	305	210	2.297	1.042	1.096	0.497	41.3	28.5	331	228				↓
119	3.38	13.65	34.67	297	204	3.167	1.436	0.497	0.225	87.9	60.6	78.8	55.0				
120	2.03	3.29	8.36	168	116	3.023	1.371	0.495	0.224	150	103	132	91.0				
121	2.03	3.29	8.36	189	130	2.514	1.140	1.101	0.499	86.1	59.4	453	312				
122	2.03	3.29	8.36	172	118	2.657	1.205	0.686	0.311	113	77.9	229	158				Stable
123*	3.38	5.32	13.51	305	210	2.755	1.249	0.676	0.307	64.8	44.7	141	97.2	19,000	64	44.1	Unstable Before Bomb.
124	3.38	5.32	13.51	267	184	3.124	1.417	0.389	0.1764	91.3	62.9	53.5	36.9	24,000	30	20.7	Unstable After Bomb.
126	3.38	5.32	13.51	458	316	3.728	1.691	1.744	0.791	82.9	57.2	340	234	20,000	222	153	Unstable After 0.36 sec.
127	3.38	5.32	13.51	520	358	4.532	2.055	1.232	0.559	105	72.4	273	188	22,000	137	94	Unstable
128	3.38	5.32	13.51	472	326	4.863	2.205	0.797	0.361	125	86.2	131	90.3				
131	3.38	5.32	13.51	307	211	2.734	1.240	0.712	0.323	50.2	34.6	115	79.3	18,000	138	95.2	Unstable
132	3.38	5.32	13.51	516	356	3.680	1.669	2.107	0.956	59.7	41.2	-					
133	3.38	5.32	13.51	292	202	1.761	0.799	1.844	0.836	22.6	15.8	-					
								-1 Zoned Triplet									
147	3.38	5.32	13.51	296	204	2.772	1.257	0.673	0.305	162	112	65.5	45.2				
148	3.38	5.32	13.51	283	195	3.037	1.377	0.477	0.216	210	145	46.5	32.1	12,000	205	141	Unstable
149*	3.38	5.32	13.51	300	207	2.765	1.254	0.667	0.302	165	114	63.1	43.5				Stable Test; 312 PSI Peak to Peak @ Bomb, Attenuating to tare amplitude in 0.08 sec.
150	3.38	5.32	13.51	308	212	2.362	1.071	1.114	0.505	137	94	182	125				
151	3.38	5.32	13.51	109	75.2	0.993	.450	0.251	0.114	62.4	43.0	23.1	15.9				
152B	3.38	5.32	13.51	527	363	4.670	2.118	1.231	0.558	267	184	127	87.6				
								-2 Zoned Triplet									
157	3.38	5.32	13.51	107	73.8	0.948	0.430	0.251	0.114	55.3	38.1	24.2	16.7				
158	3.38	5.32	13.51	264	182	3.040	1.379	0.388	0.176	208	143.	21.9	15.1				
159	3.38	5.32	13.51	316	218	2.860	1.297	0.710	0.322	157	108	64.2	44.3				
160*	3.38	5.32	13.51	316	218	2.853	1.294	0.704	0.319	159	110	64.0	44.1				Stable Test; 78 PSI Peak to Peak @ Bomb attenuating to tare amplitude in .08 sec.
161	3.38	5.32	13.51	292	201	3.056	1.386	0.479	0.217	191	132	30.9	21.3				
162	3.38	5.32	13.51	324	223	2.416	1.096	1.160	0.526	134	92.4	181	125				
163	3.38	5.32	13.51	301	208	1.751	0.794	1.789	0.811	68.3	47.1	393	271				
164	3.38	5.32	13.51	536	370	4.583	2.078	1.273	0.577	244	168	128	88.3				

III ANALYTICAL MODEL

A. Introduction and General Procedure

The analytical model described in this section can be used by the designer to select the element type and independently vary injector and chamber design parameters to determine performance and chamber heat flux predictions. The effects of allowable ranges of feed system pressure drops, element geometry and size, and hydraulic characteristics also can be evaluated by the model. The chamber length parameter can be varied parametrically to analyze the effect of length on mixing rate. The chamber contraction ratio and design (or experimental test) wall temperature need to be specified only if chamber heat flux estimates are required.

The flow chart shown in Figure 11 illustrates how the generalized analytical model is utilized to predict either cold flow or combustion performance and chamber wall heat flux. The upper left block represents required model input data which must either be specified by system design requirements or assumed as preliminary design criteria. The Injector, Chamber, and Element Selection blocks represent the designer's discretion in selecting the design combination which best satisfies all of his requirements. The upper central blocks may be bypassed if chamber heat flux estimates or combustion performance effects are not required. The bottom group of blocks convert the non-dimensional mixing parameters B_a or B_t into oxidizer-rich and fuel-rich stream tube mixture ratios. The two upper right blocks list the tables which contain generalized equations used to predict performance and chamber heat flux, respectively, for all element types.

B. Description of Calculational Procedure

The above outlined procedure can be used as a generalized model to calculate local mixing distributions. For the elements specifically mentioned, both oxidizer and fuel calculational procedures are defined step-by-step in Tables IV thru IX. For elements not listed, the appropriate generalized equations can be developed by following the modeling instructions given in the

final report. Appropriate equations to calculate hydraulic diameters at the injector face plane and spray angles are listed on the tables if applicable. The tables specify recommended values of interaction exponents and specify whether the axi-symmetric correlation B_a or the two dimensional correlation B_t labeled on Figure 12 should be utilized. As a final output from these tables, values for mixing correlation parameter, B, are determined. Values for B_{ao} or B_{to} and B_{af} or B_{tf} are then used to enter Figure 12 to determine the local mixture ratios, η_j and η_i, respectively, which are required in the combustion performance and chamber heat flux predictions to define the fuel rich and oxidizer rich stream tube mixture ratios.

If hot-fire performance and/or chamber heat flux values are required, then combustion influence parameters (Da) must be included in the calculation. For combustion performance problems several iterations may be required until the calculated combustion influence parameter converges upon the assumed value used in the equations for obtaining the parameter B as defined in Tables IV through IX. This process is demonstrated in the sample problem included at the end of this section.

The combustion influence parameter for ambient temperature GO_2/GH_2 is plotted vs. O/F in Figure 13, and for 82.6% FLOX/CH_4 in Figure 14. For other propellant combinations, the following procedure must be followed to determine the combustion influence parameter.

1. One dimensional equilibrium thermochemical data must be generated for the particular propellant combination and combustion chamber conditions (inlet temperature and pressure) over a range of mixture ratios from about 10^{-2} to 10^{2} times stoichiometric proportions. A program such as JANNAF ODE is recommended (See Reference 2).

2. From the data obtained in Step 1, the combustion influence parameter can be calculated at each mixture ratio from the terms in the right hand side of the following equation:

III.B. Description of Calculational Procedure (cont.)

$$\text{Combustion influence parameter} = \frac{dP}{P} + \frac{dA}{A} + \frac{dV}{V} = \frac{dT}{T} - \frac{dMW}{MW}$$

3. The combustion influence parameter is then plotted vs mixture ratio as shown for the two propellant combinations used in this section (Figures 13 and 14).

Using the η parameters obtained from Figure 12 the performance and chamber heat flux predictions can be determined according to the procedures outlined in Tables X and XI, respectively. The only additional data required for the performance prediction procedure outlined in Table X are values for theoretical C* and I_{sp} vs O/F for the desired propellant combination. It is recommended that this theoretical data be obtained from the JANNAF ODE computer program (Reference 2). A sample problem is included in the next section to assure the reader that he is following correctly the intended calculation procedure. The only additional data required for the chamber wall heat flux prediction procedure outlined in Table XI are values for theoretical gas temperature and gas properties vs O/F for the desired propellant combination. The theoretical gas temperature can be obtained from the Reference 2 JANNAF program and the gas properties can be obtained from other sources available to the user such as Reference 6 for conventional rocket propellants or Reference 4 for air-hydrocarbon reactants.

After calculating heat fluxes for the oxidizer rich and fuel-rich stream tubes as outlined in Table XI and comparing them with the nominal uniform mixture ratio value, the designer must visually examine his injector pattern layout to identify the local wall mixture ratio. For example, if annular fuel co-axial elements are used the wall mixture ratio will be fuel rich. Hence the wall heat flux will be more closely approximated by using ϕ_i . If external impinging F-O-F triplets are used, the wall O/F will depend upon element orientation next to the wall and whether the fuel underpenetrates ($Y < .5\ D_o$) or overpenetrates ($Y > .5\ D_o$) the oxidizer jet. In the event of like doublets, predicted wall heat flux will depend upon whether a fuel doublet or oxidizer doublet is nearest the wall. For a detailed description of how these factors influenced chamber heat flux on this program, the reader is referred to the Final Report, Reference 1.

C. SAMPLE PROBLEM FOR COLD FLOW AND HOT-FIRE PERFORMANCE

TASK: Predict the following performance parameters:

1. Cold Flow E_m @ L = 1 & 5 in.
2. Hot Fire E_m and % C* @ L = 5 in.

GIVEN DESIGN REQUIREMENTS:

		MW	T	ρ	μ
Oxidizer:	82.6% FLOX	36.8	400°R	0.86 lbm/ft^3	.95 x 1(lbm/ft-
Fuel:	CH_4	16.	800°R	0.19 lbm/ft^3	9.0 x 1(lbm/ft-

F_{vac} = 1,000 lb_f, P_c = 100 psia, O/F = 5.75, ε = 40:1

ASSUMED PERFORMANCE GOALS: 96% C*, 92% I_{sp}

C* (5.75) = 7100 fps; I_{sp} (ε = 40, 5.75) = 420

ASSUMED PRELIMINARY DESIGN PARAMETERS:

Element Type: Shear Co-Ax

	ΔP	C_d	N = 20	T_W = 1800°R
Oxid:	15 psi	.85	L = 5 in.	
Fuel:	25 psi	.75	CR = 3.0	

CALCULATIONS:

Injector Flow Rates

$$\dot{W}_t = \frac{F_{vac}}{(\%\ I_{sp})\ (I_{sp,\ theo})} = \frac{(1{,}000)}{(.92)\ (420)} = 2.59 \text{ lbm/sec}$$

$$\dot{W}_o = \frac{O/F}{1 + O/F} \cdot \dot{W}_t = \frac{5.75}{1 + 5.75} \quad (2.59) = 2.206 \text{ lbm/sec}$$

Injector Flow Rates (cont.)

$$\dot{W}_f = \frac{\dot{W}_t}{1 + O/F} = \frac{2.59}{1 + 5.75} = .384 \text{ lbm/sec}$$

Chamber Design

$$A_t = \frac{(\%C^*)\ (C^*_{theo})\ \dot{W}_t}{P_c\ g} = \frac{.96\ (7100)\ (2.59)}{(100)\ (32.2)} = 5.48 \text{ in}^2$$

$$A_c = A_t \cdot CR = 5.48\ (3.0) = 16.5 \text{ in}^2$$

$$A_e = A_t \cdot \varepsilon = 5.48\ (40) = 219 \text{ in}^2$$

Injector Design

$$V_o = \sqrt{2\ g\ \frac{\Delta P_o}{\rho_o}} = \left(\frac{12 \text{ in}}{\text{ft}}\right) \sqrt{2\ (32.2)\ \frac{15}{.86}} = 400 \text{ fps}$$

$$V_f = 12 \sqrt{2\ (32.2)\ \frac{25}{.19}} = 1100 \text{ fps}$$

$$A_o = \frac{\dot{W}_o}{N\ \rho_o\ V_o\ C_{do}} = \frac{(144\ \frac{\text{in}^2}{\text{ft}^2})\ (2.206)}{20\ (.86)\ (400)\ (.85)} = .0543 \text{ in}^2$$

$$A_f = \frac{144\ (.384)}{20\ (.19)\ (1100)\ (.75)} = .0176 \text{ in}^2$$

$$D_o = \sqrt{\frac{4\ (.0543 \text{ in}^2)}{\pi}} = 0.263 \text{ in} = D_{Ho}$$

Let Tube wall thickness (t_w) = .010 in.

$$D_{fl} = D_o + 2\ (t_w) = .263 + 2\ (.010) = .283 \text{ in.}$$

$$D_{f2} = \sqrt{D_{f1}^2 + \frac{4\,A_f}{\pi}} = \sqrt{.283^2 + \frac{4\,(.0176)}{\pi}} = .320 \text{ in.}$$

$$D_{Hf} = D_{f2} - D_{f1} = .320 - .283 = .037 \text{ in.}$$

$$Re_{do} = \frac{\rho_o\,(C_{do}\,V_o)\,D_{Ho}}{\mu_o} = \frac{(.86)\,[.85\,(400)]\,(.263)}{(.95 \times 10^{-5})\,(12\,\frac{\text{in}}{\text{ft}})} = 6.75 \times 10$$

$$Re_{df} = \frac{.19\,[.75\,(1100)]\,(.037)}{(9.0 \times 10^{-5})\,(\frac{12 \text{ in}}{\text{ft}})} = 0.54 \times 10^4$$

$$Pd_o = \frac{1}{2}\,\rho_o\,V_o^2 = \frac{.86}{2\,(32.2)}\left[\frac{400}{12 \text{ in/ft}}\right]^2 = 14.8 \text{ psi}$$

$$Pd_f = \frac{.19}{2\,(32.2)}\left[\frac{1100}{12}\right]^2 = 24.8 \text{ psi}$$

$$Pd_{eq} = \frac{Pd_o + \frac{MW_o/MW_f}{O/F}\,Pd_f}{1 + \frac{MW_o/MW_f}{O/F}}$$

$$Pd_{eq} = \frac{14.8 + \frac{(36.8/16)}{5.75}\,[24.8]}{1 + .40} = 17.6 \text{ psi}$$

$$\frac{4\,(O/F)}{MW_o/MW_f} = \frac{4\,(5.75)}{36.8/16.} = 10.0$$

The above parameter is not within 0.5 to 2.0 range. Therefore we must use Figure 15 instead of using mole fraction terms in B_a or B_t parameters.

for B_{ao} $\quad \frac{B_a\,@\,(10)}{B_a\,@\,(1)} = 2.43$

for B_{tf} $\quad \frac{B_t\,@\,(10)}{B_t\,@\,(1)} = .43$

Cold Flow Distribution

L = 1.0 in.

$$B_{ao} = \frac{(L/D_{Ho}) \left[\frac{B_{a\ @\ (10)}}{B_{a\ @\ (1.0)}}\right]}{[C_{do}\ (1 + Da_o)\ ]^{.625} \left[\frac{Re_{do}}{10^5}\right]^{.25} \left[\frac{Pd_o}{Pd_{eq}}\right]^{F_o}}$$

$$B_{ao} = \frac{\left[\frac{1.0}{.263}\right]\ [2.43]}{\left[.85\ (1 + 0)\right]^{.625}\ [6.75]^{.25} \left[\frac{14.8}{17.6}\right]^{1.0}} = 7.54$$

Use the above value of B_{ao} to find η_j from Figure 12.

$\eta_j = 0.55$; $(O/F)_j = O/F/\ \eta_j = 5.75/.55 = 10.4$

$$B_{tf} = \frac{(L/D_{Hf}) \left[\frac{B_{t\ @\ (10)}}{B_{t\ @\ (1.0)}}\right]}{\left[C_{df}\ (1 + Da_f)\right]^{1.25} \left[\frac{Re_{df}}{10^5}\right]^{.25} \left[\frac{Pd_f}{Pd_{eq}}\right]^{F_f}}$$

$$B_{tf} = \frac{\left[\frac{1.0}{.037}\right]\ [.43]}{\left[.75\ (1 + 0)\right]^{1.25}\ [.054]^{.25} \left[\frac{24.8}{17.6}\right]^{.5}} = 29.0$$

Use the above value of B_{tf} to find η_i from Figure 12.

$\eta_i = 0.66$; $\eta_i\ (O/F) = .66\ (5.75) = 3.79 = O/F_i$

$$U = \eta_j \frac{(1 - \eta_i)}{(1 - \eta_j)} = .55 \frac{(1 - .66)}{(1 - .55)} = .415$$

$$X_j = \frac{U}{1+U}\left(\frac{1+O/F_j}{1+O/F}\right) = \frac{.415}{1+.415}\left(\frac{1+10.4}{1+5.75}\right) = .495$$

$$X_i = 1 - X_j = 1 - .495 = .505$$

$$E_m = 100\left\{1 - X_j\left[\frac{(O/F)_j - (O/F)}{1+(O/F)_j}\right] - X_i\left[\frac{(O/F)-(O/F)_i}{O/F\,[1+(O/F)_i]}\right]\right\}$$

$$= 100\left[1.0 - .495\left[\frac{10.4-5.75}{1+10.4}\right] - .505\left[\frac{5.75-3.79}{5.75\,(1+3.79)}\right]\right] = 76.2\%$$

at L = 5 in. (Cold Flow)

$B_{ao} = 37.7$ $\quad \eta_j = .951$ $\quad O/F_j = 6.04$

$B_{tf} = 145$ $\quad \eta_i = .940$ $\quad O/F_i = 5.40$

$U = 1.16$ $\quad X_j = .560$ $\quad X_i = .440$

$$E_m = 100\left[1 - .56\left(\frac{0.29}{6.75}\right) - .44\left(\frac{0.35}{5.75\,(6.40)}\right)\right] = 97.2\%$$

<u>For Hot Fire Mixing at L = 5 in.</u>

From above cold flow solution at L = 5-in., $(O/F)_j = 6.04$ and $(O/F)_i = 5.40$. So from Figure 14

$Da_o = 13.9$ at $O/F_j \approx 6.04$

$Da_f = 14.0$ at $O/F_i \approx 5.40$

However, the above combustion influence parameters were for ambient ($540^{\circ}R$) temperature propellants. Thus, they must be corrected for design inlet temperatures as shown below.

Assume $Da_o\ (T_o) = [Da_o\ (T_{ref})]\ \frac{T_{ref}}{T_o}$

$$Da_o\ (400^oR) = 13.9\left(\frac{540\ ^oR}{400^oR}\right) = 18.8$$

$$Da_f\ (800\ ^oR) = 14.0\left(\frac{540^oR}{800^oR}\right) = 9.4$$

Go back and re-calculate hot fire B_{ao} & B_{tf} at L = 5 in.

$$B_{ao} = \frac{\left(\frac{5.0}{.263}\right)[2.43]}{\left[.85\ (1 + 18.8)\right]^{.625}\ [6.75]^{.25}\left[\frac{14.8}{17.6}\right]^{0.2}} = 5.07$$

$\eta_j = .313$ $\quad O/F_j = 18.4$ $\quad Da_o\ (540^oR) = 8.5$

$$Da_o\ (400^oR) = 8.5\ \frac{540}{400} = 11.5$$

Iterate on O/F_j and Da_o

Assume $Da_o \approx 14.0$

$$B_a = \left(\frac{1 + 18.8}{1 + 14}\right)^{.625}\ (5.07) = 6.03$$

$\eta_j = .415$ $\quad O/F_j = 13.8$ $\quad Da_o\ (540^oR) = 10.3$

$Da_o = 10.3\ (\frac{540}{400}) = 13.9$ $\quad$ O.K. (Close enough)

Similarly for hot fire fuel

$$B_{tf} = \frac{\left[\frac{5.0}{.037}\right]\ [0.43]}{\left[.75\ (1 + 9.4)\right]^{1.25}\ [.054]^{.25}\left[\frac{24.8}{17.6}\right]^{0.0}} = 9.25$$

$\eta_i = .32$ $\quad O/F_i = 1.84$ $\quad Da_f\ (540^oR) = 7.6$

$$Da_f\ (800^oR) = 8.6\ \frac{540}{800} = 5.1$$

On next iteration assume $Da_f \approx 6.0$

$$B_{tf} = \left[\frac{1 + 9.4}{1 + 6.0}\right]^{1.25} (9.25) = 15.2$$

$\eta_i = .45$ $\quad O/F_i = 2.59$ $\quad Da_f \ (540^{\circ}R) = 9.5$

$Da_f \ (800^{\circ}R) = 9.5 \ \frac{540}{800} = 6.4$ O.K. (Close enough)

$$U = .415 \ \frac{(1 - .45)}{(1 - .415)} = .39 \qquad X_j = \frac{.39}{1.39}\left(\frac{1 + 13.8}{1 + 5.75}\right)$$

$X_j = .615$ $\quad X_i = .385$

$$E_m = 100\left[1 - .615\left(\frac{13.8 - 5.75}{14.8}\right) - .385\left(\frac{3.16}{5.75 \times 3.59}\right)\right] = 60.7\%$$

Notice the difference from 97.2% cold flow E_m to 60.7% hot fire E_m with same propellants and chamber length. Combustion E_m at 5 in. is less than 76.2% cold flow E_m at 1 in.

$$\%C^* = \frac{(X_j)\left[C^*\ (O/F)_j\right] + (X_i)\left[C^*\ (O/F)_i\right]}{C^*\ (O/F)}$$

$$\%C^* = \frac{.615\ [5540] + .385\ [6600]}{7100} = \frac{5950}{7100} = 83.8\%$$

Note that for this initial preliminary injector design that the predicted combustion performance is significantly lower than the 96% design goal assumed. At this point 3 options are available to the designer:

1. Increase numbers of injection element, N $>$ 20, to decrease hydraulic diameters to improve efficiency.

2. Increase chamber length to improve mixing.

3. Select another element type which has higher mixing characteristics.

Option 1 may be limited by already narrow fuel annulus gap, $t_f = 1/2 (D_{f2} - D_{f1}) = .0185$ in. Option 2 for present injector requires factor of 2.5 to 3.0 increase in present chamber length and may be impractical. Option 3 appears most attractive.

Go back and re-iterate until a satisfactory design is achieved.

In any event this one hour hand calculation using the generalized charts will have prevented the designer from selecting a dismal performing injector in spite of its attractive 97.2% E_m which could be expected from experimental cold flow tests.

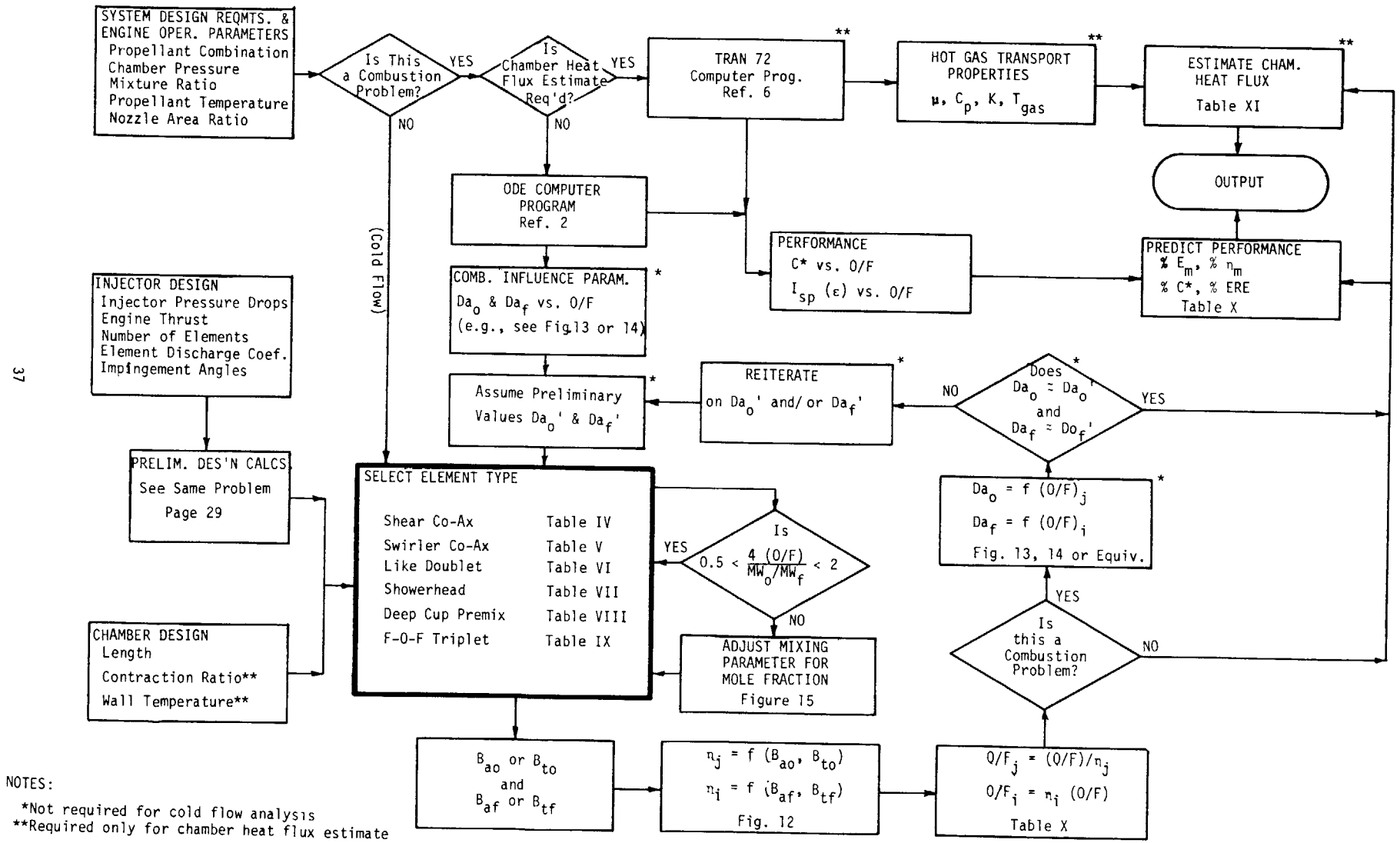

NOTES:

*Not required for cold flow analysis
**Required only for chamber heat flux estimate

Figure 11. Flow Chart for Analytical Model

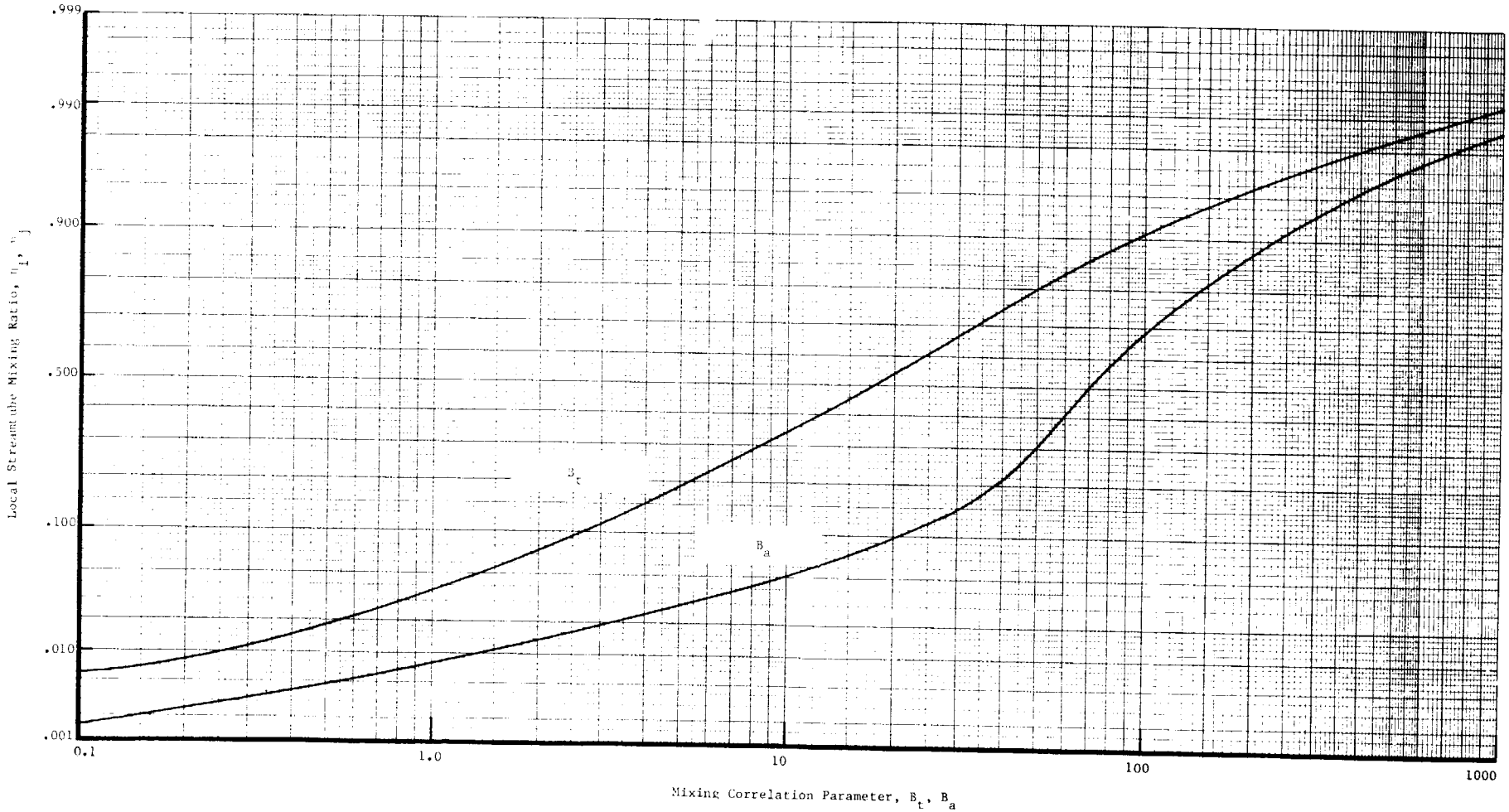

FIGURE 12. GENERALIZED MIXING CORRELATION CHART

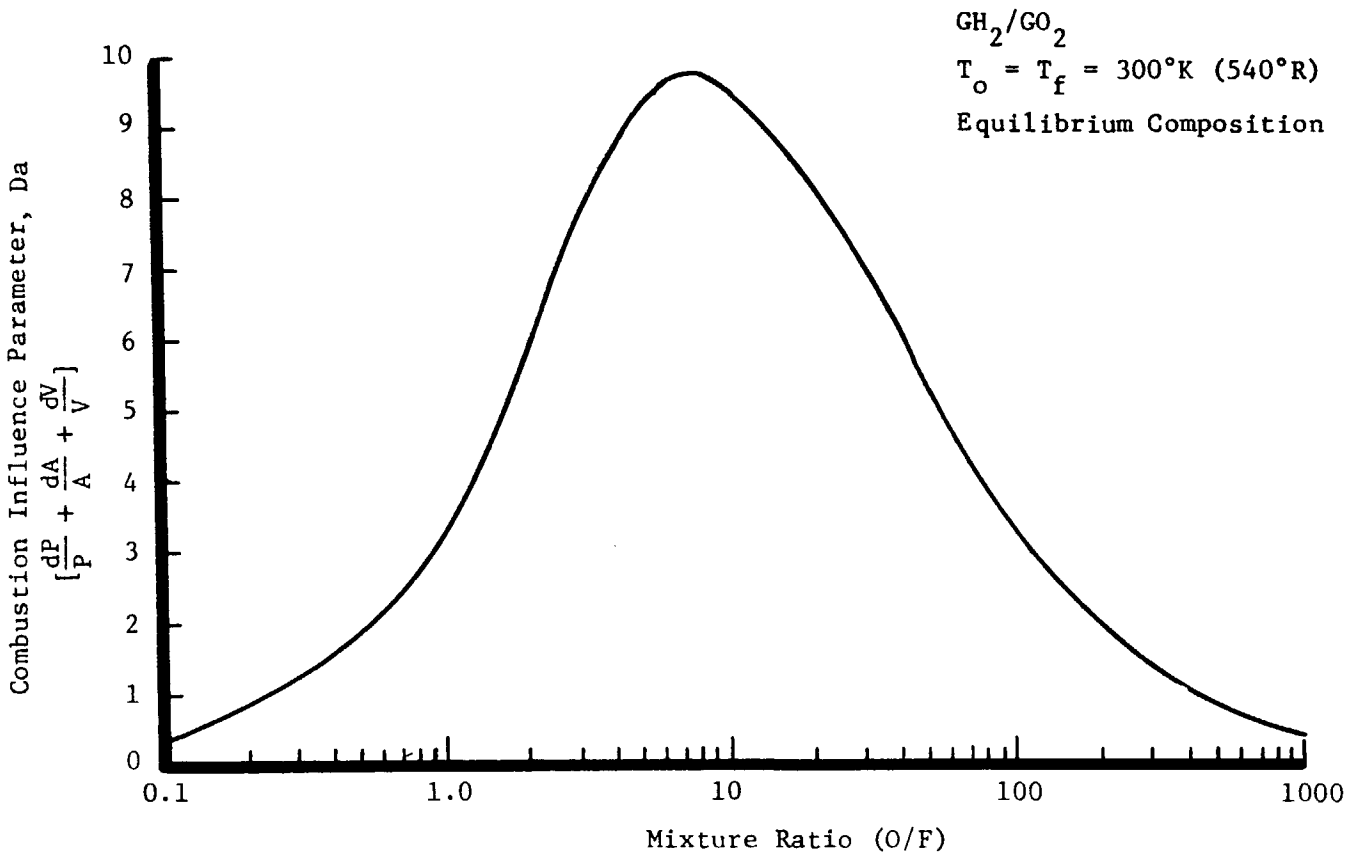

FIGURE 13. COMBUSTION INFLUENCE PARAMETER VS. MIXTURE RATIO GO_2/GH_2

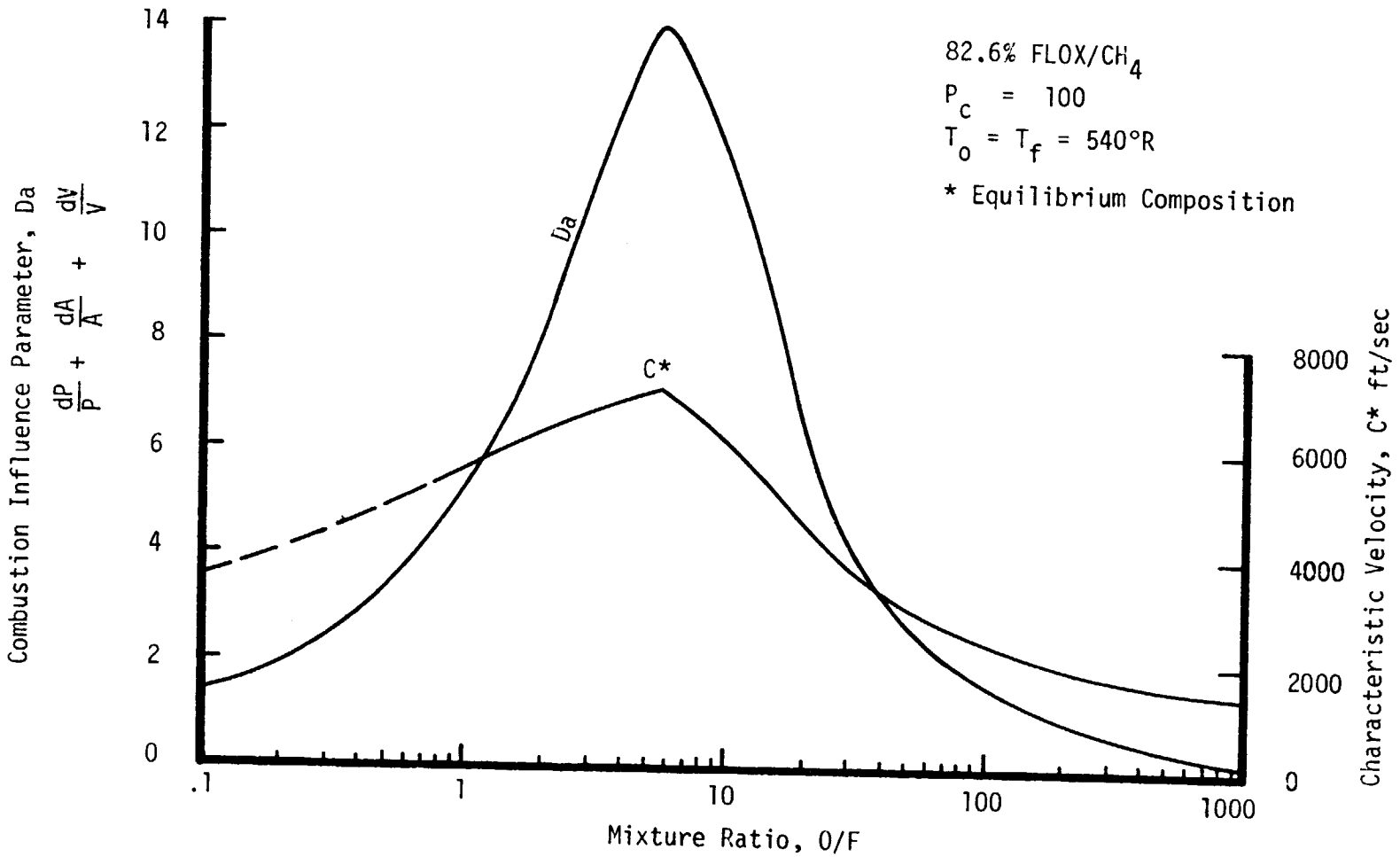

FIGURE 14. FLOX/CH_4 THERMOCHEMICAL DATA

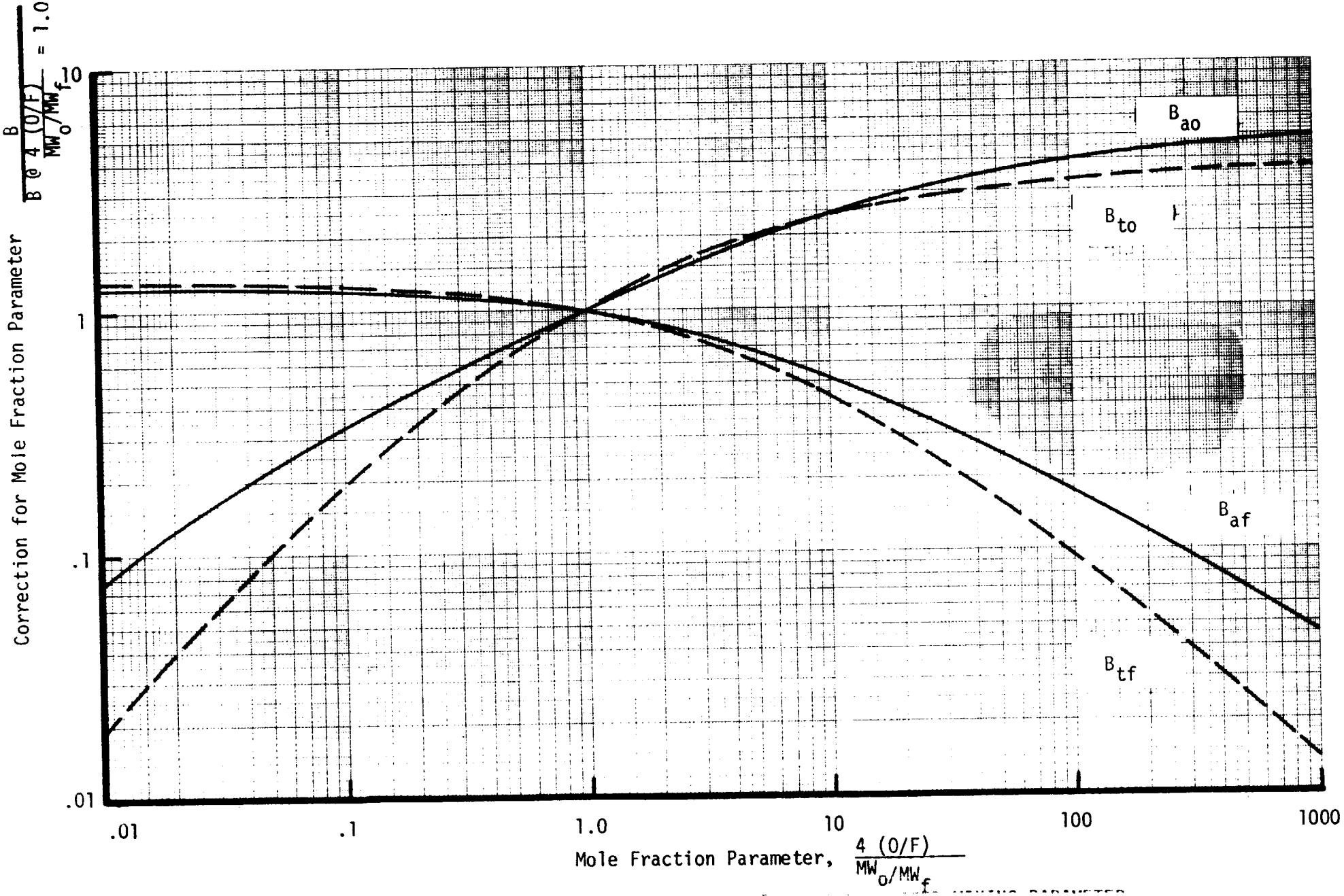
Correction for Mole Fraction Parameter $\frac{B}{B\ @\ \frac{4\ (O/F)}{MW_o/MW_f} = 1.0}$
10
1
.1
.01
B_{ao}
B_{to}
B_{af}
B_{tf}
.01
.1
1.0
10
100
1000
Mole Fraction Parameter, $\frac{4\ (O/F)}{MW_o/MW_f}$

TABLE IV

SHEAR COAXIAL ELEMENT EQUATIONS

	OXIDIZER	FUEL
Diffusion Characteristic:	Axi-Symmetric	Two-Dimensional
Hydraulic Diameter:	$D_{Ho} = \left[\frac{4\ A_o}{\pi}\right]^{1/2}$	$D_{Hf} = D_{f2} - D_{f1}$

COLD FLOW

$Da_o = 0.0$	$Da_f = 0.0$
$F_o = 1.0$	$F_f = 0.5$

HOT FIRE

$Da_o = f\ (O/F)_j$	$Da_f = f\ (O/F)_i$
$F_o = 0.2$	$F_f = 0.0$

$$B_{ao} = \frac{(L/D_{Ho}) \left[\frac{4\ (O/F)}{MW_o/MW_f}\right]^{0.45}}{\left[C_{do}\ (1 + Da_o)\right]^{0.625} \left[\frac{Re_{do}}{10^5}\right]^{.25} \left[\frac{Pd_o}{Pd_{eq}}\right]^{F_o}}$$

$$B_{tf} = \frac{(L/D_{Hf})}{\left[.8 + .2\left(\frac{4\ (O/F)}{MW_o/MW_f}\right)\right]\left[C_{df}\ (1 + Da_f)\right]^{1.25} \left[\frac{Re_{df}}{10^5}\right]^{.25} \left[\frac{Pd_f}{Pd_{eq}}\right]^{F_f}}$$

NOTES:

1. If $\left[\frac{4\ (O/F)}{MW_o/MW_f}\right]$ is not > 0.5 and < 2.0 in B_{ao} and B_{tf} equations, use mole fraction correction factor in Figure 15 to evaluate $\left[\frac{4\ (O/F)}{MW_o/MW_f}\right]$

TABLE V

SWIRLER COAXIAL ELEMENT EQUATIONS

	OXIDIZER	FUEL
Diffusion Characteristics:	Two-Dimensional	Two-Dimensional
Hydraulic Diameter:	$D_{Ho} = \left[\frac{1 - \sqrt{1 - C_{do}}}{C_{do}}\right]\left[\frac{4 A_o}{\pi}\right]^{1/2}$	$D_{Hf} = D_{f2} - D_{f1}$

COLD FLOW

$Da_o = 0.0$	$Da_f = 0.0$
$F_o = 0.5$	$F_f = 0.5$

HOT FIRE

$Da_o = f\,(O/F)_j$	$Da_f = f\,(O/F)_i$
$F_o = 0.0$	$F_f = 0.0$

$$\phi = \tan^{-1}\left[\frac{\frac{(O/F)\tan\alpha_o}{V_f}}{(O/F) + \frac{}{V_o \cos\alpha_o}}\right]$$

$$(L/D)_o^* = \left[\frac{\sqrt{1 + \frac{8}{3}\left[\frac{Re_{do}}{(1 - \sqrt{1 - C_{do}})}\right]^{.2}(1 + Da_o)\, C_{do}\tan\phi} - 1}{4\tan\phi}\right]^{1.111}$$

$$(L/D)_f^* = \left[\frac{\sqrt{1 + \frac{8}{3} C_{df}\left(1 + \frac{D_{f1}}{D_{f2}}\right)\left(1 - \frac{D_{f1}}{D_{f2}}\right)^{.8} Re_{df}^{.2}\,(1 + Da_f)\tan\phi} - 1}{4\tan\phi}\right]^{1.111}$$

$$B_{to} = \frac{(L/D_{Ho})\left[\frac{4\,(O/F)}{MW_o/MW_f}\right]^{.66}\left\{2\,(1 - \sqrt{1 - C_{do}})\left[1 + 2\,(L/D)_o^*\tan\phi\right]\right\}^{1.25}}{\left[C_{do}\,(1 + Da_o)\right]^{1.25}\left[\frac{Re_{do}}{10^5}\right]^{.25}\left[\frac{Pd_o}{Pd_{eq}}\right]^{F_o}}$$

$$B_{tf} = \frac{(L/D_{Hf})\left\{\frac{2\left[1 + 2\,(L/D)_f^*\tan\phi\right]}{1 + \frac{D_{fj}}{D_{fi}}}\right\}^{1.25}}{\left[.8 + .2\left(\frac{4\,(O/F)}{MW_o/MW_f}\right)\right]\left[C_{df}\,(1 + Da_f)\right]^{1.25}\left[\frac{Re_{df}}{10^5}\right]^{.25}\left[\frac{Pd_f}{Pd_{eq}}\right]^{F_f}}$$

NOTES:

1. If $\left[\frac{4\,(O/F)}{MW_o/MW_f}\right]$ is not > 0.5 and < 2.0 in B_{to} and B_{tf} Equations, use mole fraction correction factor in Figure 15 to evaluate $\left[\frac{4\,(O/F)}{MW_o/MW_f}\right]$

2. If design L/D $<$ (L/D)* calculated in above equation, use design L/D instead of (L/D)* in B_{to} and B_{tf} equations.

TABLE VI

LIKE ON LIKE DOUBLET ELEMENT EQUATIONS

	OXIDIZER	FUEL
Diffusion Characteristics:	Two-Dimensional	Two-Dimensional
Hydraulic Diameter:	$D_{Ho} = \left[\frac{2\,A_o}{\pi}\right]^{1/2}$	$D_{Hf} = \left[\frac{2\,A_f}{\pi}\right]^{1/2}$
COLD FLOW		
	$Da_o = 0.0$	$Da_f = 0.0$
	$F_o = 0.1$	$F_f = 0.1$
HOT FIRE		
	$Da_o = f\,(O/F)_j$	$Da_f = f\,(O/F)_i$
	$F_o = 0.0$	$F_f = 0.0$
	$\phi_o = \sin^{-1}\left[\tan \alpha_o\right]$	$\phi_f = \sin^{-1}\left[\tan \alpha_f\right]$

$$(L/D)_o^* = \left[\frac{\pi C_{do}\,(1 + Da_o)}{3 \cos \alpha_o \tan \phi_o}\right]^{.555} Re_{do}^{.111} \qquad (L/D)_f^* = \left[\frac{\pi C_{df}\,(1 + Da_f)}{3 \cos \alpha_f \tan \phi_f}\right]^{.555} Re_{df}^{0.111}$$

$$B_{to} = \frac{(L/D_{Ho}) \left[\frac{4\,(O/F)}{MW_o/MW_f}\right]^{.66} \left[\frac{2}{\pi}\,(L/D)_o^* \cos \alpha_o \tan \phi_o\right]^{1.25}}{\left[C_{do}\,(1 + Da_o)\right]^{1.25} \left[\frac{Re_{do}}{10^5}\right]^{.25} \left[\frac{Pd_o}{Pd_{eq}}\right]^{F_o}}$$

$$B_{tf} = \frac{(L/D_{Hf}) \left[\frac{2}{\pi}\,(L/D)_f^* \cos \alpha_f \tan \phi_f\right]^{1.25}}{\left[.8 + .2\left(\frac{4\,O/F}{MW_o/MW_f}\right)\right] \left[C_{df}\,(1 + Da_f)\right]^{1.25} \left[\frac{Re_{df}}{10^5}\right]^{.25} \left[\frac{Pd_f}{Pd_{eq}}\right]^{F_f}}$$

NOTES:

1. If $\left[\frac{4\,(O/F)}{MW_o/MW_f}\right]$ is not > 0.5 and < 2.0 in B_{to} and B_{tf} Equations, use mole fraction correction factor in Figure 15 to evaluate $\left[\frac{4\,(O/F)}{MW_o/MW_f}\right]$

2. If design L/D $<$ (L/D)* calculated in above equation, use design L/D instead of (L/D)* in B_{to} and B_{tf} equations.

TABLE VII

SHOWERHEAD ELEMENT EQUATIONS

	OXIDIZER	FUEL
Diffusion Characteristics:	Axi-Symmetric	Axi-Symmetric
Hydraulic Diameter: Circular:	$D_{Ho} = \left[\frac{4\,A_o}{\pi}\right]^{1/2}$	$D_{Hf} = \left[\frac{4\,A_f}{\pi}\right]^{1/2}$
Non-Circular:	$D_{Ho} = \frac{4\,ab}{2\,(a+b)}$	$D_{Hf} = \frac{4\,cd}{2\,(c+d)}$

COLD FLOW

$Da_o = 0.0$	$Da_f = 0.0$
$F_o = 0.1$	$F_f = 0.1$

HOT FIRE

$Da_o = f\,(O/F)_j$	$Da_f = f\,(O/F)_i$
$F_o = 0.0$	$F_f = 0.0$

$$Ba_o = \frac{(L/D_{Ho})\left[\frac{4\,(O/F)}{MW_o/MW_f}\right]^{0.45}}{\left[C_{do}\,(1+Da_o)\right]^{.625}\left[\frac{Re_{do}}{10^5}\right]^{.25}\left[\frac{Pd_o}{Pd_{eq}}\right]^{F_o}}$$

$$Ba_f = \frac{L/D_{Hf}}{\left[\frac{4\,(O/F)}{MW_o/MW_f}\right]^{.13}\left[C_{df}\,(1+Da_f)\right]^{.625}\left[\frac{Re_{df}}{10^5}\right]^{.25}\left[\frac{Pd_f}{Pd_{eq}}\right]^{F_f}}$$

NOTE:

1. If $\left[\frac{4\,(O/F)}{MW_o/MW_f}\right]$ is not $>$ 0.5 and $<$ 2.0 in Ba_o and Ba_f equations, use mole fraction correction factor in Figure 15 to evaluate $\left[\frac{4\,(O/F)}{MW_o/MW_f}\right]$

TABLE VIII

PREMIX (TRIPLET & PENTAD) ELEMENT EQUATIONS

	OXIDIZER	FUEL
Diffusion Characteristics:	Axi-Symmetric	Axi -Symmetric
Hydraulic Diameter:	$D_{Ho} = \left[\frac{4\ C_{d\ cup}\ A_{cup}}{\pi}\right]^{1/2}$	$D_{Hf} = \left[\frac{4\ C_{d\ cup}\ A_{cup}}{\pi}\right]^{1/2}$

COLD FLOW

$Da_o = 0.0$	$Da_f = 0.0$
$F_o = 0.1$	$F_f = 0.1$

HOT FIRE

$Da_o = f\ (O/F)_j$	$Da_f = f\ (O/F)_i$
$F_o = 0.0$	$F_f = 0.0$

$$\Delta P_{cup} = \frac{1}{2}\left[(P_{oj} - P_c - Pd_o) + (P_{fj} - P_c - Pd_f)\right]$$

$$\eta_{pj} = \exp\left[-3.5\ Pd_o/(Pd_o + \Delta P_{cup})\right]$$

$$\eta_{pi} = 1.0 - \left[\frac{P_{df}}{(Pd_f + \Delta P_{cup})}\right]^{0.7}$$

$$Ba_o = \frac{(L/D_{Ho})\left[\frac{4\ (O/F)}{MW_o/MW_f}\right]^{.45}\left[\frac{Pd_o + \Delta P_{cup}}{Pd_o}\right]^{.65}}{\left[C_{do}\ (1 + Da_o)\right]^{.625}\left[\frac{Re_{do}}{10^5}\right]^{.25}\left[\frac{Pd_o}{Pd_{eq}}\right]^{F_o}}$$

If η_j @ f$\left[Ba_o\right] < \eta_{pj}$, $\eta_j = \eta_{pj}$

TABLE VIII (cont.)

PREMIX (TRIPLET & PENTAD) ELEMENT EQUATIONS

$$Ba_f = \frac{(L/D_{Hf}) \left[\frac{Pd_f + \Delta P_{cup}}{Pd_f} \right]^{.65}}{\left[\frac{4\ (O/F)}{MW_o/MW_f} \right]^{.13} \left[C_{df}\ (1 + Da_f) \right]^{.625} \left[\frac{Re_{df}}{10^5} \right]^{.25} \left[\frac{Pd_f}{Pd_{eq}} \right]^{F_f}}$$

$$\text{If } \eta_i \text{ @ f } [\ Ba_f\ ] < \eta_{pi}, \quad \eta_i = \eta_{pi}$$

NOTES:

1. If $\left[\frac{4\ (O/F)}{MW_o/MW_f} \right]$ is not > 0.5 and < 2.0 in Ba_o and Ba_f Equations, use mole fraction correction factor in Figure 15 to evaluate

$$\left[\frac{4\ (O/F)}{MW_o/MW_f} \right]$$

TABLE IX

EXTERNAL IMPINGING TRIPLET ELEMENT EQUATIONS

	OXIDIZER	FUEL
Diffusion Characteristics:	Two-Dimensional	Two-Dimensional
Hydraulic Diameter:	$D_{Ho} = \left[\frac{4\ A_o}{\pi}\right]^{1/2}$	$D_{Hf} = \left[\frac{2\ A_f}{\pi}\right]^{1/2}$

COLD FLOW

$Da_o = 0.0$ $\qquad$ $Da_f = 0.0$

$F_o = 0.1$ $\qquad$ $F_f = 0.1$

$$\frac{Y}{D_o} = 0.62 \left(\frac{D_{Hf}}{D_{Ho}}\right) \sin \alpha_f \left[\frac{Pd_f}{Pd_o}\right]^{0.1}$$

HOT FIRE

$Da_o = f\ (O/F)_j$ $\qquad$ $Da_f = f\ (O/F)_i$

$F_o = 0.0$ $\qquad$ $F_f = 0.0$

$$\frac{Y}{D_o} = \frac{0.62}{\sqrt{1 + Da_o}} \left(\frac{D_{Hf}}{D_{Ho}}\right) \sin \alpha_f \left[\frac{Pd_f}{Pd_o}\right]^{0.5}$$

$$\phi = \sin^{-1} \left[\frac{\frac{V_f \tan \alpha_f}{V_o}}{\frac{V_f}{V_o} + \frac{O/F}{\cos \alpha_f}}\right]$$

$Om = 0.0$ if $D_{Hf} > D_{Ho}$

$$Om = \frac{\beta - \sin \beta}{\pi} \quad \text{if } D_{Hf} \leq D_{Ho}$$

where $\beta = \pi - 2 \sin^{-1} (D_{Hf}/D_{Ho})$

$$\eta_{H10} = \exp \left[- Om \ (6.0 - 2.0 \ln_e \left[\frac{4\ (O/F)}{MW_o/MW_f}\right])\right]$$

EXTERNAL IMPINGING TRIPLET ELEMENT EQUATIONS

OXIDIZER **FUEL**

If $\frac{Y}{D_o} < 0.5$

$$\eta_{H14} = [1 - Om]^{1.5} \exp\left[-(1 - 2\frac{Y}{D_o})(5.2 - 1.44 \ln_e\left[\frac{4\ (O/F)}{MW_o/MW_f}\right])\right]$$

If $\eta_{H14} < \eta_{H10}$ $\eta_{H1} = \eta_{H14}$

If $\eta_{H14} \geq \eta_{H10}$ $\eta_{H1} = \eta_{H10}$

$$\eta_{H2} = 2\frac{Y}{D_o}(1 - Om)$$

$$(L/D)_o^* = Re_{do}^{.111}\left[\frac{\pi C_{do}(1 + Da_o)}{6 \tan \phi}\right]^{.555} \qquad (L/D)_f^* = Re_{df}^{.111}\left[\frac{\pi C_{df}(1 + Da_f)}{6 \cos \alpha_f \tan \phi}\right]$$

$$Bt_o = \frac{(L/D_{Ho})\left[\frac{4\ (O/F)}{MW_o/MW_f}\right]^{.66}\left[\frac{4}{\pi}(L/D)_f^* \tan \phi\right]^{1.25} \exp(3.5\eta_{H1})}{\left[C_{do}(1 + Da_o)\right]^{1.25}\left[\frac{Re_{dc}}{10^5}\right]^{.25}\left[\frac{Pd_o}{Pd_{eq}}\right]^{F_o}}$$

If η_j @ f [B_{to}] $< \eta_{H1}$, $\eta_j = \eta_{H1}$

$$Bt_f = \frac{(L/D_{Hf})\left[\frac{4}{\pi}(L/D)_f^* \cos \alpha_f \tan \phi\right]^{1.25} \exp(1.7\eta_{H2})}{\left[.8 + .2\left(\frac{4\ (O/F)}{MW_o/MW_f}\right)\right]\left[C_{df}(1 + Da_f)\right]^{1.25}\left[\frac{Re_{df}}{10^5}\right]^{.25}\left[\frac{Pd_f}{Pd_{eq}}\right]^{F_f}}$$

If η_i @ f [B_{tf}] $< \eta_{H2}$, $\eta_i = \eta_{H2}$

TABLE IX (cont.)

EXTERNAL IMPINGING TRIPLET ELEMENT EQUATIONS

OXIDIZER

FUEL

If $\frac{Y}{D_o} \geq 0.5$

$$\eta_{H16} = \frac{1}{\left(2\frac{Y}{D_o}\right)(1 - Om)}$$

If $\eta_{H16} < \eta_{H10}$ $\eta_{H1} = \eta_{H16}$

If $\eta_{H16} \geq \eta_{H10}$ $\eta_{H1} = \eta_{H10}$

$$\eta_{H2} = (1 - Om)\left\{1.0 - .25\left(\frac{4\ (O/F)}{MW_o/MW_f}\right) \ln_e\left[2\ \frac{Y}{Do}\right]\right\}$$

$$(L/D)_o^* = Re_{Do}^{.111}\left[\frac{\pi C_{do}\ (1 + Da_o)}{12 \tan \phi}\right]^{.555} \qquad (L/D)_f^* = Re_{df}^{.111}\left[\frac{\pi C_{df}\ (1 + Da_f)}{3 \cos \alpha \tan \phi}\right]^{.555}$$

$$B_{to} = \frac{(L/D_{Ho})\left[\frac{4\ (O/F)}{MW_o/MW_f}\right]^{.66}\left[\frac{8}{\pi}\ (L/D)_o^* \tan \phi\right]^{1.25} \exp\ (3.5\ \eta_{H1})}{\left[C_{do}\ (1 + Da_o)\right]^{1.25}\left[\frac{Re_{Do}}{10^5}\right]^{.25}\left[\frac{P_{Do}}{Pd_{eq}}\right]^{F_o}}$$

If $\eta_j @ f\ [B_{to}] < \eta_{H1}$ $\eta_j = \eta_{H1}$

$$B_{tf} = \frac{(L/D_{Hf})\left[\frac{2}{\pi}\ (L/D)_f^* \cos \alpha_f \tan\phi\right]^{1.25} \exp\ (1.7\ \eta_{H2})}{\left[.8 + .2\left(\frac{4\ (O/F)}{MW_o/MW_f}\right)\right]\left[C_{df}\ (1 + Da_f)\right]^{1.25}\left[\frac{Re_{df}}{10^5}\right]^{.25}\left[\frac{Pd_f}{Pd_{eq}}\right]^{F_f}}$$

If $\eta_i @ f\ [B_{tf}] < \eta_{H2}$ $\eta_i = \eta_{H2}$

NOTES:

1. If $\left[\frac{4\ (O/F)}{MW_o/MW_f}\right]$ is not > 0.5 and < 2.0 in B_{to} and B_{tf} Equations, use mole fraction correction factor in Figure 15 to evaluate $\left[\frac{4\ (O/F)}{MW_o/MW_f}\right]$

2. If design L/D $<$ (L/D)* calculated in above equation, use design L/D instead of (L/D)* in B_{to} and B_{tf} equations.

TABLE X

GENERALIZED PERFORMANCE EQUATIONS

$$\eta_j = f \quad [B_{ao} \quad \text{or} \quad B_{to}]$$

$$\eta_i = f \quad [B_{af} \quad \text{or} \quad B_{tf}]$$

$$(O/F)_j = (O/F)/\eta_j$$

$$(O/F)_i = \eta_i \cdot (O/F)$$

$$U = \eta_j \frac{(1 - \eta_i)}{(1 - \eta_j)}$$

$$X_j = \left[\frac{U}{1 + U}\right] \left[\frac{1 + (O/F)_j}{1 + (O/F)}\right]$$

$$X_i = 1 - X_j$$

$$E_m = 100 \left\{1 - X_j \left[\frac{(O/F)_j - (O/F)}{1 + (O/F)_j}\right] - X_i \left[\frac{(O/F) - (O/F)_i}{(O/F)\,[1 + (O/F)_i]}\right]\right\}$$

$$\eta_m = 100 \left[X_j \cdot \eta_j + X_i \cdot \eta_i\right]$$

$$\%C^* = \frac{X_j \cdot C^*\,(O/F)_j + X_i \cdot C^*\,(O/F)_i}{C^*\,(O/F)}$$

$$\%ERE = \frac{X_j \cdot I_{sp}\,(O/F)_j + X_i \cdot I_{sp}\,(O/F)_i}{I_{sp}\,(O/F)}$$

TABLE XI

GENERALIZED CHAMBER HEAT FLUX EQUATIONS

Stream Tube	Nominal	Oxid.-Rich	Fuel-Rich
Mixture Ratio	(O/F)	$(O/F)_j$	$(O/F)_i$
Gas Temperature	T_{gas}	T_{gas_j}	T_{gas_i}
Specific Heat, C_p	C_p	C_{pj}	C_{pi}
Viscosity, μ	μ	μ_j	μ_i
Film Coefficient	h_g	h_{gj}	h_{gi}
Thermal Conductivity, k	k	k_j	k_i
Heat Flux	ϕ	ϕ_j	ϕ_i

$$Pr = \frac{C_p \mu}{k}$$

$$T_{gas} = f\,[O/F]$$

$$\phi = \frac{.026}{D_c^{0.2}} \frac{\mu^{0.2} C_p}{Pr^{0.6}} \left(\frac{\dot{W}_t}{A_c}\right)^{0.8} (T_{gas} - T_w)$$

IV. SYMBOLS AND ABBREVIATIONS

A	=	injector element area
B	=	non-dimensional mixing parameter
a,b,c,d	=	rectangular orifice dimension
C	=	specific heat coefficient
CR	=	contraction ratio
C*	=	characteristic velocity
D	=	diameter
Da	=	combustion influence parameter
d	=	differential
E	=	element, efficiency
ERE	=	energy release (combustion) efficiency
F	=	thrust, interaction exponent
g	=	gravitational constant
H	=	hydrogen
I	=	impulse
JANNAF	=	Joint Army NASA Navy Air Force
K	=	empirical factor
k	=	thermal conductivity
L_{cold}	=	equivalent cold flow length
L_{comb}	=	combustion chamber length
ln	=	natural logarithm
N	=	number of elements
O	=	oxygen
ODE	=	one-dimensional equilibrium
Om	=	oxidizer misimpingement fraction
O/F	=	oxidizer to fuel mixture ratio
MW	=	molecular weight
P	=	pressure
Pd	=	dynamic pressure
Pr	=	Prandtl number
R	=	gas constant
Re	=	Reynolds number
T	=	temperature
t	=	wall thickness

U	=	non-dimensional parameter
V	=	injection velocity
W	=	premix slot width (see Table I)
$\dot{W}$	=	flow rate
WP	=	wetted perimeter
X	=	length from throat, mass fraction
Y	=	penetration
α	=	impingement half angle
β	=	non-dimensional parameter
γ	=	ratio of specific heats
Δ	=	differential
ε	=	nozzle exit area ratio
η	=	mixing ratio
μ	=	viscosity
ϕ	=	heat flux, spray fan propagation angle
π	=	3.1416
ρ	=	density

Subscripts

a	=	axial, axisymmetric chamber, coaxial
comb	=	combustion
cup	=	mixing cup
d	=	discharge, diameter, delivered
e	=	exit
est	=	estimated
eq	=	equivalent (see Table I, Comments column), equivalent dynamic pressure
f	=	fuel
H	=	hydraulic
h	=	head end
i	=	refers to fuel-rich streamtube
J	=	injector
j	=	refers to oxidizer-rich streamtube

Symbols and Abbreviations (cont.)

m	=	mixing
nom	=	nominal
p	=	at constant pressure, propellant, premix
w	=	wall
o	=	oxidizer
ode	=	one-dimensional equilibrium
s	=	swirler
sp	=	specific
T	=	total, triplet
t	=	tangential, two-dimensional, thrust
theo	=	theoretical
vac	=	vacuum
x	=	length

REFERENCES

1. Calhoon, D. F., Ito, J. I., Kors, D. L., Investigation of Gaseous Propellant Combustion and Associated Injector/Chamber Design Guidelines, NASA CR-121234, NAS 3-14379, Aerojet Liquid Rocket Company, Sacramento, California, June 1973.

2. Gordon, S., and McBride, B. J., Computer Program for Calculation of Complex Chemical Equilibrium Compositions, Rocket Performance, Incident and Reflected Shocks, and Chapman-Jouguet Detonations, NASA SP-273, NASA Lewis Research Center, 1971.

3. Pieper, J. L., "ICRPG Liquid Propellant Thrust Chamber Performance Evaluation Manual," Report 178, Sept. 1968, Chemical Propulsion Information Agency.

4. Keenan, J. H., and Kaye, J., Gas Tables - Thermodynamic Properties of Air Products of Combustion and Component Gases Compressible Flow Functions, John Wiley & Sons, Inc., 1948.

5. Priem, R. J., and Yang, J. S., A Technique for Predicting High Frequency Stability Characteristics of Gaseous Propellant Combustors, (NASA Lewis Research Center report to be published).

6. Svehla, R. A., and McBride, B. J., Fortran IV Computer Program for Calculation of Thermodynamic and Transport Properties of Complex Chemical Systems, NASA-TN D-7056, January 1973.